Transactions of the ASME®

Journal of Turbomachinery

Published Quarterly by The American Society of Mechanical Engineers

VOLUME 115 • NUMBER 3 • JULY 1993

Transactions of the ASME, Journal of Turbomachinery (ISSN 0889-504X) is published quarterly (Jan., Apr., July, Oct.) for $130.00 per year by The American Society of Mechanical Engineers, 345 East 47th Street, New York, NY 10017. Second class postage paid at New York, NY and additional mailing offices. POSTMASTER: Send address change to Transactions of the ASME, Journal of Turbomachinery, c/o THE AMERICAN SOCIETY OF MECHANICAL ENGINEERS, 22 Law Drive, Box 2300, Fairfield, NJ 07007-2300.
CHANGES OF ADDRESS must be received at Society headquarters seven weeks before they are to be effective. Please send old label and new address.
PRICES: To members, $40.00, annually; to nonmembers, $130.00.
Add $24.00 for postage to countries outside the United States and Canada.
STATEMENT from By-Laws. The Society shall not be responsible for statements or opinions advanced in papers or . . . printed in its publications (B7.1, Par. 3).

INDEXED by Applied Mechanics Reviews and Engineering Information, Inc.
Canadian Goods & Services Tax Registration #126148048

TECHNICAL PAPERS

(Contents Continued)

ANNOUNCEMENTS

M. L. Shelton

B. A. Gregory

Turbine Aero and Cooling Technology,
General Electric Aircraft Engines,
Cincinnati, OH 45208

R. L. Doughty

T. Kiss

H. L. Moses

Mechanical Engineering Department,
Virginia Polytechnic Institute
and State University,
Blacksburg, VA 24061

A Statistical Approach to the Experimental Evaluation of Transonic Turbine Airfoils in a Linear Cascade

In aircraft engine design (and in other applications), small improvements in turbine efficiency may be significant. Since analytical tools for predicting transonic turbine losses are still being developed, experimental efforts are required to evaluate various designs, calibrate design methods, and validate CFD analysis tools. However, these experimental efforts must be very accurate to measure the performance differences to the levels required by the highly competitive aircraft engine market. Due to the sensitivity of transonic and supersonic flow fields, it is often difficult to obtain the desired level of accuracy. In this paper, a statistical approach is applied to the experimental evaluation of transonic turbine airfoils in the VPI & SU transonic cascade facility in order to quantify the differences between three different transonic turbine airfoils. This study determines whether the measured performance differences between the three different airfoils are statistically significant. This study also assesses the degree of confidence in the transonic cascade testing process at VPI & SU.

Introduction

Aircraft engine high-pressure turbines must operate at very high inlet temperatures and high aerodynamic loading and still provide a high level of efficiency. The resulting turbine airfoils often have high turning angles and supersonic relative exit Mach numbers. Due to cooling and mechanical requirements, large wedge angles and thick trailing edges are usually required. In this environment, typical turbine efficiency loss mechanisms, such as profile loss, trailing edge blockage, secondary flows, and coolant mixing losses, become more severe. In addition, shock structures are formed creating another loss mechanism.

In order to improve efficiency levels in aircraft engine turbines, methods of investigating the various loss mechanisms are required. However, rotating rig tests are prohibitively expensive and analytical methods for cooled, transonic turbines are still being developed. Linear cascade testing offers an economical method of investigating transonic turbine loss mechanisms that are two dimensional in nature, including investigating trailing edge shock phenomena, evaluating various airfoil designs, evaluating coolant ejection effects, and providing test data for validation of analytical tools.

However, experimental variation in linear cascades can increase to significant levels for transonic and supersonic exit Mach numbers. Defining "significant" is somewhat subjective, but most turbine aerodynamic designers would probably agree that ± 0.5 points in efficiency is a "significant" level of variation for experimentally evaluating turbine airfoil designs. There have been indications in the literature that "significant" levels of variation in transonic turbine cascade testing are typical. Mee et al. (1992) showed analytical predictions of a high level of uncertainty supported to some degree by test data. Also, Kiock et al. (1986) showed significant variation in loss measurements for exit Mach numbers greater than 0.92. Similarly, significant levels of variation have been observed in cascade testing at VPI & SU. If the levels of variation are significant at the exit Mach number of interest, single-sample experiments may lead to misleading conclusions.

The objective of this investigation is to evaluate three airfoil designs at a subsonic exit Mach number and at a supersonic exit Mach number using multiple samples and simple statistical methods. The intent of the airfoil designs is to reduce the downstream shock strength and improve the airfoil's efficiency. A matrix of 216 test points, 108 at subsonic Mach numbers and 108 at supersonic Mach numbers, was designed to evaluate the airfoils. Statistical methods used to interpret the test data include linear regression, analysis of variance, and the Duncan significance test. In addition to evaluating the airfoils, quantitative estimates for uncertainty in loss measurements, uncertainty in downstream static pressure measurements, and uncertainty in setting a desired exit Mach number were obtained for the VPI & SU transonic wind tunnel.

Description of Facility

The VPI & SU transonic wind tunnel is a cold-air, blowdown

Contributed by the International Gas Turbine Institute and presented at the 37th International Gas Turbine and Aeroengine Congress and Exposition, Cologne, Germany, June 1-4, 1992. Manuscript received by the International Gas Turbine Institute January 13, 1992. Paper No. 92-GT-5. Associate Technical Editor: L. S. Langston.

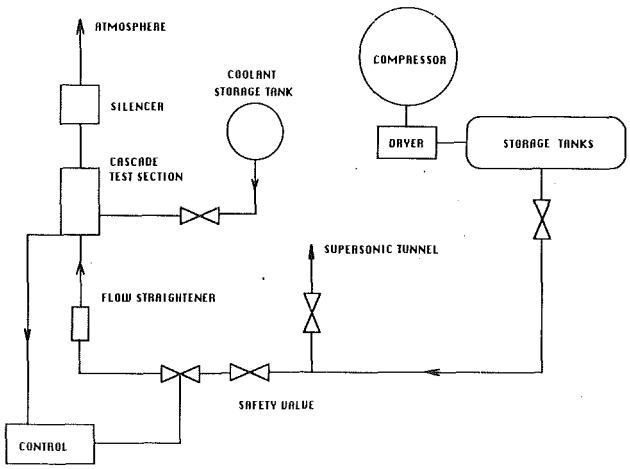

Fig. 1 Block diagram of VPI & SU transonic cascade test facility

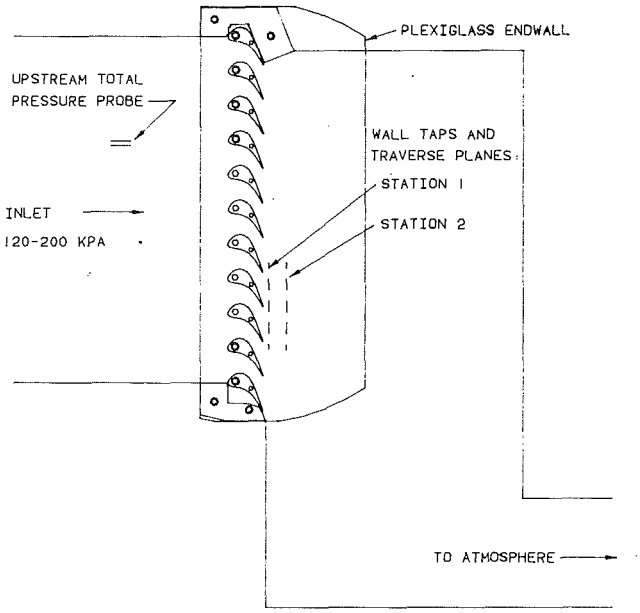

Fig. 2 Sketch of cascade test section for VPI & SU transonic wind tunnel

type fed by two storage tanks. The tanks are charged by a four-stage reciprocating compressor and the air is passed through a dryer before entering the tanks. A schematic of the facility is shown in Fig. 1. Air flow to the tunnel is controlled by a computer-operated, feedback-controlled, pneumatic valve, which sets the cascade upstream total pressure. The computer software requires calibration constants, which are determined experimentally for each desired Mach number setting. The facility also includes a storage tank for coolant simulation. Typically, CO_2 is used for the coolant simulation in order to obtain the appropriate coolant-to-gas density ratio.

For this investigation, the test section consists of eleven aluminum or stainless steel airfoils mounted on 1/2 in. plexiglass endwalls. The plexiglass endwalls are supported by 1/2 in. aluminum walls and steel angle iron. A window in the aluminum wall permits shadowgraphs or Schlieren photographs to be taken. Figure 2 shows the test section, the static pressure tap locations, and the traverse planes. The airfoils for this test have a chord of 49.45 mm, an axial chord of 38.10 mm, and a spacing of 37.26 mm. The height of the cascade is 152.4 mm, giving an aspect ratio of 4 based on axial chord. The tolerance on the airfoil pitch is ± 0.05 mm and the tolerance on the airfoil contour is also ± 0.05 mm. Station 1 is located at 1.167 axial chord from the airfoil leading edge and station 2 is located at 1.667 axial chord. For this investigation, ΔP_T traverses and wall static pressure measurements were taken only for station 1. The ΔP_T traverse is made with a single traverse probe driven by a stepper motor. The traverse probe is insensitive to the expected angle changes. An upstream total pressure probe in a low Mach number region is used to represent P_{T1}. No tailboard is used since previous studies show the free shear layer gives the best periodicity in this facility. An indication of the periodicity is shown in Figs. 3(*a*) and 3(*b*) where typical downstream ΔP_T traverse and wall static pressure measurements are given.

Figure 3(*a*) also shows an upstream total pressure measurement over a typical 18 second run time. P_{T1} remains very constant over the 18 second run time indicating the pneumatic valve control system works very well. However, there is still some variation in setting the desired Mach number. One of the objectives of this test was to quantify the uncertainty in setting the cascade isentropic Mach number, M_{2ISEN}. The capability of setting M_{2ISEN} is important in order to obtain a complete set of data from the wind tunnel. A complete set of data includes the downstream total pressure distribution, the downstream static pressure distribution, airfoil surface static pressures, and a shadowgraph. Typically, this requires three runs, one for the downstream static and total pressures, one for the airfoil surface static pressures, and one for an unobstructed shadowgraph. Ideally, all three runs are at the same M_{2ISEN}, but in reality, there will always be some variation in M_{2ISEN}.

Two separate data acquisition systems are used during a run. One system uses an electronic pressure scanner (by Pressure Systems, Inc.) to measure endwall static pressures. This system has an automated calibration system. Five sets of static pressure data are taken during a run to provide a static pressure history for the run. The other data acquisition system records ΔP_T and P_{T1} at a frequency of 40 Hz over two blade spacings during

Nomenclature

L = loss coefficient
M = Mach number
P = pressure
Pr_s = maximum to minimum static pressure ratio at airfoil exit traverse plane
R = gas constant
s = blade pitch
T = temperature
t = time
u = velocity
x = horizontal (axial) direction
y = vertical (pitchwise) direction
γ = ratio of specific heats
ΔP_T = difference between airfoil upstream total pressure and downstream total pressure = $P_{T1} - P_{T2}$
ρ = density

Subscripts

1 = upstream blade inlet
2 = downstream of blade
AVG = indicates an average value
ISEN = indicates value calculated with isentropic assumption
S = static conditions
T = stagnation or "total" conditions
x = upstream of shock
y = downstream of shock

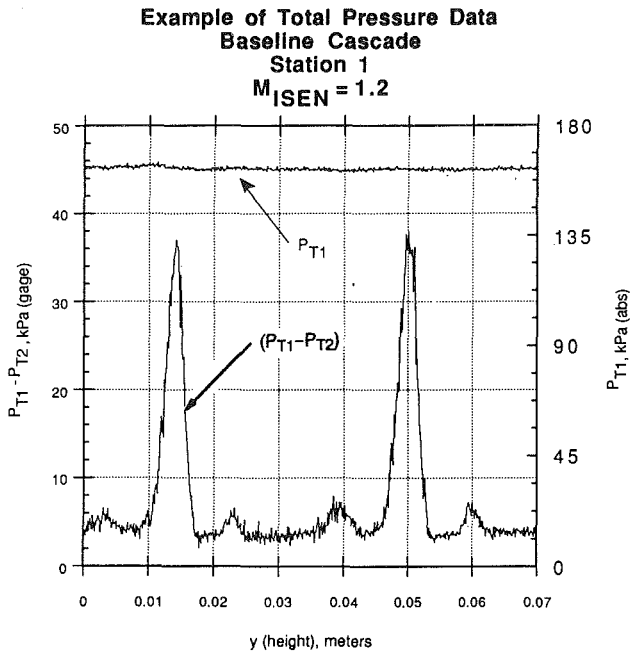

Fig. 3(*a*)

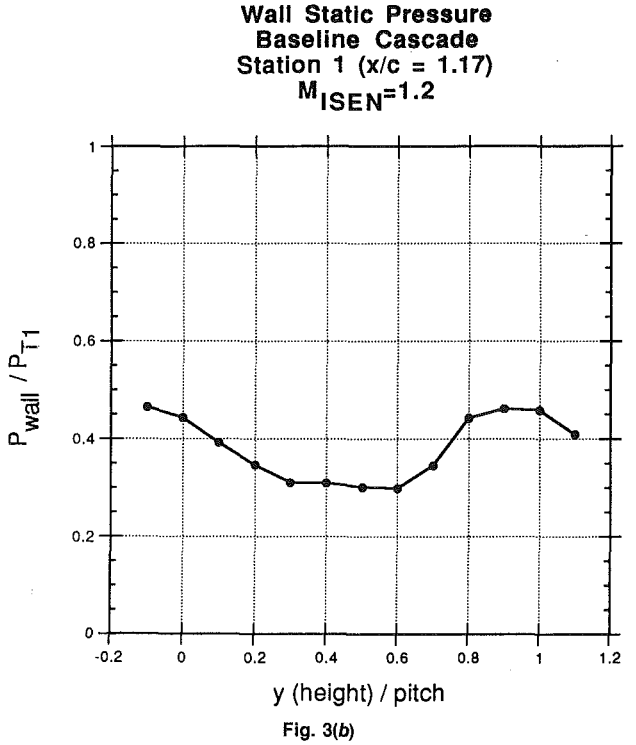

Fig. 3(*b*)

Fig. 3 Examples of upstream total, downstream total, and downstream static pressure distributions for a typical 18 second run

the 18 second run time. This system is calibrated with a free weight system before each day's testing.

Data Reduction

An isentropic Mach number, M_{2ISEN}, is defined to identify the cascade pressure ratio for a given run. The wall static pressures are arithmetically averaged over space to get P_{S2AVG}. Then, $M_{2ISEN}(t)$ is calculated at each point in time from the isentropic relationship

$$M_{2ISEN}(t)=\sqrt{\frac{2}{(\gamma-1)}\left[\left(\frac{P_{T1}(t)}{P_{S2AVG(t)}}\right)^{(\gamma-1)/\gamma}-1\right]} \quad (1)$$

$M_{2ISEN}(t)$ is then averaged over time to give M_{2ISEN}. For the downstream total pressure in supersonic flow, a bow shock is assumed to exist upstream of the probe. The normal shock relation

$$\frac{P_{T,y}}{P_{T,x}}=\left[\frac{\left(\frac{\gamma+1}{2}\right)M_x^2}{1+\left(\frac{\gamma-1}{2}\right)M_x^2}\right]^{\gamma/(\gamma-1)}\left[\frac{1}{\left(\frac{2\gamma}{\gamma+1}\right)M_x^2-\left(\frac{\gamma-1}{\gamma+1}\right)}\right]^{1/(\gamma-1)} \quad (2)$$

and the isentropic relation

$$\frac{P_{T,x}}{P_{S,x}}=\left[1+\left(\frac{\gamma-1}{2}\right)M_x^2\right]^{\gamma/(\gamma-1)} \quad (3)$$

are solved simultaneously for $P_{T,x}$ and M_x. In order to solve Eqs. (2) and (3), the following assumption is made for $P_{S,x}$:

$$P_{S,x}=P_{S2AVG}. \quad (4)$$

The loss coefficient, L, is defined as the mass-weighted average of $\Delta P_T/P_{T1}$. The following procedure is used to calculate L. For each of the 800 values of ΔP_T, the quantities $T_{S,x}$, ρ_x, and u_x are determined. $T_{S,x}$ is calculated from the adiabatic relation

$$\frac{T_{T,x}}{T_{S,x}}=\left[1+\left(\frac{\gamma-1}{2}\right)M_x^2\right]. \quad (5)$$

From the ideal gas law, ρ_x is

$$\rho_x=\frac{P_{S,x}}{RT_{S,x}}. \quad (6)$$

Finally, u_x is calculated from the definition of Mach number

$$u_x=M_x\sqrt{\gamma RT_{S,x}}. \quad (7)$$

Then, L for a single blade spacing is calculated as

$$L=\frac{\int_0^S \rho u\left(\frac{\Delta P_T}{P_{T1}}\right)dy}{\int_0^S \rho u dy}\times 100\ (L \text{ in percent}). \quad (8)$$

The L values presented later are the average of the loss calculated for two adjacent blade pitches.

Description of Experiment

Airfoils. The airfoil shapes that were tested are shown in Fig. 4. The ULTRE airfoil was originally designed with a thinner trailing edge than the baseline and LUT airfoils as indicated in Fig. 4. However, for this investigation, all of the airfoils had a 0.96 mm trailing edge thickness. The airfoils were designed with a 0 deg inlet angle to accommodate the wind tunnel. The design exit angle is approximately 67 deg at a M_{2ISEN} of 1.2. The "baseline" airfoil has a converging passage and is typical of present transonic airfoil designs. The "LUT" airfoil (Low Unguided Turning) has reduced unguided turning and a reduced wedge angle but still has a converging passage. The reduced unguided turning reduces the suction side Mach number at the trailing edge and the lower wedge angle reduces the angle between the suction side and pressure side streamlines at the trailing edge. The "ULTRE" airfoil (Unloaded Trailing Edge) has a slight converging-diverging passage to increase the pressure side Mach number and better match the suction side and pressure side static pressures at the trailing edge. The ULTRE also has about the same unguided turning as the LUT

but has a larger wedge angle due to the convex pressure side near the trailing edge used to create the *C–D* passage. A comparison of the Mach number distributions, based on an inviscid analysis, is shown in Fig. 5. The intent of both the LUT and ULTRE designs is to reduce the suction side shock strength and improve the airfoil's efficiency. The parameters of interest for this study are loss, L, and shock strength, which is indicated by the maximum to minimum downstream static pressure ratio, Pr_s, taken at the endwall.

Test Matrix. In order to limit the size of the test matrix, the experiment was designed around a single subsonic Mach number, $M_{2ISEN} = 0.82$, and a single supersonic Mach number, $M_{2ISEN} = 1.18$. Since there is some variation in the method of controlling the facility, it is difficult to set the desired M_{2ISEN} exactly. Therefore, the matrix of target Mach numbers was expanded to $M_{2ISEN} = 0.78, 0.82, 0.86, 1.14, 1.18$, and 1.22. This array of target Mach numbers permits interpolation to obtain values for L and Pr_s at the desired M_{2ISEN} of 0.82 and 1.18. Also, in order to assess the variation in the facility, each of the target Mach numbers was repeated three times in a randomized order.

The test described above was performed for each airfoil design four times for a total of twelve tests. Only one of these tests was run per day. The tests were performed in a randomized order. In the instances where the random sequence of tests called for running the same airfoil on back-to-back days, the entire cascade was still removed from the wind tunnel and then reinstalled on the next day. However, the cascades themselves were not disassembled due to time constraints (the positioning of the airfoils in the cascade represents another source of variation due to manufacturing and assembly tolerances of the airfoils). A total of 216 data points were taken, 108 at subsonic Mach numbers, and 108 at supersonic Mach numbers. A summary of the matrix is shown in Table 1.

Data Analysis. A linear regression of the loss coefficient, L, and the maximum-to-minimum downstream static pressure ratio, Pr_s, with M_{2ISEN} as the independent variable was per-

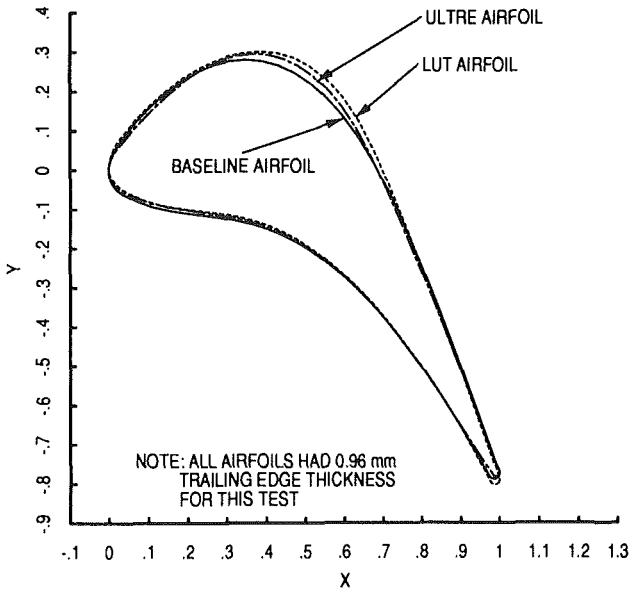

Fig. 4 Comparison of airfoil designs

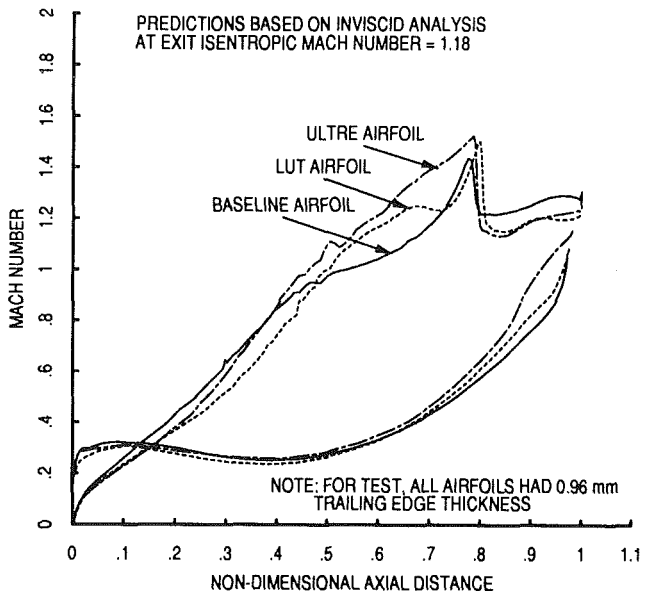

Fig. 5 Comparison of predicted airfoil Mach number distributions for $M_{2ISEN} = 1.18$

Table 1 Test matrix used for the investigation

		SUBSONIC TESTING		SUPERSONIC TESTING	
AIRFOIL	NUMBER OF REPLICATIONS PER AIRFOIL	TARGET M_{2ISEN}	NUMBER OF REPLICATIONS OF M_{2ISEN}	TARGET M_{2ISEN}	NUMBER OF REPLICATIONS OF M_{2ISEN}
BASELINE	4	0.78 0.82 0.86	3 3 3	1.14 1.18 1.22	3 3 3
LUT	4	0.78 0.82 0.86	3 3 3	1.14 1.18 1.22	3 3 3
ULTRE	4	0.78 0.82 0.86	3 3 3	1.14 1.18 1.22	3 3 3

THE REPLICATIONS FOR THE AIRFOIL TESTING WERE PERFORMED IN A RANDOMIZED SEQUENCE

FOR EACH AIRFOIL TESTING, THE REPLICATIONS OF M_{2ISEN} WERE PERFORMED IN A RANDOMIZED SEQUENCE AND WERE COMPLETED ON THE SAME DAY

formed for each airfoil for both the subsonic Mach number and the supersonic Mach number cases. A parabolic regression could have been used, but the narrow range of Mach numbers justified the convenience of using a linear regression. Also, for this experiment, the emphasis is on only $M_{2ISEN} = 0.82$ and $M_{2ISEN} = 1.18$. Prediction limits and confidence limits were also calculated for each airfoil for 95 percent confidence. The *prediction limits* define the uncertainty interval for the next *single* observation based on the data used in the regression. The *confidence limits* define the uncertainty interval for the *mean* line (or the next N observations), as calculated from the N observations used in the linear regression. Detailed explanations of the prediction limits and confidence limits are given by Ott (1988). The uncertainty for the facility is estimated by averaging the uncertainty for the three airfoils as determined by the regression analysis.

In order to compare the airfoils, the analysis of variance, ANOVA, is used to determine whether a significant difference exists. The ANOVA compares the variation *within* a subgroup of data to the variation *between* subgroups. Obviously, the differences between two subgroups must be greater than the variation within the subgroups for the subgroups to be significantly different. The ANOVA provides a mathematical method of evaluating these differences with a given level of confidence. If a significant difference exists, the Duncan method is used to determine which subgroups are significantly different. The Duncan test permits the investigator to determine mathematically the magnitude of the required difference (for a given level of confidence) between the means of the subgroups for the subgroups to be significantly different. There are several other tests similar to the Duncan test. However, the Duncan test is one of the least conservative and is more apt to show a difference between subgroups. For this reason, the Duncan test is frequently used by investigators expecting to observe differences. The ANOVA and Duncan tests were performed for $M_{2ISEN} = 0.82$ and $M_{2ISEN} = 1.18$ where L and Pr_s were calculated from the linear regression mean line. A detailed technical discussion of the ANOVA and the Duncan test is given by Ott (1988).

An estimate of the standard deviation in setting M_{2ISEN} is made from the variation in the measured M_{2ISEN}. It is assumed that the facility could be calibrated to set the fixed error between the mean measured M_{2ISEN} and the target M_{2ISEN} to zero for any desired setting. The uncertainty for the facility is estimated by averaging the uncertainty calculated for each airfoil.

Uncertainty Analysis

Ideally, before beginning any experimental effort, an uncertainty analysis would be performed to determine if the proposed apparatus had the capability of meeting the desired level of accuracy. In practice, analytically predicting the uncertainty can be difficult.

Kline and McClintock (1953) described methods of analytically estimating the uncertainty in experiments. Moffat (1981) elaborated further on this topic. Typically, the sources of error are classified as "fixed error" (or "bias") and random error. The random error is defined as "scatter" about some mean value, which can be approximated with a normal distribution. The fixed error is the difference between the measured result and an external reference, which could be a widely accepted baseline case or a case that can be deduced from conservation laws. Assuming all fixed errors have been accounted for and the experimental process is "zero-centered," the uncertainty for a result R as a function of the uncertainty in N independent variables, $x_1, x_2, \ldots, x_N$ can be calculated from

$$\delta R = \sqrt{\left(\frac{\partial R}{\partial x_1}\delta x_1\right)^2 + \left(\frac{\partial R}{\partial x_2}\delta x_2\right)^2 + \ldots + \left(\frac{\partial R}{\partial x_N}\delta x_N\right)^2} \quad (9)$$

The difficulty usually lies in quantifying the derivatives, $\partial R/\partial x_i$, and the variation in the independent variables, δx_i.

Moffat (1981) also describes three levels of replication, the Nth order, the first order, and the zeroth order. The Nth order includes variation between different researchers with physically different facilities and different instrumentation (even if the facilities and instrumentation are of the same type and by the same manufacturer). The first order includes variation due to changes in the instrument calibration, interpretation and interpolation of instrument readings, changes in atmospheric conditions, and other effects that vary in time. For the zeroth order of replication, in which the process is steady, there is no change in instrument readings, and the chief source of error is in the inaccuracies of the instrument readings.

For the purposes of evaluating the relative differences in the airfoils within the same facility, the errors on the Nth-order replication level do not have to be addressed. These include errors from the calibration methods, time response of the probes, geometric differences in the airfoils, flow exit angle variations, impact of probe on the flow field, etc. These errors are assumed to be the same for each cascade due to the relative similarity of the cascades. However, in validating analytical tools, it would be desirable to evaluate the magnitude of these errors.

The distinction between the first-order replication level and the zeroth-order replication level is somewhat difficult to define for a blowdown wind tunnel where, technically, all measurements are varying in time. For the purposes of this investigation, the zeroth-order replication level is defined as testing occurring within the same day, in fact, within a few hours for this experiment. First-order replication is defined as testing occurring on different days. Variation associated with the first-order replication level include the dismantling and assembly of the cascade into the wind tunnel test section, changes in atmospheric conditions, different tunnel operators, different sequences in starting and running the facility, etc. Unfortunately, these variations cannot be quantified analytically.

At the zeroth level of replication, however, there are variations that can be estimated. These include change in total temperature during a run (due to the pressure/temperature/volume effects in the storage tank), observed drifts in the calibration of transducers during a day, unsteadiness in the upstream total pressure, variation in downstream static pressure measurements, interpolations between the five sets of static pressure data taken during a run, etc. The resulting predictions for uncertainty to a 95 percent confidence level are

- Loss coefficient, ΔL, ± 0.1 (for L in percent)
- Isentropic exit Mach number, ΔM_{2ISEN}, ± 0.005
- Max to min exit static pressure ratio, ΔPr_s, ± 0.0003

In the uncertainty analysis, these variations are independent of Mach number. However, in practice, the uncertainty does vary with Mach number. This may be due to sources of variation at the zeroth level that cannot be quantified, including the warming up of the compressor, the warming up of electrical equipment, slight changes in ambient temperature and humidity, etc.

Discussion of Results

Uncertainty Results. The measured loss for the subsonic conditions for all three airfoils is shown in Fig. 6 with the prediction limits and in Fig. 7 with the confidence limits. Similarly, Pr_s is shown with the prediction limits in Fig. 8 and with the confidence limits in Fig. 9. A summary of the results is given in Table 2. The Duncan test indicates that the differences between the airfoils are statistically significant. Although, for the subsonic case, that the airfoils are "significantly" different is obvious from the graphic presentation of the results. In the subsonic regime, the actual un-

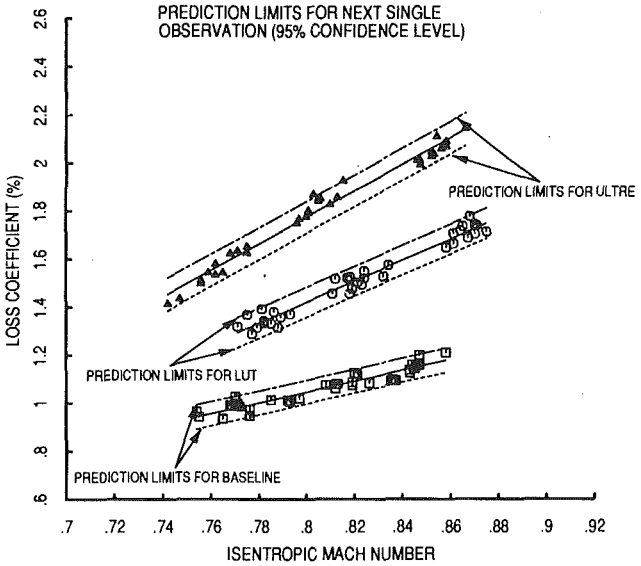

Fig. 6 Comparison of measured loss for subsonic exit Mach numbers with prediction limits for next single observation

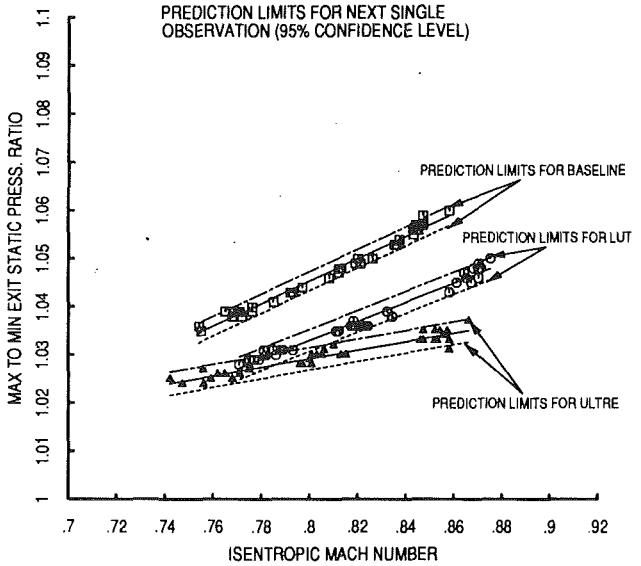

Fig. 8 Comparison of measured downstream static pressure variation for subsonic exit Mach numbers with prediction limits for next single observation

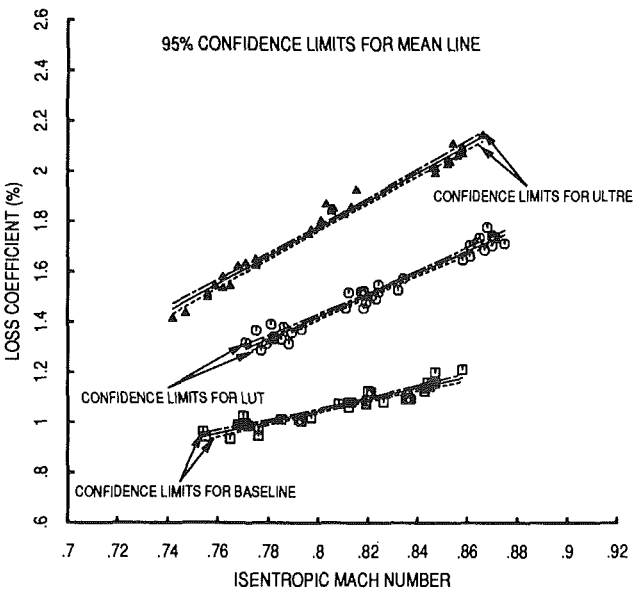

Fig. 7 Comparison of measured loss for subsonic exit Mach numbers with 95 percent confidence limits for mean line

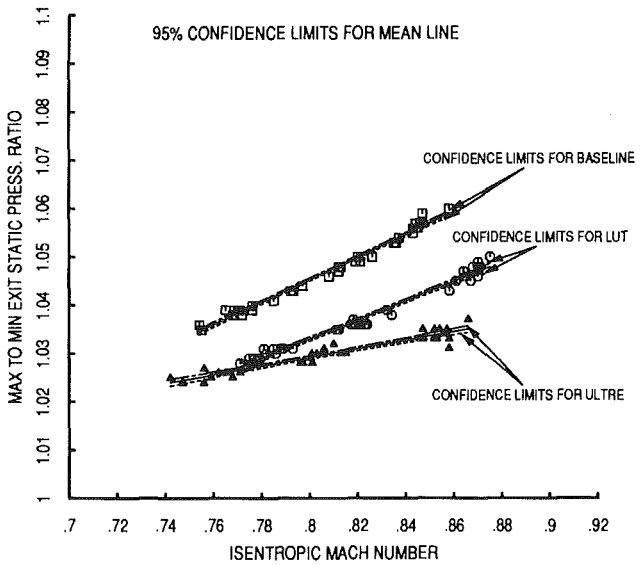

Fig. 9 Comparison of measured downstream static pressure variation for subsonic exit Mach numbers with 95 percent confidence limits for mean line

certainty for a single observation is estimated to be 0.059 in L and 0.002 in Pr_s. This compares very favorably with the predicted uncertainty of 0.1 for L and 0.003 for Pr_s. This indicates that the facility is very well controlled and reasonable conclusions could likely be drawn from single sample experiments.

However, the actual uncertainty in the supersonic regime is much higher than in the subsonic regime. The measured loss in the supersonic regime is shown in Fig. 10 with prediction limits and in Fig. 11 with confidence limits. Pr_s is shown in Fig. 12 with prediction limits and in Fig. 13 with confidence limits. A summary of the results is given in Table 3. The actual uncertainty for a single observation is estimated to be 0.44 for L and 0.021 for Pr_s. These estimates are almost an order of magnitude greater than the subsonic uncertainty estimates and the predicted uncertainty estimates. This indicates some unknown variable or variables are not being controlled.

The uncertainty for the supersonic testing is also indicated in the Duncan test for loss. The Duncan test for loss indicates the difference between the ULTRE and LUT is not significant at the 95 percent confidence level. For 90 percent confidence however, the ULTRE and LUT can be shown to be significantly different. The Duncan test for Pr_s indicates that the differences between the airfoils are statistically significant at the 95 percent confidence level.

With this uncertainty in the supersonic regime, it is not unlikely that a single-sample experiment would give misleading conclusions. Even with multisample tests, the conclusions from graphic results such as those in Fig. 10 are not obvious. Applying statistical tools permits the investigator to quantify the differences and uncertainties between subgroups objectively and to assign a numerical value to the level of confidence. The validity of the statistical tools is dependent on the assumed curve used for the regression and on how well the measured uncertainty is approximated by the probability function used

Table 2 Summary of results for M_{2ISEN} = 0.82

	RESULTS FOR LOSS - 95% CONFIDENCE				RESULTS FOR Pr_s - 95% CONFIDENCE			
AIRFOIL	MEAN L (%)	UNCERTAINTY FOR THIS TEST MATRIX	UNCERTAINTY FOR SINGLE OBSERVATION	DUNCAN TEST*	MEAN Pr_s	UNCERTAINTY FOR THIS TEST MATRIX	UNCERTAINTY FOR SINGLE OBSERVATION	DUNCAN TEST*
BASELINE	1.09	±0.0085 in L ± 0.8% of MEAN	±0.049 in L ±4.5% of MEAN	A	1.050	< 0.001 in Pr_s < 0.1% of MEAN	±0.002 in Pr_s ±0.2% of MEAN	A
LUT	1.51	±0.011 in L ±0.7% of MEAN	±0.062 in L ±4.1% of MEAN	B	1.037	< 0.001 in Pr_s < 0.1% of MEAN	±0.002 in Pr_s ±0.2% of MEAN	B
ULTRE	1.88	±0.012 in L ±0.6% of MEAN	±0.066 in L ±3.5% of MEAN	C	1.031	< 0.001 in Pr_s < 0.1% of MEAN	±0.002 in Pr_s ±0.2% of MEAN	C
AVERAGE OF ALL TESTS	1.49	±0.010 in L ±0.7% of MEAN	±0.059 in L ±4.0% of MEAN	—	1.039	< 0.001 in Pr_s < 0.1% of MEAN	±0.002 in Pr_s ±0.2% of MEAN	—

* DUNCAN TEST INDICATES SIGNIFICANT DIFFERENCE IF LETTERS ARE DIFFERENT

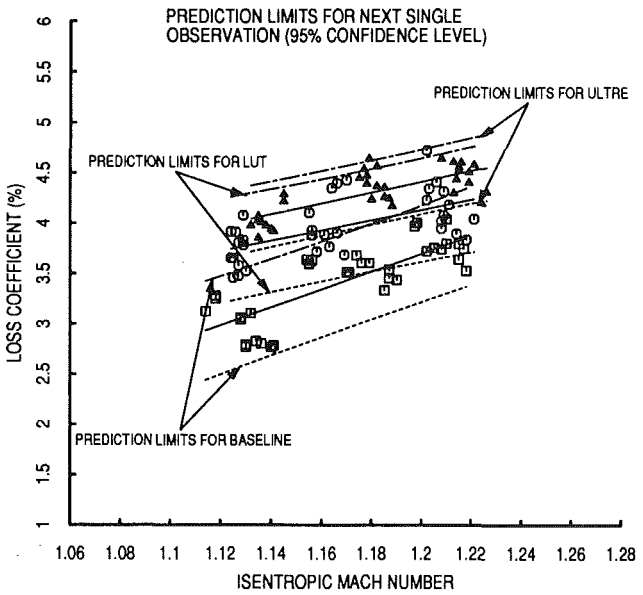

Fig. 10 Comparison of measured loss for supersonic exit Mach numbers with prediction limits for next single observation

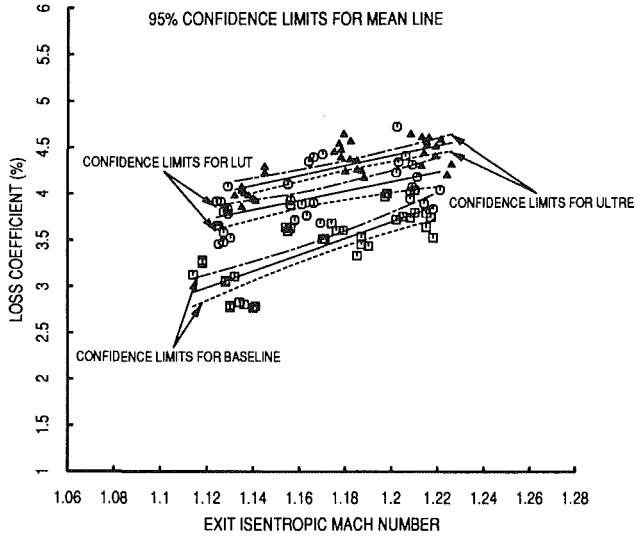

Fig. 11 Comparison of measured loss for supersonic exit Mach numbers with 95 percent confidence limits for mean line

in the statistical methods. The statistical methods used in this study are relatively simple from a statistician's viewpoint. However, as shown in this study, even simple statistical methods permit the investigator to evaluate the relatively small differences in various airfoil designs.

The large increase in uncertainties for L and Pr_s in the supersonic regime naturally leads to speculation and investigation into the source(s) of the variation. Unsteadiness in the flow field may be a source of variation. High-speed cinematography has indicated some unsteadiness in the shock structures. The impact of the traverse probe on the flow field may be another possible source of variation. The traverse probe is long and thin to minimize its effect on the flow field, but this geometry can lead to flutter problems when traversing through shocks and wakes. Condensation shocks may also be a source of variation if the dryer system is not working properly. However, this has not been established as of the writing of this paper. Statistical analyses of the test data from this investigation have not shown any consistent significant difference between day-to-day variation (i.e., first-order replication level) and same day variation (i.e., zeroth-order replication level). Mee et al. (1992) suggested that uncertainty may be a function of Reynolds number. This warrants investigation, but the facility as presently configured does not have the capability of setting the Mach number and Reynolds number independently. In the interim, the statistical approach as presented in this paper offers a method of quantifying the differences between different airfoils.

Table 4 shows the uncertainty in setting M_{2ISEN}. The uncertainty is based on the standard deviation of the measured values for M_{2ISEN}. It is assumed that the offset between the mean measured value and the target value could be calibrated to zero for any desired setting. The actual uncertainty is about 3 times higher than the predicted uncertainty for M_{2ISEN} over the entire range of Mach numbers. Since the predicted uncertainty is based on the known inaccuracies in the measurements, this implies the actual uncertainty in M_{2ISEN} is due to the repeatability of the control system of the tunnel.

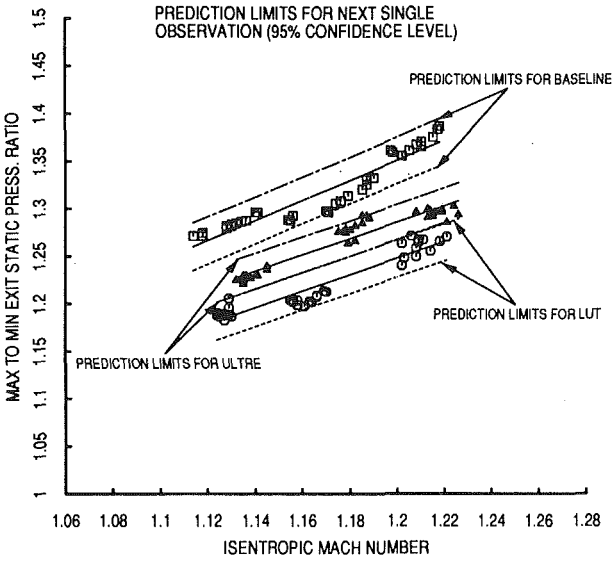

Fig. 12 Comparison of measured downstream static pressure variation for supersonic exit Mach numbers with prediction limits for next single observation

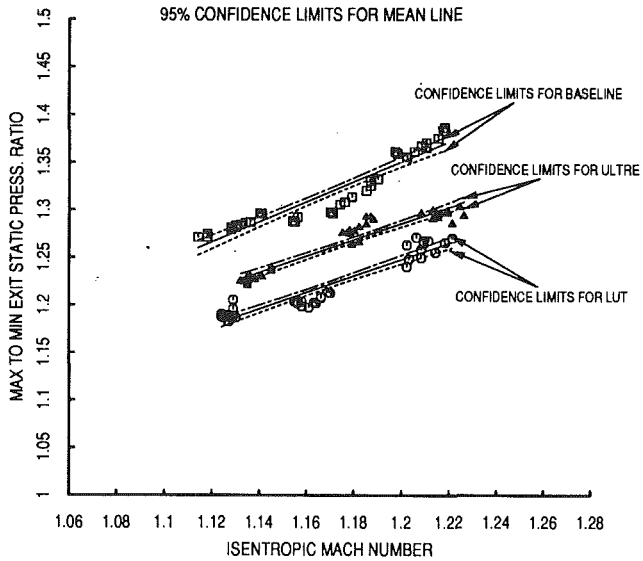

Fig. 13 Comparison of measured downstream static pressure variation for supersonic exit Mach numbers with 95 percent confidence limits for mean line

Table 3 Summary of results for $M_{2ISEN} = 1.18$

	RESULTS FOR LOSS - 95% CONFIDENCE				RESULTS FOR Pr_s - 95% CONFIDENCE			
AIRFOIL	MEAN L (%)	UNCERTAINTY FOR THIS TEST MATRIX	UNCERTAINTY FOR SINGLE OBSERVATION	DUNCAN TEST*	MEAN Pr_s	UNCERTAINTY FOR THIS TEST MATRIX	UNCERTAINTY FOR SINGLE OBSERVATION	DUNCAN TEST*
BASELINE	3.52	±0.080 in L ± 2.3% of MEAN	±0.48 in L ±13.6% of MEAN	A	1.330	±0.004 in Pr_s ± 0.3% of MEAN	±0.025 in Pr_s ±1.9% of MEAN	A
LUT	4.03	±0.096 in L ±2.4% of MEAN	±0.51 in L ±12.7% of MEAN	B**	1.231	±0.004 in Pr_s ±0.3% of MEAN	±0.020 in Pr_s ±1.6% of MEAN	B
ULTRE	4.31	±0.053 in L ±1.2% of MEAN	±0.32 in L ±7.4% of MEAN	B**	1.269	±0.003 in P_{rs} ±0.2% of MEAN	±0.019 in Pr_s ±1.5% of MEAN	C
AVERAGE OF ALL TESTS	3.95	±0.076 in L ±1.9% of MEAN	±0.44 in L ±11.1% of MEAN	—	1.277	±0.004 in P_{rs} ±0.3% of MEAN	±0.021 in Pr_s ±1.7% of MEAN	—

* DUNCAN TEST INDICATES SIGNIFICANT DIFFERENCE IF LETTERS ARE DIFFERENT
** DUNCAN TEST FOR 90% CONFIDENCE DID SHOW A SIGNIFICANT DIFFERENCE BETWEEN LUT AND ULTRE

Aerodynamic Results. The results presented in Figs. 11 and 13 and in Table 3 show the LUT and ULTRE designs achieved their objective to some degree by reducing the downstream shock strength. The ULTRE reduced the shock strength, (Pr_s − 1), by approximately 18 percent and the LUT airfoil reduced shock strength by approximately 30 percent. However, both the LUT and ULTRE designs increased the loss from the baseline airfoil. Supersonically, the LUT airfoil increased L by approximately 14.5 percent over the baseline and the ULTRE increased L by approximately 22.4 percent over the baseline. Subsonically, as shown in Table 2 and Fig. 7, the LUT airfoil increased L by 38.5 percent over the baseline and the ULTRE airfoil increased L by 72.5 percent over the baseline. While the LUT and ULTRE airfoil designs reduced the suction side shock strength, they have resulted in significant increases in loss from the baseline airfoil.

To understand the differences in the airfoil designs, first consider the geometric features and simple parameters that contribute to the trailing edge shock structure. The most obvious feature is the finite trailing edge thickness. The finite thickness trailing edge will lead to the classical overexpansion and subsequent recompression that creates the pressure side and suction side trailing edge shocks. But even with an infinitely thin trailing edge, the airfoil aerodynamics may still create a shock. Consider an infinitely thin plate with a supersonic suction side Mach number and a sonic pressure side Mach number at the trailing edge. Since there is a static pressure difference between the suction and pressure sides, one-dimensional compressible flow theory will predict a shock on the suction side at the trailing edge and an expansion around the pressure side at the trailing edge. Also, consider a converging-diverging turbine airfoil design where both the suction side and pressure side are supersonic at the trailing edge, the static pressure difference is equal to zero at the trailing edge, and there is zero trailing edge thickness. If there is any wedge angle at all, one-dimensional compressible flow theory will predict a suction side and pressure side trailing edge shock. Finally, in order to produce the lift to turn the flow, the suction side flow must

Table 4 Summary of capability of setting M_{2ISEN}

	RESULTS FOR M_{2ISEN} = 0.82				RESULTS FOR M_{2ISEN} = 1.18			
AIRFOIL	MEAN	STANDARD DEVIATION	UNCERTAINTY FOR 95% CONFIDENCE*	MEAN OFFSET*	MEAN	STANDARD DEVIATION	UNCERTAINTY FOR 95% CONFIDENCE*	MEAN OFFSET*
BASELINE	0.811	0.011	± 0.022	0.009	1.174	0.013	± 0.025	0.006
LUT	0.821	0.007	± 0.014	0.001	1.162	0.005	± 0.010	0.018
ULTRE	0.804	0.006	± 0.012	0.016	1.181	0.004	± 0.008	0.001
AVERAGE OF ALL TESTS	0.812	0.008	± 0.016	0.008	1.172	0.007	± 0.014	0.008

* UNCERTAINTY ASSUMES MEAN OFFSET COULD BE CALIBRATED TO ZERO FOR ANY ONE DESIRED SETTING

be accelerated to a lower static pressure than the cascade exit static pressure. Some sort of compression on the suction side is required to match the cascade exit static pressure, most likely in the form of a shock for supersonic flows. The geometric parameter typically used to indicate the suction side curvature downstream of the geometric throat is unguided turning, the difference between surface angle at the geometric throat and surface angle at the trailing edge. In summary, four parameters that have a significant influence on the trailing edge shock structure are the trailing edge thickness, the static pressure difference between the suction side and the pressure side, the wedge angle, and the unguided turning. All of these parameters must be considered when trying to control the trailing edge shock structure on a turbine airfoil.

With the above discussion in mind, compare the airfoil Mach number distributions shown in Fig. 5. With the lower unguided turning, the LUT and ULTRE airfoils have reduced the suction side Mach number from approximately 1.32 for the baseline to about 1.24. Since the exit isentropic Mach number is 1.18, the amount of compression required to match the exit pressure is less for the LUT and the ULTRE resulting in a reduction in the suction side shock strength from the baseline airfoil.

An example of the trade-offs in the parameters controlling the trailing edge shock structure is seen in the comparison of the LUT and the ULTRE airfoils. Both the LUT and the ULTRE have about the same unguided turning. As a result, both have about the same suction side Mach number at the trailing edge. For this investigation, both the LUT and the ULTRE have the same trailing edge thickness. The difference between the LUT and ULTRE airfoils is the ULTRE airfoil has a converging–diverging passage. The pressure side of the ULTRE airfoil becomes convex at about 90 percent axial chord as shown in Fig. 4. As a result, the pressure side isentropic Mach number on the ULTRE airfoil becomes sonic at about 90 percent axial chord. While the ULTRE design significantly reduces the static pressure difference between the pressure and suction sides at the trailing edge, the increased wedge angle of the ULTRE airfoil results in an increase in suction side shock strength relative to the LUT airfoil.

The lower unguided turning that resulted in reduced suction side shock strength also increases the airfoil loss. Once again, refer to the comparison of Mach number distributions in Fig. 5. By reducing the unguided turning, the aerodynamic loading on the aft side of the airfoil is reduced. The ULTRE and LUT designs compensate for the reduced aft loading by increasing the forward loading of the airfoil in order to produce the same lift. This results in a higher suction side peak Mach number for the LUT and the ULTRE airfoils as shown in Fig. 5. With the higher peak suction side Mach number and the lower trailing edge suction side Mach number, the suction side diffusion is much stronger on the LUT and ULTRE airfoils than the baseline airfoil. This stronger diffusion essentially manifests itself as a stronger pressure side trailing edge shock, which impinges on the suction side. The pressure side trailing edge shock is also closer to being normal to the flow on the LUT and ULTRE airfoils than on the baseline airfoil. In terms of airfoil loss, the benefit of reducing the trailing edge suction side shock strength was more than offset by the increase in the trailing edge pressure side shock strength. This is in agreement with Denton and Xu's (1990) conclusion that reduced suction side curvature downstream of the throat will increase the loss. Denton and Xu reached this conclusion with a simple control volume analysis without regard to the shock/boundary layer interaction. The losses due to the shock/boundary layer interaction will only increase for the LUT and ULTRE airfoils due to the stronger pressure side trailing edge shock impinging on the suction side.

For the off-design, subsonic case, the tendency for separation on the suction side will be stronger for the LUT and ULTRE airfoils than for the baseline airfoil because of the stronger suction side diffusion. With the converging–diverging passage of the ULTRE airfoil, separation on the pressure side downstream of the throat is also likely at the subsonic conditions. Therefore, it is not surprising that the LUT airfoil is worse than the baseline subsonically, and the ULTRE airfoil is worse than the LUT. The magnitude of the increases in loss are somewhat surprising though and warrant further investigation.

Qualitatively, the influences of trailing edge thickness, static pressure difference across the trailing edge, wedge angle, and unguided turning can be understood. Quantitatively, the trade-offs between the various airfoil design parameters are still being investigated. As shown in this paper, measurements in supersonic flow are difficult to obtain to the desired level of accuracy. However, accurate experimental measurements are necessary to validate new CFD analysis tools and the subsequent airfoil designs resulting from the improved analytical capability.

Conclusions

1 The level of uncertainty in cascade test measurements for loss coefficient and downstream static pressure distribution is significantly greater at supersonic exit Mach numbers than at subsonic exit Mach numbers.

2 For the VPI & SU facility as configured at the time of this test, the uncertainty for a single sample experiment to a 95 percent confidence level is estimated to be approximately

$$\pm 0.06 \text{ in } L \ (L \text{ in percent}) \text{ at } M_{2ISEN} = .82$$

$$\pm 0.44 \text{ in } L \ (L \text{ in percent}) \text{ at } M_{2ISEN} = 1.18$$

$$\pm 0.002 \text{ in } Pr_s \text{ at } M_{2ISEN} = 0.82$$

$$\pm 0.021 \text{ in } Pr_s \text{ at } M_{2ISEN} = 1.18$$

$$\pm 0.016 \text{ in setting } M_{2ISEN}.$$

3 Multisample experiments and simple statistical methods can be used to increase the level of confidence in evaluating airfoils at supersonic exit Mach numbers.

4 The transonic turbine airfoil shock structure is a function of many airfoil design parameters including trailing edge thickness, pressure difference across the trailing edge, wedge angle, and unguided turning.

5 Relative to the baseline airfoil, reducing unguided turning and reduced wedge angle will reduce the downstream shock strength.

6 Relative to the baseline airfoil, the efficiency benefits of reducing the downstream shock strength can be offset by the increase in strength of the trailing edge pressure side shock.

Summary

This study illustrates the difficulties in measuring small, but still significant, differences in airfoil efficiency, particularly for transonic and supersonic flow. Ideally, in the experimental process, one would continue to investigate, identify, and control the source(s) of variation until the desired level of uncertainty is reached. In practice, time and funding constraints are likely to limit the level of effort available for refining the experimental process. The statistical approach as shown in this paper gives the investigator a methodology for assessing measured differences relative to the variation in the process. Rigorously, one can argue that the validity of the approach is dependent on how well the true probability function is approximated by the normal distribution used in the data reduction. However, future improvements in turbine efficiency are likely to be incremental in nature requiring measurement of small differences to validate new designs. Methods of assessing measured differences and uncertainty will be required. The authors hope this paper will stimulate further discussion on this topic.

References

Denton, J. D., and Xu, L., 1990, "The Trailing Edge Loss of Transonic Turbine Blades," ASME JOURNAL OF TURBOMACHINERY, Vol. 112, pp. 277–285.

Kiock, R., Lehthaus, F., Baines, N. C., and Sieverding, C. H., 1986, "The Transonic Flow Through a Plane Turbine Cascade as Measured in Four European Wind Tunnels," ASME *Journal of Engineering for Gas Turbines and Power*, Vol. 108, pp. 277–284.

Kline, S. J., and McClintock, F. A., 1953, "Describing Uncertainties in Single-Sample Experiments," *Mechanical Engineering*, Jan., pp. 3–8.

Mee, D. J., Baines, N. C., Oldfield, M. L. G., and Dickens, T. E., 1992, "An Examination of the Contributions to Loss on a Transonic Turbine Blade in Cascade," ASME JOURNAL OF TURBOMACHINERY, Vol. 114, pp. 155–162.

Moffat, R. J., 1981, "Contributions to the Theory of Uncertainty Analysis for Single-Sample Experiments," *Proceedings of the 1980–81 AFOSR-HTTM-Stanford Conference on Complex Turbulent Flows*, Vol. 1, pp. 40–56.

Ott, L., 1988, *An Introduction to Statistical Methods and Data Analysis*, 3rd ed., PWS-Kent Publishing Co., Boston, MA.

F. J. G. Heyes[1]

H. P. Hodson
Mem. ASME

Whittle Laboratory,
Cambridge University
Engineering Department,
Cambridge, CB3 0DY United Kingdom

Measurement and Prediction of Tip Clearance Flow in Linear Turbine Cascades

This paper describes a simple two-dimensional model for the calculation of the leakage flow over the blade tips of axial turbines. The results obtained from calculations are compared with data obtained from experimental studies of two linear turbine cascades. One of these cascades has been investigated by the authors and previously unpublished experimental data are provided for comparison with the model. In each of the test cases examined, excellent agreement is obtained between the experimental and predicted data. Although ignored in the past, the importance of pressure gradients along the blade chord is highlighted as a major factor influencing the tip leakage flow.

Introduction

The necessary clearance between the tips of unshrouded turbine blades and the machine casing is known to produce a significant loss of efficiency. Typically, a clearance of 1 percent of the blade height is associated with a penalty of 1–3 percent of the stage efficiency (e.g., Booth, 1985). However, few, if any, of the traditional correlations (e.g., Ainley and Mathieson, 1951; Meldahl, 1941) are based on the physical processes involved.

There are two important aspects of tip leakage flow. First, there is a reduction in the amount of work that the blade extracts. This occurs because the leakage flow is not turned to the same degree as the mainstream flow and the effect manifests itself as a deviation of the flow from the exit blade angle. Of itself this does not constitute a loss because the work theoretically may be extracted in a subsequent blade row (Denton and Cumpsty, 1987). The second aspect involves the generation of entropy, within the tip gap, in the blade passage, and downstream of the blade row.

Recent detailed measurements of the flow within the tip gap of linear turbine cascades (e.g., Bindon, 1989; Dishart and Moore, 1990; Yaras and Sjolander, 1991) have started to reveal the physics governing leakage loss generation. Bindon (1989) and later Dishart and Moore (1990) showed that the loss generated within the tip gap is approximately of equal magnitude to that generated by the mixing of the leakage and mainstream flows within and downstream of the cascade. However, experiments by Yaras and Sjolander (1991) on a thin blade at high tip clearance showed that little of the loss was generated within the tip gap. Heyes et al. (1992) showed that loss generation within the tip gap reduced the leakage mass flow and therefore the overall leakage loss. In addition they showed that the angle that the tip leakage flow made with the mainstream flow at the exit of the tip gap would also influence the overall loss generation. Clearly a number of factors influence the mass flow rate and the leakage trajectory and these factors will vary along the chord and from design to design. Since these affect the loss generation process, it is necessary to determine the distribution of these quantities along the chord if accurate predictions are to be made.

Booth et al. (1982) argued that the flow over a blade tip was analogous to that through an orifice plate and that the discharge coefficients were of similar magnitude. Bindon (1986) showed that the leakage flow within the tip gap was dominated by the formation of a vena contracta and the subsequent mixing and diffusion of the flow that would ultimately fill the clearance gap if the blade were sufficiently thick. At tip gap exit he observed that for thinner parts of the blade, the leakage flow was characterized by a region of loss-free flow near the endwall and a region of high total pressure loss in the wake of the vena contracta separation bubble. Moore et al. (1989) and Moore and Tilton (1988) observed, on a much thicker blade, that the gap exit flow velocity was virtually constant across the tip gap. Heyes et al. (1992) put forward a model of the tip gap flow, based on a simpler model of Moore and Tilton, which is illustrated in Fig. 1. The model is characterized by the contraction coefficient of the vena contracta, σ, and the proportion of the leakage volume flow that mixes to form the separation bubble wake, M. The value of M will vary from 0, for regions of tips with very low values of $T\sqrt{\tau}$, to 1 for much thicker ones.

Booth et al. (1982) have also presented calculations of the leakage flow trajectories obtained from a simple model. They assumed that the chordwise pressure gradients were small so that the component of the leakage flow parallel to the blade pressure side is convected through the tip gap unchanged. The

[1]Current address: Senior Design Engineer, European Gas Turbines Ltd., Lincoln, United Kingdom.

Contributed by the International Gas Turbine Institute and presented at the 37th International Gas Turbine and Aeroengine Congress and Exposition, Cologne, Germany, June 1–4, 1992. Manuscript received by the International Gas Turbine Institute February 20, 1992. Paper No. 92-GT-214. Associate Technical Editor: L. S. Langston.

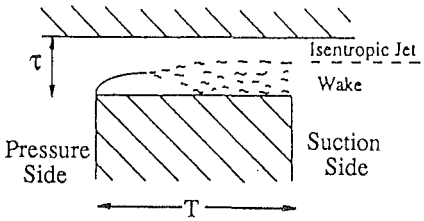

Fig. 1 Model of flow over blade tip after Heyes et al. (1992)

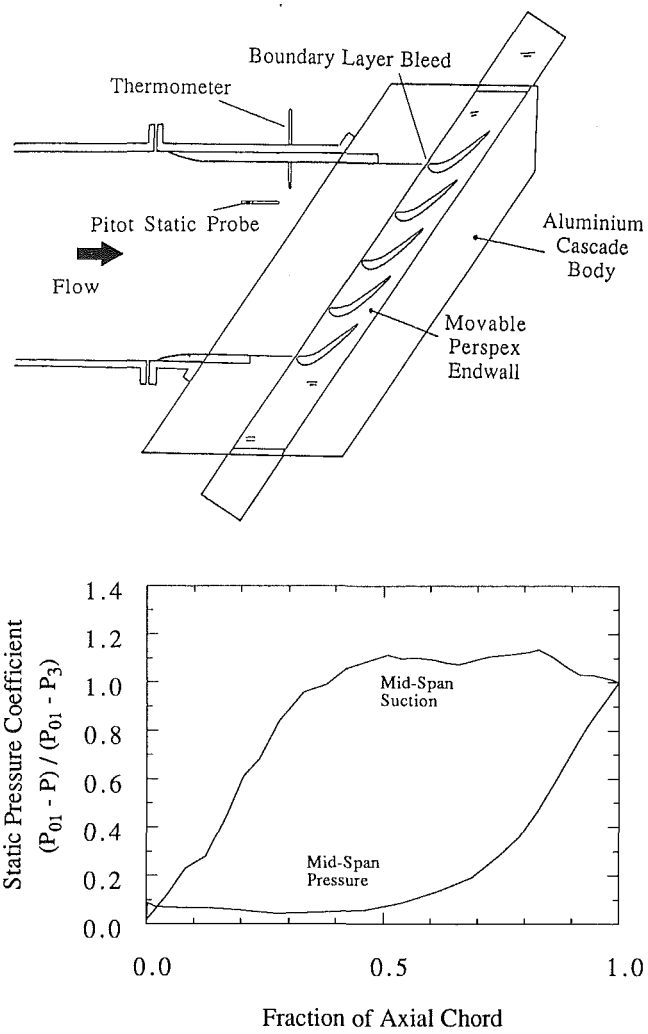

Fig. 2 General features of cascade

Table 1 Cascade geometry and test conditions

No. of Blades	5
Chord	225mm
Axial Chord	103mm
Pitch/chord ratio	0.824
Aspect ratio	2.11
Reynolds No. V_2c/ν	4.0×10^5
Inlet flow angle, α_1	32.5°
Blade exit angle, α_2	75.6°
Max. thickness / chord	14%
Zweifel Coefficient	0.73

velocity normal to the blade pressure side was then calculated from the static pressure drop from midspan on the pressure side to tip gap exit using a measured discharge coefficient of 0.8. Reasonable agreement with their experimental data was obtained.

The present paper is specifically concerned with the nature of the leakage flow over the blade tips and its variation along the chord. Detailed measurements of the leakage flow within the blade tip gap and the flow losses and deviation downstream of a cascade of turbine blades are presented. A model of the leakage flow is then described and results obtained from calculations employing the model are compared with the experimental data of the present authors and of other investigators.

Experimental Details

The Cascade. Figure 2 shows the incompressible flow cascade that was previously investigated by Heyes et al. (1992). It is based on the tip section of a model turbine that is currently under investigation. It has a large chord and so permits a detailed investigation of the flow field. The blades were cantilevered from the hub endwall. The tip clearance was changed by withdrawing the blade into the hub endwall; the distance between the hub and tip endwall therefore remained constant, independent of the tip clearance. The cascade was fitted to an open jet wind tunnel so that the exhaust was at atmospheric pressure. Table 1 gives further details of the cascade.

Instrumentation and Experimental Techniques

Exit Traverses. The flow leaving the cascade was measured at a plane 35 percent axial chord downstream of the blade trailing edge. A five-hole pneumatic probe, which had been calibrated over an angular range of ±40 deg of yaw and pitch, was used for these measurements. If the yaw angle onto the probe was found to be outside this range, the probe was rotated about an axis coincident with its head until the flow was within range of the calibration. No such difficulties were found with the pitch angle at the axial location of this traverse plane. The traverses were made over an area of one pitch by 28 percent

Nomenclature

c = chord
C_f = skin friction coefficient
C_p = static pressure coefficient $= (P_{01}-P)/(P_{01}-P_3)$
h = span
Δl = width of a computational cell
Δm = mass flow through a computational cell
M = proportion of mass flow mixing over tip
P_0 = stagnation pressure
P = static pressure
T = tip gap length in flow direction
V = velocity
Y = stagnation pressure loss coefficient $= (P_{01}-P_0)/(P_{01}-P_3)$
α = flow angle measure to axial direction
λ = surface shear stress
ρ = density
σ = contraction coefficient
τ = tip clearance

Subscripts

b = in tip separation bubble
N = component normal to blade pressure side
P = pressure side
R = radius of orifice
S = suction side
T = component tangential to blade pressure side
1 = upstream of cascade
2 = at cascade exit plane
3 = at downstream mixed-out conditions

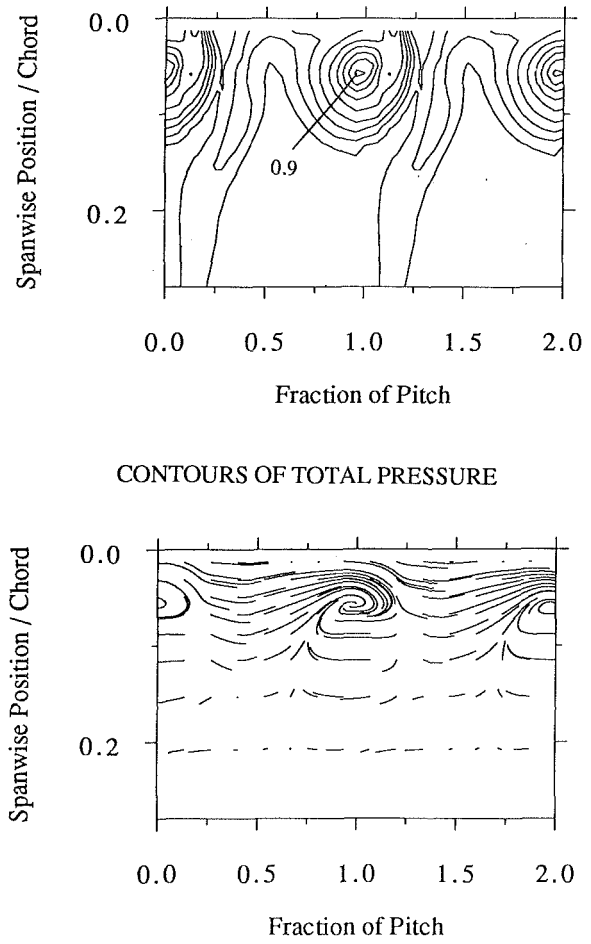

Fig. 3 Exit traverse results for *TIC* = 1.0 percent

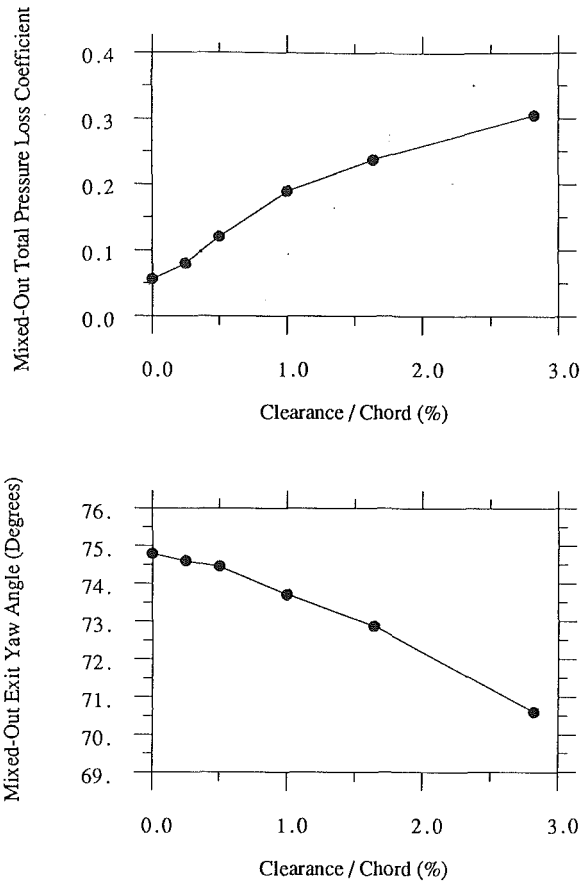

Fig. 4 Cascade mixed-out exit flow conditions for a range of tip gaps

of chord in the spanwise direction. Although this did not cover the whole of the cascade exit flow, the regions of influence of the leakage flow are contained within this area. This region was the same in extent as the area measured by Heyes et al. (1992) with a Pitot rake, although at a location farther downstream.

The diameter of the probe head was 3.29 mm; the cone semi-angle was 45 deg and the four side holes were drilled perpendicular to the side of the cone. This was to ensure minimum sensitivity of the probe to Reynolds number effects (Hodson and Dominy, 1988).

Clearance Gap Measurements. Measurements of the flow at the suction side of the tip gap were made using a single-axis hot-wire probe. The length of the probe prongs was greater than the tip gap to prevent the probe stem from causing significant blockage when fully immersed in the flow. Along each traverse there were 19 spanwise stations between blade tip and endwall. At each spanwise location, the probe was rotated about its axis and voltage measurements made over a range of probe angles. From these measurements the flow speed and direction were deduced. Further details are given by Heyes et al. (1992).

Measurements of the static pressure were made on the blade tip surface using the "micro-tapping" technique of Bindon (1986). Here 17 slots were machined across the tip of the blade in a direction perpendicular to the chord line and the slots covered with Magic Tape®. Seventeen measurements were made using each slot by puncturing the tape with a finely ground needle. The minimum spacing of the measurements was 0.25 mm or 0.8 percent of the maximum blade thickness.

Test Results

Exit Traverses. Figure 3 shows the results of the five-hole probe traverses downstream of the cascade with a clearance of 1.0 percent chord. Contours of total pressure are shown projected into a plane perpendicular to the blade exit angle. The contour interval is 0.1 ($P_{01} - P_3$). Although measurements were made only over one pitch, the results are shown repeated for clarity. The loss core generated by the leakage loss of one blade is seen to be interacting with the wake of its neighbor. The maximum value of Y_2 is 0.926.

Secondary flow lines are also shown. These were obtained by time integration of the secondary flow vector field to obtain the paths of imaginary particles. The total time for each line was identical. The secondary flow was defined as being perpendicular to the mixed-out exit flow (see below). These reveal the vortical motion in the leakage loss core. The centers of the vortex and the loss core are seen to coincide.

Similar traverses were performed for a range of clearances from 0 to 2.82 percent chord. Although they are not shown here, readers may refer to Heyes (1992) for further details. The results of all the traverses were reduced to mixed-out total pressure loss coefficients, Y_3, and exit angles α_3 by performing constant area mixing calculations over the measured flow field, i.e., a region of one pitch by 28 percent chord in the spanwise direction. These are plotted in Fig. 4. Since the cascade exit flow angle was 75.6 deg, there is approximately 0.9 deg of deviation at zero clearance for the part of the flow under consideration.

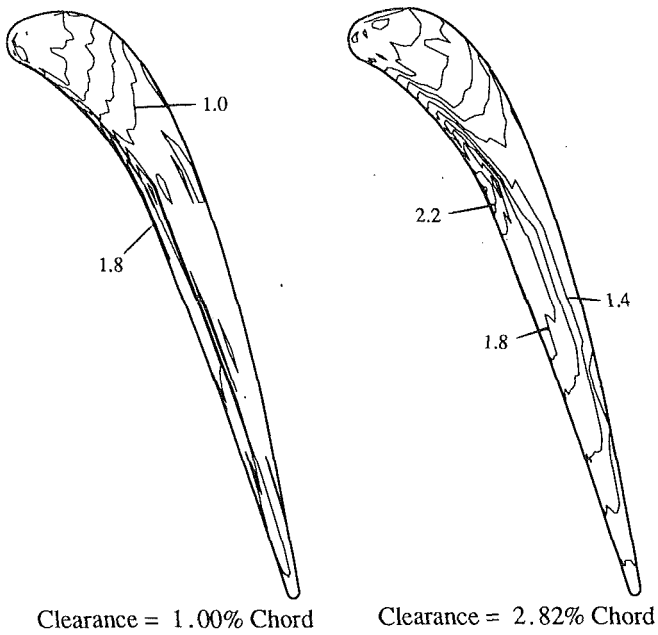

Fig. 5 Static pressure measurements on the blade tip for two tip gaps

Tip Static Pressure Distributions. Measurements of the static pressure on the blade tip for a clearance of 1 and 2.82 percent chord are shown contoured in Fig. 5. The contour interval is 0.2 ($P_{01} - P_3$). Over most of the blade they clearly show a low-pressure region near the pressure side that is associated with the vena contracta. The width of this low-pressure region is approximately 1.5 τ in the leakage flow direction, as observed by Moore et al. (1989). As the flow begins to mix out, the pressure rises until eventually it reaches the level of the static pressure on the blade suction side. Although for the smaller clearance case this mixing process has been completed by tip gap exit, for the larger clearance there is still evidence of increasing static pressure at tip gap exit over the thinner trailing third of the blade. This shows that the mixing process is incomplete (and that the mixing parameter M will therefore take a value less than 1) at tip gap exit.

Model of the Tip Leakage Flow

Mixing Within the Tip Gap. By extending the analogy between the tip gap and the orifice, the degree of mixing that occurs within the tip gap may be linked to the mixing that occurs within a circular orifice. The variation of orifice discharge coefficients with orifice length has been documented by Lichtarowicz et al. (1965). Figure 6 is a reproduction of one of their figures. It shows how the discharge coefficient varies with orifice length. If no mixing was to occur, theoretically the discharge coefficient should be the contraction coefficient, which takes the value 0.611 for incompressible flow (Milne-Thomson, 1968). This is close to the values shown for orifices of short length, and thus, by analogy, for thin parts of the blade tip. For orifices of intermediate length, the tip discharge coefficient rises sharply from its initial low value and reaches a peak at lengths near 5.5 radii. This regime is associated with the mixing of the flow to fill the orifice and thus the value of M will be expected to rise from 0 to 1 over that distance of 4.5 radii. For orifices of length greater than 5.5 radii, the discharge coefficient is seen to decrease with orifice length. This is consistent with the action of shear on the orifice walls. If there were no shear, the discharge coefficient would be expected to reach the value of 0.845 where $M = 1$.

Figure 6 also shows the result of calculations based on a model that assumes a linear variation of M from 0 to 1 over the length of the mixing region (i.e., from 1 to 5.5 radii). Before mixing, the flow is assumed to accelerate isentropically into the vena contracta. Downstream of the crest the mixing takes place. A constant shear stress is assumed to act on the orifice walls, which is given by

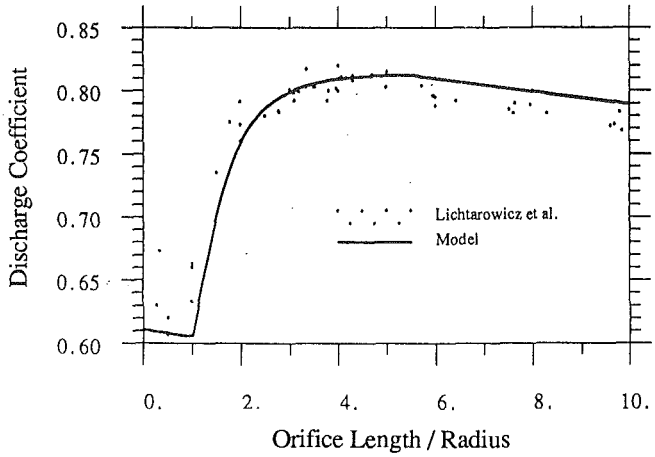

Fig. 6 Variation of discharge coefficient with orifice length

$$\lambda = C_f \frac{1}{2} \rho V^2 \tag{1}$$

where the velocity, V, is the mean value at orifice exit. The value of C_f depends on the Reynolds number of the flow based on the orifice radius, Re_R, and is given by the relationship for fully developed turbulent flow in a pipe

$$C_f = \frac{0.067}{Re_R^{0.25}} \tag{2}$$

These assumptions allow the variation of the tip discharge coefficient to be calculated, solely by using the conservation equations of mass and momentum. Figure 6 shows the results of such a prediction for a representative Reynolds number of 4000. The agreement is sufficiently adequate for the same model to be used for the turbine tip clearance flows, that is, a linear variation of M within the mixing region and a constant shear stress on the tip and endwall surfaces may be used to calculate the clearance flow perpendicular to the blade pressure side. The mixing will be assumed to take place immediately downstream of the vena contracta, over a length of 4.5τ (i.e., from $T = 1.5\tau$ to $T = 6\tau$) since the hydraulic mean diameter of the tip clearance is 2τ.

Trajectories of the Leakage Streamlines. To predict the trajectories of the leakage streamlines, a simple finite volume time-marching method is used. The scheme relies on knowledge of the pressure distribution at tip gap exit and on the blade pressure side away from the tip clearance. In this case, measured values are used, but the results of a three-dimensional Navier–Stokes solver, such as that of Dawes (1987), could be used instead.

The blade tip gap is modeled as a chordwise row of quadrilateral computational cells each having one side on the pressure side of the blade and another on the suction side, as shown in Fig. 7. The sides of each cell, AD and BC, follow the local leakage flow path and hence mass enters each control volume only at AB, and leaves only at CD. An estimate of the leakage flow is needed to determine the initial position of each cell. For this purpose a constant leakage flow angle over the whole blade (normal to the mean camber line) was found to be sufficient. As the computation progresses, the leakage flow trajectories change and thus the shapes of the control volumes are altered to ensure no flow through the sides BC and AD.

The pressure distribution around each cell must be known

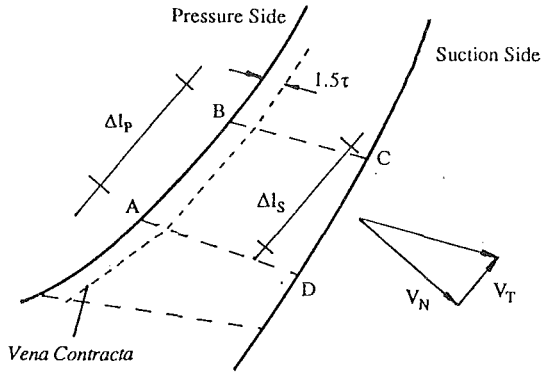

Fig. 7 Computational cell for the trajectory calculation

before the conservation of momentum equations can be employed to calculate an updated value of the leakage velocity. Along AB, it is assumed that the conditions correspond to those at the vena contracta, and so the value P_b acts on the cell pressure side. The arithmetic mean of the pressure at the points C and D is assumed to act along CD. These values are interpolated from the measured distribution at tip gap exit.

The mass flow, Δm, through the control volume, and the contraction coefficient, σ, are used with Bernoulli's equation to find the pressure at the vena contracta, P_b. If the cell occupies a length Δl_P of the pressure side, then

$$P_b = P_P - \frac{1}{2}\rho\left(\frac{\Delta m}{\rho\sigma\tau\Delta l_P}\right)^2 \tag{3}$$

where P_P is measured away from the tip gap. At the vena contracta, the momentum of the fluid parallel to the pressure side is assumed to be that inferred from the pressure measurements made on the pressure side away from the blade tip where the value is undisturbed by the leakage flow.

The pressure acting at the vena contracta at A (interpolated from the P_b values for this cell and its nearest neighbor) is assumed to act over a distance 1.5τ along AD, and then the pressure at D is assumed to act over the remainder of AD. A similar distribution is assumed for BC based on the pressure values at B and C. Although this magnitude and location of the resulting pressure forces will not be strictly correct, the approximations are acceptable if the leakage flow trajectories are parallel up to the crest of the vena contracta. The added complication of calculating the true variation of momentum and pressure up to the vena contracta for converging streamlines could not be justified for the present investigation.

Once an estimate for the mass flow through each control volume and the leakage trajectories is obtained, the calculation proceeds by the application of the equations for the conservation of momentum. The components of the pressure forces acting on the control volume and of the shear forces calculated from Eq. (1) and the mean cell exit dynamic head are resolved parallel and normal to AB. By applying these forces over a small increment in time, the changes in the components of the leakage flow momentum can be found. These changes are assumed to occur at the midpoint of CD. Once the components of momentum are updated and the value of M is determined, a new value of the mass flow rate leaving the control volume is calculated. This is equal to the mass flow rate Δm. In addition, the new leakage flow trajectory is taken to be the direction of the exit velocity. Once the new leakage trajectories are known for the whole blade, the cell boundaries are moved so that each boundary is parallel to the mean of the velocities either side of it.

The above procedure is then repeated over successive time steps until changes in the momentum flux and mass flow leaving each cell between successive iterations are reduced to less than 0.01 percent for a CFL number of approximately 0.1. This procedure gave convergence to a consistent solution, independent of the starting conditions.

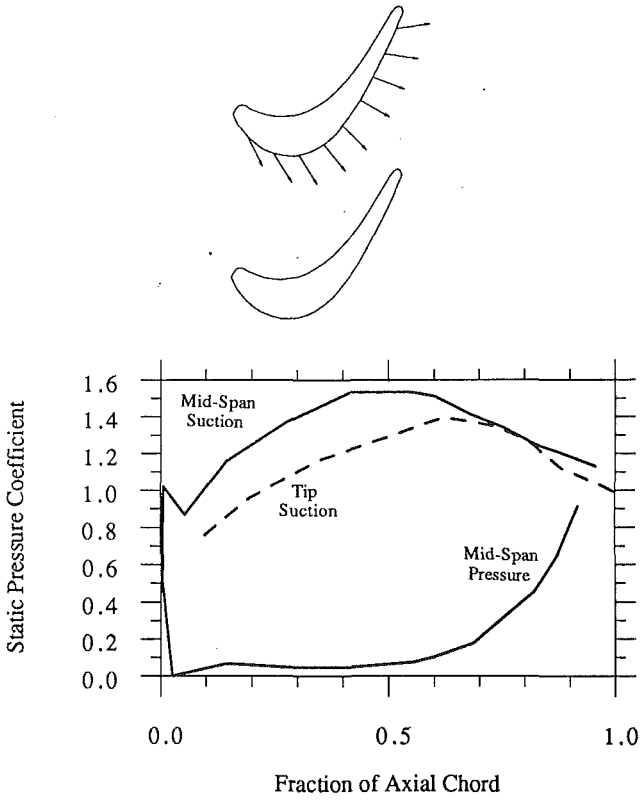

Fig. 8 Cascade and leakage flow data of Dishart and Moore (1990)

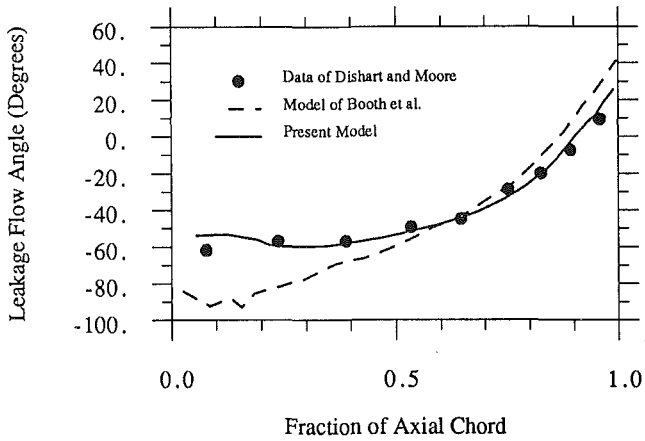

Fig. 9 Comparison of flow models with data of Dishart and Moore

Validation of Flow Model Against Experiment

Data of Dishart and Moore. Before comparisons are made with the present data, calculation results for the cascade of Dishart and Moore (1990) are presented. Figure 8 shows the reported pressure distributions at midspan and at tip gap exit and the leakage flow trajectories measured at gap exit with a three-hole pneumatic probe. The cascade Reynolds number was 5.4×10^5 and the tip clearance 2.1 percent chord.

Figure 9 shows the results of the present leakage flow calculation for the Moore cascade as the angle of the leakage flow trajectories. The angle is measured from the axial direction. Also shown are the measured data and the results of a calculation of the leakage flow trajectory put forward by Booth et al. (1982). The latter assumes that the chordwise pressure gradients are small so that the component of the leakage flow

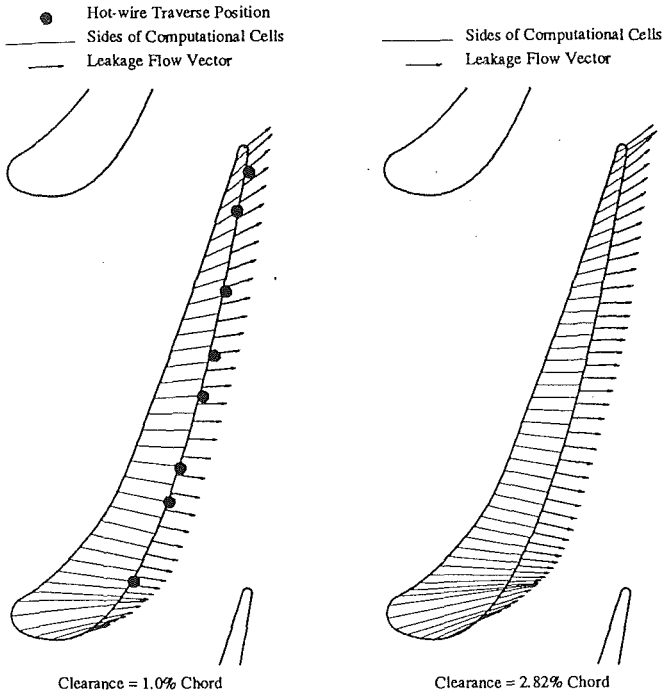

Fig. 10 Calculated leakage flow trajectories for the present cascade

parallel to the blade pressure side is convected through the tip gap unchanged. The velocity normal to the blade pressure side is calculated from the static pressure drop from midspan on the pressure side to tip gap exit and a discharge coefficient of 0.8.

The comparison shows excellent agreement between the data and the present calculation. The scheme of Booth et al. underpredicts the leakage flow angle by nearly 30 deg at the leading edge and overpredicts the value by 10 deg toward the trailing edge. The reason for the discrepancy in the models is the fact that the Booth method has no connection between the discharge coefficient and the leakage trajectories. The present calculation employs the momentum and continuity equations so that when leakage streamlines converge, the discharge coefficient decreases, and when they diverge the discharge coefficient increases. The reason for the convergence and divergence of the streamlines is linked to the static pressure gradients along the blade chord. As the static pressure falls on the blade pressure side toward the rear of the blade, the component of velocity parallel to AB increases. At the same time the pressure difference across the blade tip decreases and so the velocity component normal to AB falls, causing streamline divergence.

Present Data. Figure 10 shows the calculated distribution of leakage flow trajectories for the present cascade at two clearance values. Near the leading edge the streamlines are converging and over the remaining part of the blade (except actually at the trailing edge) the trajectories diverge.

The convergence of the flow lines over the first part of the blade arises because the pressure difference across the tip increases over the leading part of the blade, increasing the leakage velocity normal to the blade pressure side, while the pressure parallel to the pressure side remains almost constant in this region. For the case of the higher clearance, the minimum pressure on the blade suction side is farther downstream (see Fig. 12) so that more of the blade shows converging streamlines.

Hot-wire measurements at tip gap exit are compared with the calculation for the lower tip clearance value in Fig. 11. Again, agreement is excellent over the whole of the blade.

Equation (3) indicates that an easily accessible measure of the mass flow rate over the blade tip is the static pressure

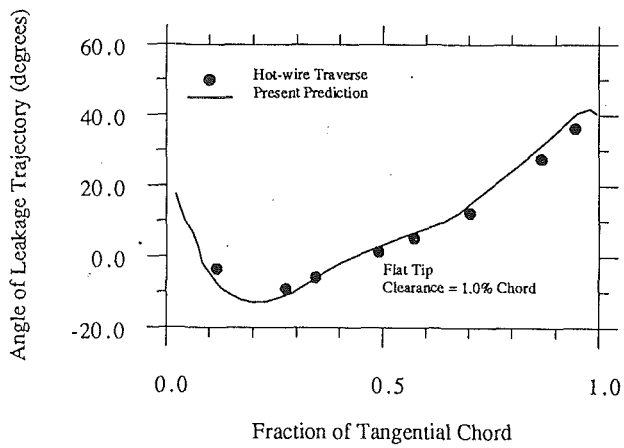

Fig. 11 Predicted and measured leakage flow trajectories for the present cascade

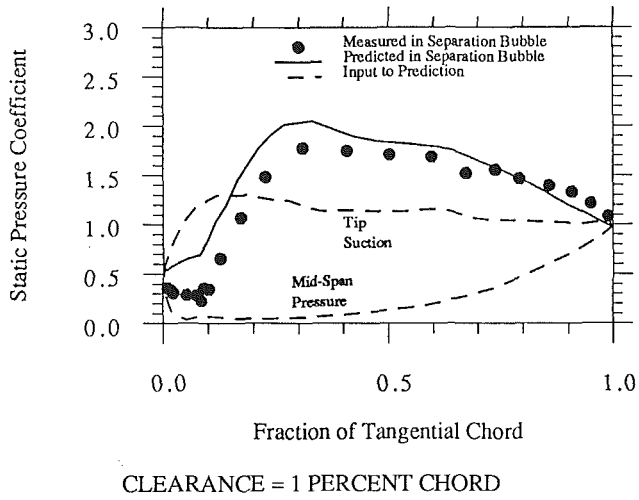

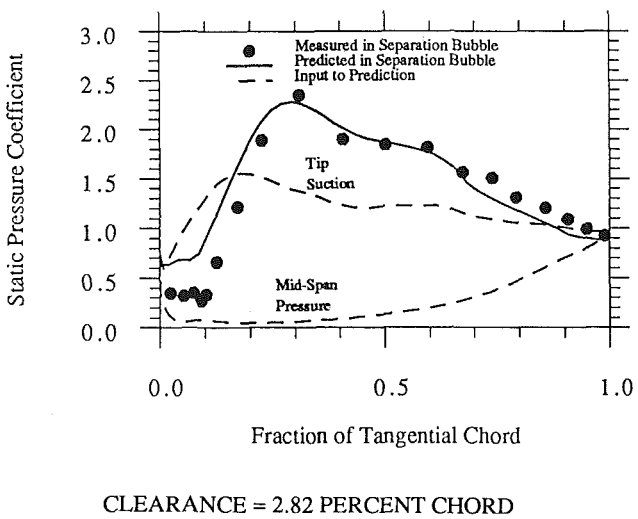

Fig. 12 Predicted and measured vena contracta pressures for the present cascade

measured in the vena contracta. The data shown in Fig. 5 are therefore used as a comparison in Fig. 12 with the calculated values of P_b for the present cascade at two clearances. The measured data, presented as a pressure coefficient C_P, are derived from the average pressure acting on the blade tip over the first 1 mm of the blade measured from the pressure side along a predicted leakage streamline. Also shown in Fig. 12

is the static pressure measured at midspan on the blade pressure side and at tip gap exit on the suction side. These data were used for the prediction. The scheme shows good agreement with the measurements, although the pressure coefficient is slightly overpredicted for much of the blade at the lower clearance. Near the leading edge of the blade in both cases, the low value of C_P in the vena contracta is associated with the converging streamlines and consequent low leakage velocity. At the trailing part of each blade the scheme underpredicts the value of C_P. This is probably due to the simplified model of the overtip mixing.

Discussion

The model of the flow within the tip gap, presented above, has been shown to agree accurately with available measurements. The model provides an important step toward the ability to calculate the total pressure losses and flow angle deviations associated with the tip clearance flows. Before the final objective can be achieved, however, the evolution of the flow within the blade passage must be determined.

The mixing of the passage and overtip leakage flows is governed by the equations of conservation of mass and momentum (Denton, 1991). These also determine the resulting deviation. In practice, the details of this mixing process do not need to be accurately modeled since the equations for conservation of mass and momentum must be satisfied globally. Of course, the pressure field that evolves as part of the iterative solution affects the magnitude and the trajectory of the leakage flow and these in turn are effectively determined by the same pressure field. In addition, distortions of the static pressure field occur in the vicinity of the tip gap. The static pressure distortion on the pressure side is a result of an inviscid process and has been highlighted by Moore and Tilton (1988). The distortion on the suction side is associated with the formation of the leakage vortex and the method by which the leakage flow and mainstream flow interact. These distortions will not be accurately predicted using coarse computational grids. However, the most important effect on the pressure field (Denton, 1991) is that which arises because the leakage flow is underturned and yet expands to the same back-pressure as the passage flow. This means that the mass flow between the blades is reduced over the entire span as the tip leakage flow will have a higher axial velocity. Since the passage flow is reduced, the blade force and, therefore, the pressure differences are also reduced. This is a large-scale effect and will be correctly modeled by a three-dimensional flow prediction code.

In the case of a compressor cascade, Storer and Cumpsty (1991) showed that the leakage losses arise almost entirely at the tip gap exit, where a shear layer forms between the leakage flow and the mainstream flow. As a consequence, they found that a three-dimensional Navier–Stokes code (i.e., Dawes, 1987) gave very good agreement with experimental observations, both in terms of leakage flow trajectories and losses without needing to predict the detail of the flow in the tip gap. In the case of a turbine cascade, some mixing usually takes place in the tip gap so that the loss generation. However, the loss that results from the mixing within the gap and the resulting flow can be determined using the above model. Thus it should be possible to combine the present model with a three-dimensional flow solver to evaluate total pressure losses and flow angle deviations associated with the tip clearance flows, although such a calculation is beyond the scope of the present paper.

Conclusions

Measurements of stagnation pressure loss and flow angles have been presented for an incompressible linear turbine cascade over a range of tip clearances. In addition, details of the flow field in the tip clearance gap have been presented.

A simple iterative calculation of the flow in the tip gap has been put forward. It relies on a time-marching scheme and uses an adaptive mesh. The method was shown to predict the leakage flow with accuracy for a range of blade geometries and flow conditions. An important effect, which has been ignored in the past, is found to be caused by the chordwise pressure gradients. When coupled to the calculation of the main flow, such as in a Navier–Stokes calculation, it is suggested that the flow losses and reduction in turning can be calculated with great accuracy.

Acknowledgments

This work was carried out with the support of the Procurement Executive of the Ministry of Defence and Rolls-Royce plc. The authors would like to thank Rolls-Royce plc for their kind permission to publish the paper.

References

Ainley, D. G., and Mathieson, G. C. R., 1951, "A Method of Performance Estimation for Axial-Flow Turbines," ARC R&M No. 2974, Dec.

Bindon, J. P., 1986, "Pressure and Flow Field Measurements of Axial Turbine Tip Clearance Flow in a Linear Cascade," Report CUED/A-Turbo TR-123, Cambridge University, United Kingdom.

Bindon, J. P., 1989, "The Measurement and Formation of Tip Clearance Loss," ASME JOURNAL OF TURBOMACHINERY, Vol. 111, pp. 257–263.

Booth, T. C., 1985, "Turbine Loss Correlations and Analysis," *Tip Clearance Effects in Turbomachines*, VKI Lecture Series 1985-05.

Booth, T. C., Dodge, P. R., and Hepworth, H. K., 1982, "Rotor Tip Leakage: Part 1—Basic Methodology," ASME *Journal of Engineering for Power*, Vol. 104, pp. 154–161.

Dawes, W. N., 1987, "A Numerical Analysis of the Three-Dimensional Viscous Flow in a Transonic Compressor Rotor and Comparison With Experiment," ASME JOURNAL OF TURBOMACHINERY, Vol. 109, pp. 83–90.

Denton, J. D., and Cumpsty, N. A., 1987, "Loss Mechanisms in Turbomachines," Proc. IMechE, *Turbomachinery—Efficiency and Improvement*, Paper No. C260/87.

Denton, J. D., 1991, private communication.

Dishart, P. T., and Moore, J., 1990, "Tip Leakage Losses in a Linear Turbine Cascade," ASME JOURNAL OF TURBOMACHINERY, Vol. 112, pp. 599–608.

Heyes, F. J. G., 1992, "Tip Leakage Flow and Control in Axial Turbines," PhD thesis, Cambridge University, to be published.

Heyes, F. J. G., Hodson, H. P., and Dailey, G. M., 1992, "The Effect of Blade Tip Geometry on the Tip Leakage Flow in Axial Turbine Cascades," ASME JOURNAL OF TURBOMACHINERY, Vol. 114, pp. 643–651.

Hodson, H. P., and Dominy, R. G., 1988, "An Investigation Into the Effects of Reynolds Number and Turbulence Upon the Calibration of 5-Hole Cone Probes," presented at 9th Symp., *Transonic and Supersonic Flow in Cascades and Turbo Machines*, St. Catherine's College, Oxford, Mar., N. C. Baines, ed.

Lichtarowicz, A., Duggins, R. K., and Markland, E., 1965, "Discharge Coefficients for Incompressible Non-cavitating Flow Through Long Orifices," *J. Mech. Eng. Sci.*, Vol. 7, No. 2, pp. 210–219.

Meldahl, A., 1941, "End Losses of Turbine Blades," *The Brown Boveri Review*, Vol. 28, No. 11, Nov.

Milne-Thomson, L. M., 1968, *Theoretical Hydrodynamics*, MacMillan & Co., Ltd., 5th ed., pp. 310–311.

Moore, J., and Tilton, J. S., 1988, "Tip Leakage Flow in a Linear Turbine Cascade," ASME JOURNAL OF TURBOMACHINERY, Vol. 110, pp. 18–26.

Moore, J., Moore, J. G., Henry, G. S., and Chaudry, U., 1989, "Flow and Heat Transfer in Turbine Tip Gaps," ASME JOURNAL OF TURBOMACHINERY, Vol. 111, pp. 301–309.

Storer, J. A., and Cumpsty, N. A., 1991, "Tip Leakage Flow in Axial Compressors," ASME JOURNAL OF TURBOMACHINERY, Vol. 113, pp. 252–259.

Yaras, M. I., and Sjolander, S. A., 1992, "Prediction of Tip-Leakage Losses in Axial Turbines," ASME JOURNAL OF TURBOMACHINERY, Vol. 114, pp. 204–210.

Incidence Angle and Pitch-Chord Effects on Secondary Flows Downstream of a Turbine Cascade

A. Perdichizzi
Dipartimento di Meccanica,
Università di Brescia,
25060, Brescia, Italy

V. Dossena
Dipartimento di Energetica,
Politecnico di Milano,
20100, Milano, Italy

This paper describes the results of an experimental investigation of the three-dimensional flow downstream of a linear turbine cascade at off-design conditions. The tests have been carried out for five incidence angles from −60 to +35 deg, and for three pitch-chord ratios: s/c = 0.58, 0.73, 0.87. Data include blade pressure distributions, oil flow visualizations, and pressure probe measurements. The secondary flow field has been obtained by traversing a miniature five-hole probe in a plane located at 50 percent of an axial chord downstream of the trailing edge. The distributions of local energy loss coefficients, together with vorticity and secondary velocity plots, show in detail how much the secondary flow field is modified both by incidence and by cascade solidity variations. The level of secondary vorticity and the intensity of the crossflow at the endwall have been found to be strictly related to the blade loading occurring in the blade entrance region. Heavy changes occur in the spanwise distributions of the pitch-averaged loss and of the deviation angle, when incidence or pitch-chord ratio is varied.

Introduction

The operating conditions of a turbine profile may extend over quite a wide range. Changes of rotational speed and flow rate are the main cause for incidence angle and expansion ratio variations. Pitch-chord ratio may also vary, when the same profile is employed in various stages with different solidities.

In the aerodynamic development of a multistage turbine the knowledge of blade row performance in terms of loss and secondary flow angle distribution is of utmost importance, both for optimizing the design, and for predicting the overall efficiency at part loads. This is true especially in low aspect ratio stages where the secondary effects are often dominant. By using loss prediction methods based on empirical correlations such as those of Ainley and Mathieson (1951), Dunham and Came (1970) and Craig and Cox (1971), only limited information can be obtained; if a reliable estimation of the secondary flow effects at off-design conditions is desired, such methods are quite inadequate. Therefore the only way to get such precious information is to carry out an experimental investigation on the selected profiles.

In the last few years a very large number of experimental works on secondary flows in turbine cascades at design conditions have been carried out. These investigations aimed to clarify the details of three-dimensional flow development (e.g., Langston et al., 1977; Marchal and Sieverding, 1977; Sharma and Butler, 1987; Hodson and Dominy, 1987a; Yamamoto, 1987), to analyze the loss production mechanism (e.g., Moore and Adhye, 1985; Gregory-Smith et al., 1988a) and to determine the development of turbulence quantities (e.g., Moore et al., 1987; Zunino et al., 1987; Gregory-Smith et al., 1988b; Perdichizzi et al., 1989). On the other hand, very few papers are available in the published literature about secondary flows at off-design conditions. Yamamoto and Nouse (1988) have shown the influence of the incidence angle on the three-dimensional flow inside a linear cascade. The investigation refers to a low-velocity cascade at moderately positive and high negative incidences. Hodson and Dominy (1987b) have reported secondary flows downstream of a high-speed linear cascade under off-design conditions, including incidence angle, pitch-chord ratio, Reynolds number, and inlet boundary layer thickness variations.

The present work aims partially to overcome the lack of data at off-design conditions, by providing detailed information on the three-dimensional flow downstream of a turbine cascade, within a wide range of incidence angles and for different cascade solidities. An additional objective of the work is to supply a set of experimental data under heavy off-design conditions, to be used for the validation of a three-dimensional viscous flow computational method (Bassi and Savini, 1992).

Experimental Details

The experimental investigation was carried out in the CNPM (Centro Nazionale per Ricerche sulla Propulsione e sull'Energetica, Milano) transonic wind tunnel, which is a blow down facility for linear turbine cascade tests. The test section, 50 mm high and 400 mm wide, allows the support of cascades with a relatively large number of blades.

The cascades consisted of blades scaled from a high-pressure stage steam turbine nozzle with an aspect ratio $h/b = 1.47$ and a geometric turning angle $\Delta\beta' = 89.4$ deg. Tests have

Contributed by the International Gas Turbine Institute and presented at the 37th International Gas Turbine and Aeroengine Congress and Exposition, Cologne, Germany, June 1-4, 1992. Manuscript received by the International Gas Turbine Institute February 11, 1992. Paper No. 92-GT-184. Associate Technical Editor: L. S. Langston.

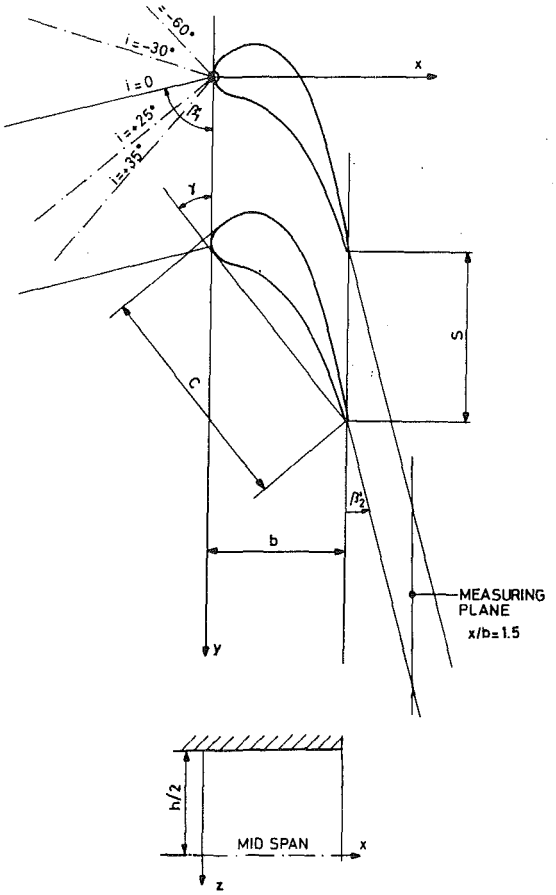

Fig. 1 Cascade geometry

been carried out on three different cascades characterized by different solidities corresponding to s/c = 0.58, 0.73, 0.87.

The changes in pitch-cord ratio were obtained simply by shifting the blades pitchwise; as a consequence, the number of blades of the cascade had to be consistently modified with the pitch value (Z = 11, 9, 8). The central blades have been instrumented by static pressure at the midspan section, in order to support information about profile velocity distribution. The cascade geometry and the relevant geometric data are shown in Fig. 1 and Table 1.

The measurements have been carried out by means of a fully automated computer-controlled data acquisition system. Downstream measurements have been carried out at a plane located at 50 percent of an axial chord from the trailing edge, by means of a miniaturized five-hole conical pressure probe presenting a head diameter of 1.5 mm. The measurement plane

Table 1 Cascade geometric data

Chord length, c	55.2 mm
Axial chord, b	34.0 mm
Aspect ratio, h/b	1.47
Inlet blade angle, β_1'	76.1 deg
Outlet blade angle, β_2'	14.5 deg
Blade turning angle, $\Delta\beta'$	89.4 deg
Stagger angle, γ	39.9 deg

Table 2 Inlet boundary layer at design conditions

Displacement thickness, δ^*	2.90 mm
Momentum thickness, θ	2.18 mm
Form factor, H	1.31
Inlet loss, $\zeta_1 \times 100$	1.18
Inlet Mach number, M_1	0.15
Outlet Mach number, M_{2is}	0.70
Reynolds number, $Re_2 \times 10^6$	0.84

was selected far enough from the trailing edge, where most of the energy dissipation has already taken place and the loss coefficient is representative of the overall energy dissipation. The measuring grid has been defined by 10 points in spanwise direction and by a 2 mm step in pitchwise direction. Further details about the experimental apparatus and the measuring procedure can be found from Bassi and Perdichizzi (1987) and Osnaghi and Perdichizzi (1990).

The cascades have been tested at five different incidence angles, i.e., −60, −30, 0, +25, +35 deg and for Mach numbers ranging from 0.3 up to 0.9. As the Mach number influence on secondary flows has already been treated in a previous paper (Perdichizzi, 1990), the following discussion refers mainly to the design expansion ratio, corresponding to M_{2is} = 0.7.

The results are presented in terms of kinetic energy loss coefficient, secondary velocity, and streamwise vorticity plots. The secondary velocity at a given pitchwise position is defined as the projection of the local velocity vector onto a plane normal to the midspan velocity. The local kinetic energy loss coefficient is defined as:

$$\zeta = \frac{q_{2is(y,z)}^2 - q_{2(y,z)}^2}{\overline{q}_{2isMS}^2}$$

The streamwise vorticity ω_s has been calculated from the axial and tangential components ω_x and ω_y; the first is directly estimated by the experimental results while ω_y is evaluated as indicated by Gregory-Smith et al. (1988a), using the spanwise component of the Crocco relation and by assuming total enthalpy to be constant. The presented vorticity contours have been nondimensionalized by using the inlet free stream velocity and the blade chord.

The upstream flow has been traversed by a flattened Pitot probe at x/b = 1.0 to determine the inlet boundary layer profile, whose integral parameters are presented in Table 2. The inlet loss is referred to the outlet isentropic condition. No significant changes of these parameters have been found for the considered incidence angles.

Nomenclature

b = axial chord
c = chord
h = span
H = form factor or horseshoe
i = incidence angle
M = Mach number
q = velocity
Re = Reynolds number = qc/ν
s = pitch
s, n, z = flow coordinate system
S = separation line
SKE = secondary kinetic energy = $\int v_2^2 + w_2^2/\overline{q}_{2isMS}^2\, dydz$
u, v, w = velocities along s, n, z
x, y, z = cascade coordinates
Z = number of blades
β = flow angle (from tangential)
β' = blade angle (from tangential)
γ = stagger angle (from tangential)
δ^* = boundary layer displacement thickness
θ = boundary layer momentum thickness
ζ = energy loss coefficient
ν = kinematic viscosity
ω = vorticity

Subscripts

1 = inlet
2 = traverse plane
2is = downstream isentropic
MS = midspan
p = pressure side
s = suction side or streamwise
SEC = secondary

Superscripts

$\overline{\ }$ = pitchwise averaged
$\overline{\overline{\ }}$ = pitch and spanwise averaged

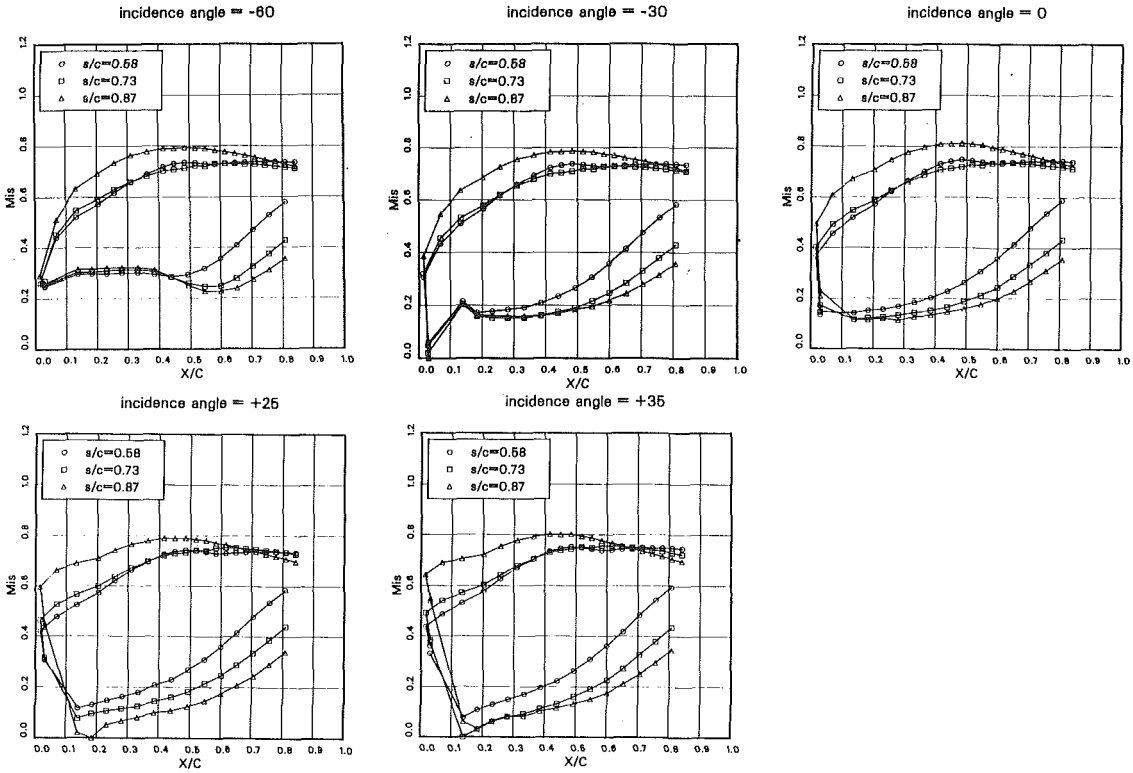

Fig. 2 Midspan insentropic Mach number distributions

Midspan Flow

The isentropic Mach number distributions measured at the midspan section for all the examined test conditions are presented in Fig. 2.

Referring to the design inlet flow angle, it can be seen that most of the flow acceleration takes place at the leading edge, producing the maximum blade loading just in the entrance region; beyond $x/c = 0.5$ the pressure on the suction surface remains constant, and the blade loading is reduced.

When the pitch is increased, the blade loading rises significantly everywhere along the blade. This is consistent with the larger momentum variation throughout the cascade. At the maximum s/c a greater acceleration, followed by a slight diffusion, takes place on the suction surface; on the pressure surface the velocity remains low for much of the blade, increasing only in the last part. The location of the stagnation point does not appear to be significantly influenced by the pitch-chord ratio.

Plots relating to incidence angles other than $i = 0$ show that the pressure distribution is strongly affected over much of the profile by the inlet flow angle variation.

At positive incidences the stagnation point moves downstream on the pressure side (up to about $x/c = 0.15$–0.20), producing an increase of circulation around the profile, and thus determining higher pressure differences between pressure and suction side in the entrance region. It has to be noticed that this effect becomes more important when increasing the pitch-chord ratio. It is not clear whether a separation bubble exists on the first part of the suction surface.

Decreasing the incidence below the nominal value, the blade loading at inlet undergoes a marked reduction and the stagnation point shifts upstream up to $x/c = 0.0$. At $i = -60$ the constant-pressure region occurring on the pressure surface for all the pitches suggests that a wide separation bubble exists. Then the boundary layer reattaches, presumably turbulent, at about $x/b = 0.4$. The diffusion behind the leading edge overspeeding is responsible for this separation. It is supposed that a less extended separation occurs at $i = -30$.

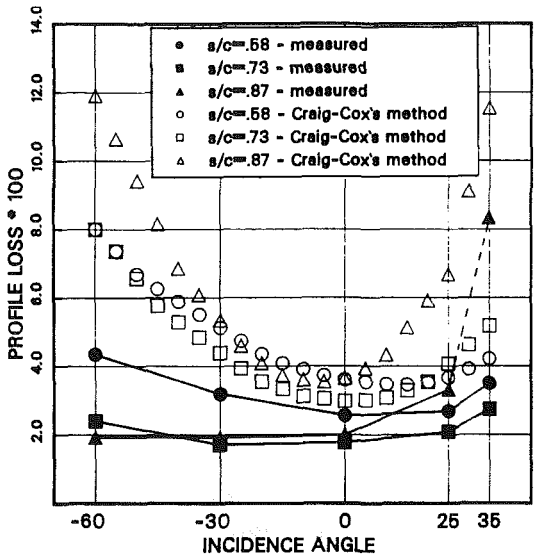

Fig. 3 Profile losses

It should be noticed that in the rear part of the profile the pressure distribution remains practically unchanged for all incidence angles.

The measured profile losses are presented in Fig. 3 together with the values predicted by the Craig-Cox method. The experimental data show a rather marked insensitivity of the profile loss to incidence, which is to be related to the thick and rounded leading edge of the profile.

The effects of the separation occurring at the minimum incidence become more important for the smallest pitch.

It should be pointed out that the steep increase of the loss found at $i = +35$ for the largest pitch is not a two-dimensional effect. As will be presently shown, the secondary flow effects in this condition are so conspicuous that they reach the midspan

section and no pure two-dimensional flow may be considered. The same consideration applies to the midspan outlet flow angle, which, under the above conditions, increases considerably (Fig. 4).

As far as the prediction is concerned, a relatively good agreement with the experiments at the design inlet angle can be noticed; the profile loss is slightly overestimated, and the pitch-chord influence is well enough captured. However, moving away from the design condition, the Craig-Cox method significantly overestimates the profile loss for both positive and negative incidences, providing unacceptable results.

Oil Flow Visualizations

To provide some information on the vortex structure developing inside the blade passage, surface oil flow visualizations have been carried out at three different inlet angles. As is well known, this technique allows one to follow the behavior of the various vortices, as it provides the traces of the near surface flow. Figure 5 shows a comprehensive view of suction surface and endwall visualizations obtained at $i = -30$, at the design inlet angle, and at $+25$ deg of incidence.

The primary separation lines, S_{1p}, S_{1s}, associated with the upstream boundary layer separation are easily visible at all the incidences, while the secondary ones S_{2p}, S_{2s}, corresponding to the horseshoe vortex separation from the endwall, can be clearly detected only at $i = +25$.

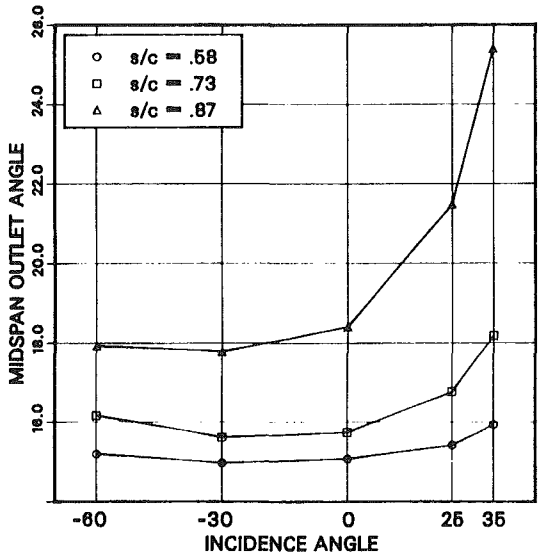

Fig. 4 Outlet flow angle

The flow field configuration appears to be greatly affected by the inlet angle. As the incidence angle is increased, the separation lines move significantly upstream of the leading edge.

At $i = -30$, the distance from the leading edge of the saddle point related to S_1 is about 0.10 c, while at $i = +25$ it becomes 0.23 c. Also the point where the separation line S_{1p} impacts the suction surface shifts significantly upstream: It moves from $x/b = 0.70$ ($i = -30$) to $x/b = 0.61$ ($i = 0$), up to $x/b = 0.45$ ($i = +25$). In a similar way the corresponding point related to S_{1s} moves from $x/b = 0.38$ to $x/b = 0.24$, up to $x/b = 0.18$. This trend is an outcome of the higher pressure difference driving the crossflow across the channel.

On the suction surface the separation line S_4 associated with the passage vortex is quite evident. The greater inclination of this line noticeable at $i = +25$ indicates a major intensity of the flow rotation within the vortex. Another clear effect is the increasing of the flow three-dimensionality: At the trailing edge the region affected by the passage vortex extends from $z/h = 0.12$ ($i = -30$) to $z/h = 0.19$ ($i = 0$), up to $z/h = 0.27$ ($i = +25$).

At $i = +25$ no traces of separation for the leading edge overspeeding are present on the suction surface. On the contrary, for $i = -30$ a separation bubble with a limited extent has been observed on the pressure side surface at $x/b = 0.10$.

Three-Dimensional Flow

Variation With Incidence. Figure 6 presents the results of the area traverses at the five incidences considered, for the design pitch-chord ratio (i.e., $s/c = 0.73$).

Zero Incidence. At the design inlet angle, the flow field appears consistent with the well-known secondary flow vortex structure. It should be pointed out that, as the measurement plane is relatively far from the trailing edge, turbulence and viscosity action have contributed to modify the flow configuration and to reduce partially the secondary vortex intensity with respect to the cascade exit plane. Relating to the classical model of the secondary flows in turbine cascades, i.e., Langston et al. (1977) and Sieverding (1985), the following features can be traced:

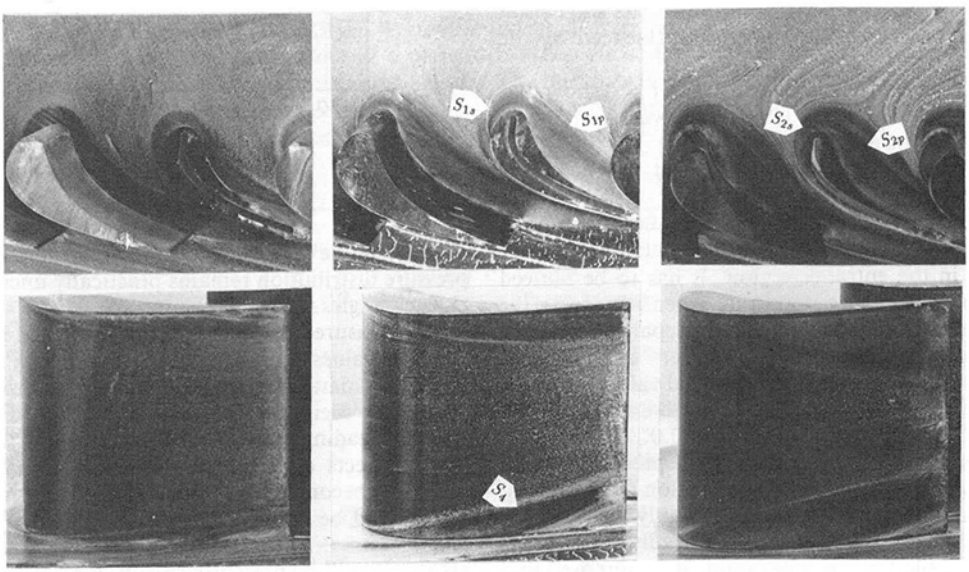

Fig. 5 Oil flow visualizations for $s/c = 0.73$ at $i = 30$, $i = 0$, and $i = +25$

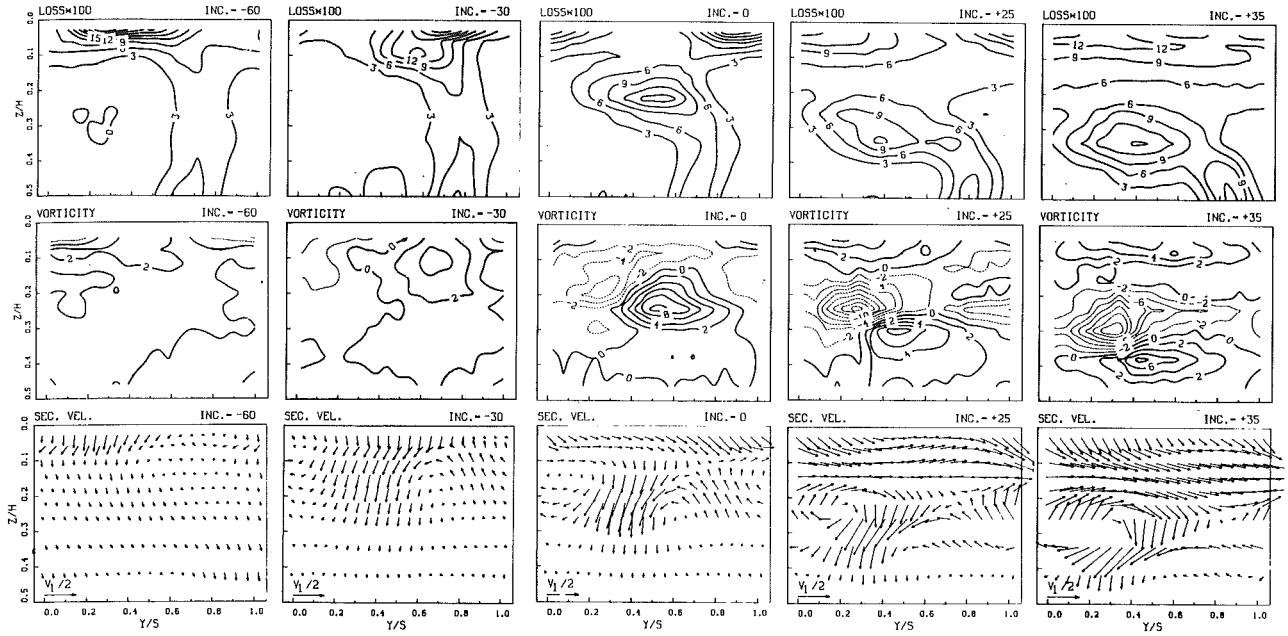

Fig. 6 Secondary velocity vectors, loss, and vorticity contours for *s/c* = 0.73

• The passage vortex, which can be identified by the clockwise rotating flow and by the negative vorticity core, appears to be relatively weak, as much of its secondary kinetic energy has been dissipated between the trailing edge and the measuring plane. However, an appreciable crossflow at the endwall remains, indicating the overall vorticity of the flow field.

• The trailing shed vorticity, which at the trailing edge originally developed as a vortex sheet, has been reorganized in a well-defined single vortex located across the wake. The shed vortex is still quite intense, as indicated by the secondary velocities and by the positive vorticity level. It is about twice the one found within the passage vortex.

• In the endwall region the spanwise secondary velocities, associated with positive vorticities, show the presence of the corner vortex. The loss core related to this vortex presents a high peak value (about 20 percent) and extends significantly in both pitchwise and spanwise direction. This loss, as suggested by Hodson and Dominy (1987a), is not only due to the dissipation of the secondary kinetic energy associated with the vortex, but it is also the result of the new endwall boundary layer swept toward the suction surface by the endwall crossflow.

• The wake appears significantly distorted toward the suction side, as the mixing process has been heavily influenced by the shed-passage vortex interaction. The position of loss core on the suction side of the wake coincides roughly with the vortex interaction region. The extension of this loss region and its distance from the endwall may be considered an index of the intensity of the secondary flow phenomena.

• No traces of the suction side leg of the horseshoe vortex are visible. Presumably it has been swept by the passage vortex.

Positive Incidence. As is well known, the secondary flow phenomena in a turbine cascade are considerably affected by the main flow deflection. This can be simply derived from the so-called transport vorticity equation, which is obtained by forming the curl of the full Navier–Stokes equation. In an intrinsic coordinate system the streamwise component can be written as follows:

$$\frac{D\omega_s}{Dt} = \omega_s \frac{\partial u}{\partial s} + \omega_n \frac{\partial u}{\partial n} + \omega_z \frac{\partial u}{\partial z} + \nu \nabla^2 \omega_s$$

If the viscous term is neglected, it follows that in the entrance region of a linear turbine cascade the rate of change of the streamwise vorticity ω_s depends only on the normal vorticity ω_n (due to the inlet boundary layer) and on the velocity gradients $\partial u/\partial n$ in the normal direction, as ω_s and ω_z are zero. Therefore when the incidence angle is increased, larger secondary flow effects must be expected, as larger velocity gradients take place between suction and pressure surface (see Fig. 2). The same feature may be drawn if s/c is increased.

Referring to the traverse results at $i = +25$ and $i = +35$, presented in Fig. 6, it can be seen that by increasing the incidence the secondary flow field experiences dramatic changes:

• The negative vorticity level increases considerably, denoting a much more intense passage vortex. This effect is a direct consequence of the high blade loading taking place in the entrance region (Fig. 2). At $i = +35$ the peak vorticity within the passage vortex is about 2.5 times the one found at design condition.

• The shed vorticity, on the contrary, remains roughly at the same level; this result is in contrast with the one presented by Hodson and Dominy (1987b), where a shed vorticity has been reported that rises appreciably at positive incidences. As the incidence is increased, a second positive vorticity core appears in the endwall region, showing a stronger intensity of the corner vortex.

• Both passage and shed vortex migrate toward the midspan, therefore the extension of the two-dimensional flow from the midspan section is progressively reduced.

• In most of the flow field the secondary velocities grow considerably, reaching the same order of magnitude of the inlet velocity. At the endwall there is an intense crossflow, which extends to about 20 percent of the blade height, revealing a large amount of the overall streamwise vorticity.

• The loss core on the suction side of the wake shifts toward the midspan in agreement with the higher intensity of the passage vortex. The peak value remains practically unchanged, but the overall loss is much greater, because of the higher secondary velocities occurring in both the vortex and the endwall regions. A larger loss appears out also in the wake presumably due to the leading edge overspeeding.

Negative Incidence. At the considered negative incidences the flow turning $\Delta\beta$ is considerably reduced as it decreases from 88.2 (design value) to 27.7 deg ($i = -60$). The following effects can be observed:

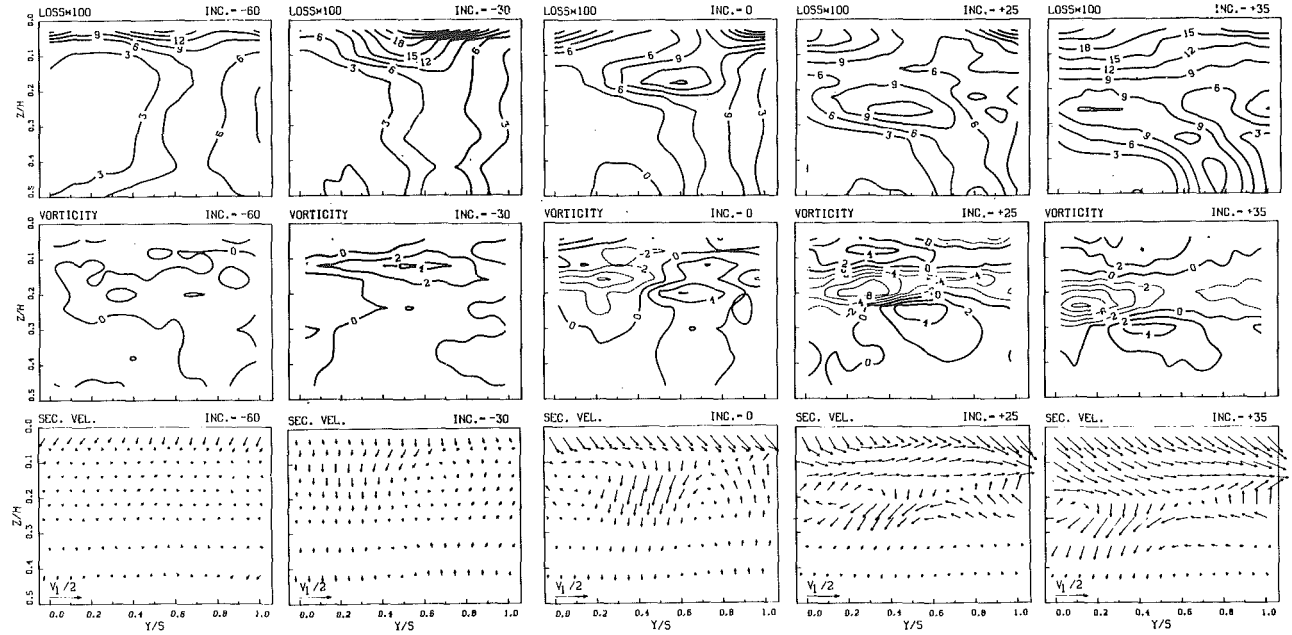

Fig. 7 Secondary velocity vectors, loss, and vorticity contours for $s/c = 0.58$

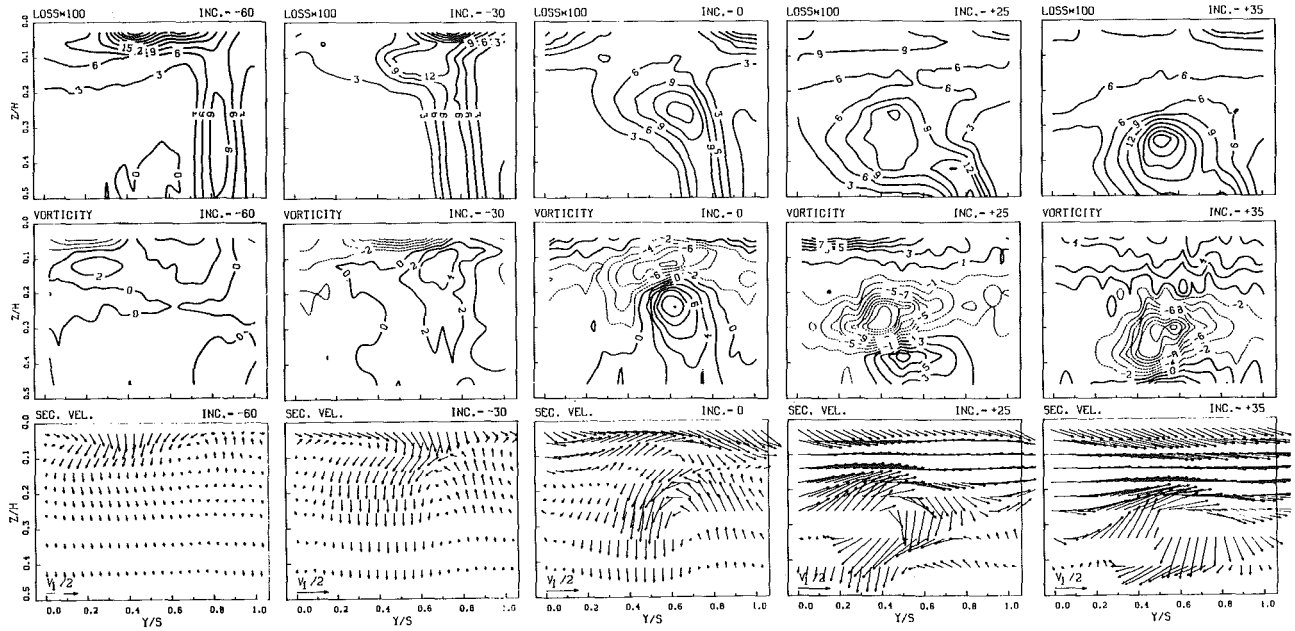

Fig. 8 Secondary velocity vectors, loss, and vorticity contours for $s/c = 0.87$

- The passage vortex experiences a drastic weakening and the secondary velocities in general become quite small. Both positive and negative vorticity are substantially lower and therefore the three-dimensional effects remain confined in the endwall region, leaving a two-dimensional flow along most of the blade height.
- On the pressure side of the wake, relatively far from the shed vortex, a clockwise rotating vortex is visible that should be mostly attributed to the pressure side leg of the horseshoe vortex, as suggested by Yamamoto and Nouse (1988). Indeed, at negative incidence this vortex is presumably stronger because of the high turning angle around the leading edge and the related overspeeding. No evident effect of the vortex interaction with the separation bubble on the pressure side was noted.
- The crossflow between the pressure and the suction side of the channel, which at zero and positive incidence was quite intense, is virtually absent. However, a very thin crossflow is thought to exist in the layer closest to the wall. It turns out that the crossflow intensity is very sensitive to the blade loading on the first part of the profile, but much less to the loading at the rear, after most of the flow turning has occurred and the secondary flows have developed.
- At -60 deg of incidence the loss distribution does not appear to be largely modified with respect to a normal boundary layer. This is the effect of the absence of the rolling action of the passage vortex on the inlet boundary layer. There is a single loss core close to the endwall with a high peak value, that is about 25 percent. This should be mostly related to the new endwall boundary layer developed throughout the cascade fed into the passage vortex. A contribution is supposed to come also by the pressure side leg of the horseshoe vortex.

Variation With Pitch-Chord Ratio. The influence of the pitch variation on the secondary flow field can be seen by comparing the results of the exit area traverses for $s/c = 0.58$ and $s/c = 0.87$, presented in Figs. 7 and 8, respectively.

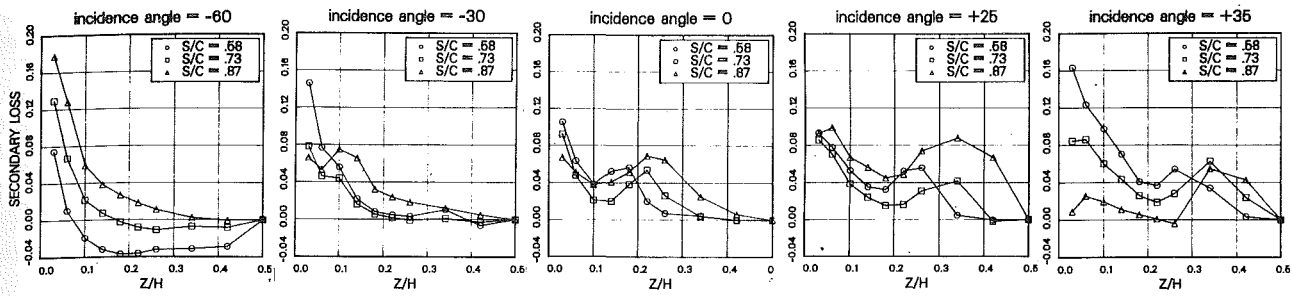

Fig. 9 Spanwise secondary loss distributions at different incidence angles

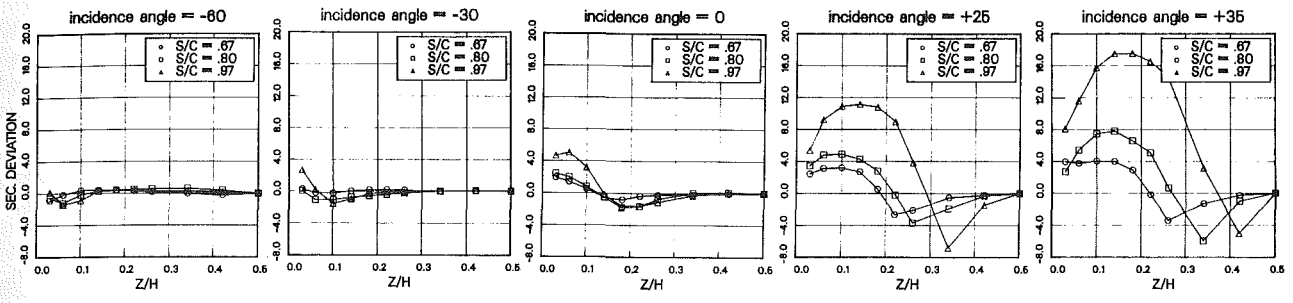

Fig. 10 Spanwise distributions of secondary flow angle deviation at different incidence angles

As the pitch is increased, the secondary velocities become generally greater for all the inlet conditions, but at positive incidence they undergo a truly dramatic growth; the flow field is dominated by a quite intense passage vortex and by an impressive crossflow extending up to $z/h = 0.26$. The peak of the negative vorticity is about twice the one at the smallest pitch and the secondary kinetic energy grows considerably all over the plane. These phenomena are the effects of the high loading occurring on the blade because of the contemporary presence of a large pitch-chord ratio and a high flow turning (Fig. 2).

There is another striking effect denoted by these results: Due to the occurrence of strong passage vortices, the region affected by the secondary phenomena extends up to the midspan; therefore the two passage vortices occurring in the upper and lower part of the blade passage interact. At this condition the overall loss is significantly increased; the loss contours present a wide core with a high peak value, at about 24 percent, located just in the center of the passage vortex. It should be noticed that at the midspan no wake can be discerned and therefore no two-dimensional flow can be considered. It is thought that in this very complex flow configuration the interaction of the two vortices, together with a presumed high turbulence and large Reynolds stresses, are responsible for such an important energy dissipation.

As far as the results for the smallest s/c, it has been found that the flow configuration is qualitatively similar to the one at the design cascade solidity, but with a general reduction of all the three-dimensional effects, i.e., the secondary velocities and the vorticity values. As noted above, when lower streamwise vorticities occur, the secondary phenomena are more confined in the endwall region and, even at a large incidence, there remains a two-dimensional flow for a wide blade height extent.

At the lowest incidence the wake appears to be heavily distorted to a major extent at the midspan. It is presumed that the H_p vortex interaction with the two-dimensional separation bubble on the pressure side beyond the leading edge (Fig. 2) is responsible for this phenomenon. In similar conditions, i.e., at large negative incidences, Yamamoto and Nouse (1988) have shown that new secondary flows arise that transport the low-momentum fluid within the separated region from the endwall toward the midspan. Here the low-energy fluid is accumulated and through a mixing process diffuses along the pitch; as a result midspan losses are greater than at the endwall. This result is surprising since, although the secondary vorticity was quite low, appreciable three-dimensional effects arose, affecting even the midspan flow.

It follows that also in these conditions it is not possible to consider the midspan flow as a two-dimensional reference flow, to be used for the estimation of the secondary effects.

An interesting feature that should be noted is that this phenomenon appears only at the smallest pitch-chord ratio; some weak traces can also be seen for the design pitch at the smallest incidence. It is presumed that the migration of the low-energy fluid toward the midspan occurs only when the passage vortex is very weak or virtually absent.

Mass-Averaged Results

The traverse data have been mass averaged across the pitch to get the spanwise distribution of the loss coefficient and of the exit angle. The secondary losses and deviation angles plotted in Figs. 9 and 10 are defined as:

$$\bar{\zeta}_{\mathrm{SEC}(z)} = \bar{\zeta}_{(z)} - \bar{\zeta}_{MS} \quad \Delta\beta_{\mathrm{SEC}(z)} = \bar{\beta}_{2MS} - \bar{\beta}_{2(z)}$$

The midspan values are assumed to be representative of the two-dimensional reference flow.

At the lowest incidence the loss distribution presents the maximum at the endwall and looks not too much different from the one of a boundary layer. For the lowest pitch the presence of negative values reveals that, as already noticed, the midspan flow is affected by secondary effects.

As the incidence angle is increased, the endwall loss decreases as the low-energy fluid is removed from the endwall by the passage vortex and is convected toward the midspan; as a consequence a peak is produced in the loss distribution. For larger pitch-chord ratios the position of the peak moves even more toward the midspan in agreement with the passage vortex behavior.

The yaw angle distribution at negative incidence presents very small underturning and overturning angles only close to the endwall, confirming the weakness of the secondary phenomena. Conversely, increasing the incidence, large overturning and underturning take place and the extension of the two-dimensional flow is progressively reduced. This trend is consistent with the greater intensity of passage and shed vortex previously shown.

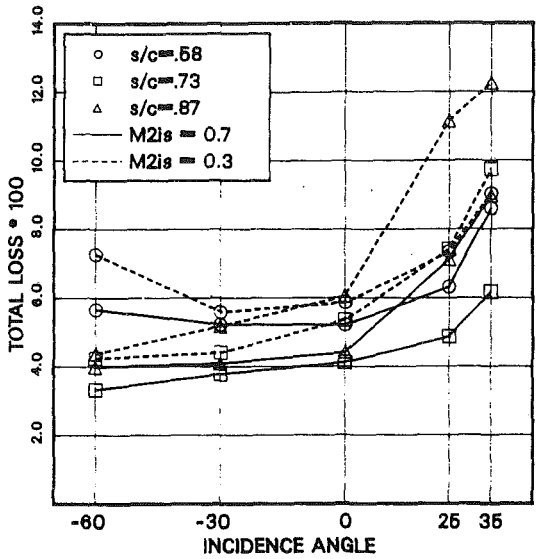

Fig. 11 Overall loss distributions for $M_{2is} = 0.7$ and for $M_{2is} = 0.3$

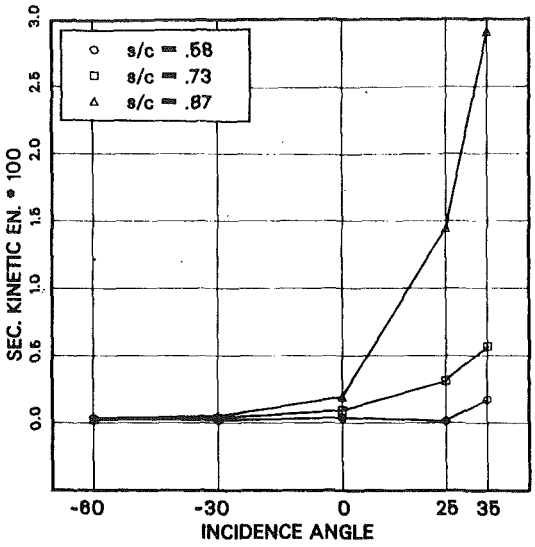

Fig. 13 Secondary kinetic energy

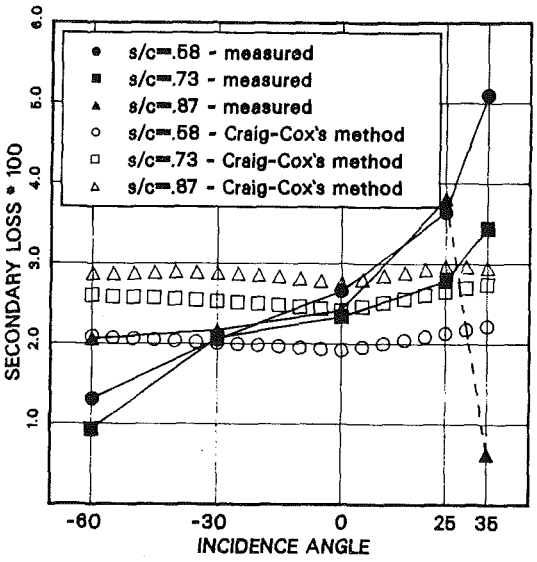

Fig. 12 Measured and predicted secondary losses

The large influence produced by the pitch-chord ratio should also be noted: At $s/c = 0.87$ both overturning and underturning angles are nearly twice the ones occurring at $s/c = 0.73$, and at $i = +35$ the difference between the maximum overturning and underturning becomes as great as 20 deg; however it has to be pointed out that in this last condition the secondary deviation distribution is not fully correct, as the three-dimensional effects have become so large as to affect the midspan values.

The overall loss $\bar{\bar{\zeta}}$, evaluated by the pitch and span mass average of the results, is plotted in Fig. 11, while Fig. 12 shows the secondary loss ζ_{SEC} obtained by subtracting the midspan value $\bar{\zeta}_{MS}$ from the overall loss. The dashed line indicates that the assumption considering the secondary flow superimposed on an undisturbed two-dimensional flow in the central part of the blade channel is no more valid. To complete the data, the overall secondary kinetic energy coefficient SKE is presented in Fig. 13.

It can be seen that the overall loss remains low even for high negative incidence, as the separation effects are counterbalanced by smaller secondary losses.

With increasing incidence, the overall loss undergoes a sharp increase that is particularly marked for the largest s/c. As shown in Fig. 13, this is mostly related to the growth of the secondary loss. However, at $i = +35$ for the largest pitch, it cannot be stated how much loss is due to secondary flows and how much is an incidence effect on two-dimensional flow. Observing the huge growth of SKE (up to 3 percent of the outlet kinetic energy), it appears clear that important dissipations take place when the secondary vortices of the two half-channels interact each other.

This is supported also by the results at $M_{2is} = 0.3$ presented in Fig. 11. While at $i = 0$ the overall loss is only slightly higher than at $M_{2is} = 0.7$, at positive incidences the loss increase is substantially higher ($\bar{\bar{\zeta}}$ grows up to 12 percent). Reducing the Mach number means the secondary flows shift toward the midspan (Perdichizzi, 1990), and therefore a strong interaction between counterrotating vortices, constrained in the midspan region, takes place.

The results plotted in Fig. 12 show that at design conditions Craig and Cox's correlation works reasonably well, as the level of the secondary losses is captured. But when the inlet angle is varied, both for positive and negative incidences, the relevant changes of the secondary losses are not adequately predicted, and large errors (up to 0.03) have been found.

Conclusions

The performance of a high-pressure steam turbine profile has been investigated for a wide range of off-design conditions. Detailed quantitative information has been reported for each combination of five incidence angles and three pitch-chord ratios. Data include profile Mach number distributions, area plots, spanwise deviation angle and loss distributions, profile and secondary losses.

The changes of the secondary flow structure in a downstream plane have been shown in detail. A clear relationship between the blade loading in the first part of the blade passage and the intensity of the secondary flows has been observed: High levels of streamwise vorticity and intense crossflows at the endwall take place at large incidence angles and low solidities. Heavy modifications have been found in the deviation angle distributions: The maximum overturning angle varies from almost zero up to 15 deg.

As the incidence angle and the pitch-chord ratio are increased, the region covered by secondary flows extends progressively toward the midspan. For extreme conditions the vortices of the two halves of the flow channel meet at midspan and interact with each other; as a consequence the overall secondary loss and the exit flow angle undergo a huge increase.

The application of the Craig and Cox's method provided

unrealistic secondary loss estimation, especially at inlet angles different from the design.

The comprehensive body of data here presented can be a useful reference for evaluating secondary flow effects in designing new turbines, or for establishing more up-to-date correlations for secondary loss and deviation angle prediction.

Finally, these data are also suitable to be utilized for assessing the accuracy of viscous three-dimensional methods, under quite different loading conditions, for which viscous effects vary significantly.

Acknowledgments

The authors wish to thank Ansaldo Componenti s.r.l. for the permission to publish the experimental data and Dr. M. Savini for the oil flow visualizations. The invaluable support by Mr. C. De Ponti and Mr. G. B. Daminelli is gratefully acknowledged.

References

Ainley, D. C., and Mathieson, G. C. R., 1951, "A Method of Performance Estimation for Axial-Flow Turbines," British Aeronautical Research Council, R&M 2974.

Bassi, F., and Perdichizzi, A., 1987, "Secondary Flow Development Downstream of a Turbine Cascade," *Proceedings 1987 Tokyo Gas Turbine Congress*, Vol. II, pp. 123–130.

Bassi, F., and Savini, M., 1992, "Secondary Flows in a Transonic Cascade: Validation of a Three-Dimensional Navier Stokes Code," ASME Paper No. 92-GT-62.

Craig, H. R., and Cox, H. J. A., 1971, "Performance Estimation of Axial Flow Turbines," *Proceedings of the Institution of Mechanical Engineers*, Vol. 185 32/71, pp. 403–423.

Dunham, J., and Came, P. M., 1970, "Improvement to the Ainley-Mathieson Method of Turbine Performance Prediction," ASME *Journal of Engineering for Power*, Vol. 92, pp. 252–256.

Gregory-Smith, D. G., Graves, C. P., and Walsh, J. A., 1988a, "Growth of Secondary Losses and Vorticity in an Axial Turbine Cascade," ASME JOURNAL OF TURBOMACHINERY, Vol. 110, pp. 1–8.

Gregory-Smith, D. G., Walsh, J. A., Graves, C. P., and Fulton, K. P., 1988b, "Turbulence Measurements and Secondary Flows in a Turbine Rotor Cascade," ASME JOURNAL OF TURBOMACHINERY, Vol. 110, pp. 479–485.

Hodson, H. P., and Dominy, R. G., 1987a, "Three-Dimensional Flow in a Low-Pressure Turbine Cascade at Its Design Condition," ASME JOURNAL OF TURBOMACHINERY, Vol. 109, pp. 177–185.

Hodson, H. P., and Dominy, R. G., 1987b, "The Off-Design Performance of a Low-Pressure Turbine Cascade," ASME JOURNAL OF TURBOMACHINERY, Vol. 109, pp. 201–209.

Langston, L. S., Nice, M. L., and Hooper, R. M., 1977, "Three-Dimensional Flow Within a Turbine Cascade Passage," ASME *Journal of Engineering for Power*, Vol. 1, pp. 21–28.

Marchal, P., and Sieverding, C. H., 1977, "Secondary Flows Within Turbomachinery Bladings," AGARD Conf. on Secondary Flow in Turbomachines, AGARD CP-214, Paper No. 11.

Moore, J., and Adhye, R. Y., 1985, "Secondary Flow and Losses Downstream of a Turbine Cascade," ASME *Journal of Engineering for Gas Turbines and Power*, Vol. 107, pp. 961–968.

Moore, J., Shaffer, D. M., and Moore, J. G., 1987, "Reynolds Stresses and Dissipation Mechanism Downstream of a Turbine Cascade," ASME JOURNAL OF TURBOMACHINERY, Vol. 109, pp. 258–267.

Osnaghi, C., and Perdichizzi, A., 1990, "Aerodynamic Measurements in Turbine Cascades at High Mach Number," *Proceedings of 10th Symposium on Measuring Techniques for Transonic and Supersonic Flows in Cascades and Turbomachines*, Von Karman Institute, Sept. 17–18.

Perdichizzi, A., Ubaldi, M., and Zunino, P., 1989, "Secondary Flows and Reynolds Stress Distributions Downstream of a Turbine Cascade at Different Expansion Ratios," AGARD Conf. on Secondary Flows in Turbomachines, AGARD CP-269, Paper No. 6.

Perdichizzi, A., 1990, "Mach Number Effects on Secondary Flow Development Downstream of a Turbine Cascade," ASME JOURNAL OF TURBOMACHINERY, Vol. 112, pp. 643–651.

Sharma, O. P., and Butler, T. L., 1987, "Predictions of Endwall Losses and Secondary Flows in Axial Flow Turbine Cascades," ASME JOURNAL OF TURBOMACHINERY, Vol. 109, pp. 229–236.

Sieverding, C. H., 1985, "Recent Progress in the Understanding of Basic Aspects of Secondary Flow in Turbine Blade Passages," ASME *Journal of Engineering for Gas Turbines and Power*, Vol. 107, pp. 248–257.

Yamamoto, A., 1987, "Production and Development of Secondary Flows and Losses in Two Types of Straight Turbine Cascades: Part 1: Stator Case," ASME JOURNAL OF TURBOMACHINERY, Vol. 108, pp. 186–193.

Yamamoto, A., and Nouse, H., 1988, "Effects of Incidence on Three-Dimensional Flows in a Linear Turbine Cascade," ASME JOURNAL OF TURBOMACHINERY, Vol. 110, pp. 486–496.

Zunino, P., Ubaldi, M., and Satta, A., 1987, "Measurements of Secondary Flows and Turbulence in a Turbine Cascade Passage," ASME Paper No. 87-GT-132.

APPENDIX

Blade Profile Coordinates

	X p.side	Y p.side		X s.side	Y s.side
1	0.0000	0.0000	56	33.9238	40.5980
2	0.1266	1.2015	57	33.6978	39.3938
3	0.5682	2.3260	58	33.4659	38.1907
4	1.2929	3.2927	59	33.2290	36.9807
5	2.2484	4.0319	60	32.9864	35.7878
6	3.3661	4.4902	61	32.7381	34.5880
7	4.5870	4.8152	62	32.4843	33.3895
8	5.7987	5.1725	63	32.2249	32.1920
9	6.9927	5.5851	64	31.9601	30.9958
10	8.1684	6.0474	65	31.6900	29.8008
11	9.3293	6.5455	66	31.4146	28.6069
12	10.4767	7.0742	67	31.1340	27.4143
13	11.6063	7.6398	68	30.8482	26.2229
14	12.7107	8.2531	69	30.5570	25.0329
15	13.7841	8.9192	70	30.2599	24.2367
16	14.8237	9.6369	71	29.9566	22.6572
17	15.8290	10.4020	72	29.6468	21.4719
18	16.7993	11.2108	73	29.3299	20.2884
19	17.7343	12.0603	74	29.0048	19.1071
20	18.6337	12.9475	75	28.6705	17.9284
21	19.4976	13.8693	76	28.3259	16.7527
22	20.3264	14.8226	77	27.9697	15.5805
23	21.1212	15.8047	78	27.6010	14.4121
24	21.8828	16.8126	79	27.2186	13.2481
25	22.6126	17.8438	80	26.8216	12.0890
26	23.3120	18.8959	81	26.4087	10.9355
27	23.9828	19.9665	82	25.9782	9.7885
28	24.6268	21.0534	83	25.5280	8.6490
29	25.8427	23.2681	84	25.0562	7.5184
30	26.4190	24.3924	85	24.5611	6.3978
31	26.9775	25.5256	86	24.0418	5.2881
32	27.5200	26.6666	87	23.4975	4.1904
33	28.0475	27.8146	88	22.9252	3.1072
34	28.5711	28.9689	89	22.3199	2.0421
35	29.0621	30.1287	90	21.6769	0.9993
36	29.5518	31.2932	91	20.9940	-0.0178
37	30.0317	32.4619	92	20.2691	-1.0054
38	30.5023	33.6344	93	19.4964	-1.9560
39	30.9640	34.8104	94	18.6701	-2.8603
40	31.4169	35.9898	95	17.7952	-3.7179
41	31.8524	37.1724	96	16.8745	-4.5259
42	32.2978	38.3580	97	15.8858	-5.2484
43	32.7259	39.5466	98	14.8302	-5.8695
44	33.1472	40.7379	99	13.7264	-6.4003
45	33.5603	41.9317	100	12.5720	-6.8085
46	33.6002	42.0093	101	11.3764	-7.0725
47	33.6608	42.0721	102	10.1571	-7.1834
48	33.7369	42.1149	103	8.9339	-7.1322
49	33.8221	42.1340	104	7.7277	-6.9220
50	33.9091	42.1278	105	6.5566	-6.5646
51	33.9908	42.0968	106	5.4319	-6.0800
52	34.0600	42.0437	107	4.3598	-5.4880
53	34.1111	41.9729	108	3.3440	-4.8037
54	34.1397	41.8905	109	2.3846	-4.0420
55	34.1444	41.8031	110	1.4855	-3.2103
			111	0.7048	-2.2883
			112	0.1975	-1.1919

Shock Formation in Overexpanded Tip Leakage Flow

J. Moore
Mechanical Engineering Department,
Virginia Polytechnic Institute and
State University,
Blacksburg, VA 24061-0238

K. M. Elward
Gas Turbine Engineering and Development,
General Electric Company,
Schenectady, NY 12345

Shock formation due to overexpansion of supersonic flow at the inlet to the tip clearance gap of a turbomachine has been studied. The flow was modeled on a water table using a sharp-edged rectangular channel. The flow exhibited an oblique hydraulic jump starting on the channel sidewall near the channel entrance. This flow was analyzed using hydraulic theory. The results suggest a model for the formation of the jump. The hydraulic analogy between free surface water flows and compressible gas flows is used to predict the location and strength of oblique shocks in analogous tip leakage flows. Features of the flow development are found to be similar to those of compressible flow in sharp-edged orifices. Possible implications of the results for high-temperature gas turbine design are considered.

Introduction

Tip leakage flow through the clearance gaps of unshrouded turbomachinery blades is known to cause reductions in efficiency and performance (Roelke, 1973; Hourmouziadis and Albrecht, 1987). It is also known that enhanced heat transfer to the tips of turbine rotor blades, resulting from the separation and reattachment of the leakage flow, can be a major factor in determining blade life in high-temperature gas turbines (Moore et al., 1989). There have therefore been many recent studies of flow and heat transfer in tip gaps (Bindon, 1987; Metzger and Bunker, 1989; Metzger et al., 1991; Yaras et al., 1989). But most of these studies have considered only incompressible flow, and features of compressible flow such as overexpansion to high supersonic Mach numbers, shock formation within the tip gap, and shock boundary layer interaction have received little attention. It is important that this compressible flow physics be understood sufficiently well to be included in the turbine design process.

Consider, for example, turbine rotor blades in gas turbines operating with transonic flow. Around the airfoil, the flow accelerates to supersonic Mach numbers near the suction surface in regions of low static pressure. Similarly flow passing through the tip clearance gap will accelerate as the pressure falls. But its path is not as smooth as that around the airfoil profile. Efforts are made to reduce the leakage flow by using sharp corners, for example on the pressure side, and cavities. The flow may, therefore, overexpand locally and exhibit regions of supersonic flow and complex compressible flow structure.

In an attempt to shed some light on compressible flow development in tip gaps, Henry and Moore (Moore et al., 1989) made a preliminary study using a water table flow simulation. Using the hydraulic analogy between free surface liquid flow and two-dimensional compressible flow (Johnson, 1964; Laitone, 1952), they gained some insight into possible Mach number distributions and shock patterns to be found in turbine tip clearance gaps. It appeared that overexpansion of flow around the pressure surface corner leads to an oblique shock wave, which extends from the inlet corner region to the shroud wall at about two tip gap heights into the tip gap and then reflects back to the turbine blade tip. For tip gap exit pressures corresponding to blade suction surface Mach numbers greater than 1.0, they found local maximum Mach numbers within the tip gap in the range of about 1.5 to 1.8.

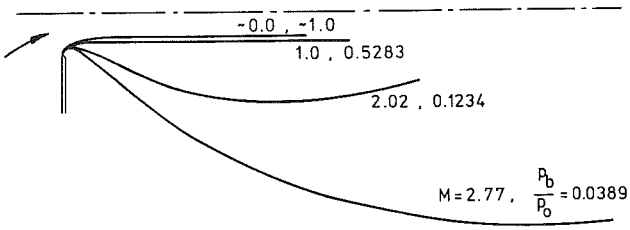

Fig. 1 Free streamlines for inviscid flow of air from a half-slit with various back pressures; calculated by Benson and Pool

Compressible Orifice Flows. Although little was found in the literature about compressible tip gap flows, much research has been done on compressible orifice flows. Benson and Pool (1965) describe early research in this area.

Benson and Pool numerically solved the equations for steady, isentropic flow of air through a two-dimensional slit. They then compared the results with Schlieren photographs and interferograms. Figure 1 shows the computed free streamlines for various back pressures. The flows range from incompressible flow $p_b/p_o \sim 1.0$, $M \sim 0.0$, to sonic flow, $p_b/p_o = 0.5283$, $M = 1.0$, to choked flow, $p_b/p_o = 0.0389$, $M = 2.77$.

Consider flow accelerating along the orifice wall to the sharp corner. If the back pressure is low enough to cause supersonic flow, this flow will undergo a Prandtl-Meyer expansion at the corner to the free-stream Mach number. As a result the flow turns through the corresponding expansion of angle. The free streamline then continues to turn through a further 90 deg to the point of its maximum (downward) slope. Subsequently the jet reaches a maximum width followed by a contraction (as the free streamline turns upward again).

Contributed by the International Gas Turbine Institute and presented at the 37th International Gas Turbine and Aeroengine Congress and Exposition, Cologne, Germany, June 1-4, 1992. Manuscript received by the International Gas Turbine Institute January 13, 1992. Paper No. 92-GT-1. Associate Technical Editor: L. S. Langston.

For subsonic and sonic flow, the jet simply contracts to an asymptotic jet width. This width is $\pi/(\pi+2)=0.61$ of the slit width for incompressible flow and 0.74 of the slit width for sonic flow, as seen in Fig. 1. With supersonic flow, the jet width contracts and then expands. At a free-stream Mach number of about 1.3 ($p_b/p_o \sim 0.36$), the maximum width of the jet is equal to the slit width. At choked flow, the maximum width is about five times the slit width.

Norwood (1961) performed a computational study similar to that of Benson and Pool. He concentrated mostly on flow near the slit. He also performed experimental work on jet reattachment in two-dimensional models of a flapper valve. The geometry of these was like that of the slit in Fig. 1 except that downstream of the minimum area a straight wall was inclined downward at an angle of 22-1/2 deg to the horizontal. This effectively produced a tip gap with a sharp inlet corner and a linearly increasing height. Norwood visualized the flow with shadowgraph pictures.

At low upstream stagnation pressures ($p_b/p_o > \sim 0.23$), the jet in Norwood's models followed the horizontal wall like the subsonic and just supersonic flows in Fig. 1. Further increase in the upstream pressure ($p_b/p_o < \sim 0.23$), however, caused the jet to jump to the inclined wall. Norwood noted that in his two-dimensional models the flow jumped at a relatively constant pressure ratio. This suggested that the only characteristic parameter for the flow development was the Mach number. It also indicated that the phenomenon of reattachment on the inclined wall was, initially at least, a compressibility effect depending on the Mach number rather than a frictional effect.

In a shadowgraph picture of flow along the inclined wall, Norwood observed two features of interest in the present study. The first was "a teardrop-shaped region," or "bubble," at the edge of the orifice where the flow is rapidly accelerating and the streamlines are highly curved. Norwood argued that the pressure in the bubble was very low because of the entrainment of the air inside into the main stream. The second interesting feature was an oblique shock just downstream of the throat starting on the inclined wall at the end of the bubble. This is due to the change in direction the supersonic flow encounters when it contacts the wall.

Hydraulic Analogy. Hydraulic analogies are used to translate water table results into useful compressible flow ideas. Two procedures are suggested in the literature, the classical analogy, as used by Henry and Moore, and a modified analogy, which was found to be more relevant to the present work.

The classical analogy compares the reversible change in depth of a shallow water flow with the two-dimensional isentropic flow of an ideal gas. The velocity of a wave moving on the free surface, taken as $\sqrt{gh}$, is considered analogous to the speed of sound in the gas, $\sqrt{kRT}$. So the Mach number, $M = v/\sqrt{kRT}$, and the Froude number $F = v/\sqrt{gh}$, are also analogous. From continuity and energy considerations, the water depth ratio is related to the following aerodynamic ratios:

$$\frac{h}{h_o} \equiv \left[\frac{\rho}{\rho_o} = \sqrt{\frac{p}{p_o}} = \frac{T}{T_o}\right]. \tag{1}$$

When comparing the results of water and air flows there are two limitations to this analogy:

1 The "analogue gas" described by Eq. (1) has a ratio of specific heat capacities, $k=2$, instead of 1.4 for air.

2 When shock waves are present, the isentropic assumption of the analogy is violated.

These limitations were discussed by Ippen and Harleman (1952), who also noted that most supersonic flows are made up of combinations of compression shocks and expansions. They therefore compared hydraulic and gas flows with shock and rarefaction waves to see if there was a more appropriate analogy. They found that the density ratio was the only aerodynamic property that agreed reasonably well with the hydraulic depth ratio, i.e.,

$$\frac{h}{h_o} \cong \frac{\rho}{\rho_o}. \tag{2}$$

The modified hydraulic analogy proposed by Ippen and Harleman was then "to use the measured depth ratio at any point in the flow field only to determine the analogous density ratio. Such quantities as pressure and local Mach number are then calculated from the measured density ratio by means of the applicable aerodynamic relations."

Wave Velocity. In practice, two factors, in addition to the water depth, h, influence the wave velocity of water tables. These are the wavelength, λ, and the surface tension of the water.

The term shallow water refers to $h \ll \lambda$, and it is for wavelengths much larger than the water depth that the wave velocity is $\sqrt{gh}$. So it is desirable to test at small water depths with waves of long wavelength. Laitone (1952) has noted that it is difficult to use a flowing water channel with a depth of only 0.6 cm because of flow nonuniformities over the fixed bottom. This observation agrees with Johnson's experimental evidence that depths of the order of 0.6 to 1.3 cm are best (Johnson, 1964). Wavelengths should then be of the order of 10 cm.

Capillary waves arise when the surface of the water vibrates as a membrane. Johnson reports that reducing the surface

Nomenclature

A, B, C, D, E = test configuration, Fig. 3
F = Froude number
g = acceleration due to gravity
h = tip gap height or water depth
k = ratio of specific heat capacities = c_p/c_v
l = length
M = Mach number
Nu = Nusselt number
p = static pressure
R = gas constant
T = temperature or surface tension
v = velocity
w = water channel half-width
x, y = Cartesian coordinates, Fig. 2
x_i = distance from orifice edge to the point of intersection of the free streamline with the orifice wall
β = oblique hydraulic jump angle
δ = deflection or turning angle
λ = wavelength of water wave
ρ = density
σ = oblique shock angle

Subscripts

b = back or downstream conditions
d = dimple
i = intersection point
m = line of median heights
max = maximum
p = line of maximum heights
0 = total or upstream conditions
1 = conditions upstream of shock or hydraulic jump
2 = conditions downstream of shock or hydraulic jump
∞ = fully developed

tension as much as possible will help lessen the effect of these waves relative to the gravity waves. Laitone also suggests that their relative effect may be practically eliminated by using a larger model.

Present Contribution. The present study is aimed at further understanding the mechanism of shock formation near the inlet of the tip clearance gap. The flow structure is related to the development of compressible flow in sharp-edged orifices. Particular features of interest include the length scale of the formation process and the strength of the shocks produced.

The experiments were performed on the same water table used by Henry and Moore, with some modification. Larger scale models were used to improve the hydraulic analogy and to increase the resolution of the flow structure. The modified hydraulic analogy of Ippen and Harleman (1952) is used to calculate analogous compressible gas flows.

Experimental Apparatus and Procedure

Water Table. The water table apparatus used in this study is described by Elward (1989). The table itself consists of two large tanks each about 0.22 m^3 in volume on either end of a glass table of dimensions 0.91×0.61 m. Flow across the table is provided by a pump.

Measurement of the water heights was accomplished by a traversing micrometer with a least count of 0.001 in. (0.0254 mm). Distances in either the longitudinal or latitudinal directions were measured with 0.1 in. (2.54 mm) least count scales, each fitted with a vernier scale allowing measurement to the nearest 0.01 in. (0.254 mm).

The table was level to within 0.25 mm across the entire table surface. Since the various test sections used were no larger than 19.8 × 7.6 cm, the table within the test section was level to within about 0.08 mm.

As mentioned previously, it is desirable to reduce the surface tension of the water as much as possible. Johnson reports using photographic wetting agents to accomplish this. The surface tension in the present tests was kept at about 30 dynes/cm by adding 4 ml of Kodak Photoflo 600 per gallon of water.

Test Sections. The test sections used for this investigation were constant area channels (or orifices) assembled using two rectangular aluminum blocks. The corner at the leading edge (entrance to the channel) was machined as sharp as possible to ensure an entrance modeling a sharp-edged orifice. Also, the channel sidewall and the upstream side of the blocks were machined smooth to avoid interference with the flow.

A representative sketch of the test section is shown in Fig. 2. The desired flow regime is sketched within the test section. The location of the origin and the axes used to measure channel coordinates are also shown in the figure. The length/width ratios of the channels were chosen such that the waves formed near the corners of the channel entrance intersected within the channel, but their reflections from the channel centerline did not intersect the channel wall.

In all, five test cases were studied. These are summarized in Fig. 3, labeled as cases *A* through *E*. There are two basic configurations, symmetric and one-sided. For the symmetric configurations, cases *B* and *C*, the blocks were placed as shown in the example of Fig. 2. In doing so, a tip gap with an inviscid shroud wall and its mirror image are modeled. To obtain the one-sided geometries, cases *A*, *D*, and *E*, a strip of stainless steel sheet metal was placed along the length of the water table to give the proper channel width. In these cases, the tip gap and a shroud wall are modeled.

Also seen in Fig. 3, two channel length to half-width ratios (l/w) were chosen to provide different geometries. Cases *A*, *B*, and *C* all have $l/w = 2.6$, but each has a different half-width, *w*. In this way, the effect of scaling on the flow can be examined. Configurations *D* and *E* have $l/w = 1.32$ and the same half-width, but different overall water depth ratios, h_b/h_o. Thus, the effect of h_b/h_o ($\sqrt{p_b/p_o}$ by the classical hydraulic analogy) can be investigated. In addition, configurations *A* and *D* can be compared to examine the effect of geometry on the flow. Both have similar half-widths and h_b/h_o, but each has a different l/w.

The locations for the measurement of h_o and h_b are shown in the sample configuration in Fig. 2. Three criteria were used in choosing values for these depths. First, h_o was chosen such

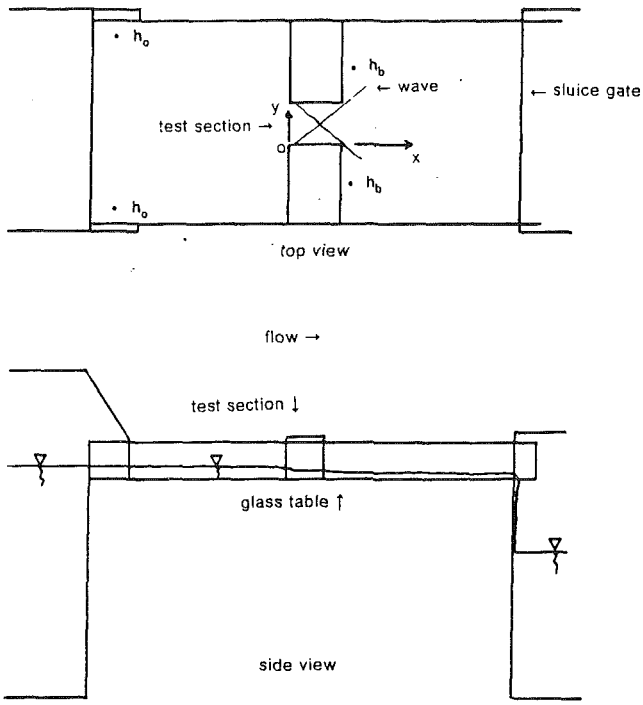

Fig. 2 Representative test section and flow regime

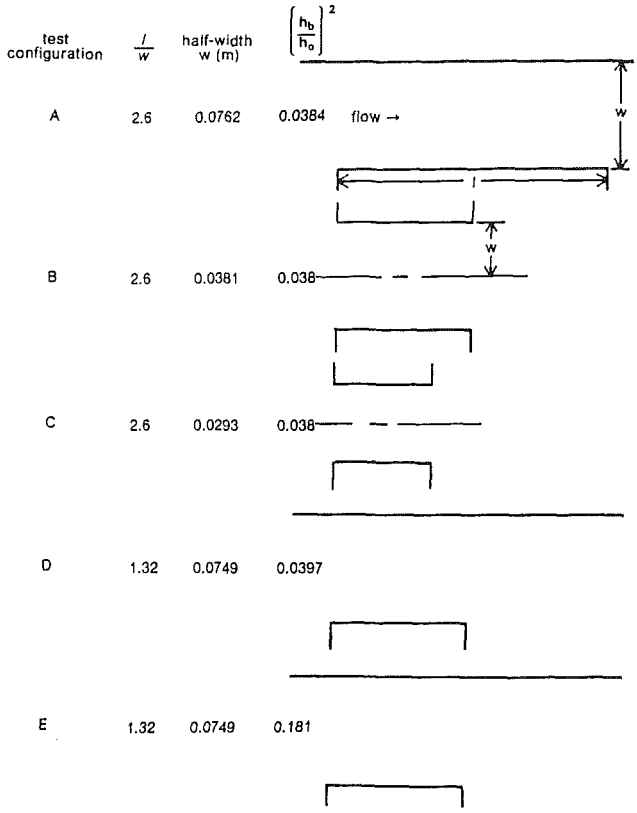

Fig. 3 Test section configurations

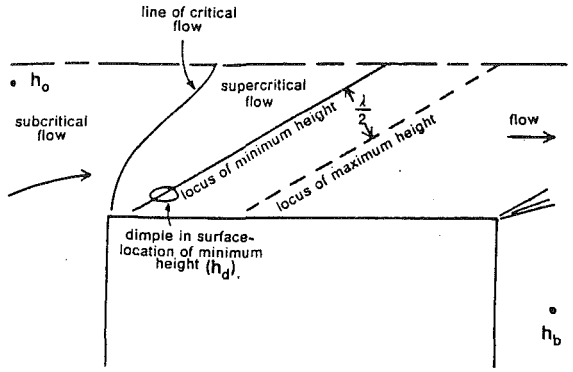

Fig. 4 Schematic of flow in the water channel

that the depth of water in the channel would be in the range of 0.6 to 1.3 cm, where the hydraulic analogy would hold best. It was decided to choose h_b very low to give high Froude numbers and stronger hydraulic jumps. Finally, h_o and h_b were selected to give overall height ratios, h_b/h_o, which would yield pressure ratios similar to those used by Norwood (1961). During the course of each test, h_o remained constant to within 0.002 in. (0.05 mm).

For each test a set of water heights upstream and in the channel was taken. Moving along a line at a fixed distance from the channel wall, a fixed y value, surface height measurements were taken at points along the direction of flow (in the positive x direction). This was done across the entire channel half-width, creating a grid of water heights, which could then be easily converted to a grid of height ratios, h/h_o, for use in data analysis.

Experimental Results

Major Features of Channel Flow. Flow observed on the water table is shown schematically in Fig. 4. The figure shows one-half of the symmetric channel flow with the direction of flow from left to right. Starting from h_o, the flow accelerates from subcritical ($F<1$, $h/h_o>2/3$) to critical ($F=1$, $h/h_o=2/3$). As seen from the shape of the line of critical flow in Fig. 4, the flow accelerates more rapidly near the corner of the channel. The flow then remains supercritical ($F>1$, $h/h_o<2/3$) throughout the rest of the channel.

Associated with the rapid acceleration of the flow around the corner of the channel entrance is a location of minimum water height, h_d. The location of minimum height appears as a dimple in the water surface. This dimple is the beginning of a trough or line of minimum water height, which extends to the centerline, gradually becoming less sharp.

The trough is the beginning of an oblique hydraulic jump, which is also shown in Fig. 4. This jump results from the turning of the flow after it accelerates around the corner. The distance measured perpendicularly from the trough to the line labeled locus of maximum height corresponds to one-half of the wavelength ($\lambda/2$) of the hydraulic jump.

The flow then exits the channel and expands to the downstream water height, h_b. At the corner of the channel exit, an expansion fan is present, as seen in Fig. 4.

Test Results. The results of the five test cases are presented here. First, the results of the basic configuration, Case *B* in Fig. 3, are presented along with the analysis used to obtain the results. Then, a summary of the corresponding results for the other four cases will be presented.

The basic configuration was symmetric with $(h_b/h_o)^2 = 0.038$. Surface height measurements were taken and a contour plot of h/h_o was prepared. This plot, along with a plot of corresponding Froude numbers, appears in Fig. 5. Note the

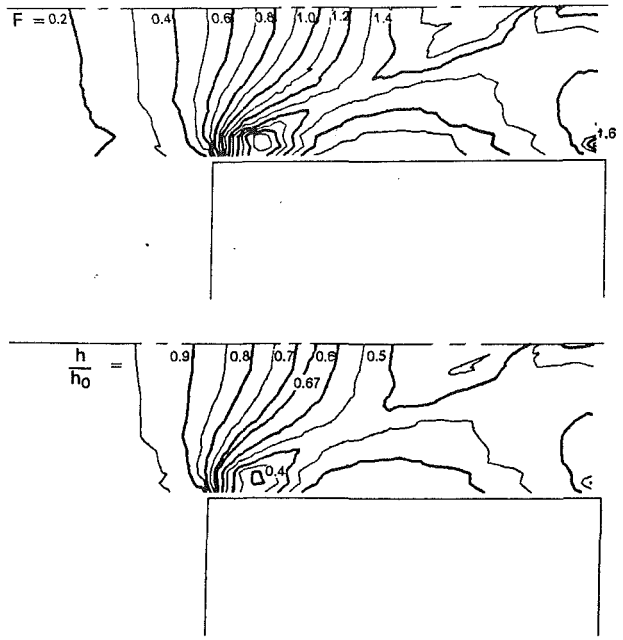

Fig. 5 Contours of Froude number and height ratio, case *B*

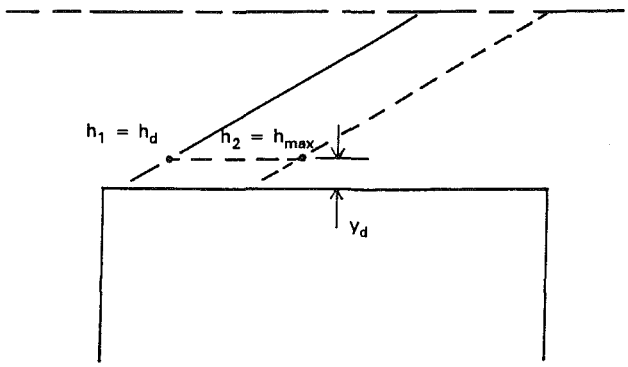

Fig. 6 Quantities used to determine strength of jump

regions of flow in Fig. 5 correspond to those described in the flow schematic in Fig. 4.

Figure 5 also shows the rapid acceleration of the flow around the corner with a dimple occurring at $x=1.14$ cm, $y=0.38$ cm. The height ratio at this point is $h_d/h_o=0.394$. Associated with this minimum height ratio is a maximum or dimple Froude number, F_d. For this case, $F_d=1.75$.

The hydraulic jump discussed for the schematic of Fig. 4 was seen to exist in all the test cases. In order to compare the jumps observed in each case, oblique hydraulic jump relations from classical hydraulic theory are used to determine the strength and angle of each wave. The analysis used is presented below, with reference to the schematics shown in Figs. 6 and 7.

As Fig. 6 shows, the minimum water height, h_d, is defined as h_1, or the water height just before the hydraulic jump. The height just after the hydraulic jump, h_2, is define as the maximum height the water reaches along the line $y=y_d$, where y_d is the y coordinate of the dimple. In doing so, the ratio h_2/h_1, a measure of the strength of the hydraulic jump, can be found.

For comparison, a method was developed for predicting the angle of the wave from the measured surface heights. This is based on the conceptual model of free streamline flow intersecting a wall. Figure 7 shows this schematically. In examining the data, it is helpful to note the location on the channel wall where the oblique wave forms. This location was estimated from the contour plots of Fig. 5. An average of the loci of

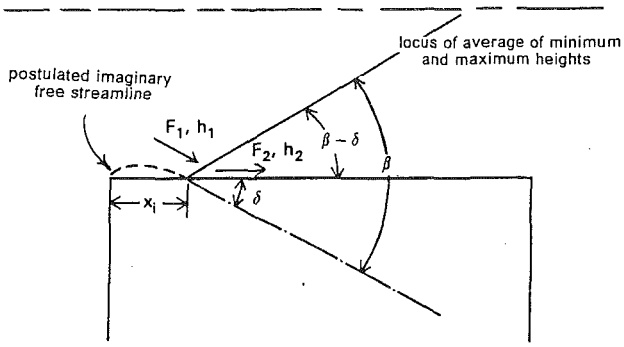

Fig. 7 Quantities used to determine jump angle

maximum and minimum heights was drawn. The point where this median line intersects the channel wall is then considered the location of the wave formation. The distance from the channel entrance to this point of intersection, x_i, is as shown in Fig. 7. It is the point where the "free streamline" contacts the wall causing the flow to turn.

To calculate the angle of the wave, the following equations are used in reference to Fig. 7 (Ippen, 1982)

$$F_1 = \sqrt{2\left(\frac{h_o}{h_1} - 1\right)} \tag{3}$$

$$\sin\beta = \frac{1}{F_1}\sqrt{\frac{1}{2}\frac{h_2}{h_1}\left(\frac{h_2}{h_1}+1\right)} \tag{4}$$

$$\tan(\beta-\delta) = \frac{\tan\beta}{\left(\frac{h_2}{h_1}\right)} \tag{5}$$

For the basic configuration, case B,

$$\frac{h_1}{h_o} = \frac{h_d}{h_o} = 0.394 \text{ and } \frac{h_2}{h_o} = 0.651$$

resulting in

$$\frac{h_2}{h_1} = 1.65.$$

Using these values in the above equations yields

$$F_1 = 1.75$$

$$\beta = 57.6 \text{ deg}$$

$$\beta - \delta = 43.6 \text{ deg}$$

resulting in

$$\delta = 14.0 \text{ deg}$$

The measured angle, $\beta - \delta$, obtained in this case is 31 deg.

The other four cases were treated in a similar manner. Calculations were performed for all cases as above. The results of these calculations and the corresponding measurements are summarized in Table 1.

The measured wavelengths of the oblique hydraulic jumps are shown in Table 2. They are also expressed in channel half-widths, λ/w, and in terms of the dimple water depth, λ/h_d.

Discussion of Results

In this section, the oblique wave structure measured on the water table and its relevance to oblique shock wave formation in compressible tip gap flows are discussed. The validity of the water table models and of the simple hydraulic theory of the oblique wave formation are considered. The modified hydraulic analogy is applied to the data and the results are compared with available data and calculations for compressible flow through sharp-edged orifices.

Table 1 Summary of water table results

test config	l/w	half-width w(m)	$\left(\frac{h_b}{h_o}\right)^2$	$\frac{h_d}{h_o} = \frac{h_1}{h_o}$	$\frac{h_2}{h_1}$	F_d	β-δ° calc	meas	δ° calc
A	2.6	0.076	0.0384	0.40	1.49	1.75	40	37	11
B	2.6	0.038	0.038	0.39	1.65	1.75	44	31	14
C	2.6	0.029	0.038	0.44	1.41	1.60	45	31	10
A	2.6	0.076	0.0384	0.40	1.49	1.75	40	37	11
D	1.32	0.075	0.0397	0.28	2.09	2.29	31	35	20
E	1.32	0.075	0.181	0.35	1.59	1.93	35	28	13

Table 2 Wavelengths of oblique hydraulic jumps

test config	λ (cm)	$\frac{\lambda}{w}$	$\frac{\lambda}{h_d}$
A	6.4	0.84	7.8
B	3.4	0.89	4.1
C	3.0	1.02	3.7
A	6.4	0.84	7.8
D	6.2	0.83	9.4
E	3.7	0.50	5.3

Wave Angles. The measured angles, $\beta - \delta$, of the wave relative to the channel sidewall, as shown in Table 1 for cases A through E, are 37, 31, 31, 35, and 28 deg, respectively. The angles calculated using the data and classical hydraulic theory were 40, 44, 45, 31, and 35 deg, respectively. Since the classical theory was developed for uniform supercritical flow encountering a wedge imposing a uniform turning angle, whereas the present flow involves a nonuniform overexpanded flow around a corner impinging on a wall, some difference is to be expected. Overall, the largest models with the low downstream height (h_b/h_o) gave the best agreement, within three or four degrees.

Wavelengths. Page (1952) gives the equation for the velocity of a wave moving on the surface of a fluid as

$$V = \sqrt{\left(\frac{g\lambda}{2\pi} + \frac{2\pi T}{\rho\lambda}\right)\tanh\left(\frac{2\pi h}{\lambda}\right)}. \tag{6}$$

Figure 8 is a plot of wave velocity as a function of wavelength λ and water depth h as given by Eq. (6). This plot is for tap water with the reduced surface tension T of 30 dynes/cm, used in the present tests. It shows the effect of the surface tension term of Eq. (6). For small wavelengths, the velocity of the surface wave tends toward infinity. If the surface tension term is neglected, the velocities will approach zero for smaller and smaller wavelengths. As λ increases, the velocity approaches $\sqrt{gh}$. Since this is the velocity used in the analogy, it is important to run experiments in the range where velocity is not a function of wavelength, at larger wavelengths and/or more shallow depths.

The present tests were run with water depths between 0.66 and 1.38 cm, and the measured wavelengths, from Table 2, were from 3.0 to 6.4 cm. The ranges of operation of the five tests are shown in Fig. 8. It appears that tests A and D came closest to satisfying the requirement of the hydraulic analogy. In those cases, the values of the λ/h_d were 7.8 and 9.4, respectively. In the three other tests, B, C, and E, the values were smaller, between 3.7 and 5.3.

The measured wavelengths in Table 2 show that for given flow conditions, wavelength varies as channel half-width. For cases A through D, with $(h_b/h_o)^2 = 0.038$, the wavelength expressed in half-widths remains approximately constant, about

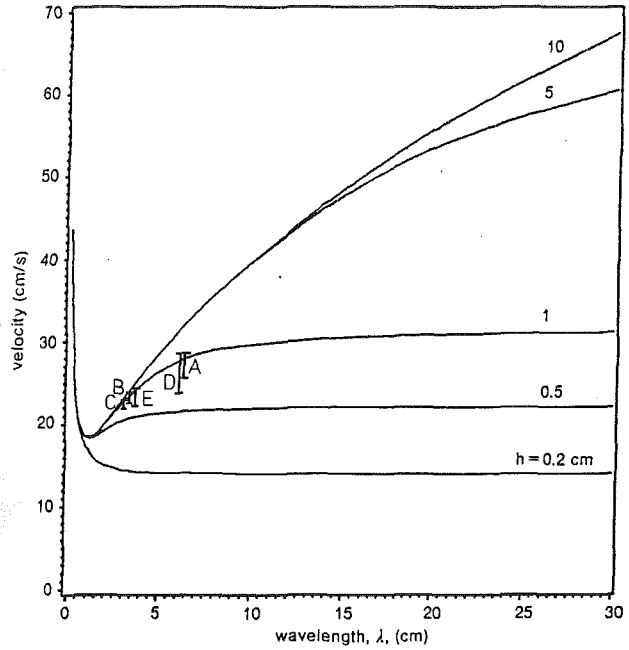

Fig. 8 Wave velocity as a function of wavelength and water depth: $T = 30$ dynes/cm

$\lambda/w = 0.9$. This agrees with Laitone's observation that a larger model will give larger wavelengths, thus reducing the effects of capillary waves. It also explains why the largest scale models, *A* and *D*, exhibit better shallow water behavior than the smaller models, *B* and *C*.

Analogous Compressible Flow. Using the modified hydraulic analogy of Ippen and Harleman, the compressible flows analogous to the measured water table flows may be calculated. Here, we consider the compressible flow analogous to the flow in Fig. 7. We wish to determine the Mach number M, the density ρ, and the oblique shock angle σ, corresponding to the Froude number F, the water depth h, and the oblique hydraulic jump angle β.

In the modified analogy, Eq. (2),

$$\frac{\rho_1}{\rho_o} = \frac{h_1}{h_o} \tag{7}$$

and

$$\frac{\rho_2}{\rho_1} = \frac{h_2}{h_1}. \tag{8}$$

The equations for the Mach number and the oblique shock angles corresponding to Eqs. (3)–(5) are then

$$M_1 = \sqrt{\frac{2}{k-1}\left[\left(\frac{\rho_o}{\rho_1}\right)^{k-1} - 1\right]} \tag{9}$$

$$\sin\sigma = \frac{1}{M_1}\sqrt{\frac{\dfrac{\rho_2}{\rho_1}}{\dfrac{k+1}{2} - \left(\dfrac{k-1}{2}\right)\dfrac{\rho_2}{\rho_1}}} \tag{10}$$

and

$$\tan(\sigma - \delta) = \frac{\tan\sigma}{\dfrac{\rho_2}{\rho_1}}. \tag{11}$$

Table 3 shows the results for air with $k = 1.4$. Comparing the results of Tables 1 and 3, we see that the Mach numbers are lower, 1.40–1.84, than the Froude numbers, 1.60–2.29; the shock angles are larger than the jump angles by 8–12 deg; but the calculated turning angles, δ, are about the same.

Table 3 Modified hydraulic analogy

test config	$\frac{\rho_1}{\rho_0} = \frac{h_1}{h_0}$	M_1 (k = 1.4)	$\frac{\rho_2}{\rho_1} = \frac{h_2}{h_1}$	σ-δ°	δ°
A	0.40	1.50	1.49	48	11
B	0.39	1.50	1.65	54	12
C	0.44	1.40	1.41	54	9
A	0.40	1.50	1.49	48	11
D	0.28	1.84	2.09	43	20
E	0.35	1.62	1.59	43	13

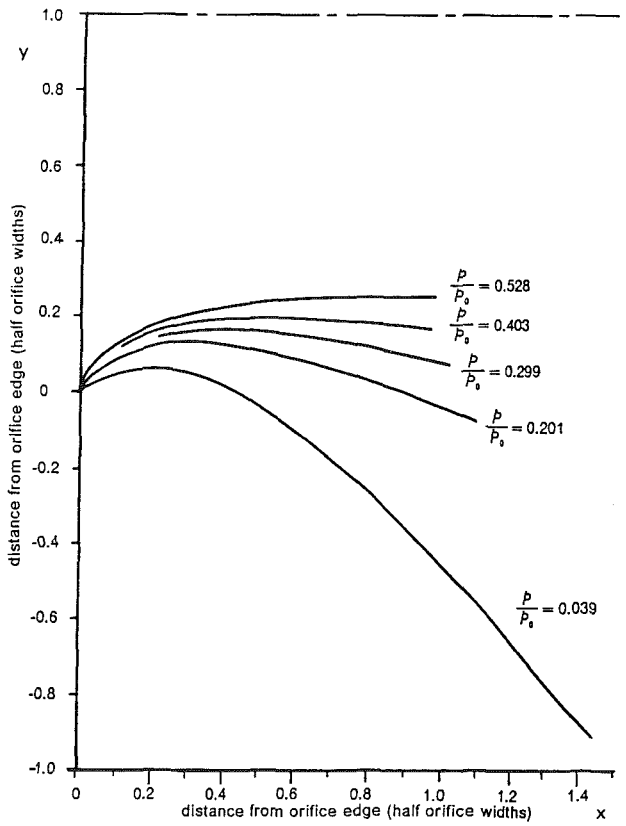

Fig. 9 Norwood's calculated free streamlines from a half-slit

Effective Wall Location of Wave Formation. Figure 9 shows the free streamlines calculated for sharp-edged orifice flows by Norwood.

From the free streamline results of Benson and Pool and of Norwood, Fig. 10 was constructed. This figure shows the distance, x_i, from the orifice entrance to the point of intersection of the free streamline with a line drawn from the orifice edge parallel to the orifice centerline, plotted against the free-stream Mach number. This distance is plotted as x_i/w, or the distance in orifice half-widths. The figure shows that at higher Mach numbers, the free streamline intersects the "wall" closer to the orifice edge. As the Mach number decreases, the free streamline intersects the wall farther and farther downstream. The free streamline becomes parallel to the wall at a pressure ratio of about 0.36 or $M \sim 1.3$, as suggested by the results of Benson and Pool.

Figure 10 also plots the data for the five water table cases against the Mach number, M_1, from Table 3. Two points are plotted for each case, the location of the intersection of the line of median heights with the channel wall, denoted by the

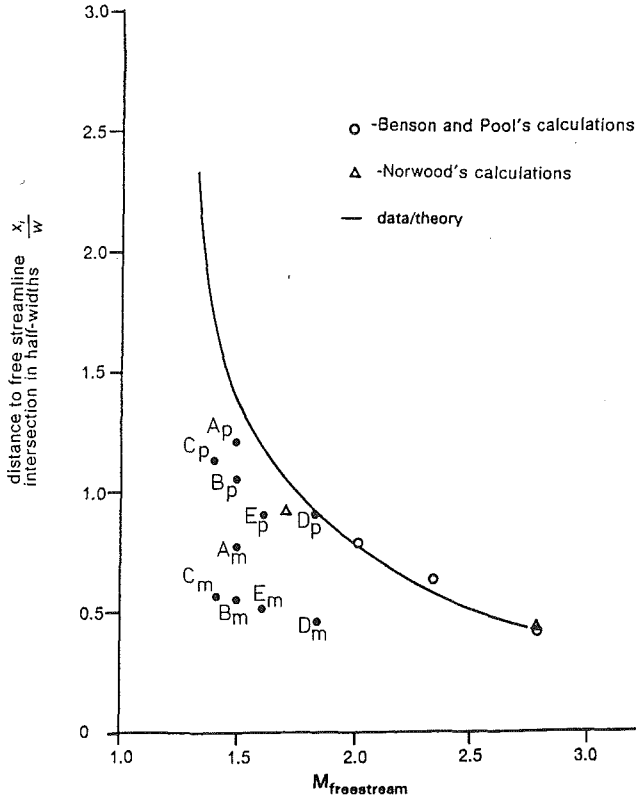

Fig. 10 Comparison of free streamline intersection with channel sidewall

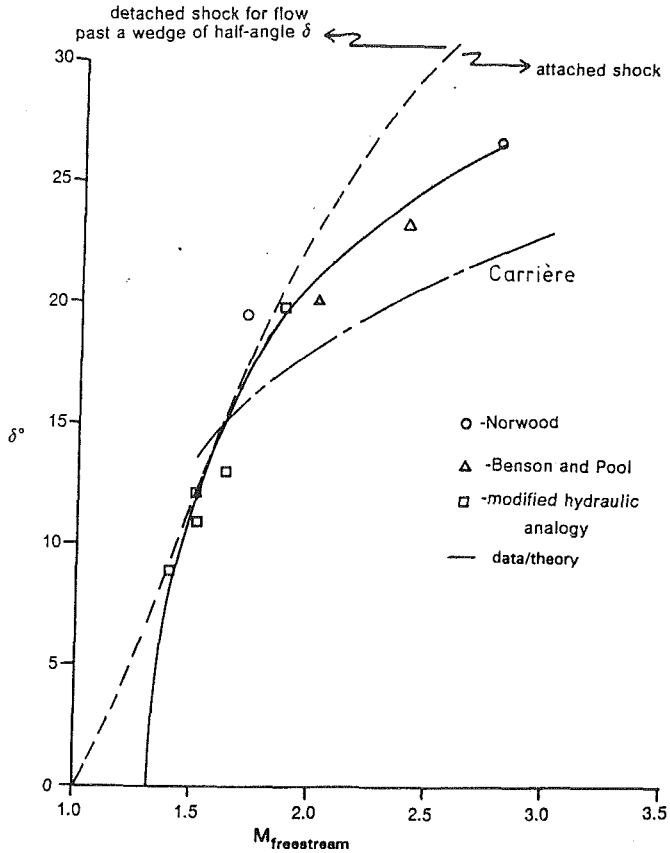

Fig. 11 Compressible flow turning angles

symbol m, and the location of the intersection of the line of maximum heights with the channel wall, denoted by the symbol p. The intersections for the lines of maximum height agree well with the wall locations predicted from the calculated compressible flow free streamlines. These data lie in the range $x_i/w = 0.9$–1.2. The trend in the data follows the predicted variation with free-stream Mach number; and tests A and D give the best agreement.

The angles of turn, δ, or equivalently the angles with which the free streamlines intersect the wall, are plotted against free-stream Mach number in Fig. 11. The figures shows the turning angles from Table 3 and the free streamline angles of Benson and Pool and of Norwood. As was seen in Fig. 10, for Mach numbers above about 1.3, the free streamline intersects the wall. The angle of intersection then becomes steeper as the Mach number increases. There is excellent agreement between the present results and the calculated compressible flow results.

The line of minimum Mach number required for an attached shock for a given δ is also shown on Fig. 11. The present data lie in the range M = 1.4–1.84 and they follow this line very closely. This implies that the shock formation is like that of an attached shock on a wedge of half-angle, δ.

Another interpretation of the shock formation is that it is like turbulent reattachment in supersonic flow. Carriere (1970) has presented a correlation of experimental results for two-dimensional flow. Again, Fig. 11 shows that this is in reasonable agreement with the data, but the trend is toward somewhat lower turning angles, or later reattachment, at higher Mach numbers. This perhaps supports the argument by Norwood that the phenomenon of reattachment on his inclined wall was a compressibility effect rather than a frictional effect.

Analogous Wave Formation in Compressible Flows. The results in Fig. 10 and 11 may be used to predict oblique shock formation in compressible flows. For example, consider a flow with a free-stream Mach number of 1.8, that is, a minimum pressure $p_1/p_o = 0.174$ (with $k = 1.4$). Figures 10 and 11 give

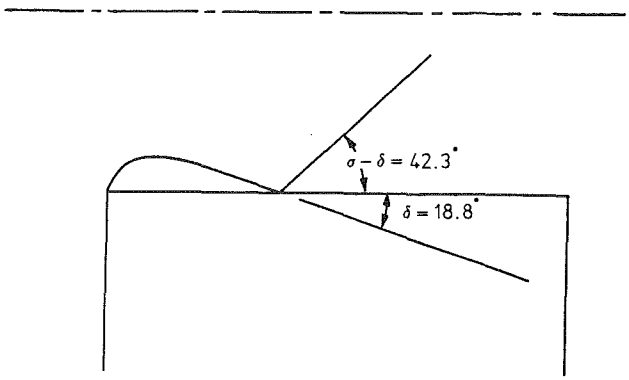

Fig. 12 Predicted shock formation in compressible gas flow with $M_{freestream} = 1.8$

the wave location and turning angle as $x_i/w = 0.96$ and $\delta = 18.8$ deg, respectively. Equations (9) and (10) may then be solved to get $\sigma = 61.1$ deg and $\sigma - \delta = 42.3$ deg. The resulting predicted flow is shown plotted in Fig. 12.

Implications for Jet Engine Heat Transfer. The two-dimensional, incompressible turbulent flow calculations of Moore et al. (1989) showed an area of enhanced heat transfer on the pressure side of a turbine blade tip as shown in Fig. 13. The heat transfer was enhanced by up to 1.8 times the downstream fully developed value in the first two to three tip gap heights. The estimated intersection of the free streamline with the sidewall of x_i/w between 0.4 and 1.4, observed in Fig. 10, would indicate a shock forming within this region of already enhanced heat transfer. The shock-boundary layer interaction could serve to further enhance the heat transfer. Increased heat transfer would lead to higher metal temperatures and increased rates of oxidation and material weight loss. This would reduce

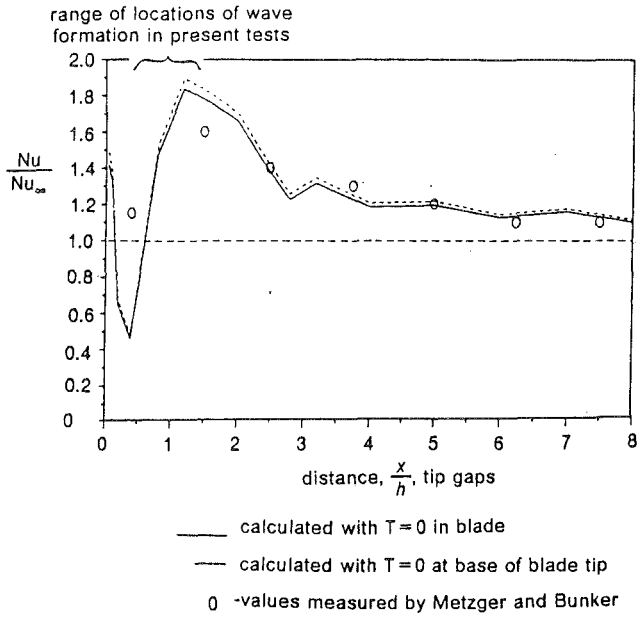

Fig. 13 Enhanced heat transfer to turbine blade tip

both the expected useful life of the turbine blade and the turbine efficiency.

Conclusions

Tests to study the formation mechanism of shocks in sharp-edged rectangular channels were performed to gain insight into the compressible flow in tip clearance gaps of turbomachinery blading. The flow was modeled on a water table using the hydraulic analogy. Tests were run with equivalent back pressure ratios, p_b/p_o, of about 0.04 and 0.2 on channels with aspect ratios (length to half-width, l/w) of 2.6 and 1.32.

The results observed on the water table suggest a model for the formation of an oblique hydraulic jump near the inlet to the channel. As the flow enters the channel, it accelerates around the corner, creating a region of minimum water height. The "free streamline" separates from the wall at the channel entrance; and, for Froude numbers greater than about 1.3, it curves back to intersect the channel sidewall. At this point, the free-stream flow is abruptly turned parallel to the sidewall, giving rise to an oblique hydraulic jump.

In the cases tested, the flow accelerated around the corner, reaching maximum Froude numbers of 1.6 to 2.3. A hydraulic jump at an angle of 28 to 37 deg to the channel wall appeared to start at the sidewall within 0.4–1.4 half-widths of the channel entrance. The results were analyzed using the hydraulic theory of oblique wave formation in supercritical flow over a wedge. This indicated that the flow was turned through an angle of 10 to 20 deg by the wall.

The modified hydraulic analogy of Ippen and Harleman and the theory of oblique shock wave formation in supersonic flow over a wedge allow analogous compressible flow behavior to be predicted. This gives maximum free-stream Mach numbers of 1.4 to 1.8, wave angles of 43 to 54 deg, and turning angles of 9 to 20 deg; as the free-stream Mach number increases, the angle of turn also increases. These predicted results compare well with the results of compressible sharp-edged orifice flow calculations found in the literature.

It appears that in a turbine, after separating from the inlet corner, the flow reattaches on the blade tip and an oblique shock is formed at 0.4–1.4 tip gap heights into the clearance gap. The resulting shock-boundary layer interaction may contribute to further enhancement of already high heat transfer to the blade tip in this region. This in turn could lead to higher blade temperatures and adversely affect blade life and turbine efficiency.

On the water table, for similar operating conditions, the ratio of the wavelength of the oblique hydraulic jump to the channel half-width was approximately constant. The largest scale models therefore came closest to satisfying the requirement of the hydraulic analogy that the wavelength be much greater than the water depth. The best agreement between the water table results analyzed using the modified hydraulic analogy and corresponding compressible flow results was obtained with the largest scale models.

Acknowledgments

The authors wish to thank Rolls-Royce plc, Aero Division, for supporting this work under a cooperative agreement with Virginia Polytechnic Institute and State University.

References

Benson, R. S., and Pool, D. E., 1965, "Compressible Flow Through a Two-Dimensional Slit," *Int. J. Mech. Sci.*, Vol. 7, pp. 315–336.

Bindon, J. P., 1987, "Measurement of Tip Clearance Flow Structure on the End-Wall and Within the Clearance Gap of an Axial Turbine Cascade," *Int. Conf. on Turbomachinery—Efficiency Prediction and Improvement*, Cambridge, United Kingdom, IMechE, pp. 43–52.

Carriere, P., 1970, "Analyse Theorique du Decollement et du Recollement Turbulents au Bord de Fuite d'un Aubage aux Vitesses Supersoniques," *Flow Research on Blading*, L. S. Dzung, ed., Elsevier Pub. Co., New York, pp. 210–242.

Elward, K. M., 1989, "Shock Formation in Overexpanded Flow—A Study Using the Hydraulic Analogy," M.S. Thesis, Virginia Polytechnic Institute and State University, Blacksburg, VA, Apr.

Hourmouziadis, J., and Albrecht, G., 1987, "An Integrated Aero/Mechanical Performance Approach to High Technology Turbine Design," AGARD Conference Proceedings No. 421 on Advanced Technology for Aero Gas Turbine Components, Paris, France.

Ippen, A. T., 1982, "Mechanics of Supercritical Flow," *Classic Papers in Hydraulics*, ASCE, New York.

Ippen, A. T., and Harleman, D. R. F., 1952, "Certain Quantitative Results of the Hydraulic Analogy to Supersonic Flow," *Proceedings of the 2nd Midwestern Conference on Fluid Mechanics*, Ohio Engineering Station Bulletin #149.

Johnson, R. H., 1964, "The Hydraulic Analogy and Its Use With Time Varying Flows," G.E. Research Laboratory Report No. 64-RL-(3755c), Aug.

Laitone, E. V., 1952, "A Study of Transonic Gas Dynamics by the Hydraulic Analogy," *J. of the Aeronautical Sciences*, Apr., pp. 265–272.

Metzger, D. E., and Bunker, R. S., 1989, "Cavity Heat Transfer on a Transverse Grooved Wall in a Narrow Flow Channel," ASME *Journal of Heat Transfer*, Vol. 111, pp. 73–79.

Metzger, D. E., Dunn, M. G., and Hah, C., 1991, "Turbine Tip and Shroud Heat Transfer," ASME JOURNAL OF TURBOMACHINERY, Vol. 113, pp. 502–507.

Moore, J., Moore, J. G., Henry, G. S., and Chaudhry, U., 1989, "Flow and Heat Transfer in Turbine Tip Gaps," ASME JOURNAL OF TURBOMACHINERY, Vol. 111, pp. 301–309.

Norwood, R. E., 1961, "Two Dimensional Transonic Gas Jets," Sc.D. Thesis, Massachusetts Institute of Technology, Cambridge, MA, June.

Page, L., 1952, *Introduction to Theoretical Physics*, D. Van Nostrand Company, Inc., New York.

Roelke, R. J., 1973, "Turbine Design and Application," A. J. Glassman, ed., NASA SP-290, pp. 125–131.

Yaras, M., Yingkang, Z., and Sjolander, S. A., 1989, "Flow Field in the Tip Gap of a Planar Cascade of Turbine Blades," ASME JOURNAL OF TURBOMACHINERY, Vol. 111, pp. 276–283.

S. H. Moustapha
Chief,
Turbine Aerodynamics,
Pratt & Whitney Canada, Inc.,
Montreal, Quebec, Canada

W. E. Carscallen
Senior Research Officer,
Combustion and Fluids Engineering Laboratory,
National Research Council,
Ottawa, Ontario, Canada

J. D. McGeachy
Professor,
Department of Mechanical Engineering,
Queen's University,
Kingston, Ontario, Canada

Aerodynamic Performance of a Transonic Low Aspect Ratio Turbine Nozzle

This paper presents detailed information on the three-dimensional flow field in a realistic turbine nozzle with an aspect ratio of 0.65 and a turning angle of 76 deg. The nozzle has been tested in a large-scale planar cascade over a range of exit Mach numbers from 0.3 to 1.3. The experimental results are presented in the form of nozzle passage Mach number distributions and spanwise distribution of losses and exit flow angle. Details of the flow field inside the nozzle passage are examined by means of surface flow visualization and Schlieren pictures. The performance of the nozzle is compared to the data obtained for the same nozzle tested in an annular cascade and a stage environment. Excellent agreement is found between the measured pressure distribution and the prediction of a three-dimensional Euler flow solver.

Introduction

Modern small turbomachines are the response of gas turbine engine manufacturers to the market demand for compact, fuel-efficient engines. Typical features employed in the turbine section of these engines are high pressure ratio and stage loading, combined with blade passages of small aspect ratio, high turning, and transonic Mach numbers. The resulting flow field within the turbine passages is highly three dimensional and prone to increased losses. The turbine designer must develop and exploit an improved understanding of the factors affecting the loss mechanisms in order to produce more efficient gas turbines.

A number of detailed experimental studies have been carried out in recent years to investigate the flow in a turbine passage. To date, most of these studies have been done in low-speed cascades due to their simplicity and low cost. Examples of subsonic testing are Sjolander (1975), Langston et al. (1976), Binder and Romey (1983), Sieverding et al. (1984), Yamamoto and Yanagi (1985), Mobarak et al. (1988), and Wegener et al. (1989). Such tests have provided a sound basis for clarifying the fundamental aspects of the flow field in a turbine passage and helped in identifying the major flow and geometric parameters affecting the various loss components.

The influences of compressibility and shock-boundary layer interaction on the flow and related losses are not fully understood but are needed to verify and calibrate the available numerical techniques. Most of the published data refer to rotor sections tested in a large aspect ratio planar cascade. Graham and Kost (1979) tested two different rotor profiles with a turning angle of 128 deg and an aspect ratio of 2.0. The blades were tested over a range of exit Mach number from 0.7 to 1.4 and incidence from -20 to $+8$ deg. The results indicated the sensitivity of the cascade performance to the blade-back curvature and incidence. The importance of Schlieren pictures in showing the shock-boundary layer interaction was emphasized. Camus et al. (1984) reported tests for a blade (120 deg turning, 2.4 aspect ratio) at various Mach numbers (0.7 to 1.2), Reynolds numbers, and incidences. The shock–boundary layer interaction was shown to extend across the whole span and endwall. Perdichizzi (1989) investigated the flow field downstream of a blade with an aspect ratio of 1.0 and a turning angle of 84 deg up to a Mach number of 1.55. The importance of secondary losses was found to diminish as the Mach number increased. With increasing Mach number, the passage vortex moved closer to the endwall, the loss core diminished in magnitude, and the flow overturning and underturning decreased. Mee et al. (1992) conducted a study on a cascade with 111 deg turning, aspect ratio of 3, and Mach numbers between 0.7 and 1.1. They were able to define the individual contributions of boundary layer loss, shock loss, and mixing loss at different Mach number regimes. Detemple-Laake (1991) performed tests on a highly loaded rotor blade (105 deg turning) in a 2.1 aspect ratio planar cascade. The parameters varied were the inlet flow angle (-10 to $+25$ deg incidence) and the exit Mach number (0.8 to 1.3). The passage vortex shifted toward the side wall until the cascade was choked and then remained in the same position for all supersonic Mach numbers. The shock–boundary layer interaction did not extend to the side wall region whereas the trailing edge shock did.

Limited studies exist on the effect of Mach number on the performance of turbine nozzles where three-dimensional effects are dominant due to the low aspect ratio. Horton (1989) compared the predictions of a three-dimensional viscous flow solver to the measurements performed on a nozzle with an aspect ratio of 0.62 and a turning angle of 75 deg over a range of Mach number from 0.9 to 1.3. The investigations of Dominy

Contributed by the International Gas Turbine Institute and presented at the 37th International Gas Turbine and Aeroengine Congress and Exposition, Cologne, Germany, June 1–4, 1992. Manuscript received by the International Gas Turbine Institute January 28, 1992. Paper No. 92-GT-31. Associate Technical Editor: L. S. Langston.

and Harding (1989) involve three alternative nozzles with an aspect ratio of 0.7 and a turning angle of 65 deg tested at 0.83 and 0.95 exit Mach number. Recently, Arts and deRouvroit (1992) tested a nozzle guide vane with a turning angle of 75 deg in a two-dimensional cascade at various Mach numbers (0.7 to 1.0), Reynolds numbers, and turbulence intensities. The loss coefficient was almost constant over the range Mach number tested.

Williamson and Moustapha (1986) tested a low aspect ratio (0.6), high turning angle (76 deg) transonic (exit Mach number 1.2) nozzle as part of a highly loaded turbine stage. The nozzle was tested in an annular cascade and in a stage environment over a range of exit Mach number from 0.67 to 1.2. Building on this work, in order to obtain additional and more detailed information on the three-dimensional flow field in the nozzle as a function of Mach number, the midspan section of the nozzle was tested in a large-scale planar cascade. This paper presents the performance of the nozzle over a range of exit Mach numbers from 0.3 to 1.36.

Experimental Methods

Nozzle Cascade. The large-scale planar cascade constructed for this experimental investigation was an exhauster type with five nozzle passages. The cascade test section is shown in Figs. 1 and 2. The cascade was operated by a 2-MW exhauster facility, capable of continuously drawing 5 kg/s of air. Inlet air to the cascade was drawn through a rectangular bellmouth with a 5:1 elliptically shaped cross section. The distance from the bellmouth to the leading edge of the vanes was such that the inlet boundary layer that grew on the cascade endwalls was 11.3 percent vane span in thickness. The boundary layer on the sidewalls and the vortices in the corners bounded by the sidewalls and the endwalls were bled off by adjustable sidewall boundary layer bleeds. An adjustable perforated aluminum tailboard was used to establish the flow periodicity and to eliminate shock wave reflection. In order to permit flow visualization during the shakedown and the detailed tests, the front endwall was replaced with one constructed from clear plexiglass.

The vane profile used in the present investigation is the mean section of a nozzle designed for a gas generator research turbine with a pressure ratio of 3.8 and a stage loading of 2.5. Details of the stage design and experimental results related to the performance of the nozzle and the stage have been documented by Williamson and Moustapha (1986). The nozzle tested in the present cascade is scaled 4.3 times engine size and 1.4 times the research turbine stage. This provided for ample space for comprehensive flow visualization studies and minimum probe interference at representative Mach numbers. Figure 3 shows the vane profile and the main geometric parameters. The hub and tip sections for the actual nozzle, tested in the stage configuration (Moustapha and Williamson, 1986), are shown for reference. The nozzle aspect ratio is 0.64, turning angle 76 deg, and design exit Mach number 1.16. The vane coordinates are given in Table 1 in order to help researchers evaluate the accuracy of their inviscid and viscous flow codes.

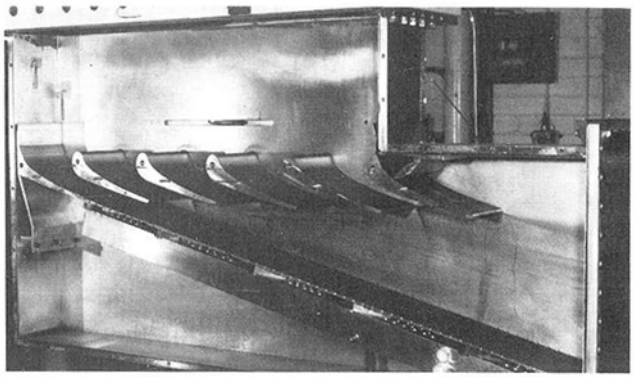

Fig. 1 Experimental facility

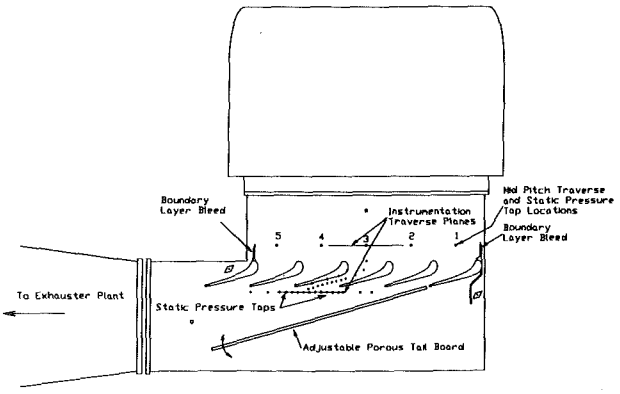

Fig. 2 Transonic nozzle cascade

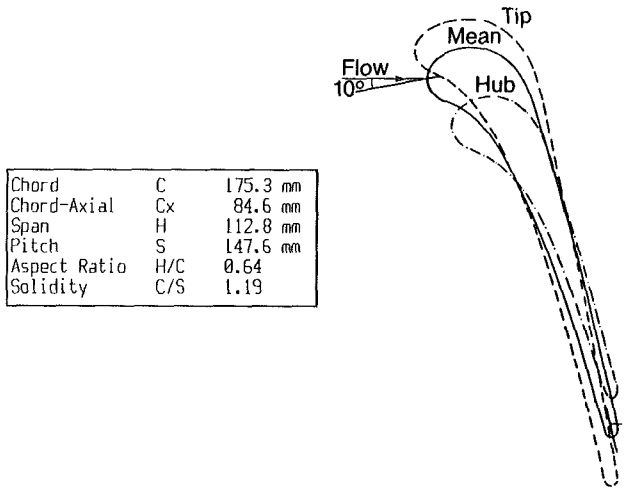

Chord	C	175.3 mm
Chord-Axial	Cx	84.6 mm
Span	H	112.8 mm
Pitch	S	147.6 mm
Aspect Ratio	H/C	0.64
Solidity	C/S	1.19

Fig. 3 Vane profile and geometric parameters

Instrumentation and Flow Visualization. Instrumentation was designed to explore nozzle passage pressure distributions, exit flow angles, and total pressure losses. The two vanes

Nomenclature

C = vane chord
Cx = vane axial chord
C/S = vane solidity
Cpo = local total pressure loss coefficient = $(P_{om1} - P_{o2})/(P_{om1} - P_{sm2})$
$\overline{Cpo}$ = pitchwise mean of Cpo
$\overline{\overline{Cpo}}$ = area-weighted spanwise mean of Cpo
H = nozzle span
H/C = nozzle aspect ratio
M = Mach number
Po = local total pressure
Pr = nozzle total to static pressure ratio = P_{om1}/P_{sm2}
Ps = static pressure
V = local velocity
x = axial distance from vane leading edge

Subscripts

1 = nozzle inlet plane
2, e = nozzle exit plane
m = mean
ms = midspan

Table 1 Vane coordinates

X	Y upper	Y lower
-1.813392	1.912752	1.912752
-1.796688	2.017872	1.784736
-1.746720	2.127312	1.675440
-1.680048	2.206656	1.596096
-1.613376	2.260080	1.545696
-1.546848	2.303712	1.512864
-1.480176	2.339712	1.487952
-1.313568	2.402064	1.413936
-1.146816	2.431296	1.314288
-0.980208	2.431584	1.179936
-0.813600	2.403792	1.001808
-0.646992	2.345184	0.775584
-0.480384	2.250720	0.503569
-0.313776	2.108016	0.192816
-0.147168	1.886976	-0.149760
-0.063792	1.727424	-0.331776
0.019584	1.518912	-0.520704
0.102816	1.253520	-0.716544
0.186192	0.967392	-0.919872
0.269424	0.675216	-1.130832
0.352800	0.378864	-1.350288
0.436032	0.078336	-1.578816
0.519408	-0.226656	-1.816848
0.686016	-0.861696	-2.317968
1.019232	-2.157264	-3.411072
1.185984	-2.844144	-3.986352
1.269216	-3.196800	-4.280688
1.310976	-3.376368	-4.386096
1.352592	-3.556080	-4.417200
1.385856	-3.701664	-4.417200
1.419264	-3.848400	-4.425840
1.452528	-3.996288	-4.415328
1.485792	-4.145184	-4.390992
1.502496	-4.220208	-4.369104
1.519200	-4.308480	-4.308480

bounding the center nozzle passage were equipped with four static taps at midspan on the suction surface and one tap on the trailing edge of the pressure surface at the nozzle throat. Ten taps were positioned midway between the two vanes on the endwall. Five vanes of the cascade had static taps at 30 percent axial chord to allow measurement of periodicity. Uncertainty in the measurement of endwall and vane static pressures was estimated to be ± 1.0 percent of the reading. The upstream and downstream traverse planes were located at 65 and 25 percent axial chord from the nozzle leading and trailing edges, respectively (Figs. 1 and 2).

A United Sensor 4.75-mm-dia wedge probe was used to measure total temperature, total pressure, and yaw angle. The wedge probe was operated under computer control, being automatically nulled via a binary search routine at each preselected measurement station. The wedge probe was calibrated over a Mach number range of 0.4 to 1.2 with particular attention being paid to the transonic calibration, Mach number 0.95 to 1.05. Effect of yaw angle on the calibration was also investigated. The wedge probe measured total pressure correctly when aligned to within ± 10 deg of flow angle. The wedge probe was limited in approach to the wall when the total pressure port was at 4 mm from the endwall. Uncertainty in the measurement of total pressure at the design pressure ratio was estimated to be ± 0.5 percent of the reading. Although the uncertainty in the measurement of flow direction was estimated to be ± 0.6 deg, the ability of the nulled wedge probe to indicate true flow direction in shear flows (i.e., crossing the vane wake) is presently not quantified but is expected to be no greater than ± 2 deg. Additional error analysis was reported by Carscallen and Oosthuizen (1989). Inlet boundary layer profiles were measured using a 1.6-mm-dia total head probe.

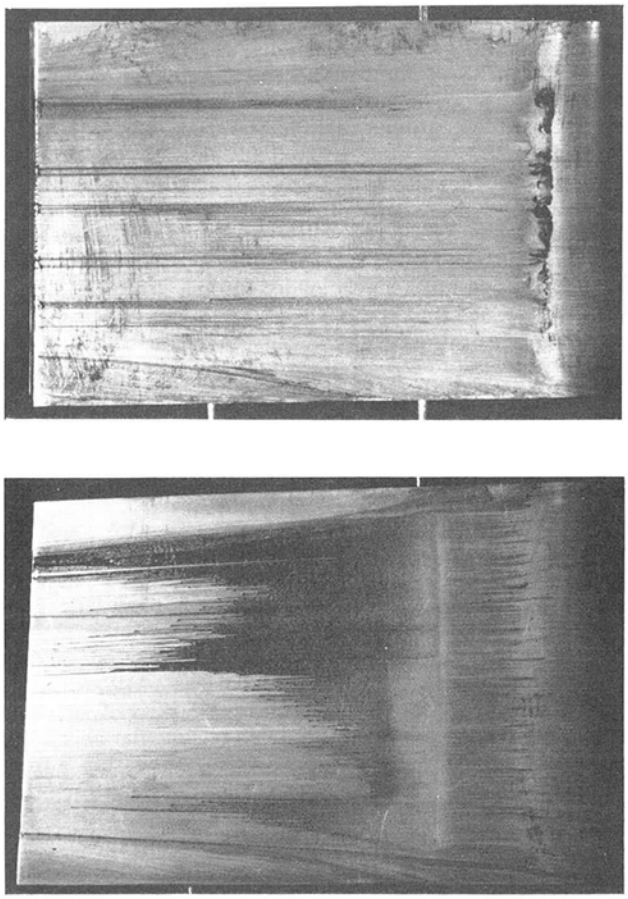

Fig. 4(*b*) Flow visualization on nozzle suction surface, $M_e = 1.2$

Data acquisition was performed using a Hewlett Packard 3045C system. L.C. Smith traverse gear, controlled by the HP system, was used to traverse the wedge and total head probes in the pitchwise, spanwise, and yaw directions. Static pressures were scanned and measured by a ganged miniature Scanivalve system. Wedge and total head probe pressures were measured with stand alone Statham pressure transducers. Control of the Scanivalve, and measurement and recording of the pressure transducers were carried out by the HP system.

Flow visualization, using an oil mixture, was used to help interpret data from the planar cascade, with emphasis on the suction surface and the endwall. A satisfactory mixture was lampblack pigment and cooking oil. A Schlieren system was used to look at the endwall shock structure.

Cascade Flow Conditions. In a cascade test section with small number of blades, inlet flow uniformity and outlet flow periodicity must be carefully established, so that the flow simulates as closely as possible that in an infinite cascade. The inlet flow uniformity in the pitchwise and the spanwise directions was globally verified by comparison of spanwise inlet velocity profiles taken at the five midpitch traverse locations. In addition, detailed pitchwise and spanwise traversing was done for the center nozzle passage. The outlet flow periodicity was established by checking endwall static pressure, exit total pressure, and angle in the pitchwise direction. The flow uniformity and periodicity were checked over the range of cascade operating conditions and also verified by means of the oil flow

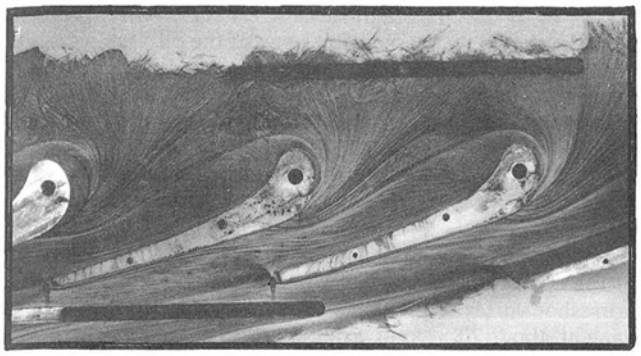

Fig. 5 Flow visualization on nozzle endwall, $M_e = 0.7$

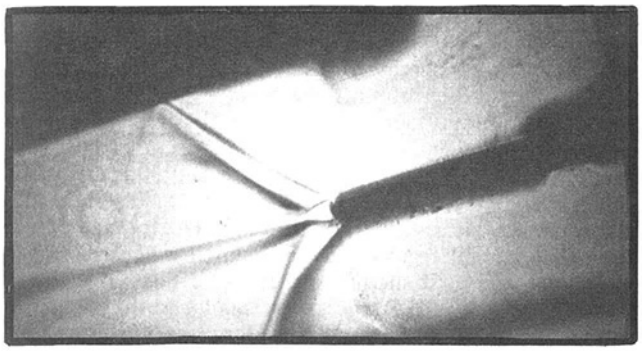

Fig. 6 Schlieren visualization, $M_e = 1.2$

visualizations and wool tufts. Ambient air condition was monitored before the test to ensure adequate margins against shock condensation.

Experiments were conducted at seven nominal pressure ratios ranging from a low subsonic exit Mach number of 0.3 to a supersonic Mach number of 1.36, corresponding to total to static pressure ratios across the nozzle of 1.07 to 3.0. At the design exit Mach number of 1.16 (inlet number 0.11), the vane Reynolds number was 2×10^5 based on inlet conditions and the measured inlet root mean square turbulence level was about 0.2 percent. The inlet boundary layer thickness at each end wall was about 11.3 percent of the nozzle span.

Nozzle Passage Flow

The flow structure in the nozzle passage was explored in detail at three exit Mach numbers: 0.7, 1.0, and 1.2, corresponding to a nozzle pressure ratio of 1.4, 1.9, and 2.3. Qualitative measurements included oil and Schlieren flow visualizations on the suction surface and the endwall (Figs. 4, 5, and 6). Quantitative measurements involved static pressure measurements at the midspan of the vane surface and at the midpitch of the endwall (Figs. 7 and 8). The following is a discussion of these results and comparison with prediction methods and previously reported data for the nozzle tested in an annular configuration.

Figures 4(*a*) and 4(*b*) show oil flow visualization on the suction surface at Pr = 1.4 and 2.3, respectively. The leading edge is to the right of the figure. For the subsonic case, Fig. 4(*a*), there is a clearly visible dark spanwise region near the leading edge in the picture (about 50 percent axial chord). This is evidence of a short laminar separation bubble with turbulent reattachment as shown by the oil traces. The location of the separation bubble coincides with the measured weak suction peak (Fig. 7, Pr = 1.4). For the supersonic case (Fig. 4*b*), the separation region, as shown by a light spanwise band, is longer and farther downstream (about 70 percent axial chord). Again, this agrees with the location of the measured suction peak in

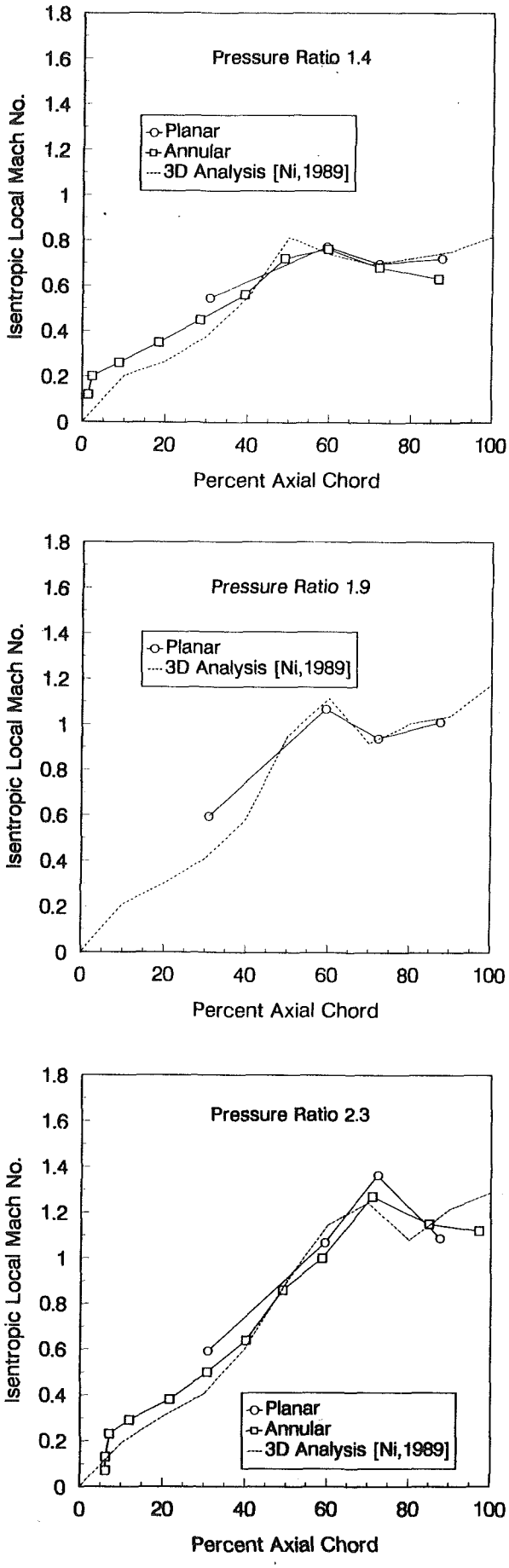

Fig. 7 Nozzle suction surface Mach number distribution at midspan

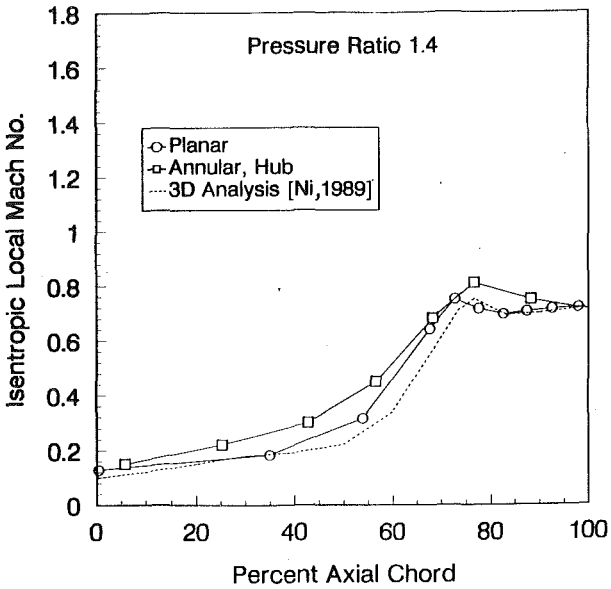

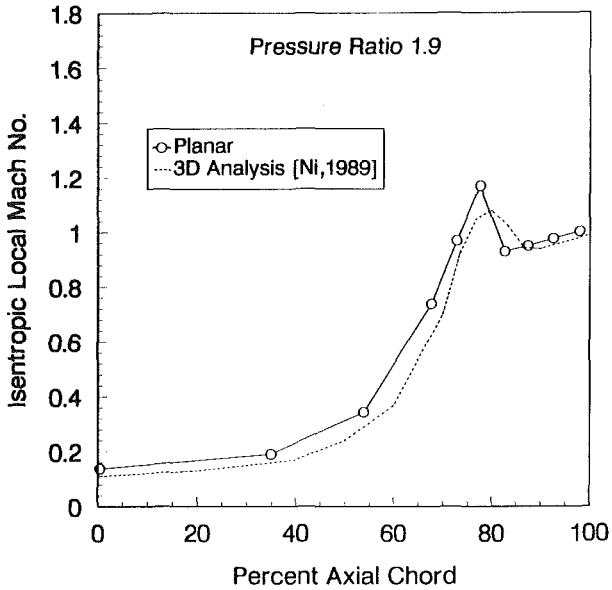

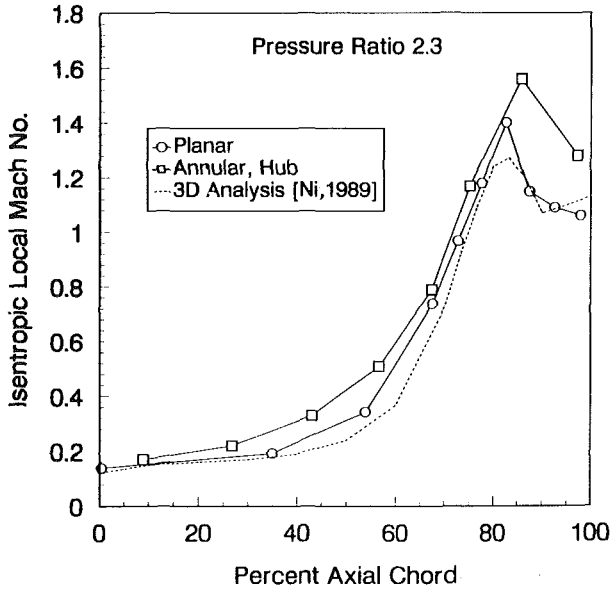

Fig. 8 Nozzle endwall Mach number distribution at midpitch

Fig. 7, Pr = 2.3. The high shear stress region after reattachment, as shown by the scouring away of the oil, implies a fully turbulent boundary layer. At both Mach numbers, one easily notes that the oil traces are nearly parallel between 15 and 85 percent span, thus suggesting that the flow is nearly two dimensional in this region.

Details of the secondary flow field could be explained by means of Figs. 4 and 5. The endwall flow characteristics, shown in Fig. 5 for $M_e = 0.7$, are similar to the results reported by Langston et al. (1976) and Sieverding (1985). The rolling up of the endwall boundary layer in front of the nozzle into the horseshoe vortex resulted in a separation saddle point for each vane at about 20 percent axial chord upstream of the nozzle leading edge. The saddle point divided the endwall flow along the stagnation streamline into two distinct regions of three-dimensional flow. On one side of the stagnation streamline is the suction leg of the horseshoe vortex wrapping around the leading edge. On the other side is the pressure leg of the horseshoe vortex merging with the passage vortex to form a single vortex, which lifts off the endwall and rolls onto the suction surface at about 30 percent axial chord (Fig. 4*a*). For both Mach numbers, oil traces on the suction surface show the separation line starting at zero span and 30 percent axial chord and ending at 15 percent span at the trailing edge. The separation line clearly splits the suction surface into the endwall three-dimensional region and the main flow nearly two-dimensional region. It should be mentioned that for all Mach numbers the endwall oil traces were similar to the one shown in Fig. 5. The results presented in Figs. 4 and 5 suggest that the structure of the secondary flow field is independent of Mach number.

Figure 6 is a Schlieren image at $M_e = 1.2$, showing the trailing edge shock pattern, which consisted of a separation and reattachment shock following both suction and pressure surfaces, similar to that reported by Graham and Kost (1979). It can be noticed that the tailboard satisfactorily attenuated reflection of the incident trailing shocks. The footprint of the trailing edge shock intersected the nozzle suction surface at the location of the separation region in Fig. 4(*b*) and the peak Mach number in Fig. 7, Pr = 2.3. It is also worth noting from Fig. 4(*b*) that the shock does not appear to penetrate the endwall secondary flow region.

Measured static pressures in the nozzle passage were converted isentropically to Mach number using the measured upstream total pressure. The results are shown in Figs. 7 and 8 at pressure ratios of 1.4, 1.9, and 2.3. From the measured data, it is seen that the location of adverse pressure gradient moves downstream with increase in Mach number. The shock emanating from the trailing edge of one vane swings downstream as the Mach number increases and thus impinges at a further downstream location on the suction surface. The axial shift of the measured peak was in line with the flow visualization presented in Figs. 4 to 6.

Analytical predictions using the Ni and Bogoian (1989) three-dimensional inviscid flow solver are shown. Remarkable agreement is displayed between the measurement and the prediction in terms of the location and the magnitude of the peak Mach number at all pressure ratios. The experimental results reported by Williamson and Moustapha (1986) for the same nozzle tested in an annular cascade are also shown. Good agreement is seen between the midspan data of the planar and annular cascade. The midpitch values are slightly higher for the annular nozzle due the higher Mach number levels on the hub of the annular cascade.

Nozzle Downstream Flow Field

Spanwise traversing was conducted at a distance 25 percent axial chord downstream of the trailing edge and covering more

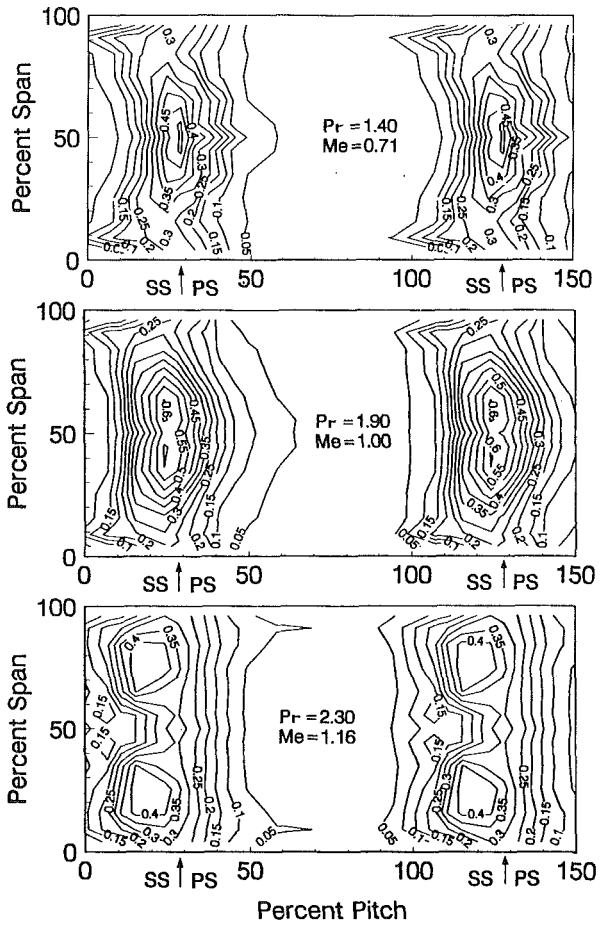

Fig. 9 Nozzle total pressure loss contours

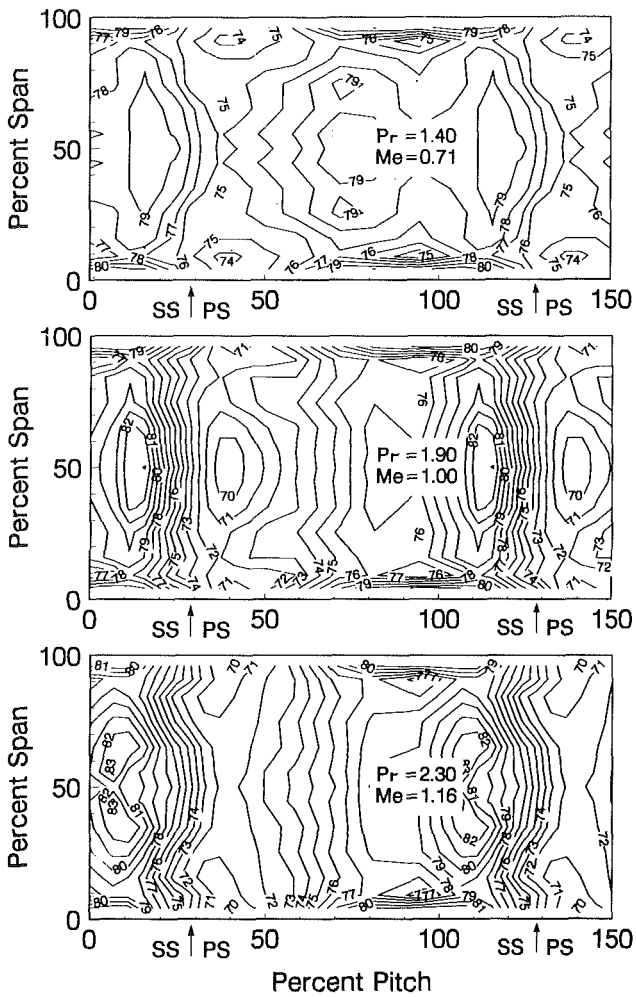

Fig. 10 Nozzle exit flow angle contours

than one vane pitch. Figures 9 and 10 present contours of total pressure loss coefficient and exit flow angle for three exit Mach numbers. The footprints of the nozzle trailing edge on the traverse plane are at about 30 percent and 130 percent pitch, as shown by the arrows, with the pressure surface (PS) of the vane to the right and the suction surface (SS) to the left.

At exit Mach number of 0.71, there is a loss peak (Fig. 9) at midspan and roughly centered in the wake. As the Mach number increases, the high loss region divides and migrates toward the endwalls and the suction surface side of the wake. At $M_e = 1.16$, the two loss peaks are located 10 percent pitch from the center of the wake and 20 percent span from the endwalls. The magnitude of the loss in these regions increases with Mach number ($M_e = 0.71$ to 1.0) and then decreases. From Fig. 9, it is apparent that the width of the wake increases with Mach number and that the wake profile is not two dimensional at the three Mach numbers. For all Mach numbers, no loss core related to the secondary vortex displaced in Figs. 4 and 5 is found. However, the skewness of the loss contours at 10 percent span (particularly at $M_e = 0.71$ and 1.0) is evidence of the secondary loss region and has been documented by other investigators (e.g., Langston et al., 1976, and Sieverding, 1985).

The exit flow angle contours in Fig. 10 show gradual change in flow direction across the main part of the flow with underturning near the pressure surface to overturning near the suction surface. The flow angle change in this area varies from about 4 deg at $M_e = 0.71$, to 12 deg at $M_e = 1.0$ and 8 deg at $M_e = 1.16$. The pitchwise location of the steepest gradient in flow angle shifts toward the suction surface as the Mach number is increased, and coincides with the location of the loss peak discussed in Fig. 9. The endwall region at all three

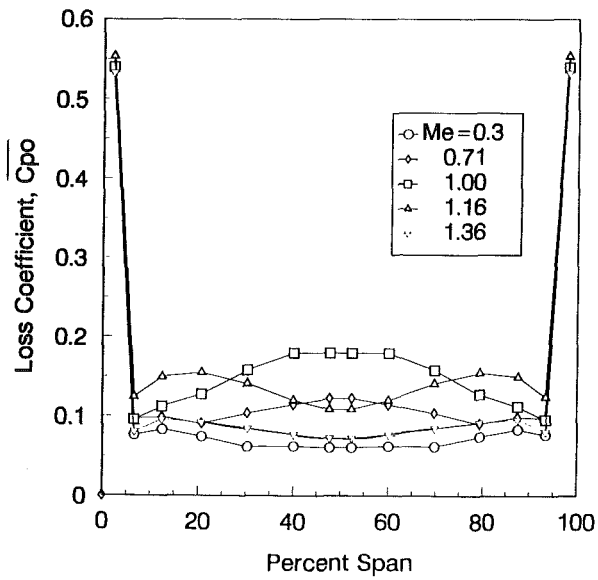

Fig. 11 Nozzle spanwise distribution of losses

Mach numbers shows a high overturning of 80 deg extending from about nozzle midpitch toward the suction surface.

Nozzle Spanwise Performance

Pitchwise area averaging of the total pressure losses and the exit flow angles presented in Figs. 9 and 10 was carried out at

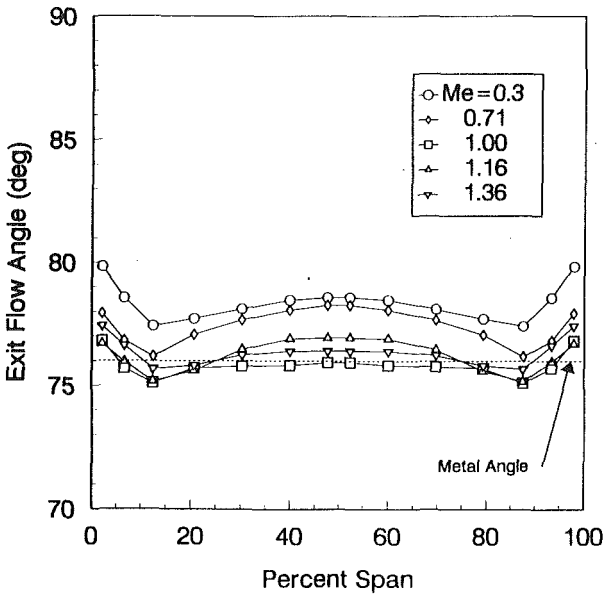

Fig. 12 Nozzle spanwise distribution of exit flow angle

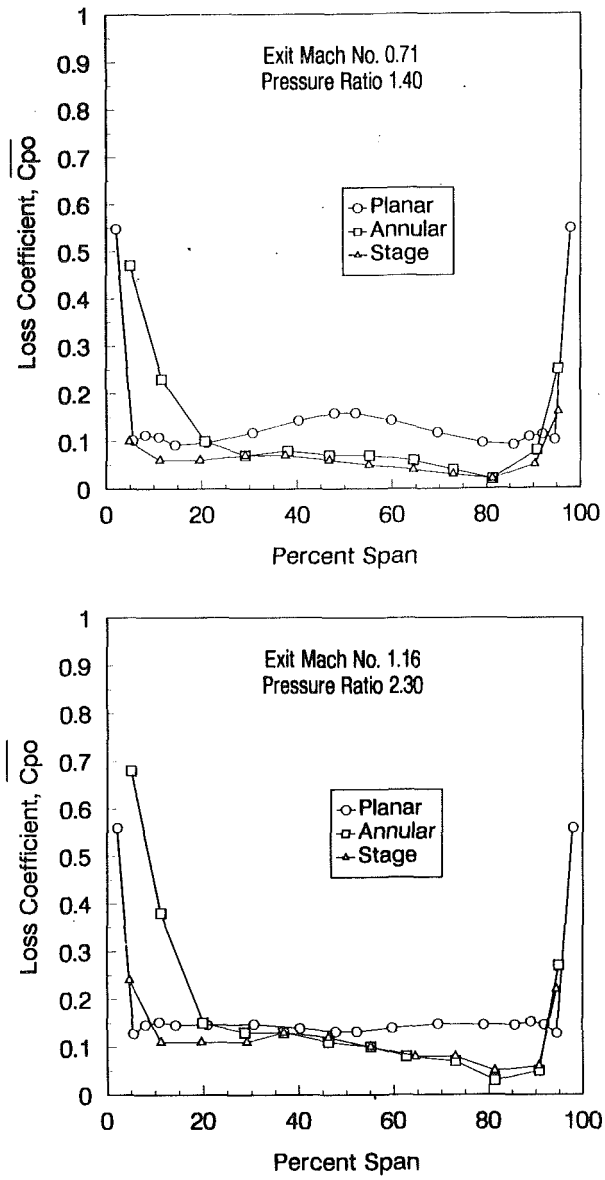

Fig. 13 Nozzle spanwise distribution of losses

each spanwise location. The results are shown in Figs. 11 and 12 for five nozzle pressure ratios. In the main flow region, the overall loss level increases with Mach number, peaks at a value of 1.0, and then decreases. The peaking stems from the fact that at low supersonic Mach numbers the shock wave from the trailing edge of the adjacent vane impinges on the uncovered suction surface farther upstream than is the case at higher Mach numbers where the shock is more oblique. Although the shock-boundary layer interaction is a function of shock strength, the greater development distance of the disturbed boundary layer and the angle of the impinging shock wave play a significant role in determining the magnitude of the observed loss coefficient. The loss distribution between 20 and 80 percent span for M_e = 0.71, 1.0, and 1.16 confirms the trend in the contours discussed in Fig. 9. It is also interesting to notice that the overall level of loss is minimum and roughly equal at M_e = 0.3 and 1.36. The exit angle distribution, Fig. 12, shows that the general level, and hence the deviation with respect to the vane metal angle, is strongly influenced by the exit Mach number.

While the flow visualization, Fig. 4, indicates a nearly two-dimensional flow on the vane suction surface between 15 and 85 percent span, the loss and flow angle distribution, Figs. 11 and 12, show a variation across this region, the amount and nature of which is a function of Mach number. This variation indicates that the flow along the midspan of the vane suction surface is more complex than indicated by the flow visualization, and that it is not a two-dimensional flow typical of the midspan flow over a nozzle vane of high aspect ratio.

In the endwall region, the exit angle distributions displayed a classical secondary flow overturning and underturning, which is similar at all Mach numbers. The minimum flow angle measured (maximum underturning) occurred at a fixed 15 percent span location, which agreed perfectly with the trailing edge location of the separation line discussed with Fig. 4. The results presented in Figs. 4 and 12 appear to be in contrast to the findings of Perdichizzi (1990) and Detemple-Laake (1991) where the penetration of the secondary vortices and the magnitude of the overturning and underturning were influenced by the exit Mach number. Their tests were conducted on rotor blade sections with large aspect ratio, higher flow turning, and thicker inlet boundary layer when compared to the present investigation.

The spanwise performance of the present planar nozzle cascade was compared in Figs. 13 and 14 with the results of the same nozzle tested in an annular and a stage configuration (Williamson and Moustapha, 1986) and with the prediction of a three-dimensional Euler code (Ni and Bogoian, 1989).

At both Mach numbers, the loss levels for the annular and stage cases are lower in the outer half of the passage. This is due to the radial pressure gradient in the annular geometry, which results in lower Mach numbers toward the outer wall, as compared to the planar cascade, and hence lower losses. Earlier work by Moustapha and Williamson (1986) established the influence of the downstream rotor presence on the performance of the present nozzle geometry. Their investigations concluded that the measured high losses in the hub region of a transonic, high turning and low aspect ratio nozzle, when tested in an annular configuration, could be substantially reduced by the design and operation of a downstream rotor. In Fig. 13, it is interesting to see the inner 20 percent loss levels for the planar cascade matched better those measured for the nozzle tested in a stage environment. Also the extent of the secondary flow regions is more in line with the stage data. Exit flow angles in Fig. 14 revealed the same conclusions as the losses between the planar, annular, and stage cases. The agree-

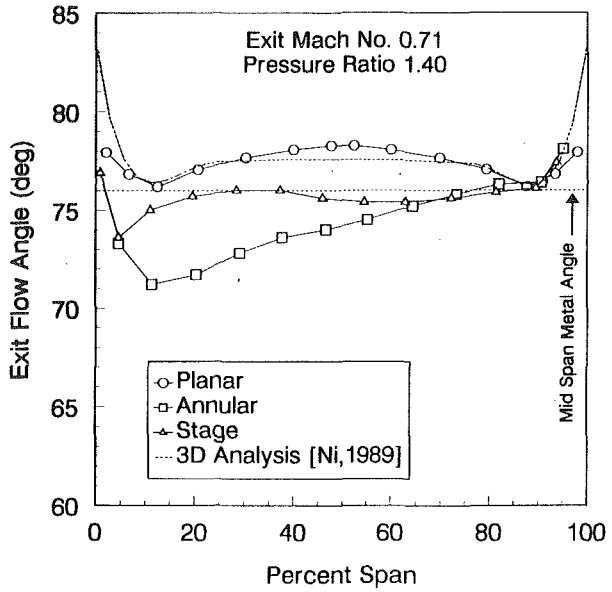

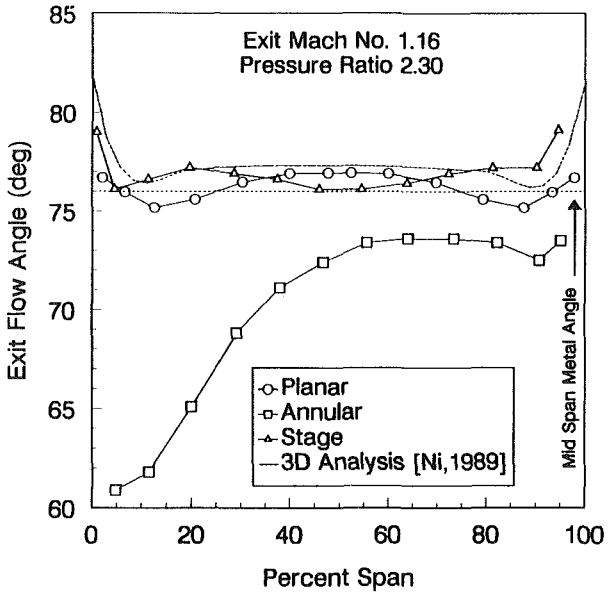

Fig. 14 Nozzle spanwise distribution of exit flow angle

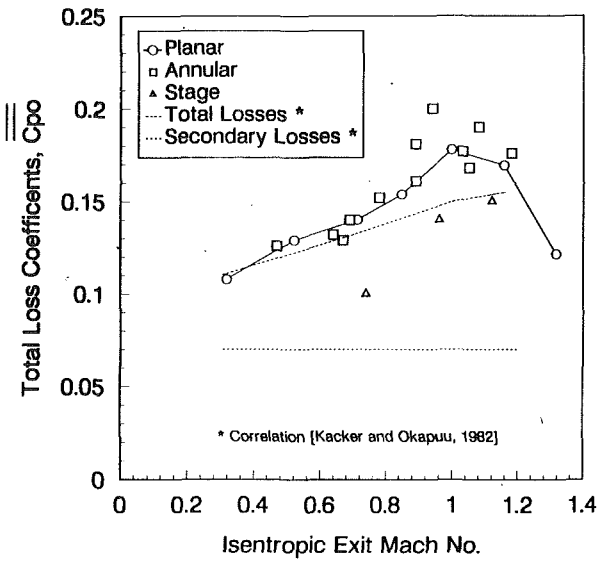

Fig. 15 Variation of nozzle loss with exit Mach number

ment between the exit angle distribution of the planar and the stage cases at the nozzle design pressure ratio is good.

The inviscid three-dimensional flow solver predicted extremely well the level and the distribution of the exit flow angle as function of exit Mach number, as well as the location of the endwall secondary vortices.

Nozzle Overall Performance

In addition to the spanwise performance of turbine nozzles, the designer is interested in their overall performance as a function of Mach number. This is particularly required at the early stages of a turbine design where the selection of the nozzle and rotor operating pressure ratios will define the loss levels and hence the efficiency of the turbine. In addition, a proper understanding of the transonic loss characteristics of turbine airfoils and the factors affecting them will help the designer to optimize the profile shape for minimum loss. Total losses and angular deviation data are also needed to review and calibrate the analytical tools periodically.

Area-weighted averaging of the mean spanwise distribution of total pressure loss coefficients at the downstream plane is plotted in Fig. 15 as a function of exit Mach number. The transonic drag rise characteristic of the nozzle is in general agreement with results published by previous investigators: Graham and Kost (1979), Martelli and Boretti (1985), and Perdichizzi (1990). The reduction in losses above an exit Mach number of 1.0 is related to the swing of the shock system and was discussed in detail in the previous sections (Figs. 7, 8, and 11). From this variation one may conclude that it is advantageous to operate the nozzle at higher than design pressure ratio, provided that the downstream rotor can be designed to cater for the higher inlet Mach number.

The measured nozzle total losses from the annular cascade and the stage configuration are also plotted in Fig. 15. Reasonable agreement could be seen between the planar and the annular data in terms of the loss level and the value of exit Mach number at which the loss peaks. The loss correlation of Kacker and Okapuu (1982) generally underpredicts the data and overpredicts the stage results. The area between the loss data and the constant value of secondary loss, as predicted by the correlation, represents the profile, trailing edge, and shock loss components.

The midspan deviation, defined as the difference between the measured midspan exit flow angle and the vane metal angle, is plotted in Fig. 16. Values from other investigations, the correlation by Ainley (1948), and the three-dimensional analysis are also plotted. The results show a general decrease of deviation with increase in exit Mach number.

Conclusions

The main objective of the present investigation is to document the overall performance of a turbine nozzle with an aspect ratio of 0.64 and a turning angle of 76 deg. The nozzle has been tested in a large-scale planar cascade over a range of exit Mach number from 0.3 to 1.36.

The flow visualization studies performed on the nozzle endwall and suction surface supported the experimental data very well. The shock-induced separation on the suction surface was evident from the perfect match between the location of the shock impingement, the adverse pressure gradient, and the separation region.

The results are compared to data secured earlier for the same nozzle geometry tested in an annular and a stage configuration. Very good agreement was obtained between the distribution of surface pressure, total pressure losses, and exit flow angle

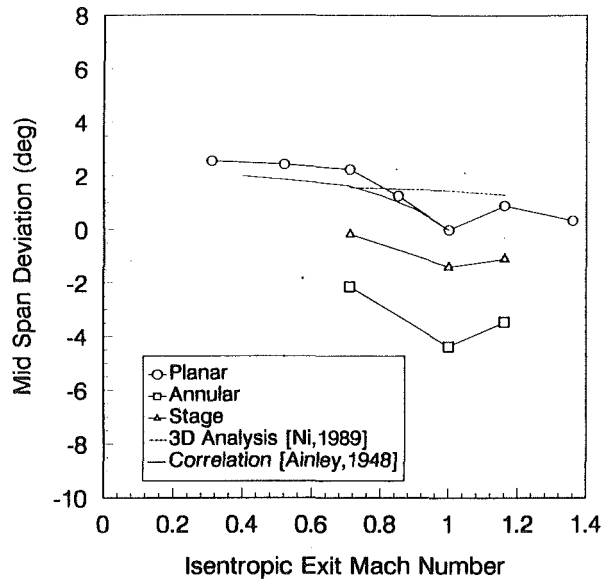

Fig. 16 Variation of midspan deviation with Mach number

for the three test vehicles. The measured nozzle passage surface Mach number distributions and the spanwise variation of exit flow angle were properly predicted by a three-dimensional Euler flow solver at all Mach numbers.

The endwall and suction surface flow visualization and the exit flow angle distribution suggested that, for this nozzle configuration, the secondary flow pattern and the spanwise penetration of the resulting vortices were independent of the exit Mach number. There is a lack of sufficient data in the literature on the effect of compressibility on the secondary flow field in turbine airfoils. Available loss correlations do not account for such effects, particularly at supersonic exit Mach numbers where the profile losses and shock-boundary layer interaction play a more important role in determining the total losses.

The overall nozzle performance as a function of Mach number confirmed other studies about the need to understand and properly predict the transonic drag rise characteristics of turbine airfoils to improve turbine efficiency. The total loss measured for the present nozzle at an exit Mach number of 1.36 was about 30 percent lower than the loss at the design Mach number of 1.16.

While several aspects of the flow in this transonic turbine nozzle cascade have been correlated, details of the spatial distribution of the various loss components in the main flow region and their interaction mechanism remain to be explored. Detailed loss measurements in the endwall region of the nozzle passage and at different downstream locations are planned to investigate the effect of Mach number on the secondary losses.

Acknowledgments

The work reported here is part of a joint research program carried out by the National Research Council of Canada and Pratt and Whitney Canada Inc. Contributions by Dr. R. G. Williamson, Dr. U. W. Schaub, and Mr. P. Hunt from NRC, Mr. A. Lem from PWC, and Dr. S. A. Sjolander from Carleton University, are gratefully acknowledged.

References

Ainley, D. G., 1948, "The Performance of Axial Flow Turbines," *Proc. I.Mech.E.*, Vol. 159.

Arts, T., and deRouvroit, M. L., 1992, "Aero-Thermal Performance of a Two-Dimensional Highly Loaded Transonic Turbine Nozzle Guide Vane: A Test Case for Inviscid and Viscous Flow Computations," ASME JOURNAL OF TURBOMACHINERY, Vol. 114, pp. 147–154.

Binder, A., and Romey, R., 1983, "Secondary Flow Effects and Mixing of the Wake Behind a Turbine Stator," ASME *Journal of Engineering for Power*, Vol. 105, pp. 40–46.

Camus, J. J., Denton, J. D., Soulis, J. V., and Scrivener, C. T. J., 1984, "An Experimental and Computational Study of Transonic Three-Dimensional Flow in a Turbine Cascade," ASME JOURNAL OF TURBOMACHINERY, Vol. 106, pp. 414–420.

Carscallen, W. E., and Oosthuizen, P. H., 1989, "The Effect of Secondary Flow on the Redistribution of the Total Temperature Field Downstream of a Stationary Turbine Cascade," AGARD-CP-469.

Detemple-Laake, E., 1991, "Detailed Measurements of the Flow Field in a Transonic Turbine Cascade," ASME Paper No. 91-GT-29.

Dominy, R. G., and Harding, S. C., 1989, "An Investigation of Secondary Flows in Nozzle Guide Vanes," AGARD-CP-469.

Graham, C. G., and Kost, F. H., 1979, "Shock Boundary Layer Interaction on High Turning Transonic Turbine Cascades," ASME Paper No. 79-GT-37.

Horton, G. C., 1989, "Secondary Flow Predictions for Transonic Nozzle Guide Vane," AGARD-CP-469.

Kacker, S. C., and Okapuu, U., 1982, "A Mean Line Prediction Method for Axial Flow Turbine Efficiency," ASME *Journal of Engineering for Power*, Vol. 104., pp. 111–119.

Langston, L. S., Nice, M. L., and Hooper, R. M., 1976, "Three Dimensional Flow Within a Turbine Cascade Passage," ASME Paper No. 76-GT-50.

Martelli, F., and Boretti, A., 1985, "A Simple Procedure to Compute Losses in Transonic Turbines Cascades," ASME Paper No. 85-GT-21.

Mee, D. J., Baines, N. C., Oldfield, M. L. G., and Dickens, T. E., 1992, "An Examination of the Contributions to Loss on a Transonic Turbine Blade in Cascade," ASME JOURNAL OF TURBOMACHINERY, Vol. 114, pp. 155–162.

Mobarak, A., Khalafallah, M. G., Osman, A. M., and Heikal, H. A., 1988, "Experimental Investigation of Secondary Flow and Mixing Downstream of Straight Turbine Cascades," ASME JOURNAL OF TURBOMACHINERY, Vol. 110, pp. 497–503.

Moustapha, S. H., Okapuu, U., and Williamson, R. G., 1987, "The Influence of Rotor Blade Aerodynamic Loading on the Performance of a Highly Loaded Turbine Stage," ASME JOURNAL OF TURBOMACHINERY, Vol. 109, pp. 155–162.

Ni, R. H., and Bogoian, J., 1989, "Prediction of 3D Multi-stage Turbine Flow Field Using a Multiple-Grid Euler Solver," AIAA Paper No. 89-0203.

Perdichizzi, A., 1990, "Mach Number Effects on Secondary Flow Development Downstream of a Turbine Cascade," ASME JOURNAL OF TURBOMACHINERY, Vol. 112, pp. 643–651.

Sieverding, C. H., Van Hove, W., and Boletis, E., 1984, "Experimental Study of the Three-Dimensional Flow Field in an Annular Turbine Nozzle Guide Vane," ASME *Journal of Engineering for Gas Turbines and Power*, Vol. 106, pp. 437–444.

Sieverding, C. H., 1985, "Recent Progress in the Understanding of Basic Aspects of Secondary Flows in Turbine Blade Passages," ASME *Journal of Engineering for Gas Turbines and Power*, Vol. 107, pp. 248–257.

Sjolander, S. A., 1975, "The End Wall Boundary Layer in an Annular Cascade of Turbine Nozzle Guide Vanes," Carleton U. TRME/A75-4.

Wegener, D., Quest, J., and Hoffman, W., 1989, "Secondary Flow in a Turbine Guide Vane With Low Aspect Ratio," AGARD-CP-469.

Williamson, R. G., and Moustapha, S. H., 1986, "Annular Cascade Testing of Turbine Nozzles at High Exit Mach Numbers," ASME *Journal of Fluids Engineering*, Vol. 108, pp. 313–320.

Williamson, R. G., Moustapha, S. H., and Hout, J. P., 1986, "The Effect of Downstream Rotor on the Measured Performance of a Transonic Turbine Nozzle," ASME JOURNAL OF TURBOMACHINERY, Vol. 108, pp. 269–274.

Yamamoto, A., and Yanagi, R., 1985, "Production and Development of Secondary Flows and Losses Within a Three-Dimensional Turbine Stator Cascade," ASME Paper No. 85-GT-217.

Separated Flow in a Low-Speed Two-Dimensional Cascade: Part I—Flow Visualization and Time-Mean Velocity Measurements

A. M. Yocum
Applied Research Laboratory,
Pennsylvania State University,
State College, PA 16804

W. F. O'Brien
Virginia Polytechnic Institute
and State University,
Blacksburg, VA 24061

This study was conducted for the purpose of providing a more fundamental understanding of separated flow in cascades and to provide performance data for fully stalled blade rows. Cascades of a single blade geometry and a solidity of unity were studied for three stagger angles and the full range of angle of attack, extending well into the stalled flow regime. Results are presented from flow visualization and time-mean velocity measurements of stalled flow in the cascade. Surface and smoke flow visualization revealed that the blade stagger angle is a key parameter in determining the location of the separation line and the occurrence of propagating stall. Time-mean velocity measurements obtained with a dual hot split-film probe also showed that the separated velocity profiles within the blade passages and the profiles in the wake have distinctly different characteristics depending on the stagger angle.

Introduction

Two-dimensional cascade tests and analysis have historically played a key role in the development of axial-flow turbomachinery. In the early years of axial-flow compressor, pump, and turbine design, various organizations conducted numerous cascade tests from which a wealth of design information was obtained. These early cascade tests were usually parametric studies where the effects of various geometric and operating parameters were studied. From this large source of experimental data, correlations were developed that form the basis for many current-day design procedures. Horlock (1973) presents the design correlations, which were developed from both the British data and the NACA data. Lieblein (1965) presents correlations that represent the NACA data in the familiar NASA Special Publication 36. The range in angle of incidence for the many tests used to develop the design correlations was sufficiently wide to define the positive and negative incidence stall points. For these investigations and correlations, stall was usually defined as the point where the loss or drag coefficient is twice its minimum value. However, limited fundamental data and no detailed performance data can be found in the literature for cascades operating far beyond the initial stall point.

Unlike the many investigations used to develop design correlations, the subject of this investigation is the fundamental behavior and the overall performance of fully stalled cascades. In these papers, the terminology "fully stalled" refers to flow separation that originates at or very near the leading edge of the blades. The question may be raised as to what is the practical engineering significance of a study of fully stalled flow in a two-dimensional cascade. After all, the purpose of a good design is to produce a machine that will operate on or near the maximum efficiency condition and with a margin as large as is practically possible between the operating condition and the stall point. However, in an effort to provide lighter, efficient, and more compact aviation gas turbine engines, the designer is often forced to accept a smaller stall margin. Thus, even with elaborate control systems designed to prevent an engine from entering the stalled flow regime, compressor stall in engines may be triggered by inlet flow distortions, lighting of afterburners, or other transient phenomena.

The post-stall behavior of compressors must also be given serious consideration to assure that rapid recovery from the stalled condition can be achieved. A fundamental knowledge of the two-dimensional behavior of fully stalled cascades, particularly as it relates to the effects of design variables, is important in understanding the stalled flow in the compressor. Post-stall compressor models, such as those of Sexton (1980), Takata and Nagano (1972), and Cousins and O'Brien (1985) require stalled cascade performance information to predict the transient post-stall behavior of a compressor. System models such as those of Greitzer (1976) and Davis and O'Brien (1991) also require the axisymmetric post-stall performance of the compressor as input. It would be advantageous if this axisymmetric performance could be estimated from fundamental cascade data and other appropriate models to account for three-dimensional effects. Greitzer (1980) in a review article on compressor stall phenomena stated that it seems a disproportionate amount of effort has gone into solving the flow fields upstream and downstream of the blade rows, while the models used for

Contributed by the International Gas Turbine Institute and presented at the 37th International Gas Turbine and Aeroengine Congress and Exposition, Cologne, Germany, June 1-4, 1992. Manuscript received by the International Gas Turbine Institute March 5, 1992. Paper No. 92-GT-356. Associate Technical Editor: L. S. Langston.

representing the flow within the blade rows are over 25 years old.

In addition to the possible application of stalled cascade performance data to compressor studies, the data can be of value in the off-design analysis of pumps. As for compressors, a fundamental understanding of stalled flow and basic performance data can be used with appropriate models to analyze the starting characteristics of pumps. Even though data from stationary cascades cannot be used in the design and analysis of radial flow impellers, information from the present study may find application in estimating the far off-design performance of centrifugal pump and compressor impellers and radial vaned diffusers. An additional application for the information and data of this investigation is in the evaluation or verification of Computational Fluid Dynamics (CFD) codes. Increasingly, researchers are computing turbomachinery flows that contain separated flow regions. The data and flow visualizations of this study provide cases for comparing both two-dimensional and three-dimensional separated flow calculations.

As previously mentioned, two-dimensional cascade studies of fully stalled flow have not been included in the vast number of cascade tests conducted to obtain design information. However, a review of the literature is not only important to illustrate this point, but also to provide important guidance on the manner of conducting cascade tests. Several cascade tunnel characteristics and parameters should be controlled or monitored to assure useful and accurate cascade performance data are obtained. The significant cascade characteristics and parameters are the two dimensionality of the flow, the Reynolds number based on the blade chord, and the inlet free-stream turbulence level. As historical background, Gostelow (1984) cites the earliest cascade tests as being reported by Christiani (1928) in Germany and Harris and Fairthorne (1928) in England. The data of Harris and Fairthorne were used by the British in the late 1930s for the design of early axial-flow compressors. In early cascade tests, the importance of obtaining truly two-dimensional flow was unknown. Consequently, the tests of several investigators, such as Constant (1937) and Bogdonoff (1948) were conducted with the axial velocity ratio (AVR) significantly greater than one, indicating the flow was not truly two dimensional. Erwin and Emery (1951) expressed the need to obtain true two-dimensional flow and stated five conditions that should be met to verify that two-dimensional flow does exist in the spanwise direction. They were able to approach true two-dimensional behavior by the development of the porous side wall technique for continuous removal of the boundary layer from the side walls of the cascade. For the current investigation, which is concerned with the somewhat gross features of fully stalled flow, the side wall boundary layers were not removed by suction to provide an axial velocity ratio of one. However, the two-dimensional nature of the flow was investigated using surface flow visualization, and the axial velocity profiles were measured from which the AVR was evaluated.

An additional parameter that affects the two-dimensionality of the flow is the aspect ratio. If slots and porous side walls are used to remove the boundary layer completely, an aspect ratio of one will yield good two-dimensional flow. For solid side walls, however, Pollard and Gostelow (1967) recommend an aspect ratio of three to preclude secondary flow effects on the center plane of the cascade. They also state that even for aspect ratios up to five, the axial velocity ratio will be greater than unity, if the working section has solid walls.

Rhoden (1952) conducted extensive tests to evaluate the effects of Reynolds number on the performance of a cascade. From these tests it was observed that there exists a critical Reynolds number below which laminar separation is likely to occur, resulting in a sharp increase in losses and a decrease in turning. Above the critical value, the Reynolds number does not significantly affect cascade performance. The value of the critical Reynolds number was found to vary between different tests, but generally fell within the range from $\mathrm{Re} = 2 \times 10^5$ to 5×10^5.

A decrease in the free-stream turbulence intensity has the same effect as a decrease in Reynolds number. Low turbulence intensity will delay transition and thus promote laminar separation and a decrease in the cascade performance. Gostelow (1984) states that although the effects of Reynolds number and turbulence intensity are closely related, they must be treated separately. Whatever its level, the importance of the turbulence intensity on the performance of a cascade requires that it at least be measured, simply to completely define the conditions under which the cascade tests were conducted.

Roberts (1975a, 1975b) did extensive studies of the effects of low Reynolds number and laminar separation on the performance of axial-flow compressor cascades. Excluding turbulent separation due to off-design conditions, Roberts described four types of flow regimes. Clayton and Massey (1967) also studied flow separation in a cascade at low Reynolds number. Both of these studies are concerned with laminar separation, while the current investigation is concerned with separation and full blade stall due to high incidence angles.

Stenning and Kriebel (1958) investigated propagating stall in a circular cascade and a single stage axial-flow compressor. The motivation for their work was to be able to predict rotating stall frequencies in actual machines. A circular two-dimensional cascade was developed with the plan of obtaining information in the simplest possible case where propagating stall could be sustained. Included in this work was the development of an analysis that would predict propagation speed and wave lengths of stall cells. This analysis is valid for small perturbations and blade rows of high solidity. Stenning and Kriebel (1958) later proposed an inviscid vortex shedding model for rotating stall that was not limited to small perturbations.

Measurements and smoke flow visualization were used by Sovran (1959) to study rotating stall in an axial-flow compressor and in a two-dimensional cascade. Flow visualization studies in the axial-flow compressor showed clearly the conditions existing upstream and downstream of the rotor during rotating stall, but could not show the details of the flow within the passage. For this reason a stationary two-dimensional cascade was used to study the details of propagating stall. For

Nomenclature

AVR = axial velocity ratio
E = anemometer bridge voltage
E_{f_n} = calibration parameter of the dual split-film probe for sensor n
i = incidence angle
k = thermal conductivity of the fluid
Re = Reynolds number
s = blade spacing
T_a = tunnel air temperature
T_{film} = temperature of the fluid
film $= \dfrac{T_s + T_a}{2}$
T_s = hot-film sensor temperature
u = local x component of velocity
v = local y component of velocity
V = average velocity
V_x = x component of the average velocity
V_x = y component of the average velocity
x, y, z = Cartesian coordinates
α_1 = inlet flow angle
α_2 = exit flow angle
α^* = angle of attack
ξ = stagger angle

the two-dimensional cascade, flow visualization revealed regions of severe reverse flow and large flow distortions extending a considerable distance upstream of the cascade. Sovran also noted that for conditions when rotating stall occurred, the phenomena closely resembled a Karman vortex street. After further investigating this phenomenon, Sovran suggested that propagating stall is controlled more by the overall characteristics of the system than by the details of the flow.

Cheers and Funnel (1965) examined the available published data on stall propagation speeds in cascades, isolated rotors, and a rotor with a stator, and correlated the data with a modified shape parameter similar to one proposed by Gault (1957) for describing stalling characteristics of isolated airfoils. They found that for stationary and rotating blade rows with the highest incidence at the tip, the propagation speed correlated with their shape factor. However, for rotating blade rows with the highest incidence at the root or midsection, stall propagation speed showed no dependence on blade geometry. They also noted that as the incidence angle increased well beyond where stall initially occurs, multiple cells coalesce to form one or two large cells of large amplitude with a substantial change in propagation speed. From the works of Sorvan (1959) and Cheers and Funnel (1965) the effects of blade shape on stall performance seem to be small, with the major contributions caused by overall cascade geometry.

The present investigation consisted of experimental and numerical phases where the cascade flow field and overall cascade performance were studied. Flow visualization studies were conducted as an initial part of the experimental phase to evaluate the two dimensionality of the cascade flow and to determine the degree and type of unsteadiness. Velocity and pressure measurements with pneumatic probes were made throughout the cascade flow field. The flow field upstream of the cascade was traversed with pneumatic probes in both the span and pitch directions. These measurements were conducted to quantify the two dimensionality of the flow, measure the boundary layer on the side walls and to determine the magnitude of the disturbance of the flow upstream of the cascade caused by the stalled blades. Velocity measurements within the blade passage and downstream of the cascade were made with a dual split-film probe. The dual split film probe has the capability of measuring the velocity magnitude and angle for two-dimensional flow over the full range of direction of 360 deg. Using the direction determined by the split-film probe, a pneumatic probe was aligned with the flow at each location and the total and static pressure were measured. These data were needed to evaluate the total pressure loss of the cascade. For all of the cascade tests, a single blade geometry and solidity of one were used. Cascades with stagger angles of 25, 36.5, and 45 deg were evaluated. For a limited number of cases, the effects of Reynolds number were determined by making the measurements at nominal Reynolds numbers of 50,000, 100,000, 150,000, as well as the usual 200,000.

This paper presents the results of the flow visualization studies and the time-mean velocity measurements. Part II of the paper presents the results of the experimental performance evaluation and the numerical results. The following sections describe the cascade test facility, the flow visualization procedures, and the velocity measurement procedures with the dual split-film probe. The measurement results are then presented. Conclusions are made regarding the general nature of the stalled flow as affected by the stagger angle.

Test Facility

A test facility specifically designed for investigating cascade flows with very high angles of attack and fully stalled blades was utilized in this study. The facility is shown pictorially in Fig. 1. The settling section interior cross section was 1.2 m (4 ft) square, while the nozzle discharge was 0.3 m square, providing a contraction ratio of 16:1. This large contraction ratio and the smooth nozzle contour provided a flow to the cascade test section with uniform velocity and small wall boundary layers.

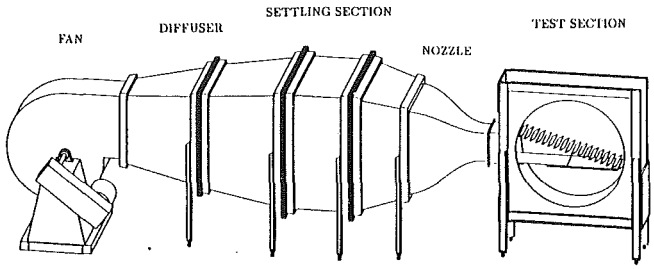

Fig. 1 Pictorial of the cascade tunnel

Honeycomb and screens were used to reduce the free-stream turbulence level to a level sufficiently low to conduct smoke flow visualization. An inlet control valve provided a range of velocities between 15 and 48 m/s in the test section. The control of the velocity over this range was utilized to evaluate the effects of Reynolds number on the cascade performance. The maximum Mach number at the inlet to the cascade was 0.15. A unique feature of the test facility was the large number of blades necessary for conducting cascade studies at very large inlet angles. Typical cascade tunnels usually have five or seven blades, while the present facility has eighteen blades. The blades were mounted between two large plexiglass disks 1.4 m in diameter. Each individual blade could be rotated about its mounting bolt, allowing the stagger angle to be varied. In addition, the assembly of blades and plexiglass disk could be rotated within the cascade housing, enabling the inlet angle and thus the angle of attack to be varied independently of the stagger angle. The large number of blades was necessary at large inlet angles in order to maintain a constant height of the cascade tunnel. At very high angles of attack, a larger number of blades was utilized. Also as the inlet angle was varied, the length of the top and bottom inlet walls varied. Removable plexiglass inlet walls of various lengths were installed, which clamped against the side walls of the cascade tunnel. Sheet metal extensions on the inlet duct overlapped the removable walls so that different walls of precise length were not required for each angle of attack.

The geometry of the blades and cascade nomenclature used in this investigation are shown in Figs. 2 and 3, respectively. The blades, which were manufactured from plates of aluminum, consisted of a circular arc suction surface and a flat pressure surface. The blade chord length was 65.5 mm, and the span of the blades was 308.0 mm, yielding an aspect ratio of 4.7:1. For the present investigation the blades were mounted in the cascade with a spacing of 65.5 mm, providing the desired solidity of unity.

For the purpose of quantifying the velocity field upstream of the cascade, flow surveys with a cobra-type pneumatic probe were made from side wall to side wall in the span direction and over a distance of four blade spacings in the pitch direction (Russ, 1987). The measurements show that the flow in the spanwise direction is uniform to within 1 m/s outside of the wall boundary layers. The boundary layers on the side walls varied in thickness from approximately 14 mm to 29 mm, depending on which wall is considered, and on the pitch location of the measurement. Even for the maximum measured boundary layer thickness of 29 mm, the blades were subjected to uniform flow over 81 percent of the span. No attempt was made to remove the boundary layer with suction upstream of the cascade, nor were porous side walls used to remove the boundary layer through the cascade. The turbulence intensity and mean velocity were also measured at an array of points, and at four different inlet velocities. The inlet velocities corresponded to Reynolds numbers based on the blade chord of

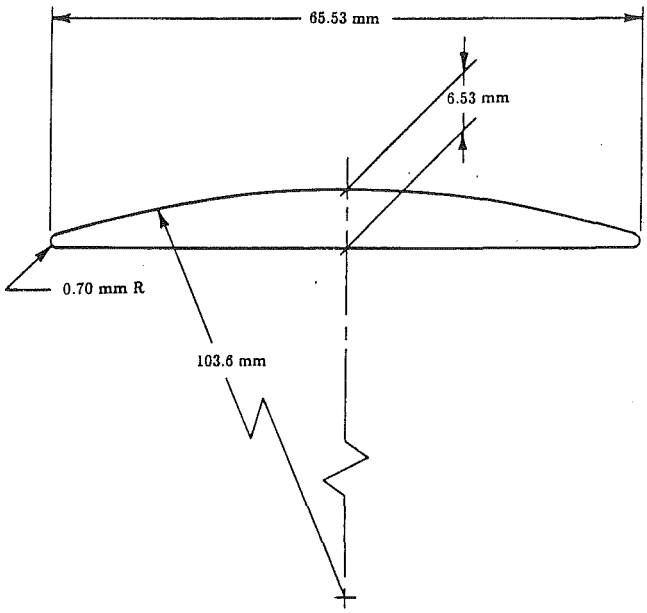

Fig. 2 Cascade blade geometry

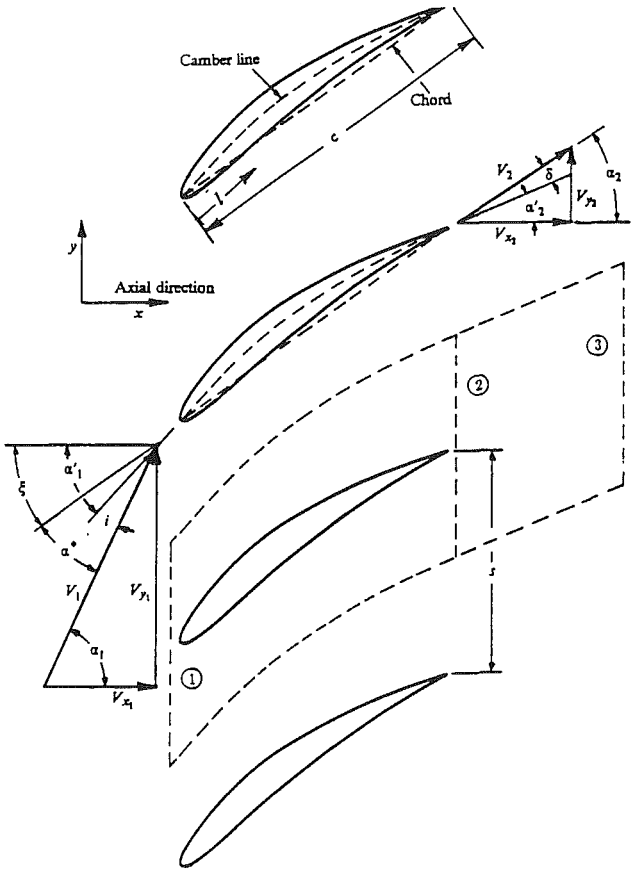

Fig. 3 Cascade geometry and velocity triangles

200,000, 150,000, 100,000, and 57,000. The array of measurement locations consisted of three span locations outside of the side wall boundary layers, with 25.4 mm increments in the pitch direction. The turbulence intensities ranged from 1.1 to 1.3 percent for all inlet velocities and measurement locations. The point-to-point variation in mean velocity was always found to be less than 1 m/s, consistent with the results from the cobra probe surveys.

Flow Visualization Procedures

Two types of flow visualization were conducted to obtain a qualitative understanding of the nature of the stalled flow prior to making detailed velocity and pressure surveys of the flow field. Russ (1987) conducted surface flow visualization tests using a mixture of titanium dioxide and diesel fuel to indicate the flow pattern on the pressure and suction blade surfaces and the rear side wall. These tests were conducted for the same array of test conditions as the tests for measuring the cascade performance. The purposes of the surface flow visualization tests were to determine the two dimensionality of the flow and to locate the separation line on the blade surface. The oil-flow visualization technique is described by Squire et al. (1962), and additional details of the test procedure for this investigation are given by Russ (1987).

To observe stalled flow, the flow in the blade-to-blade plane of the cascade had to be made visible. Visualization of flow away from a surface is most commonly performed by the injection of tracer particles. These particles must be of sufficiently small size to follow the flow accurately and of sufficient concentration and suitable composition to reflect or scatter enough light to make the flow visible. In air tunnels, smoke or fog is typically the substance used as a tracer. For this investigation, additional hardware was designed and manufactured to enable a thin sheet of fog to be injected on the vertical centerplane of the cascade.

In selecting a source of smoke or fog, some features or characteristics were considered essential. The smoke or fog must be nontoxic and noncarcinogenic, the generation device must be capable of continuous operation, and the generation must be convenient and controllable. A fog generator designed for use in theatrical productions was selected as a source of fog that would meet the above requirements. The fogging agent was obtained commercially in prefilled pressurized cans. The generation device consisted of a control valve and a heating element with a thermostat control. The fogging agent was heated as it was transported through a helical coil of tubing surrounding the heating element. Upon expanding and mixing in the surrounding air, the fluid formed a thick dense cloud of fog. A method of injecting the fog into the tunnel was necessary that would not disturb the flow or create a large wake. Griffin and Votaw (1973) and Griffin and Ramberg (1977) have conducted flow visualization studies in a wind tunnel using an aerosol injected into the flow through slots near the trailing edge of an airfoil. The airfoil was located upstream of the test section in the nozzle of the tunnel. The favorable pressure gradient in the nozzle prevented the boundary layers on the injection airfoil from becoming excessively large. An injection airfoil similar to the one used by Griffin et al. (1973, 1977) was used in the current investigation. However, the tunnel flow velocities of interest in the current investigation were much larger than the 8 m/s tunnel flow velocities used in these references. To provide a flow rate of fog sufficient for the fog injection velocity to match the tunnel velocity, pressurized air from the settling section of the tunnel was removed and mixed with fog. The mixture re-entered the tunnel through the settling section, where small ducts inside the tunnel carried the air–fog mixture to the injection airfoil located in the tunnel nozzle. This arrangement required an auxiliary fan, which needed to produce a pressure rise only as great as the losses in the fog injection system.

A plan view of the fog injection system is shown in Fig. 4. A section was added to the settling section of the tunnel, which contained a vertical strut bisecting the section. The front of the strut was open to remove air from the settling section without creating any flow disturbances. The rear section of the strut served as a duct to transfer the fog–air mixture to an upper duct in the tunnel nozzle, one of two ducts that supplied the injection airfoil. A cross section of the injection airfoil is

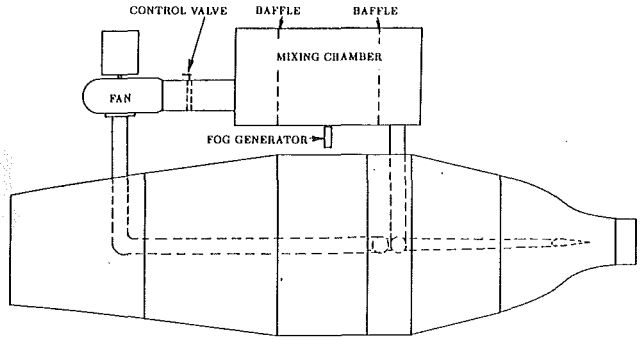

Fig. 4 Plan view of the fog injection system

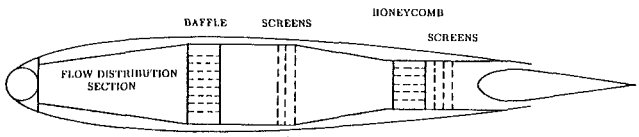

NACA 0015
254 mm CHORD

Fig. 5 Cross section of the fog injection airfoil

shown in Fig. 5. To provide a uniform sheet of fog with low turbulence, the inside of the airfoil contained many of the components of a typical wind tunnel. A baffle in the airfoil caused a sufficient back pressure to force the flow to become evenly distributed along the span. The airfoil profile was an NACA 0015 with a 254 mm chord. This system provided a sufficiently uniform and stable sheet of fog for conducting flow visualization studies. The width of each slot on the injection airfoil was 2.4 mm, providing an initial sheet of fog 4.8 mm thick. The sheet diffused a small amount before reaching the cascade, with a final thickness of approximately 9.5 mm. The diffusion of the fog was a result of the free-stream turbulence, which was visible in the flow visualization.

Still-shot photography was used to freeze the flow such that the details of the separated flow could be observed. The room was darkened and a strobe flash with a 3 ms. duration was used to illuminate and freeze the flow. Still-shot photographs using Polaroid type 47 film were taken of the cascade flow for a stagger angle of 36.5 deg, high, medium, and low velocities, and a full range of angle of attack.

High-speed photography was employed to observe the unsteadiness of the cascade flow. A Hycam II 16 mm high-speed rotating prism camera was used at a speed of 4000 frames per second. To maximize the light scattered by the fog, several high-intensity lights were used to illuminate the flow from the rear, with the camera positioned in the front. Griffin and Ramberg (1977) conducted tests to determine the light scattering properties of smoke and fog, and found that the light was scattered with a higher intensity if the incident light was from the rear. High-speed motion pictures were taken for test conditions, which included three stagger angles, the full range in angle of attack, and for some cases, high and low-speed flow.

Time-Mean Velocity Measurements With a Dual Split-Film Probe

One of the main objectives of this investigation was to determine the performance of cascades with stalled flow. To evaluate the overall performance parameters such as the deflection angle, force coefficients, and total pressure loss, the velocity magnitude and direction as well as the static and total pressure must be determined. Measurements of flow velocity

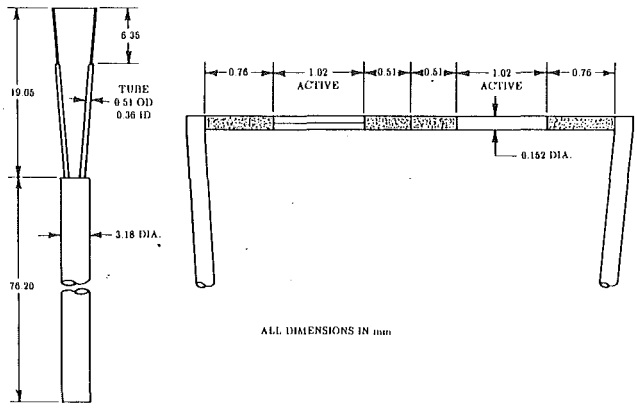

Fig. 6 Dual split-film probe

with pneumatic probes are very difficult in regions of separated flow where steep velocity gradients, very low velocities and regions of reverse flow may exist. Because of the difficulties in measuring velocity with pneumatic probes, the velocity and total and static pressure were measured in different test series with different types of instruments. To eliminate the flow angle ambiguity possible with single split film probes, a dual split film probe was employed that consisted of two pairs of split films on a single cylindrical substrate, as shown in Fig. 6. The measured velocity angle was used in the subsequent test series to align a pneumatic probe with the flow, and thereby measure the total and static pressure. The split of one pair was offset from the other by 90 degs. For steady flow, the common direction indicated by both pairs of films was taken as the true direction of the flow.

The dual split-film probe was manufactured by TSI Incorporated. A similar probe was originally designed and manufactured for research conducted by Mark et al. (1979). This probe was used to measure separated flows behind two-dimensional airfoils with deflected spoilers. This is the only other known reported work that used a dual split-film probe for measuring separated flows.

The probe was used in the constant temperature mode using standard hot-wire/hot-film electronics. For a split-film probe, the sum of the heat transfer from the two film segments indicates the velocity magnitude, while the difference between the heat transfer from the two segments of the split-film probe is indicative of the velocity direction. Several methods have been proposed for calibrating split-film probes (Jorgensen, 1982; TSI Inc., 1999; Richter, 1985). The calibration method of Richter (1985) requires a more detailed calibration, but is applicable and more accurate over a wider range of flow angles and velocities. This method consists of obtaining a calibration map of the bridge voltage of sensor one versus the bridge voltage of sensor two. The calibration map is formed by two sets of approximately orthogonal curves: one set of curves representing constant values of velocity and the other set of curves corresponding to constant flow angle. A modified version of this calibration approach was used in this investigation as described in detail by Yocum (1988). Calibration coefficients were formed to account for the possible variation in the tunnel air temperature. For one split-film pair, the calibration coefficients E_{f_1} and E_{f_2} were defined as:

$$E_{f_1} \equiv \frac{E_1^2}{k_1(T_{s1} - T_a)} \tag{1}$$

$$E_{f_2} \equiv \frac{E_2^2}{k_2(T_{s2} - T_a)} \tag{2}$$

The dual split-film probe was mounted in a wind tunnel with a special calibration device, which enabled the probe to be rotated 360 deg around the axis of the sensors. The tunnel air

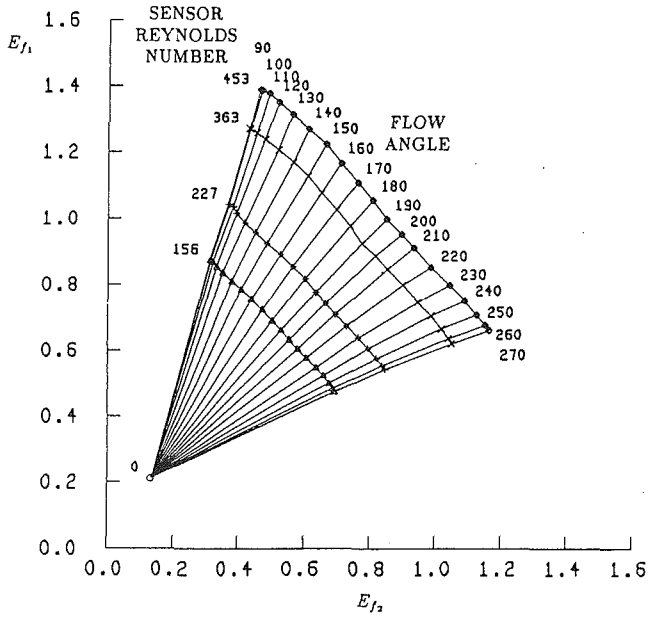

Fig. 7 Calibration data for sensors 1 and 2 for flow angles from 90 to 270 deg

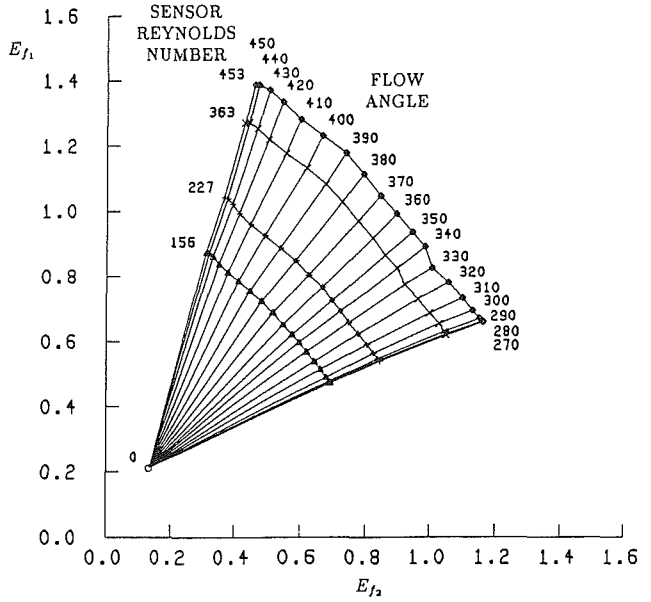

Fig. 8 Calibration data for sensors 1 and 2 for flow angles from 270 to 450 deg

speed was varied to provide a calibration for the velocity magnitude. The velocity magnitude was expressed in dimensionless form as the Reynolds number based on probe diameter, with the viscosity of the air evaluated at the measured tunnel air temperature. Results for one sensor pair of E_{f_1} versus E_{f_2} are presented in Figs. 7 and 8. The lines emanating from the point of zero speed are lines of constant flow angle relative to the probe. The lines approximately perpendicular to the constant angle lines are for constant velocity or Reynolds number. Two figures are required to present the data for one sensor pair, because as seen, the data for the range from 90 to 270 deg with 180 deg at the center would lie directly over the data for the other half of the range, which has 0 deg at the center. This characteristic of the data also illustrates the ambiguity of flow angle with a single sensor pair, and demonstrates the need for a second sensor pair to resolve the flow angle. Calibration data

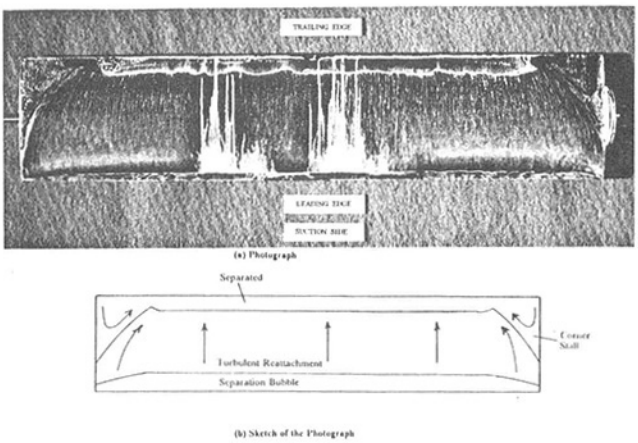

Fig. 9 Surface flow pattern for $\xi = 25$ deg and $\alpha^* = 17.5$ deg

for the other sensor pair are not presented for the sake of brevity. However, the data for the other sensor pair were similar, except with the range in angles going from 0 to 180 deg with the center angle in the two calibration maps being 90 and 270 deg.

Application of the dual split-film calibration data for measuring the velocity magnitude and angle in the cascade is described in detail by Yocum (1988). Although simple interpolation can be employed to evaluate the velocity magnitude and angle for steady flow, a modified procedure must be employed when the flow is unsteady and when only time-averaged anemometer signals are recorded.

Results and Discussion

Surface Flow Visualization and Axial Velocity Ratio. Surface flow visualization tests were conducted for the purpose of determining the location of the flow separation line on the blades and to evaluate qualitatively the two dimensionality of the flow. These tests were reported in detail by Russ (1987). The results of evaluating the axial velocity ratio, AVR, from the time-mean velocity measurements are presented along with the surface flow visualization so that the surface flow visualization can be used to explain the trends observed. The AVR is a quantitative measure of the two dimensionality of the flow. The axial velocity ratio was evaluated for the midplane of the cascade by numerical integration of the measured velocity. The axial velocity ratio is defined as:

$$\text{AVR} = \frac{V_{x_2}}{V_{x_1}} = \frac{\int_0^s u_2 dy}{\int_0^s u_1 dy} \tag{3}$$

For an incompressible and two-dimensional flow, conservation of mass requires that the average axial velocity upstream V_{x_1} equals the average axial velocity downstream V_{x_2}, and thus the AVR would be unity. However, if the flow area is restricted by boundary layer growth and/or separation from the tunnel walls, V_{x_2} will be greater than V_{x_1}.

Samples of the surface flow visualization results are presented for the cascade with a 25 deg stagger angle, for angles of attack just preceding and following the initial full stall condition. Shown in Fig. 9 is a photograph and a sketch of the flow visualization on the suction surface of the blade for a cascade with a stagger angle ξ of 25 deg and an angle of attack α^* of 17.5 deg. The symmetric blade has a camber angle of 18 deg; thus this condition corresponds to an incidence angle of 8.5 deg. As will be shown in subsequent results, this angle

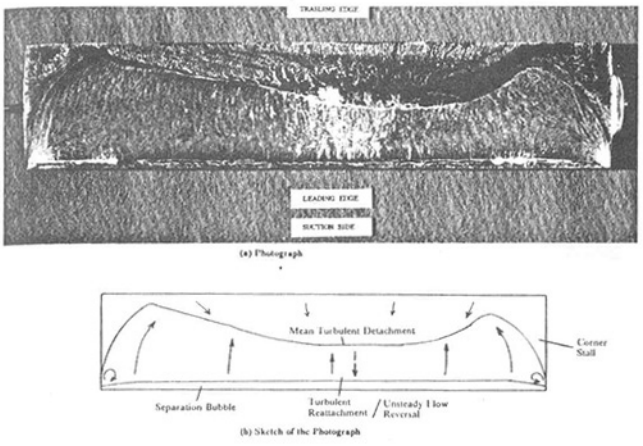

Fig. 10 Surface flow pattern for $\xi = 25$ deg and $\alpha^* = 20$ deg

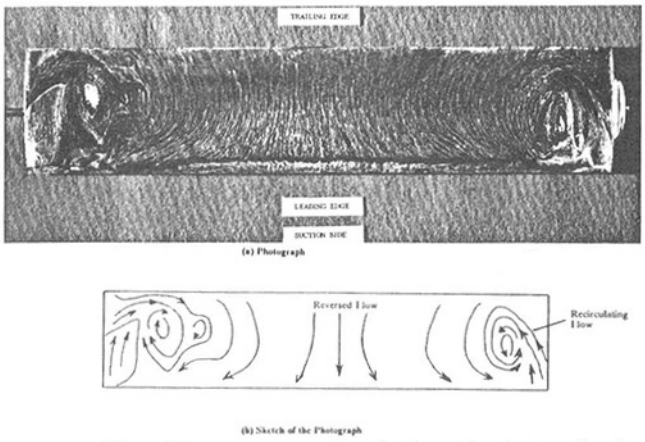

Fig. 11 Surface flow pattern for $\xi = 25$ deg and $\alpha^* = 25$ deg

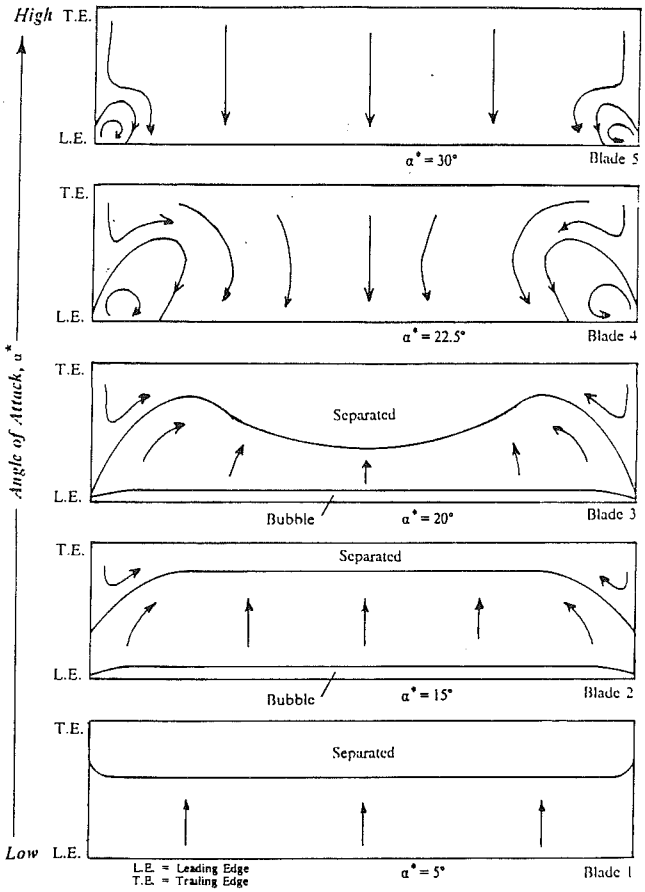

Fig. 12 Summary of the three-dimensional flow on the blade suction surface

of attack is an operating condition just preceding a full leading edge stall. The figure indicates that the flow is two dimensional over approximately 75 percent of the center region of the blade. A laminar separation bubble is evident at the leading edge, followed by a reattached turbulent boundary layer. A laminar separation bubble was observed for all tests with a positive incidence angle (angle of attack, $\alpha^* > 9$ deg) less than the incidence angle of full stall. The turbulent boundary layer is seen to separate near the trailing edge of the blade at approximately the 85 percent chord location. Figure 9 also shows that a region of reverse flow is present at both ends of the blade. This corner stall is typical of cascades with solid side walls where the tunnel wall boundary layer separates due to the adverse pressure gradient imposed by the mean flow of the cascade. The corner stall significantly increases the blockage of the flow passage, resulting in an AVR greater than unity and significantly altered cascade performance. Thus, even though the streaklines and separation lines make the flow appear to be two dimensional over a large proportion of the center of the blade, the flow in the center region is affected by the corner stall through a decrease in the pressure gradient accompanying the increased passage blockage.

Figure 10 shows the surface flow visualization for an angle of attack of 20 deg. As in the previous figure, a laminar separation bubble, followed by a reattached turbulent layer and subsequent turbulent boundary layer separation, are indicated. It is seen that the turbulent boundary layer separation line is farther from the trailing edge and is not symmetric about the center of the blade. The conditions just preceding full stall were found to be the only conditions where the streaklines deviated significantly from a symmetric pattern. Also note that the separation line just outside of the corner stall region is nearer to the trailing edge than the separation line for the center portion of the blade. When the AVR results are presented, it will be shown that this flow pattern has a somewhat unexpected effect on the value of the axial velocity ratio, which is evaluated at the midplane of the cascade. The explanation for the observed flow pattern is that the blockage of the corner stall region causes the flow outside of the corner separated region to accelerate such that it has sufficient momentum to delay separation to a location nearer to the trailing edge.

Results from the surface flow visualization test for $\xi = 25$ deg and $\alpha^* = 25$ deg are presented in Fig. 11. At this angle of attack the flow separates from the leading edge of the blade, referred to in this paper as full stall. Reverse flow is present on the entire central region of the blade with swirling flow regions indicated at the ends of the blades. The reverse flow streaklines have significant curvature, except on the line of symmetry at the center of the blade. The curvature in the streaklines indicates the flow is not two dimensional, but the symmetry suggests that a fairly uniform region of separated flow exits over the center 75 percent of the blade.

A summary of the results of the surface flow visualization tests for a range in angle of attack from 5 to 30 deg is presented in Fig. 12. The sketch of the flow pattern for an angle of attack of 5 deg (incidence angle, $i = -4$ deg) shows that for this negative incidence a laminar separation bubble is not present, but that laminar separation occurs at approximately the 60 percent chord location. Blade sketches 2, 3, and 4 in Fig. 12 summarize the flow patterns discussed above with the visualization photographs. The fifth sketch illustrates how the surface flow pattern changes as the angle of attack is increased

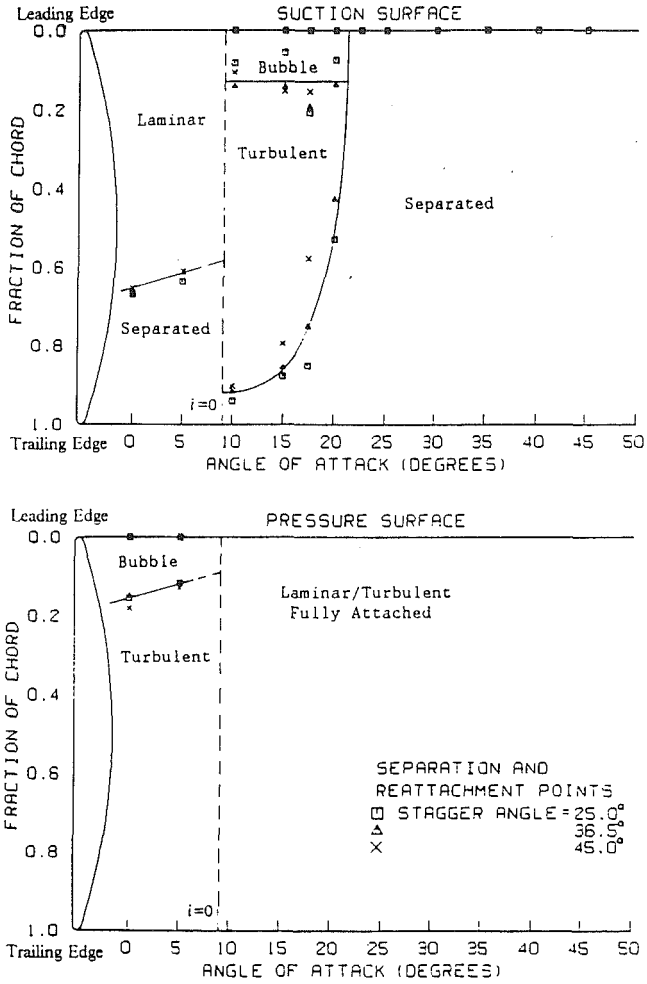

Fig. 13 Summary of the midspan boundary layer development for $Re_c = 2.0 \times 10^5$ and $Tu = 1.1$ percent

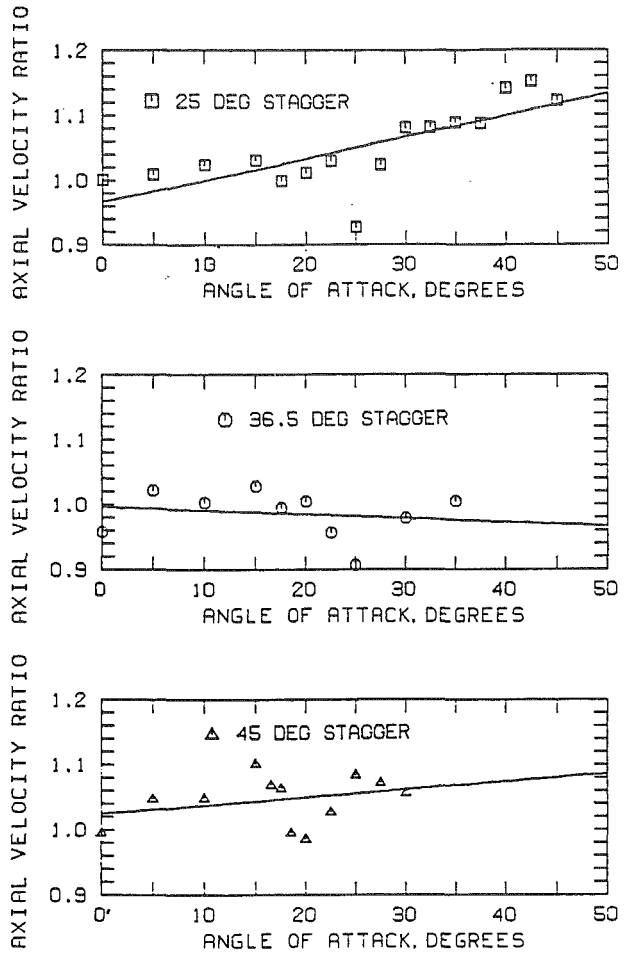

Fig. 14 Axial velocity ratio for cascades with staggers of 25, 36.5, and 45 deg

beyond the initial occurrence of full stall. It is seen from the fifth sketch that the streaklines become straighter over most of the blade, and that the swirling flow patterns near the ends of the blade extend over a smaller region and have less effect on the primary flow.

The quantitative information, which can be determined from the surface flow visualization, is the location of the separation line at the midspan of the blade. Figure 13 summarizes the type of boundary layer on the blade surface and location of separation as a function of angle of attack for both the suction and pressure surfaces of the blade. Data for the three stagger angles of 25, 36.5, and 45 deg are presented. To help identify the various flow regions, curves have been fit to the mean data. The curve representing the turbulent boundary layer separation location generally follows the data for the stagger angle of 36.5 deg. For a stagger of 25 deg, separation occurs nearer the trailing edge, and for a stagger of 45 deg the separation occurs closer to the leading edge. Thus, it is observed that the stagger angle significantly affects the location of separation. Subsequent smoke flow visualization results and the time-mean velocity measurements will show that the stagger angle is also a key parameter in determining the stability of the stalled flow and the nature of the flow in the blade-to-blade plane.

The axial velocity ratio (AVR) data were computed from the time-mean velocity measurements made just downstream of the cascade. The data for the cascades of each of the three stagger angles are plotted in Fig. 14 as a function of angle of attack. To illustrate the general trend in the data, a straight line has been fit to the data using a least-squares technique. Realizing that a value of the axial velocity ratio greater than unity results from an increase in blockage of the flow by the wall boundary layer and corner stall, it is expected that the AVR should increase with increasing angle of attack. For the stagger angles of 25 and 45 deg, the AVR does increase with angle of attack. For the 36.5 deg stagger cascade, the AVR is approximately constant, with a slight decrease with increasing α^*. It should be observed that for all three cascades, a drop in the AVR occurs near 20 to 25 deg angle of attack. Recalling that full stall initially occurred near these angles of attack, the drop in the AVR appears to be associated with the highly three-dimensional nature of the flow at these conditions. Because the surface flow visualization indicated that three-dimensional flow occurred near the initial full-stall condition, the AVR evaluated for the midplane of the cascade is not indicative of the blockage associated with the wall stall.

Smoke Flow Visualization and Time-Mean Velocity Measurements. Smoke flow visualization tests were conducted to examine qualitatively the nature of the stalled flow and to determine the existence and type of unsteadiness. Separated flows are usually unsteady. However, an ordered unsteadiness in the form of a propagating stall is also possible. The existence and type of unsteadiness is important in itself, particularly if design variables affect the occurrence of propagating stall and the propagating speed. It was also important to know whether the flow was unsteady when evaluating the data from the pressure and velocity measurements.

Still shot photographs were initially taken over a range of angle of attack for the cascade with 36.5 deg stagger. These

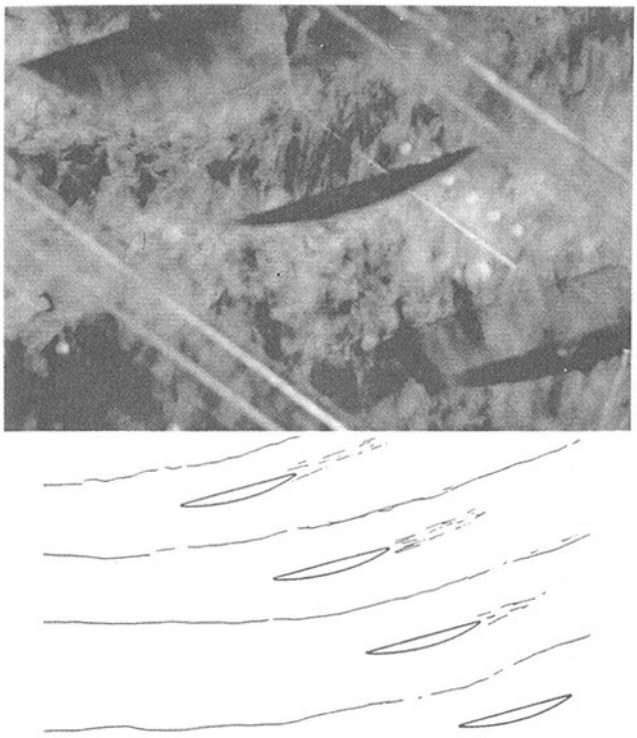

Fig. 15 Photograph and sketch of the smoke flow visualization for ξ = 36.5 deg and α^* = 15 deg

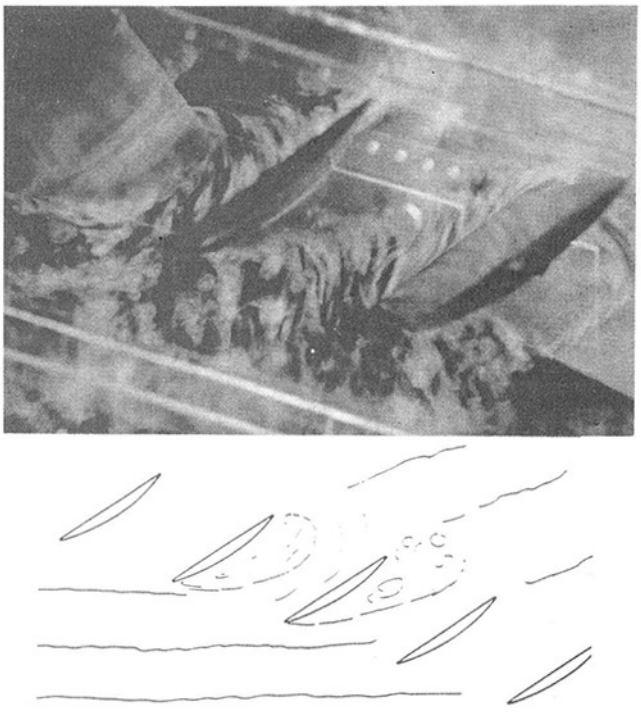

Fig. 17 Photograph and sketch of the smoke flow visualization for ξ = 36.5 deg and α^* = 35 deg

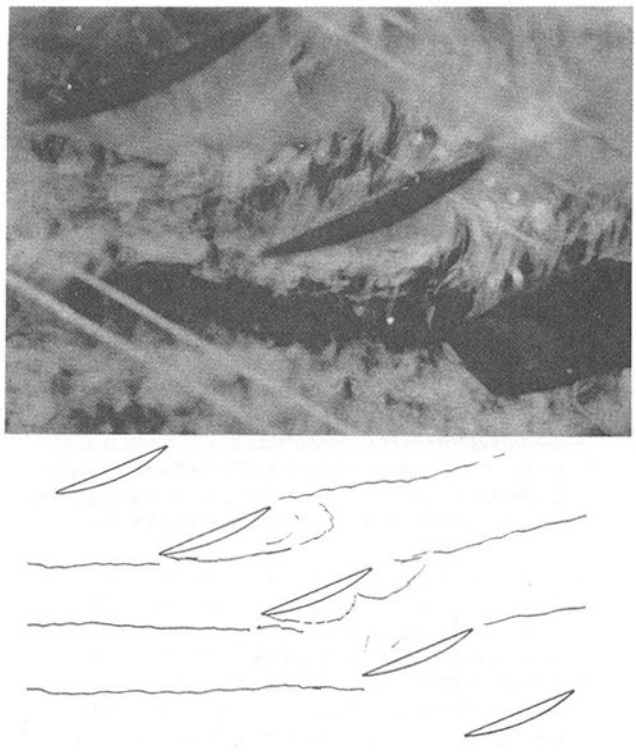

Fig. 16 Photograph and sketch of the smoke flow visualization for ξ = 36.5 deg and α^* = 25 deg

photographs were taken to determine whether high-speed photography would reveal the flow structures of interest. Figures 15, 16, and 17 are sample photographs of the flow at angles of attack of 15, 25, and 35 deg. In Fig. 15, the smoke reveals the free-stream turbulence and a possible separation region near the trailing edge of the airfoil. For this angle of attack, the boundary layers appear to be attached over most of the blade. Mixing in the wakes of the airfoils is evident from the more diffuse smoke in these regions. Figures 16 and 17 show the flow for angles of attack of 25 and 35 deg, respectively. For both of these photographs, large separated regions are evident. It appears that the flow separates from the leading edge of the blades and that the size of the separated region increases with an increase in angle of attack. It is also evident in both Figs. 16 and 17 that the separated regions at this instant in time are not identical in the two neighboring passages. In Figure 16 the separated region in the middle passage is larger and contains more diffuse smoke than the separated region in the passage below. In the passage below the middle passage, the separated region is smaller, with greater contrast in the smoke along the edge and with the smoke appearing to curl into the separated region. The differences observed in the two passages of Fig. 16 are similar to what would be expected if propagating stall were present. However, conclusive evidence with regard to the existence of propagating stall required high-speed motion pictures.

High-speed motion pictures taken at 4000 frames per second were subsequently studied at 16 frames per second, providing a reduction in speed by a factor of 250 to 1. With this reduction in speed, propagating stall was easily identified when present. The stagger angle of the cascade blades was found to be the major parameter in determining the occurrence of propagating stall. For the 25 deg stagger cascade, propagating stall was not observed even at angles of attack as large as 45 deg. For the cascades with stagger angles of 36.5 and 45 deg, propagating stall was observed at all angles of attack of 20 deg and greater. Contrary to what may have been expected, the flow did not restabilize at high angles of attack, but continued to reveal propagating stall superimposed on a mean full stall. The propagating stall evident in the films showed the classical blockage of a passage, the flow diversion upstream of the cascade around the blockage, and the subsequent recovery (or complete flushing out) in the passage behind the propagating cell. Ahead of the stall cell, the increase in angle of attack caused by the flow diverging around the blockage resulted in the next blade stall-

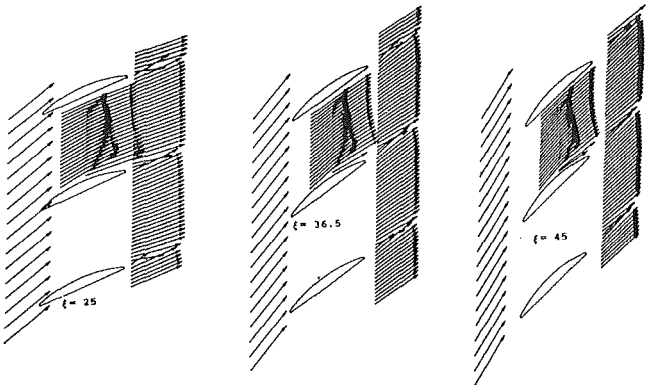

Fig. 18 Blade-to-blade and discharge velocity profiles for three stagger angles and $\alpha^* = 15$ deg

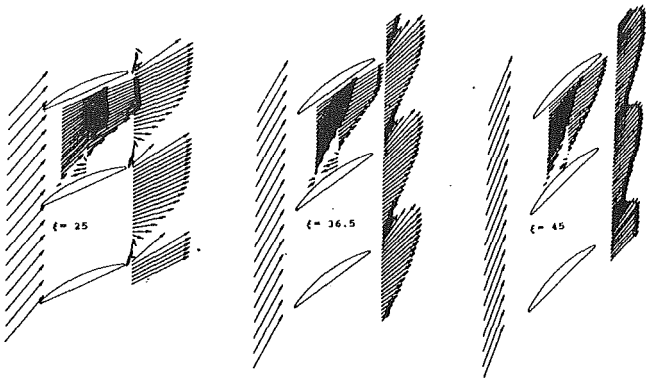

Fig. 20 Blade-to-blade and discharge velocity profiles for three stagger angels and $\alpha^* = 25$ deg

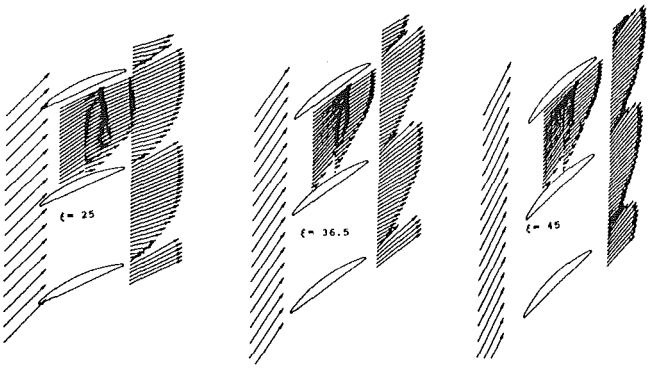

Fig. 19 Blade-to-blade and discharge velocity profiles for three stagger angles and $\alpha^* = 20$ deg

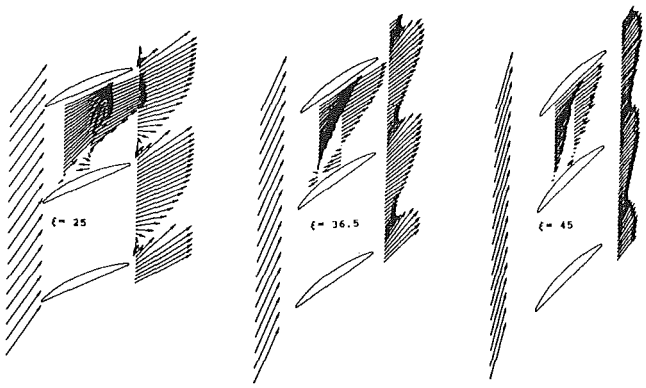

Fig. 21 Blade-to-blade and discharge velocity for three stagger angles and $\alpha^* = 30$ deg

ing. It was also observed that stall propagation was associated with almost complete blockage of a passage and not just an increase in blockage from the mean. For the 25 deg stagger cascade the stall cells did not propagate, and in this case the passages were observed never to be completely blocked.

The frequency of occurrence of propagating stall was studied by Piatt (1986) using the motion picture film obtained in the present study. This quantity is of interest in order to obtain an indication of the degree of unsteadiness. The frequency of occurrence is probably controlled by both the tunnel characteristics that affect the triggering mechanism of propagating stall, and the geometry of the cascade itself. By dividing the blade spacing by the propagation speed and multiplying by the frequency of occurrence, the fraction of time that a blade passage undergoes propagating stall is computed. Although the results of this calculation show scatter, some general trends with respect to angle of attack can be made. At an angle of attack of 20 deg, propagating stall is present approximately 20 percent of the time. At higher angles of attack, propagating stall is present between 40 and 90 percent of the time. For cases where propagating stall is present 90 percent of the time, it is apparent that severe fluctuations in the flow are occurring almost continuously. In these cases, the time-averaged velocity measurements will indicate a flow field that is strongly influenced by unsteady mixing in the blade passage.

Both the surface oil-flow visualization and the smoke flow visualization showed that the blade stagger angle strongly affected the characteristics of the separated flow. The time-mean velocity measurements also indicate that the characteristics of the blade-to-blade velocity profiles were strongly dependent on the stagger angle. Figures 18–21 compare the velocity profiles for the three stagger angles tested for four angles of attack. Figure 18 presents the results for an angle of attack of 15 deg. At this angle of attack the turbulent boundary layer separates near the trailing edge, and no reverse flow regions were indicated at the measurement locations. In this figure, the velocity profiles within the blade passage primarily indicate potential flow characteristics. The observed increase in velocity when traversing the passage from the pressure to suction surfaces is typical of a loaded blade. Downstream of the cascades the velocity is seen to be uniform, except for a small wake region. Figures 19–21 present comparisons of the velocity profiles for the three cascades with progressively increasing angles of attack. In Fig. 19 the angle of attack is 20 deg, which is a condition just preceding a full leading edge stall. No reverse flow velocity vectors were measured, but the viscous effects for this condition are seen to extend well into the blade passage. At this angle of attack, it is apparent that the stagger angle determines the extent of the passage affected by the viscous flow.

Figures 20 and 21 present the velocity profiles for angles of attack of 25 and 30 deg, respectively. These figures show large reverse flow regions and dramatically demonstrate the strong effects of the stagger angle on the characteristics of the stalled flow velocity profiles. For the cascade with 25 deg stagger angle, the flow is characterized by two distinct regions: a recirculating flow region and a region with essentially inviscid flow. The cascades with stagger angles of 36.5 and 45 deg do not show distinct regions, but instead show that the entire passage is affected by the viscous effects and the recirculating flow. Comparing the profiles for the 25 deg stagger cascade in Figs. 20 and 21, it is seen that the increase in angle of attack from 25 to 30 deg has very little effect on the size of the separated flow region. The results for the cascade with a stagger angle of 36.5 deg show that separated flow affects a greater portion of the passage to a greater degree as the angle of attack increases from 25 to 30 deg. The results for the cascade with

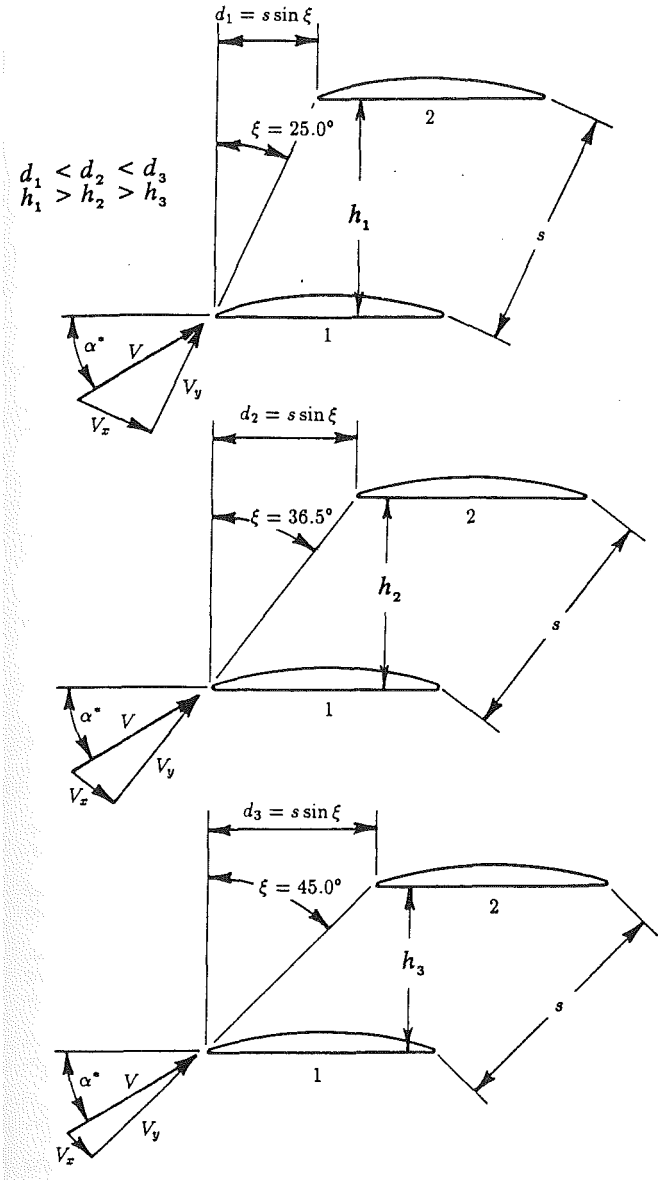

Fig. 22 Sections of three cascades of different staggers, illustrating how stagger affects blade interaction

a stagger of 45 deg and an angle of attack of 25 deg show that the entire passage is affected by the stalled flow, and that the additional increase in the angle of attack to 30 deg has little effect on the extent of the passage affected by the stalled flow.

The results of the time-mean velocity measurements are clearly consistent with the characteristics of the stalled flow observed in the smoke flow visualization. Recall that the smoke flow visualization did not show a propagating stall with the 25 deg stagger cascade, and that the lack of stall propagation was associated with a less-than-complete blockage of the passage by the recirculating region. These observations are consistent with the observation in the velocity profile measurements that the recirculating region did significantly increase in size with increasing angle of attack, and that two distinct flow regions existed. Propagating stall was observed for 36.5 and 45 deg stagger cascades as a result of almost complete blockage of the passage by the stall cell. Again, this is consistent with the measured velocity profiles, which showed that the entire passage was affected by the stalled flow.

Several possible causes for the observed strong effects of stagger can be deduced with physical reasoning. One possible cause becomes apparent when examining how stagger alters the amount of blade interaction near the leading edge. In Fig. 22, sketches of three cascades of blades are presented to illustrate staggers of 25, 36.5, and 45 deg. When viewed with respect to the blade chord, it is seen that increasing the stagger has the effect of sliding the upper blade away from the leading edge of the lower blade. The distance d illustrated in the figure is greater for cascades with larger stagger angles. Flow entering the blade passage from around the leading edge of the lower blade encounters the influence of the neighboring blade above, and is directed into the passage at a shorter distance from the leading edge for smaller staggered cascades. Consequently, for small stagger angle cascades, the separated region extends a shorter distance into the blade passage. A second geometric effect of the stagger angle is that the perpendicular distance between blades, designated as h in Fig. 22, is smaller for higher stagger cascades. Thus, for a given size of the recirculating flow region, the fraction of the passage affected by the recirculating flow will be greater for higher stagger angle cascades.

A third way in which the stagger angle may affect the stalled flow characteristics is related to the comparative values of the axial and tangential velocity components. Velocity triangles are included in Fig. 22 to illustrate the change in V_x and V_y with stagger angle for a constant value of angle of attack. It is seen that the axial velocity component becomes smaller and the tangential component larger as the stagger angle increases. On this basis, it is reasonable to expect that the flow of a larger stagger cascade is more easily diverted around the separated region, again resulting in the effects of the separated region extending further into the blade passage.

Summary and Conclusions

Results have been presented from surface flow visualization, smoke flow visualization, and time-mean velocity measurements of stalled flow in a low-speed two-dimensional cascade of airfoils. For each type of test, the results indicated that the blade stagger angle is a key parameter in determining the characteristics of the separated and fully stalled flow. Surface flow visualization was used to evaluate the two dimensionality of the flow and to determine the location of the separation line on the blades. A laminar separation bubble near the leading edge was observed for all positive incidence angles below the angle of full stall. The reattached turbulent boundary layer separated at a shorter distance from the leading edge for the cascades with the larger stagger angles. Also, fully stalled flow occurred at a slightly lower angle of attack for the cascades with greater stagger. The transition from separation near the midchord to full stall occurred for each cascade in the range from 17.5 to 22.5 deg angle of attack.

Smoke flow visualization studies were conducted to study qualitatively the nature of the separated flow, and to investigate the existence and type of unsteadiness. From these tests it was concluded that the separated region extends further into the blade passage for larger stagger cascades at the same angle of attack. Consequently, the blockage of the passage by the separated flow is greater for the cascades with larger stagger angles. The stability of the stalled flow and the occurrence of propagating stall was found to be related to the passage blockage, and thus the stagger angle of the cascade. The stalled flow becomes unstable and propagating stall occurs for cascades with large stagger angles. In this investigation, propagating stall was observed for the 36.5 and 45 deg stagger cascades. Propagating stall was never observed for the 25 deg stagger cascade, even at angles of attack as high as 45 deg. For the cascades where propagating stall was found to occur, it occurred for all angles of attack greater than or equal to the full-stall inception angle. Propagating stall was found to result from complete or almost complete blockage of the passage, and did not result from just an increase in blockage associated with transition to full stall.

The results from the time mean-velocity measurements fur-

ther illustrated the effects of the blade stagger angle on the characteristics of the stalled flow. The measured velocity profiles were consistent with the qualitative observation made from the smoke flow visualization. For the lowest stagger cascade, $\xi = 25$ deg, two distinct regions of the flow existed: a region of nearly potential or inviscid flow and a viscous region of recirculating flow. For the larger stagger cascades, the two distinct regions were not evident, and the effects of the recirculating flow region were seen to extend across the entire passage. Thus, the velocity profiles for the larger stagger cascades exhibited greater blockage of the passage as also observed in the smoke flow visualization. In Part II of this paper, the relationship between the observed flow characteristics and the overall performance of the cascades will be presented.

Acknowledgments

This investigation was sponsored by the Air Force Office of Scientific Research under the direction of Dr. James Wilson. The support of the AFOSR is greatly appreciated.

References

Bogdonoff, S. M., 1948, "NACA Cascade Data for the Blade Design of High Performance Axial-Flow Compressors," *Journal of Aeronautical Sciences*, Feb.

Cheers, F., and Funnel, G. C, 1965, "Note on the Speed of Stall Propagation in a Cascade of Aerofoils," *The Aeronautical Quarterly*, Vol. XVI, Part 2, pp. 179–186.

Christiani, K., 1928, "Experimentelle Untersucung eines Tragflugelprofils bei Gitteranordnung," *Luchfahrtfers 2*.

Clayton, B. R., and Massey, B. S., 1967, "Flow Separation in an Aerofoil Cascade," *Journal of the Royal Aeronautical Society*, Vol. 71, No. 680, pp. 559–565.

Constant, H., 1937, "Performance of Cascades of Aerofoil," ARC R&M 1768.

Cousins, W. T., and O'Brien, W. F., 1985, "Axial-Flow Compressor Stage Post-stall Analysis," *AIAA Paper No. 85-1349*.

Davis, M. W., Jr., and O'Brien, W. F., 1991, "A Stage-by-Stage Post-stall Compression System Modeling Technique," *AIAA Journal of Propulsion and Power*, Vol. 7, No. 6, pp. 997–1005.

Erwin, J. R., and Emery, J. C., 1951, "Effect of Tunnel Configuration and Testing Technique on Cascade Performance," NACA Report No. L016.

Gault, D. E., 1957, "A Correlation of Low-Speed, Airfoil-Section Stalling Characteristics With Reynolds Number and Airfoil Geometry," NACA Technical Note 3963.

Gostelow, J. P., 1984, *Cascade Aerodynamics*, Pergamon Press, New York.

Greitzer, E. M., 1976, "Surge and Rotating Stall in Axial-Flow Compressors, Part I: Theoretical Compression System Model," ASME *Journal of Engineering for Power*, Vol. 98, pp. 190–198.

Greitzer, E. M., 1980, "REVIEW-Axial Compressor Stall Phenomena," ASME *Journal of Fluids Engineering*, Vol. 102, pp. 134–151.

Griffin, O. M., and Votaw, C. W., 1973, "The Use of Aerosols for the Visualization of Flow Phenomena," *International Journal of Heat and Mass Transfer*, Vol. 16, pp. 217–219.

Griffin, O. M., and Ramberg, S. E., 1977, "Wind Tunnel Flow Visualization With Liquid Particle Aerosols," *Proceedings of the International Symposium on Flow Visualization*, pp. 65–73.

Harris, R. S., and Fairthorne, R. A., 1928, "Wind Tunnel Experiments With Infinite Cascades of Aerofoils," ARC R&M 1206.

Horlock, J. H., 1973, *Axial-Flow Compressors, Fluid Mechanics and Thermodynamics*, Robert E. Krieger Publishing Co., Huntington, NY.

Jorgensen, F. E., 1982, "Characteristics and Calibration of a Triple-Split Probe for Reversing Flows," DISA Information No. 27.

Lieblein, S., 1965, "Experimental Flow in Two-Dimensional Cascades," *Aerodynamic Design of Axial-flow Compressors*, NASA SP-36, Chap. VI, pp. 183–226.

Mark, M. D., Seetharam, H. C., Kuhn, W. G., and Bright, J. T., 1979, "Aerodynamics of Spoiler Control Devices," AIAA Paper No. 79-1873.

Piatt, D. R., 1986, "Development of a Geometric Model for the Study of Propagating Stall Inception Based on Flow Visualization in a Linear Cascade," M. S. Thesis, Mechanical Engineering, Virginia Polytechnic Institute and State University, Blacksburg, VA.

Pollard, D., and Gostelow, J. P., 1967, "Some Experiments at Low Speed on Compressor Cascades," ASME *Journal of Engineering for Power*, Vol. 89, pp. 427–436.

Rhoden, H. G., 1952, "Effects of Reynolds Number on the Flow of Air Through a Cascade of Compressor Blades," Aeronautical Research Council Reports and Memoranda No. 2919.

Richter, H., 1985, "Measurements of Two-Dimensional Periodical Flow Behind Turbine Guide-Vanes by Means of a Split-Fiber Probe," *Dantec Information No. 1*, DANTEC Elektronik, Denmark, pp. 10–12.

Roberts, W. B., 1975a, "The Experimental Cascade Performance of NACA Compressor Profiles at Low Reynolds Number," ASME *Journal of Engineering for Power*, Vol. 97, pp. 454–459.

Roberts, W. B., 1975b, "The Effect of Reynolds Number and Laminar Separation on Axial Cascade Performance," ASME *Journal of Engineering for Power*, Vol. 97, pp. 261–274.

Russ, T. W., 1987, "A Surface Flow Visualization Study of Boundary Layer Behavior on the Blades of a Solid-Wall Compressor Cascade at High Angles of Attack," M. S. Thesis, Mechanical Engineering, Virginia Polytechnic Institute and State University, Blacksburg, VA.

Sexton, M. R., 1980, "An Investigation of the Dynamic Stalling Characteristics of Rotating Axial-Flow Compressor Blades," Ph.D. Dissertation, Mechanical Engineering, Virginia Polytechnic Institute and State University, Blacksburg, VA.

Sovran, G., 1959, "The Measured and Visualized Behaviour of Rotating Stall in an Axial-Flow Compressor and in a Two-Dimensional Cascade," *Transactions of the American Society of Mechanical Engineers*, Vol. 81, pp. 24–34.

Squire, L. C., Maltby, R. L., Keating, R. F. A., and Stanbrook, A., 1962, "The Surface Oil Flow Technique," *Flow Visualization in Wind Tunnels Using Indicators*, NATO AGARDograph No. 70, North Atlantic Treaty Organization Advisory Group for Aerospace Research and Development, pp. 1–74.

Stenning, A. H., and Kriebel, A. R., 1958, "Stall Propagation in a Cascade of Airfoils," *Transactions of the American Society of Mechanical Engineers*, Vol. 80, pp. 777–790.

Takata, H., and Nagano, S., 1972, "Nonlinear Analysis of Rotating Stall," ASME *Journal of Engineering for Power*, Vol. 94, Series A, No. 4, pp. 279–293.

TSI Inc., 1999, "TSI Split Film Sensor, Calibration and Application," *TSI Technical Bulletin 20*, St. Paul, MN.

Yocum, A. M., 1988, "An Experimental and Numerical Investigation of the Performance of Compressor Cascades With Stalled Flow," Ph.D. Dissertation, Mechanical Engineering, Virginia Polytechnic Institute and State University, Blacksburg, VA.

Separated Flow in a Low-Speed Two-Dimensional Cascade: Part II—Cascade Performance

A. M. Yocum
Applied Research Laboratory,
Pennsylvania State University,
State College, PA 16804

W. F. O'Brien
Virginia Polytechnic Institute
and State University,
Blacksburg, VA 24061

This study was conducted for the purpose of providing a more fundamental understanding of separated flow in cascades and to provide performance data for fully stalled blade rows. Cascades of a single blade geometry and a solidity of unity were studied for three stagger angles and the full range of angle of attack extending well into the stalled flow regime. The Reynolds number was also varied for a limited number of cases. Results from velocity and pressure measurements made in the cascade and the overall cascade performance evaluated from these measurements are presented. In addition, results from a numerical simulation of the flow through a cascade of flat plate airfoils are used to illustrate further the effects of blade stagger and to define the correct limits for the cascade performance. The results indicate that the slope of the total pressure loss versus angle of attack curve for the flow immediately downstream of the cascade is steeper for cascades with greater stagger. The normal force coefficient was found to increase to a peak value near the angle of attack where full leading edge stall first occurs. A further increase in angle of attack results in a decline in the normal force coefficient. The peak value of the normal force coefficient is greater and occurs at a higher angle of attack for the cascades with smaller stagger.

Introduction

In the field of axial-flow turbomachinery, the two-dimensional cascade model is often used experimentally or numerically to investigate the fundamental flow characteristics and overall performance of blade rows. Traditionally, cascade tests have been used to measure blade row performance as a function of airfoil geometry, cascade geometry, and operating parameters. These types of tests usually span the range in incidence angle from the negative to positive incidence stall conditions. However, prior to this investigation, no investigations have been conducted that thoroughly examine the post-stall flow characteristics and performance of two-dimensional cascades. The current investigation was conducted for the purposes of providing a more fundamental understanding of separated flow in cascades and to provide performance data for fully stalled blade rows. A knowledge of the characteristics of stalled flow in cascades and the overall performance data can be applied to the development of improved blade models for use in post-stall analysis or far off-design performance prediction of compressors and pumps. In addition, the flow visualization results and the detailed velocity and pressure data can be used to evaluate the capabilities of two- and three-dimensional CDF codes in predicting stalled flows. In the present investigation, cascades with a single blade geometry, a solidity of unity, and stagger angles of 25.0, 36.5, and 45.0 deg were studied over a full range of angle of attack extending well into the stalled flow regime.

Part I of this paper presented the results of blade surface flow visualization, smoke flow visualization, and time-mean velocity measurements. The oil-flow technique for surface flow visualization was used to evaluate the two-dimensionality of the flow and to determine the location of the separation line. The smoke flow visualization tests were conducted to examine qualitatively the nature of the stalled flow and to determine the existence and type of unsteadiness. Although the time-mean velocity surveys are an integral part of the flow field measurements and cascade performance evaluation, these results were presented in Part I of this paper to complete the description of the velocity field and to illustrate the effects of cascade stagger angle on the flow characteristics. The results from the time-mean velocity measurements were used to align a total pressure probe with the flow and subsequently to evaluate the overall cascade performance parameters. This paper will describe the total and static pressure measurements and the overall performance of the cascades. In this investigation, the cascade performance is expressed in terms of a normal force coefficient and a mass-averaged total pressure loss coefficient. Numerical predictions of the cascade flow field and performance are also presented. The Navier–Stokes equations for flow through a cascade of flat plate airfoils were solved using the SIMPLER algorithm (Patankar, 1980). The results from the numerical study were used to determine the trends in the performance parameters at angles of attack far exceeding those that were practical for testing. For example, numerical

Contributed by the International Gas Turbine Institute and presented at the 37th International Gas Turbine and Aeroengine Congress and Exposition, Cologne, Germany, June 1–4, 1992. Manuscript received by the International Gas Turbine Institute March 5, 1992. Paper No. 92-GT-357. Associate Technical Editor: L. S. Langston.

results were obtained for inlet flow angles α_1 as great as 85 deg.

A survey of the literature concerning cascade tests was presented in Part I of this paper. This discussion of the literature served to illustrate proper cascade test procedures and to document the nonexistence of data describing fully stalled performance of cascades. To complete this survey of the literature on topics relevant to stalled flow in cascades, a review of the literature pertaining to analytical and numerical methods for predicting stalled flow performance of cascades will be presented.

An early approximate analytical procedure for analyzing fully stalled flow in a cascade was reported by Horlock (1973) and Cornell (1954). Cornell solved for the potential flow through a flat plate cascade, assuming the separated region started at the leading edge and was bounded by a free streamline. Along the free streamline, pressure and velocity were assumed constant. Assuming all mixing and losses occurred downstream of the cascade, he calculated the losses and deflection resulting from complete mixing of the jet and the wake. This approach enabled the effects of incidence, stagger, and solidity to be included. However, the assumptions of a free-streamline and no losses within the blade passage neglect much of the important physics of the flow.

In a recent publication by Moses and Thomason (1986) a control volume approach was used to obtain algebraic equations with which to estimate the performance of a fully stalled compressor blade row. The flow was assumed to separate from the leading edge and a loss factor k was defined to account for mixing within the blade passage. At the trailing edge plane the flow was assumed to consist of two regions, a jet of high velocity and a wake where the velocity is assumed to be essentially zero. The size of the separated region did not enter into the calculation. The goal of the procedure was to provide a simple approach for estimating the losses and normal forces, which would approach the correct limits as the throughflow is reduced to zero. When compared with the very limited data of O'Brien et al. (1983), the results were shown to give the correct trends. The results from this approximate procedure are highly dependent on the relationship suggested for calculating the loss factor k. The authors assumed the loss factor was proportional to the blade chord and inversely proportional to the mass flow rate per blade passage. The effects of stagger and angle of attack were not included in the approximation for k.

At an intermediate level of approximation between the method just described and a solution of the Navier–Stokes equations, extensions of boundary layer theory have been made by Moses et al. (1978) to allow separated flow to be studied. Moses et al. (1981), and O'Brien et al. (1983) applied this approach to cascade flow, simultaneously solving the inviscid flow and the integral boundary layer equations. Since a simultaneous solution procedure was used rather than the common interactive procedures, the singularity at the separation point was avoided. Comparisons of results from this approach were compared with experimental data of Tkacik (1982). The method gave correct trends, but did not predict nearly as steep a rise in the losses when the flow separates as was observed experimentally. For very large separated regions where the inviscid region is very small or nonexistent, the method can no longer be applied.

When the details of the flow are required and when the separated region is large, solution of the Navier–Stokes equations (or Reynolds-averaged equations) is required. However, many of the Navier–Stokes cascade codes were developed for analyzing compressible flow in the transonic regime, and may not run efficiently for low-speed or incompressible flows or flows with large separated regions. Examples of cascade codes that solve the Navier–Stokes equations for transonic flow are reported by Shamroth et al. (1984), Weinberg et al. (1986), Steger et al. (1980), and Schäfer et al. (1985). These computer codes all employ some form of time marching, implicit method of solution. Hah (1983, 1984) has solved the Reynolds-averaged Navier–Stokes equations for compressible flow through a two-dimensional cascade and for three-dimensional flow through a rotor. Hah's approach is based on a control volume formulation and a pressure corrector type of solution procedure. These investigations are concerned with stall phenomena and the blade row performance at a stalled condition. However, the changes in performance as the angle of attack is increased far beyond initial stall are not reported.

Rosenfeld and Wolfshtein (1982) have solved the Navier–Stokes equations for the case of incompressible, laminar, separated flow through a two-dimensional cascade. With the assumptions of incompressible two-dimensional flow, a vorticity-stream function type of formulation was employed. This formulation eliminates the pressure from the governing equations, simplifying the solution procedure. Rosenfeld and Wolfshtein solved the governing equations using a directly constructed nonorthogonal grid system. Results were presented for sepa-

Nomenclature

AVR = axial velocity ratio
c = chord length
C_{F_n} = dimensionless normal force coefficient
$C_{M_{mc}}$ = dimensionless moment coefficient about the midchord point
C_p = blade pressure coefficient
C_{p_s} = static pressure coefficient
C_{p_t} = total pressure coefficient
$C_{p\ \mathrm{yaw}}$ = pneumatic probe yaw angle calibration coefficient
$C_{p\ \mathrm{static}}$ = pneumatic probe static pressure calibration coefficient
$C_{p\ \mathrm{total}}$ = pneumatic probe total pressure calibration coefficient
F_n = component of force normal to the blade chord per unit span
F_t = component of force tangent to the blade chord per unit span
F_x = x component of force on the blade per unit span
F_y = y component of force on the blade per unit span
i = incidence angle
p_s = static pressure
p_{sb} = local static pressure on the blade
$p_{s\ \mathrm{ind}}$ = static pressure indicated by pneumatic probe
p_t = total pressure
Re = Reynolds number
s = blade spacing
u = local x component of velocity
v = local y component of velocity
V = average velocity
V_x = x component of the average velocity
V_y = y component of the average velocity
x, y, z = Cartesian coordinates
α_1 = inlet flow angle
α_2 = exit flow angle
α_1' = inlet blade metal angle
α_2' = exit blade metal angle
α^* = angle of attack
δ = deviation angle
ϵ = flow deflection or turning angle
θ = camber angle
ξ = stagger angle
ρ = mass density
ω_2 = mass-averaged total pressure loss coefficient at station 2
ω_3 = total pressure loss coefficient for the fully mixed flow

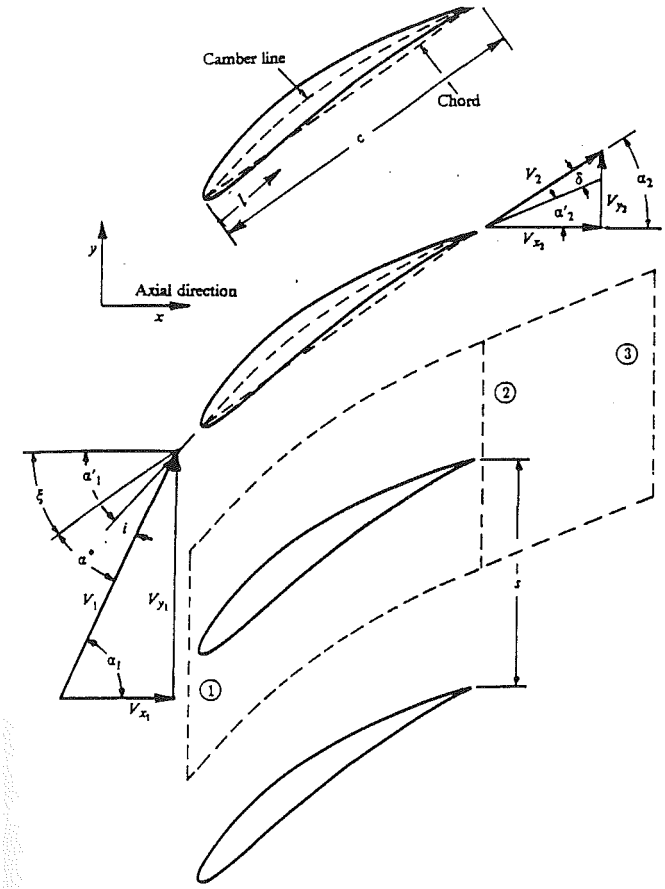

Fig. 1 Cascade geometry and velocity triangles

rated flow, but cascade performances for very large angles of attack were not investigated.

The preceding literature review of analytical and numerical methods for predicting cascade performance and the literature review in Part I on cascade testing have shown that data describing the flow characteristics and cascade performance for fully stalled blade rows are not available. Therefore, the purpose of this investigation is to determine, for various stagger angles, cascade flow field characteristics and cascade performance at very large angles of attack. The following sections describe the cascade performance parameters, the test facility, and the experimental procedure followed for the pressure measurements. The numerical procedure used in the investigation is briefly described. Both the experimental and numerical results are presented and discussed. Conclusions regarding the effects of angle of attack, Reynolds number, and stagger angle are given.

Cascade Performance Evaluation

The parameters used to describe the cascade performance will be defined and described in this section. Figure 1 defines the nomenclature used to describe the cascade geometry and the velocity vectors. The dashed lines in the figure also define control volumes, which are used to derive relationships between the velocity profiles, pressure, and blade forces. Station 1 is upstream of the cascade and can be arbitrarily located, if desired, at a position where the velocity is uniform. Station 2 is immediately downstream of the cascade where the velocity is nonuniform due to the boundary layer wakes and separated regions. Station 3 is at a hypothetical position far downstream, where the flow is again uniform. The actual location of station 3 is unknown and depends on the rate of mixing downstream of the cascade. However, the pressure and velocity at this station can be determined for fully mixed flow by applying the laws of conservation of mass and momentum. The velocity vectors V_1, V_2, and V_3 represent the average velocities at the respective locations. The velocity at a point location in the flow field will be represented by the velocity components in the x and y directions, u and v respectively. The average inlet velocity, V_1, is used as the reference velocity in forming the dimensionless flow field and performance parameters.

A dimensionless blade pressure coefficient is defined by

$$C_p = \frac{p_{t_1} - p_{s_b}}{\frac{1}{2}\rho V_1^2} \tag{1}$$

where p_{t_1} is the total pressure upstream of the cascade and p_{sb} is the static pressure on the surface of the blade. Similar pressure coefficients are defined to express the total and static pressure anywhere in the flow field in dimensionless form.

$$C_{p_t} = \frac{p_{t_1} - p_t}{\frac{1}{2}\rho V_1^2} \tag{2}$$

$$C_{p_s} = \frac{p_{t_1} - p_s}{\frac{1}{2}\rho V_1^2} \tag{3}$$

Two parameters are needed to describe the overall performance of a cascade. One parameter must specify either the deflection of the flow by the blade or the force on the blade. The second parameter must specify the efficiency of the cascade and can be expressed as an efficiency, a static pressure rise coefficient, a drag coefficient, or as a total pressure loss coefficient. In cascade data and correlations used for designing blade rows, the flow deflection aspect of cascade performance is usually expressed as the flow discharge angle, α_2, or the deviation angle, δ. For cascades operating near the minimum loss conditions, the blade wakes are small and the flow changes direction very little as the wakes mix. However, for cascades operating at large angles of attack and consequently with large separated regions, a very significant change in the flow direction will accompany the mixing of the wakes. Under these conditions the force on the blade is more indicative of the cascade performance, and, therefore, the normal force coefficient was selected as one parameter for representing the cascade performance in this investigation. Results illustrating how the average flow angle changes from station 2 to 3 are also presented. Mass-averaged total pressure loss coefficients for stations 2 and 3 were selected to represent the efficiency aspect of the cascade performance.

Dimensionless force and moment coefficients can be defined as:

$$C_{F_n} = \frac{F_n}{\frac{1}{2}\rho V_1^2 c} \tag{4}$$

$$C_{M_{mc}} = \frac{M_{mc}}{\frac{1}{2}\rho V_1^2 c^2} \tag{5}$$

Since we are concerned with two-dimensional cascades, the blade force and moment in the above coefficients are for a unit length of the blade span. If the pressure on the blade surface is known, the force and moment on the blade (neglecting shear forces) can be obtained by integrating the pressure distribution. Thus,

$$C_{F_n} = \int_0^1 \frac{p_{s_{ps}}}{\frac{1}{2}\rho V_1^2} d\left(\frac{l}{c}\right) - \int_0^1 \frac{p_{s_{ss}}}{\frac{1}{2}\rho V_1^2} d\left(\frac{l}{c}\right)$$

$$= \int_0^1 (C_{p_{ss}} - C_{p_{ps}}) d\left(\frac{l}{c}\right) \quad (6)$$

where *ps* and *ss* designate the pressure and suction surfaces, respectively, and *l* is the distance along the chord line. Similarly the moment coefficient for the moment about the midchord can be expressed in terms of the pressure distribution as:

$$C_{M_{mc}} = \int_0^1 (C_{p_{ss}} - C_{p_{ps}}) \left(\frac{l}{c} - 0.5\right) d\left(\frac{l}{c}\right) \quad (7)$$

Using the above equations, the normal force and moment coefficients can be evaluated from the measured pressure distribution on the blade. These measurements will be described in the following sections. The forces on the blade can also be evaluated by applying the integral form of the conservation of momentum equation to the control volume surrounding the blade using the velocity and pressure measurements made at station 2. Also, the pressure and velocity at the hypothetical location, station 3, can be evaluated using the conservation of mass and momentum equations. Applying the *x*-momentum equation to the control volume from station 1 to 2, the following equation is obtained:

$$-F_x + \int_0^s (p_{s1} - p_{s2}) dy = \rho \int_0^s (u_2^2 - u_1^2) dy \quad (8)$$

The term on the right side of Eq. (8) is not zero for nonuniform flow even if the flow is purely two-dimensional and the axial velocity ratio (AVR) is unity. If the AVR $\neq$ 1, additional terms would also be needed to account for the flow crossing the sides of the control volume in the plans perpendicular to the span of the airfoil. Equation (8) can be expressed in dimensionless form as:

$$C_{F_x} = \frac{F_x}{\frac{1}{2}\rho V_1^2 c} = \frac{s}{c}\left[\int_0^1 (C_{p_{s2}} - C_{p_{s1}}) d\left(\frac{y}{s}\right) - 2\int_0^1 \left[\left(\frac{u_2}{V_1}\right)^2 - \left(\frac{u_1}{V_1}\right)^2\right] d\left(\frac{y}{s}\right)\right]$$

$$= \frac{s}{c}\left[\overline{C_{p_{s2}}} - \overline{C_{p_{s1}}} - 2\left(\overline{\left(\frac{u_2}{V_1}\right)^2} - \overline{\left(\frac{u_1}{V_1}\right)^2}\right)\right] \quad (9)$$

The *x*-momentum equation applied to the control volume from station 2 to 3 yields:

$$\int_0^s (p_{s_2} - p_{s_3}) dy = \rho \int_0^s (u_3^2 - u_2^2) dy \quad (10)$$

where $u_3 (u_3 \neq f(y))$ by definition can be obtained from the continuity equation,

$$u_3 = V_{x_3} = \frac{1}{s}\int_0^s u_2 dy \quad (11)$$

With p_{s2} and u_2 determined experimentally, Eqs. (10) and (11) can be used to calculate the static pressure at the hypothetical location 3, where the flow is fully mixed. In dimensionless form, the static pressure at location 3 is:

$$C_{p_{s3}} = \frac{p_{t_1} - p_{s_3}}{\frac{1}{2}\rho V_1^2} = \int_0^1 C_{p_{s2}} d\left(\frac{y}{s}\right) - 2\int_0^1 \left(\frac{u_2}{V_1}\right)^2 d\left(\frac{y}{s}\right) + 2\left(\frac{V_3}{V_1}\right)^2 \quad (12)$$

The *y*-momentum equation can be applied in a similar manner. Since the flow in the *y* direction is periodic with a period of *s*, there is no net pressure force on the upper and lower control volume boundaries or net momentum flux through these boundaries. For the control volume from station 1 to station 2, the blade force is equated to the net flux of momentum through the ends of the control volume:

$$-F_y = \rho \int_0^s (u_2 v_2 - u_1 v_1) dy \quad (13)$$

or expressed nondimensionally;

$$C_{F_y} = \frac{F_y}{\frac{1}{2}\rho V_1^2 c} = 2\frac{s}{c}\int_0^1 \left(\frac{u_1}{V_1}\frac{v_1}{V_1} - \frac{u_2}{V_1}\frac{v_2}{V_1}\right) d\left(\frac{y}{s}\right) \quad (14)$$

For the control volume from station 2 to station 3, the *y*-momentum equation yields:

$$\rho u_3 v_3 s - \rho \int_0^s u_2 v_2 dy = 0 \quad (15)$$

Solving for v_3, the following expression is obtained:

$$v_3 = \frac{1}{u_3 s}\int_0^s u_2 v_2 dy \quad (16)$$

With u_3 and v_3 given by Eqs. (11) and (16), respectively, the angle of the flow when the wakes are fully mixed is given simply by:

$$\alpha_3 = \tan^{-1}\left(\frac{v_3}{u_3}\right) \quad (17)$$

As the flow wakes mix out from station 2 to station 3, the average flow angle will increase. At this point an average α_2 has not been defined. It is desirable to have the average angle at station 2 reflect the true force on the blade, as well as the conservation of momentum from station 2 to 3. For this reason α_2 is defined as the inverse tangent of the *y* momentum over the *x* momentum,

$$\alpha_2 = \tan^{-1}\frac{\int_0^s \rho u_2 v_2 dy}{\int_0^s \rho u_2^2 dy} \quad (18)$$

It can be observed that the quotient in Eq. (18) is equivalent to the mass-averaged v_2 over the mass-averaged u_2. With α_2 defined above, the deflection or turning angle for the cascade is given by:

$$\epsilon_{12} = \alpha_1 - \alpha_2 \quad (19)$$

Equations (9) and (14) provide expressions for evaluating C_{Fx} and C_{Fy}, respectively. The above expressions can be combined to yield a second means of evaluating the normal and tangential blade force coefficient:

$$C_{F_n} = C_{F_y} \cos \xi - C_{F_x} \sin \xi \quad (20)$$

Thus far, the forces on the blades and the deflection of the flow have been considered without reference to the efficiency of the cascade. It it naturally the designer's desire to have the cascade turn the flow as much as possible with minimal losses. One way of expressing the efficiency of a cascade is in terms of a total pressure loss coefficient. The total pressure varies across the wake of the blades; thus, an average total pressure is needed to indicate the overall performance of a blade row. The mass flow-based average is the appropriate method. The mass-averaged total pressure loss coefficient for station 2, ω_2, is defined as:

$$\omega_2 = \frac{\overline{\Delta p_t}}{\frac{1}{2}\rho V_1^2} = \frac{\frac{1}{sV_{x_2}}\int_0^s (p_{t_1} - p_{t_2}) u_2 dy}{\frac{1}{2}\rho V_1^2} \tag{21}$$

Additional total pressure losses occur as the blade wakes mix out from stations 2 to 3. The flow is uniform at station 3, thus averaging the total pressure at this location is not necessary. The total pressure at station 3 can be computed from p_{s3}, u_3, and v_3, which are given by Eqs. (10), (11), and (16), respectively.

$$p_{t_3} = p_{s_3} + \frac{1}{2}\rho(u_3^2 + v_3^2) \tag{22}$$

The loss coefficient ω_3 is given by:

$$\omega_3 = \frac{p_{t_1} - p_{t_3}}{\frac{1}{2}\rho V_1^2} \tag{23}$$

$$\omega_3 = C_{p_{s3}} + \left(\frac{u_3}{V_1}\right)^2 + \left(\frac{v_3}{V_1}\right)^2 \tag{24}$$

Test Facility and Experimental Procedure

The test facility was described in detail in Part I of this paper, particularly with regard to the unique features of the facility, which enable flows at very large inlet angles and fully stalled flows to be studied. Figure 2 presents front and top views of the cascade test section, which show the reference coordinate system, the traverse locations, and the rear wall static pressure tap locations. The velocity measurements made using the dual split-film probe (described in Part I of this paper) and pressure measurements made with a five-hole probe were conducted at the axial location of the downstream traversing slot on the midspan plane of the cascade. The upstream traversing slot shown in Fig. 2, was used to measure the total and static pressure and the variation in flow direction, which may result from the blockage of the blade passages by the separated flow. For these upstream measurements a three-hole probe was used in a non-nulling mode by first conducting calibration tests, which provided a yaw angle pressure coefficient and total and static pressure coefficients. These calibration coefficients were obtained as a function of the probe Reynolds number and the flow angle relative to the probe in the yaw direction. The probe calibration and data reduction procedure is described in detail by Yocum (1988) and is analogous to the procedure used for five-hole probes described by Treaster and Yocum (1979).

The static pressure wall taps upstream of the cascade were used to assess the periodicity of the flow and also to indicate the upstream static pressure for initially setting the cascade inlet velocity. The taps downstream of the cascade were used to indicate the periodicity of the flow at the exit of the cascade. Six additional wall taps (not shown in Fig. 2) were equally spaced across the discharge of the center blade passage and were used to indicate the variation in static pressure across the passage. However, due to the complex three-dimensional nature of the flow in the end wall regions, these static taps were found not to be indicative of the static pressure at the cascade midplane, as determined by the pneumatic probe surveys.

A commercially available United Sensor Model #DC-125-12-CD five-hole probe was used to measure the total and static pressure profiles at the discharge of the cascade. A sketch of the probe is shown in Fig. 3. This type of probe was selected because the sensing element had the desired geometric features, although only three of the five holes were actually used for measuring the pressures. The curved shape of the end of the probe allows the probe to be inserted in the flow from a transverse direction, while the tip of the probe is aligned with the flow. With this tip geometry the probe created a minimal disturbance of the flow in the vicinity of the measurement.

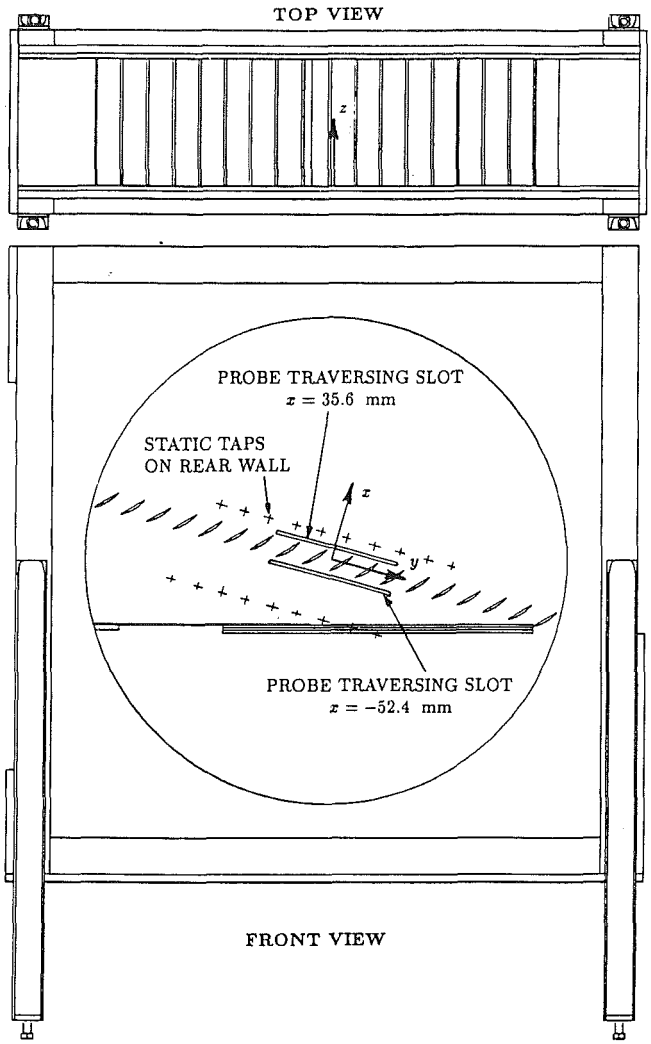

Fig. 2 Front and top views of the test section showing the coordinate system, the traverse locations, and the static taps

With highly loaded and stalled blades, large variations and very steep gradients in the velocity and pressure are present in the y direction across the cascade discharge. Because of the difficulties in using a pneumatic probe to determine the velocity direction in flows with steep gradients, the dual split-film probe was used to measure the velocity magnitude and direction. The experimental procedure and the results from the dual split-film probe measurements were presented in Part I of this paper. In an independent series of tests, the five-hole probe was aligned with the flow using the flow angle determined with the split-film probe. With the probe aligned with the flow, the only probe calibration necessary was to determine the static pressure coefficient. Because of the velocity and pressure gradients in the y direction, only holes 4 and 5, which were positioned in a constant y plane, were used to indicate the static pressure. Therefore, the static pressure calibration coefficient was defined as:

$$C_{p\ \text{static}} = \frac{p_{s\ \text{ind}} - p_{s\ \text{true}}}{p_1 - p_{s\ \text{ind}}} \tag{25}$$

where

$$p_{s\ \text{ind}} = \text{indicated static pressure} = \frac{p_4 + p_5}{2} \tag{26}$$

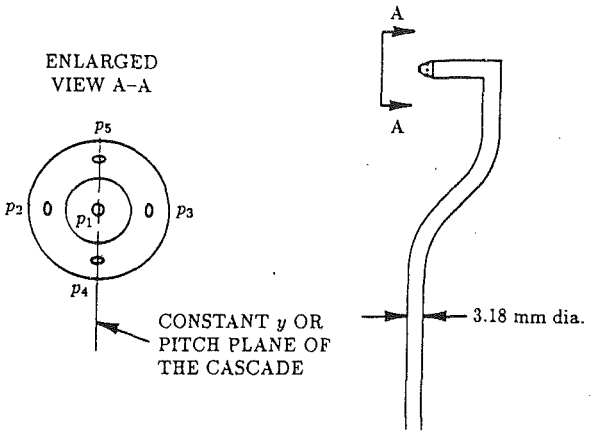

Fig. 3 Sketch of the five-hole probe

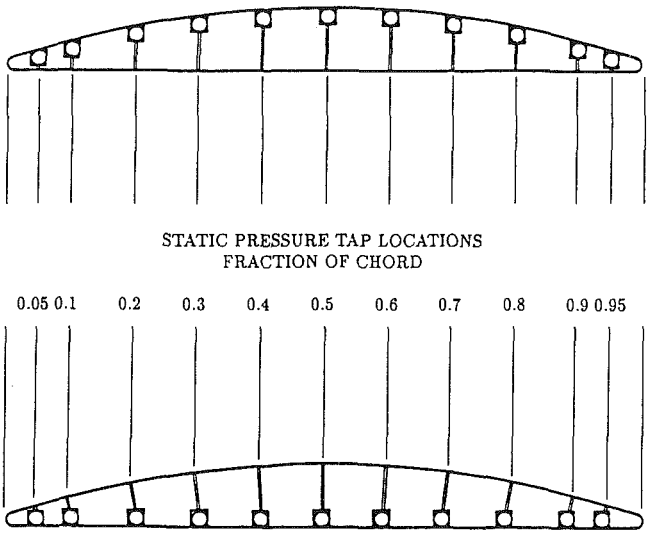

Fig. 4 Cross section of the two center blades

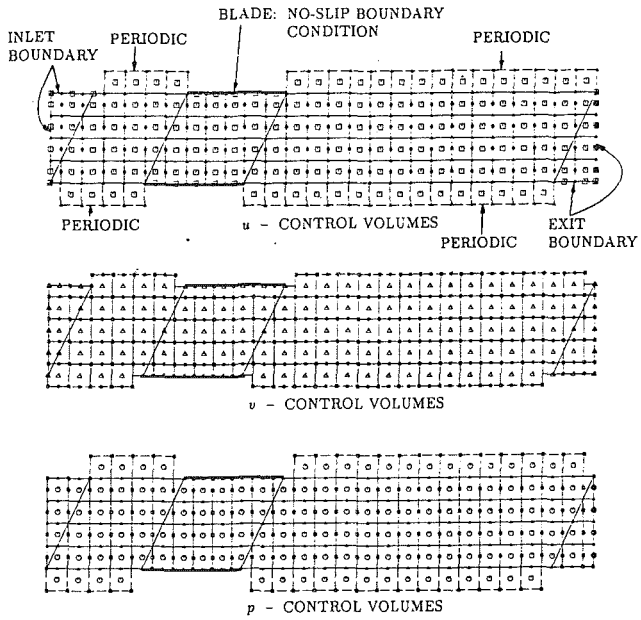

Fig. 5 Typical staggered grid used for calculating the flow through a cascade of flat plate airfoils

To assess the influence of the probe Reynolds number, calibration tests to determine the static pressure coefficient were conducted over a range of velocities. The calibration results indicated that over the probe Reynolds number range tested (approximately 3000 to 9000) the static pressure coefficient had a constant value of 0.094. Although the probe calibration is independent of Reynolds number, the nonzero value of the static pressure coefficient reveals that holes 4 and 5 do not directly indicate the correct static pressure, and that the calibration was necessary.

Eleven static pressure taps on both surfaces of the center blade passage were used to measure the pressure distribution on the blade surfaces. Figure 4 shows the cross section of the two center blades and illustrates the location of the taps. As shown in the figure, the taps and pneumatic connections were manufactured by machining slots in the opposite blade surface, imbedding tubes in the slots, and restoring the blade contour with a filler material. The taps were then drilled from the sides opposite the slots using a 0.5 mm drill bit. All tests were at low Mach number, essentially providing incompressible flow.

Numerical Procedure

Stalled flow through a cascade was numerically simulated by solving the Navier–Stokes equations using the SIMPLER algorithm of Patankar (1980). Although the Navier–Stokes equations were employed, some simplifying assumptions were made. It was assumed that the flow was two dimensional, steady, incompressible and that the viscosity was constant. An additional assumption was made that did not affect the governing equations, but that geometrically simplified the solution domain. It was assumed that the blades could be modeled by infinitely thin flat plates. This assumption greatly simplified the solution procedure by eliminating the need for body-fitted curvilinear coordinates. With these simplifying assumptions, it is apparent that an extremely accurate prediction of the velocity and pressure fields would not be achieved. However, the effects of blade stagger, solidity, and angle of attack could be investigated. Most importantly, the cascade performance could be studied at angles of attack far beyond the angles that were physically practical for testing in a cascade tunnel. Inlet angles of 85 deg or angles of attack within 5 deg of flow parallel to the cascade were numerically simulated.

The SIMPLER algorithm is a well-known and often-used method for solving the elliptic Navier–Stokes equations. Therefore, the details of the procedure will not be given here. The SIMPLER algorithm and its derivatives are solution procedures that link the solution of the momentum equations to the continuity equation through a pressure correction equation. In the SIMPLER algorithm, the pressure correction is used only to correct the velocity components, and an additional set of simultaneous equations are solved to obtain the pressure. Although the computation time per outer loop iteration for the SIMPLER method is greater, fewer required iterations result in an overall savings in computational time.

A staggered grid was used, as is common with pressure-based procedures, to avoid the odd-even decoupling between the pressure nodes. In a staggered grid, the nodes for the u-velocity component are offset 1/2 grid spacing in the x direction from the pressure nodes, and the nodes for the v-velocity component are offset 1/2 grid spacing in the y direction. Figure 5 illustrates the layout of a staggered grid for a cascade of flat plates and also identifies the various boundary conditions.

The power-law scheme was used to represent the combined convection and diffusion terms. This scheme very accurately approximates the exact solution to the one-dimensional convection-diffusion equation. For convection-dominated flow, the scheme reduces to an upwind difference; while for diffusion-dominated flow, the power-law scheme is equivalent to a

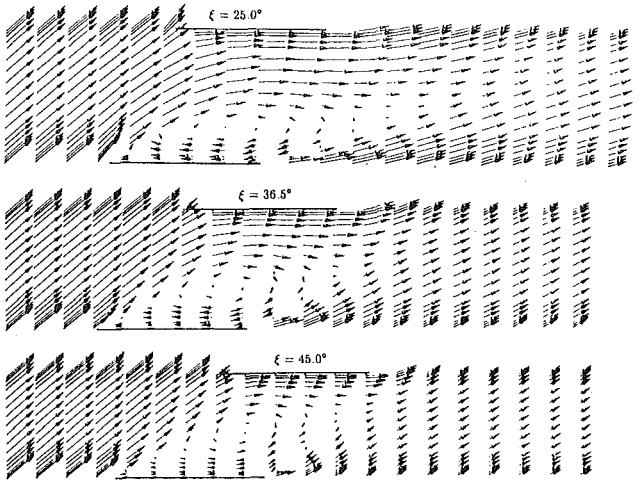

Fig. 6 Numerically predicted velocity vector field for three staggers with $\alpha^* = 40$ deg and Re = 200,000

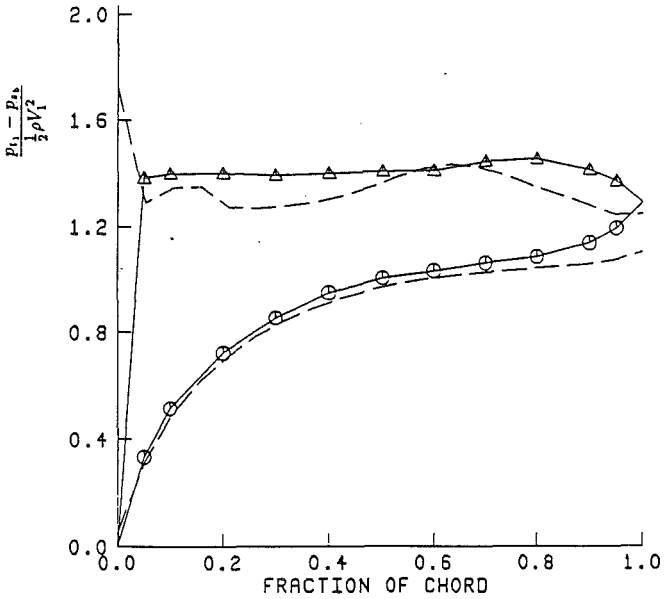

Fig. 7 Predicted and measured blade pressure distributions for ξ = 25 deg, α^* = 30 deg and Re = 200,000

central difference. At cell Reynolds numbers where both convection and diffusion are significant, the power-law scheme provides coefficients for the discretized momentum equation, which correctly account for the relative levels of convection and diffusion.

Results and Discussion

Before discussing the results from the pressure measurements and the overall cascade performance, we should recall the primary characteristics of the flow determined from the flow visualization and time-mean velocity measurements, which were presented in Part I of this paper. The cascade stagger angle was found to be a key parameter in determining the characteristics of the stalled flow and the occurrence of propagating stall. For the low stagger (ξ = 25 deg) cascade, the stalled flow was characterized by two distinct regions—a jet region of essentially inviscid flow and a wake region where the effects of the recirculating flow were concentrated. These two distinct regions resulted in less than complete blockage of the passage, and as a result the stalled region was stable and propagating stall was never observed. For the cascades with staggers of 36.5 and 45 deg, two distinct regions were not apparent and the flow in the entire passage was affected by the flow recirculation. Propagating stall for these two cascades was observed for all angles of attack equal to or greater than the angle where full stall first occurred. It will be seen that the losses across the passage and the blade pressure distribution also reflect these observed characteristics. A sample of the *numerical* results for the velocity field is given in Fig. 6 for the cascades of the three stagger angles. These vector fields also illustrate the characteristics of two distinct flow regions for the 25 deg stagger cascade, but with almost the entire passage affected by the recirculating flow for the other two stagger angles.

Figures 7–12 illustrate the blade pressure distributions and the discharge total and static pressure profiles for the three cascades at an angle of attack at 30 deg. The pressure distribution for the 25 deg stagger cascade, Fig. 7, shows that for fully stalled flow the pressure within the recirculating region is nearly constant. Constant pressure within the separated region is an assumption often made when analyzing separated flow over airfoils; thus, this assumption would be valid for a cascade of low stagger. However, Figs. 9 and 11 show that as the stagger angle increases, the variation of the pressure within the separated region also increases. For the 45 deg stagger cascade, the variation in pressure in the separated region is quite significant. The characteristics of the pressure distribu-

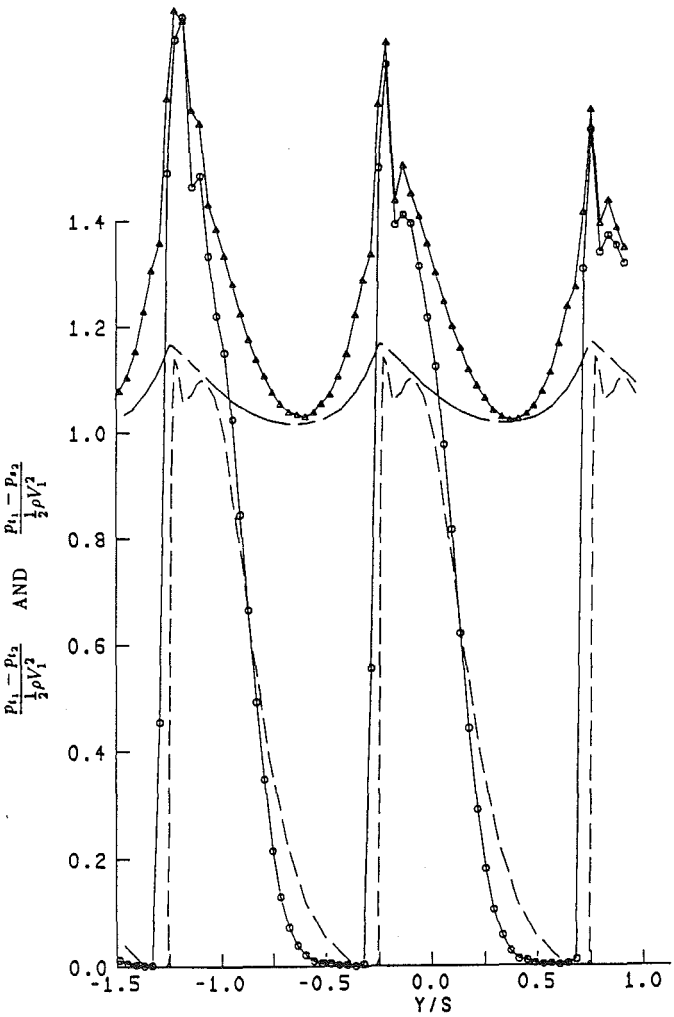

Fig. 8 Predicted and measured pressure profiles downstream of the cascade for ξ = 25 deg, α^* = 30 deg, and Re = 200,000

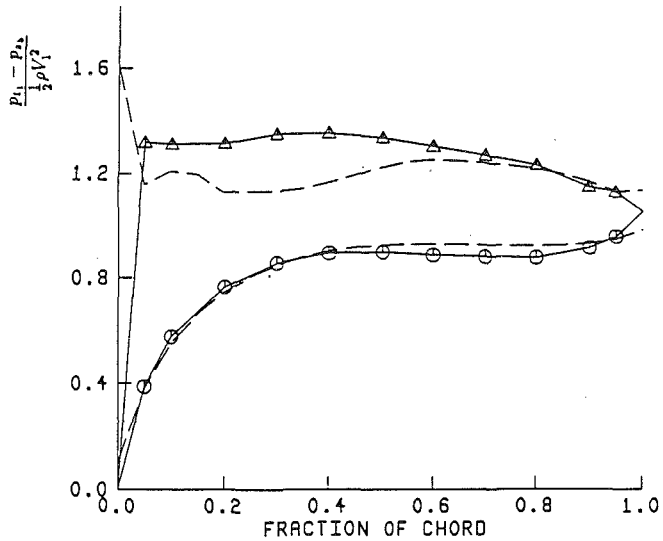

Fig. 9 Predicted and measured blade pressure distributions for ξ = 36.5 deg, α^* = 30 deg and Re = 200,000

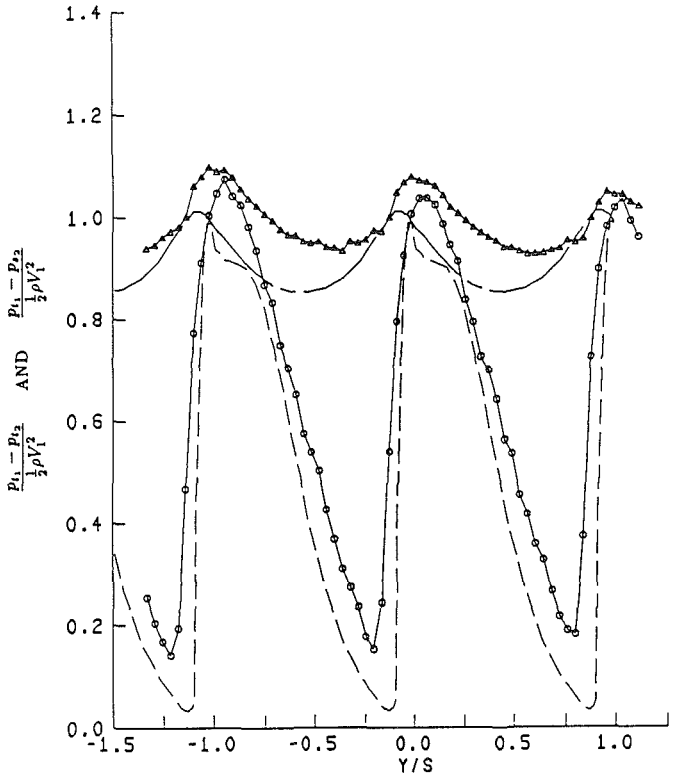

Fig. 10 Predicted and measured pressure profiles downstream of the cascade for ξ = 36.5 deg, α^* = 30 deg and Re = 200,000

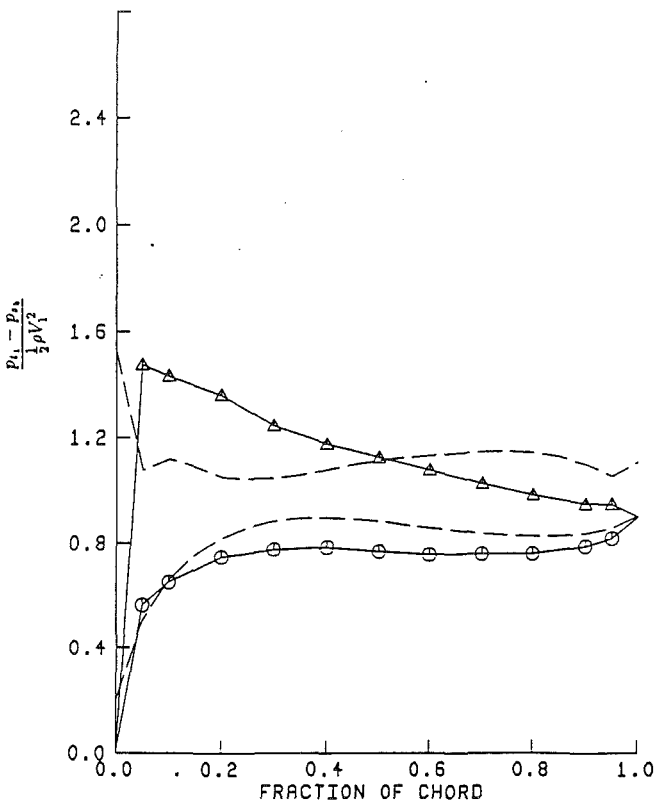

Fig. 11 Predicted and measured blade pressure distributions for ξ = 45 deg, α^* = 30 deg, and Re = 200,000

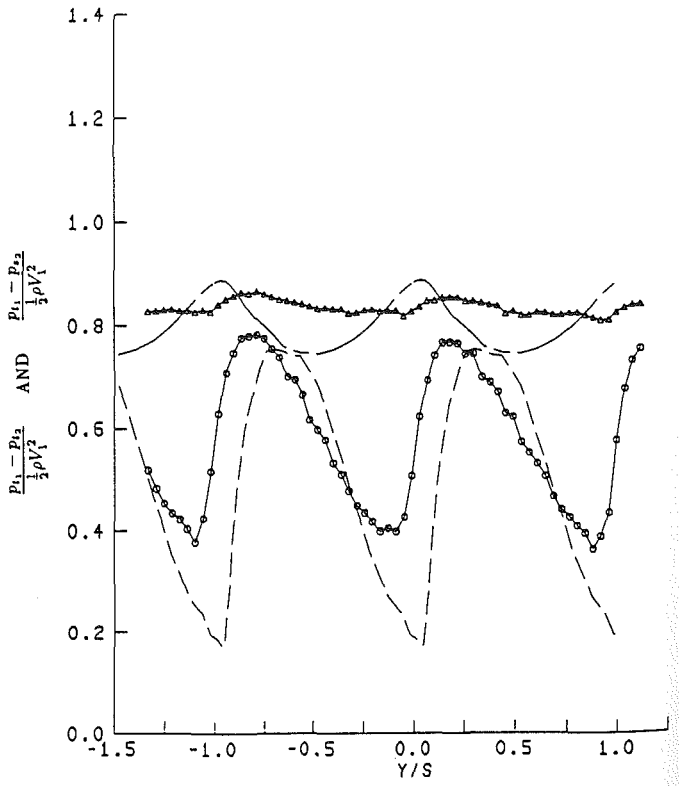

Fig. 12 Predicted and measured profiles downstream of the cascade for ξ = 45 deg, α^* = 30 deg, and Re = 200,000

tions are consistent with the expected behavior based on the difference in the flow characteristics for the different stagger angles. For the 25 deg stagger cascade, where the flow is characterized by two distinct regions, the flow curvature within the separated region is small and the pressure is therefore approximately constant. For the larger stagger cascades the recirculating region occupies a greater portion of the passage and the recirculating flow has greater curvature. The greater curvature results in a pressure variation in the separated region.

The numerically predicted pressure distribution for the 25 deg stagger cascade is in fairly good agreement with the experimental results. However, it is seen that the agreement is not

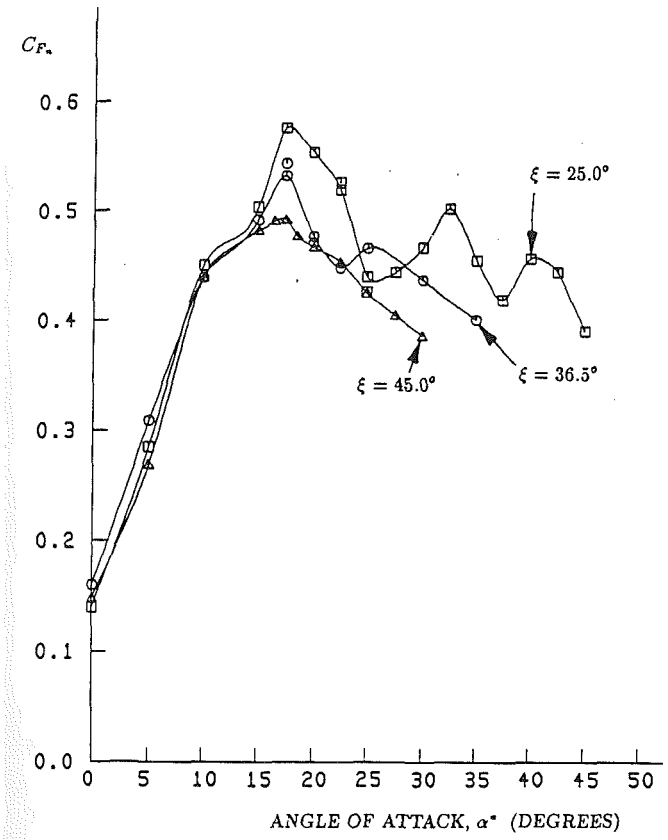

Fig. 13 Normal force coefficient evaluated from the measured blade pressures for three stagger angles and Re = 200,000

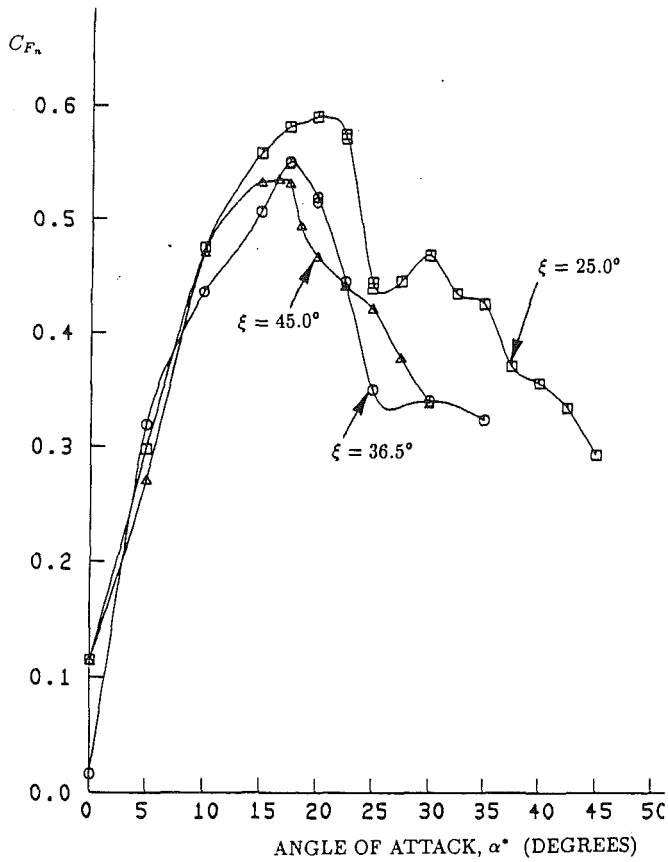

Fig. 14 Normal force coefficient evaluated from the downstream velocity and pressure profiles for three stagger angles and Re = 200,000

as good for the high stagger cascades. This deterioration of the agreement between the predicted and measured pressures suggest that the pressure in the separated regions of the higher stagger cascades is strongly influenced by the unsteady flow and turbulent mixing, which are neglected in the numerical model.

The total and static pressure distributions at the cascade discharge are presented in Fig. 8, 10, and 12. Note that as a result of the dimensionless form selected for representing the total pressure, the pressure coefficient represents the local total pressure loss. In Fig. 8 the results for ξ = 25 deg again show two distinct flow regions. One region exists where there is no total pressure loss, whereas very large losses are observed in the wake region. For the larger stagger cascades, Figs. 10 and 12 illustrate that the losses are distributed over the entire passage width, and two distinct flow regions cannot be identified. The predicted pressure profiles show similar trends, although an absence of a turbulence model results in the maximum loss being undepredicted.

Curves of the normal force coefficient evaluated from the blade pressure distributions and the downstream velocity and pressure profiles are presented in Figs. 13 and 14, respectively. The normal force coefficient evaluated from the numerical results is presented in Fig. 15. The results for the normal force coefficient exhibit similar trends and peak values for both methods. If the flow were truly two dimensional and steady, identical results would confirm the accuracy of the various measurements. In the angles of attack preceding stall, it is seen that the two sets of data are nearly identical. This consistency does confirm that there were no major errors in the data acquisition. The difference in the curves computed the two ways for angles of attack where the cascades are stalled can be attributed to three-dimensional and unsteady flow effects. Notice that for some conditions, two data points are given for the same angle of attack. These double points indicate the test

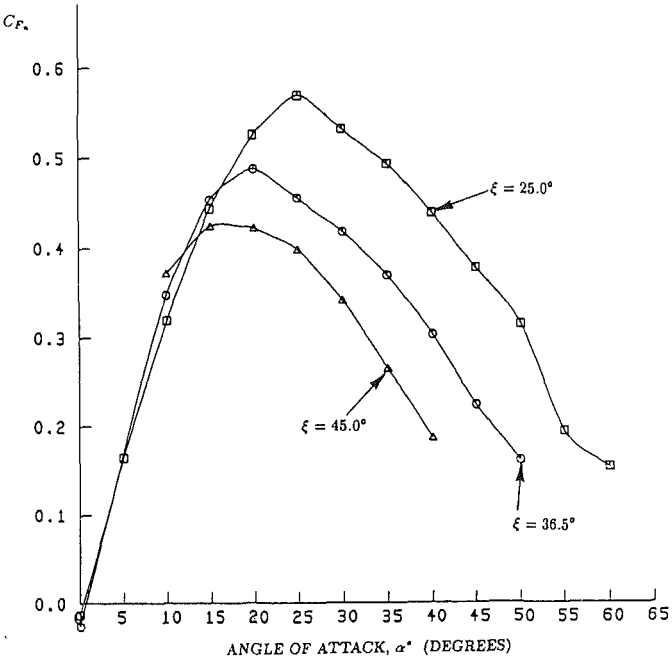

Fig. 15 Normal force coefficient evaluated from the numerical results for three stagger angles and Re = 200,000

at this condition was repeated to assure that the characteristic of the curves represent the real time-average performance of the cascade and were not a function of the data sampling. Also, in the stalled-flow operating regime, tests were conducted at increments in angle of attack of 2.5 deg to define fully the

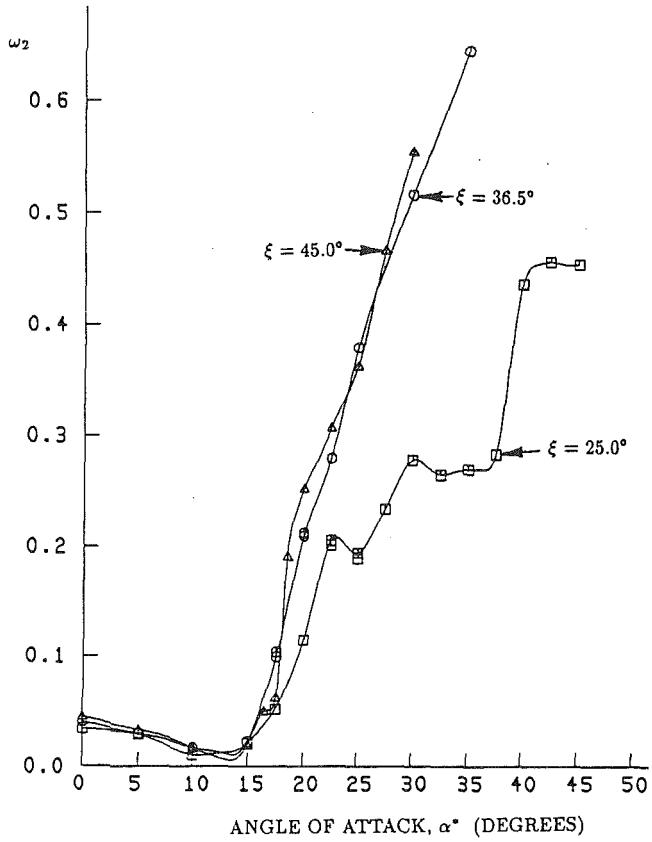

Fig. 16 Mass average total pressure loss coefficient evaluated from the experimental data at the downstream measurement station for three stagger angles and Re = 200,000

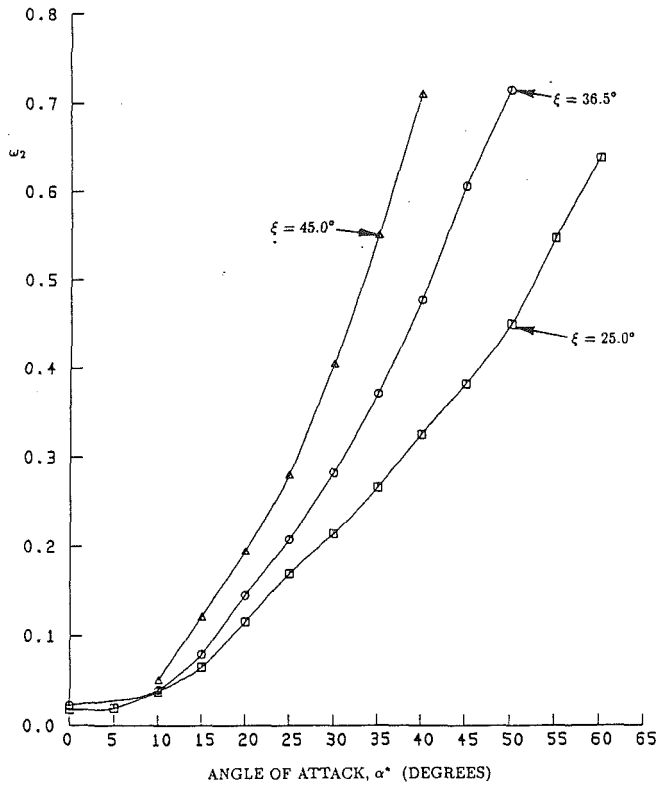

Fig. 17 Mass average total pressure loss coefficient evaluated from the numerical results for Re = 200,000

characteristics of the performance curves. The fluctuating nature of the curves suggests that various three-dimensional and/or unsteady flow characteristics may only exist over a small range in angle of attack. If the flow phenomena only changed in size or intensity, a smoother variation in the normal force coefficient would be expected.

The normal force coefficient determined from the numerical results, Fig. 15, exhibits the same trends as the experimental results presented in Figs. 13 and 14. An asset of the numerical results, despite the fact that the magnitudes of the force coefficient may not be well predicted, is that the variations in the force coefficient curves associated with changes in stagger are clearly evident. The normal force coefficient increases to a peak value near the condition where full stall initially occurs. The force coefficient then decreases and approaches a value of zero at the angle of attack where the flow is parallel to the cascade. Both the experimental and numerical results show that the peak value is greater and the peak occurs at a larger angle of attack for cascades with smaller stagger angle.

The mass-averaged total pressure loss coefficient data evaluated at the cascade discharge are given in Figs. 16 and 17. Figure 16 presents the loss curves evaluated from the experimental results, while Fig. 17 gives the results from the numerical simulation. In Fig. 16, the experimental loss curves for stagger angles of 36.5 and 45 deg are seen to be nearly identical. In contrast, the slope of the loss curve for the 25 deg stagger cascade is much less than the slope of the curves for the other staggers. The characteristics of the loss curves correlate with the extent of the passage affected by the recirculating flow. The recirculating flow was seen to affect the flow across the entire passage of the larger stagger cascades, as evidenced by the velocity profiles and the distribution of total pressure losses across the passage. For the 25 deg stagger cascade two distinct flow regions were observed, with one region being an inviscid or loss free region. Correspondingly, the losses for the 25 deg stagger cascade are smaller in magnitude.

The numerical results in Fig. 17 again show the correct trends, but with a smaller slope of the predicted loss curves and with a more continuous variation in the slope associated with changes in stagger. The discrepancy between the slopes of the experimental and predicted results may be a result of not modeling the turbulence, or may also result from the assumptions of zero thickness and flat plate blades. The greater losses for the 36.5 and 45 deg stagger cascade are a result of the greater mixing associated with the entire flow in the passage being affected by the recirculating flow. The extent of the recirculating flow is determined by the cascade geometry and not the turbulent mixing. Therefore, the blade thickness and curvature effects are believed to cause the discrepancy between the experimental and numerical results. Both the additional blockage of the blade thickness and the blade curvature, which directs the reverse flow over the rear part of the blade toward the center of the passage, cause the recirculating region to extend over a greater portion of the blade passage. The question can then be raised as to why each curve is not affected a similar amount, such that the loss curve for ξ = 45 deg would have a steeper slope than the curve for ξ = 36.5 deg. For the cascades with staggers of 36.5 and 45 deg, the data of Figs. 10 and 12 show that the entire passage has been affected by the separated flow and that no portion of the flow is free of losses. Under these circumstances, where the losses are distributed across the entire passage, it is reasonable to expect that additional geometric changes would not further increase the losses. If this rationale is correct, the loss curves for the 36.5 and 45 deg stagger cascades represent the limiting case of maximum losses for any cascade with this solidity.

The loss curves in Figs. 16 and 17 are for the losses incurred by the flow a short distance downstream of the cascade. It is

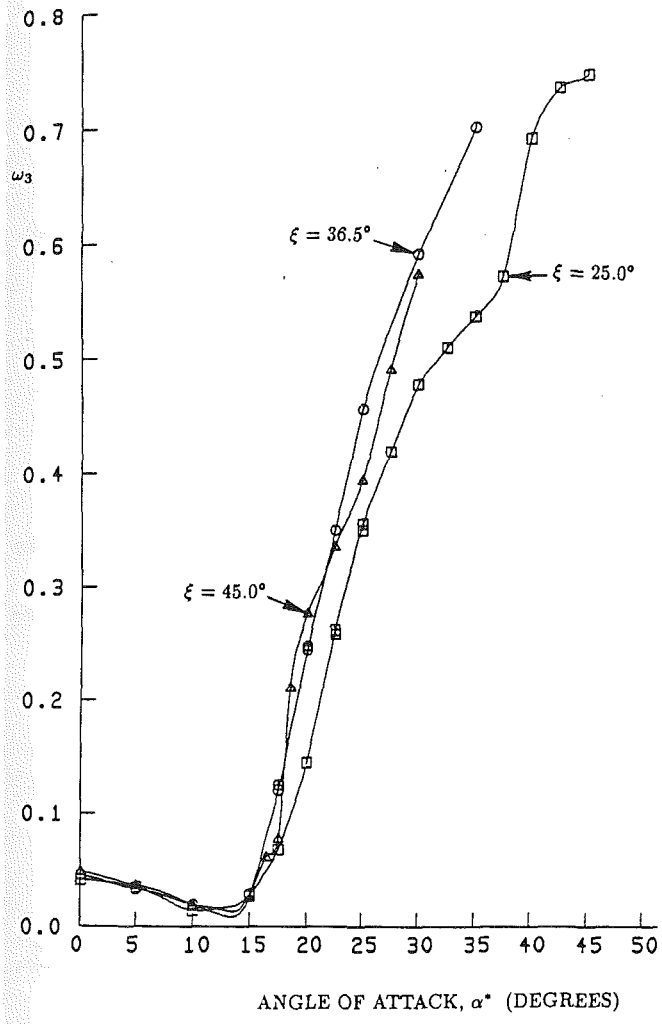

Fig. 18 Total pressure loss coefficient for fully mixed flow evaluated from experimental data for three stagger angles and Re = 200,000

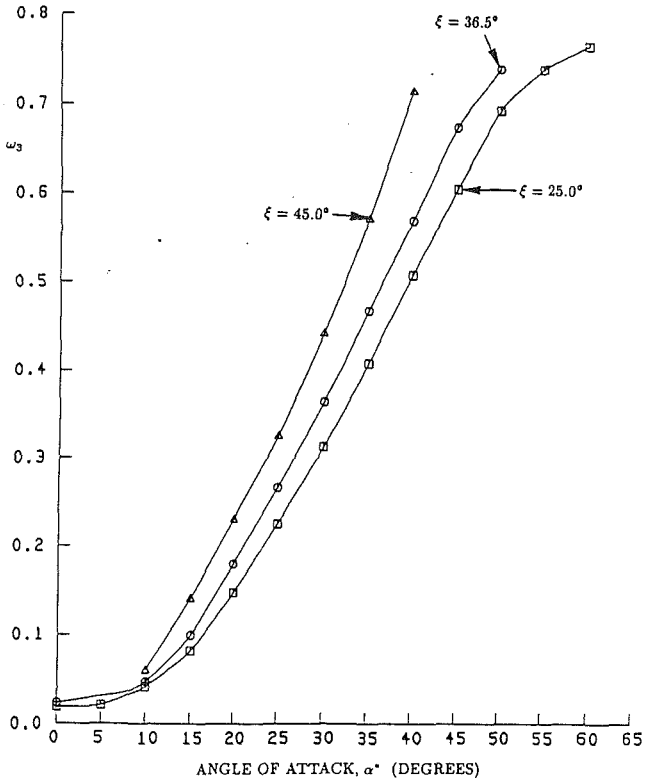

Fig. 19 Total pressure loss coefficient for fully mixed flow evaluated from the numerical results for Re = 200,000

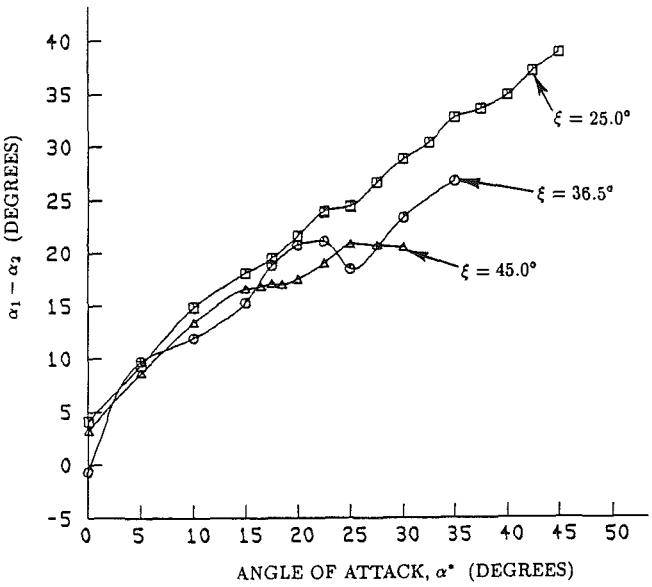

Fig. 20 Measured flow deflection downstream of the cascade for three stagger angles and Re = 200,000

most likely that these losses and the associated blockage determine the stalling characteristics of the blade row. However, when modeling the overall performance of a single blade row or multiple blade rows, additional losses or loss mechanisms should be included that account for the mixing of the wakes downstream of the blade rows. The hypothetical location where complete mixing occurs has been designated as station 3. The equations for evaluating the flow properties at station 3 were given in the section on Cascade Performance Evaluation.

Curves of the total pressure loss coefficients for the fully mixed flow are presented in Figs. 18 and 19. The loss data in these figures were calculated from the experimentally and numerically determined flow fields, respectively. Examining these figures, it is seen that the differences between the curves for the different staggers are much smaller than the differences observed for the losses at station 2. For the 36.5 and 45 deg stagger cascades, the losses were caused by viscous mixing of the flow across most of the blade passage. For the 25 deg stagger cascade, two distinct regions of the flow existed, implying that much less mixing occurred within the passage for this configuration. However, as the flow becomes fully mixed further downstream from the cascade, greater mixing will occur for the 25 deg stagger cascade than will occur for the other two cases. In other words, it appears that the total losses are more nearly equal at station 3 for each stagger than at station 2, with the main difference being where the mixing losses occur. For the 36.5 and 45 deg stagger cascades, much of the mixing and the associated losses occur within the blade passage. For the 25 deg stagger cascade the greater part of the mixing losses occur downstream of the cascade.

The two independent performance parameters, C_{Fn} and ω, are sufficient to describe the cascade performance completely. However, the flow deflection will also be presented to illustrate further the stalled performance of cascades as affected by the cascade stagger angle. Figures 20 and 21 present the flow de-

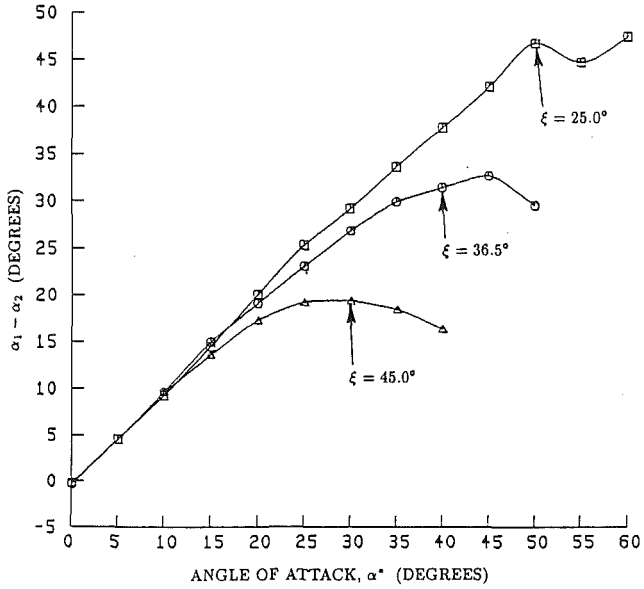

Fig. 21 Numerically predicted flow deflection at the downstream measurement location for three stagger angles and Re = 200,000

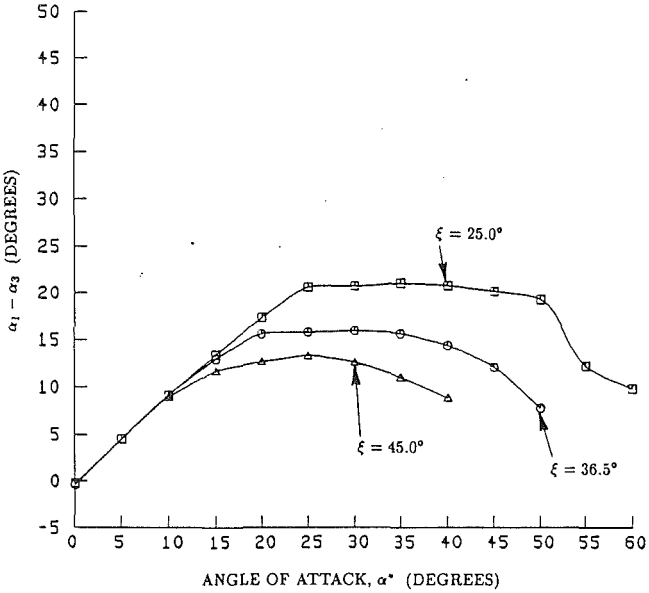

Fig. 23 Flow deflection for the fully mixed flow evaluated from the numerical results for three stagger angles and Re = 200,000

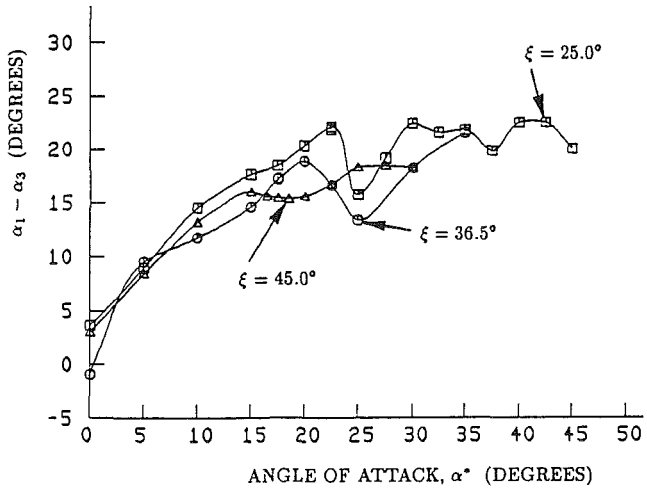

Fig. 22 Flow deflection for the fully mixed flow evaluated from the experimental data for three stagger angles and Re = 200,000

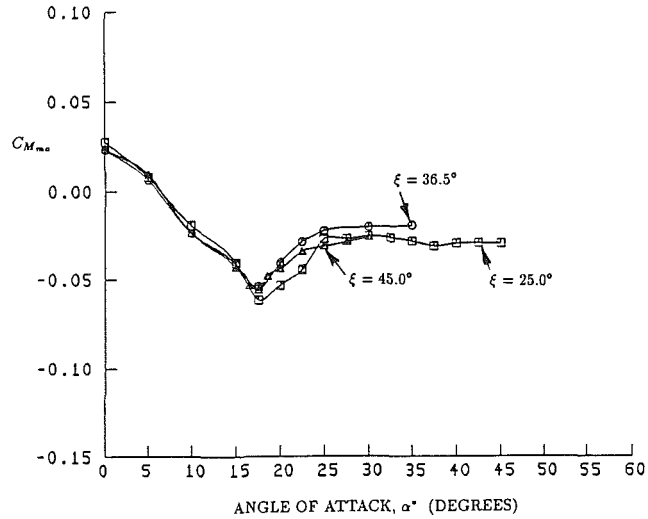

Fig. 24 Moment coefficient about the blade midchord evaluated from the experimental data for three stagger angles and Re = 200,000

flections for station 2, which were evaluated from the experimental and numerical results, respectively. Figures 22 and 23 present similar data for the deflection of the fully mixed flow. The deflection angle ($\alpha_1 - \alpha_2$), shown in Figs. 20 and 21, is seen to increase approximately linearly until the blade stalls for the cascades with staggers of 36.5 and 45 deg. For the cascade with a stagger of 25 deg, the curve continues to rise well beyond the stall point. The physical reason for this behavior is that the flow leaves the pressure side of the blades nearly parallel to the surface until the separated region has grown to the extent that it affects the complete passage. These trends are shown quite clearly in Fig. 21 by the deflection angles computed from the numerically predicted flow field. Recalling that α_2 was calculated as the inverse tangent of the quotient of the tangential to axial momentum, the linear nature of the ($\alpha_1 - \alpha_2$) curve for ξ = 25 deg, illustrates that the momentum of the flow at station 2 is dominated by the inviscid region of the flow near the pressure surface. From Figs. 22 and 23 it is seen that the deflection angle of the fully mixed flow does not exhibit a linear nature past the stall point. These curves are seen to level off and decline as the stall point is exceeded. Since the y momentum is conserved from stations 2 to 3, it is the change in the axial momentum that must cause the increased losses and the decrease in the deflection angle as the flow mixes. The change in axial momentum results from the pressure forces acting on the flow due to the rise in static pressure from station 2 to station 3. In Fig. 8, the static pressure for the 25 deg stagger cascade is seen to vary significantly across the passage discharge. The low pressure in the wake of the separated region makes a large contribution to the pressure force acting on the flow, and consequently, it significantly affects the fully mixed flow angle and the total pressure losses.

A final parameter that is important in the mechanical design of blades is the moment coefficient. In this investigation, the moment was calculated about the midchord location of the blade and was designated as C_{Mmc}. In Fig. 24, the moment coefficient is plotted versus the angle of attack. The curves for each stagger are seen to be quite similar. The moment is negative for all but large negative flow incidences on the blade. The negative sign of the coefficient indicates the leading edge region of the blade is more heavily loaded than the trailing edge region. The maximum moment occurs just at or just

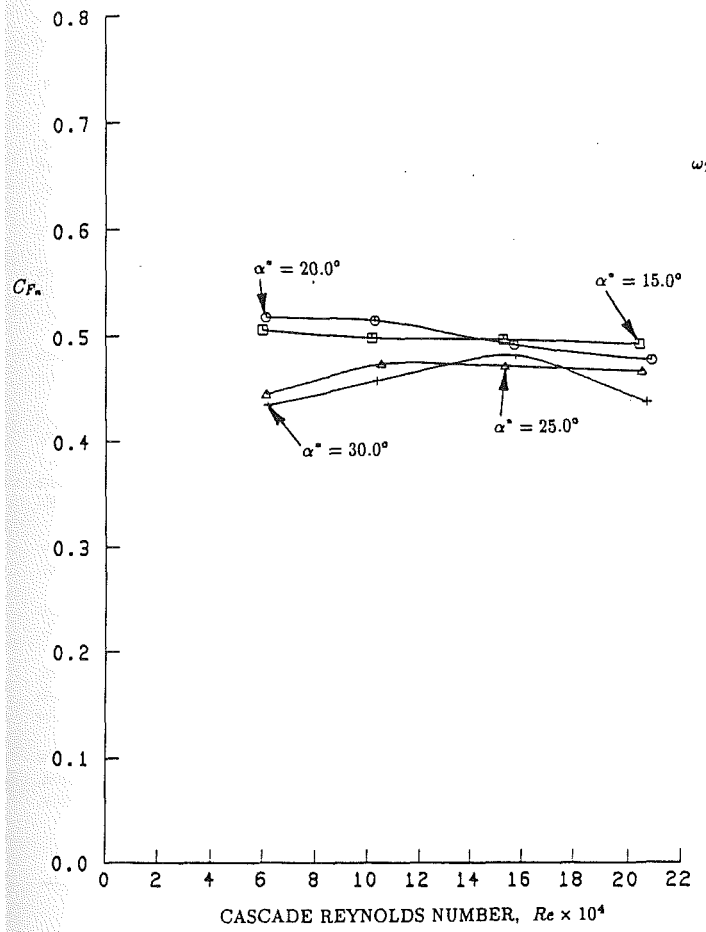

Fig. 25 Normal force coefficient evaluated from the experimental blade pressures as a function of Reynolds number for ξ = 36.5 deg

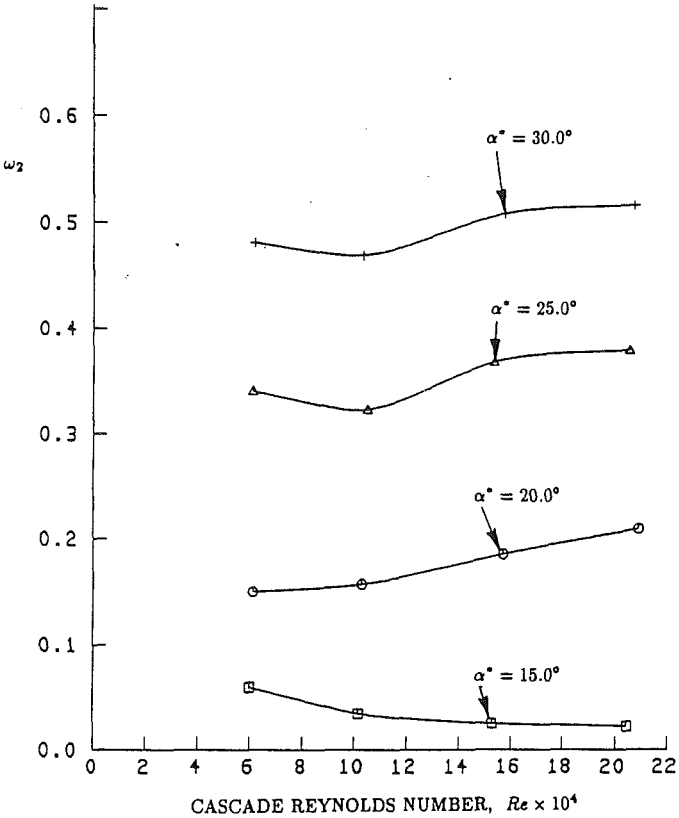

Fig. 26 Mass-averaged total pressure loss coefficient at the downstream measurement location as a function of Reynolds number for ξ = 36.5 deg

before full stall occurs. Although no extremely large variations in the moment are observed, a fluctuation of the moment from the stalled to unstalled value might need to be included in a fatigue or vibration analysis of the blades.

All the data presented to this point have been for a nominal Reynolds numbers of 200,000 based on the cascade inlet velocity and the blade chord. Two final figures are presented to illustrate the effects of variations in Reynolds number on the performance of a stalled cascade. Compressor and pump blading usually operates at high Reynolds numbers, well above 200,000. For a cascade that is not stalled, tests reported in the literature indicate the losses and flow deflection are constant above a critical Reynolds number in the neighborhood of 200,000. A precise critical Reynolds number cannot be specified, because it is known to vary with the free-stream turbulence level and the blade camber and loading. Below the critical Reynolds number, laminar separation may occur, which will result in an order of magnitude increase in the total pressure loss. Curves of C_{Fn} and ω_2 as a function of Reynolds number are given for several angles of attack in Figs. 25 and 26. Although variations in the loss coefficient and the normal force coefficient are evident, the variations are small relative to the full range of C_{Fn} and ω_2 observed over the operating range from attached to fully stalled flow. The variations are also small relative to the order of magnitude increase associated with laminar separation at low Reynolds numbers.

Summary and Conclusions

Results for blade pressure distributions and total and static pressure profiles measured in a two-dimensional cascade under fully stalled conditions (i.e., separation from the blade leading edge) have been presented. The total and static pressure profiles were measured with a pneumatic probe by aligning the probe with the flow at the angle determined with a dual split-film probe. The characteristics of the pressure data are consistent with the characteristics of the flow observed from the flow visualization and time-mean velocity measurements presented in Part I of this paper. The total pressure profiles for the 25 deg stagger cascade revealed a region of essentially inviscid (loss-free) flow, and a region of high losses in the wake of the recirculating region. For the 36.5 and 45 deg stagger cascade, two distinct regions were not evident and the losses were found to extend across the entire blade passage. Associated with the larger recirculating region, the mass-averaged total pressure loss was shown to increase at a much greater rate with increases in the angle of attack for the larger stagger cascades. The differences between the slopes of the loss curves for the various staggers are less significant for the fully mixed flow than for the losses directly downstream of the cascade. The normal force coefficient was found to rise to a peak value at the point where full stall occurred, and then decrease with additional increases in angle of attack. The peak values of the normal force coefficient and the angle of attack where the peak occurred were greater for the smaller stagger cascades.

The performance curves calculated from the numerically predicted flow fields showed the same trends as the experimental results. The influence of stagger on the performance curves was more pronounced and easily observed. Trends in the performance curves at angles of attack far exceeding those possible to test experimentally were also obtained from the numerical simulation. Numerical test cases were run for each stagger at angles of attack up to the condition where the flow was within 5 deg of being parallel to the cascade (i.e., within 5 deg of α_1 = 90 deg). These results showed that the losses continue to rise as the limiting angle of attack is approached.

The normal force coefficient continues to decline after the peak value and appears to approach zero as the inlet angle approaches 90 deg.

A final conclusion is that the Reynolds number, within the range from 50,000 to 200,000, does not have a significant effect on the performance of fully stalled cascades. In this range of Reynolds number, the shear layers of the separated flow are turbulent in nature, and therefore no change in the performance of the cascade would be expected until the flow becomes completely laminar at very low Reynolds numbers.

Acknowledgments

This investigation was sponsored by the Air Force Office of Scientific Research under the direction of Dr. James Wilson. The support of the AFOSR is greatly appreciated.

References

Cornell, W., 1954, "The Stall Performance of Cascades," *Proceedings, 2nd National Conference of Applied Mechanics*, ASME, New York.

Hah, C., 1983, "Modeling of Turbulent Flow Fields Through Cascade of Airfoils at Stall Condition," AIAA Paper No. 83-1743.

Hah, C., 1984, "A Numerical Study of Three-Dimensional Flow Separation and Wake Development in an Axial Compressor Rotor," ASME Paper No. 84-GT-34.

Horlock, J. H., 1973, *Axial-Flow Compressors, Fluid Mechanics and Thermodynamics*, Huntington, NY, Robert E. Krieger Publishing Co., ©, 1958, Reprinted.

Moses, H. L., Jones, R. R., and O'Brien, W. F., 1978, "Simultaneous Solution of the Boundary Layer and Freestream With Separated Flow," *AIAA Journal*, Vol. 16, No. 1, pp. 61-66.

Moses, H. L., Thomason, S. B., and Jones, R. R., 1981, "Simultaneous Solution of the Inviscid Flow and Turbulent Boundary Layers for Compressor Cascade," AIAA Paper No. 81-1476.

Moses, H. L., and Thomason, S. B., 1986, "An Approximation for Fully-Stalled Cascades," *AIAA Journal of Propulsion and Power*, Vol. 2, No. 2, pp. 188-189.

O'Brien, W. F., Moses, H. L., Thomason, S. B., and Yocum, A. M., 1983, "High-Angle-of-Attack Cascade Measurements and Analysis," *Proceedings, 6th International Symposium on Air-Breathing Engines*, AIAA, New York, pp. 643-648.

Patankar, S. V., 1980, *Numerical Heat Transfer and Fluid Flow*, Hemisphere Publishing Corporation, New York.

Rosenfeld, M., and Wolfshtein, M., 1982, "Numerical Solution of Viscous Flow Around Arbitrary Airfoils in a Straight Cascade," *Proceedings, Eighth International Conference on Numerical Methods in Fluid Dynamics*, Springer-Verlag, New York.

Schäfer, O., Frühauf, H.-H., Bauer, B., and Guggolz, M., 1986, "Application of a Navier-Stokes Analysis to Flows Through Plane Cascades," ASME *Journal of Engineering for Gas Turbines and Power*, Vol. 108, pp. 103-111.

Shamroth, S. J., McDonald, H., and Briley, W. R., 1984, "Prediction of Cascade Flow Fields Using the Averaged Navier-Stokes Equations," ASME *Journal of Engineering for Gas Turbines and Power*, Vol. 106, pp. 383-390.

Steger, J. L., Pulliam, T. H., and Chima, R. V., 1980, "An Implicit Finite Difference Code for Inviscid and Viscous Cascade Flow," AIAA Paper No. 80-1427.

Tkacik, P. T., 1982, "Cascade Performance of Double Circular Arc Compressor Blades at High Angles of Attack," M.S. Thesis, Mechanical Engineering, Virginia Polytechnic Institute and State University, Blacksburg, VA.

Treaster, A. L., and Yocum, A. M., 1979, "The Calibration and Application of Five-Hole Probes," *Instrument Society of America Transactions*, Vol. 18, No. 3, pp. 23-34.

Weinberg, B. C., Yang, R.-J., McDonald, H., and Shamroth, S. J., 1986, "Calculations of Two and Three-Dimensional Transonic Cascade Flow Fields Using the Navier-Stokes Equations," ASME *Journal of Engineering for Gas Turbines and Power*, Vol. 108, pp. 93-102.

Yocum, A. M., 1988, "An Experimental and Numerical Investigation of the Performance of Compressor Cascades with Stalled Flow," Ph.D. Dissertation, Mechanical Engineering, Virginia Polytechnic Institute and State University, Blacksburg, VA.

Experimental Study on the Three-Dimensional Flow Within a Compressor Cascade With Tip Clearance: Part I—Velocity and Pressure Fields

S. Kang[1]

C. Hirsch
Professor.
Mem. ASME

Vrije Universiteit Brussel,
Department of Fluid Mechanics,
1050 Brussel, Belgium

Experimental results from a study of the three-dimensional flow in a linear compressor cascade with stationary endwall at design conditions are presented for tip clearance levels of 1.0, 2.0, and 3.3 percent of chord, compared with the no-clearance case. In addition to five-hole probe measurements, extensive surface flow visualizations are conducted. It is observed that for the smaller clearance cases a weak horseshoe vortex forms in the front of the blade leading edge. At all the tip gap cases, a multiple tip vortex structure with three discrete vortices around the midchord is found. The tip leakage vortex core is well defined after the midchord but does not cover a significant area in traverse planes. The presence of the tip leakage vortex results in the passage vortex moving close to the endwall and the suction side.

Introduction

Research on the three-dimensional flow in axial turbomachinery with tip gap can be traced back to the 1920s as reviewed by Prasad (1977). Most of the investigations on axial compressor flow fields have been concerned with rotor wake characteristics (Lakshminarayana and Poncet, 1974; Hirsch and Kool, 1977; Kool et al., 1978) and with the interaction region of the casing wall boundary layer, the wake and the tip leakage flow (Davino and Lakshminarayana, 1982; Hunter and Cumpsty, 1982). The behavior of the flow fields inside and behind an axial rotor has been examined by Dring et al. (1982), Joslyn and Dring (1985), and Inoue and Kuroumaru (1984). Experimental studies with special emphasis on the leakage flow development near and in the tip clearance have been conducted by Bindon (1985a, b) and Moore and Tilton (1988) for linear turbine cascades, and by Lakshminarayana et al. (1982, 1987), Inoue and Kuroumaru (1989), Inoue et al. (1991), and Storer and Cumpsty (1991) for axial compressors. The tip leakage flow and its subsequent rolling up into a vortex have been clearly demonstrated and described originally by Rains (1954) and subsequently by Lakshminarayana (1970). More recently, Chen et al. (1991), based on the slender body theory in external aerodynamics, proposed an approximate method for analyzing compressor tip clearance flow. Numerical computation of the three-dimensional flow in a passage with tip clearance has also been reported recently (Hah, 1986; Storer and Cumpsty, 1991) using the Navier-Stokes equations, showing satisfactory prediction on both the overall effects and certain local details near and inside the tip clearance. But for further validation of the computational codes, detailed measured data and physical interpretations are necessary.

This paper presents more information on the secondary flow and vorticity within and behind a linear compressor cascade, with tip clearance, of a NACA 65-1810 blade profile at design conditions, and to present the overall features of the tip leakage vortex, such as the evolution of its size, center position, and vorticity. The investigation is presented in two parts. In part I, the overall secondary flows, total pressures losses and static pressures are discussed; in part II (Kang and Hirsch, 1993), the main attention will be focused on the vorticity field.

Experimental Facility and Instrumentation

The experimental facility, instrumentation, and measurement accuracy have been described by Kang and Hirsch (1991). Hence only a short review is presented here.

The present investigations were carried out in the low-speed compressor cascade wind tunnel of the Department of Fluid Mechanics, Vrije Universiteit Brussel (VUB). The test section of the wind tunnel consists of two parallel end plates, aligned horizontally, between which a cascade with seven NACA 65-1810 blades is installed. The blades, with flat tips, are cantilevered from the upper wall of the cascade. The lower wall, supported by four screws and stiffed horizontally by other four screws, can be adjusted to produce tip clearance with an

[1]Permanent address: Power Engineering Dept., Harbin Institute of Technology, Harbin 150006, People's Republic of China.

Contributed by the International Gas Turbine Institute and presented at the 37th International Gas Turbine and Aeroengine Congress and Exposition, Cologne, Germany, June 1-4, 1992. Manuscript received by the International Gas Turbine Institute February 20, 1992. Paper No. 92-GT-215. Associate Technical Editor: L. S. Langston.

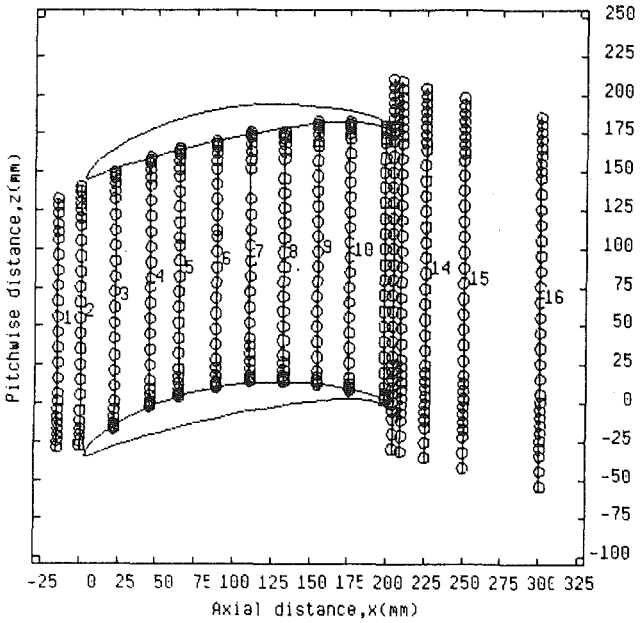

Fig. 1 Cascade coordinate system and traverse measurement point distribution in a spanwise (*y* axis) section

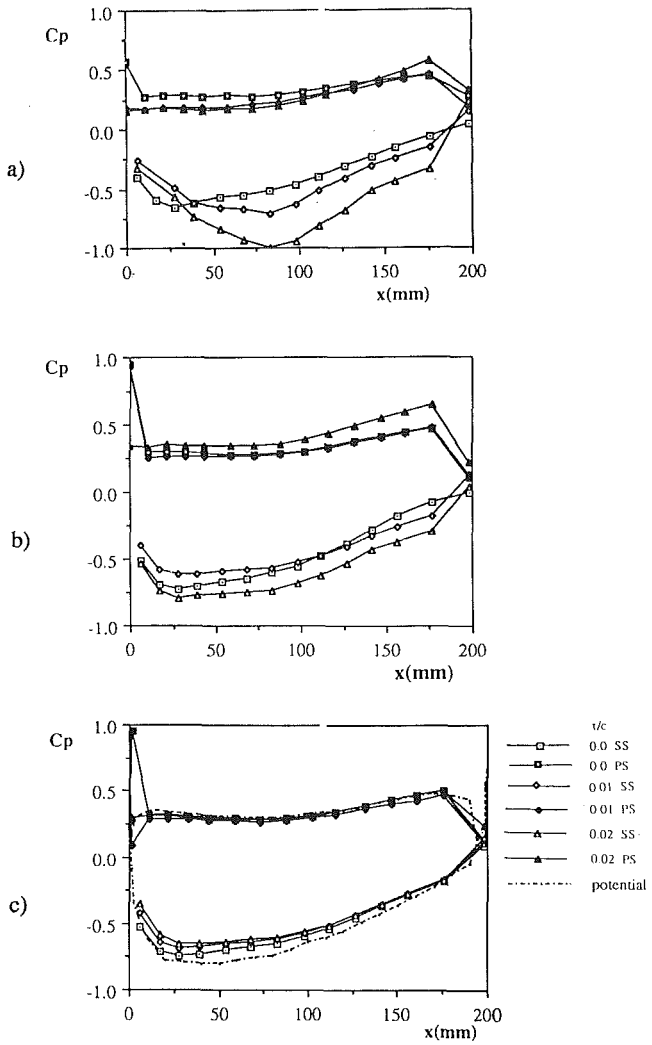

Fig. 2 Static pressure distribution on blade surface in three span positions: (*a*) 1.5 percent, (*b*) 15 percent, and (*c*) midspan

uncertainty of ±0.1 mm for the seven tip gaps. The tip clearance spaces in the present study were 1.0, 2.0, and 3.3 percent of chord. The periodicity is shown from the uncertainty of the static pressure coefficients on the lower wall of the leading and trailing edges of the measured passage. For 2.0 percent clearance as an example, the periodicity is better than 1 percent. The blade aspect ratio is 1.0.

Traverse measurements with a five-hole probe were conducted, at tip clearance of 1.0 and 2.0 percent, in the passage with the middle blade as its pressure side. There were 16 traverse planes (Fig. 1) from 7.5 percent chord upstream of the leading edge to 50 percent chord downstream of the cascade exit plane. In each of the traverse planes 24 stations from suction side to pressure side and 33 stations behind the cascade were arranged. Fifteen points in each station are recorded from near the endwall to midspan. In order to obtain some information on the flow in the whole span region, more points (26 points in span) are taken in the traverse plane No. 14 for 1.0 percent tip clearance, covering 98 percent of the span.

The five-hole probe with external size of 2.6 mm is mounted on a support located downstream and fixed to the upper wall of the cascade, from which the probe can be inserted into the flow field. The static pressures of blade surfaces and endwall were also recorded by static pressure tubes.

The five-hole probe was fully calibrated in a jet (Kang, 1989). The accuracies of the measured velocity and total pressure are 1 percent of the inlet midspan values from where all the reference parameters were taken. The uncertainty of the measured flow direction is better than 1 deg.

The methods used for visualizing the three-dimensional flow inside the linear compressor cascade included oil film and titanium dioxide, cotton threads, white paint-trace, and black ink-trace. For the last two methods, a very thin plastic paper was pasted on the visualized surface; photos were taken after tearing it off. All the flow visualization studies had been filmed in motion with a video camera. The visualization studies are conducted on the clearances of 0.0 to 3.3 percent.

Test Conditions

With the tip clearances, all the inlet flow conditions, except the dynamic pressure, were not significantly different from those without tip clearance reported by Kang and Hirsch (1991). The test Reynolds number, based on blade chord, was about 2.9×10^5; free-stream turbulence intensity was 3.4 percent. The

Nomenclature

c = blade chord
C_p = static pressure
H = shape factor
l = blade span
LE = leading edge
PS = pressure side
P_y = coordinate of passage vortex center from low wall
P_z = coordinate of passage vortex center from suction side
s = pitch
SS = suction side
TE = trailing edge
u, u_a = axial velocity, mass-averaged axial velocity
V_1 = inlet resultant velocity
x, y, z = axial, spanwise, and pitchwise distance
δ = boundary layer thickness
δ^* = displacement thickness
θ = momentum thickness
τ = tip clearance

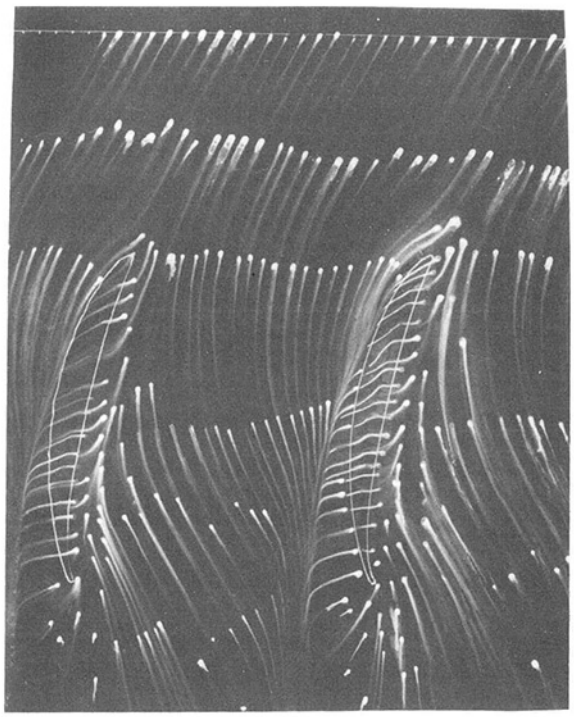

Fig. 3 Paint-trace visualization on the endwall, at 2.0 percent tip clearance

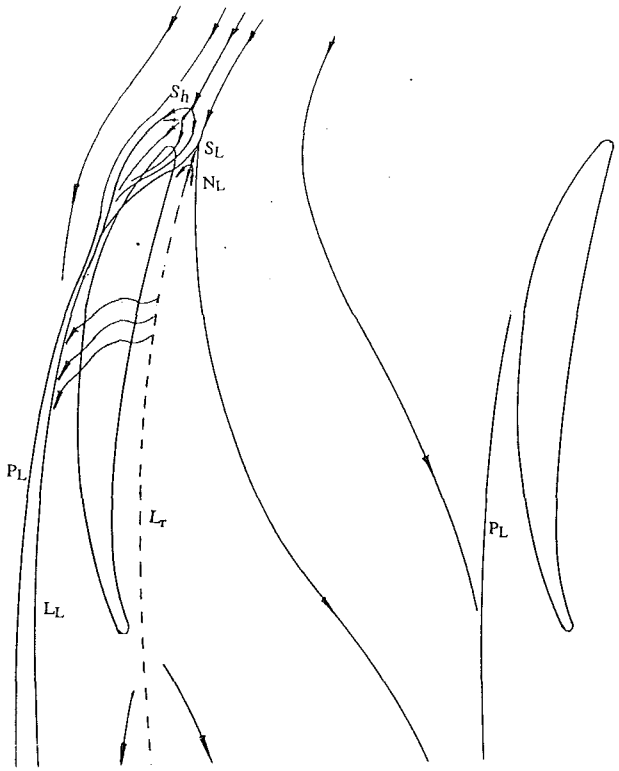

Fig. 5 Schematic of the flow pattern on the wall at $\tau/c = 0.02$

Fig. 4 Ink-trace visualization on the blade tip surface, at 2.0 percent tip clearance

mass-averaged air inlet and outlet angles, measured 40 percent chord upstream and 25 percent chord downstream were 29.3 and -2.5 deg, compared to the design values of 30 and -4.02 deg, respectively. The inlet boundary layer was turbulent. The integral parameters of the inlet endwall boundary layer, at 40 percent chord upstream of the leading edge, are summarized as follows:

$$\delta/c = 0.2 \qquad \delta^*/c = 0.0144$$

$$\theta/c = 0.0118 \qquad H = 1.22$$

Static Pressure Distribution on Blade Surfaces

The measured static pressure distributions on the blade surfaces at three spanwise positions, $y/l = 0.015$, 0.15, and 0.5 (midspan), are given in Fig. 2 for tip clearances, 0.0, 1.0, and 2.0 chord with potential calculation. The values closest to the trailing edge were obtained from the five probe readings at the measured point near the blade surfaces on traverse plant No. 11, 2 mm ahead of the exit plane. It is seen from Figs. 2(*b*) and 2(*c*) that the pressure distributions at the spanwise positions far away from the blade tip (15 percent and midpan) have qualitatively similar shapes for different tip clearances with some change in the pressure values, especially in the first half chord on the suction surface. The shift, resulting in unloading, may be caused by the motion of the tip leakage flow, which is to be expected as the midspan is just a half blade chord away from the tip. As in the case without tip gap, the pressure peaks on the suction surface with tip clearances are also located at about 15 percent chord downstream of the leading edge at 15 percent span and midspan.

Near the blade tip (Fig. 2*a*), however, the static pressure distribution is significantly different from the other spanwise positions. In the vicinity of the leading edge, it shows small unloading, then strong reloading takes place around the midchord. Undoubtedly, this is related to the generation of the tip leakage flow and the motion of the corresponding tip leakage vortex. The pressure increase on the suction side near the leading edge is due to the interaction with the fluid passing through the tip gap from the pressure side, where the tip leakage vortex originates; see later discussions. The increment of blade force, from 20 chord downstream of the leading edge, results from the low-pressure core of the tip leakage vortex. A similar behavior has been mentioned by Graham (1986) in his investigation of a tip clearance cascade in a water rig, with larger gaps.

Surface Flow Visualization

Extensive visualizations for 0.0, 1.0, 2.0, and 3.3 percent clearance have been analyzed in detail and reported by Kang (1991b). In this paper only the analysis referring to the 2.0 percent clearance will be presented.

Figure 3 shows the paint-trace pattern of the endwall around and under the blades and Fig. 4 shows the ink-trace pattern of a blade tip surface. The topological patterns of the endwall and blade surface skin-friction lines or limiting streamlines, deduced from the visualizations, are respectively shown in Figs. 5 and 6.

Endwall Flow Pattern. As seen from Fig. 3, the skin-fric-

tion line, approaching the blade leading edge, splits into two branches at a point in front of the leading edge. This is a saddle point, labeled S_h in Fig. 5, resulting in the formation of a leading edge horseshoe vortex. Its suction side branch turns around the leading edge and joins with the separation line of the tip leakage vortex at about 25 percent chord downstream. The pressure side branch stretches downstream a short distance, then changes its direction at about 5 percent chord, and finally passes through the tip gap and tends to join with the suction side branch. Sjolander and Amrud (1987) also found, at their smaller clearance ($\tau/c = 0.96$ percent), that the pressure side leg of the vortex was swept back over the blade tip with the first 10 percent of chord length. This effect was, however, not seen for the 1.0 percent tip clearance, where the pressure side branch stretches always downstream, similar as the case of zero clearance. When the tip size was increased to 3.3 percent, the saddle point S_h disappeared and no leading edge horseshoe vortex could be seen.

The deepest impression on Fig. 3 is the formation of a reattachment line near the pressure side and a separation line near the suction side, as respectively sketched by L_r and L_L in Fig. 5. The line L_L is the separation line of the tip leakage vortex. From a detailed analysis of the visualizations, a separation line close to L_L, indicated as P_L on Fig. 5, can be identified. The paint-traces around the midpitch converge to this line, which is certainly the separation line of the passage vortex. The flow divergence from the reattachment line L_r implies a flow toward the endwall. As a result, a node and a saddle point will be topologically generated at the leading edge region, as shown in Fig. 5 by N_L and S_L. Besides, it is seen in Fig. 3 that the limiting streamlines issued from the reattachment line L_r toward the pressure side are all going into the gap at almost right angles to the pressure surfaces, except near the leading and the trailing edges where the pressure-driven leakage flows are small.

Even though the origin of the separation line of the tip leakage vortex is not easily identified from Fig. 3, the origin might possibly be the saddle point S_L. The apparent rolling-up of the tip leakage vortex starts just downstream of the leading edge in the suction side corner. Inside the gap the vortex may be mixed with the leakage flow.

Blade Surface Flow Pattern. One of the new observations in the present visualizations is the flow pattern on the blade tip surface. It is seen from the ink-trace visualization of Fig. 4 at 2.0 percent clearance that the limiting streamlines, diverging from about the middle of the blade profile, converge toward the tip edges over about 70 percent chord length from the leading edge. Near the trailing edge reverse flow takes place. As a result, a saddle and a node point were formed at the leading edge region, and two nodes divided by a saddle were formed in the region of about 70 to 86 percent chord as schematically shown in Fig. 6 by S_t, N_t, N_{tp}, and N_{ts}. Figure 6 shows the schematic flow pattern of the blade tip surface, together with the "opened-up" pressure and suction surfaces.

From the visualizations on the pressure and suction surfaces, see Kang (1991b) for details, it was observed that near the tip, the paint-traces also converged to the corresponding blade tip edges. These observations are schematically shown in Fig. 6. As a result, Fig. 7 presents a multiple tip vortex structure based on the visualizations. It consists of the well-known tip leakage vortex, a tip separation vortex, and a secondary vortex. The convergent line along the suction side edge in Fig. 6 may be the separation line of the secondary vortex, which has an opposite rotation sense to the tip leakage vortex. The presence and rotation of this vortex can be evidenced from the secondary flow charts in the suction side corner; see Fig. 13 and later discussion. The other convergence line along the pressure side edge in Fig. 6 may be the separation line of the tip separation vortex. This vortex, in a section, is similar to the so-called

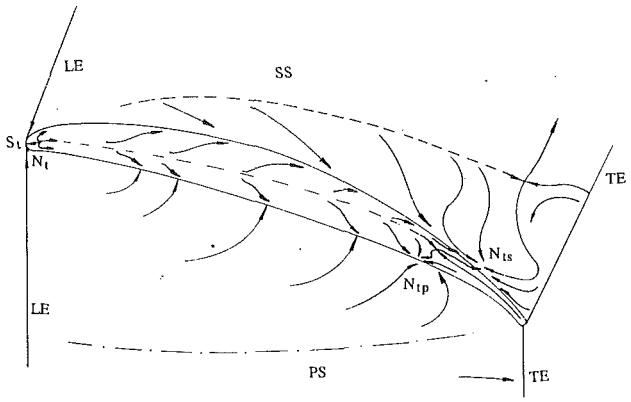

Fig. 6 Schematic of the flow pattern on the blade tip, with "opened-up" pressure and suction surfaces

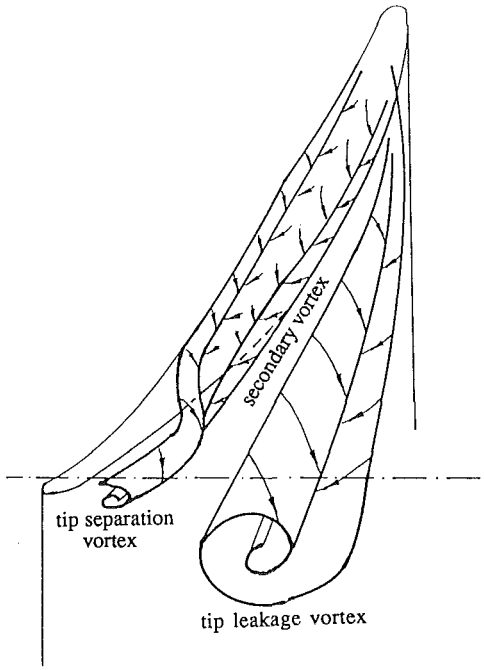

Fig. 7 Schematic of the vortex structure around the tip

separation bubble or vena contracta, as referred to by Rains (1954) and Moore and Tilton (1988). However, it is really not a separation bubble but a vortex aligning along the tip. Both of the separation lines along the blade edges issued from the saddle point S_t (Figs. 4 and 6) at the leading edge and terminated at two nodes N_{tp} and N_{ts} near the trailing edge. These two nodes are generally unstable; they may change from node to degenerated node or spiral node. When they are spiral nodes, the oil, converged to the separation lines and stacked around the singular points, was shed into the flow field, as can be seen also from the video film. According to topological criteria, there must be a saddle point between the two nodes N_{tp} and N_{ts}, as shown in Fig. 6. Because of the presence of the saddle, the tip separation vortex turns it toward the suction side from where it stretches toward the trailing edge along the corner, see Fig. 7.

It is noted that Rains (1954) assumed that the tip leakage flow was two dimensional and normal to the camber line of the blade. But from the present tests, it is concluded that limiting streamlines on the blade tip surface are generally nei-

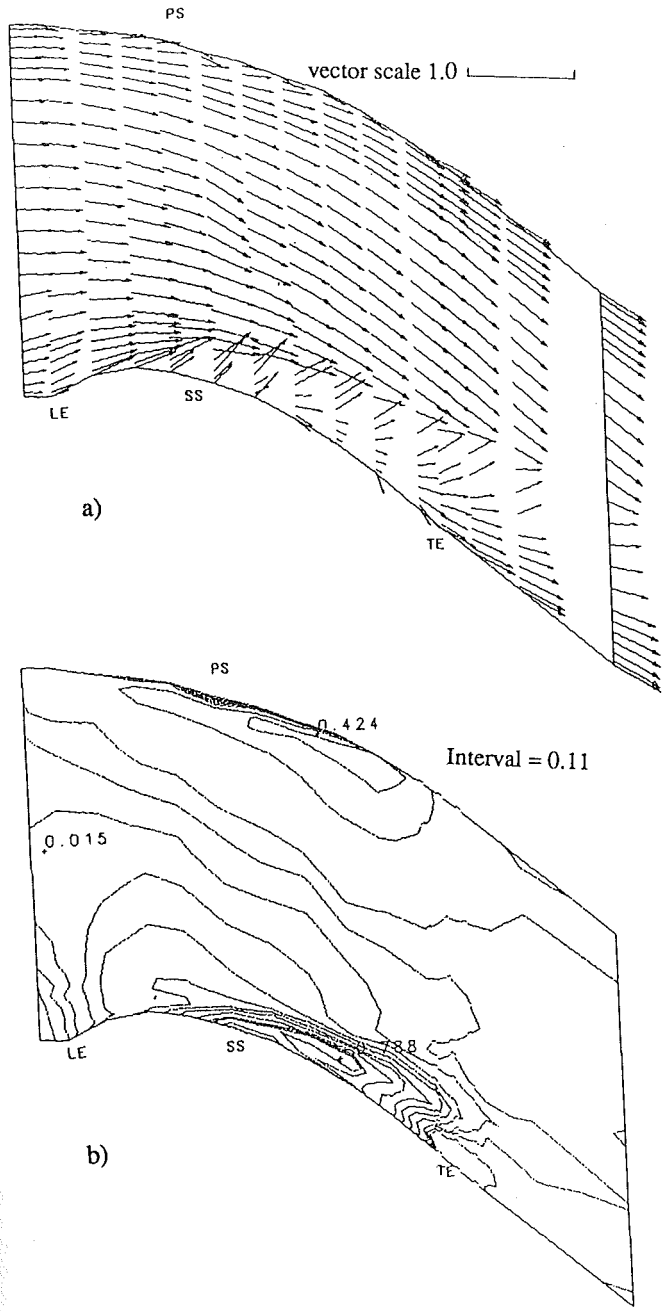

Fig. 8 (*a*) velocity vector plot and (*b*) static pressure contour near the wall ($y/l = 0.02$) at $\tau/c = 0.02$

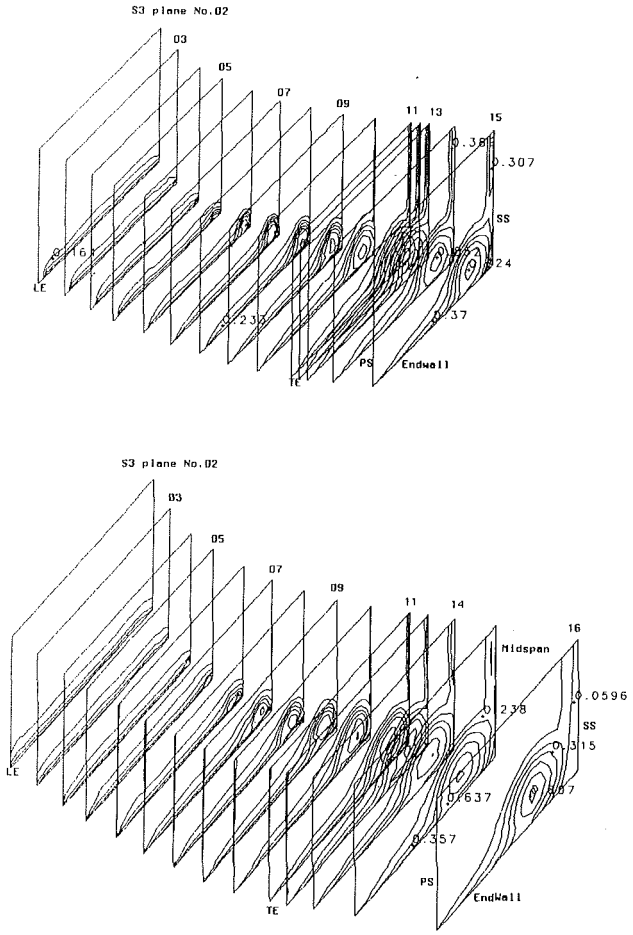

Fig. 9 Contours of total pressure loss on traverse planes at (*a*) $\tau/c = 0.01$, and (*b*) $\tau/c = 0.02$, interval = 0.14 in range of 0 ~ 2.4

ther normal to the suction side nor to the camber line within the gap. On the stationary endwall, however, the limiting streamlines around the midchord in the pressure side are approximately normal to the pressure surface. Hence, the flow inside the tip gap is strongly three dimensional almost over the whole chord length.

Secondary Flows and Total Pressure Losses

For a better understanding of the three-dimensional flow structure, the measured data are analyzed with the interactive flow visualization program CFView, developed in the Dept. of Fluid Mech., VUB (Vucinic et al., 1992). Some of the plots of the total and static pressure coefficients and secondary flow velocities are shown in Figs. 8–11 and more details can be found from Kang (1991a).

Within the Blade Passage. The velocity vector plot and static pressure contour on the blade to blade surface near the endwall at 2.0 percent span are shown in Fig. 8. It is observed from Fig. 8(*a*) that a strong secondary flow is developed near the endwall. The flow near the suction side converges to a particular line, i.e., the separation line of the tip vortex, which can be identified as the line L_L of Fig. 6; this separation line starts from about the first 10 percent chord, which is consistent with the visualization observations. Due to the development of the tip leakage vortex, a low-pressure trough is formed on the endwall near the suction side around the midchord (Fig. 8*b*). The low-pressure core increases with tip gap. Associated with it, the total pressure loss reaches its high values.

Figure 9 shows the contours of total pressure loss on all the traverse planes from the leading edge to downstream of the exit at 1.0 percent and 2.0 percent tip clearances. Figure 10 shows a selection of the secondary flow vector plots for the traverse plane No. 10 (88 percent *c*) and 15 (125 percent) at the clearance of 1.0 percent. The secondary flow vectors were obtained by projecting the measured velocities on the plane normal to the flow direction at midspan at the same pitch coordinate (Kang and Hirsch, 1991). The first impression from the plots in Figs. 9 and 10 is the generation and development of the tip leakage vortex with high total pressure loss and strong rotation motion. It is seen that the isolines in the suction side corner with high values are quasi-circular and are well consistent with the rotation center of the tip vortex. Even though the presence of the tip leakage vortex can be evidenced at about 10 percent chord downstream of the leading edge from the visualizations (Figs. 3 and 5) and from the near-wall velocity

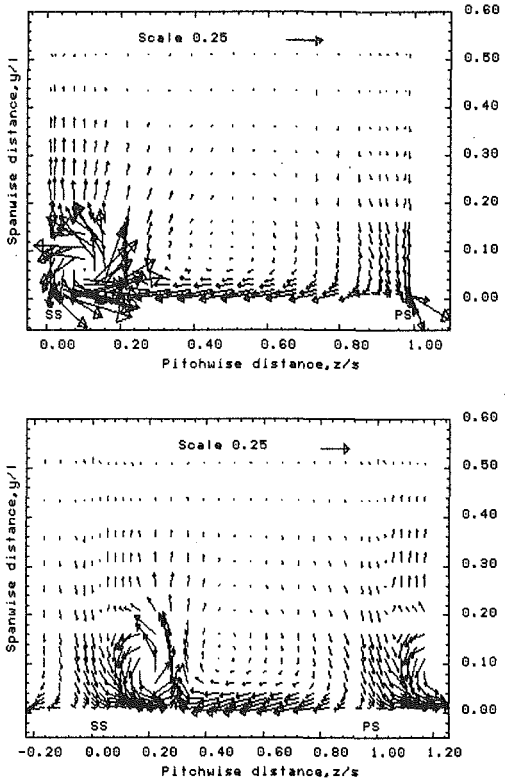

Fig. 10 Secondary velocity vectors at $\tau/c = 0.01$ on traverse planes (*a*) No. 10 (88 percent *c*), and (*b*) No. 15 (150 percent *c*)

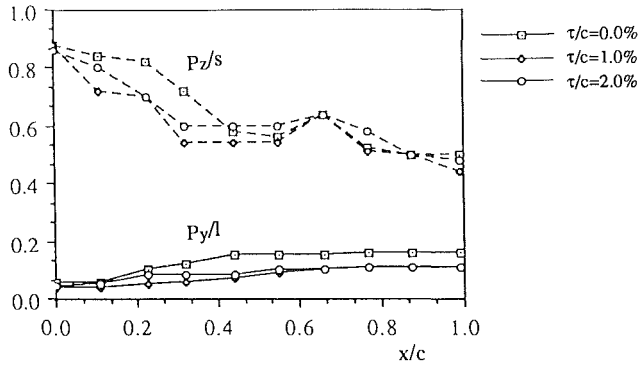

Fig. 11 Position of passage vortex center in cross section

vector chart of Fig. 8(*a*), the apparent rotation or the quasi-circular isolines can be identified from the S_3 plane No. 6 (44 percent *c*). Due to its very small size, more information cannot be obtained near the leading edge with the present measurement method with a 2.6 mm five-hole probe. As noted by Sjolander and Amrud (1987), the starting point of the leakage vortex at larger tip gaps is shifted axially. In the present study, the shifting is characterized by the less apparent rotation on the secondary flow plots at $\tau/c = 2.0$ percent compared to $\tau/c = 1.0$ percent.

Figure 11 shows the approximate coordinates P_y and P_z of the passage vortex core center, defined by the distance of the rotation center from the endwall and from the passage suction side. Those data were read from the secondary vector charts of Fig. 10 in each traversed plane for different tip clearances, including the zero clearance. It is found that the tendency of the passage vortex center in the pitchwise direction is similar for the three clearance cases in the rear half-chord region. In the front half-chord, however, the passage vortex in the cases with tip gap is closer to the suction side than the zero tip gap

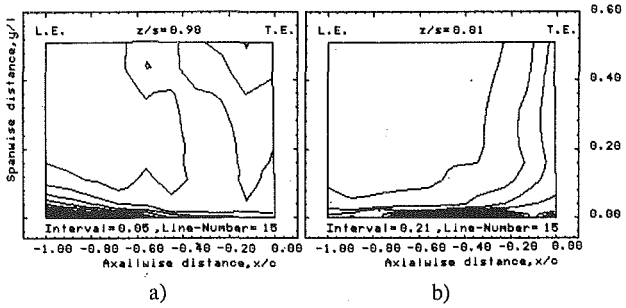

Fig. 12 Contours of total pressure losses (*a*) near pressure surface ($z/s = 0.98$), and (*b*) near suction surface ($z/s = 0.01$) at $\tau/c = 0.01$

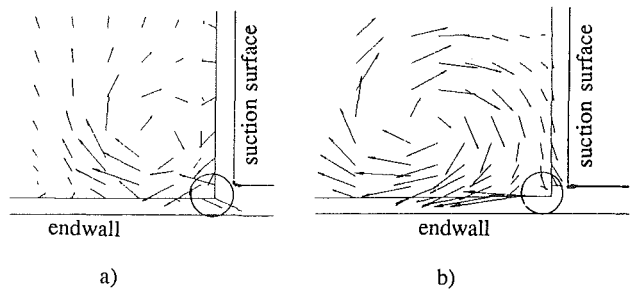

Fig. 13 Zooms of the secondary velocity vector in the suction side corner for 2.0 percent clearance on the S_3 planes, (*a*) No. 7 (55 percent *c*), and (*b*) No. 11 (98 percent *c*)

case. The reason may be that the low-energy fluids of the blade pressure surface and endwall boundary layers in the pressure side corner have been driven through the tip gap to the suction side corner in the adjacent passage as observed from the visualization. As a result, the endwall boundary layer of the pressure side is thin. This can be identified from the total pressure loss coefficient contours in Fig. 9. It is seen that close to the leading edge planes, the total pressure coefficient contours are basically uniform over the whole pitch for the two clearance cases. But starting from the traverse plane No. 3, the loss is going to lower values in the pressure side corner but to higher values in the suction side corner. Hence the passage vortex or the rotation of the passage secondary flow shifts to the suction side.

In the spanwise direction, the vortex has almost the same height P_y near the leading edge plane. Downstream of the leading edge, the vortex tends to go up and then almost keeps at a constant height from midchord to trailing edge. It is observed in Fig. 11 that generation of the tip leakage vortex results in the passage vortex moving close to the endwall.

More evidence on the behavior of the leakage flow can be viewed from Fig. 12, which shows the contours of total pressure losses near the pressure surface ($z/s = 0.98$) and the suction surface ($z/s = 0.01$). It is seen that the start of the high loss region near the suction surface (Fig. 12*b*) just corresponds to the start of the significant decrease in pressure side (Fig. 12*a*). Therefore, it can be concluded that the tip leakage flow or the resulting tip leakage vortex would largely be influenced by viscous effect and depends upon the thickness of the inlet boundary layer and Reynolds number, even though the driving force may be due to inertia, as described by Rains (1954).

Figure 13 shows zooms of the secondary velocity vector in the suction side corner on the S_3 plane No. 7 (55 percent *c*) and 11 (98 percent *c*) for 2.0 percent clearance. From this figure the tip separation and secondary vortices in the multiple vortex structure shown in Fig. 7 can be evidenced. It was found from the measured secondary flow velocities that in the extreme corner, a small weak rotation in opposite sense to the tip leakage vortex exists, from planes No. 6 to 9 (Fig. 13*a*), but in the same sense as the tip leakage vortex near trailing edge

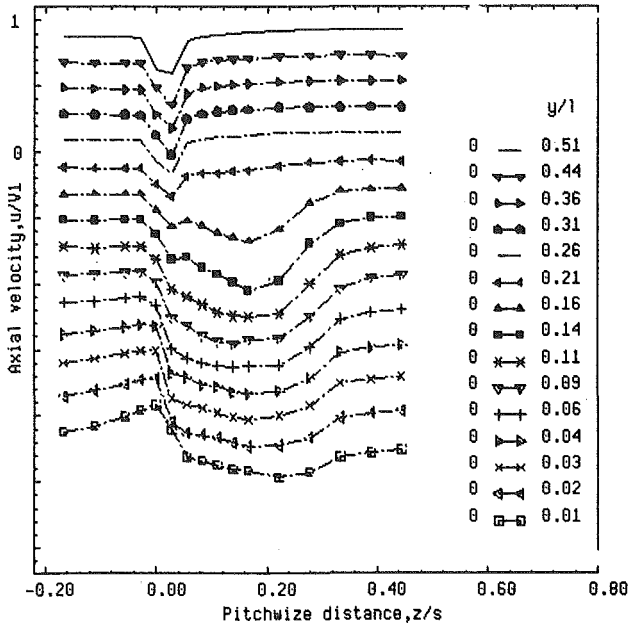

Fig. 14 Spanwise development of the axial velocity on transverse plane No. 14 (112.5 percent *c*) for $\tau/c = 0.01$

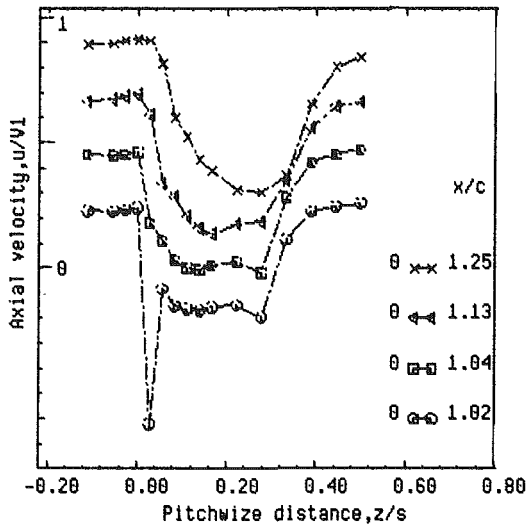

Fig. 15 Axial development of the axial velocities near the tip leakage vortex center at $y/l = 0.09$ for $\tau/c = 0.01$

planes No. 10 and 11 (Fig. 13*b*). The rotation around the midchord is believed to be associated with the secondary vortex, but that near the trailing edge is believed to be associated with the separation vortex, as schematically drawn in Fig. 7. This means that the secondary vortex may be mixed before reaching the trailing edge, due to its weak and opposite sense, or that due to its small size, it could not be measured with the present facility.

Behind the Passage. Figure 14 shows the spanwise development of the axial velocities on traverse plane No. 14 (112.5 percent chord behind the cascade) at $\tau/c = 0.01$. Figure 15 shows the axial development of the axial velocities near the tip leakage vortex center at $y/l = 0.09$ for 1.0 percent clearance from 2 to 25 percent downstream of the trailing edge. It is seen from Fig. 14, and also from Figs. 9 and 10 that even though the tested model is a linear cascade, the wake flow is still dominated by significant three dimensionality. With the existence of the tip clearance, the wake has been fully distorted except near midspan. The profiles in Fig. 15 have two defect

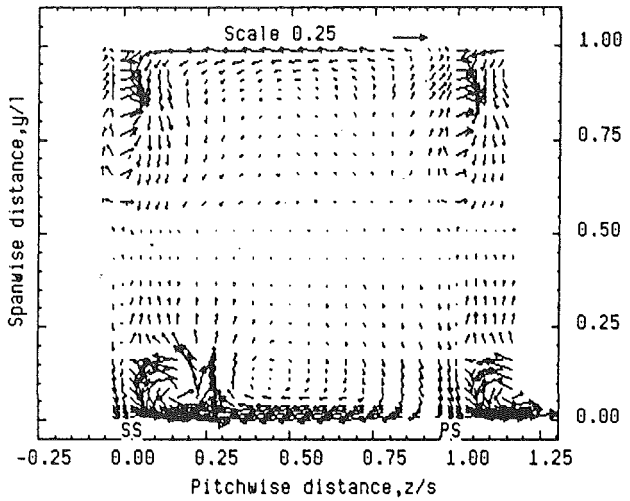

Fig. 16 Full-span secondary flow vectors on the traverse plane No. 14 (112.5 percent *c*) for $\tau/c = 0.01$

regions near the trailing edge; one corresponds to the blade wake, the other to the core of the tip vortex. But with the development along the streamwise direction the former tends to disappear due to the interaction between the wake and the tip leakage vortex.

The multiple tip vortex structure, i.e., the secondary vortex and the separation vortex in Fig. 7, was not observable in all the downstream traverse planes. They may be mixed with or entrained into the wake and/or the tip leakage vortex, due to their small size and weak vorticities.

A measurement over the full span was also conducted in the traverse plane No. 14, even though it was believed that the influence of the tip clearance is confined only within a half span. The result is shown in Fig. 16 for the secondary velocity vector. It is seen that the flow features in the upper half span are fairly similar to those of the previous measurements in the lower half span with no tip gap (Kang and Hirsch, 1991).

Summary. A weak horseshoe vortex will be generated in front of the leading edge at smaller clearance under the present conditions. In the 1.0 and 2.0 percent clearances, the vortex is evidenced from the probe measurements and visualizations. But with further increase of the clearance, the vortex will not occur, as observed from the visualization at 3.3 percent clearance.

The passage and tip leakage vortices have different properties in compressor cascades. The tip leakage vortex is basically formed from the low-energy fluid coming from the pressure and suction surface boundary layers near the tip and from the endwall boundary layers around the tip. It has a distinctive core being seen not only from the vector plots of secondary velocity but also from the total pressure and/or the static pressure coefficient contours. For the passage vortex, the fluid rotating with it is partly viscous from the boundary layers and partly inviscid from outside of the boundary layers. Therefore, the rotation center of the passage vortex is not always coincident with higher loss and/or lower static pressure. For turbine cascades such as those mentioned by Langston et al. (1977) and Marchal and Sieverding (1977), the much stronger horseshoe vortex, with its pressure side leg rolling up most of the low-momentum fluids in the incoming boundary layer into it, will be merged into the passage vortex in its downstream development. Thus a distinct low-energy or static pressure region may exist around the passage vortex center.

The multiple tip vortices shown in Fig. 7, based on visualizations and measurements, is a first observation of this phenomenon in cascade. Even though the accuracy of the measured data in the extreme suction side corner, Fig. 13, may be affected

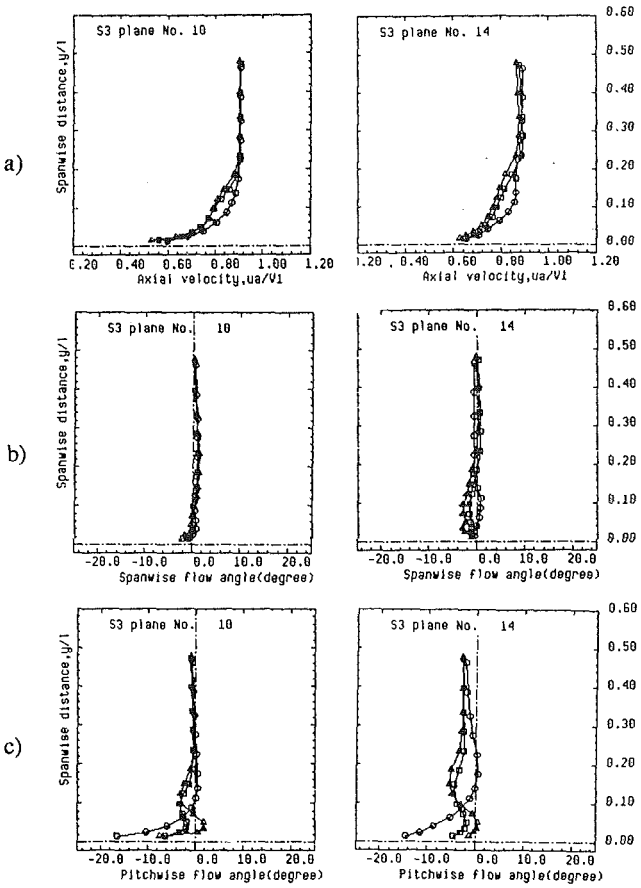

Fig. 17 Pitchwise mass-averaged profile of (*a*) axial velocities, and (*b*) pitchwise and (*c*) spanwise flow angles on S_3 planes No. 10 (88 percent *c*) and No. 14 (112.5 percent *c*); circle, $\tau/c = 0.0$; square, $\tau/c = 0.01$; triangle, $\tau/c = 0.02$

by the solid walls, the authors believe that the multiple vortex structure shown in Fig. 7 is possible and correct at least qualitatively. It is noted that Sjolander and Amrud (1987) also mentioned multiple tip vortices in a turbine cascade study. But their "first vortex," corresponding to the secondary vortex in the present paper, has the same sense as the tip leakage vortex, which was deduced only based on their suction surface static pressure contours.

Pitchwise-Averaged Parameters

The data for each traverse plane were averaged across the pitch, taking the definitions given by Kang (1990). Figure 17 shows a selection of the axial velocities, and pitchwise and spanwise flow angles in traverse planes No. 10 and 14. With the present test conditions, moderate turning angle and low flow speed, the averaged axial velocity profiles on each traverse plane in the front half-chord are similar to each other for all three cases, except for a small difference in magnitude. But the averaged pitchwise flow angles show significantly less overturning near the endwall for the cases with tip clearance, starting from the S_3 plane No. 3 (11 percent chord). The lower overturning is attributed to the opposite actions of the tip leakage vortex and the passage vortex.

From midchord to downstream, the pitchwise mass-averaged axial flow velocity profiles for 1.0 and 2.0 percent tip gaps (Fig. 17*a*) are not still parabolalike but have two turning points along the profiles, which is related to the influence of the wakelike profile (see Part II of this paper: Kang and Hirsch, 1993) in the tip vortex core and the wake flow. With the development of the tip leakage vortex, the averaged flow angle profile (Fig. 17*c*) shows overturning, underturning, and overturning from midspan to the wall. The overturned region farthest away from the wall is most probably associated with the passage secondary flow, i.e., the rotation of the passage vortex. But the under- and overturning regions near the wall are related to the opposite rotation of the tip leakage vortex and the passage vortex. The underturning increases and the overturning decreases with increasing tip gap, which is consistent with the increase of the circulation of the tip vortex (see Part II of this paper). Although there are significant spanwise flows in the suction side corner and inside the wake, the pitchwise mass-averaged spanwise flow angles (Fig. 17*b*) are quite small, especially inside the passage. It is found that behind the cascade, the averaged spanwise flow angle profile is bent and has its extreme value near the endwall. The extreme value is positive for the zero tip clearance but negative for the both tip clearances. The negative value increases with increasing tip gap.

Conclusions

The three-dimensional flow in a linear compressor cascade with 1.0, 2.0, and 3.3 percent clearances has been discussed in this paper, and the following conclusions are drawn:

A weak horseshoe vortex is formed from the blade leading edge at small clearance. In addition to the normally known tip leakage vortex, two other small vortices were observed in the tip region; one of them was rolled up by the flow separated from the pressure side edge; the other was from the suction side edge. Hence the flow inside the gap is fully three dimensional almost over the whole chord.

The tip leakage vortex had a quasi-circular core with high total pressure loss and low static pressure value. The core of the passage vortex, however, was not accompanied by the occurrence of high loss and low static pressure.

Generation of the tip leakage vortex resulted in the passage vortex moving close to the endwall and to the suction side of the passage.

Even in the linear cascade, the two-dimensional blade surface pressure is not the simple driving force of the leakage flow. The motion of the tip vortex arouses a strong reloading by which the leakage flow is reinforced.

The pitchwise mass-averaged profiles, with and without tip clearance, were basically the same upstream of midchord for all the parameters, but were significantly different downstream of midchord.

References

Bindon, J. P., 1986a, "Visualisation of Axial Turbine Tip Clearance Flow Using a Linear Cascade," CUED/A-Turbo/TR 122.

Bindon, J. P., 1986b, "Pressure and Flow Field Measurements of Axial Turbine Tip Clearance Flow in a Linear Cascade," CUED/A-Turbo/TR 123.

Chen, T. G., Greitzer, M. E., Tan, C. S., and Marble, F. E., 1991, "Similarity Analysis of Compressor Tip Clearance Flow Structure," ASME JOURNAL OF TURBOMACHINERY, Vol. 113, pp. 260–271.

Davino, R., and Lakshminarayana, B., 1982, "Turbulence Characteristics in the Annulus-Wall Boundary Layer and Wake Mixing Region of a Compressor Rotor Exit," ASME *Journal of Engineering for Power*, Vol. 104, pp. 561–570.

Dring, R. P., Joslyn, H. D., and Hardin, L. W., 1982, "An Investigation of Axial Compressor Rotor Aerodynamics," ASME *Journal of Engineering for Power*, Vol. 104, pp. 84–96.

Graham, J. A. H., 1986, "Investigation of a Tip Clearance Cascade in a Water Analogy Rig," ASME *Journal of Engineering for Gas Turbines and Power*, Vol. 108, pp. 38–46.

Hah, C., 1986, "A Numerical Modeling of Endwall and Tip-Clearance Flow of an Isolated Compressor Rotor," ASME *Journal of Engineering for Gas Turbines and Power*, Vol. 108, pp. 15–21.

Hirsch, C., and Kool, P., 1977, "Measurement of the Three-Dimensional Flow Field Behind an Axial Compressor Stages," ASME *Journal of Engineering for Power*, Vol. 99, pp. 168–180.

Hunter, I. H., and Cumpsty, N. A., 1982, "Casing Wall Boundary Layer Development Through an Isolated Compressor Rotor," ASME Paper No. 82-GT-18.

Inoue, M., and Kuroumaru, M., 1984, "Three-Dimensional Structure and Decay of Vortices Behind an Axial Flow Rotation Blade Row," ASME *Journal of Engineering for Gas Turbines and Power*, Vol. 106, pp. 561–569.

Inoue, M., and Kuroumaru, M., 1989, "Structure of Tip Clearance Flow in an Isolated Axial Compressor Rotor," ASME JOURNAL OF TURBOMACHINERY, Vol. 111, pp. 250–256.

Inoue, M., and Kuroumaru, M., Iwamoto, T., and Ando, Y., 1991, "Detection of a Rotating Stall Precursor in Isolated Axial Flow Compressor Rotors," ASME JOURNAL OF TURBOMACHINERY, Vol. 113, pp. 281–289.

Joslyn, H. D., and Dring, R. P., 1985, "Axial Compressor Stator Aerodynamics," ASME *Journal of Engineering for Gas Turbines and Power*, Vol. 107, pp. 485–493.

Kang, S., 1989, "Five-Hole Probe Calibration," Vrije Universiteit Brussel, Dept. of Fluid Mechanics, Report No. VUB-TN-43.

Kang, S., 1990, "3-D Flows in a Linear Compressor Cascade at Design Conditions," Vrije Universiteit Brussel, Dept. of Fluid Mechanics, Report No. VUB-TN-44.

Kang, S., 1991a, "Experimental Study on the Three Dimensional Flow Within Compressor Cascade With Tip Clearances," Vrije Universiteit Brussel, Dept. of Fluid Mechanics, Report No. VUB-TN-45.

Kang, S., 1991b, "Topological Analysis on the Three Dimensional Flow in a Linear Compressor Cascade With Tip Clearance," Vrije Universiteit Brussel, Dept. of Fluid Mechanics, Report No. VUB-TN-46.

Kang, S., and Hirsch, Ch., 1991, "Three Dimensional Flows in a Linear Compressor Cascade at Design Conditions," ASME paper No. 91-GT-114.

Kang, S., and Hirsch, Ch., 1993, "Experimental Study on the Three-Dimensional Flow Within a Compressor Cascade With Tip Clearance: Part II—The Tip Leakage Vortex," ASME JOURNAL OF TURBOMACHINERY, Vol. 115, this issue, pp. 444–452.

Kool, P., DeRuyck, J., and Hirsch, C., 1978, "The Three-Dimensional Flow and Blade Wake in an Axial Plane Downstream of an Axial Compressor Rotor," ASME Paper No. 78-GT-66.

Lakshminarayana, B., 1970, "Method of Predicting the Tip Clearance Effects in Axial Flow Turbomachinery," ASME *Journal of Basic Engineering*, Vol. 92, pp. 467–480.

Lakshminarayana, B., and Poncet, A., 1974, "A Method of Measuring Three-Dimensional Wakes in Turbomachinery," ASME *Journal of Fluids Engineering*, Vol. 96, pp. 87–91.

Lakshminarayana, B., Pouagare, M., and Davino, R., 1982, "Three-Dimensional Flow Field in the Tip Region of a Compressor Rotor Passage, Part I: Mean Velocity Profiles and Annulus Wall Boundary Layer," ASME *Journal of Engineering for Power*, Vol. 104, pp. 760–771.

Lakshminarayana, B., Zhang, J., and Muthy, K. N. S., 1987, "An Experimental Study on the Effects of Tip Clearance on Flow Field and Losses in Axial Flow Compressor Rotor," ISABE 87-7045, pp. 273–290.

Langston, L. S., Nice, M. L., and Hooper, R. M., 1977, "Three-Dimensional Flow Within a Turbine Blade Passage," ASME *Journal of Engineering for Power*, Vol. 99, pp. 21–28.

Marchal, P., and Sieverding, C. H., 1977, "Secondary Flow Within Turbomachinery Bladings," *Secondary Flows in Turbomachines*, AGARD CP-214.

Moore, J., and Tilton, J. S., 1988, "Tip Leakage Flow in a Linear Turbine Cascade," ASME JOURNAL OF TURBOMACHINERY, Vol. 110, pp. 18–26.

Prasad, C. R. K., 1977, "Tip Clearance Effect in Axial Flow Turbomachines," Indian Institute of Science, Report No. ME-TURBO-1-77.

Rains, D. A., 1954, "Tip Clearance Flow in Axial Compressors and Pumps," California Institute of Technology, Mech. Eng. Laboratory, Report 5.

Sjolander, S. A., and Amrud, K. K., 1987, "Effects of Tip Clearance on Blade Loading in a Planar Cascade of Turbine Blades," ASME JOURNAL OF TURBOMACHINERY, Vol. 109, pp. 237–245.

Storer, J. A., and Cumpsty, N. A., 1991, "Tip Leakage Flow in Axial Compressors," ASME JOURNAL OF TURBOMACHINERY, Vol. 113, pp. 252–259.

Vucinic, D., Pottiez, M., Sotiaux, V., and Hirsch, Ch., 1991, "CFView, An Advanced Interactive Visualization System Based on Object-Oriented Approach," AIAA-92-0072.

Experimental Study on the Three-Dimensional Flow Within a Compressor Cascade With Tip Clearance: Part II—The Tip Leakage Vortex

S. Kang[1]

C. Hirsch
Professor.
Mem. ASME

Vrije Universiteit Brussel,
Department of Fluid Mechanics,
1050 Brussel, Belgium

An analysis of the experimental data of a linear compressor cascade with tip clearance is presented with special attention to the development of the tip leakage vortex. A method for determining the tip vortex core size, center position, and vorticity or circulation from the measured data is proposed, based on the assumption of a circular tip vortex core. It is observed that the axial velocity profile passing through the tip vortex center is wakelike. The vorticity of the tip vortex increases rapidly near the leading edge and reaches its highest values at a short distance downstream, from which it gradually decreases. In the whole evolution, its size is growing and its center is moving away from both the suction surface and the endwall, approximately in a linear way.

Introduction

The study of the tip leakage vortex through the vorticity field has received an increasing interest in the published literature. Lakshminarayana and Horlock (1962) analyzed the vorticity of the tip leakage vortex for an isolated compressor blade by employing a vortex meter. Determination of vorticity directly from the measured velocity field was done recently by Inoue and Kuroumarou (1984) on the flow field behind an axial compressor rotor, and Gregory-Smith et al. (1988) in an axial turbine cascade. Measurements of the circulation in the tip leakage vortex were performed by Inoue et al. (1986) for a compressor rotor and Yaras and Sjolander (1990) for a planar turbine cascade. Their data showed the behavior of the tip vortex downstream of the cascade exit. Obviously, it is necessary to investigate the tip vortex behavior in its whole evolving history.

The influence of the tip gap on the blade loading and on the behavior of the whole secondary flow field has been examined in the companion part of this paper (Kang and Hirsch, 1993). A multiple tip vortex structure has been deduced, based on the flow visualizations and traverse measurements, as shown in Fig. 1. The vortex structure consists of three discrete vortices, i.e., tip separation vortex, secondary vortex, and tip leakage vortex. This part will present further discussions on the experiment data of the linear compressor cascade with tip clearance, but with special attention to the development of the tip leakage vortex, such as the evolution of its size, center position, and vorticity or circulation.

Velocity Profiles

The velocity profiles near the tip leakage vortex axis are examined first. The vortex axis is defined here as the line passing through the vortex center and is mainly along the chordwise direction.

Figure 2 shows the spanwise distribution of the axial and pitchwise velocities and the pitchwise distribution of the spanwise velocity, as an example, for 2.0 percent tip clearance at different axial position. It is found that the axial velocity (Fig. 2*a*) in all the corresponding traversed planes shows a wakelike shape around the tip vortex center. Escudier et al. (1980) reported, according to their study on the classification of confined vortex flow regimes, that at sufficiently high Reynolds number the vortex core is turbulent and its profile is wakelike. In the present case, at a Reynolds number of 2.9×10^5, the inlet boundary layer flow is turbulent. Hence the core of the tip vortex, formed from the leakage flow mostly coming from the endwall and blade surface boundary layers (see Part I), should be turbulent. The growth of the depression part of the axial velocity profiles with axial distance shows the growth of the tip vortex core. It is observed that inside the passage the wakelike profile is sharp but diffuses rapidly behind the cascade. Comparing the profiles for two tip clearances, it is found that at 1.0 percent clearance the diffusion is stronger than at

[1]Permanent address: Power Engineering Dept., Harbin Institute of Technology, Harbin 150006, People's Republic of China.

Contributed by the International Gas Turbine Institute and presented at the 37th International Gas Turbine and Aeroengine Congress and Exposition, Cologne, Germany, June 1-4, 1992. Manuscript received by the International Gas Turbine Institute February 27, 1992. Paper No. 92-GT-432. Associate Technical Editor: L. S. Langston.

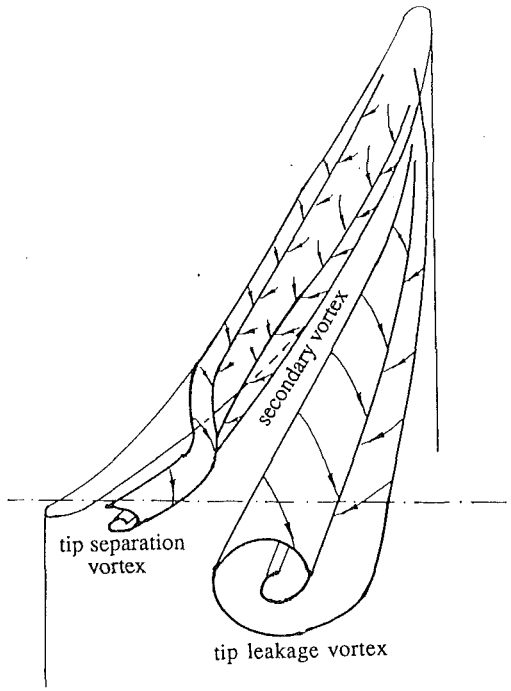

Fig. 1 Schematic of the vortex structure around the tip, from Part I of this paper (Kang and Hirsch, 1993)

2.0 percent. The reason may be that the vortex core at 1.0 percent clearance is much closer to the wall (see later discussions on the vortex center location) and is more affected by the wall boundary layer.

The spanwise and pitchwise velocities in Figs. 2(*b*) and 2(*c*) around the tip vortex center show **Z**-shaped profiles, which indicate the rotation of the tip vortex. The nonzero value of spanwise velocity far away from the tip vortex center is obviously associated with the evolution of the passage vortex.

Vorticity in the Whole Field

The vorticity in the measured field is calculated from the following formula, based on the definition of vorticity vector with the incompressible and inviscid assumptions, see Appendix Eq. (A4),

$$\Omega_x = \left(\frac{\partial v}{\partial z} - \frac{s}{1}\frac{\partial w}{\partial y}\right)$$

$$\Omega_y = \frac{v}{u}\Omega_x + \frac{1}{2}\frac{1}{u}\frac{\partial C_{pt}}{\partial z}$$

$$\Omega_z = \frac{w}{u}\Omega_x - \frac{1}{2}\frac{1}{u}\frac{s}{1}\frac{\partial C_{pt}}{\partial y} \qquad (1)$$

where the velocities are normalized with the inlet velocity, y

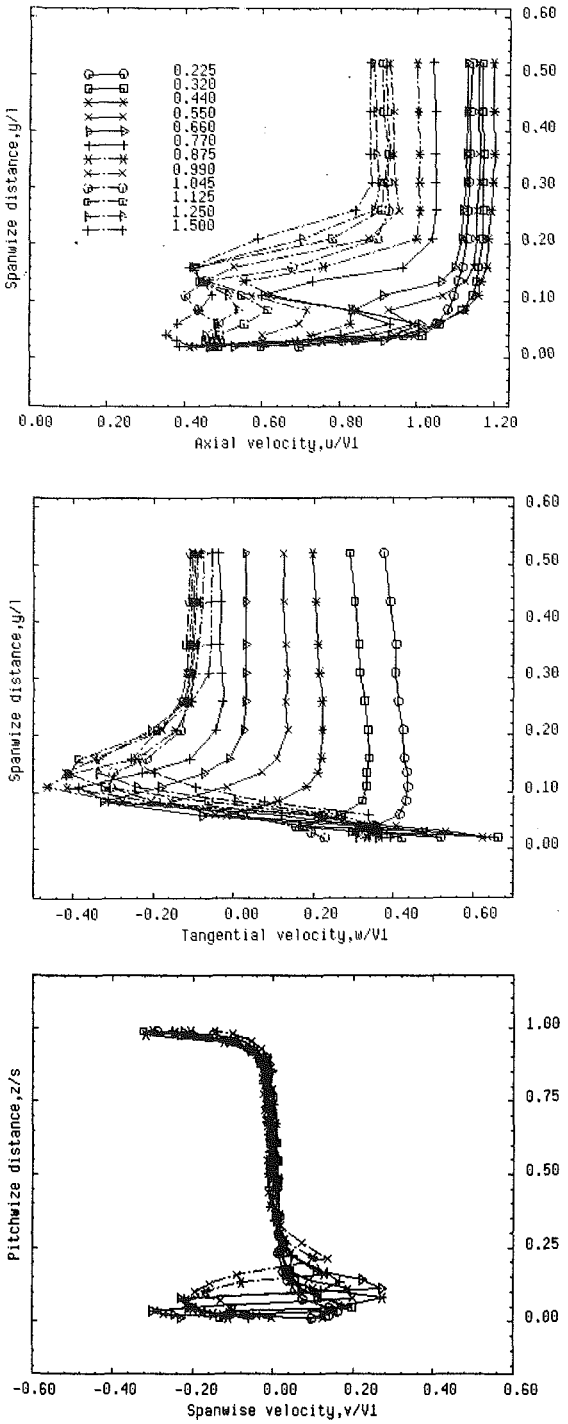

Fig. 2 Profiles passing through tip vortex center with different *x/c* at $\tau/c = 0.02$, (*a*) and (*b*) spanwise profiles of *u* and *w*, (*c*) pitchwise profiles of *v*

Nomenclature

c = blade chord
C_p = static pressure coefficient
C_{pt} = total pressure coefficient
l = blade span
L_y = coordinate of tip vortex center from low wall
L_z = coordinate of tip vortex center from suction side
LE = leading edge
PS = pressure side
p_t = total pressure
R = vortex core radius
s = pitch
SS = suction side
TE = trailing edge
u, v, w = axial, spanwise and pitchwise velocities
u_t = blade speed
V_1 = inlet resultant velocity
V_u = circumferential velocity of a vortex
x, y, z = axial, spanwise, and pitchwise distances
β_1, β_2 = inlet and outlet flow angles
β_m = average flow angle, midspan flow angle
Γ = circulation
ρ = density
τ = tip clearance
ω = angular velocity
$\Omega_x, \Omega_y, \Omega_z, \Omega_s$ = axial, spanwise, pitchwise, and streamwise vorticities

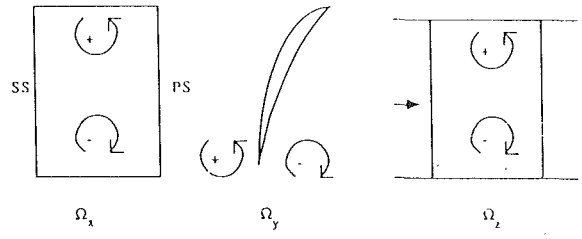

Fig. 3 Illustration of vorticity signs

with span l, z with pitch s. A similar method was used by Gregory-Smith et al. (1988) and Yaras and Sjolander (1990).

The illustration of vorticity signs is given in Fig. 3. The isolines of the three vorticity components on the S_3 (traverse) planes are shown in Fig. 4, the coordinates of the traverse planes being given in Fig. 1 of Part I. Figure 5 shows the vorticity vectors on the S_3 plane No. 15 at the clearance of 0.0, 1.0, and 2.0 percent. These plots are directly drawn from the data calculated by using Eq. (1) without any smoothing. Hence the unrealistic values in some points may be due to the differentiation of the scattered experimental data.

It is seen from Fig. 4(*b*) that the pitchwise vorticity across the pitch is uniform near the endwall in the S_3 plane No. 1, 7.5 percent chord upstream of the leading edge. This shows the uniform shear flow of the inlet boundary layer. But the minus value (see Fig. 3 for sign definition) of the axial vorticity (Fig. 4*a*) near the endwall in the plane is partly due to the turning of the inlet vorticity filament, and indicates the early stage of the passage vortex. Starting from S_3 plane No. 3 (11 percent chord) the axial vorticity shows remarkably high values in the suction side corner. The quasi-circular isovorticity lines with positive values in the corner refer to the tip vortex core, according to the sign definition given in Fig. 3, and the negative values over a large range of the passage represent the passage vortex. It is observed by using the CFView visualization program that, due to the interaction of the tip leakage vortex with the passage vortex, a relatively small region with higher negative value is formed above the tip vortex after S_3 plane No. 5 (32 percent chord). It can be deduced that there might be a three-dimensional surface with zero vorticity, surrounding the tip vortex.

Behind the cascade exit, for example on S_3 plane No. 16 in Fig. 4(*a*), the flat elliptic loops with their long axes along the spanwise direction are referred to the trailing vortex sheet. Because of the two-dimensional geometry, comparatively little vorticity is shed in the wake and the wake is not quite clear on the streamwise vorticity plots. But from the contours of spanwise vorticity (Fig. 4*c*), the wake can be easily identified from the straight isolines perpendicular to the endwall near midspan. Also from the vector plots in Fig. 5, it is seen that the spanwise vorticity in the two sides of the wake has opposite directions, directed toward the endwall in the pressure side or toward the midspan in the suction side.

As expected, the contours of spanwise (Fig. 4*b*) and pitchwise vorticities (Fig. 4*c*) show two loops, with opposite sign values, in the two sides of the tip vortex center, due to the depression of the velocity profiles in Fig. 2. Because of the influence of the endwall and blade suction surface boundary layers on the tip vortex motion, the two loops are not exactly symmetric. Even so, it still can be suggested with fair confidence, based on the closed circular isolines of the total and static pressure coefficients (see Fig. 9 in Part I) and the axial vorticities (Fig. 4*a*) around the tip vortex center, that after the tip vortex is rolled up, (*i*) its core is circular; and (*ii*) the variation of the vorticity inside its core is linear and axially symmetric. This feature of axial symmetry was also reported by Yaras and Sjolander (1990) from their downstream measurements on a turbine blade cascade.

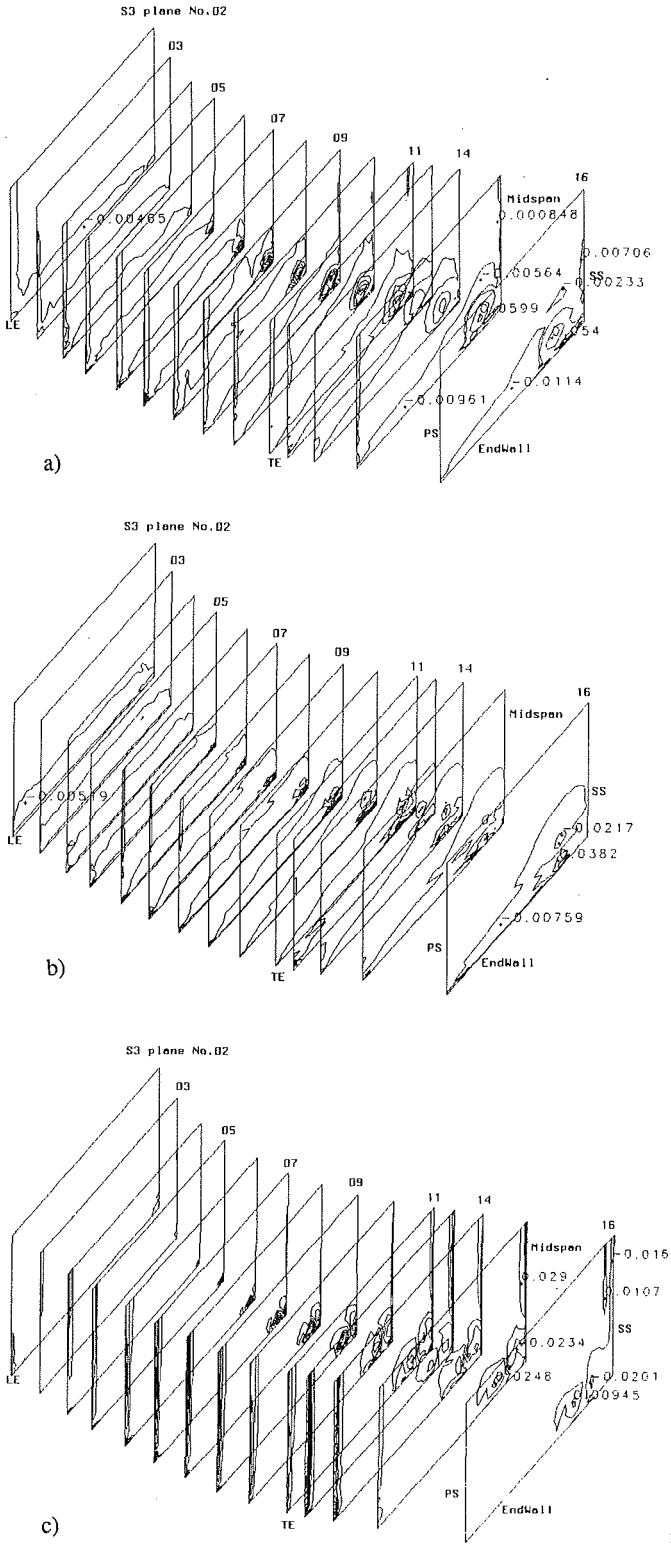

Fig. 4 Contours of vorticities at $\tau/c = 0.02$, (*a*) axial vorticity, (*b*) pitchwise vorticity, (*c*) spanwise vorticity

In addition, the rolling-up process of the leakage vortex can be clearly observed from the vorticity vector plots in the traverse planes, for example in S_3 plane No. 15 for 1.0 and 2.0 percents clearances in Fig. 5. As a comparison, Fig. 5 also shows the vorticity vector plots in the same plane at zero tip clearance, from which the skewed wake due to the interaction of the passage secondary flow, the concentrated shed vortex

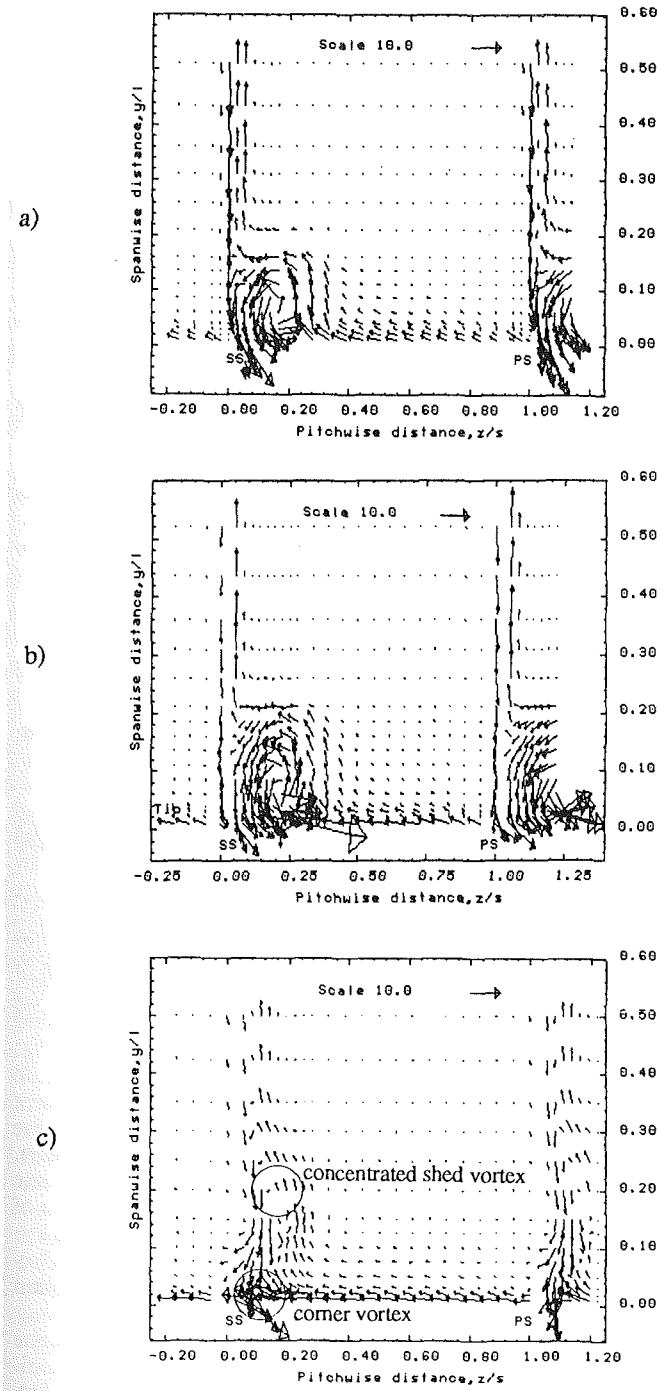

Fig. 5 Vector plots of vorticity on S_3 plane No. 15 for (*a*) $\tau/c = 0.01$, (*b*) $\tau/c = 0.02$, and (*c*) $\tau/c = 0.0$

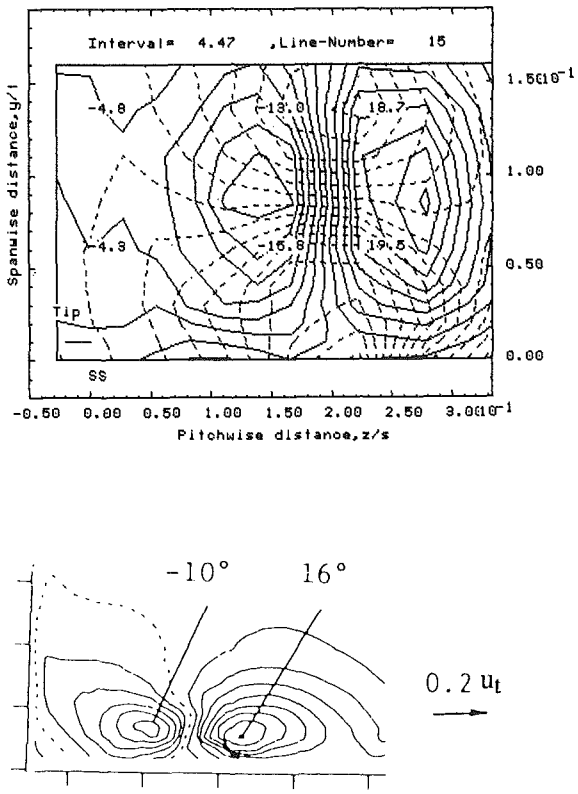

Fig. 6 Isolines of flow angles: (*a*) measured spanwise (solid lines) and pitchwise (dashed lines) flow angles in S_3 plane No. 15 at $\tau/c = 0.01$, in which the numbers are the values of spanwise flow angle, and (*b*) after *Inoue et al. (1989)*

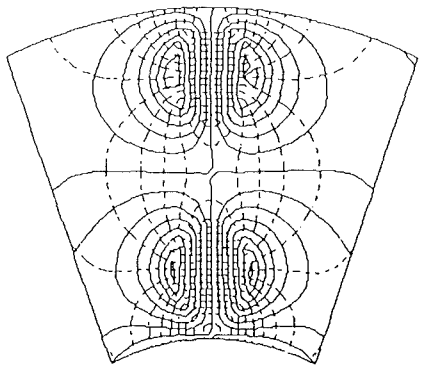

Fig. 7 Isolines of spanwise (solid lines) and pitchwise (dashed lines) flow angles within an annular cascade with a pair of imaginary vortices with a circular core

defined in the previous paper (Kang and Hirsch, 1991), and the corner vortex close to the wall can be identified.

Vorticity of the Tip Vortex Core

To explore the features of the tip vortex, based on the experimental data, an approximate method based on the supposition that the vortex has a circular core and its vorticities are all concentrated inside the core, is developed. The tip vortex is considered as a Rankine vortex and rotates as a solid body with constant angular velocity $\omega/2$. The size and center location of the tip leakage vortex in each of the transverse planes can be determined from the isoline plots of the measured spanwise and pitchwise flow angles. As an example, Fig. 6(*a*) shows the isolines of the measured flow angles in S_3 plane No. 15 (25 percent chord behind the cascade) for 1.0 percent clearance. As a comparison, Fig. 7 shows the isolines of the flow angles induced by a pair of vortices, imagined in a passage of an annular cascade, with circular solid body cores. Two conclusions can be drawn from these two plots: (*i*) The vortex center is located at the cross point of the isolines of the two flow angles with zero value; (*ii*) the diameter of the vortex core is approximately equal to the length of the straight portion, passing through the vortex center, along either of the flow angle contours.

With these two conclusions, the geometry of the tip leakage vortex, characterized by L_y, L_z and core radius R defined in Fig. 8, can be determined from the experimental data. Consequently, its vorticity and circulation can be calculated in the following approximate way. Since the circumferential velocity V_u induced by a vortex with circular solid core takes its largest

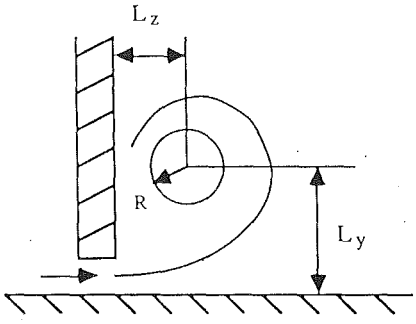

Fig. 8 Definition of tip vortex geometry

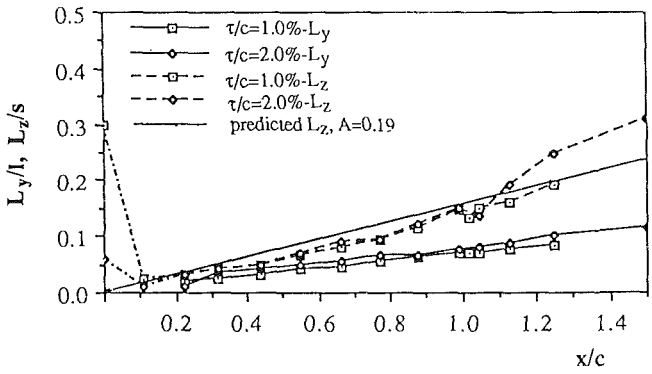

Fig. 9 Evolution of tip vortex core location in the mainstream direction, compared to the predications by Chen et al. (1991). The dot-dashed lines correspond to the positions of maximum streamwise vorticity.

values along the edge of the solid core, it can be approximately read from the experimental data of spanwise velocity component v in the point where $y=L_y$, $z=L_z+R$. If the spanwise velocity at this point is not the largest, then the largest in the small region around it is taken as V_u. Thus the vorticity and circulation, normalized by V_1/s and $V_1 s$ respectively, can be calculated from following formula:

$$\omega = 2\,\frac{V_u/V_1}{R/s} \quad \text{and} \quad \Gamma = \pi\omega\,\frac{R^2}{s^2} \tag{2}$$

Geometry of the Vortex Core. Figure 9 shows the measured positions, L_y and L_z, of the tip vortex core center and Fig. 10 shows its core radius R for two values of tip clearance. The zero point of L_z within the passage is in the suction side, as shown in Fig. 8; behind the exit it is on the line drawn from the blade trailing edge in the direction of the designed outflow angle. The values of L_z at $x/c=0.0$ and 0.11 in dot-and-dash lines correspond to the positions where the streamwise vorticities at the same axial coordinate take the largest value. In Part I, it is shown that a horseshoe vortex is formed in front of the blade leading edge, at the measured clearance cases, and its suction side leg is merged together with the rolling-up leakage flow some distance downstream. Hence, the value at $x/c=0.0$ is most probably the center of the suction side leg of the horseshoe vortex. It is seen that the horseshoe vortex, acted on by the traverse pressure gradient, is quickly moved toward the suction side, from $L_z/s=0.3$ at $x/c=0.0$ to 0.025 at $x/c=0.11$ for 1.0 percent tip clearance as an example, and the suction side leg of the horseshoe vortex is closer to suction side at larger clearance. It is observed from Figs. 9 and 10 that as the tip vortex stretches downstream, the center of the tip vortex is gradually moving far away from both of the solid walls, characterized with the growth of L_y and L_z, with its core radius R growing. The growth of L_y and L_z almost obeys a linear relation with the axial distance. With increasing clearance, the spanwise coordinate of the vortex center is increased, but the pitchwise coordinate inside the passage changes less.

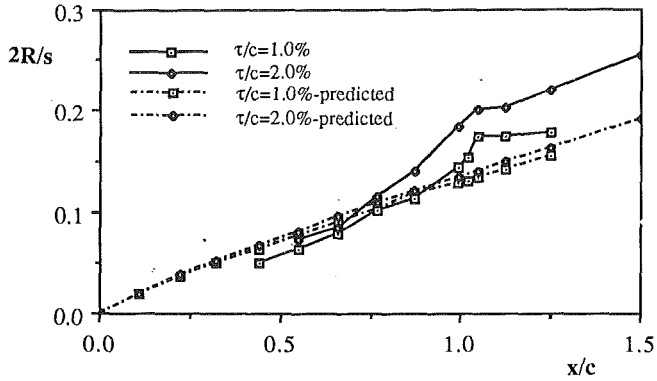

Fig. 10 Evolution of the core radius in the main stream direction, with predictions following Lakshminarayana (1970)

Chen et al. (1991) proposed a formula to predict the pitchwise position of the tip vortex center inside the compressor passage, based on similarity analysis, as

$$\frac{L_z/s}{x/c} = A\left(\sqrt{\frac{c(\tan\beta_1-\tan\beta_2)}{s\cos\beta_m}}\right)_{\text{midspan}} \tag{3}$$

They suggested the constant $A=0.46$. But it is seen from Fig. 9 that for the present linear cascade with stationary endwall, the data are rather close to $A=0.19$.

Yanagida (1989) and Inoue and Kuroumaru (1989) measured the tip vortex trajectories from the coordinates of the low total or static pressures on the endwall. These data were used by Chen et al. (1991) to set up their model. The large difference between the model and the present data in the line slope, i.e., the constant A, may be partly related to the different way of determining the center location, and partly to the influence of the relative motion between the blade tip and the endwall. The action of the relative motion tends to drag the tip vortex toward the pressure side in compressor cascades. It is seen from Fig. 6 that the isolines of the pitchwise flow angle inside the tip vortex core are perpendicular to the endwall for the present stationary cascade (Fig. 6*a*) but seriously inclined against the wall for the case (Fig. 6*b*) of Inoue and Kuroumaru (1989). These inclined isolines will doubtlessly affect the local static and total pressure distribution on the wall. Therefore, both of the methods for determining tip vortex trajectory from the low static and/or total pressure positions on the wall are not accurate, especially when the influences of the relative motion and other kinds of secondary flows are strong.

The core radius R presented in Fig. 10 is the averaged value of those measured respectively in spanwise and pitchwise directions from the isoline plots of the flow angles (Fig. 6*a*). Because of the constraint of the present facility, the scales of the tip leakage vortex close to the leading edge plane cannot be determined from the plots of flow angles. It is seen that downstream of the exit, the core radius varies in the axial direction with nearly a linear relation. The different behavior of the core radius inside and outside of the passage may be related to the different behavior of the vortex in the two regions. Inside the passage, except for viscous diffusion, the rolling up of the vorticity near the tip dominates its behavior. But downstream it mainly decays with distance due to fluid viscosity. The rapid increment of the radius immediately downstream of the exit may be due to the sudden release of the blade boundary.

Based on inviscid flow and constant blade loading along the chord, Rains (1954) set up a theory to predict the tip vortex radius, which has been used by Lakshminarayana (1970) in his theoretical model. Comparing the values predicted with the

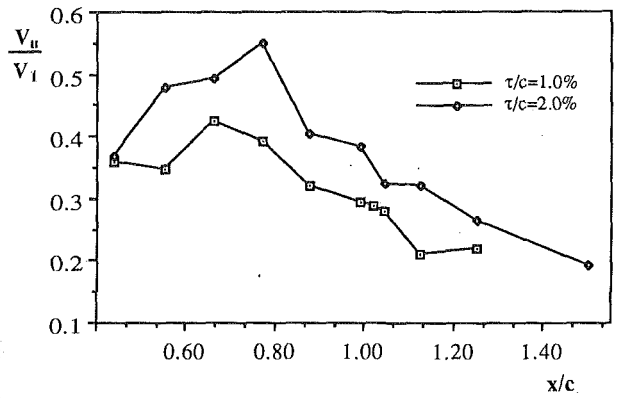

Fig. 11 Evolution of the circumferential velocity at the tip vortex edge

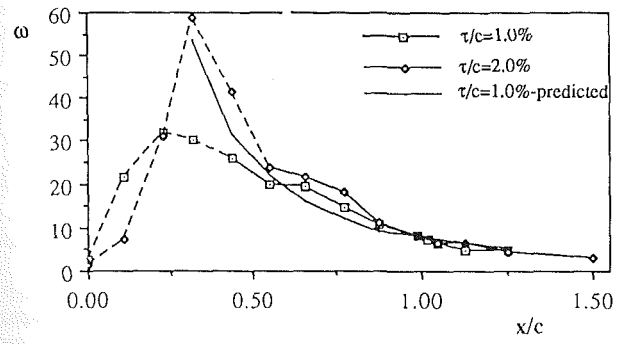

Fig. 12 Evolution of the vorticities of the tip vortex core, with the predicted values following Lakshminarayana (1970)

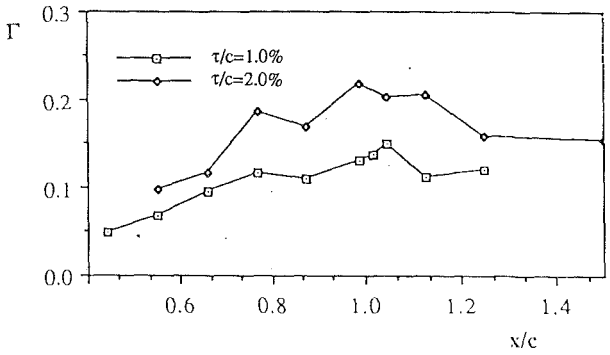

Fig. 13 Evolution of the circulations of the tip vortex core

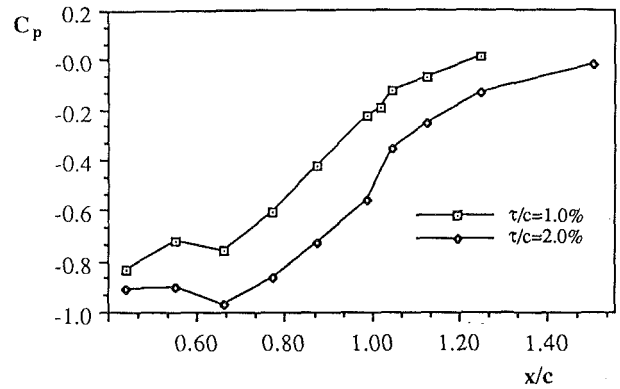

Fig. 14 Static pressure at the center of the tip vortex core

present data by using Rains' method, it is noted in Fig. 10 that caution should be taken when using it in the rear portions and downstream of the passage. In addition, the experimental data show a stronger dependence upon the clearance level than the predictions.

Vorticity and Circulation of the Vortex Core. The circumferential velocities obtained in the vortex core edge on each of the transverse planes are shown in Fig. 11 for the two clearances. With the known values V_u, the vorticities (or angular velocities) and circulations can be calculated from Eq. (2) as shown in Figs. 12 and 13. Due to the measurement difficulty, the information on the vorticity of the tip vortex close to the leading edge is missing. The curve drawn near the leading edge ($x/c<0.44$) with a dashed line in Fig. 12 is the largest streamwise vorticity, calculated with Eq. (A5), in the suction side corner. This portion of the curves refers to the suction side leg of the horseshoe vortex and the early stage of the tip leakage vortex. From Fig. 12, more conclusions can be drawn on the features of the tip vortex: In the leading edge plane a weak horseshoe vortex is formed with relatively less vorticity, then the vorticity is increased rapidly with the leakage flow and the size of the tip vortex core is small. It achieves its largest value at a point after a short distance downstream. Even though the subsequent leakage flow still tends to increase the vorticity, the vorticity decay and streamwise adverse pressure gradient are also increased. Also the growth of the core radius reduces the vorticity, averaged over the core cross area.

Figure 12 also shows predictions according to Lakshminarayana (1970). Since the predicted vorticity is less dependent on the tip space, except near the leading edge, only the predictions on the 1.0 percent clearance case are presented in Fig. 12. It is seen that the predictions show a good correlation with the experimental data in the rear part of the passage and downstream.

With the vorticity of the tip vortex monotonously decreasing in the rear part of the passage, the corresponding circulation shown in Fig. 13, however, increases with a peak near the trailing edge. The growth of the circulation indicates the increment of the total vorticity of the tip vortex minus decay and diffusion in chordwise direction. Downstream of the exit, the circulation of the tip vortex goes down rapidly and then tends to remain constant far downstream. The large values immediately downstream of the exit may be related to the action of the blade wake. Because the rotation sense of the tip vortex is the same as that of the trailing edge vortex, some of the vorticities of the trailing vortex sheet, close to the tip vortex, are merged into the tip vortex as seen from the vector plot of Fig. 5. Further downstream, its circulation is quickly decreased. It is seen that with increasing tip clearance the circulation increases.

Static Pressure at the Vortex Center. Figure 14 shows the static pressure coefficients at the tip vortex center. Normally, the static pressure is the lowest in the region within the vortex core. It is seen that the static pressure at the vortex center is basically increasing with distance for the two tip clearances, but is decreasing with tip clearance.

Conclusions

Detailed examination and discussion on the tip vortex formed in the linear compressor cascade at design conditions have been presented, from which the following conclusions are drawn:

The axial velocity profile passing through the tip vortex center shows a wakelike shape, which is diffusing while moving downstream. The diffusion rate is affected by the wall boundary layer, especially when the vortex center is closer to the wall at smaller clearance.

A new method for determining the tip vortex trajectory, core radius, and vorticity from the transverse measured data is proposed, based on the supposition that the core is circular. It is shown that the method has an acceptable accuracy.

It is found that the vorticity of the tip vortex increases rapidly near the leading edge and reaches it highest values at a short distance downstream of the leading edge, from which it gradually decreases toward the exit. With increasing clearance, the vortex circulation increases. The vorticity can be well predicted by the theory of Lakshminarayana (1970), except near the leading edge.

During the tip vortex evolution, its center is moving away from both the blade suction surface and the endwall, approximately in a linear relation with distance. But it is observed that the slope of the linear relation for the pitchwise position of the tip vortex center is very different from that predicted by Chen et al. (1991).

References

Chen, T. G., Greitzer, M. E., Tan, C. S., and Marble, F. E., 1991, "Similarity Analysis of Compressor Tip Clearance Flow Structure," ASME JOURNAL OF TURBOMACHINERY, Vol. 113, pp. 260–271.

Escudier, M. P., Bornstein, J., Zehnder, J., and Maxworthy, T., 1980, "The Classification of Confined Vortex Flow Regimes," *Vortex Flows*, ASME, pp. 15–24.

Gregory-Smith, D. G., Graves, C. P., and Walsh, J. A., 1988, "Growth of Secondary Losses and Vorticity in an Axial Turbine Cascade," ASME JOURNAL OF TURBOMACHINERY, Vol. 110, pp. 1–8.

Inoue, M., and Kuroumaru, M., 1984, "Three-Dimensional Structure and Decay of Vortices Behind an Axial Flow Rotation Blade Row," ASME *Journal of Engineering for Gas Turbines and Power*, Vol. 106, pp. 561–569.

Inoue, M., Kuroumaru, M., and Fukuhara, M., 1986, "Behavior of Tip Leakage Flow Behind an Axial Compressor Rotor," ASME *Journal of Engineering for Gas Turbines and Power*, Vol. 108, pp. 7–14.

Inoue, M., and Kuroumaru, M., 1989, "Structure of Tip Clearance Flow in an Isolated Axial Compressor Rotor," ASME JOURNAL OF TURBOMACHINERY, Vol. 111, pp. 250–256.

Kang, S., and Hirsch, Ch., 1991, "Three-Dimensional Flows in a Linear Compressor Cascade at Design Conditions," ASME Paper No. 91-GT-114.

Kang, S., and Hirsch, Ch., 1993, "Experimental Study on the Three-Dimensional Flow Within a Compressor Cascade With Tip Clearance: Part I—Velocity and Pressure Fields," ASME JOURNAL OF TURBOMACHINERY, Vol. 115, this issue, pp. 435–443.

Lakshminarayana, B., 1970, "Method of Predicting the Tip Clearance Effects in Axial Flow Turbomachinery," ASME *Journal of Basic Engineering*, Vol. 92, pp. 467–480.

Lakshminarayana, B., and Horlock, J. H., 1962, "Tip-Clearance Flow and Losses for an Isolated Compressor Blade," ARC R&M 3316.

Rains, D. A., 1954, "Tip Clearance Flow in Axial Compressors and Pumps," California Institute of Technology, Mech. Eng. Laboratory, Report 5.

Sjolander, S. A., and Amrud, K. K., 1987, "Effects of Tip Clearance on Blade Loading in a Planar Cascade of Turbine Blades," ASME JOURNAL OF TURBOMACHINERY, Vol. 109, pp. 237–245.

Storer, J. A., and Cumpsty, N. A., 1991, "Tip Leakage Flow in Axial Compressors," ASME JOURNAL OF TURBOMACHINERY, Vol. 113, pp. 252–259.

Yanagida, M., Machida, Y., and Takata, H., 1989, "A Study on the Mechanism of Stall Margin Improvement of Casing Treatment," *Trans. Japan Society Mechanical Eng.*, Vol. 55, No. 518, Series B [in Japanese].

Yaras, M., and Sjolander, S. A., 1990, "Development of the Tip-Leakage Flow Downstream of a Planar Cascade of Turbine Blades: Vorticity Field," ASME JOURNAL OF TURBOMACHINERY, Vol. 112, pp. 609–617.

APPENDIX

Calculation of Vorticity

The components of the vorticity vector are obtained in the Cartesian coordinate system, defined as x, y, and z in the axial, spanwise, and pitchwise directions:

$$\Omega_x = \frac{\partial v}{\partial z} - \frac{\partial w}{\partial y}$$

$$\Omega_y = \frac{\partial w}{\partial x} - \frac{\partial u}{\partial z}$$

$$\Omega_z = \frac{\partial u}{\partial y} - \frac{\partial v}{\partial x} \tag{A1}$$

The axial component can be determined from the measured data in a transverse plane. Making some assumptions, the spanwise and pitchwise components can also be obtained from such data. Assuming incompressible flow and neglecting viscous effects, the following equation can be used as an alternative way:

$$\mathbf{V} \times \boldsymbol{\Omega} = \frac{1}{\rho} \nabla p_t \tag{A2}$$

Taking its y and z components,

$$w\Omega_x - u\Omega_z = \frac{1}{\rho} \frac{\partial p_t}{\partial y}$$

$$u\Omega_y - v\Omega_x = \frac{1}{\rho} \frac{\partial p_t}{\partial z} \tag{A3}$$

If the vorticity components are normalized with inlet velocity V_1 and pitch s, for example, $\Omega_x s/V_1$, then the final formula is

$$\Omega_x = \left(\frac{\partial v}{\partial z} - \frac{s}{1} \frac{\partial w}{\partial y} \right)$$

$$\Omega_y = \frac{v}{u} \Omega_x + \frac{1}{2} \frac{1}{u} \frac{\partial C_{pt}}{\partial z}$$

$$\Omega_z = \frac{w}{u} \Omega_x - \frac{1}{2} \frac{1}{u} \frac{s}{1} \frac{\partial C_{pt}}{\partial y} \tag{A4}$$

where the velocities are normalized with inlet velocity V_1, y, with span l, z with pitch s.

The streamwise vorticity was taken as the component of vorticity in the main flow direction, defined as the midspan flow, rather than the component in the local flow direction. Thus the streamwise vorticity becomes

$$\Omega_s = \Omega_x \cos \beta_m + \Omega_z \sin \beta_m \tag{A5}$$

where β_m is the pitchwise flow angle at midspan but varying with pitchwise distance.

It is found that the vorticity of the tip vortex increases rapidly near the leading edge and reaches it highest values at a short distance downstream of the leading edge, from which it gradually decreases toward the exit. With increasing clearance, the vortex circulation increases. The vorticity can be well predicted by the theory of Lakshminarayana (1970), except near the leading edge.

During the tip vortex evolution, its center is moving away from both the blade suction surface and the endwall, approximately in a linear relation with distance. But it is observed that the slope of the linear relation for the pitchwise position of the tip vortex center is very different from that predicted by Chen et al. (1991).

References

Chen, T. G., Greitzer, M. E., Tan, C. S., and Marble, F. E., 1991, "Similarity Analysis of Compressor Tip Clearance Flow Structure," ASME JOURNAL OF TURBOMACHINERY, Vol. 113, pp. 260–271.

Escudier, M. P., Bornstein, J., Zehnder, J., and Maxworthy, T., 1980, "The Classification of Confined Vortex Flow Regimes," *Vortex Flows*, ASME, pp. 15–24.

Gregory-Smith, D. G., Graves, C. P., and Walsh, J. A., 1988, "Growth of Secondary Losses and Vorticity in an Axial Turbine Cascade," ASME JOURNAL OF TURBOMACHINERY, Vol. 110, pp. 1–8.

Inoue, M., and Kuroumaru, M., 1984, "Three-Dimensional Structure and Decay of Vortices Behind an Axial Flow Rotation Blade Row," ASME *Journal of Engineering for Gas Turbines and Power*, Vol. 106, pp. 561–569.

Inoue, M., Kuroumaru, M., and Fukuhara, M., 1986, "Behavior of Tip Leakage Flow Behind an Axial Compressor Rotor," ASME *Journal of Engineering for Gas Turbines and Power*, Vol. 108, pp. 7–14.

Inoue, M., and Kuroumaru, M., 1989, "Structure of Tip Clearance Flow in an Isolated Axial Compressor Rotor," ASME JOURNAL OF TURBOMACHINERY, Vol. 111, pp. 250–256.

Kang, S., and Hirsch, Ch., 1991, "Three-Dimensional Flows in a Linear Compressor Cascade at Design Conditions," ASME Paper No. 91-GT-114.

Kang, S., and Hirsch, Ch., 1993, "Experimental Study on the Three-Dimensional Flow Within a Compressor Cascade With Tip Clearance: Part I—Velocity and Pressure Fields," ASME JOURNAL OF TURBOMACHINERY, Vol. 115, this issue, pp. 435–443.

Lakshminarayana, B., 1970, "Method of Predicting the Tip Clearance Effects in Axial Flow Turbomachinery," ASME *Journal of Basic Engineering*, Vol. 92, pp. 467–480.

Lakshminarayana, B., and Horlock, J. H., 1962, "Tip-Clearance Flow and Losses for an Isolated Compressor Blade," ARC R&M 3316.

Rains, D. A., 1954, "Tip Clearance Flow in Axial Compressors and Pumps," California Institute of Technology, Mech. Eng. Laboratory, Report 5.

Sjolander, S. A., and Amrud, K. K., 1987, "Effects of Tip Clearance on Blade Loading in a Planar Cascade of Turbine Blades," ASME JOURNAL OF TURBOMACHINERY, Vol. 109, pp. 237–245.

Storer, J. A., and Cumpsty, N. A., 1991, "Tip Leakage Flow in Axial Compressors," ASME JOURNAL OF TURBOMACHINERY, Vol. 113, pp. 252–259.

Yanagida, M., Machida, Y., and Takata, H., 1989, "A Study on the Mechanism of Stall Margin Improvement of Casing Treatment," *Trans. Japan Society Mechanical Eng.*, Vol. 55, No. 518, Series B [in Japanese].

Yaras, M., and Sjolander, S. A., 1990, "Development of the Tip-Leakage Flow Downstream of a Planar Cascade of Turbine Blades: Vorticity Field," ASME JOURNAL OF TURBOMACHINERY, Vol. 112, pp. 609–617.

APPENDIX

Calculation of Vorticity

The components of the vorticity vector are obtained in the Cartesian coordinate system, defined as x, y, and z in the axial, spanwise, and pitchwise directions:

$$\Omega_x = \frac{\partial v}{\partial z} - \frac{\partial w}{\partial y}$$

$$\Omega_y = \frac{\partial w}{\partial x} - \frac{\partial u}{\partial z}$$

$$\Omega_z = \frac{\partial u}{\partial y} - \frac{\partial v}{\partial x} \tag{A1}$$

The axial component can be determined from the measured data in a transverse plane. Making some assumptions, the spanwise and pitchwise components can also be obtained from such data. Assuming incompressible flow and neglecting viscous effects, the following equation can be used as an alternative way:

$$\mathbf{V} \times \Omega = \frac{1}{\rho} \nabla p_t \tag{A2}$$

Taking its y and z components,

$$w\Omega_x - u\Omega_z = \frac{1}{\rho}\frac{\partial p_t}{\partial y}$$

$$u\Omega_y - v\Omega_x = \frac{1}{\rho}\frac{\partial p_t}{\partial z} \tag{A3}$$

If the vorticity components are normalized with inlet velocity V_1 and pitch s, for example, $\Omega_x s/V_1$, then the final formula is

$$\Omega_x = \left(\frac{\partial v}{\partial z} - \frac{s}{1}\frac{\partial w}{\partial y}\right)$$

$$\Omega_y = \frac{v}{u}\Omega_x + \frac{1}{2}\frac{1}{u}\frac{\partial C_{pt}}{\partial z}$$

$$\Omega_z = \frac{w}{u}\Omega_x - \frac{1}{2}\frac{1}{u}\frac{s}{1}\frac{\partial C_{pt}}{\partial y} \tag{A4}$$

where the velocities are normalized with inlet velocity V_1, y, with span l, z with pitch s.

The streamwise vorticity was taken as the component of vorticity in the main flow direction, defined as the midspan flow, rather than the component in the local flow direction. Thus the streamwise vorticity becomes

$$\Omega_s = \Omega_x \cos \beta_m + \Omega_z \sin \beta_m \tag{A5}$$

where β_m is the pitchwise flow angle at midspan but varying with pitchwise distance.

DISCUSSION

N. A. Cumpsty[1] and E. M. Greitzer[2]

Tip clearance flow is a major cause of loss in axial compressors and one of the principal sources of uncertainty in performance prediction so any clarification is to be welcomed. The authors have collected and presented a prodigious amount of data for a cascade of compressor blades and we would like to offer a few observations.

The flow in cascades differs from that inside compressors in several ways, but the most important difference is the nature of the inlet boundary layer on the endwall. For a compressor this is unsteady, but, more significantly, the flow direction varies as the wall is approached; for the cascade the flow direction is uniform and is referred to as collateral. The change in frame of reference not only contributes to the flow direction variation in a compressor, but produces a variation in the magnitude of the velocity through the boundary layer near the hub or casing of a compressor that is qualitatively different than that near the endwall of a cascade. (The significance of these particular features of a compressor is very well demonstrated by Wadia and Beacher, 1990.) This does suggest that there is limited utility in studying the fine detail of cascade flow in the endwall region where the differences from a real

[1]Whittle Laboratory, Cambridge University, Cambridge, United Kingdom.

[2]Gas Turbine Laboratory, Massachusetts Institute of Technology, Cambridge, MA 02139.

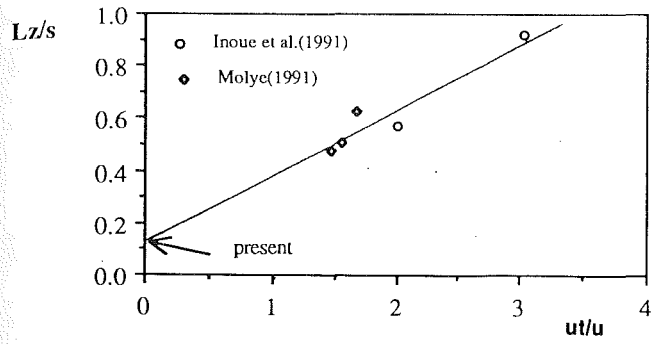

Fig. 15 Variation of tip vortex loci with blade speed

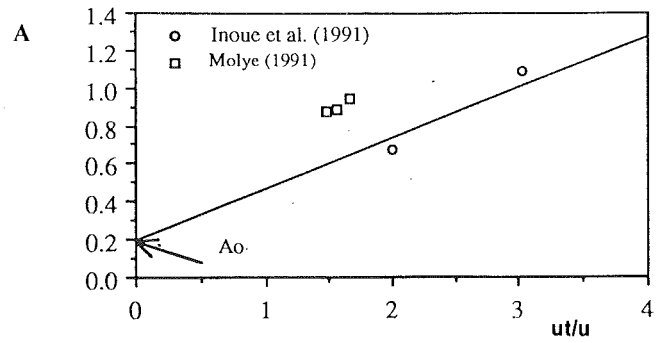

Fig. 16 Variation of factor A with blade speed

compressor are most marked. It would therefore be unfortunate if the impression were created that all the flow patterns observed in cascade and described in these papers were to be found in compressors if sufficient care were taken.

In Part II the authors compare their measured loci of the clearance vortex with the predictions of the simple method of Chen et al. (1991) and find that to obtain reasonable agreement the coefficient A should be much smaller than that proposed by Chen et al. We would offer the following observations:

(*i*) J. A. Storer, in the discussion of the paper by Chen et al., also showed that a smaller value of A was needed to match measurements he had obtained in a cascade flow.

(*ii*) Chen et al. found that their simple model gave good predictions for the position of the vortex for a large number of different compressor rotors, using the value $A = 0.46$ they recommended, providing strong support for this approach in the case, which is of practical interest.

(*iii*) Storer, also in the discussion of the paper by Chen et al., compared the model of Chen et al. with the results of a reliable Navier-Stokes solver for a blade with a noncollateral inlet flow, in this case a stator hub with clearance. The Chen et al. method agreed well with the Navier-Stokes solution in this case.

(*iv*) Navier-Stokes solutions have also made it possible to carry out experiments that would have been expensive or impossible to do physically; one of these is to explore the effect of a moving or stationary wall over rotor tips. The calculations show that the motion of the wall past the tips has a minimal effect on the flow, since the shear stresses are so small, but it is the skewing of the inlet profile that is important.

Storer's lucid discussion reinforces the differences between cascade and compressor flows. It is our belief that measurements and calculations in linear cascades with collateral inlet boundary layers on the endwalls do have use, but the differences between such cascade flows and the flows in actual compressors always need to be borne in mind.

Additional Reference

Wadia, A., and Beacher, B. F., 1990, "Three-Dimensional Relief in Turbomachinery Blading," ASME JOURNAL OF TURBOMACHINERY, Vol. 112, pp. 587-598.

Authors' Closure

We greatly appreciate the observations made by Prof. Cumpsty and Prof. Greitzer. It is quite correct that there is a great difference between the flows in a cascade and a real machine. Even though it is deeply felt that a linear cascade cannot simulate the effects of the inlet flow skew and the relative motion between the blade tip and the casing, the investigation on a cascade flow still remains useful since many factors influencing the secondary flow and tip leakage flow are the same. Also, due to its simple geometry, some of the detailed flow mechanisms are ease to analyze.

Two reasons for the fact that the coefficient A in Eq. (3) is much less than that of Chen et al. (1991) have been discussed in the paper. One is connected to the different way to locate the vortex trace; the other is due to the influence of the relative motion.

The relative motion has an important influence upon the secondary flow development, as shown by many authors, for example, Storer and Cumpsty (1991) and Inoue et al. (1991). It causes the skewing of the inlet boundary layer and tends to drag the tip leakage vortex to the pressure side.

If one recognizes the main factors that affect the trajectory of the leakage vortex core, such as tip clearance τ, pressure difference ΔP, density ρ, time t (see Chen et al.), and blade speed u_t, then dimensional analysis shows that the pitchwise loci L_z can be expressed in the following formula:

$$\frac{L_z}{\tau} = f\left(\frac{t}{\tau}\sqrt{\frac{\Delta P}{\rho}}, \frac{tu_t}{\tau}\right) \tag{4}$$

The time t can be calculated from the axial velocity, u, as

$$t = \frac{x}{u} \tag{5}$$

Since L_z increases linearly in the mainstream direction, as proved by the simple model of Chen et al. (1991) and in the present study, Eq. (4) can be written as

$$\frac{L_z/s}{x/c} = \frac{c}{s} \cdot f\left(\frac{1}{u}\sqrt{\frac{\Delta P}{\rho}}, \frac{u_t}{u}\right) \tag{6}$$

Inoue et al. (1991) and Moyle et al. (1992) presented the static pressure contours at the casing wall for different flow coefficients at a clearance of 1.7 and 0.6 percent chord, respectively. From these contours, the rolling-up of a tip leakage vortex could be identified along a pressure trough. It is observed from their results, for example Fig. 6 of Inoue et al. (1991), that at the flow coefficient 0.5, the tip vortex in the traverse section near the rotor exit is located at about 57 percent pitch from the suction side; but by reducing the flow coefficient to 0.33, i.e., increasing blade speed 1.52 times, the vortex has been dragged to about 92 percent pitch from the suction side. This shows a great influence of the relative motion on the tip leakage vortex loci. Figure 15 presents the loci of the tip vortices at the rotor exit as a function of u_t/u. The locus of the tip vortex near the trailing edge at the present case is also indicated in Fig. 15 for 1.0 percent clearance. It is seen that the variation of the loci with u_t/u is close to a linear relation. It follows that Eq. (6) can be expressed as

$$\frac{L_z/s}{x/c} = \left(A_0 + A_u \frac{u_t}{u}\right)\sqrt{\frac{c(\tan\beta_1 - \tan\beta_2)}{s\cos\beta_m}} \tag{7}$$

in which the pressure difference in Eq. (6) has been replaced with an average loading, as done by Chen et al. (1991). Com-

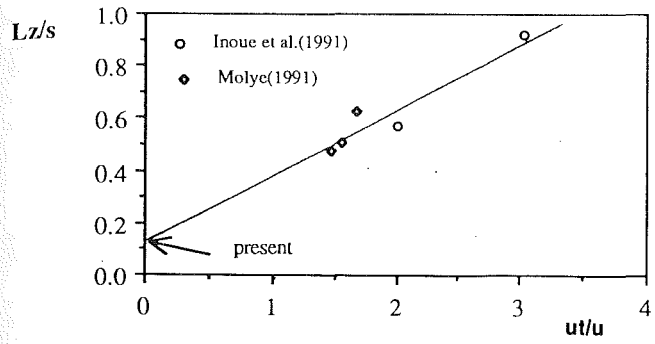

Fig. 15 Variation of tip vortex loci with blade speed

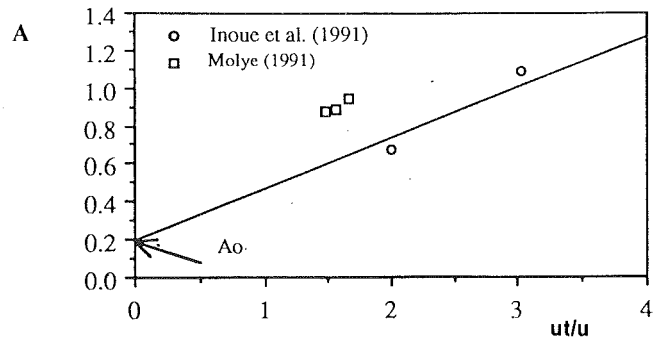

Fig. 16 Variation of factor A with blade speed

compressor are most marked. It would therefore be unfortunate if the impression were created that all the flow patterns observed in cascade and described in these papers were to be found in compressors if sufficient care were taken.

In Part II the authors compare their measured loci of the clearance vortex with the predictions of the simple method of Chen et al. (1991) and find that to obtain reasonable agreement the coefficient A should be much smaller than that proposed by Chen et al. We would offer the following observations:

(*i*) J. A. Storer, in the discussion of the paper by Chen et al., also showed that a smaller value of A was needed to match measurements he had obtained in a cascade flow.

(*ii*) Chen et al. found that their simple model gave good predictions for the position of the vortex for a large number of different compressor rotors, using the value $A = 0.46$ they recommended, providing strong support for this approach in the case, which is of practical interest.

(*iii*) Storer, also in the discussion of the paper by Chen et al., compared the model of Chen et al. with the results of a reliable Navier-Stokes solver for a blade with a noncollateral inlet flow, in this case a stator hub with clearance. The Chen et al. method agreed well with the Navier-Stokes solution in this case.

(*iv*) Navier-Stokes solutions have also made it possible to carry out experiments that would have been expensive or impossible to do physically; one of these is to explore the effect of a moving or stationary wall over rotor tips. The calculations show that the motion of the wall past the tips has a minimal effect on the flow, since the shear stresses are so small, but it is the skewing of the inlet profile that is important.

Storer's lucid discussion reinforces the differences between cascade and compressor flows. It is our belief that measurements and calculations in linear cascades with collateral inlet boundary layers on the endwalls do have use, but the differences between such cascade flows and the flows in actual compressors always need to be borne in mind.

Additional Reference

Wadia, A., and Beacher, B. F., 1990, "Three-Dimensional Relief in Turbomachinery Blading," ASME JOURNAL OF TURBOMACHINERY, Vol. 112, pp. 587-598.

Authors' Closure

We greatly appreciate the observations made by Prof. Cumpsty and Prof. Greitzer. It is quite correct that there is a great difference between the flows in a cascade and a real machine. Even though it is deeply felt that a linear cascade cannot simulate the effects of the inlet flow skew and the relative motion between the blade tip and the casing, the investigation on a cascade flow still remains useful since many factors influencing the secondary flow and tip leakage flow are the same. Also, due to its simple geometry, some of the detailed flow mechanisms are ease to analyze.

Two reasons for the fact that the coefficient A in Eq. (3) is much less than that of Chen et al. (1991) have been discussed in the paper. One is connected to the different way to locate the vortex trace; the other is due to the influence of the relative motion.

The relative motion has an important influence upon the secondary flow development, as shown by many authors, for example, Storer and Cumpsty (1991) and Inoue et al. (1991). It causes the skewing of the inlet boundary layer and tends to drag the tip leakage vortex to the pressure side.

If one recognizes the main factors that affect the trajectory of the leakage vortex core, such as tip clearance τ, pressure difference ΔP, density ρ, time t (see Chen et al.), and blade speed u_t, then dimensional analysis shows that the pitchwise loci L_z can be expressed in the following formula:

$$\frac{L_z}{\tau} = f\left(\frac{t}{\tau}\sqrt{\frac{\Delta P}{\rho}}, \frac{tu_t}{\tau}\right) \tag{4}$$

The time t can be calculated from the axial velocity, u, as

$$t = \frac{x}{u} \tag{5}$$

Since L_z increases linearly in the mainstream direction, as proved by the simple model of Chen et al. (1991) and in the present study, Eq. (4) can be written as

$$\frac{L_z/s}{x/c} = \frac{c}{s} \cdot f\left(\frac{1}{u}\sqrt{\frac{\Delta P}{\rho}}, \frac{u_t}{u}\right) \tag{6}$$

Inoue et al. (1991) and Moyle et al. (1992) presented the static pressure contours at the casing wall for different flow coefficients at a clearance of 1.7 and 0.6 percent chord, respectively. From these contours, the rolling-up of a tip leakage vortex could be identified along a pressure trough. It is observed from their results, for example Fig. 6 of Inoue et al. (1991), that at the flow coefficient 0.5, the tip vortex in the traverse section near the rotor exit is located at about 57 percent pitch from the suction side; but by reducing the flow coefficient to 0.33, i.e., increasing blade speed 1.52 times, the vortex has been dragged to about 92 percent pitch from the suction side. This shows a great influence of the relative motion on the tip leakage vortex loci. Figure 15 presents the loci of the tip vortices at the rotor exit as a function of u_t/u. The locus of the tip vortex near the trailing edge at the present case is also indicated in Fig. 15 for 1.0 percent clearance. It is seen that the variation of the loci with u_t/u is close to a linear relation. It follows that Eq. (6) can be expressed as

$$\frac{L_z/s}{x/c} = \left(A_0 + A_u \frac{u_t}{u}\right)\sqrt{\frac{c(\tan\beta_1 - \tan\beta_2)}{s\cos\beta_m}} \tag{7}$$

in which the pressure difference in Eq. (6) has been replaced with an average loading, as done by Chen et al. (1991). Com-

paring Eq. (7) to Eq. (3), it is found that the factor A in Eq. (3) can be expressed as

$$A = \left(A_0 + A_u \frac{u_t}{u} \right) \tag{8}$$

It is seen that the suggested $A = 0.19$ from the present results only represents the case with zero blade speed, that is, $A_0 = 0.19$. In the simple model of Chen et al. (1991), $A = 0.46$, the influence of the relative motion was included implicitly.

Figure 16 shows the variation of the factor A with blade speed, with the data from Inoue et al. (1991), Moyle et al. (1992), and the present data, A_0, at the same conditions as Fig. 15. From the limited data in Fig. 16, it is suggested that the factor A_u is close to 0.27. The difference of Moyle's data from this line may be due to the difference of blade camber. The blades in Moyle's rotor are C4 profiles, but NACA 65 series are used in Inoue's case and the present one. It is apparent that further study on the influence of relative motion upon the tip vortex loci is needed.

References

Inoue, M., Kuroumaru, M., Iwamoto, T., and Ando, Y., 1991, "Detection of a Rotating Stall Precursor in Isolated Axial Flow Compressor Rotors," ASME JOURNAL OF TURBOMACHINERY, Vol. 113, pp. 281–289.

Moyle, I. N., Walker, G. J., and Shreeve, R. P., 1992, "Stator-Averaged, Rotor Blade-to-Blade Near-Wall Flow in a Multistage Axial Compressor With Tip Clearance Variation," ASME JOURNAL OF TURBOMACHINERY, Vol. 114, pp. 668–674.

Investigation of Tip Clearance Phenomena in an Axial Compressor Cascade Using Euler and Navier-Stokes Procedures

R. F. Kunz[1]
Graduate Student.
Mem. ASME

B. Lakshminarayana
Evan Pugh Professor of
Aerospace Engineering.
Fellow ASME

A. H. Basson
Graduate Student.

Department of Aerospace Engineering,
The Pennsylvania State University,
University Park, PA 16802

Three-dimensional Euler and full Navier-Stokes computational procedures have been utilized to simulate the flow field in an axial compressor cascade with tip clearance. An embedded H-grid topology was utilized to resolve the flow physics in the tip gap region. The numerical procedure employed is a finite difference Runge-Kutta scheme. Available measurements of blade static pressure distributions along the blade span, dynamic pressure and flow angle in the cascade outlet region, and spanwise distributions of blade normal force coefficient and circumferentially averaged flow angle are used for comparison. Several parameters that were varied in the experimental investigations were also varied in the computational studies. Specifically, measurements were taken and computations were performed on the configuration with and without: tip clearance, the presence of an endwall, inlet endwall total pressure profiles and simulated relative casing rotation. Additionally, both Euler and Navier-Stokes computations were performed to investigate the relative performance of these approaches in reconciling the physical phenomena considered. Results indicate that the Navier-Stokes procedure, which utilizes a low Reynolds number k-ϵ model, captures a variety of important physical phenomena associated with tip clearance flows with good accuracy. These include tip vortex strength and trajectory, blade loading near the tip, the interaction of the tip clearance flow with passage secondary flow, and the effects of relative endwall motion. The Euler computation provides good but somewhat diminished accuracy in resolution of some of these clearance phenomena. It is concluded that the level of modeling embodied in the present approach is sufficient to extract much of the tip region flow field information useful to designers of turbomachinery.

Introduction

The execution rate performance of efficient CFD codes on modern vector processors has reached $O(10^2)$ MFLOPS. Researchers can now obtain three-dimensional full Navier-Stokes solutions using $O(10^5)$ grid points in $O(10^0)$ CPU hours. Such capability has offered, among other things, the ability to perform large-scale viscous simulation studies to develop an improved understanding of particular physical processes in turbomachines.

The physics of tip clearance flows have received a great deal of attention from both experimental and computational investigators in the gas turbine field. This is primarily due to the importance of complex endwall and clearance phenomena in determining stage performance. The trend toward more highly loaded, lower aspect ratio blades intensifies the importance of these physics to the turbomachinery engineer.

Several of the dominant physical processes involved in tip clearance flows, including blade unloading and vorticity transport, are primarily rotational inviscid in nature. For this reason, several very useful tip clearance models have been devised based on various approximations to the Euler equations, with and without viscous corrections (Rains, 1954; Lakshminarayana, 1970; Moore and Tilton, 1988; Chen et al., 1991; Yaras et al., 1992). There are also several considerations that warrant the use of viscous analyses to provide more detailed simulation of tip clearance flows. The characteristics of the boundary layers along the blades near the tip, and on the tip and casing surfaces themselves, significantly influence flows with tip clearance. Typical of these phenomena are the often separated flow near the suction surface-casing endwall interface, the influence of relative casing wall rotation, and blockage induced by the boundary layer, which develops on the blade tip. Also, the generation and decay of vorticity must be modeled (or rely on artificial diffusion) in subsonic inviscid flow computations.

[1]Current address: Engineer, Knolls Atomic Power Laboratory, Schenectady, NY.

Contributed by the International Gas Turbine Institute and presented at the 37th International Gas Turbine and Aeroengine Congress and Exposition, Cologne, Germany, June 1-4, 1992. Manuscript received by the International Gas Turbine Institute February 27, 1992. Paper No. 92-GT-299. Associate Technical Editor: L. S. Langston.

Tip clearance effects have been incorporated in viscous turbomachinery flow field computations by numerous researchers in recent years. Often a "thin blade" approximation is used to model the tip geometry. This allows for the convenient specification of a periodic boundary in the tip gap region, while retaining a standard **H**-grid topology. This approach has been utilized by many investigators; including Storer and Cumpsty (1991), Bansod and Rhie (1990), Hah and Reid (1992), Kunz and Lakshminarayana (1992), to name a few recent examples. The grid near the casing becomes highly skewed due to the "pinching" of the blade tip, when this simple approach is used. However, for thin blade profiles this approach has been shown to provide a good engineering approximation when modeling the flow in the tip gap region.

Several alternative grid topologies can be incorporated to resolve the tip gap region directly. Rai (1989), Beach (1990), and Choi and Knight (1991) have used patched **O-H**-grid structures, with stacked **O**-grids in the gap region. Watanabe et al. (1991) recently implemented an overlapping **C-H** topology with stacked **H**-grids in the tip region. An "embedded" **H**-grid topology has found recent popularity in gas turbine applications with tip clearance (Moore and Moore, 1989; Cleak and Gregory-Smith, 1992; Liu et al., 1991; Briley et al., 1991; Basson et al., 1991). All of the mentioned approaches have in common that they provide significantly smoother meshes, more precise geometric representation, and improved flow field resolution in the tip clearance region.

In this paper, an Euler/Navier–Stokes flow solver has been used to study a variety of tip clearance phenomena. The code, described in detail by Kunz and Lakshminarayana (1992), was recently modified to accommodate the embedded **H**-grid topology. In earlier work by the present authors (Basson et al., 1991), the approach was used to simulate the flow in a linear compressor cascade with clearance. Although the emphasis of that work was on grid generation, it was found that the method provided good predictions of near-tip blade pressure and wake flow angle distributions when compared with experimental data. Also, it was observed that for the relatively thick compressor cascade blade considered, the embedded **H**-grid solution provided better agreement with these experimental measurements than a solution that incorporated a "pinched" standard **H**-grid.

A series of numerical investigations has been performed since that preliminary work, and the results of these are presented and interpreted in this paper. The goals of the present work are:

1 Evaluate the relative performance of Navier–Stokes and Euler analyses in predicting a variety of tip clearance physics. Also, provide some additional results comparing and contrasting the embedded and standard **H**-grid topologies in viscous flow computations.

2 Perform a series of parametric investigations using the viscous flow code and compare these results with available experimental data.

3 Perform an additional parametric simulation study incorporating the effect of relative endwall motion.

4 Draw conclusions, based on the results of the above, on the physical nature of flows with tip clearance and evaluate the capability and limitations of the viscous analysis in reconciling these phenomena.

Experimental and Numerical Procedures

Experimental Procedures. The configuration chosen for computational study in this paper is the so-called "Liverpool Cascade." This configuration was the subject of a variety of experimental tip clearance flow investigations undertaken by the second author in earlier work (see Lakshminarayana and Horlock, 1965; Lakshminarayana, 1970). Extensive details of the facility are provided by Lakshminarayana and Horlock (1965). A brief overview is provided here. A low-speed cascade tunnel in the turbomachinery laboratory at Liverpool University was used for the experimental investigations. The cascade had nine "split" blades of 10C430C50 profile, of chord length 0.152 m, set at a 36 deg stagger. The blades were cantilevered from a solid frame as shown in Fig. 1. One side of the tunnel was movable, allowing the distance between the two halves of the split blades, 2τ (Fig. 1), to be adjusted. The aspect ratio of the unsplit blades was 4.8 and the space-chord ratio was 1.00. For the tests detailed below, the air inlet and outlet angles were 51 and 31 deg, respectively, and the Reynolds number based on chord length and flow velocity at midspan was 2.0×10^5. Figure 1 provides a schematic of the experimental configuration.

Three series of experiments were performed, designated A, B, and C in Fig. 1. In Experiment A, the blades were separated a distance 2τ and the upstream velocity profile was uniform (Fig. 1*a*). This served to isolate tip clearance physics without the influence of an endwall or the interaction between passage secondary motion and the tip gap flow. The cascade flow field in Experiment A consists of a row of antisymmetric leakage vortex pairs. The plane of symmetry of these vortex pairs lies

Nomenclature

c = chord length = 0.152 m

C_N = normal force coefficient $= \dfrac{\mathbf{L}\cdot\mathbf{n}}{0.5\rho_{\text{ref}}q_{\text{ref}}^2 c}$

C_P = static pressure coefficient $= \dfrac{p - p_{\text{ref}}}{0.5\rho_{\text{ref}}q_{\text{ref}}^2}$

i, j, k = grid indices

l = height of split blade = 0.362 m

$\mathbf{L}$ = lift per unit span

$\dot{m}$ = mass flow rate

$\mathbf{n}$ = unit normal to blade chord line

ni, nj, nk = limits of grid indices

$nile, nite$ = streamwise indices at leading, trailing edges

$njss, njps$ = pitchwise indices at suction, pressure surfaces

p = pressure

$\mathbf{q}$ = total velocity vector

$\mathbf{q}_{2D}$ = total velocity vector at midspan and midpassage

s = distance along chord

t = pitch = 0.152 m

u, v, w = Cartesian velocity components

x, y, z = Cartesian coordinates (Figs. 1, 2)

α = flow angle = atan (v/u)

α_t = angle of vortex core trajectory

γ = stagger angle of cascade (= 36 deg)

ρ = density

τ = one-half gap height (Fig. 1)

ξ, η, ζ = curvilinear coordinates

ω = vorticity vector

Superscripts and Subscripts

— = mass-weighted pitchwise average, $\overline{\phi} = \dfrac{\int_0^t \rho u \phi dy}{\int_0^t \rho u\, dy}$

gap = through the clearance gap

inlet = inlet

ref = *local* inlet reference value $[q_{\text{ref}}(z) = q_{\text{inlet}}(z)]$

midspan = value at midspan ($k = 1$)

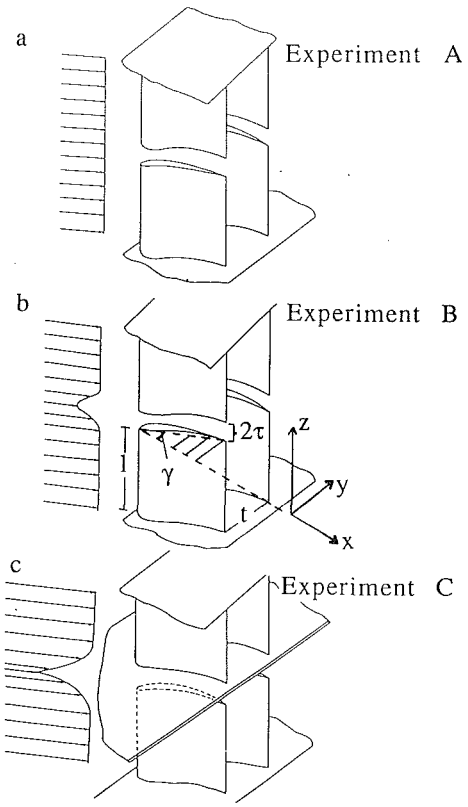

Fig. 1 Schematic of experimental configurations (note: $z = 0$ is located 0.04 chord inboard of the cascade symmetry plane [$k = nk$]; for the cases with clearance, this corresponds to the blade tip [$\tau/c = 0.04$])

halfway between the tips of the split blades. In Experiment B, a plate was inserted well upstream of the cascade to provide a nonuniform inlet flow (Fig. 1*b*). The motive of these studies was to investigate the interaction between leakage flow and the weak secondary flow due to blade to blade turning of an inlet normal vorticity profile. In Experiment C, a thin wall was inserted in the center of the gap (Fig. 1*c*) to simulate the presence of an endwall. The endwall gives rise to significantly stronger passage secondary motion, since the inlet vorticity gradient is larger and is sustained by viscous shear at the endwall. Additionally, a boundary layer develops along the endwall in the tip gap, which gives rise to additional blockage of the clearance flow. By also running Experiments B and C with zero clearance, Lakshminarayana and Horlock (1965) were able to observe and compare the isolated secondary flows in these cases, without the presence of the tip clearance flow.

Numerical Procedures. A three-dimensional Navier–Stokes flow solver was used for the computational studies presented herein. A complete description of the governing equations and numerical procedures implemented is available from Kunz and Lakshminarayana (1992). A brief overview is provided here.

The code is a three-dimensional compressible Full Navier–Stokes (FNS) solver, which includes a low Reynolds number k–ϵ turbulence model. The seven governing transport equations (continuity, momentum, energy, k, ϵ) are cast in time-dependent conservation form, in generalized curvilinear coordinates. An explicit Runge–Kutta scheme is used for temporal discretization. Second-order central finite differences are used for spatial discretization, and for the computations presented herein, fourth difference artificial dissipation is added to the discrete equations for stability. Standard turbomachinery boundary conditions are implemented; appropriate boundary conditions are also available that allow the code to be run in Euler mode. The code was modified (details from Basson et al., 1991) to accommodate the embedded **H**-grid topology.

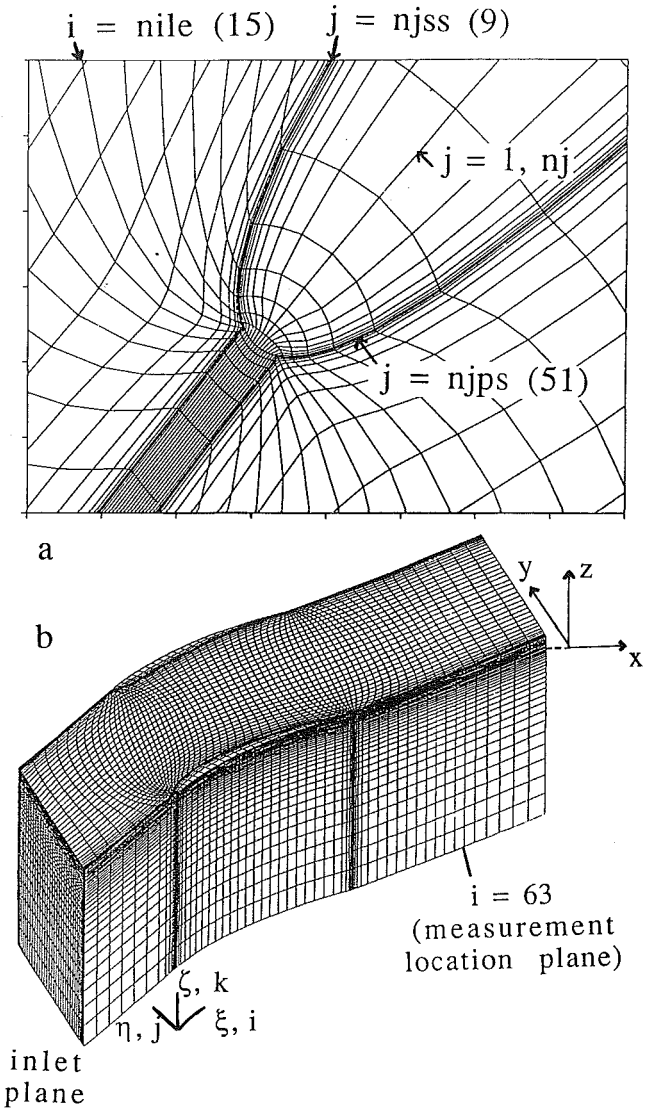

Fig. 2 Views of computational mesh and nomenclature: (*a*) detail of leading edge; (*b*) view of three-dimensional grid

All the grids were generated using a two-dimensional algebraic-elliptic approach described briefly here. For the embedded grids, the blade profile is mapped to a rectangular region within the topological boundary of an **H**-grid. For the tip gap region, an **H**-grid is embedded within this cut-out in such a way that continuous, smooth grids are obtained in the pitchwise and streamwise directions. The "pinched" **H**-grid in the tip region is generated by skewing a standard **H**-grid to fill the tip gap. As the cascade under investigation utilized uniform profile blades, the algebraic-elliptic grid generation procedure was only used to generate two-dimensional grids in the blade to blade plane. These were then stacked using a simple geometric series distribution scheme to provide appropriate spanwise clustering. Further grid generation details are available from Basson et al. (1991).

Figures 2(*a*) and 2(*b*) show views of the 69 × 59 × 35 (axial, pitchwise, spanwise) computational mesh used in the Navier–Stokes computations. Of these, 5984 points were used in the tip gap itself [17 (blade to blade) × 32 (chordwise) × 11 (tip to gap centerline)]. In Fig. 2(*a*), a leading edge detail of the computational mesh is provided. A view of the three-dimensional grid is shown in Fig. 2(*b*), and the location of the experimental wake measurement plane is also provided. Since the focus of the present investigation was on the tip gap flow, the *hub* endwall was not resolved. Specifically, the $k = 1$

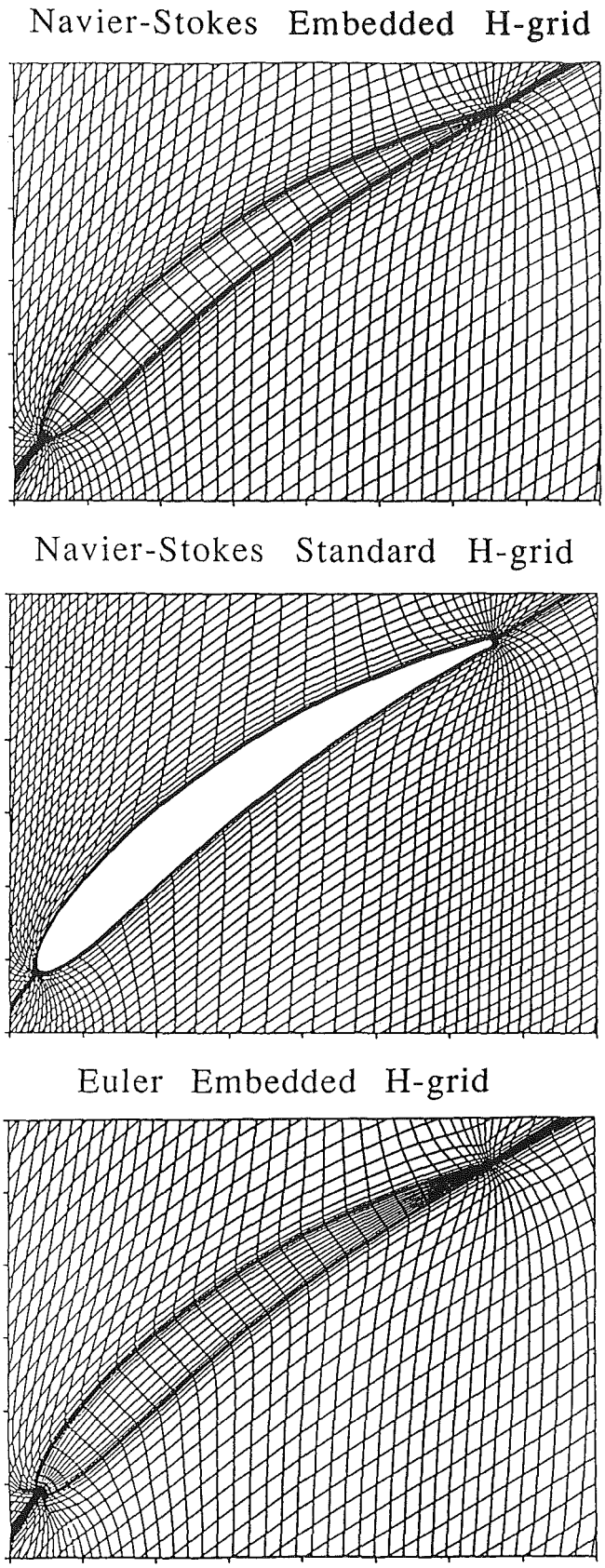

Fig. 3 Cross-sectional views of three grids used in numerical studies

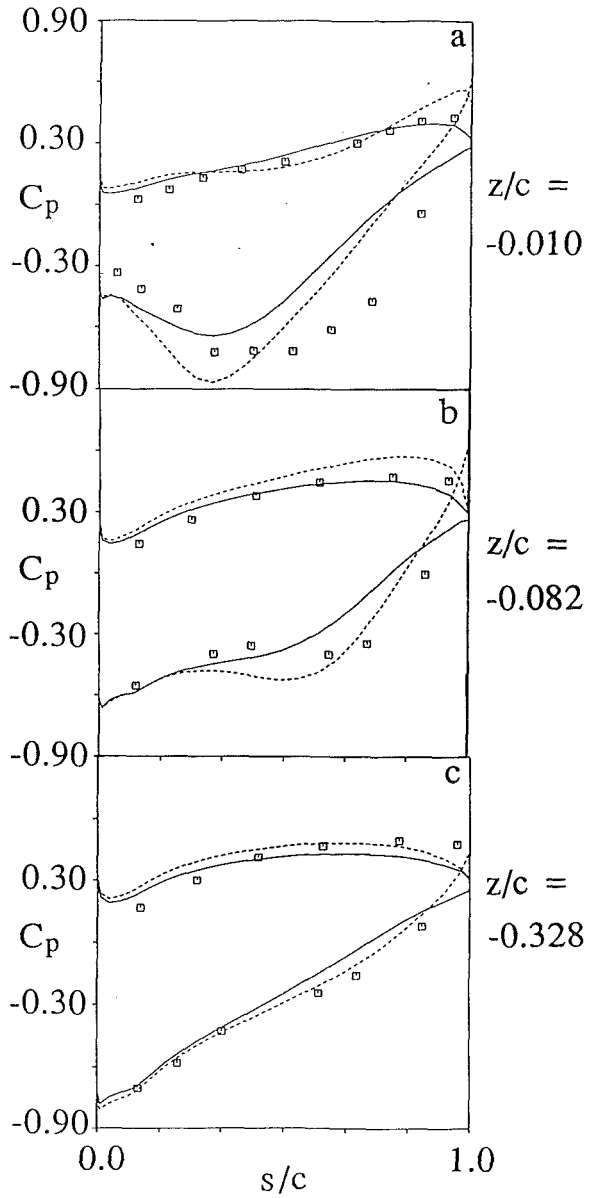

Fig. 4 Comparison of computed and measured blade static pressure coefficient at three spanwise locations; measured values (symbols), Navier-Stokes (solid line), Euler (short dashed line)

boundary (Fig. 2*b*) was treated as an inviscid symmetry boundary, thereby reducing the grid requirements in the spanwise direction. The boundary was situated approximately 2/3 chord inboard of the blade tip. The gap centerline boundary, k = nk, was treated as either an inviscid symmetry boundary or a viscous boundary depending on whether Experiment A, B or C was simulated. The computations were performed at an inlet Mach number of 0.2 to accommodate the compressible formulation of the flow solver.

Results and Discussion

Experiment A. The flow solver was first applied to Experiment A, detailed above. The clearance gap for which the computations were performed was 0.04 chord (τ/c = 0.04, see Fig. 1). Three calculations were done, including an Euler solution using an embedded **H**-grid, a Navier-Stokes solution using a "pinched" standard **H**-grid and a Navier-Stokes solution using the embedded **H**-grid shown in Fig. 2. In Fig. 3, cross-sectional views of the computational grids used for these three studies are provided. For all three grids, 69 and 35 points were used in the streamwise and spanwise directions, respectively. In the pitchwise direction, 59 grid points were used for the two Navier-Stokes calculations and 45 points were used for the Euler calculation, since very high clustering was not required near the blade surfaces.

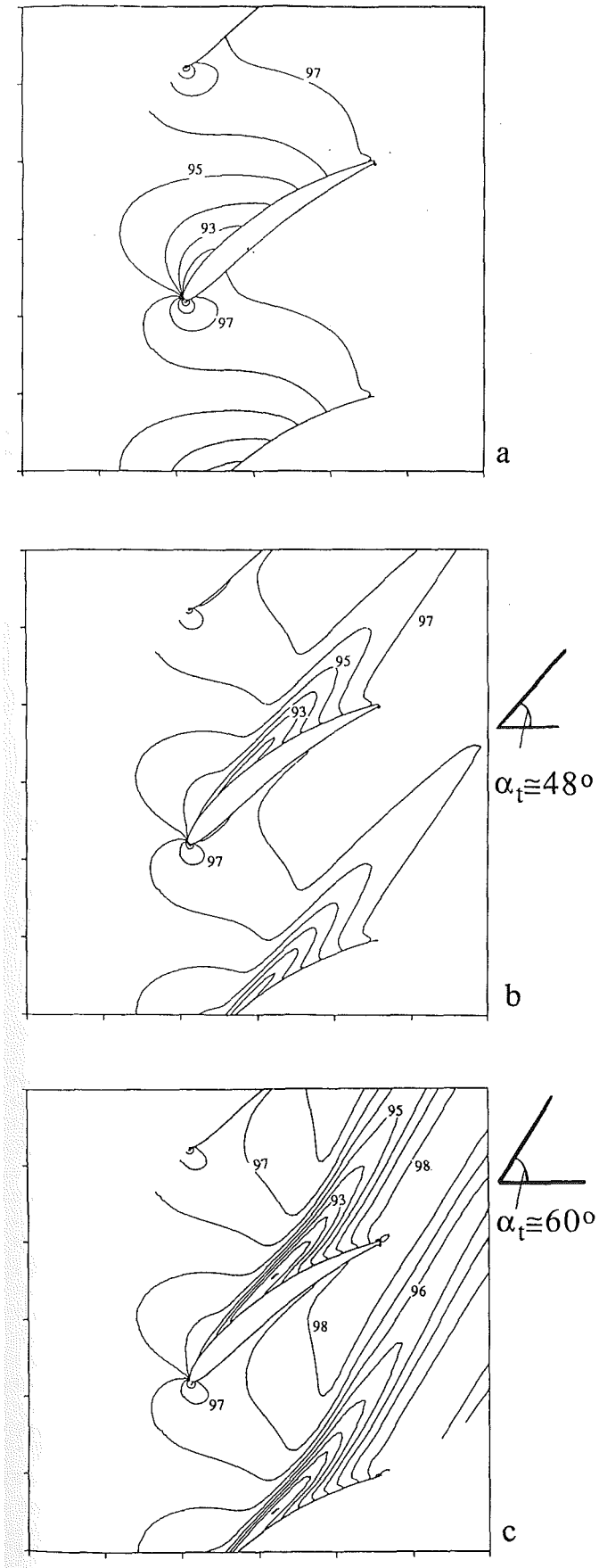

Fig. 5 Blade-to-blade contours of static pressure (kPa) predicted by the Navier-Stokes and Euler simulations: (*a*) Navier-Stokes, midspan grid slice; (*b*) Navier-Stokes, grid slice just inboard of tip; (*c*) Euler, grid slice just inboard of tip

As mentioned above, predicted blade pressures and wake flow angle contours from the embedded **H**-grid and "pinched" standard **H**-grid Navier-Stokes computations were compared in the work of Basson et al. (1991), and these results are not repeated here. New results of section normal force coefficient and gap mass flow rate are included below for these two Navier-Stokes grid topologies.

Figures 4 show predicted Navier-Stokes (embedded **H**-grid) and Euler blade surface pressure distribution at spanwise locations very near the tip ($z/c = -0.01$), near the tip ($z/c = -0.08$), and far from the tip ($z/c = -.33$). In Fig. 4(*c*), Euler and Navier-Stokes solutions are compared with measured values well away (0.33 chord) from the tip. Agreement is good for both numerical solutions, considering that only 35 grid points were used in the streamwise direction on the blade surfaces. At 0.01 and 0.08 chord inboard of the tip, both computations show the characteristic migration of the suction peak toward midchord. This pressure drop on the suction surface is due to the presence of a leakage vortex adjacent to the suction surface. At both 0.01 and 0.08 chord inboard of the tip, the Navier-Stokes solution agrees reasonably well with the experimental data. At both locations, the viscous solution underpredicts the magnitude of the suction peak, and predicts the location of this peak approximately 10 percent chord upstream of the measured peak. Apparently, the Navier-Stokes analysis predicts that the tip vortex is shed somewhat too close to the leading edge. The unloading on the pressure surface is predicted well, especially by the Navier-Stokes code.

The Euler solution also provides qualitatively good predictions of the near-tip blade pressure distribution. A suction peak is predicted that is somewhat higher than both the Navier-Stokes and experimental values, and again the location of the suction peak seems to be somewhat too close to the leading edge. Nevertheless, the important feature of increase in suction pressure due to the presence of the tip vortex is captured by the inviscid procedure.

Figure 5(*a*) shows blade to blade pressure contours at midspan ($k = 1$) as predicted by the Navier-Stokes code (embedded **H**-grid). This conventional "two-dimensional" distribution contrasts with pressure contours one grid plane inboard of the tip ($k = 24$), as shown in Fig. 5(*b*). Clearly evident is the trajectory of the tip clearance vortex, whose low pressure core is seen to make approximately a 48 deg angle with the axial direction. The core pressure of the decaying vortex is seen to increase approximately linearly with distance along its trajectory up to the cascade exit plane. The core pressure is then seen to increase toward ambient more slowly.

Figure 5(*c*) provides computed blade-to-blade pressure contours, one grid plane inboard of the tip ($k = 24$), for the Euler solution. Unlike the blade surface pressure distributions, a significant discrepancy between Euler and Navier-Stokes solutions is now seen. Specifically, the tip clearance vortex trajectory is curved in the inviscid simulation. At the cascade exit plane, the low pressure core is seen to make approximately a 60 deg angle with the axial direction. This turning of the vortex trajectory away from axial may be attributable to increased mass flow through the gap, due in turn to the lack of viscous blockage in the gap. This item is discussed further below.

Measured and computed contours of outlet flow angle are presented in Fig. 6. The location of this outlet plane is one-half chord axially downstream of the cascade exit plane, as labeled in Fig. 2(*b*). The Navier-Stokes solution using the embedded **H**-grid is seen to provide good agreement with experiment in prediction of exit flow angle distribution. The tight "binding" of the flow angle contours represents the vortex core. Clearly, the size, strength, and trajectory of the tip clearance vortex are captured with good accuracy. The viscous simulation predicts that the vortex is somewhat closer to the gap centerline than the measured vortex.

Outlet flow angle contours predicted by the Euler solution

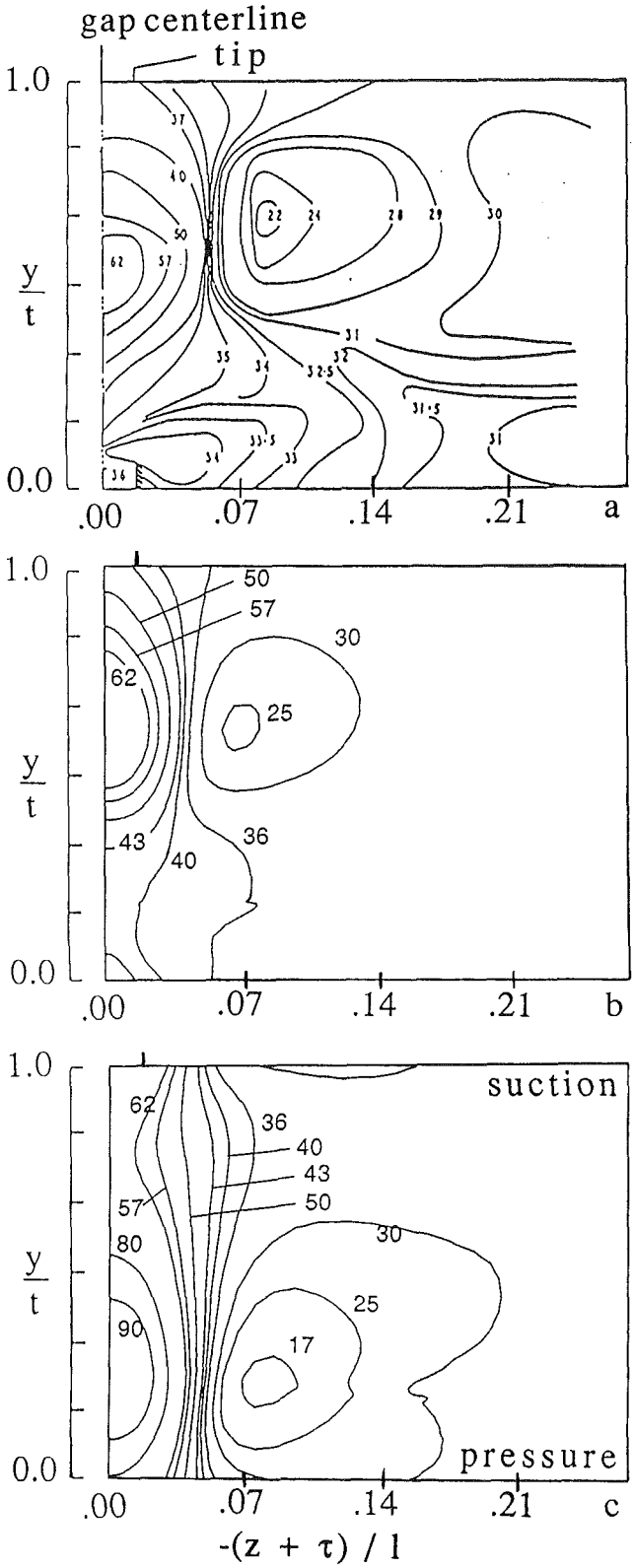

Fig. 6 Contours of flow angle, α (deg) at outlet measurement plane: (*a*) experimental; (*b*) Navier-Stokes; (*c*) Euler

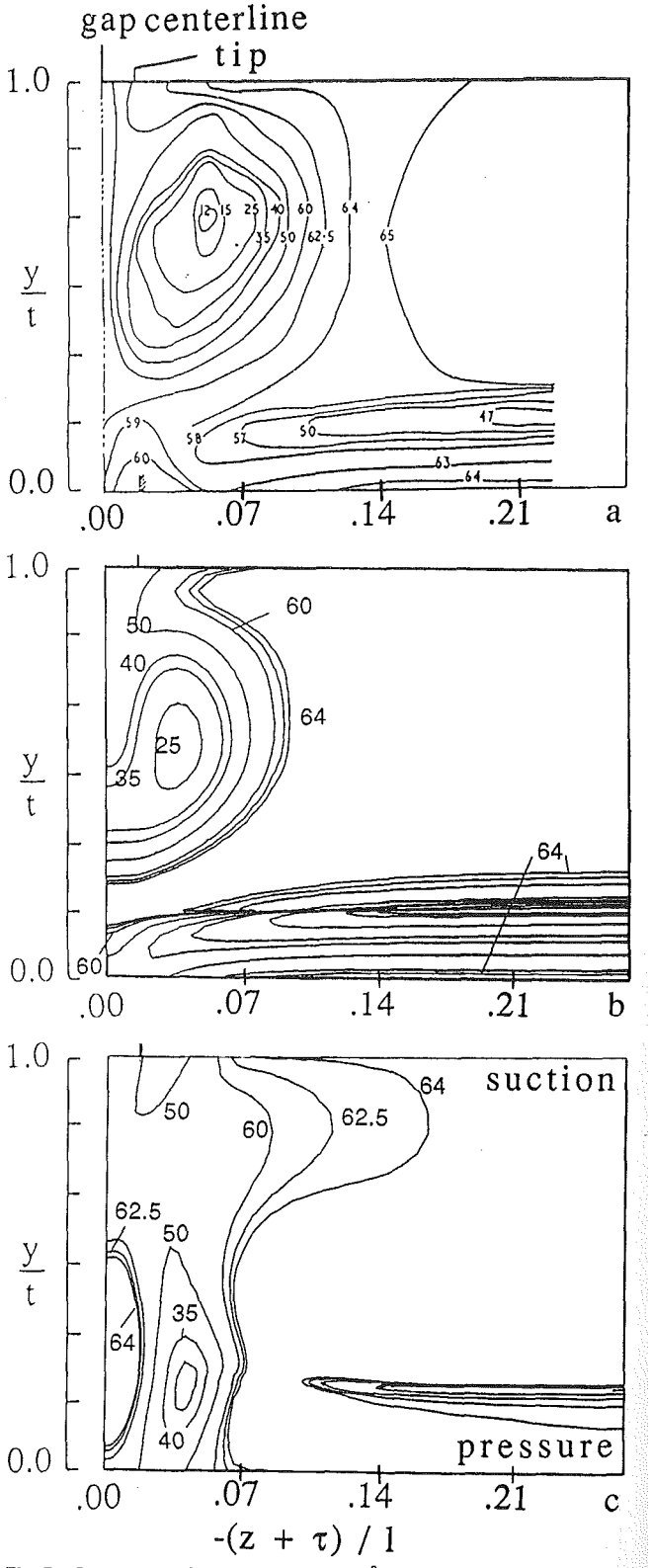

Fig. 7 Contours of dynamic pressure ($\rho q^2/2$, in percent of inlet dynamic head) at outlet measurement plane: (*a*) experimental; (*b*) Navier-Stokes; (*c*) Euler

using the embedded **H**-grid are shown in Fig. 6(*c*). The vortex trajectory is seen to be significantly different from the experimental data, as evidenced by the location of the core (compare with Figs. 6*a* and 6*b*). Also, the range of flow angles is seen to be somewhat higher than the Navier–Stokes solution. This suggests that the Euler code predicts a stronger vortex, consistent with the increase in the magnitude of the suction peak observed in Figs. 4(*a*) and 4(*b*). As mentioned in the introduction, vorticity generation in subsonic Euler computations relies exclusively on artificial dissipation, whether inherent in the numerical scheme or purposefully added to the discrete equation set. Such production, then, is highly grid dependent, and therefore caution must be exercised in interpretation of vortical Euler solutions (see Hirsch, 1990, for example).

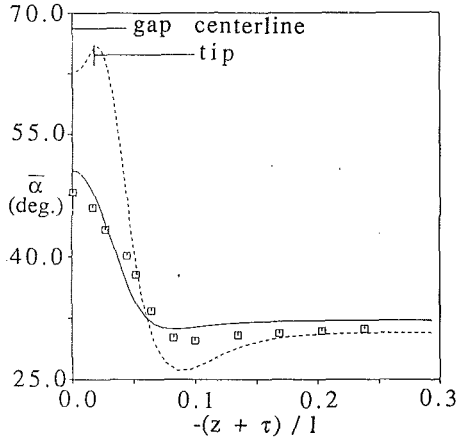

Fig. 8 Comparison of computed and measured spanwise distribution of mass-weighted, pitchwise averaged outlet flow angle; measured values (symbols), Navier-Stokes (solid line), Euler (short dashed line)

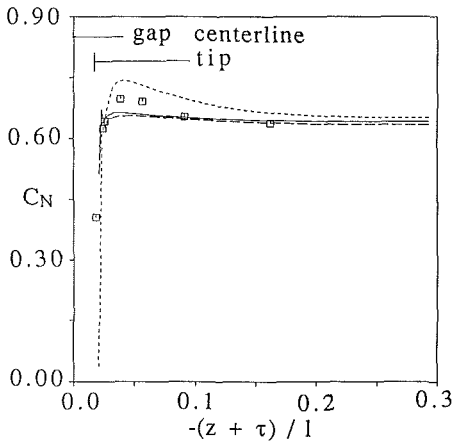

Fig. 9 Comparison of computed and measured spanwise distribution of blade normal force coefficient; measured values (symbols), Navier-Stokes, embedded H-grid (solid line), Navier-Stokes, "pinched" standard H-grid (long dashed line), Euler (short dashed line)

In the Euler calculation, the leakage velocities are larger, and hence leakage fluid tends to move somewhat farther away from the suction surface before interacting with the main flow and rolling up into a vortex. Also, as mentioned above, increased leakage velocities tend to convect the vortex toward the pressure surface. These items are further evidenced in Fig. 7, which shows contours of normalized dynamic head at the outlet measurement plane, as provided by experimental measurement and Navier-Stokes and Euler solutions. In Fig. 7(*b*), the location of the tip vortex at this outlet location is predicted to be close to midpassage, by the Navier-Stokes solution, in good agreement with experimental observation. This can be seen by comparison of the relative location of low dynamic pressure regions in the vortex core and wake (note that the computational grid did not exactly follow the wake centerline trajectory, which gave rise to the "drifting" of the wake into the computational domain). The outlet location of the tip vortex, predicted by the Euler solution, is again seen to be in poorer agreement with experiment in Fig. 7(*c*).

Figure 8 shows a plot of the variation of mass-weighted, pitchwise-averaged flow angle with span, at the outlet measurement plane. Comparison is made in this figure between Navier-Stokes, Euler, and measured values. The viscous results are in good agreement with experimental data. Specifically, as the tip gap centerline is approached, average flow angle is seen to decrease from its midspan value (overturning), due to the presence of the vortex. Average flow angle then rapidly increases to a peak of approximately 50 deg, 3 deg higher than

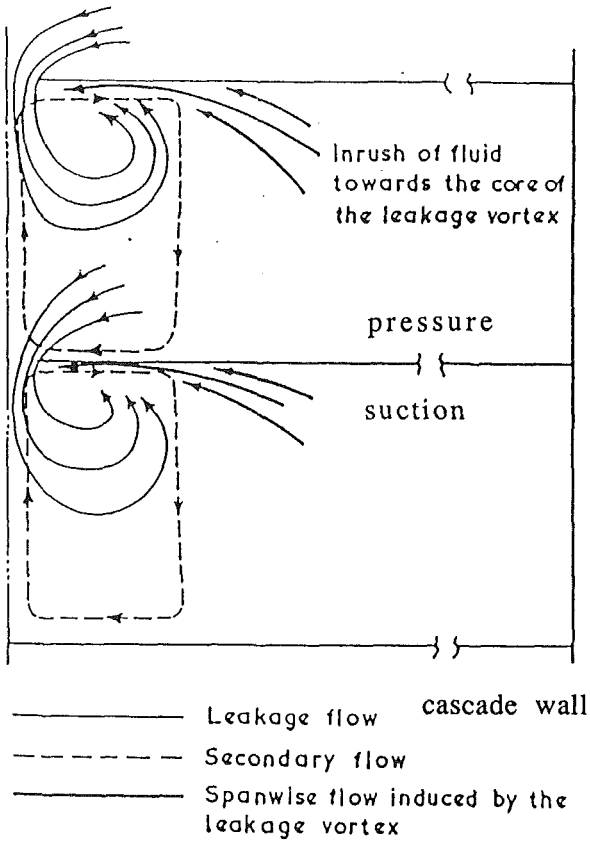

Fig. 10 Nature of leakage and secondary flows in a cascade with nonuniform upstream flow (adapted from Lakshminarayana and Horlock, 1965)

the measured value. The inviscid results show qualitatively good agreement, though again, an overprediction of vortex strength is seen. The Euler procedure shows that the vortex influences the passage flow field as far as 15 percent span inboard of the tip, while data and the Navier-Stokes solution indicate that the influence of the leakage vortex is confined to a region approximately 10 percent span inboard of the tip.

For moderate clearances, the decrease in suction side pressure near the tip due to the presence of the vortex can yield a slight increase in section lift inboard of the tip. In Fig. 9, the spanwise distribution of normal force coefficient is plotted for Experiment A. Included in this plot are measured values, and computed values using the Euler analysis, the Navier-Stokes analysis using the embedded **H**-grid, and for comparison, the Navier-Stokes analysis using the "pinched" standard **H**-grid. All three solutions capture qualitatively the increase in section lift, whose peak is located approximately 4 percent chord inboard of the tip. The Euler and Navier-Stokes predictions straddle the measured values. This is consistent with previous observations that the Euler and Navier-Stokes solutions slightly overpredict and underpredict, respectively, the strength of the clearance vortex. The section lift provided by the "pinched" standard **H**-grid Navier-Stokes solution shows some oscillatory behavior near the tip, but is essentially in good agreement with data and the other Navier-Stokes solution.

For the moderate clearance considered, $\tau/c = 0.04$, not all of the spanwise vorticity bound in the blade is shed at the tip. This gives rise to the so-called "retained lift" at the tip, evident in the measurements in Fig. 9. This feature is captured qualitatively in all of the numerical solutions, though the Navier-Stokes solution is seen to provide a less severe drop in C_N as the tip is approached.

Experiment B. The previous investigations served to isolate the effect of tip clearance on the passage and downsteam flow

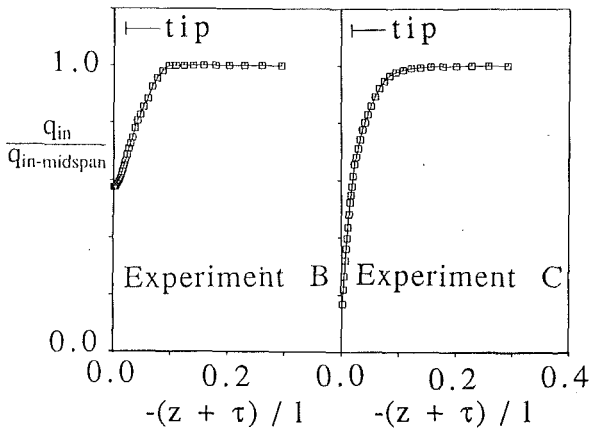

Fig. 11 Inlet total velocity profiles for: (*a*) Experiment B and (*b*) Experiment C

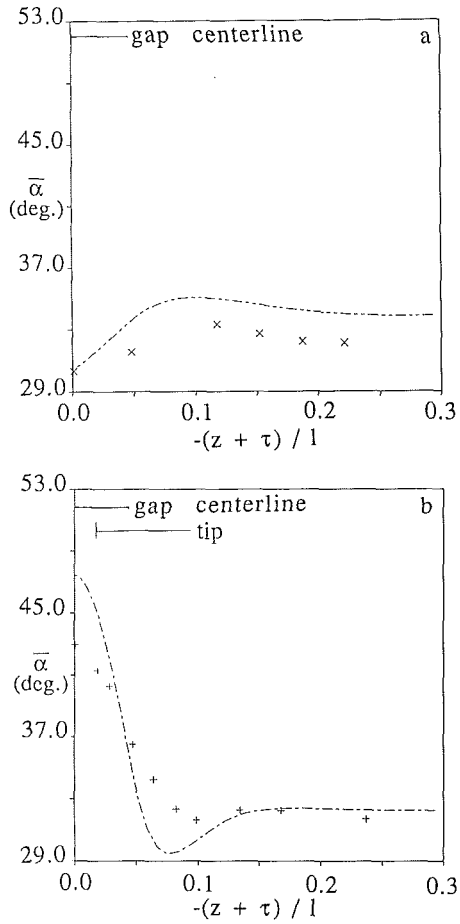

Fig. 12 Comparison of computed and measured spanwise distribution of mass-weighted, pitchwise averaged outlet flow angle; measured values (symbols), Navier-Stokes (line); (*a*) Experiment B, τ/c = 0.00; (*b*) Experiment B, τ/c = 0.04

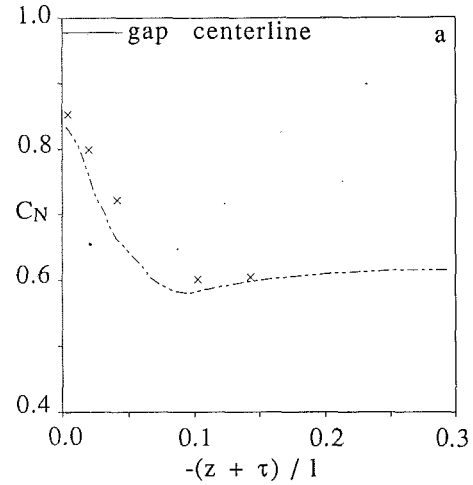

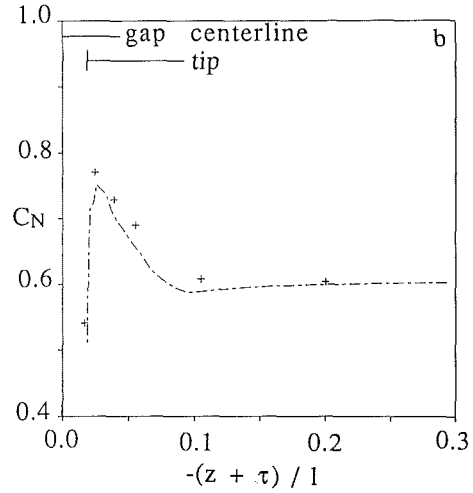

Fig. 13 Comparison of computed and measured spanwise distribution of blade normal force coefficient; measured values (symbols), Navier-Stokes (line); (*a*) Experiment B, τ/c = 0.00; (*b*) Experiment B, τ/c = 0.04

field without the presence of an endwall or secondary motion due to the transport of an inlet vorticity profile. In an axial compressor, endwall boundary layers on the hub and casing are turned in the blade row. The circumferential force acting on this endwall fluid, of nonuniform streamwise momentum, gives rise to secondary flow. Near the tip, the sense of the secondary motion is opposite that of the tip clearance vortex. This is illustrated schematically in Fig. 10, which has been adapted from Lakshminarayana and Horlock (1965).

In Experiment B, the contribution of passage secondary flow was incorporated by generating a normal (to the streamwise direction) vorticity profile upstream of the blade row. This wake (see Fig. 1*b*) was generated in the laboratory by inserting a plate along the cascade symmetry plane well upstream of the cascade. In Fig. 11(*a*), measured total velocity one-half chord upstream of the inlet plane and a short distance downstream of the profile generating plate is shown. This profile was used in constructing inlet boundary conditions for the Navier-Stokes simulation.

In Figs. 12(*a*) and 12(*b*), average flow angle variation with span is plotted for the cases with no tip gap and with the same gap of 0.04 chord used in Experiment A (distance from gap centerline to tip = 0.04*c*). For the case with no clearance, the influence of secondary flow is clearly evident. Some underturning is observed as the tip centerline is approached, followed by a more significant average overturning (refer to schematic, Fig. 10). These phenomena are very well captured by the Navier-Stokes simulation. The somewhat offsetting effects of endwall secondary flow and tip clearance flow are apparent in Fig. 12(*b*). Specifically, the measured and predicted average flow angles are noticeably lower (≅3–4 deg) than in Experiment A, where no passage secondary flow was present (see Fig. 8). Apparently, the Navier-Stokes simulation underpredicts the influence of the secondary motion somewhat. This is evidenced by an approximately 4 deg overprediction of gap centerline average flow angle, compared to approximately 3 deg for Experiment A. This may be due to numerical diffusion of the inlet vorticity profile as it is transported through the discretized domain. Comparison of Figs. 12(*a*) and 12(*b*) shows

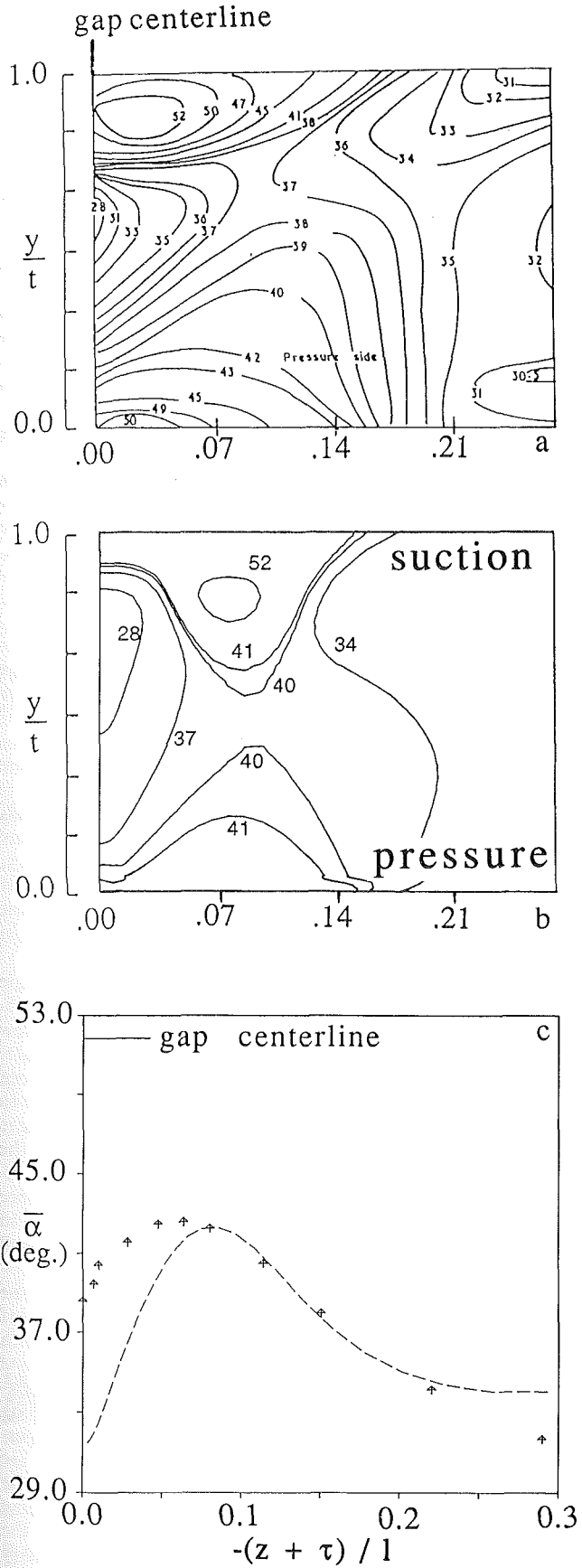

Fig. 14 Contours of flow angle at outlet measurement plane for Experiment C, τ/c = 0.00; (*a*) measured; (*b*) predicted; (*c*) comparison of computed and measured spanwise distribution of mass-weighted, pitchwise averaged outlet flow angle for Experiment C, τ/c, = 0.00; measured values (symbols), Navier-Stokes (line)

that predicted average midspan flow angle is 1.6 deg more for Experiment B with no clearance than for the case with clearance. This variation is due to the proximity of the $k = 1$ no-flow-through boundary to the tip ($k = 1 \cong 2/3$ chord inboard of tip).

Figures 13(*a*) and 13(*b*) show spanwise distribution of blade normal force coefficient for Experiment B cases with τ/c = 0.00 and τ/c = 0.04. When no clearance is present, a significant increase in section lift is observed near the tip. This is caused by overturning of the flow due to secondary motion. In Fig. 13(*b*), where τ/c = 0.04, the normal force distribution is similar to the no-clearance case, except near the tip where the blade ends. In both cases, the Navier–Stokes results are remarkably good. The effect of the interaction between secondary flow and leakage flow on near-tip loading is captured accurately. These results are encouraging, considering the importance of near tip loading predictions in modern low aspect ratio blading design.

Experiment C. By inserting a thin plate along the gap centerline, Lakshminarayana and Horlock (1965) were able to incorporate the influence of an endwall in their experimental investigation of tip clearance phenomena. In the laboratory, this plate extended from the end of the upstream plate used in Experiment B to the cascade exit plane (see Fig. 1*c*). The endwall total velocity profile, measured one-half chord upstream of the cascade, was much steeper than in Experiment B, as shown in Fig. 11(*b*), due to the presence of the endwall. This experiment served to incorporate the effects of stronger secondary motions and the additional blockage present in the gap itself on the near tip cascade flow field. In the numerical simulation, the measured inflow velocity profile, shown in Fig. 11(*b*), was used to construct inlet boundary conditions, and the endwall ($k = nk$, refer to Fig. 2*b*) boundary was changed from a symmetric no-flow-through boundary to a viscous no-slip boundary.

When the cascade was operated with an endwall but with no clearance, a strong secondary flow pattern was observed. In Figs. 14(*a*) and 14(*b*), measured and computed contours of passage flow angle, α, are shown at the downstream measurement plane. A large region of flow underturning is evident, on the suction side of the wake, which extends well away from the endwall. This is due to a large region of separated flow in the suction surface-endwall corner. This phenomenon is common in compressor cascades, stators, and rotors, and has been observed by researchers in the absence of leakage flow. In the present cascade, the influence of strong secondary motion itself is apparent in the exit flow angle distribution. Specifically, significant overturning ($\alpha_{min} \cong 27$ deg) is observed near the endwall at midpassage in both the experiment and the Navier–Stokes simulation.

Although the effect of secondary motion on flow angle is captured well, the flow angle distribution in the suction surface-endwall separation region is in some error. The location of maximum underturning ($\cong 52$ deg) is predicted to be farther from the endwall and wake centerline. In Fig. 14(*c*), spanwise mass-averaged flow angle distributions are plotted for this no-clearance case. The general trend of underturning then overturning with span is captured, but the Navier–Stokes solution significantly overpredicts the average overturning near the gap centerline due to the error in predicting the location of the region of underturning arising from flow separation.

In Figs. 15(*a*) and 15(*b*), the exit flow angles are compared for Experiment C with a tip clearance of 0.04 chord. A number of interesting features are accessible in these figures. The secondary flow is seen to persist in both experiment and Navier–Stokes simulation as evidenced by flow overturning of approximately 5 deg ($\alpha_{min} \cong 27$ deg) near the endwall at midpassage. The presence of the tip clearance vortex is seen to have two effects. The secondary motion "pushes" the leakage vor-

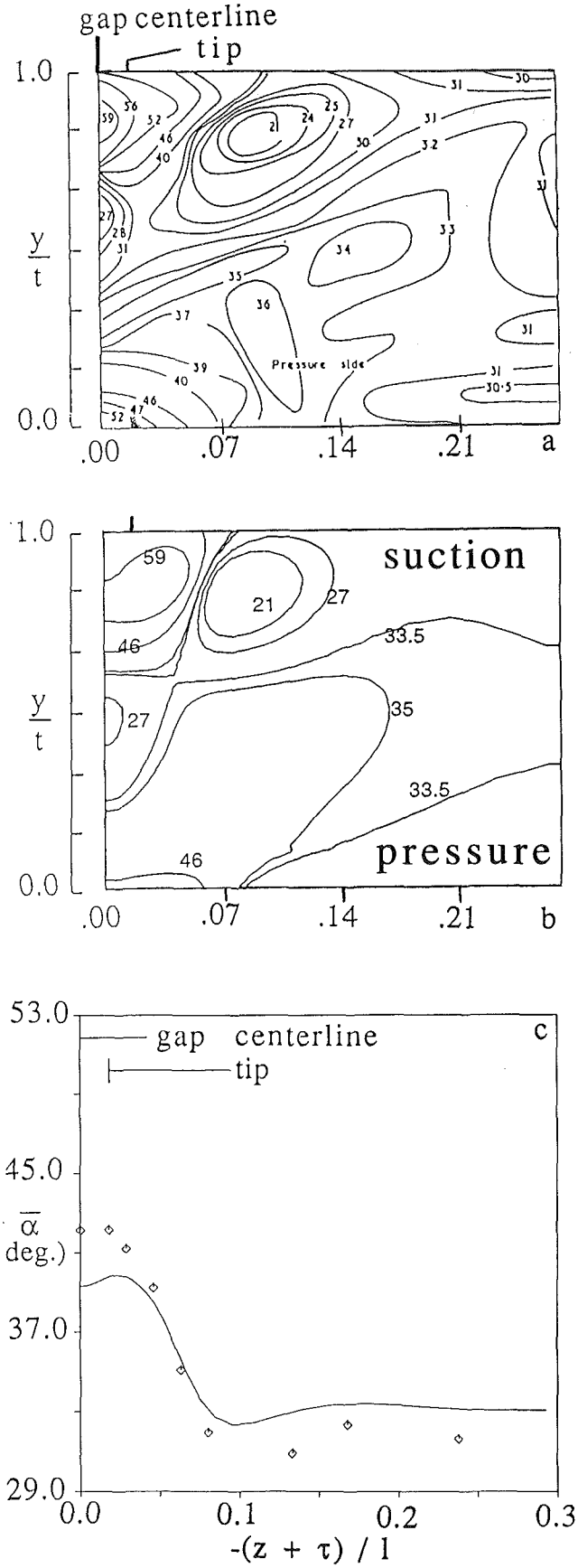

Fig. 15 Contours of flow angle at outlet measurement plane for Experiment C, τ/c = 0.04; (*a*) measured; (*b*) predicted; (*c*) comparison of computed and measured spanwise distribution of mass-weighted, pitchwise averaged outlet flow angle for Experiment C, τ/c = 0.04; measured values (symbols), Navier-Stokes (line)

tex toward the suction side (compare with Experiment A, Fig. 6). Also, spanwise flow along the suction surface is induced by the tip vortex (see Fig. 10), and this injects high-momentum fluid into the suction surface-endwall corner, reducing flow separation there. The Navier-Stokes simulation does an excellent job in resolving these complex interactions. This is further evidenced in Fig. 15(*c*), which shows that the Navier-Stokes code accurately predicts the spanwise distribution of average flow angle.

Additional Results and Discussion. The presentation above corresponds to comparison of measured and computed flow field parameters and interpretation of these results. In this section, the Navier-Stokes simulations are interrogated further and compared to one another. Additionally, the results of a Navier-Stokes solution, for which experimental measurements could not be taken, are presented. Specifically, Experiment C was rerun with a clearance of 0.04 chord, with simulated endwall rotation.

The influence of endwall rotation on the clearance flow in turbomachines can be significant. Recently Yaras and Sjolander (1992) and Yaras et al. (1992) presented their work on the effects of endwall rotation on the clearance flow in turbines. They performed experimental investigations where endwall rotation was simulated in a turbine cascade by rotating an endwall "belt" adjacent to the blade tips. They observed many interesting phenomena due to the endwall rotation, including reduced mass flow rate through the gap, and transport of passage and tip clearance vortices back toward the suction side of the wake.

The additional numerical study undertaken here is a Navier-Stokes compressor cascade analogy to the experimental turbine cascade studies of Yaras and Sjolander (1992) and Yaras et al. (1992). The present simulation of wall motion corresponds to that of a compressor rotor with a practical value of flow coefficient. Specifically, along the entire endwall boundary, $k = nk$ (see Fig. 2*b*), a pitchwise velocity of 0.5 $q_{\text{in-midspan}}$ was imposed. Aside from this, the code was run as for Experiment C, with τ/c = 0.04. The results of this study are included in the presentations below.

In Fig. 16, comparisons of spanwise-averaged flow angle distribution are made between the various Navier-Stokes solutions. Figure 16(*a*) shows the influence of secondary flow strength on flow angle in cases with moderate tip clearance. The influence of weak secondary flow (Experiment B) is seen to decrease net underturning due to the leakage flow. When strong secondary flow is present (Experiment C) the leakage vortex induced underturning is reduced significantly by the overturning due to secondary motion. Alternatively, the influence of flow separation on the suction surface provides more underturning well away from the tip gap $[-(z+t)/1 \cong 0.04$ to 0.10] than in Experiments A and B, where suction side-endwall separation was zero and small, respectively.

The influence of this flow separation is very evident in the cases with no clearance, as shown in Fig. 16(*b*). In the case of weak secondary flow, average flow angle increases slightly with span due to a small suction surface-endwall separation zone discussed earlier. In Experiment C, the effect of flow separation is more significant as seen by increased underturning away from the gap centerline. In Fig. 16(*c*), the three Experiment C results, with different clearances and wall motion, are compared. Clearly captured are the average underturning near the gap centerline due to the tip vortex and the underturning due to flow separation away from the gap centerline. In the case with simulated endwall rotation, the endwall boundary layer is seen to skew significantly and the average flow angle approaches 90 deg at the endwall. The relative motion between the blade and the endwall augments the leakage flow in the case of a compressor, giving rise to higher underturning angles near the wall $[-(z+t)/1 = 0.00$ to 0.04]. The leakage vortex

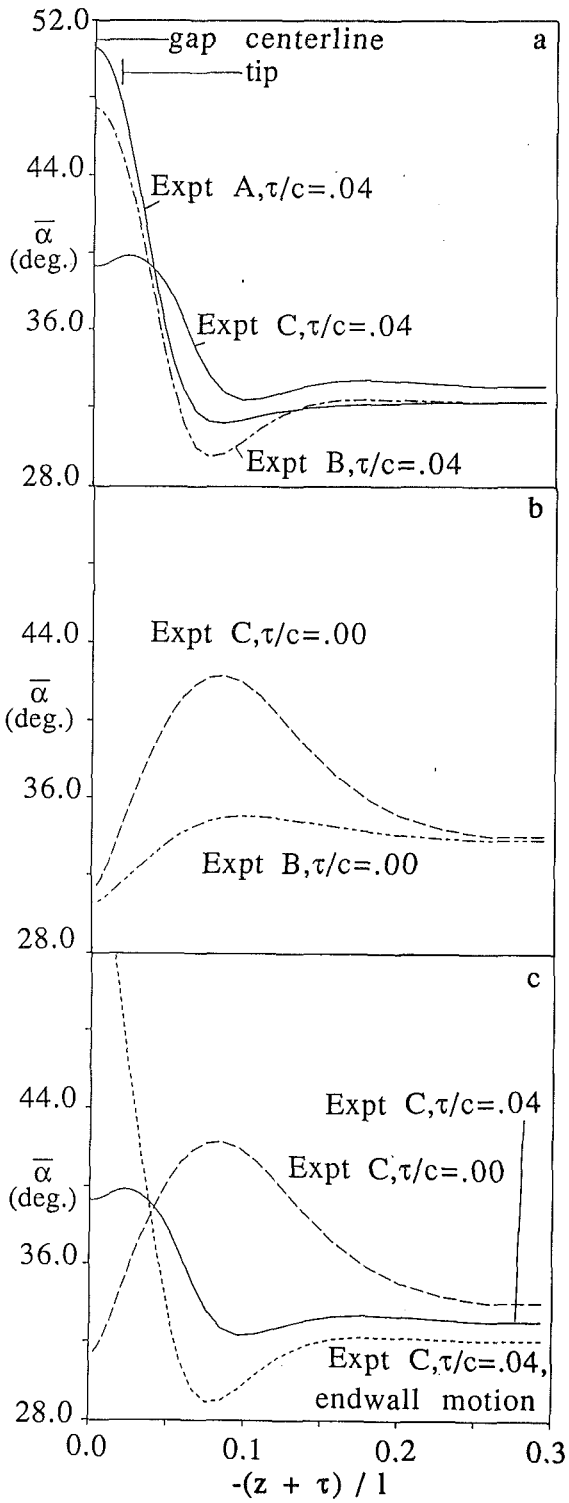

Fig. 16 Comparison of computed spanwise distributions of mass-weighted, pitchwise-averaged outlet flow angle; (*a*) Experiments A, B, C for τ/c = 0.04; (*b*) Experiments B, C for τ/c = 0.00; (*c*) Experiments C for τ/c = 0.04, τ/c = 0.00, and τ/c = 0.04 with simulated endwall rotation

is convected by the wall motion toward the pressure surface. This along with the reduced endwall flow separation decreases underturning in the region $[-(z+t)/1>0.04]$ from those observed without wall motion.

In Fig. 17, a plot of flow velocity vectors in the gap region at midchord for several of the computed cases is provided. These figures are included to provide some qualitative indication of the effects of mesh type and clustering, viscosity, and endwall treatment on the nature of the computed flow field in the gap. The embedded **H**-grid Navier–Stokes solutions are seen to provide qualitative development of boundary layers on the tip surface and endwall when present. These boundary layers reduce the leakage mass flow and strength of the tip vortex. The leakage velocities are generally higher for the Euler case and, of course, no tip surface or endwall boundary layers develop. All computations correctly predict the outward flow near the pressure surface toward the tip. It is noted that the imposed endwall velocity ($=0.5\ q_{\text{in-midspan}}$) is approximately 1/2 the peak gap cross flow velocity for the case with endwall motion.

In Fig. 18, the mass flow rate through the gap is plotted for the three Experiment A computations. In Fig. 18(*a*), accumulated mass flow is plotted against chord for Euler, Navier–Stokes with embedded **H**-grid, and Navier–Stokes with "pinched" standard **H**-grid calculations. Clearly the mass flow rate predicted by the Euler computation is significantly higher than that of the Navier–Stokes solutions. The inviscid solution predicts a total mass flow rate through the gap of approximately 2.3 percent of inlet mass flow rate compared to 1.6 percent for the embedded **H**-grid Navier–Stokes solution and 1.8 percent for the "pinched" grid Navier–Stokes solution. These observations are consistent with the flow vectors plotted in Fig. 17, and the previous observation that the angle that the Euler vortex trajectory makes with axial is too large. In Fig. 18(*b*), the normalized local mass flow rate through the gap is plotted against chord. All three solutions agree qualitatively, but the peak mass flow rate predicted by the Euler solution is closer to 2/3 chord, while the embedded **H**-grid Navier–Stokes procedure predicts a location of approximately 1/2 chord.

Figure 19 compares embedded **H**-grid Navier–Stokes mass flow rate predictions for the four experiments run with clearance (A, B, C, C with simulated endwall rotation). In Fig. 19(*a*), total mass flow through the gap is seen to decrease slightly with a weak secondary flow present (compare Experiments A and B), and is seen to decrease dramatically when an endwall is present with stronger secondary motion (Experiment C). The decrease in mass flow due to an endwall arises from increased blockage in the gap (see flow vectors, Fig. 17). Decrease in mass flow is also due to blockage induced by secondary motion, which is oppositely directed to the gap flow near the endwall. Simulated endwall rotation increases mass flow through the gap for Experiment C, which is as expected. In Fig. 19(*b*), normalized local mass flow rate through the gap is plotted against chord for these four Navier–Stokes solutions.

In Fig. 20, contours of dynamic pressure at the outlet measurement plane are provided for Experiments C. For the two cases with no endwall motion, comparison is made with experimental values. With no clearance (Fig. 20*a*), a high loss region is seen near the gap centerline close to the suction side of the cascade wake. This corresponds to the aforementioned separation zone, which develops at the suction surface-endwall interface near the trailing edge of the blade row. Consistent with the flow angle distribution for this case (refer to Fig. 14), the predicted location of minimum dynamic head is located slightly more inboard of the tip than the measured location. The magnitude of losses in dynamic head due to secondary flow and flow separation are predicted reasonably well. For the case with clearance (Fig. 20*b*), a distinct vortex is evidenced. This vortex is seen to reduce the extent of the high-loss, low dynamic head region since spanwise flow of high-momentum fluid is induced along the suction surface (see Fig. 10). In this case, the prediction of interactions between and mixing losses due to leakage flow, secondary flow, and separation are predicted well, including the location of the vortex core.

The computed contours of normalized dynamic pressure for

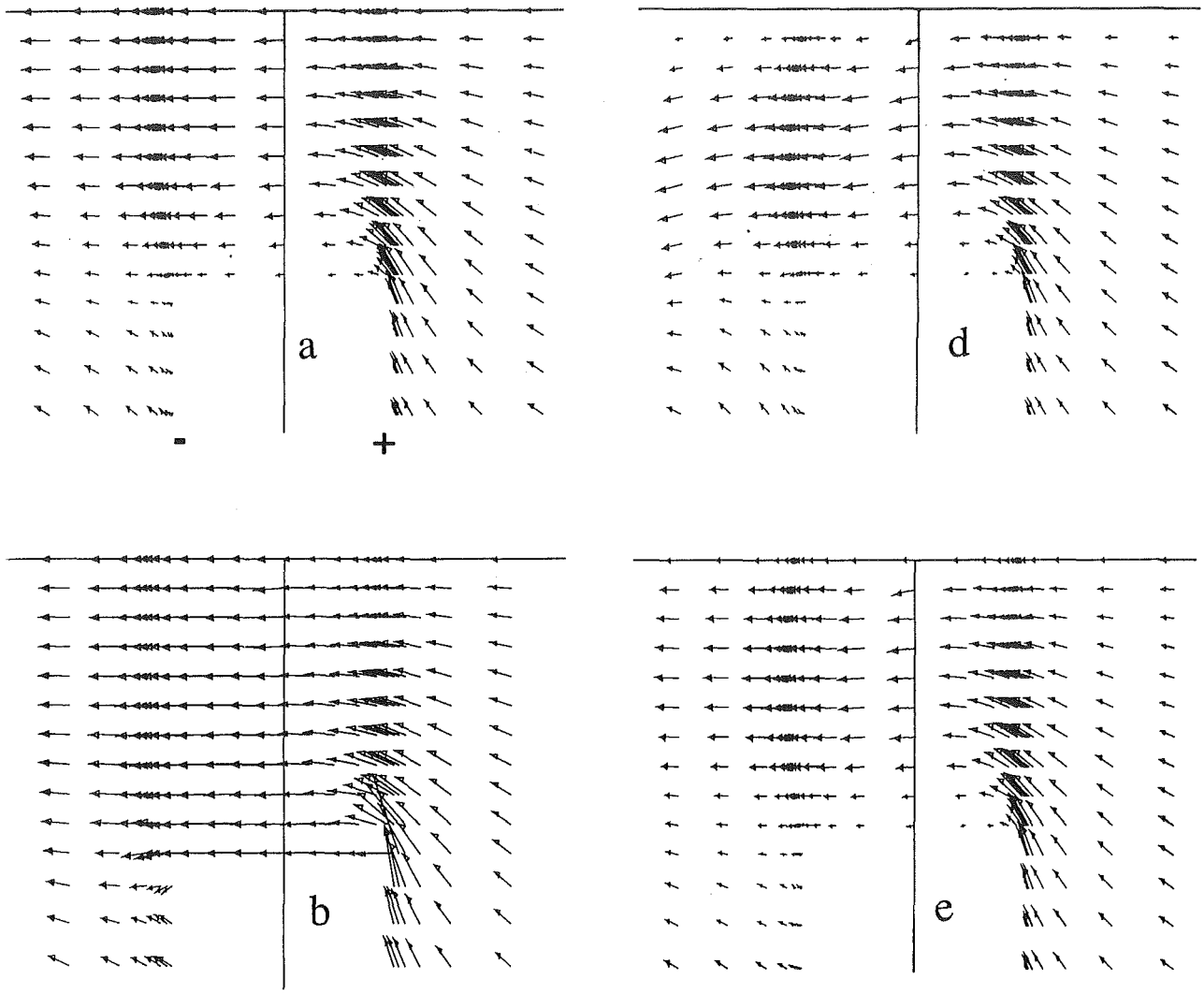

Fig. 17 Velocity vectors in the tip gap region at midchord; (*a*) Experiment A, N-S, embedded H-grid; (*b*) Experiment A, Euler, embedded H-grid; (*c*) Experiment A, N-S, "pinched" standard H-grid; (*d*) Experiment C, no endwall motion; (*e*) Experiment C, endwall motion

the case with simulated endwall rotation is shown in Fig. 20(*c*). Clearly the motion of the endwall has caused the tip clearance vortex to be carried toward midpassage. Analogous to the results and discussions of Yaras et al. (1992), modification of the vortex trajectory is due is part to the increased (decreased in Yaras' turbine cascade) mass flow rate through the gap (inviscid effect) and in part to the viscous dragging effect induced by the endwall motion. The vortex is seen to be stretched due to endwall motion.

In Fig. 21, contours of local vorticity dotted with the mid-span mean flow velocity ($\omega \cdot q_{2D}$) are presented at four chordwise locations for Experiment C, with $\tau/c = 0.04$ and no endwall motion. These plots provide qualitative indication of the nature of the developing tip clearance vortex and its interaction with the passage secondary motion and vortex. At 1/3 chord, the tip vortex has begun to form, its pitchwise width approximately equal to the local blade thickness. Also evident is a small and comparatively weak counterrotating vortex (secondary vortex) inboard of and further away from the suction surface than the forming tip vortex. By 2/3 chord, an identifiable core has formed as the clearance vortex has grown and moved both inboard of the tip and away from the suction surface. The other vortex has diffused but remains adjacent to the tip vortex. Endwall secondary flow is seen to interact with the leakage vortex at the cascade exit plane as evidenced by positive values of $\omega \cdot q_{2D}$ near the endwall and pressure surfaces. The leakage vortex has grown in diameter to approximately 2/5 cascade pitch at this trailing edge plane. At the outlet measurement plane, the tip vortex has diffused some-

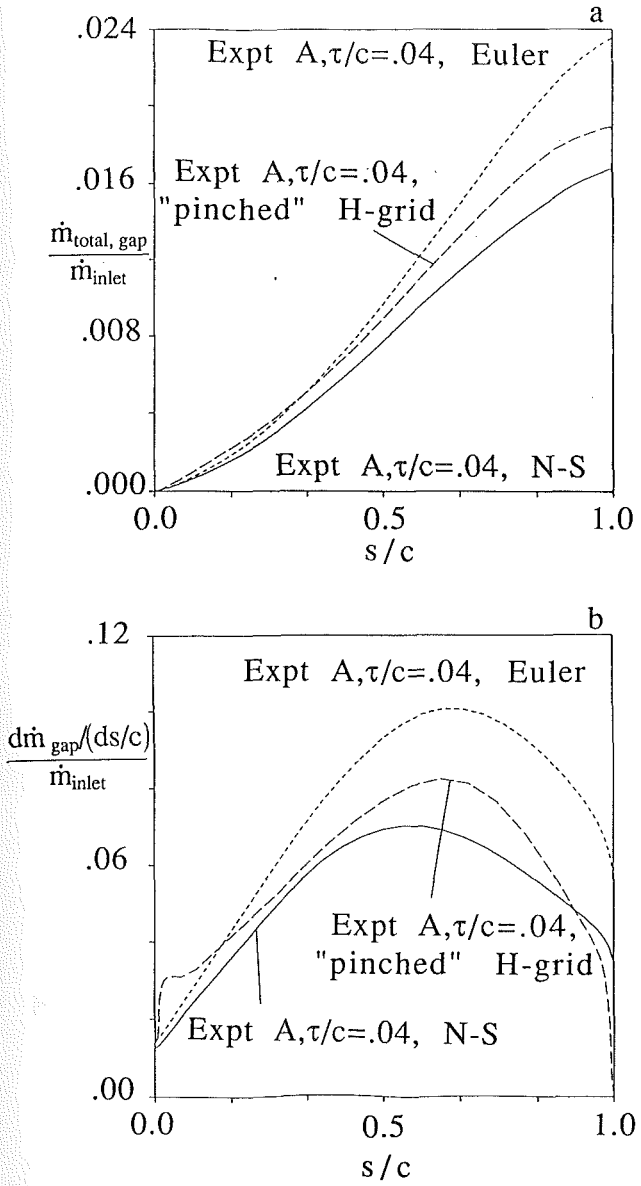

Fig. 18 Comparison of predicted mass flow rates through the gap for Experiment A using Euler, Navier-Stokes with an embedded H-grid, and Navier-Stokes with a "pinched" standard H-grid; (*a*) accumulated mass flow through the gap; (*b*) variation of incremental mass flow rate through the gap with chord

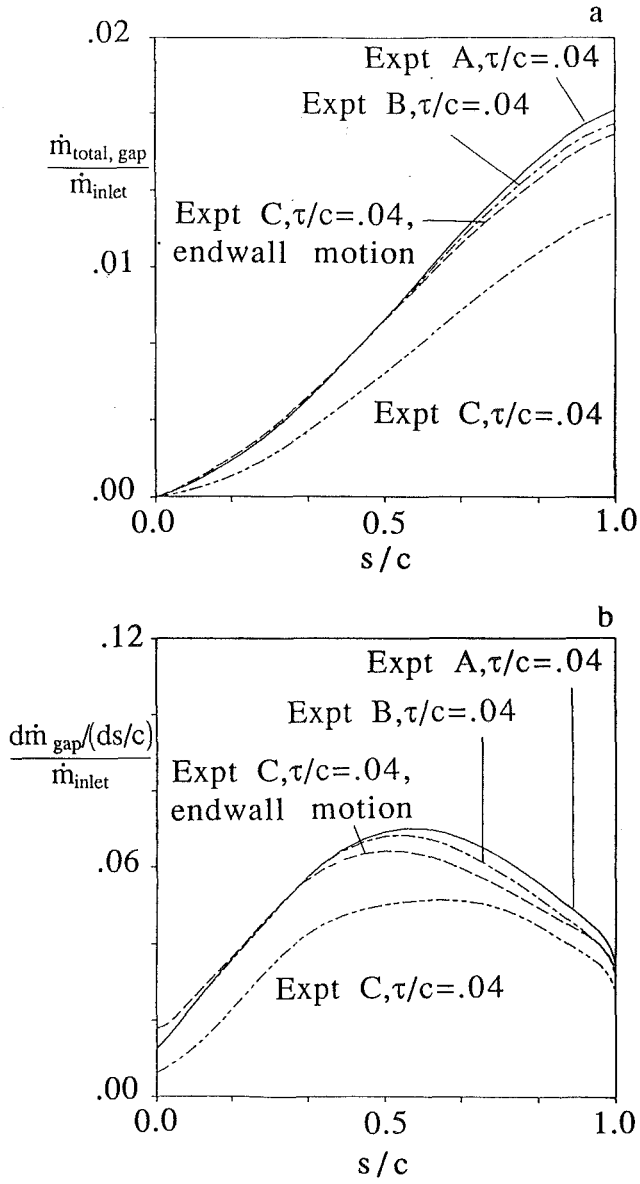

Fig. 19 Comparison of predicted mass flow rates through the gap for Experiment A with τ/c = 0.04, Experiment B with τ/c = 0.04, Experiment C with τ/c = 0.04, and Experiment C with τ/c = 0.04 and simulated endwall rotation; (*a*) accumulated mass flow through the gap, (*b*) variation of incremental mass flow rate through the gap with chord

what, but, as discussed above, its pitchwise location is seen to have been restricted to the suction side of the wake by the secondary motion.

Conclusion

A series of computational simulations of tip clearance flow in a compressor cascade has been undertaken using a Navier-Stokes/Euler code that can accommodate a grid topology that explicitly resolves the flow in the tip gap region. The following observations and conclusions apply:

1 The inviscid analysis provided qualitative representation of some of the important physical phenomena in a compressor cascade flow with tip clearance, including blade unloading due to the formation of a tip clearance vortex. The Navier-Stokes simulation was seen to provide better agreement with the experimental data in predicting vortex trajectory and strength, and is presumed to provide more accurate tip gap mass flow rate predictions.

2 Additional results were presented that suggest that a "pinched" standard **H**-grid topology can provide good engineering approximation in viscous flow computations with tip clearance. However, significant discrepancy in predicted tip gap mass flow rate was observed between solutions that incorporated the two topologies.

3 The embedded **H**-grid Navier-Stokes procedure was shown to provide good representation of the dominant physical mechanisms in turbomachinery flows with tip clearance, including the strength and trajectory of the tip clearance vortex, blade loading phenomena including lift retained at the tip, and the interaction of passage secondary flow and tip clearance flow. This was evidenced by comparison of the results of several parametric investigations with available experimental measurements of flow angle, blade loading, and dynamic head in the cascade investigated.

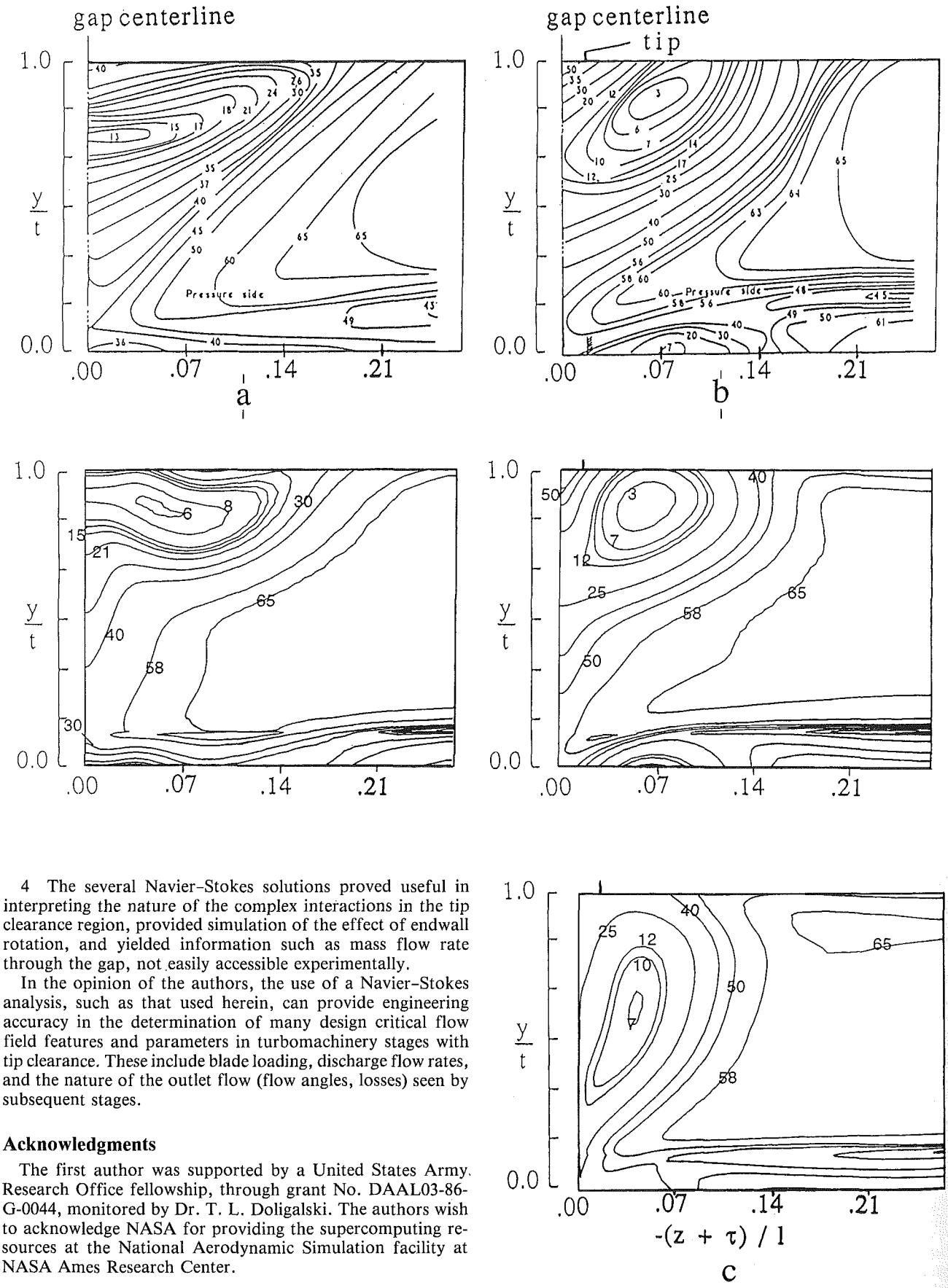

4 The several Navier–Stokes solutions proved useful in interpreting the nature of the complex interactions in the tip clearance region, provided simulation of the effect of endwall rotation, and yielded information such as mass flow rate through the gap, not easily accessible experimentally.

In the opinion of the authors, the use of a Navier–Stokes analysis, such as that used herein, can provide engineering accuracy in the determination of many design critical flow field features and parameters in turbomachinery stages with tip clearance. These include blade loading, discharge flow rates, and the nature of the outlet flow (flow angles, losses) seen by subsequent stages.

Acknowledgments

The first author was supported by a United States Army Research Office fellowship, through grant No. DAAL03-86-G-0044, monitored by Dr. T. L. Doligalski. The authors wish to acknowledge NASA for providing the supercomputing resources at the National Aerodynamic Simulation facility at NASA Ames Research Center.

References

Bansod, P., and Rhie, C. M., 1990, "Computation of Flow Through a Centrifugal Impeller With Tip Leakage," AIAA Paper No. 90-2021.

Fig. 20 Comparison of measured and computed normalized dynamic pressure ($\rho q^2/2$, in percent of inlet dynamic head) contours at cascade outlet plane for (*a*) Experiment C, τ/c = 0.00; (*b*) Experiment C, τ/c = 0.04; (*c*) Experiment C, τ/c = 0.04, simulated endwall rotation

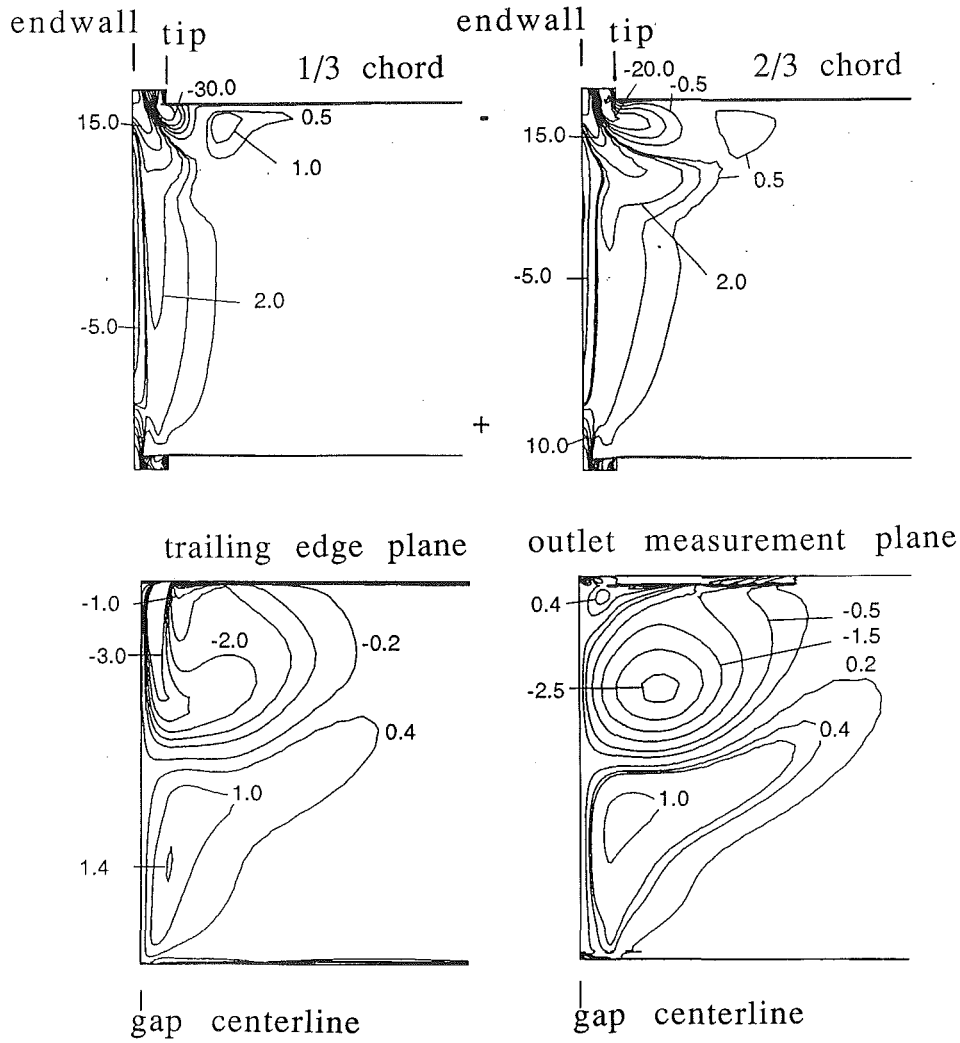

Fig. 21 Contours of $\omega \cdot q_{2D}$ normalized by $|q_{2D}|^2/c$) at four streamwise locations for Experiment C, τ/c = 0.04, no endwall motion; note that contour level increments are *not* constant

Basson, A. H., Kunz, R. F., and Lakshminarayana, B., 1991, "Grid Generation for Three-Dimensional Turbomachinery Geometries Including Tip Clearance," AIAA Paper No. 91-2360; *AIAA Journal of Propulsion and Power*, in press.

Beach, T. A., 1990, "An Interactive Grid Generation Procedure for Axial and Radial Flow Turbomachinery," AIAA Paper No. 90-0344.

Briley, W. R., Roscoe, D. V., Gibeling, H. J., Buggelin, R. C., Sabnis, J. S., Johnson, P. D., and Huber, F. W., 1991, "Computation of Flow Past a Turbine Blade With and Without Tip Clearance," ASME Paper No. 91-GT-56.

Chen, G. T., Greitzer, E. M., Tan, C. S., and Marble, F. E., 1991, "Similarity Analysis of Compressor Tip Clearance Flow Structure," ASME JOURNAL OF TURBOMACHINERY, Vol. 113, pp. 260–271.

Choi, D., and Knight, C. J., 1991, "A Study on H and O-H Grid Generation and Associated Flow Codes for Gas Turbine 3D Navier–Stokes Analyses," AIAA Paper No. 91-2365.

Cleak, J. G. E., and Gregory-Smith, D. G., 1992, "Turbulence Modeling for Secondary Flow Prediction in a Turbine Cascade," ASME JOURNAL OF TURBOMACHINERY, Vol. 114, pp. 590–598.

Hah, C., and Reid, L., 1992, "A Viscous Flow Study of Shock-Boundary Layer Interaction, Radial Transport, and Wake Development in a Transonic Compressor," ASME JOURNAL OF TURBOMACHINERY, Vol. 114, pp. 538–547.

Hirsch, C., 1990, *Numerical Computation of Internal and External Flows*, Vol. 2, Wiley, pp. 395–401.

Kunz, R. F., and Lakshminarayana, B., 1992, "Three-Dimensional Navier–Stokes Computation of Turbomachinery Flows Using an Explicit Numerical Procedure and a Coupled k–ϵ Turbulence Model," ASME JOURNAL OF TURBOMACHINERY, Vol. 114, pp. 627–642.

Lakshminarayana, B., and Horlock, J. H., 1965, "Leakage and Secondary Flows in Compressor Cascades," British Aeronautical Research Council (ARC) Report, Reports & Memoranda #3483.

Lakshminarayana, B., 1970, "Methods of Predicting the Tip Clearance Effects in Axial Flow Turbomachinery," ASME *Journal of Basic Engineering*, Vol. 92, p. 467.

Liu, J. S., Minkkinen, G., and Bozzola, R., 1991, "Analytical and Experimental Determination of Tip Clearance Effects in a High Work Turbine Rotor," ASME Paper No. 91-GT-197.

Moore, J., and Moore, J. G., 1989, "Shock Capturing and Loss Prediction for Transonic Turbine Blades Using a Pressure Correction Method," ISABE Paper No. 89-7017.

Moore, J., and Tilton, J. S., 1988, "Tip Leakage Flow in a Linear Turbine Cascade," ASME JOURNAL OF TURBOMACHINERY, Vol. 110, pp. 18–26.

Rai, M. M., 1989, "Three-Dimensional Navier–Stokes Simulations of Turbine Rotor-Stator Interaction: Part I—Methodology," *AIAA Journal of Propulsion*, Vol. 5, No. 3, May–June.

Rains, D. A., 1954, "Tip Clearance Flows in Axial Flow Compressors and Pumps," California Institute of Technology, Hydrodynamics and Mechanical Engineering Laboratories, Report No. 5.

Storer, J. A., and Cumpsty, N. A., 1991, "Tip Leakage Flow in Axial Compressors," ASME JOURNAL OF TURBOMACHINERY, Vol. 113, pp. 252–259.

Watanabe, T., Kanazawa, I., Nozaki, O., and Tamura, A., 1991, "A Numerical Analysis of the Flow Passing Through a Cascade With Tip Clearance," *JSME International Journal*, Series II, Vol. 34, No. 2, p. 134.

Yaras, M. I., and Sjolander, S. A., 1992, "Effects of Simulated Rotation on Tip Leakage in a Planar Cascade of Turbine Blades: Part I—Tip Gap Flow," ASME JOURNAL OF TURBOMACHINERY, Vol. 114, pp. 652–659.

Yaras, M. I., Sjolander, S. A., and Kind, R. J., 1992, "Effects of Simulated Rotation on Tip Leakage in a Planar Cascade of Turbine Blades: Part II—Downstream Flow Field and Blade Loading," ASME JOURNAL OF TURBOMACHINERY, Vol. 114, pp. 660–667.

Measurement of the Three-Dimensional Tip Region Flow Field in an Axial Compressor

R. C. Stauter
United Technologies Research Center,
East Hartford, CT 06108

A two-color, five-beam LDV system has been configured to make simultaneous three-component velocity measurements of the flow field in a two-stage axial compressor model. The system has been used to make time-resolved measurements both between compressor blade rows and within the rotating blade passages in an axial compressor. The data show the nature and behavior of the complex, three-dimensional flow phenomena present in the tip region of a compressor as they convect downstream. In particular, the nature of the tip leakage vortex is apparent, being manifested by high blockage as well as the expected vortical motion. The data indicate that the radial flows associated with the tip leakage vortex begin to decrease while within the rotor passage, and that they temporarily increase aft of the passage.

Introduction

The flow field within the airfoil rows of a multistage axial compressor is influenced by many different aerodynamic phenomena, both inviscid and viscous, interacting in a very complex fashion. One very significant phenomenon is the leakage flow through the finite clearance between the rotating blade tip and the stationary tip casing shroud. Not only does the leakage flow represent a loss in the airfoil performance in its tip region; it also induces a significant vortex that forms near the suction side of each airfoil in the tip region of the blade passage. The presence of the tip leakage vortex (TLV) has very significant implications for such things as the mixing behavior, blockage, unsteady loading on subsequent airfoil rows, etc. Furthermore, it has recently been postulated by Adamczyk et al. (1993) on the basis of a numerical experiment, that the behavior of the TLV plays a key role in the onset of compressor stall.

Thus, because of the significant and generally detrimental effect due to the presence of tip leakage flows and vortices, this subject has been the focus of a number of research efforts. A review of many of these studies is given by Peacock (1981, 1983). Considering that every turbomachine must have some form of tip clearance, Peacock concluded that relatively little research has been done specifically addressing tip clearance phenomena up to that time, that much of the research has been done on a piecemeal basis, and that much work remained to be done for an adequate understanding to be achieved.

Part of the problem is the difficulty involved in making the measurements required for a detailed understanding of both the flow through the tip clearance of a rotor blade, and the flow disturbance that results in the passage, namely the tip leakage vortex. The presence of the TLV reveals itself as a region of high total pressure loss as well as a region of vortical fluid motion. Many researchers have used probe methods to map out the flow field along rotor exit planes (e.g., Dring et al., 1982, 1983). However, probes are intrusive and have somewhat limited utility in making measurements inside blade passages or within the blade clearance. Probes are also relatively difficult to scan circumferentially and axially at the same time, making it difficult to track various phenomena as they develop in the throughflow direction.

Inoue et al. (1986) made detailed hot-wire measurements downstream of an isolated rotor to determine the three-dimensional exit flow field as a function of varying tip gap. This work was extended by Inoue and Kuroumaru (1989) with a hot wire probing into the tip clearance itself to make three-component measurements of the clearance jet. In this way, the structure of the tip leakage flow in the clearance, and the structure and trajectory of the developing TLV within the passage very near the tip casing were mapped out and correlated with exit plane surveys.

Storer and Cumpsty (1991) used a flattened pitot probe to measure the jet in the tip clearance of airfoils mounted in a linear cascade and compared the data to a Navier–Stokes solver. Their work demonstrated that the static pressure near the end of the blade controls the distribution of flow through the tip clearance.

Moyle et al. (1992) used an array of high-response pressure sensors mounted over the rotor to measure and track the TLV-caused pressure disturbance through the rotor passage. Their results suggest that the relative blade-to-wall motion found in a rotor plays an important role in controlling the tip clearance leakage flow.

Murthy and Lakshminarayana (1986) used a laser-Doppler velocimeter (LDV) to make two-component measurements of the tip region flow field within and aft of an axial compressor blade passage. They were able to detect and track the TLV

Contributed by the International Gas Turbine Institute and presented at the 37th International Gas Turbine and Aeroengine Congress and Exposition, Cologne, Germany, June 1-4,1992. Manuscript received by the International Gas Turbine Institute February 20, 1992. Paper No. 92-GT-211. Associate Technical Editor: L. S. Langston.

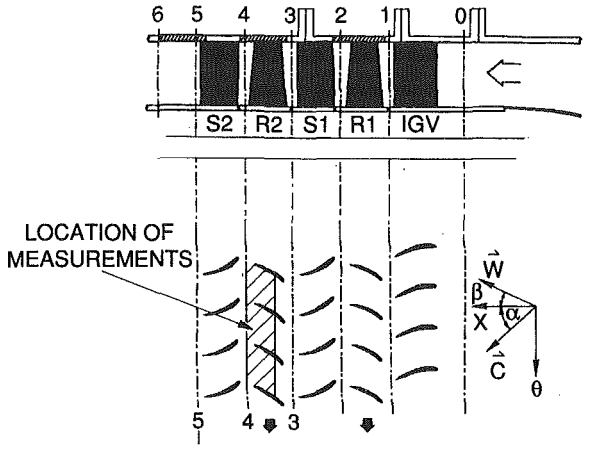

Fig. 1 UTRC Large-Scale Rotating Rig flow path

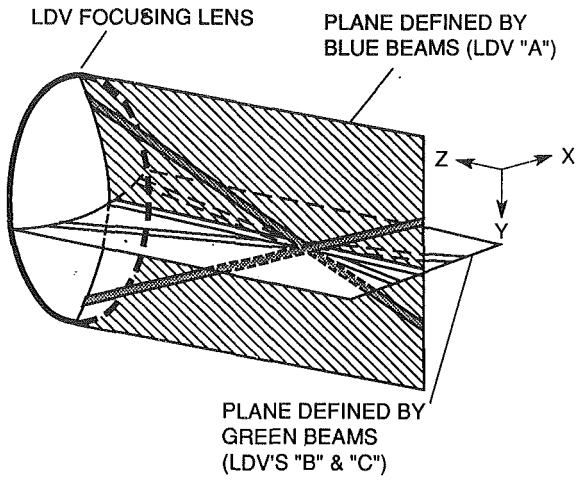

Fig. 2 Three-component LDV five-beam configuration

flow disturbances through the passage. Also, Lakshminarayana and Murthy (1988) made total pressure surveys with a probe in the rotating frame in conjunction with the LDV measurements both within and aft of a compressor rotor. In this way, they were able to correlate the pressure field and velocity field effects of the TLV.

Thus, experimental investigations of tip clearance phenomena have been made with surface pressures, with pressures and three-component velocities from probes having the limitations mentioned above, and with two-component laser velocimetry measurements. The TLV is fundamentally three dimensional in character, and measurements of the three-dimensional flow field aft of, and especially within, a rotating blade passage have been difficult to achieve. This paper describes a two-color, three-component LDV system and the results from its application to the measurement of the tip region flow field within and aft of a compressor blade row.

Experimental Facility

The experiment was conducted using a two-stage axial compressor model installed in the United Technologies Research Center Large-Scale Rotating Rig 2 (LSRR2). The two-stage model has previously been extensively studied with pneumatic pressure instrumentation including full-span airfoil pressure distributions and downstream transverse measurements for both the stators and the rotors, and with surface flow visualization. In addition, a series of two-component LDV circumferential traverses has been performed at midspan between the second rotor and the second stator and aft of the second stator. Hence, the LSRR2 is well documented and there exists a large database (Dring et al., 1982, 1983; Joslyn and Dring 1985; Stauter et al. 1991) with which to reference the current experiment.

The inlet flow to the LSRR2 is drawn from ambient air and the flow field throughout the facility is essentially incompressible. The two-stage compressor model has a 5 ft (1.52 m) tip diameter and a hub/tip ratio of 0.8. The midspan wheel speed (at $r/R = 0.9$) is $U_m = 153$ f/s (46.7 m/s) and the nominal design flow coefficient is $C_x/U_m = 0.510$. The flow path, depicted in Fig. 1, consists of a row of inlet guide vanes (IGV) followed by two similar stages: Rotor 1, Stator 1, Rotor 2, and Stator 2. The only difference between the stages is that the Rotor 1 stagger angle is closed 3 deg more than that of Rotor 2. The IGV, rotor, and stator rows each consist of 44 airfoils.

Instrumentation

The objective of the current work was to make detailed flow field measurements in the tip region to characterize the vortical flows induced by the compressor blade tip clearance. It is well known that the flow field in the tip region of an axial compressor is highly three dimensional with significant gradients (temporal and spatial) within tight physical confines. It is important that the instrumentation being utilized be capable of resolving the relevant phenomena without unduly affecting them. The laser-Doppler velocimeter (LDV) technique enables the instantaneous, nonintrusive measurement of local flow velocities within a relatively small measurement volume. Turbomachinery applications of one and two-component LDV systems are relatively common with the axial and tangential velocities being the components most typically measured. However, because of the inherent three dimensionality of turbomachine flow fields, a method of measuring the complete velocity vector has long been desired. Chesnakas and Dancey (1990) describe three-component LDV measurements in an axial compressor, but in general, such data from turbomachinery flow fields are quite scarce. The current measurement technique uses a two-color, three-component system to make time-resolved measurements of the three-dimensional velocity vector at specified locations within the LSRR2 flow field.

In the optical configuration used in the current experiment, two blue (488 nm) and three green (514.5 nm) beams are oriented so as to define two orthogonal planes, as shown in Fig. 2. The beam arrangement is similar to that of a conventional

Nomenclature

A, B, C = designating LDV channels
B_x = airfoil axial chord
C = velocity in absolute frame
C_p = pressure coefficient
LE = leading edge
PS = pressure surface
SS = suction surface
R = tip radius
TE = trailing edge
TLV = tip leakage vortex
U_m = rotor blade speed at midspan
V = individual sample velocity
W = velocity in relative frame
x, r, Θ = rig cylindrical coordinate system
x, y, z = local Cartesian coordinate system for LDV
α = absolute frame flow angle (from axial)
β = relative frame flow angle (from axial)
β' = viewing projection angle
ΔC_r = $C_{r,\max} - C_{r,\min}$ at a given span location
ϕ = LDV beam crossing half-angle
Φ = flow coefficient

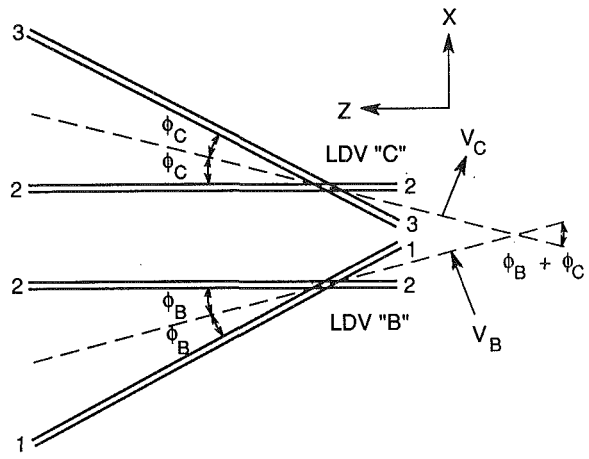

Fig. 3 Single color (green), two-component LDV beam configuration

two-component LDV system with the addition of a center beam. The "y" velocity is measured directly by the blue beam arrangement since it is a conventional, single-channel LDV (LDV "A"). Frequency shifting is accomplished by a 40 MHz Bragg cell.

The green beam arrangement, shown in Fig. 3, can be regarded as two single-channel, dual-beam LDVs: LDV "B," which is comprised of beams 1 and 2, and LDV "C," which is madeup of beams 2 and 3. Both of these single-channel LDVs share the center beam, and both lie in the same plane. Channel separation between the "B" and "C" component is accomplished by frequency shifting beams 1 and 3 by different amounts. Beam 1 is shifted by -80 MHz and beam 3 is shifted by $+40$ MHz. Beam 2, the center beam, is unshifted. Thus, the signal frequency from LDV "B" is the Doppler frequency on a carrier of 80 MHz, while LDV "C" produces a Doppler frequency riding on a carrier of 40 MHz.

The signals are collected in backscatter by two photomultiplier tubes: one for the blue scattered light and one for the green. The blue signal is downshifted for an effective frequency shift of 10 MHz. The signals from LDV "B" and LDV "C" are separated by appropriate bandpass filtering,and then each is downmixed for effective frequency shifts of 10 MHz on each channel. The beam bisectors for LDV "B" and LDV "C", which in dual beam velocimetry are normal to the measured velocity component, are at angles ϕ_B and ϕ_C to the optical axis of the overall system, which is defined by the center beam. Thus, the velocities sensed by both LDV "B" and LDV "C" are in general composed of a transverse component (the "x" velocity, perpendicular to the center beam) and an on-axis component (the "z" velocity, parallel to the center beam). Each measured velocity, V_i, can be expressed as:

$$V_i = V_x \cos \phi_i \pm V_z \sin \phi_i \quad i = B, C \tag{1}$$

By arranging LDVs "B" and "C" such that ϕ_B and ϕ_C are equal, and by combining the measured "B" and "C" velocities, the orthogonal components of the velocity vector can be resolved as:

$$V_x = (V_B + V_C)/2 \cos \phi \tag{2}$$

$$V_y = V_A \tag{3}$$

$$V_z = (V_B - V_C)/2 \sin \phi \tag{4}$$

This five-beam configuration results in three coincident probe volumes. Since the two green probe volumes have identical crossing angles, their sizes are also identical. The probe volume characteristics are summarized in Table 1.

Error Analysis

As with all measurement techniques, LDV is subject to various error sources. A number of researchers have analyzed LDV errors sources and their effect on the measurements. Their works have been assembled and well summarized by Patrick (1985), focusing on conventional dual-beam velocimetry.

Table 1 Probe volume characteristics

Color	Half Angle ϕ degrees	Length mm	Diameter mm	Fringe Spacing μm
Green	3.966	0.844	0.0583	3.719
Blue	4.957	0.693	0.0554	2.824

The nonorthogonal measurement of velocity components leads to the coupling of measurement errors. Orloff and Snyder (1982) give a good general discussion of LDV coupling effects on individual error propagation. The essence of the problem results from the fact that V_z (typically a small number) is determined by taking the difference of two relatively large quantities, V_B and V_C, and dividing it by a small quantity. As implied by Eq. (4), reducing this error effect is dependent on making ϕ as large as possible. The magnitude of the beam crossing half-angle ϕ is dictated by the size of the access window to the flow, the required standoff distance, and realistically, the prohibitive cost of large-diameter optics. In this particular optical/electronic configuration, there is also a trade-off between maximizing ϕ and having adequate bandwidth to maintain the frequency separation between V_B and V_C.

As indicated by Table 1, the green half-angle was 3.966 deg. Thus, any error in V_B or V_C was multiplied by a factor of $1/2 \sin \phi$, or in this case, by 7.22. Conversely, the calculation of V_x results in reducing individual measurement errors by $1/2 \cos \phi$, or by nearly one half. These effects present themselves most notably in the determination of V_z as both systematic bias and random error.

The systematic bias occurs because the relatively small value of ϕ causes this optical configuration to be very sensitive to mis-alignment error. The derivation of Eqs. (2) and (4) requires that (1) ϕ_B and ϕ_C be equal and that (2) the three green beams be coplanar. In practice, these two independent requirements were satisified by carefully aligning a calibration jet perpendicular to the z axis with the jet flow in two different orientations to the beam plane, and making two independent adjustments to the center green beam in order to null V_z. A "zero" ensemble average value for V_z, which ranges in time (because of random effects and hardware thermal variations) over less than $\pm 0.0065 U_m$, was typically achieved. However, observations of the experimental data indicate that the systematic bias varied $\pm 0.016 U_m$ from day to day. This larger bias was monitored by making reference measurements aft of the rotor before and after each day's data run.

The random error is primarily due to counter processor digitization error and results in random uncertainly in each individual velocity measurement. A ± 1 count processor uncertainty leads to $\pm 0.029 U_m$ uncertainty in individual V_z for the velocity range of the experiment. While this effect tends to be canceled by calculating the ensemble average of a sample distribution, it does increase the uncertainty band around the mean. Furthermore, it may mask any turbulence effects in the calculation of the rms of V_z.

Experiment

The LSRR2 two-stage compressor model was operated at its design point of $\Phi = 0.51$. The Rotor 2 blade tip geometry was a simple, squared-off design. The tip clearances were nominally set at 1 percent of chord. The blade-to-blade variation caused the actual tip clearances to range from approximately 1 percent to 1.25 percent of chord. Furthermore, the particular LDV technique used requires that the access window be optically flat. The use of an optical flat to approximate the curved

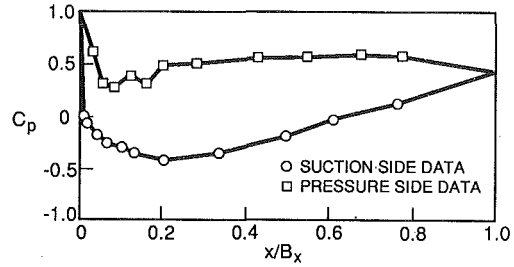

Fig. 4 Aerodynamic loading near rotor 2 blade tip (95.8 percent span)

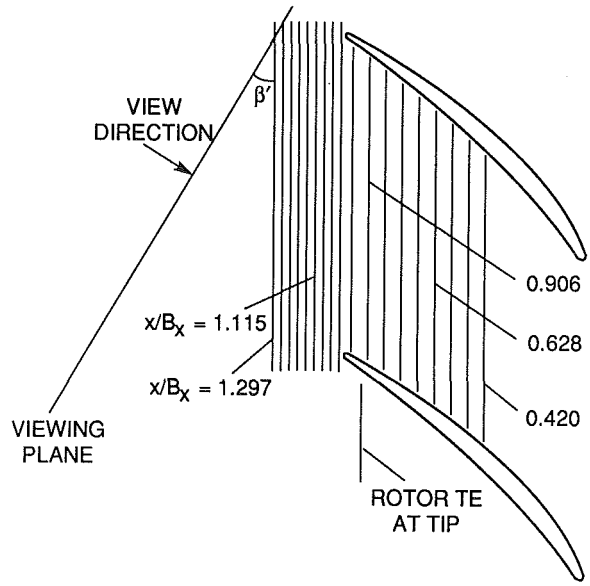

Fig. 5 Axial measurement stations

tip casing shroud produced a local, circumferential variation in the tip clearance of 0.0 to −0.4 percent of chord. The aerodynamic loading near the Rotor 2 tip (95.8 percent span) is presented in Fig. 4.

Data were acquired in radial scans at several axial locations within and aft of Rotor 2 at a circumferential position near the midgap position of the downstream stator row. At each of the axial measurement stations, the LDV probe volume was radially transversed from the tip casing (to within 98.4 percent span) to a span fraction of at least 83 percent. Span fraction is defined here as the fractional distance from the hub casing. At several of the measurement stations, the radial scan was continued to midspan. The axial stations where data were acquired are summarized in Table 2 and schematically depicted in Fig. 5.

A data sample considered of a velocity triplet (V_A, V_B, and V_C). Each velocity triplet was tagged with the instantaneous rotor position and sorted into one of 64 circumferential increments, or bins, across an average rotor blade passage. It is average in the sense that the data from all 44 rotor passages are overlaid into a single average passage; however, it is time-resolved in that all data retain their specific temporal relationship with the rotor blade. The tagging and sorting technique is further described by Stauter et al. (1991).

For this experiment, the LDV was oriented off-axis from the LSRR2, that is, the optical axis was not aligned with the radial axis, but rather it was offset so that r axis was separated from the local LDV z axis by 12 deg. Such an orientation permits closer approach to the access windows with the probe volume. At each measurement location, 20,000 data samples were acquired and sorted into the 64 bins across the "average" rotor passage, as indicated above. The acquired velocity triplets in each sorting bin were transformed into the local LDV co-

Table 2 Data acquisition axial stations

x/B_x Rotor 2 LE is 0.0	Span Fraction (from Hub Casing) at Maximum Immersion of LDV Probe Volume
0.420	0.500
0.495	0.833
0.559	0.833
0.628	0.500
0.698	0.833
0.767	0.833
0.837	0.833
0.906	0.500
0.976*	0.833
1.010	0.833
1.045	0.833
1.080	0.833
1.115	0.500
1.149	0.167
1.184	0.833
1.219	0.833
1.253	0.833
1.297	0.500

* Due to the taper of the rotor blade, this station is aft of the trailing edge in the tip region.

ordinate system (V_x, V_y, V_x) using Eqs. (2)-(4) and processed using the AEDC method (see Abernathy and Thompson, 1973) for eliminating spurious samples. The ensemble mean and rms for each bin were calculated and transformed to the LSRR2 coordinate system (C_x, C_r, C_Θ).

The reader is referred to Stauter et al. (1991) for a description of the technique for seeding the flow field. Briefly stated, plastic microspheres were used. The data were acquired with 0.9 and 1.25 μm particles, depending on availability.

Results

Three-component flow field velocity data have been acquired at the axial stations listed in Table 2. The following discussion presents an overview of the acquired data, focusing on the general nature of tip leakage vortex development and behavior. The present analysis has only begun to extract a small fraction of the available information. Considerable analysis remains.

To examine the development of the TLV qualitatively through and aft of the rotor passage, the velocity data are first presented at several of the axial stations with vector and contour plots across the rotor passage, starting at the far upstream location (42 percent of chord) and continuing downstream to 130 percent of chord. Figure 6(a, b, c) shows two vector plots and one contour plot for $x/B_x = 0.420$, well inside the passage. The vectors represent the velocity field in the rotor (relative) frame as projected onto a plane at a viewing angle β' as shown in Fig. 5. The contour plot represents the magnitude of the axial velocity component. These choices are further explained below. The vector and contour plots are bounded by the tip casing on the top, the suction surface of the rotor blade on the right, the pressure side on the left, and midspan on the bottom. Due to the orientation of the LDV optical axis relative to the blades, as described above, the flow region adjacent to the suction surface was never in the shadow region; hence, the flow field is mapped out up to and immediately adjacent to the suction surface while the region next to the pressure surface is shadowed and displays an increasing shadow region as the immersion of the probe volume increases. The index marks

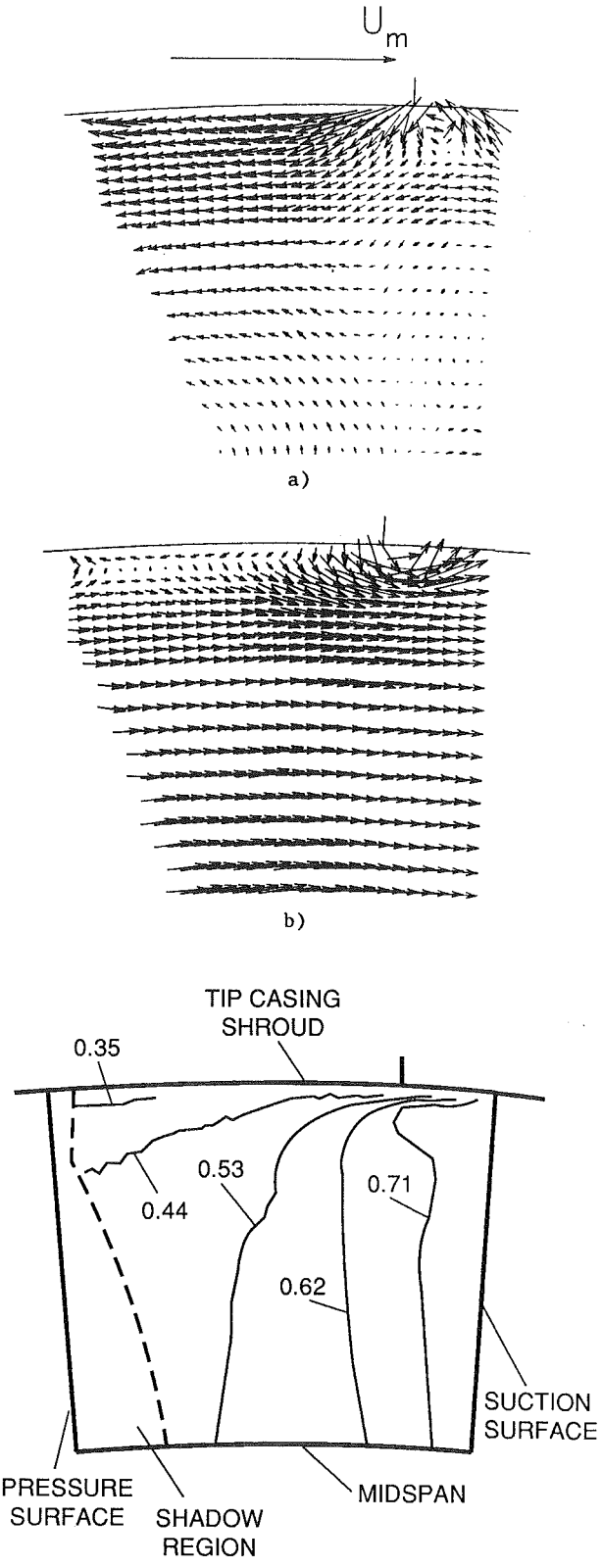

Fig. 6 At x/B_x = 0.420: (*a*) vector plot, β' = 41.4 deg (average β at midspan); (*b*) vector plot, β' = 57.1 deg (average β at $\Delta C_{r,max}$); (*c*) contour plot of axial velocity, C_x/U_m

seen on the tip casing profiles indicate the position, relative to the flow field, of the Rotor 2 midspan trailing edge.

One of the most significant effects of the TLV is the radial flow induced in the flow field. Such flows are believed to play an important role in the mixing process (e.g., Adkins and Smith, 1982). This is particularly important here as the TLV is generally adjacent to low-momentum endwall boundary layer fluid. Thus, one way to assess the qualitative effect of the TLV on the flow field is to compute the variation in the quantity ΔC_r for a given span location. This quantity, which is the difference between the maximum and minimum radial velocity, will be at a maximum at the span location that passes closest to the center of the vortex. This concept is used here to examine the behavior and effect of the TLV.

As indicated above, the vector plots are projections of the velocity field at a view angle of β'. To examine the overall secondary flow field at any given station, it would seen most natural to make the projection angle β' equal to the average midspan relative flow angle. This is the value of β' that is used in Fig, 6(*a*). However, in order to examine the flow in the tip region, specifically the flow in and around the TLV, an angle more representative of the average relative flow angle in the tip region is used so as to make the viewing angle more aligned with the tip region throughflow and, in particular, with the vortex core. The β' value chosen for this was the average relative flow angle at the span location of the vortex core which was taken to be the span location with the largest values of ΔC_r. This is the angle used for β' in Fig. 6(*b*). With either viewing angle, the vector plot displays a two-dimensional picture of the secondary flow. The component of velocity normal to the viewing plane would seem to be the natural choice for plotting as contours in order to complete the presentation of the velocity field. However, the value of β', as defined, varies with axial position. This, as well as the flow diffusion through the passage, cause the passage average of the velocity normal to the local viewing plane to vary with axial location. The changing average level of the normal velocity makes it difficult to examine the development of flow blockage associated with the TLV. Thus, the axial velocity was chosen for presentation with contour plots, as the pseudo-third-component, because its passage average is constant with axial distance and its variations are more directly related to the flow blockage. Thus, the axial velocity is presented in Fig. 6(*c*).

It is seen that, in general, the vector plots show little radial velocity at this location (x/B_x = 0.42) with the exception that near the suction surface at the tip casing, it is seen that a small region of vortical flow has formed. It is consistent with a flow pattern that would be formed by a tip leakage jet. It should be noted that the use of different projection angles changes the location of the apparent center of the TLV. The contour plot shows a small throughflow deficit at this location. It presents itself as a distortion of the cross-passage axial velocity gradient near the tip. However, at this location both the effect and extent of the tip leakage flow is quite small.

Figure 7 shows the vector and contour plots for x/B_x = 0.628. Vortical motions are seen over a larger part of the tip casing-suction surface corner region than they were at the upstream location in Fig. 6. The vortical motion does not appear as a vortex per se in Fig. 7(*a*); however, if the projection angle is increased to 51 deg, the average flow angle at the span location exhibiting the largest ΔC_r, the rollup of the vortex becomes more evident as seen in Fig. 7(*b*). The depth and extent of the deficit (Fig. 7(*c*)) have also significantly increased.

Figure 8 shows the vector and contour plots at x/B_x = 0.906. The depth and circumferential extent of the deficit have decreased somewhat, but the deficit seems to cover a greater radial extent. The vector plot (Fig. 8(*a*)) shows significant vortical motion, but the center of the vortex rollup is not readily apparent, even when viewed at the larger value of β' (Fig. 8(*b*)).

The flow field aft of the rotor trailing edge at x/B_x = 1.115 is displayed in Fig. 9. Compared with the previous axial location, the depth and both the circumferential and radial extent of the deficit have increased significantly. The vector plot (Fig. 9(*a*)) at the midspan angle projection clearly shows significant

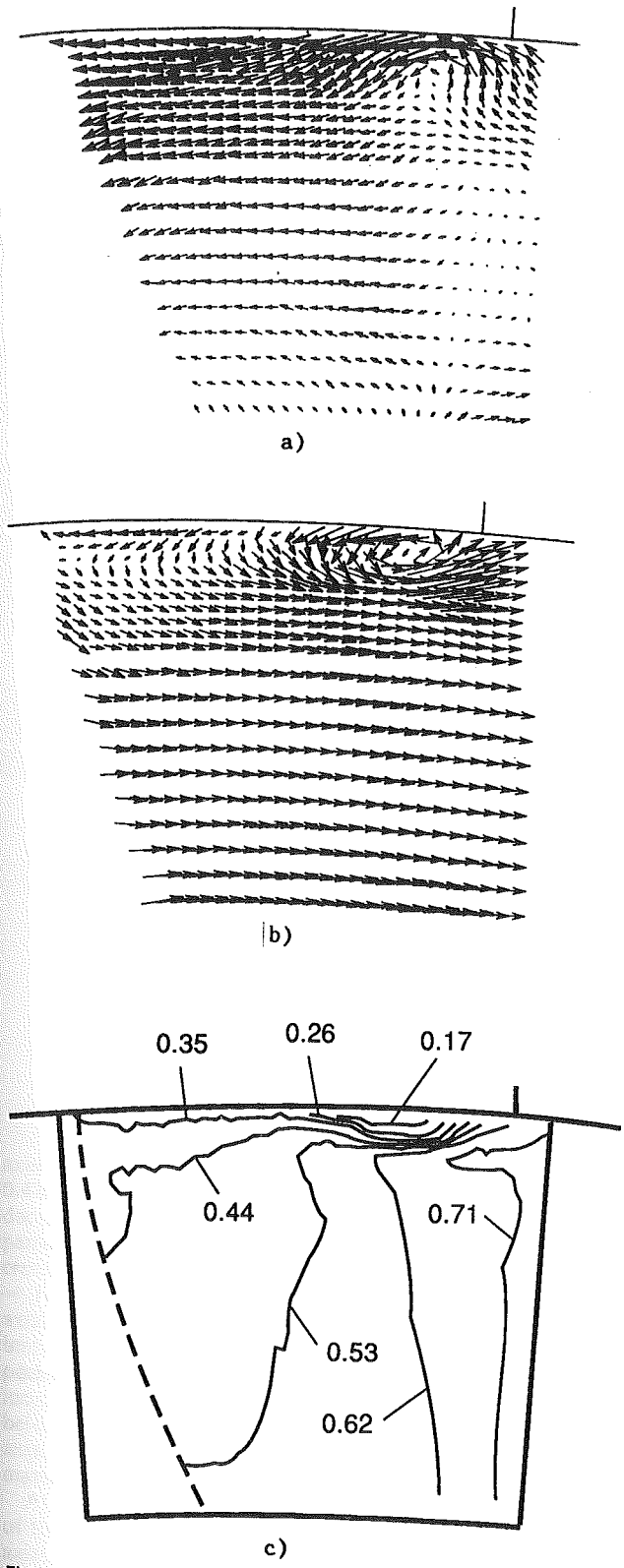

Fig. 7 At $x/B_x = 0.628$: (*a*) vector plot, $\beta' = 37.8$ deg (average β at midspan); (*b*) vector plot, $\beta' = 52.9$ deg (average β at $\Delta C_{r,\max}$); (*c*) contour plot of axial velocity, C_x/U_m

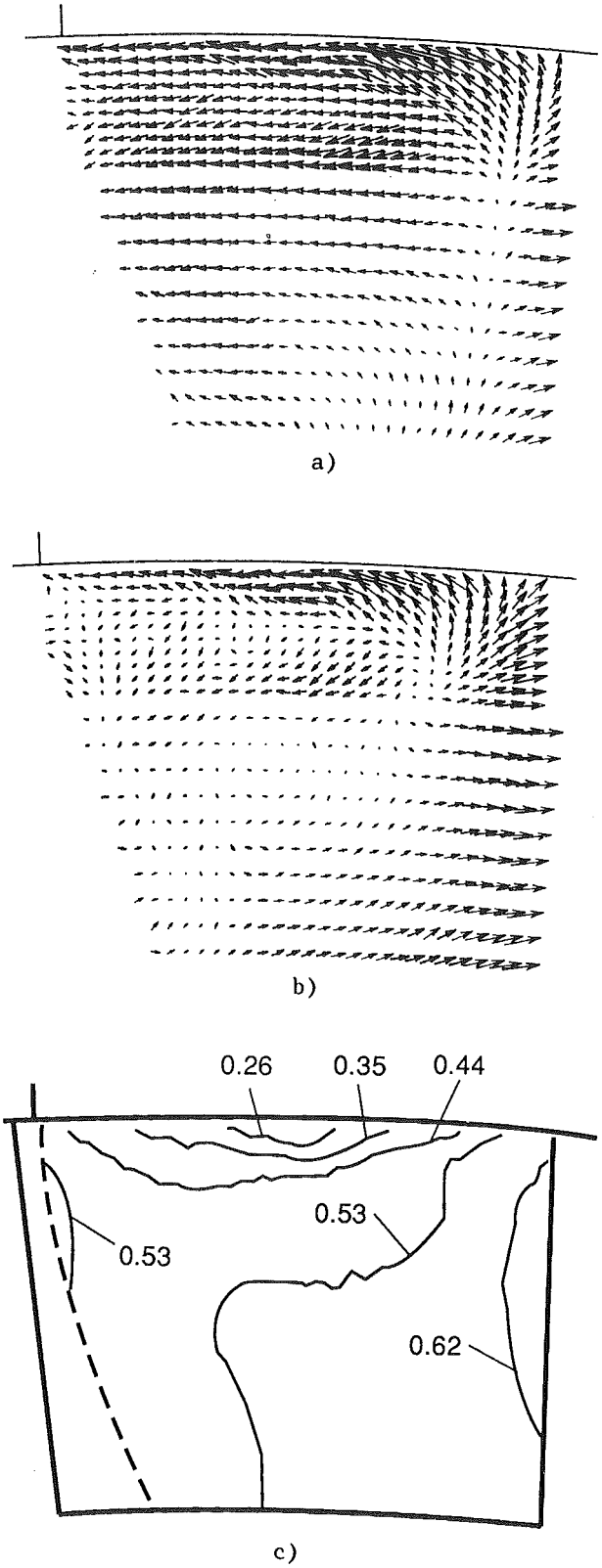

Fig. 8 At $x/B_x = 0.906$: (*a*) vector plot, $\beta' = 36.1$ deg (average β at midspan); (*b*) vector plot, $\beta' = 41.0$ deg (average β at $\Delta C_{r,\max}$); (*c*) contour plot of axial velocity, C_x/U_m

vortical flow; however, the center of the vortex rollup is more clearly evident when the tip region β' value is used (Fig. 9(*b*)). The vector plot viewed at an angle representative of the tip region flow angle clearly shows vortex rollup. The vector plot also shows significant radial outflow, especially near the suction surface side of the blade wake. It appears that this radial outflow may be feeding into and reinforcing the TLV, which seemed to be decaying at the $x/B_x = 0.906$ station.

Figure 10 presents the data at $x/B_x = 1.297$. The depth and extent of the axial velocity deficit have decreased while the vector plots shows the flow dominated by radial outflow with

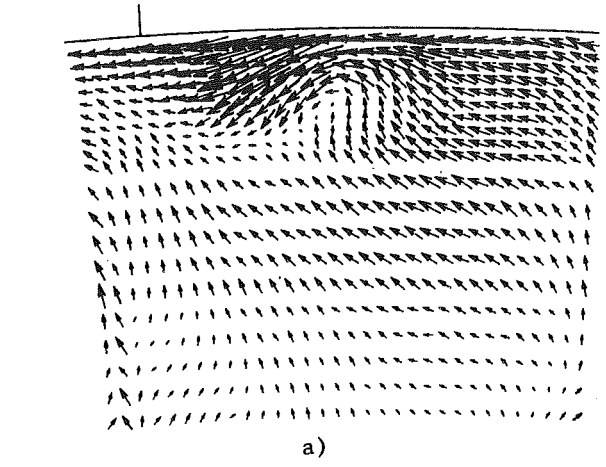

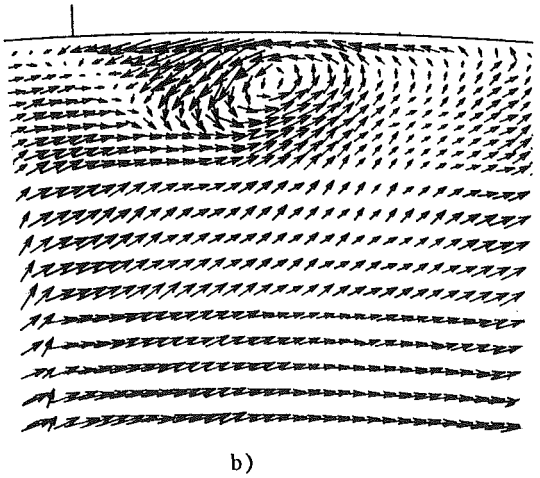

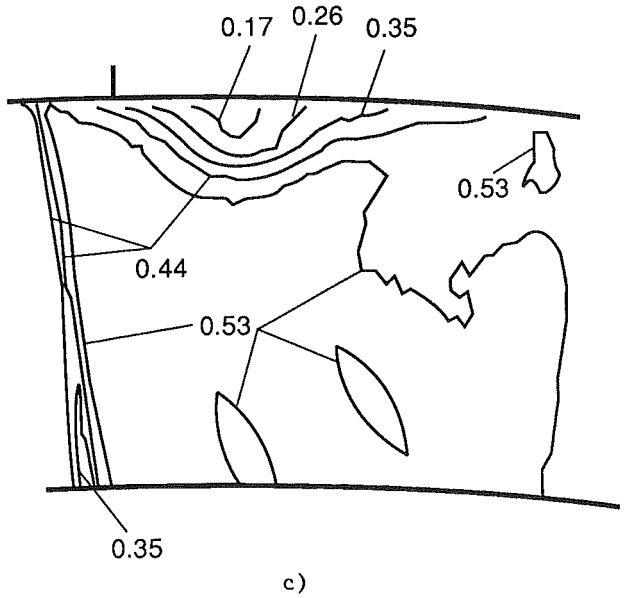

Fig. 9 At x/B_x = 1.115: (*a*) vector plot, β' = 36.1 deg (average β at midspan); (*b*) vector plot, β' = 45.6 deg (average β at $\Delta C_{r,\max}$); (*c*) contour plot of axial velocity, C_x/U_m

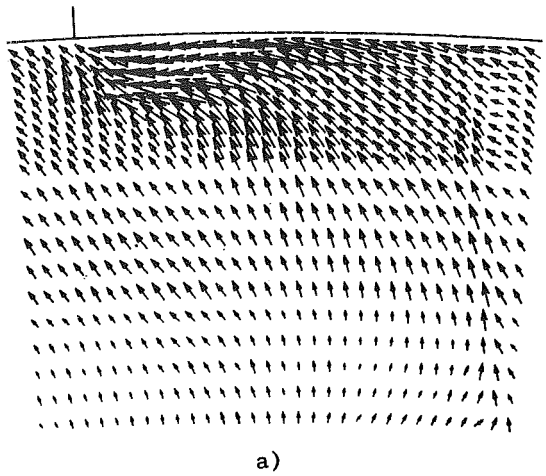

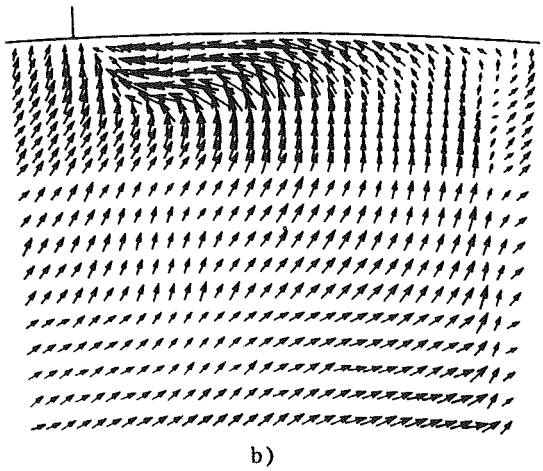

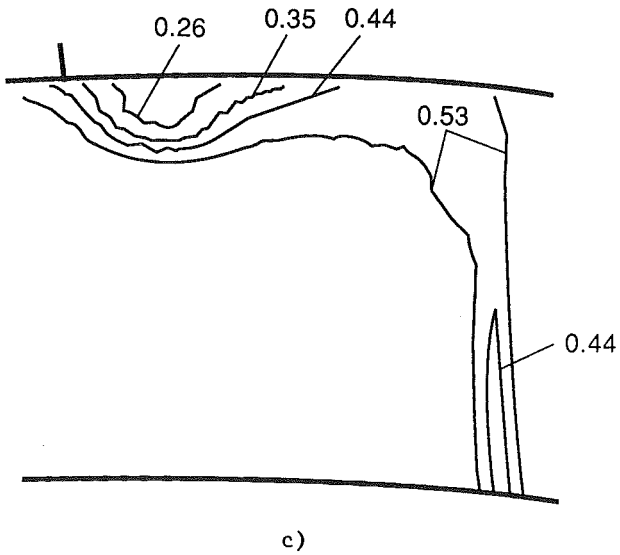

Fig. 10 At x/B_x = 1.297: (*a*) vector plot, β' = 33.5 deg (average β at midspan); (*b*) vector plot, β' = 39.1 deg (average β at $\Delta c_{r,\max}$); (*c*) contour plot of axial velocity, C_x/U_m

the exception of the deficit region. The radial outflow so dominates the secondary flow that the center of the vortex rollup is obscured.

One interesting aspect of the TLV suggested by the preceding plots is its apparent decay while still within the passage. This is in agreement with the findings of Lakshminarayana and Murthy (1988). Even more interesting and surprising is the subsequent increase in associated radial flows aft of the passage. In order to illustrate this variation as a function of the axial distance, the quantity $\Delta C_{r,\max}$ has been plotted at all the

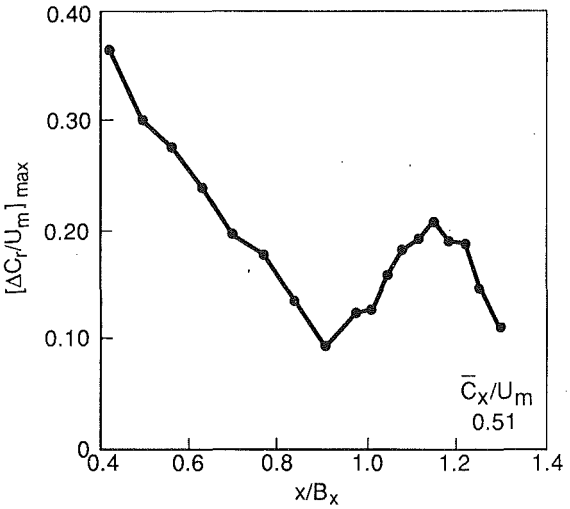

Fig. 11 Maximum $[\Delta C_r/U_m]$ versus axial location

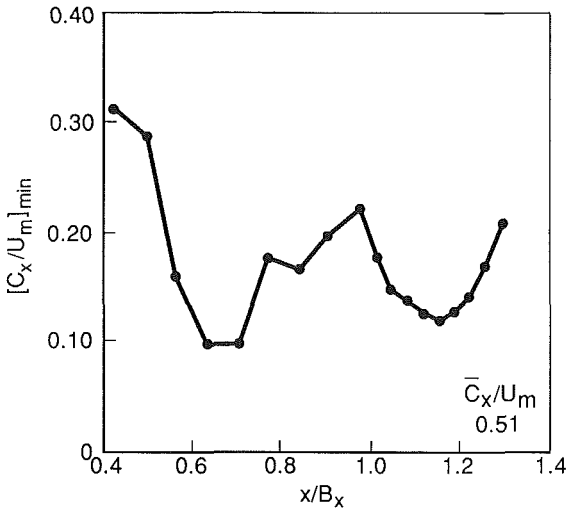

Fig. 12 Minimum $[C_x/U_m]$ versus axial location

axial stations in Fig. 11. At the far upstream station, x/B_x = 0.420, ΔC_r is at its largest value for this data set, and it steadily decreases through the passage. At the trailing edge of the passage, it has reached its minimum. However, it starts increasing aft of the passage, reaches a local maximum at x/B_x = 1.149, and then decreases again. The development of the axial velocity deficit can be characterized by plotting the minimum C_x in the endwall region against the axial distance as presented in Fig. 12. This figure shows the depth of the deficit increasing until about 75 percent chord within the passage before it starts to decrease. Aft of the passage, the maximum axial velocity deficit follows the increase and decrease of the maximum ΔC_r.

At all the axial stations discussed above, the apparent center of the vortex rollup does not coincide with the center of the axial velocity deficit, but rather, the maximum axial velocity deficit is generally closer to the tip casing and toward the pressure surface. This does not change if the velocity component normal to the vector projection plane is used (which is more nearly the passage throughflow component). This is consistent with what is seen in the plots of Inoue et al. (1986) where both the secondary velocity and kinetic energy are mapped out at the exit field. One might expect that the low-energy flow would coalesce at the vortex core. However, in the case of the TLV, low-energy tip casing boundary layer fluid is being continually scraped off the endwall and carried into the passage. Thus, the side of the vortex that feeds such fluid into the passage coincides with the center of the axial deficit.

Summary and Conclusions

A five-beam, two-color LDV system has been developed and used to map out the tip region flow field in a two-stage axial compressor. Detailed measurements have been made both aft of the rotor passage as well as within the rotor passage. By using appropriate transformations, the secondary flow field, and in particular, the behavior of the tip leakage vortex (TLV), have been studied.

Using the maximum difference in radial velocity at any given span as a measure of the vortex effect on the flow field, it has been shown that the TLV is relatively small in extent and effect at the far upstream passage location, and that it decays through the passage until aft of the trailing edge, at which point the radial flows start increasing again, reaching a peak at 115 percent of chord, after which, they start decreasing again.

The axial velocity deficit is seen to be almost imperceptible at the far upstream station. It grows in extent and depth, but it also starts to decay before reaching the trailing edge of the rotor passage. Aft of the rotor passage, it again grows in strength and then begins to decrease, corresponding to the maximum ΔC_r of the TLV.

The center of the axial velocity deficit associated with the TLV does not coincide with the apparent center of the vortex rollup.

Acknowledgments

This work was supported by funding from the Pratt and Whitney Aircraft Group of United Technologies Corporation and by internal corporate funding.

References

Abernathy, R. B., and Thompson, J. W., 1973, "Handbook—Uncertainty in Gas Turbine Measurements," Arnold Engineering Development Center, AEDC-TC-73-5, Appendix D.

Adamczyk, J. J., Celestina, M. L., and Greitzer, E. M., 1993, "The Role of Tip Clearance in High-Speed Fan Stall," ASME JOURNAL OF TURBOMACHINERY, Vol. 115, pp. 28–39.

Adkins, G. G., and Smith, L. H., Jr., 1982, "Spanwise Mixing in Axial-Flow Turbomachines," ASME *Journal of Engineering for Power*, Vol. 104, pp. 97–110.

Chesnakas, C. J., and Dancey, C. L., 1990, "Three-Component LDA Measurements in an Axial-Flow Compressor," *Journal of Propulsion and Power*, Vol. 6, No. 4, pp. 474–481.

Dring, R. P., Joslyn, H. D., and Hardin, L. W., 1982, "An Investigation of Compressor Rotor Aerodynamics," ASME *Journal of Engineering for Power*, Vol. 104, No. 1, pp. 84–96.

Dring, R. P., Joslym H. D., and Wagner, J. H., 1983, "Compressor Rotor Aerodynamics," *Viscous Flow Effects in Turbomachines*, AGARD-CP-351, Paper No. 24, Copenhagen, Denmark.

Inoue, M., Kuroumaru, M., and Fukuhara, M., 1986, "Behavior of Tip Leakage Flow Behind an Axial Flow Compressor Rotor," ASME *Journal of Engineering for Gas Turbines and Power*, Vol. 108, pp. 7–13.

Inoue, M., and Kuroumaru, M., 1989, "Structure of Tip Clearance Flow in an Isolated Axial Compressor Rotor," ASME JOURNAL OF TURBOMACHINERY, Vol. 111, pp. 250–256.

Joslyn, H. D., and Dring, R. P., 1985, "Compressor Stator Aerodynamics," ASME *Journal of Engineering for Gas Turbines and Power*, Vol. 107, pp. 485–493.

Lakshminarayana, B., and Murthy, K. N. S., 1988, "Laser-Doppler Velocimeter Measurement of Annulus Wall Boundary Layer Development in a Compressor Rotor," ASME JOURNAL OF TURBOMACHINERY, Vol. 110, pp. 377–385.

Moyle, I. N., Walker, G. J., and Shreeve, R. P., 1992, "Stator-Averaged Rotor Blade-to-Blade Near-Wall Flow in a Multistage Axial Compressor With Tip Clearance Variation," ASME JOURNAL OF TURBOMACHINERY, Vol. 114, pp. 668–674.

Murthy, K. N. S., and Lakshminarayana, B., 1986, "Laser Doppler Velocimeter Measurement in the Tip Region of a Compressor Rotor," *AIAA Journal*, Vol. 24, No. 5, pp. 807–814.

Orloff, K. L., and Snyder, P. K., 1982, "Laser Doppler Anemometer Measurements Using Non-orthogonal Velocity Components: Error Estimates," *Journal of Applied Optics*, Vol. 21, No. 2, pp. 339–344.

Patrick, W. P., 1985, "Error Analysis for Benchmark Fluid Dynamic Ex-

periments, Part I: Error Analysis Methodology and the Quantification of Laser Velocimeter Error Sources," UTRC Report R85-151772.

Peacock, R. E., 1981, "Blade Tip Gap Effects in Turbomachines—A Review," Report No. NPS67-81-016, Naval Postgraduate School, Monterey, CA.

Peacock, R. E., 1983, "A Review of Turbomachinery Tip Gap Effects," *International Journal of Heat and Fluid Flow*, Vol. 4, Mar. 1983, pp. 3-16.

Stauter, R. C., Dring, R. P., and Carta, F. O., 1991, "Temporally and Spatially Resolved Flow in a Two-Stage Axial Compressor: Part 1—Experiment," ASME JOURNAL OF TURBOMACHINERY, Vol. 113, pp. 219-226.

Storer, J. A., and Cumpsty, N. A., 1991, "Tip Leakage Flow in Axial Compressors," ASME JOURNAL OF TURBOMACHINERY, Vol. 113, pp. 252-259.

periments, Part I: Error Analysis Methodology and the Quantification of Laser Velocimeter Error Sources," UTRC Report R85-151772.

Peacock, R. E., 1981, "Blade Tip Gap Effects in Turbomachines—A Review," Report No. NPS67-81-016, Naval Postgraduate School, Monterey, CA.

Peacock, R. E., 1983, "A Review of Turbomachinery Tip Gap Effects," *International Journal of Heat and Fluid Flow*, Vol. 4, Mar. 1983, pp. 3-16.

Stauter, R. C., Dring, R. P., and Carta, F. O., 1991, "Temporally and Spatially Resolved Flow in a Two-Stage Axial Compressor: Part 1—Experiment," ASME JOURNAL OF TURBOMACHINERY, Vol. 113, pp. 219-226.

Storer, J. A., and Cumpsty, N. A., 1991, "Tip Leakage Flow in Axial Compressors," ASME JOURNAL OF TURBOMACHINERY, Vol. 113, pp. 252-259.

DISCUSSION

N. A. Cumpsty[1]

Although it has been known for at least forty years that the tip region is of particular importance for compressor performance, there are still many aspects that we do not understand. Optical methods of velocity measurement are particularly suited to the investigation of rotor tip flows and the present paper is a welcome addition.

I do however have some points that I am not clear about and would like some clarification. For example, the trend in the ΔC_r shown in Fig. 11 is puzzling. So too is the absence of an apparently clear vortex at $x/B_x = 0.906$, while it returns it full force at $x/B_x = 1.115$. Does the author have any explanation? Can we be entirely sure that it is not a problem associated with the measurement technique?

In connection with the experimental technique, I am concerned with the widely distributed radial velocities shown in Figs. 10(a) and 10(b). A rough estimate suggests radial velocities of about 6 percent of mean blade speed over most of the domain. Over most of the region the variation of the vectors in the θ-directon is small, so the continuity equation indicates that radial gradients in radial velocity ($\partial C_r/\partial r$) would be compatible with equal axial velocity gradients ($\partial C_x/\partial$x). The results show almost uniform radial velocity and this does suggest measurement error. Can the author comment on this and perhaps carry out some check on the magnitudes?

[1]Whittle Laboratory, Cambridge University, Cambridge, United Kingdom.

Author's Closure

The author would like to thank Professor Cumpsty for raising two very valid issues regarding the data presented in the paper.

The first issue, the on-again, off-again behavior of the tip leakage vortex, is admittedly unexpected and difficult to explain. This flow field is currently being studied by CFD, but results are not yet available. The behavior was first strongly suggested by preliminary data acquired at just a few of the axial locations. This unusual phenomenon was noted and a much more detailed set of data was acquired nearly a year later using a procedure designed to eliminate radial velocity measurement errors and other such problems from being blamed. In short, the sequence in which the data were acquired was radial plane by radial plane rather than by axial plane. This was used to insure that the vortex behavior variations from axial plane to axial plane were not caused by any temporal variations in the LDV alignment (or in any other thing). This eliminates the possibility of measurement error from being responsible for the phenomenon.

The second issue raised was whether or not the apparent overall level of outward radial velocity, particularly in the aft measurement planes, without any apparent axial plane acceleration violated the continuity condition. Integrating the axial velocity over the outboard region of each axial plane revealed that this flow field is indeed accelerating in the aft region. A continuity check with a series of control volumes of varying axial extent indicated that the continuity condition is satisfied. Residuals calculated from the control volume mass balances were consistent with or better than the systematic bias errors described in the Error Analysis section.

Radial Transport and Momentum Exchange in an Axial Compressor

R. P. Dring
United Technologies Research Center,
East Hartford, CT 06108

The objective of this work was to examine radial transport in axial compressors from two perspectives. The first was to compare the mixing coefficient based on a secondary flow model (using measured radial velocities) with that based on a turbulent diffusion model. The second was to use measured airfoil pressure forces and momentum changes to assess the validity of the assumption of diffusive radial transport, which is common to both models. These examinations were carried out at both design and off-design conditions as well as for two rotor tip clearances. In general it was seen that radial mixing was strongest near the hub and that it increased dramatically at near-stall conditions. It was also seen that radial transport could cause large differences (≈ 100 percent) between the force on an airfoil and the change in momentum across the airfoil at the same spanwise location.

Introduction

The compressor designer has at his or her disposal analytical resources that have led to a very high level in every measure of compressor performance. However, much of this improvement has occurred in the core flow region where the flow is often essentially two dimensional. There are still numerous problems associated with the three-dimensional nature of the flow. For this reason it seems likely that gaining control of the three dimensional features of the flow will produce the next generation of improvements.

The computational community is energetically pursuing this goal, but the current cost of three-dimensional inviscid and viscous flow solvers suggests that the historical quasi-two-dimensional design approach will be in use for some time to come, albeit with better modeling of the three-dimensional features of the flow.

Throughflow analysis is one such two-dimensional design tool and it is at the heart of the compressor design process. It is an essentially axisymmetric model of the flow in a compressor. It is used to predict the spanwise distributions of the flow parameters within and between the airfoil rows. Most importantly, it defines the velocity triangles for which the airfoil contour at each span location must be designed.

Throughflow analysis normally does not account for flow crossing the meridional stream surfaces. These radial transport effects arise both from deterministic, three-dimensional secondary flows (Adkins and Smith, 1982) and from turbulent diffusion (Gallimore and Cumpsty, 1986). With the inclusion of these effects, throughflow analysis can, to some degree, account for the impact that radial transport has on velocity triangles and on airfoil design.

Adkins and Smith (1982) devised a method to estimate radial mixing due to deterministic convection caused by mainstream non-free-vortex flow, endwall boundary layers, airfoil end clearances, airfoil end shrouding, and airfoil boundary layer and wake centrifugation. The mixing phenomenon was modeled as a diffusion process with the mixing coefficient related to the estimated radial velocities. "The nature of the assumption employed restricts the method to design-point-type applications for which losses are relatively small and significant regions of separated flow are not present."

Gallimore and Cumpsty (1986) took a different view of the mechanism causing radial mixing, namely that is was dominated by turbulent diffusion and not by deterministic secondary flows. This view was supported by their measurements of trace gas diffusion. Like Adkins and Smith, they also modeled the mixing phenomenon as a diffusion process; however, their mixing coefficient was based on turbulent transport.

Since the publication of these two papers there has been considerable effort expended examining the two approaches. Wisler et al. (1987) acquired trace gas and hot-wire data indicating that "both secondary flows and turbulent diffusion play important roles depending on (spanwise, circumferential, and axial) location...and loading level." De Ruyck and Hirsch (1988) presented a computational method including both convective and turbulent transport effects. They determined that when radial velocities exceeded about 5 percent of the main velocity, convection dominated turbulent diffusion. Leylek and Wisler (1991) used extensive numerical modeling (three-dimensional Navier–Stokes solutions) at design and off-design conditions, compared it with trace gas data, and showed that both secondary flow and turbulent diffusion play important roles. Li and Cumpsty (1991) examined the impact of anisotropic inhomogeneous turbulence. Goto (1992) used both hot-wire anemometry and trace gas testing to examine the effects of rotor tip clearance. Wennerstrom (1991) presented a review of predictive efforts for transport phenomena in axial compressors in general, and of the Adkins and Smith and Gallimore and Cumpsty models in particular.

The present paper describes the results of an analysis of an extensive data base acquired for two compressors in the UTRC large-scale rotating rig (5 ft dia). One is an isolated rotor (Dring et al., 1982; AGARD, 1990) and the other is the second stage

Contributed by the International Gas Turbine Institute and presented at the 37th International Gas Turbine and Aeroengine Congress and Exposition, Cologne, Germany, June 1–4, 1992. Manuscript received by the International Gas Turbine Institute January 13, 1992. Paper No. 92-GT-364. Associate Technical Editor: L. S. Langston.

of a two-stage compressor (Dring and Joslyn, 1986; Joslyn and Dring, 1989; Dring and Spear, 1991; AGARD, 1990). The features of the data that contribute to the discussion of radial transport are that it includes: (1) full-span radial-circumferential transverse measurements of the total and static pressures and the flow yaw and pitch angles with high spatial resolution in both the rotating and stationary frames of reference, and (2) full-span measurements of the suction and pressure surface static pressures on the rotors and stators. The transverse data enabled the calculation of radial-circumferential arrays of the three velocity components and the airfoil surface static pressure data enabled the calculation of the axial and tangential components of the pressure forces on the airfoils.

The airfoils of both the isolated rotor and the two-stage compressor have hub corner separation in varying degrees over the entire speed-line. It is reasonable to question whether the amount of corner separation present in these compressors causes them to be "atypical" (see Cumpsty's discussion at the end of Joslyn and Dring, 1985). The amount of corner separation on the airfoils of the isolated rotor and the two-stage compressor could probably be reduced through design refinement; however, the success of such refinement can only be determined through documentation of the loss and deviation, and through surface flow visualization. Pressure distributions alone can be misleading. Since this kind of in-depth information is seldom available, it is difficult to say whether the present compressor is atypical. However, corner separation is not a peculiarity, but rather it is a feature common to a wide variety of compressors and operating conditions. A partial list of its occurrences is given by Dring and Spear (1991). For this reason, the isolated rotor and the two-stage compressor are felt to give a reasonable basis for the following analysis.

In brief, this paper examines: (1) comparisons between the diffusion coefficient computed from the Adkins and Smith (1982) model using the measured radial velocities and the diffusion coefficient computed from the Gallimore and Cumpsty (1986) correlation, and (2) the extent to which radial mixing can reconcile the large differences between the spanwise distributions of the force on the airfoils and the change in fluid momentum across the airfoils. The paper does not examine the various secondary flow models used by Adkins and Smith (1982).

Background

This section of the paper presents some background information about radial mixing and some observations concerning the Adkins and Smith model.

In throughflow analysis, mixing must be applied to any three of the parameters that, in the absence of radial transport, are conserved along stream surfaces. It is the pitchwise mass-averages of these quantities that are conserved (Dring and Oates, 1990). These mass-averaged parameters might include: absolute total enthalpy, absolute total pressure, and angular momentum. Rothalpy is also conserved along stream surfaces (in the absence of radial transport) because it is a linear combination of absolute total enthalpy and angular momentum. Rotary total pressure is also conserved and for incompressible flow it is a linear combination of the absolute total pressure and angular momentum.

In the discussion that follows, the restriction of the application of the Adkins and Smith (1982) model to design-point, relatively low loss, unseparated flow will be violated since hub corner separation is present to some degree on every airfoil to be analyzed. However, since only the diffusion model (based on measured radial velocities) and not the secondary flow models of Adkins and Smith is being examined, the comparisons are believed to be valid.

In the following discussion there will be frequent reference to several equations presented by Adkins and Smith (1982). For the sake of completeness their salient features are described here.

Equation (40) . . . relates the axial derivative of a diffusing quantity to two terms (of a Taylor series), the first being the tangential area-average of (C_r/C_x) and the second being the tangential area-average of $(C_r/C_x)^2$.

Equation (42) . . . relates the mixing coefficient to the tangential area-average of $(C_r/C_x)^2$. It is similar to Eq. (3) below but with an area-average instead of a mass-average.

Equation (43) . . . describes the growth and decay of the mixing coefficient as a function of axial distance downstream of an airfoil row.

In the formulation of the Adkins and Smith (1982) model, "the first term in Eq. (40) . . . disappeared because the cross-passage average of the spanwise velocity must be zero to satisfy continuity." The average of the spanwise velocity will be zero only if the average is a pitchwise area-average. The integrand in the first term in their Eq. (40) is the velocity component ratio (C_r/C_x). The average of (C_r/C_x) will only be zero if a mass-average is used because the mass-average eliminates the C_x in the denominator (see the nomenclature).

Nomenclature

A = const, used in Eq. (4)
B = airfoil chord
B_x = airfoil axial chord
C = absolute flow speed
cl/B = rotor tip clearance-to-chord ratio
Cp = pressure coefficient = $(P - P_{t,\,\text{inlet}})/Q_{Um}$
E = dimensionless mixing coefficient = $(\epsilon/C_x * L_s)$ or (ϵ/L_s)
f = a generic function
H = absolute total enthalpy
I = rothaply
L_s = axial stage length
M = momentum, defined in Eqs. (5) and (6)
ND = nominal-design conditions
NS = near-stall conditions
P = pressure
Q_{Um} = dynamic pressure based on U_m
r = radial coordinate
t = airfoil maximum thickness
U_m = wheel speed at midspan
W = relative flow speed
WO = wide-open conditions
x = axial coordinate
α = absolute yaw angle from axial
β = relative yaw angle from axial
δ = boundary layer thickness
θ = angular coordinate
ϵ = dimensional mixing coefficient
ρ = density
τ = airfoil pitch
Φ = flow coefficient = C_x/U_m
Ω = rotation rate
ω = stage static pressure rise loss coefficient, used in Eq. (4) = $(\Delta P_{s,\,\text{ideal}} - \Delta P_{s,\,\text{actual}})/\rho U_m^2$

Subscripts

abs = absolute
h = hub (inner diameter, 0 percent span)
m = midspan
mc = midchord
r = radial component
rel = relative
s = static
t = total, or tip (outer diameter, 100 percent span)
x = axial component
θ = tangential component

Superscripts

$-a$ = pitchwise area-average; $f^{-a} = \int_0^\tau f d\theta / \int_0^\tau d\theta$
$-m$ = pitchwise mass-average; $f^{-m} = \overline{\rho C_x f}^a / \overline{\rho C_x}^a$

This distinction between averaging procedures is significant because the same average is applied to the second term in their Eq. (40), which determines the mixing coefficient (ϵ) in their Eq. (42). In the present work, calculations of the mixing coefficient based on measured circumferential distributions of C_r and C_x showed differences as large as a factor of 2 between the two averages. These differences were usually largest where the mixing coefficient was largest. The source of the difference between the area and mass-averages is that C_r is usually large where C_x is small, causing the area-average of (C_r/C_x) to be larger than the mass-average. The largest differences occurred at near-stall conditions.

In calculating the mixing coefficient [Eq. (42)] Adkins and Smith "did not allow for viscous dissipation of the secondary flow field," i.e., they assumed that the integrand (C_r/C_x) was not a function of axial position. This resulted in a mixing coefficient that increased linearly with axial distance. They empirically suppressed this increase with a variety of terms in Eq. (43).

If (C_r/C_x) varies with axial distance, Adkins and Smith's Eq. (42) takes on the following form:

$$\epsilon = \frac{\partial}{\partial x}\left(x^2 \overline{\left(\frac{C_r}{C_x}\right)^2}^m\right) \tag{1}$$

To explore this issue, the axial variation (decay) of the mass-average of $(C_r/C_x)^2$ was examined using data acquired on the isolated rotor. Full-span traverse data (i.e., dense radial-circumferential arrays of the static pressure and the three velocity components) had been acquired at four axial locations aft of the rotor (from 10 to 110 percent B_x aft) and at four flow coefficients ranging from wide-open ($\Phi = 0.95$) to a near-stall condition ($\Phi = 0.65$). The data suggested a power law decay for the mass-average of $(C_r/C_x)^2$ with an exponent between -0.5 and -1.0. Thus, instead of having a mixing coefficient that increases linearly, as in Adkins and Smith's Eq. (42), the -0.5 exponent produces a mixing coefficient that increases with an exponent of $+0.5$. The -1.0 exponent produces a constant mixing coefficient. These results eliminate much of the need for the terms suppressing the linear increase in the mixing coefficient in Adkins and Smith's Eq. (43).

Radial Mixing: Secondary Flow and Turbulent Diffusion

This section of the paper demonstrates that the turbulent diffusion correlation of Gallimore and Cumpsty generally gives a higher level of mixing than does the secondary flow model of Adkins and Smith (when the latter is based on measured radial velocities).

The relationship describing the radial diffusive mixing of any parameter (f) in throughflow analysis can be written as follows:

$$\frac{\partial f}{\partial x} = \epsilon\left(\frac{\partial^2 f}{\partial r^2}\right) \tag{2}$$

This is Adkins and Smith's Eq. (41) and Eq. (43) from De Ruyck and Hirsch (1988). The dimensionless diffusion coefficients (E) for the various models are summarized as follows.

Adkins and Smith's Eq. (42) divided by L_s and based on a mass instead of an area-average:

$$E = \left(\frac{\epsilon}{L_s}\right) = \left(\frac{x - x_{mc}}{L_s}\right)\overline{\left(\frac{C_r}{C_x}\right)^2}^m \tag{3}$$

Gallimore and Cumpsty's Eq. (9) where $A = 0.4$:

$$E = \left(\frac{\epsilon}{C_x L_s}\right) = A\left(\frac{t}{L_s}\right)\left[\frac{2\omega\left(\frac{t}{L_s}\right)}{3\Phi^2}\right]^{1/3} \tag{4}$$

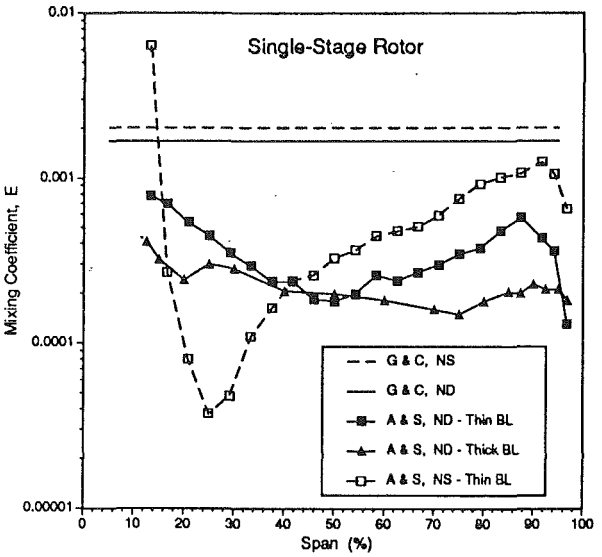

Fig. 1 Dimensionless mixing coefficient (E) for a single-stage rotor, 30 percent B_x aft, at nominal-design (ND) and near-stall (NS) conditions

Note that in Eq. (3), ϵ has the dimension of length, while in Eq. (4), ϵ the dimension of length squared per unit time.

These equations were evaluated (1) for the isolated rotor at a plane 30 percent aft of the rotor trailing edge, and (2) for the two-stage compressor at traverse planes downstream of the first and second-stage stators and downstream of the second-stage rotor. The original linear increase with axial distance in Adkins and Smith's Eq. (42) has been retained here in Eq. (3). The terms suppressing the linear increase in Adkins and Smith's Eq. (43) would reduce the values calculated here by 10 to 15 percent. The static pressure rise loss term (ω) in Eq. (4) was estimated from measured performance and A was set equal to 0.4, as recommended by Gallimore and Cumpsty. The isolated rotor results are shown in Fig. 1 and the two-stage compressor results are shown in Fig. 2.

The data in Fig. 1 are for the isolated rotor operating at its nominal-design flow coefficient ($\Phi = 0.85$, solid lines indicated by ND) and at a near stall condition ($\Phi = 0.65$, dotted lines, indicated by NS). The nominal design point data are shown for thin and thick inlet boundary layers (δ = 5 to 10 percent span, and δ = 37 percent span) while at the near-stall condition only the thin inlet boundary layer data are shown. The results of Eq. (3) are indicated by A&S, the lines with the symbols indicating the radial locations of the circumferential traverses. The results of Eq. (4) are indicated by horizontal lines labeled G&C. For all conditions, the mixing coefficient based on using measured radial velocities in Eq. (3) is much smaller than that based on the turbulent diffusion model, Eq. (4).

The results in Fig. 1 are consistent with those of De Ruyck and Hirsch (1988). Their analysis for this rotor operating at $\Phi = 0.75$ indicated that "radial redistributions...(for this rotor)...are not very significant and are dominated by turbulent diffusion." They used a "data matching" procedure to deduce the value of A in the Gallimore and Cumpsty (1986) correlation, Eq. (4). They estimated a value of $A = 0.1$ for the nominal-design case ($\Phi = 0.85$), and $A = 0.3$ for the near-stall case ($\Phi = 0.65$). The value proposed by Gallimore and Cumpsty (and used in the present work) was $A = 0.4$. These 75 and 25 percent reductions would lower the turbulent diffusion results of Eq. (4) into the same range as the convective transport results of Eq. (3). Trace gas measurements taken on this rotor by Wagner et al. (1985) also support the observation that the mixing was very weak. They noted that mixing "across the rotor was very close to what it would have been with no airfoils present." All of this suggests that a mixing coefficient less than 0.0005 has a negligible effect on the flow.

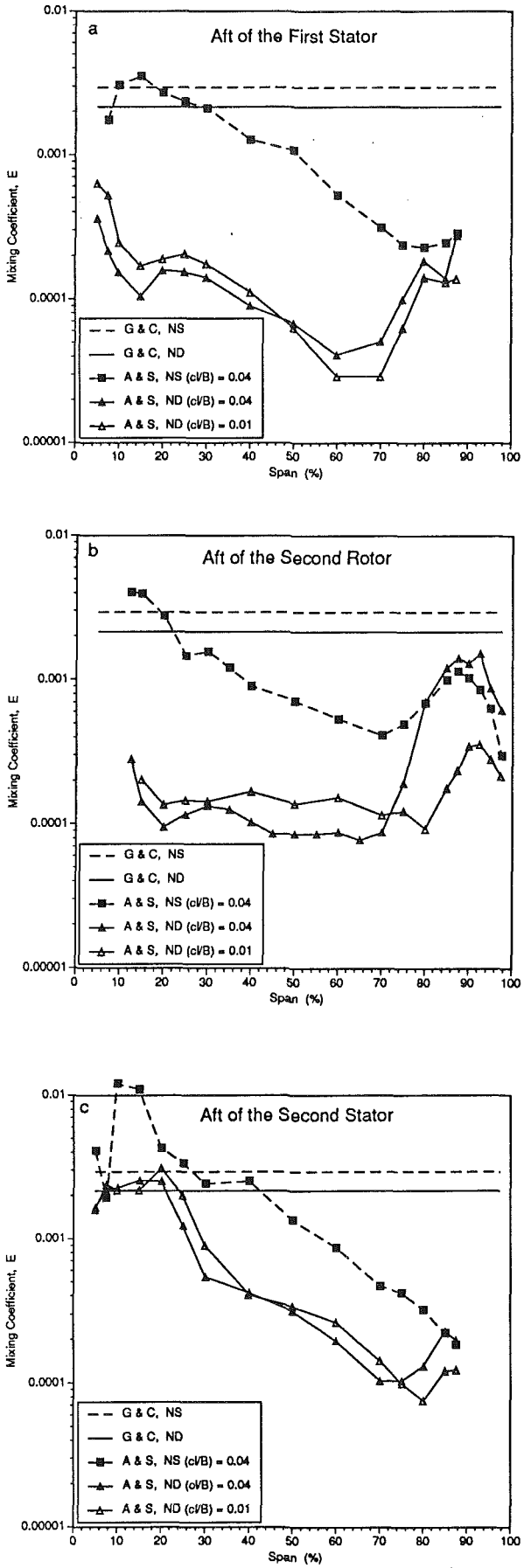

Fig. 2 Dimensionless mixing coefficient for a two-stage compressor aft of the first stator (Sta. 3), the second rotor (Sta. 4), and the second stator (Sta. 5), at nominal-design (ND) and near-stall (NS) conditions

The data in Fig. 2 follow the same format as in Fig. 1. The results of Eq. (3) are indicated by A&S and those of Eq. (4) by G&C. Equation (3) was evaluated at a plane 18 percent B_x aft of the first stator (Fig. 2*a*), at a plane 24 percent B_x aft of the second rotor (Fig. 2*b*), and at a plane 18 percent B_x aft of the second stator (Fig. 2*c*). The results of Eq. (4) are the same for all three planes. Data are shown for the compressor operating at its nominal-design flow coefficient ($\Phi = 0.51$, solid lines, indicated by *ND*) and at a near-stall condition ($\Phi = 0.45$, dotted lines, indicated by *NS*). At nominal-design conditions data are shown for small and large rotor tip clearances ($cl/B = 0.01$ and 0.04), while at near-stall only the large-clearance data are shown. The small clearance is representative of engine conditions. The large-clearance data were included because rotor tip clearance was expected to have a strong impact on mixing. The stator hubs were stationary and had no clearance.

The primary effect of rotor tip clearance is aft of the rotor (Fig. 2*b*). Mixing in the tip region (from 75 to 100 percent span) increases dramatically with tip clearance but its level in this region is insensitive to flow coefficient (as seen in data not included here for the sake of brevity). For the rotor at design conditions, convective mixing is dominated by tip leakage effects. At near-stall conditions there is a large increase in mixing across most of the span. The corner separation that grows near the hub becomes the dominant contributor. As with the isolated rotor above, turbulent mixing (Eq. (4)) is generally predicted to be much stronger than convective mixing (Eq. (3)). Previous studies (Joslyn and Dring, 1989) have shown this rotor to have good performance and to have only a relatively small hub corner separation. Perhaps then, the low levels of convective mixing it produces should not be surprising.

The convective mixing aft of the first and second stators (Figs. 2*a* and 2*c*) is insensitive to rotor tip clearance but very sensitive to flow coefficient. The second stator is the more heavily loaded of the two and the effect of this can be seen in the relatively high level of convective mixing it produces. The high levels near the hub of the second stator are due to a hub corner separation that grows form 40 to 75 percent span as the flow coefficient drops from nominal-design conditions to near-stall. At design conditions, convective mixing near the hub of the second stator is comparable to that predicted for turbulent mixing. At near-stall conditions convective mixing is dominant near the hub for both stators. The strong spanwise dependence of the mixing coefficient is not modeled by Gallimore and Cumpsty.

To summarize what has been discussed this far, the turbulent diffusion correlation of Gallimore and Cumpsty (1986) generally gives a higher level of mixing than does the secondary flow model of Adkins and Smith (1982) when the latter is based on measured radial velocities. A similar observation was made by Gallimore and Cumpsty (1986) when they compared turbulent effects based on trace gas diffusion with convective effects based on measured radial shifts of the location of peak trace gas concentration. In another similar comparison by Wisler et al. (1987), in their Fig. 16, the two models gave very nearly the same value for the diffusion coefficient in the midspan region; however, the Adkins and Smith (1982) value was based on calculated secondary flows and not on measured radial velocities as in the present comparison.

Finally, at near-stall conditions, mixing near the hub due to secondary flow (based on measured radial velocities) far exceeds that predicted for turbulent diffusion.

Wake Mixing, Blockage, and Momentum

The focus of this paper is radial transport in axial compressors. The following sections will examine the impact of radial transport on the exchange of momentum. However, some necessary ground work will be presented in this section.

In the axial region between two airfoil rows, circumferential gradients due to the total pressure wake of the upstream airfoil row cause "tangential blockage" (AGARD, 1981). This blockage can have a powerful impact on the nature of the flow (Dring and Spear, 1990). The decay of these wakes causes the flow to approach axisymmetry and the tangential blockage to decay to zero. This nonisentropic tangential mixing also causes a loss in total pressure. Note that: (1) In a homenthalpic flow, circumferential gradients due to potential flow do not produce a loss in total pressure as they decay to zero, and (2) since the mixing process is adiabatic and since entropy is reference frame independent, the total pressure loss due to wake mixing is also reference frame independent.

For simplicity the following discussion will be limited to the case of turbomachines with constant hub and tip radii. While airfoil wake mixing is occurring in an annular region, various flow properties are conserved whether or not radial transport is occurring. They include mass flow, total enthalpy (or rothalpy), angular momentum, and axial momentum. In a throughflow calculation, if the total pressure is held constant while the blockage decays to zero, there is an increase in axial momentum. For axial momentum to be conserved when blockage is decaying, there must be a loss in total pressure. When there is no radial transport, specific tangential momentum (rC_θ) is constant along stream surfaces as well as on a radially mass-averaged basis. However, even when there is no radial transport and no wake mixing, axial momentum ($P + \rho C_x^2$) is generally not constant along stream surfaces. It is only constant on a radially area-averaged basis. These conservation conditions for axial and tangential momentum may be expressed as follows:

$$M_x = \int_{r_h}^{r_t} \tau_m \left(\frac{r}{r_m}\right) (\overline{P}^a + \rho \overline{C}_x^a \overline{C}_x^m)' \, dr \tag{5}$$

$$M_\theta = \int_{r_h}^{r_t} \tau_m \left(\frac{r}{r_m}\right) (\rho \overline{C}_x^a \overline{C}_\theta^m) r dr \tag{6}$$

Both of these quantities are constant in the axial gaps between airfoil rows (if r_h and r_t are constant). Note that M_x is a force while M_θ is a torque.

Airfoil Force and Flow Momentum Change

In this section it will be demonstrated that radial transport can cause very large differences between the force on an airfoil and the change in momentum across the airfoil at the same spanwise location.

The relationship between the force on an airfoil and the change in momentum of the fluid as it transits the airfoil passage will be examined using measurements from the two-stage compressor. The measured surface static pressure distributions were used to calculate the spanwise distributions of the axial and tangential components of force on the rotor and stator airfoils. The pressure force is representative of the total force since the skin friction force is relatively small. The full-span traverse data (measurements of static pressure and the three velocity components over two airfoil pitches) acquired at planes aft of the first stator, the second rotor, and the second stator were used to calculate the spanwise distributions of the axial and tangential momentum at each plane. The data will be examined at three flow coefficients: wide-open ($\Phi = 0.55$ indicated by *WO*), nominal-design ($\Phi = 0.51$ indicated by *ND*), and near-stall ($\Phi = 0.45$ indicated by *NS*) and at the small and large rotor tip clearances ($cl/B = 0.01$ and 0.04). For the sake of brevity, not all of the data from the 24 combinations of flow coefficient, rotor tip clearance, and airfoil will be presented here. Only enough data will be shown to demonstrate the trends.

The axial and tangential components of the force on each airfoil and the change in momentum across each airfoil are shown in Figs. 3–6. The thick lines with solid symbols indicate

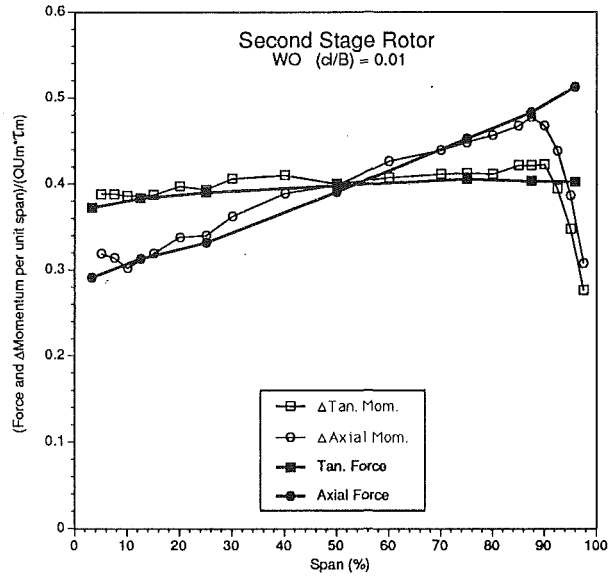

Fig. 3 Airfoil force and momentum change for the second stage rotor at wide-open conditions (*WO*, $\Phi = 0.55$) and the small rotor tip clearance ($cl/B = 0.01$)

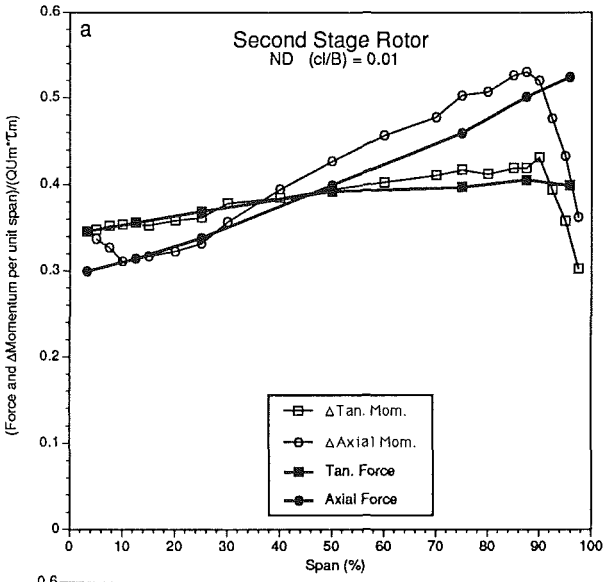

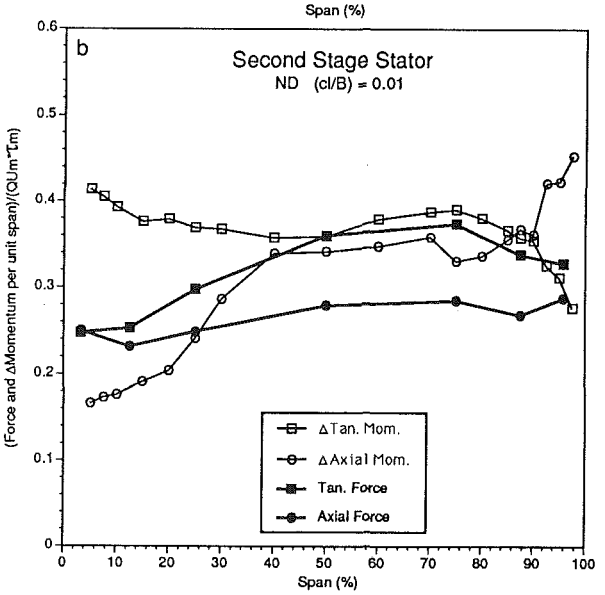

Fig. 4 Airfoil force and momentum change for the second stage rotor and stator at nominal-design conditions (*ND*, $\Phi = 0.51$) and the small rotor tip clearance ($cl/B = 0.01$)

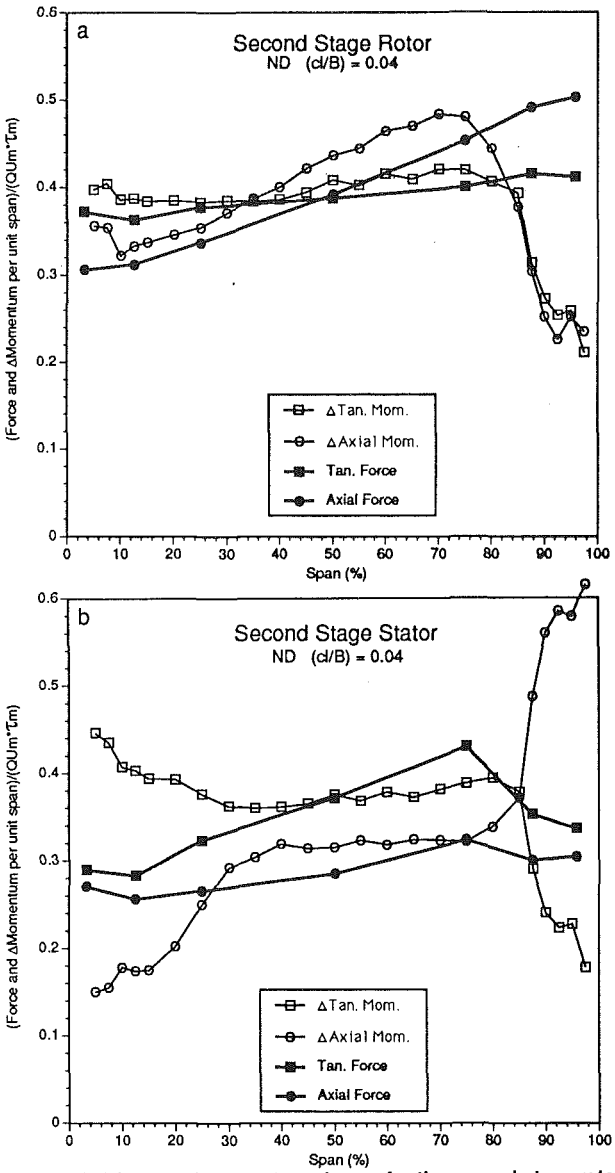

Fig. 5 Airfoil force and momentum change for the second stage rotor and stator at nominal-design conditions (*ND*, Φ = 0.51) and the large rotor tip clearance (*cl/b* = 0.04)

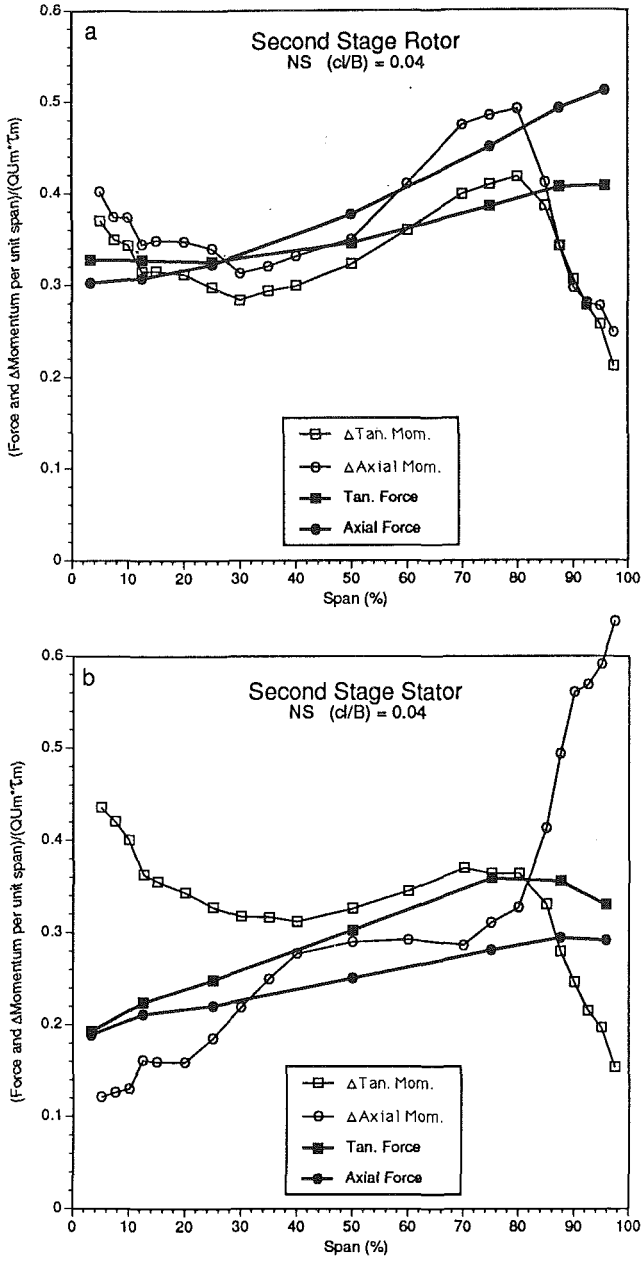

Fig. 6 Airfoil force and momentum change for the second stage rotor and stator at near-stall conditions (*NS*, Φ = 0.45) and the larger rotor tip clearance (*cl/B* = 0.04)

the pressure force components measured at seven spanwise locations on each airfoil. The thin lines with the hollow symbols indicate the measured changes in flow momentum occurring between the traverse planes up and downstream of the airfoil. The axial component of momentum is the dimensionless form of the integrand in Eq. (5). The tangential component is the dimensionless form of the integrand in Eq. (6) without the final factor of r. It represents the tangential force, not torque. When integrated from hub to tip according to Eqs. (5) and (6) the force and momentum changes across each airfoil must agree. Any differences are measurement error. The standard deviation for this error was 8 percent (for 3 flow coefficients, 2 clearances, 2 airfoils, and 2 components, i.e., 24 comparisons).

If these results had been plotted versus stream-function from hub to tip, and if there has been no transport across streamsurfaces, the distributions of force and momentum change would have been the same. However, since there is transport across streamsurfaces, and since the data are plotted versus radius, the distributions do not have to be the same. The differences between the radial distributions of force and momentum change are a measure of the strength of the radial transport.

The rotor data for the wide-open condition *WO* with the small tip clearance (Fig. 3) illustrate the closest local agreement that was obtained between the force and the momentum change. There is close agreement out to about 90 percent span where tip leakage causes the momentum change to drop off. This agreement indicates that radial transport was very weak over most of the span for the rotor at these conditions.

The rotor and stator data for the nominal-design condition *ND* with the same small rotor tip clearance are shown in Figs. 4(*a*) and 4(*b*). The results for the rotor are comparable to those at the wide-open condition (Fig. 3). The stator, however, has large differences between the force and momentum change, especially near the hub. This indicates that at these conditions, radial transport for the rotor is weak but that it is strong for the stator near the hub. These results are similar to those for the stator at the wide-open condition (not shown).

The rotor and stator data for the nominal-design condition *ND* with the large rotor tip clearance are shown in Figs. 5(*a*)

and 5(*b*). Increasing the rotor tip clearance had a significant impact on the pressure distribution at the rotor tip (data not shown) but it did not cause the force to drop off like the momentum did. Comparing Figs. 4 and 5 shows that increasing the clearance had little impact on the rotor and stator force distributions but that it caused large alterations in the momentum changes from 70 percent span to the tip. This indicates that increasing the rotor tip clearance has greatly increased radial transport in the tip regions of both the rotor and the stator. Rotor tip clearance had the same effect at the other two flow coefficients.

The rotor and stator data for the near-stall condition *NS* with the large rotor tip clearance are shown in Figs. 6(*a*) and 6(*b*). Comparing Figs. 5 and 6 shows that reducing the flow coefficient has degraded the correspondence between the force and the momentum change. This indicates an increase in radial transport over most of the span for both airfoils. Note that for the stator, near the hub, the change in tangential momentum exceeds the tangential force on the airfoil by a factor of 2. Any attempt to calculate the stator pressure distribution in the hub region from the measured up and downstream flow conditions will result in a predicted pressure distribution that has twice the tangential force of the measured pressure distribution, as demonstrated by Dring and Spear (1991) (Fig. 11).

The conclusions that one draws from these comparisons are: (1) that there can be very large differences ($\approx$100 percent) between the force on an airfoil and the change in momentum across the airfoil at the same spanwise location, and (2) that these differences grow dramatically as rotor tip clearance increases and as flow coefficient decreases toward near-stall conditions.

These local imbalances between the spanwise distributions of airfoil force and fluid momentum change suggest that there are strong radial transport mechanisms at work. This is examined in the following section.

Throughflow Modeling

In this section it will be demonstrated that the type of diffusive radial mixing described by Eq. (2) cannot describe the force and momentum imbalances seen in the previous section.

The two-stage compressor has been the subject of extensive prior throughflow modeling at both the design and near-stall flow conditions, and for both the large and small rotor tip clearances (Dring and Joslyn, 1986, 1987; Dring and Oates, 1990). All of these analyses used as input the measured spanwise distributions of airfoil total pressure loss, airfoil exit flow angle, and blockage (or its equivalent). The predicted spanwise distributions of static pressure, absolute and relative total pressure and incidence and axial velocity were compared to the measured distributions. In general excellent agreement was obtained.

Because these calculations gave accurate predictions of the pressure and velocity distributions they also gave accurate predictions of the changes in fluid momentum across the airfoil rows, i.e., accurate predictions of the measured momentum changes presented in Figs. 4, 5, and 6. Since the calculation accurately predicted the measured momentum changes, airfoil-to-airfoil flow analyses based on these predictions, in general, could never duplicate the measured airfoil pressure distributions (as demonstrated by Dring and Spear, 1991, in their Fig. 11). They compared the measured and predicted pressure distributions for the stator at 12.5 percent span for the near-stall, large-clearance condition. The prediction used the traverse data to define the up and down-stream conditions. The 100 percent difference between the force and the momentum change at 12.5 percent span (Fig. 6*b*) caused the tangential forces of the measured and predicted pressure distributions also to have the 100 percent difference.

In an effort to quantify the effect of the forces on the airfoils, a series of throughflow calculations were carried out in which the spanwise distributions of airfoil total pressure loss and exit flow angle were adjusted until agreement was reached between the spanwise distributions of the measured force on the airfoil and the predicted change in the fluid momentum. Not surprisingly, the loss and exit angle distributions deduced in this way were very different from the measured distributions (see Figs. 7*a* and 7*b* for the rotor and Figs. 8*a* and 8*b* for the stator). In addition, the calculated radial distributions of total pressure, angular momentum, and axial velocity were also very different from the measurements (Figs. 7 and 8). The question to be answered was whether or not radial diffusive mixing (which is used by both Adkins and Smith, 1982, and Gallimore and Cumpsty, 1986), as represented by Eq. (2) could be used to improve this agreement.

A mixing calculation was added to the throughflow analysis. For a specified value of the dimensionless mixing coefficient in Eq. (4) the mixing relationship in Eq. (2) was solved such that: (1) the mixed quantities (absolute total enthalpy, absolute total pressure, and angular momentum) were conserved on a full-span mass-averaged basis, and (2) they had zero normal derivatives at the hub and tip. The second-stage rotor and stator were examined separately.

Throughflow analysis results for the second-stage rotor with the compressor operating at the near-stall flow coefficient ($\Phi = 0.45$) and with the large tip clearance ($cl/B = 0.04$) are summarized in Fig. 7. Spanwise distributions of the rotor total pressure loss and exit flow angle are shown in Figs. 7(*a*) and 7(*b*). The total and static pressures, specific angular momentum, and axial velocity for the traverse plane 24 percent of B_x aft of the rotor are shown in Figs. 7(*c*), 7(*d*) and 7(*e*). The "Base" distributions are those computed earlier by Dring and Oates (1990) using the measured losses and exit flow angles (and no mixing). They are generally in excellent agreement with the measured data. The results for the present calculation (which duplicates the measured force on the airfoil) are shown for three values of the mixing coefficient, 0.000 (no mixing), 0.020 (a relatively high value), and 0.200 (a very high value).

The diffusive mixing model, Eq. (2), is smoothing the flow but its impact is inconsequential and it is not driving the prediction toward the measured results. The trends for the axial velocity (Fig. 7*e*) are similar to those for the absolute flow angle (i.e., incidence on a downstream stator) where differences occurred up to 10 deg, which were insensitive to mixing.

Similar results for the second-stage stator operating at the same conditions ($\Phi = 0.45$ and $cl/B = 0.04$) are summarized in Fig. 8. These results are for the traverse plane, which is 18 percent of B_x aft of the stator trailing edge. Here again, the diffusive mixing model is smoothing the flow, but its impact is small and it is not driving it toward the measured results. The relative flow angle (i.e., incidence on a downstream rotor) differed from the measured profile by as much as 15 deg and was very insensitive to mixing.

These comparisons represent a worst case situation, i.e., near-stall flow conditions and a large rotor tip clearance. However, it can be seen by comparing the nominal-design, small-clearance data in Fig. 4 with the wide-open, large-clearance data in Fig. 6, that similar results (albeit less severe) would have been produced if the nominal-design case had been the subject of the throughflow analysis. Although the differences would be smaller at nominal-design conditions, diffusive mixing would not drive the throughflow prediction toward the measured results.

The results presented in Figs. 7 and 8 suggest that there is a strong radial mixing process occurring within and shortly downstream of the airfoil rows. Since the dominant radial flow mechanism in these airfoil rows is hub corner separation, it seems likely that this separation is also contributing to the radial mixing.

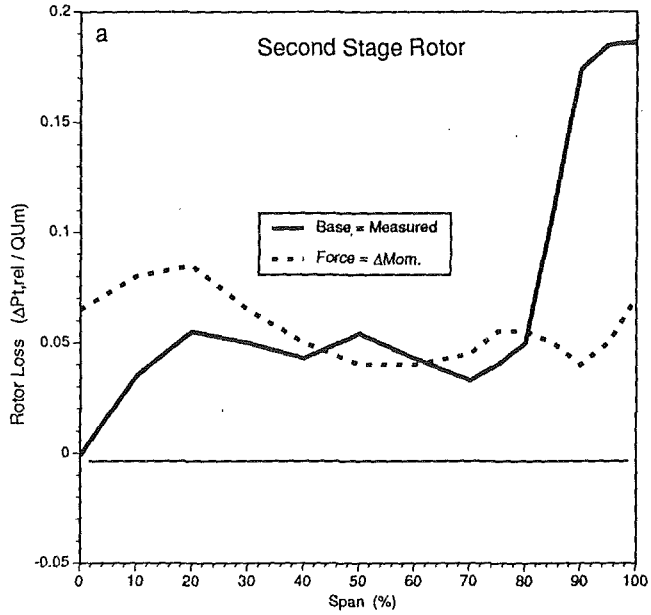

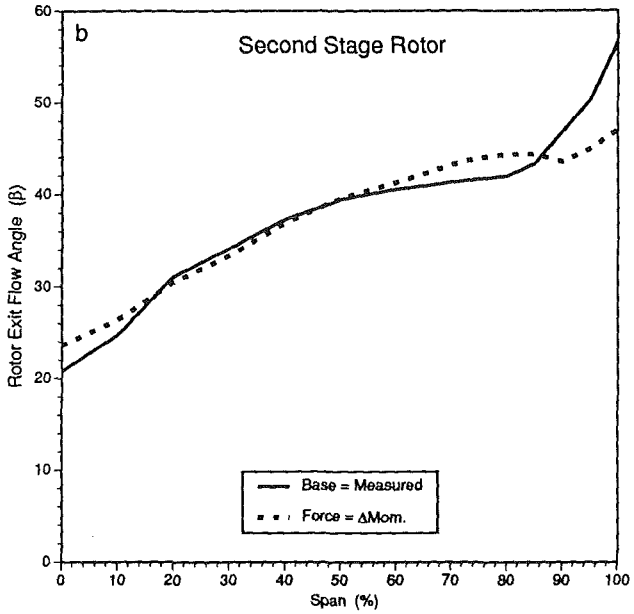

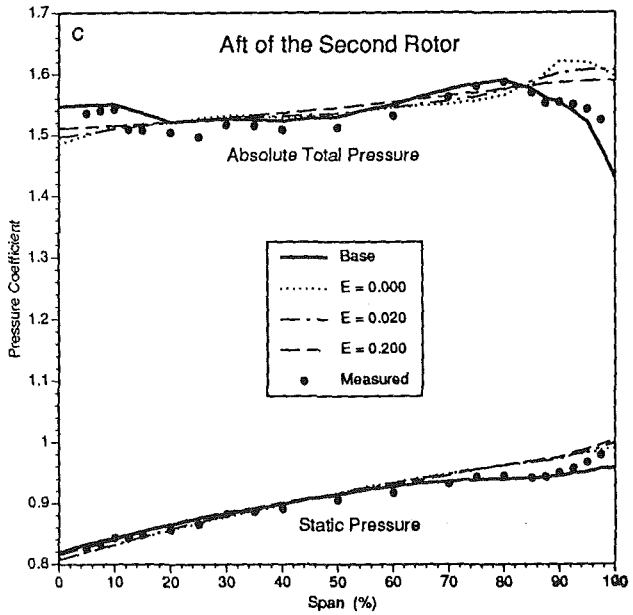

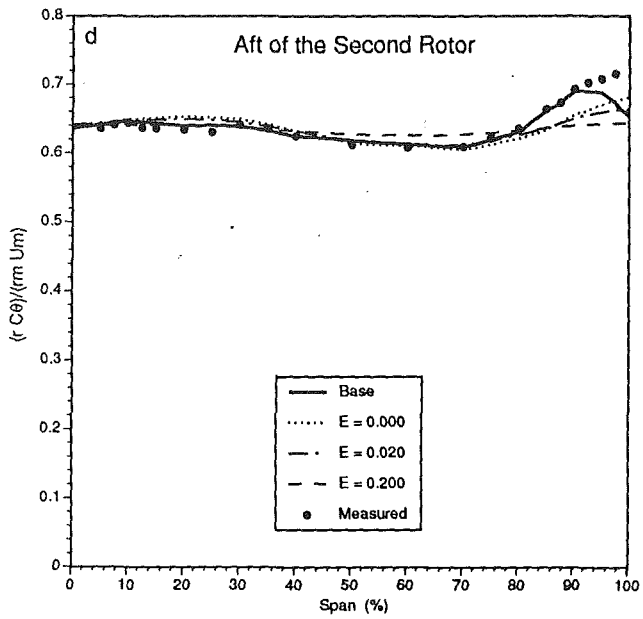

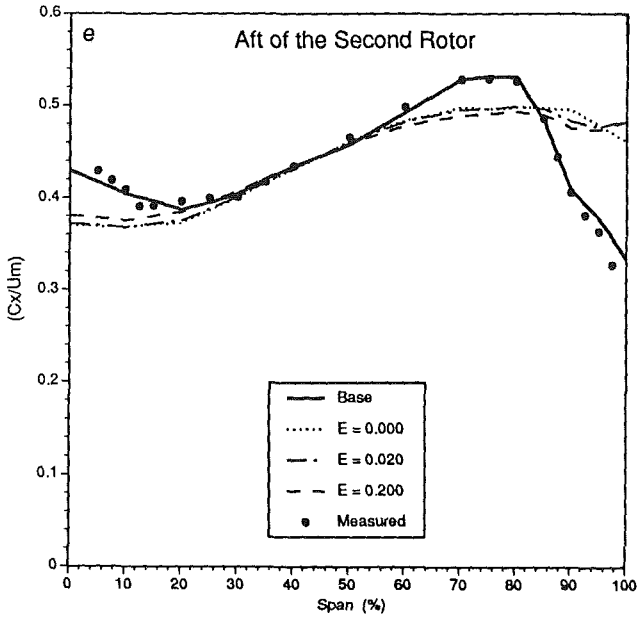

Fig. 7 Rotor throughflow predictions based on (1) measured loss and deviation and (2) matching the force on the rotor, for near-stall flow conditions (*NS*), large tip rotor clearance (*cl/B* = 0.04), 24 percent B_x aft of the rotor trailing edge

This assessment of diffusive mixing in the throughflow analysis of a low-speed compressor suggests that the radial mixing process for absolute total pressure and angular momentum is something other than the type of diffusion process described by Eq. (2). The gradients in the measured results (e.g., Figs. 8*c* and 8*d*) cannot be produced by such a diffusion process, regardless of the choice of diffusion coefficient.

Conclusions

The objective of this work was to examine radial transport in axial compressors from two perspectives. The first was to compare the mixing coefficient based on a secondary flow model (using measured radial velocities) with that based on a turbulent diffusion model. The second objective was to use measured airfoil pressure forces and momentum changes to assess the validity of the assumption of diffusive radial transport that is common to both models. These objectives lead to the following three major conclusions:

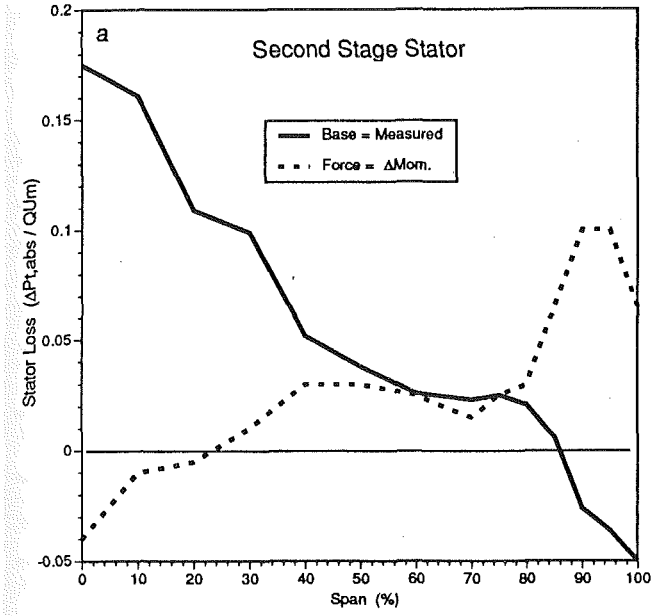

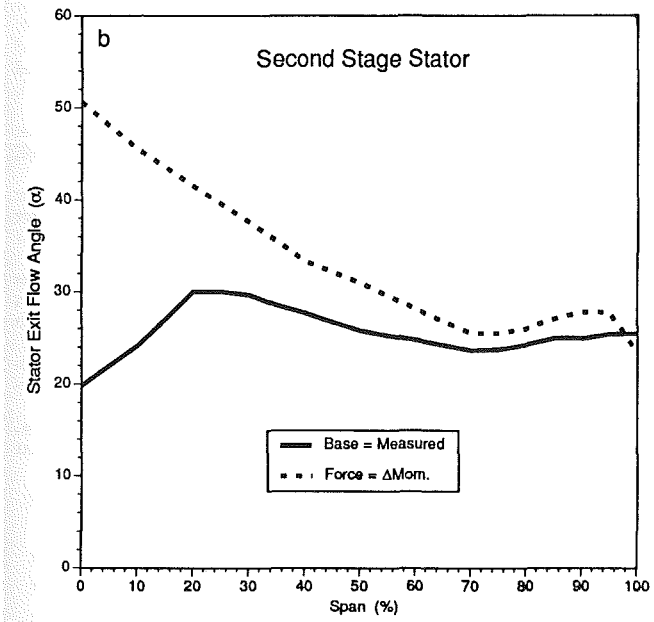

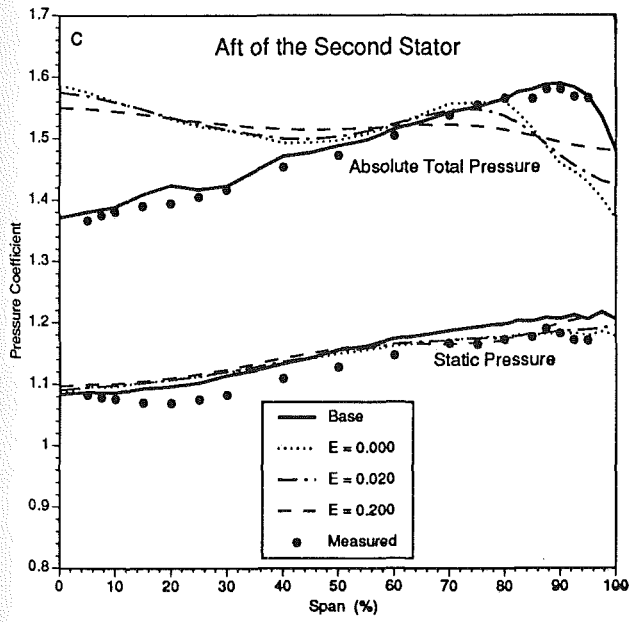

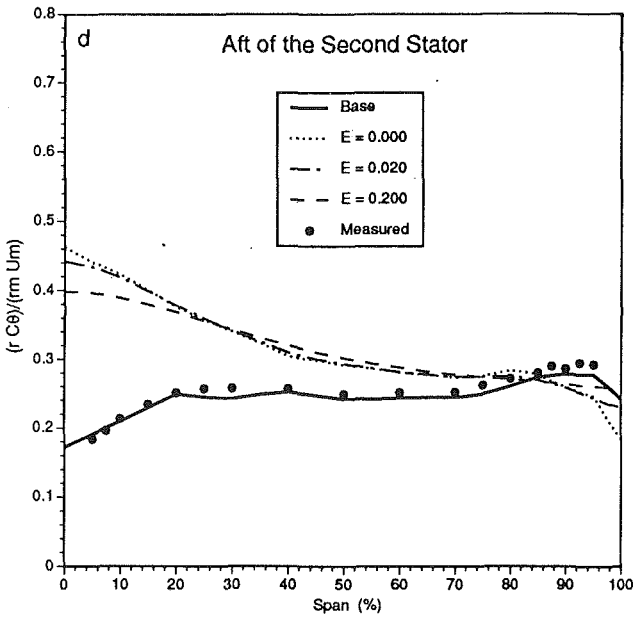

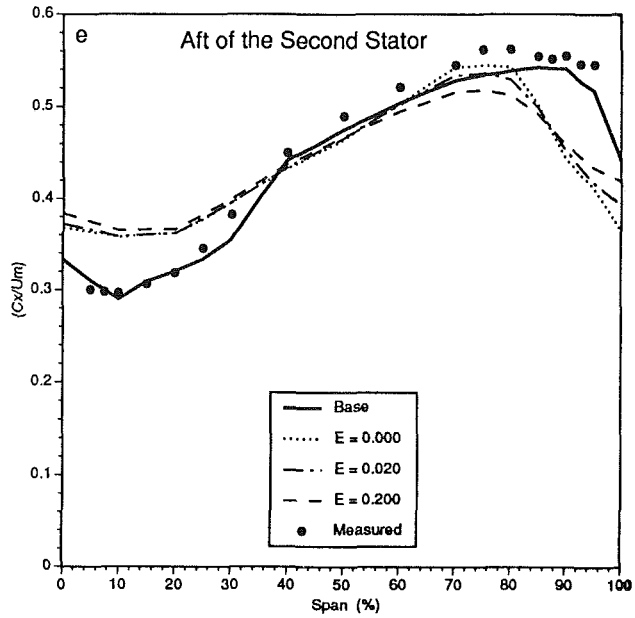

Fig. 8 Stator throughflow predictions based on (1) measured loss and deviation, and (2) matching the force on the stator, for near-stall flow conditions (*NS*), large tip rotor clearance (c/B = 0.04), 18 percent B_x aft of the stator trailing edge

- The turbulent diffusion correlation of Gallimore and Cumpsty (1986) generally predicts a higher level of mixing than does the secondary flow model of Adkins and Smith (1982) when the latter is based on measured radial velocities. However, at near-stall conditions, mixing near the hub due to secondary flow exceeds that predicted for turbulent diffusion (see Figs. 1 and 2).
- There can be very large differences ($\approx$ 100 percent) between the force on an airfoil and the change in momentum across the airfoil at the same spanwise location. These differences grow dramatically as the rotor tip clearance increases and as the flow coefficient decreases toward near-stall conditions (see Figs. 3–6).
- The diffusive mixing model in Eq. (2) smooths the flow but its impact is very small and it is not in general driving it toward the measured results (see Figs. 7 and 8). This is true at both nominal-design and near-stall conditions.

Additional observations and conclusions are as follows:

1 The secondary flow mixing coefficient in Eq. (1) should be based on mass-averaging.

2 The decay of radial velocity with axial distance suggests an axially constant mixing coefficient, or at most a square root increase (versus an initially linear increase).

3 In earlier work on this compressor it has been demonstrated that hub corner separation is often the dominant source of total pressure loss and blockage. It is evident here that it may also be a strong driver for radial mixing. Conversely, when corner separation is weak, as on the rotor of the two-stage compressor, loss, blockage, and radial mixing are all reduced.

4 When the difference between the local force on an airfoil and the local change in momentum across the airfoil is small (as in Fig. 3) then transport due to secondary flow and/or turbulent diffusion may be the dominant mechanism for radial mixing.

5 The observations made here about the nature of radial transport and momentum exchange not only provide a basis for examining data from other compressors, but they also provide a basis for examining the results of three-dimensional Navier–Stokes computations.

6 The results of this study point to the need to use three-dimensional Navier–Stokes calculations in compressor design and analysis, particularly when strong radial flow effects are anticipated.

Acknowledgments

I would like to express my gratitude to a number of people for their helpful and patient support in carrying out the work reported here. I am indebted to Frank Paoletti of Pratt & Whitney Canada, Ltd., for his guidance in modifying the throughflow code and to Lisa Vaughn of UTRC for her faithfulness in running the code. The discussions and suggestions of Harris Weingold and David Spear of the Pratt & Whitney Aircraft Commerical Engine Business group are also appreciated.

References

Adkins, G. G., Jr., and Smith, L. H., Jr., 1982, "Spanwise Mixing in Axial-Flow Turbomachines," ASME *Journal of Engineering for Power*, Vol. 104, pp. 97–110.

AGARD, 1981, "Propulsion and Energetics Working Group 12 on Through-flow Calculations in Axial Turbomachines," AGARD-AR-175, p. 329.

AGARD, 1990, "Test Cases for Computation of Internal Flows in Aero Engine Components," AGARD-AR-275.

DeRuyck, J., and Hirsch, C., 1988, "A Radial Mixing Computation Method," ASME Paper No. 88-GT-68.

Dring, R. P., Joslyn, H. D., and Hardin, L. W., 1982, "An Investigation of Axial Compressor Rotor Aerodynamics," ASME *Journal of Engineering for Power*, Vol. 104, pp. 84–96.

Dring, R. P., and Josly, H. D., 1986, "Through-flow Analysis of a Multistage Axial Compressor: Part I—Aerodynamic Input; Part II—Analytical-Experimental Comparisons," ASME JOURNAL OF TURBOMACHINERY, Vol. 108, pp. 17–31.

Dring, R. P., and Joslyn, H. G., 1987, "Through-flow Analysis of a Multistage Compressor Operating at Near-Stall Conditions," ASME JOURNAL OF TURBOMACHINERY, Vol. 109, pp. 483–491.

Dring, R. P., and Oates, G. C., 1990, "Through Flow Theory for Nonaxisymmetric Turbomachinery Flow: Part I—Formulation; Part II—Assessment," ASME JOURNAL OF TURBOMACHINERY, Vol. 112, pp. 320–337.

Dring, R. P., and Spear, D. A., 1991, "The Effects of Wake Mixing on Compressor Aerodynamics," ASME JOURNAL OF TURBOMACHINERY, Vol. 113, pp. 600–607.

Gallimore, S. J., and Cumpsty, N. A., 1986, "Spanwise Mixing in Multistage Axial Flow Compressors: Part I—Experimental Investigation; Part II—Throughflow Calculations Including Mixing," ASME JOURNAL OF TURBOMACHINERY, Vol. 108, pp. 2–16.

Goto, A., 1992, "Three-Dimensional Flow and Mixing in an Axial Flow Compressor With Different Rotor Tip Clearances," ASME JOURNAL OF TURBOMACHINERY, Vol. 114, pp. 675–685.

Joslyn, H. D., and Dring, R. P., 1985, "Axial Compressor Stator Aerodynamics," ASME *Journal for Gas Turbines and Power*, Vol. 107, pp. 485–493.

Joslyn, H. D., and Dring, R. P., 1989, "Multi-stage Compressor Airfoil Aereodynamics: Part I—Airfoil Potential Flow Analysis; Part II—Airfoil Boundary-Layer Analysis," *AIAA Journal of Propulsion and Power*, Vol.. 5, No. 4, pp. 457–468.

Leylek, J. H., and Wisler, D. C., 1991, "Mixing in Axial Flow Compressors: Conclusions Drawn From 3-D Navier–Stokes Analysis and Experiments," ASME JOURNAL OF TURBOMACHINERY, Vol. 113, pp. 161–174.

Li, Y. S., and Cumpsty, N. A., 1991, "Mixing in Axial Flow Compressors: Part I—Test Facilities and Measurements in a Four-Stage Compressor; Part II— Measurements in a Single Stage Compressor and a Duct," ASME JOURNAL OF TURBOMACHINERY, Vol. 113, pp. 139–160.

Wagner, J. H., Dring, R. P., and Joslyn, H. D., 1985, "Inlet Boundary Layer Effects in an Axial Compressor Rotor: Part I—Blade-to-Blade Effects; Part II—Throughflow Effects," ASME *Journal of Engineering for Gas Turbines and Power*, Vol. 107, pp. 374–386.

Wennerstrom A. J., 1991, "A Review of Predictive Efforts for Momentum Transport Phenomena in Axial Flow Compressors," ASME JOURNAL OF TURBOMACHINERY, Vol. 113, pp. 175–179.

Wisler, D. C., Bauer, R. C., and Okiishi, T. H., 1987, "Secondary Flow, Turbulent Diffusion, and Mixing in Axial-Flow Compressors," ASME JOURNAL OF TURBOMACHINERY, Vol. 109, pp. 455–482.

Investigation of Compressor Rotor Wake Structure at Peak Pressure Rise Coefficient and Effects of Loading

J. Prato

B. Lakshminarayana

Department of Aerospace Engineering,
The Pennsylvania State University,
University Park, PA 16802

This paper reports an experimental study of the three-dimensional characteristics of the mean velocity in the trailing-edge, near-wake, and far-wake regions of a highly loaded low-speed compressor rotor. The wake structure and decay characteristics are compared with the wake data in the same compressor with moderate loading. The experimental investigation was carried out using a rotating five-hole probe. The flow field was surveyed at various radial and axial locations downstream of the compressor rotor. Variations in the axial, tangential, and radial components of mean velocity at various axial and radial locations were derived from the data and compared with earlier data at lower loading to discern the effects of loading. It was found that the higher loading had the following effects: Higher total velocity defects were observed in the hub-wall region, increased wake growth rate in the tip region, faster decay of static pressure difference in the trailing-edge region, larger initial wake width in the trailing-edge region, increased rate of growth of the semi-wake width in the trailing-edge region, increased decay rate of radial velocity in the trailing-edge region, and decreased decay rate of the radial velocity in the far-wake region. Far wake properties were almost identical in both cases.

Introduction

The flow through a compressor stage is highly three-dimensional and complex, including such phenomena as radial flows in boundary layers, hub and annulus-wall boundary layer growth, vortex shedding, tip leakage flow, scraping vortex and spanwise flows. These are in addition to three-dimensional inviscid effects. Rotor wakes, which represent the flow field downstream of the rotor, are not only influenced by upstream flow field conditions but are also controlled by such parameters as blade loading, aspect ratio, blade spacing, hub–tip ratio, inlet turbulence intensity, three-dimensional pressure gradients, distance from the trailing edge, rotor–stator spacing, tip clearance, and centrifugal and Coriolis forces induced by curvature and rotation. The rotor wake is a major source of unsteadiness, noise, and aerodynamic inefficiency in turbomachinery. Understanding rotor wakes is important for establishing improved aerodynamic efficiency and design criteria, for predicting noise levels and for determining the stall, surge, vibration, and flutter characteristics of turbomachinery. Numerical codes have been successfully employed to predict rotor flow fields, but experimental data are needed not only to validate these codes but also to contribute to the data base and ultimately a more complete understanding of the flow fields in turbomachinery. Most recent attempts at rotor wake flow field measurement have been conducted by Reynolds et al. (1979), Dring et al. (1982), Hirsch et al. (1978), Ravindranath and Lakshminarayana (1980), Strazisar et al. (1989), and Gallus et al. (1982). Of these attempts very few have given a comprehensive survey (three velocity components at an array of axial and radial stations) of the wake at different blade loading: This motivated the research reported in this paper.

The objective of the present research is to determine experimentally the three-dimensional wake characteristics of a highly loaded compressor rotor and examine the effects of blade loading on the structure of the rotor wake characteristics. The study is aimed at a detailed survey of the flow field at four radial stations and several axial locations. A rather recent phenomenon to get attention is that of spanwise mixing, which results in the radial redistribution of the flow properties in the downstream direction. Since only four radial locations have been surveyed, interpretation of spanwise mixing effects will not be attempted; rather the focus will be the effects of loading on the wake and pressure profiles and their decay characteristics in the trailing-edge, near and far-wake regions. The trailing-edge region covers trailing edge to about 5 percent chord downstream, the near-wake region up to about 40 percent of chord, and the far-wake region is beyond 40 percent chord.

The present data are compared to those of Ravindranath and Lakshminarayana (1980) obtained from the same compressor under moderate loading. At the time of Ravindranath's

Contributed by the International Gas Turbine Institute and presented at the 37th International Gas Turbine and Aeroengine Congress and Exposition, Cologne, Germany, June 1–4, 1992. Manuscript received by the International Gas Turbine Institute January 28, 1992. Paper No. 92-GT-32. Associate Technical Editor: L. S. Langston.

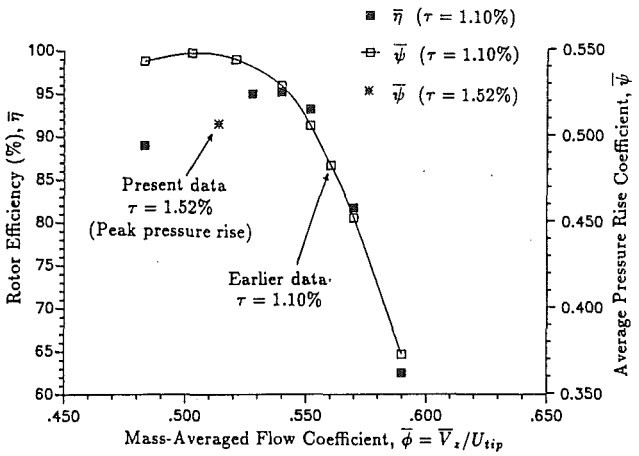

Fig. 1 PSU AFC performance curve

experiment the PSU axial flow compressor had a tip clearance of $\tau = 1.1$ percent operating at a pressure rise coefficient of $\bar{\psi} = 0.486$ and a corresponding flow coefficient of $\bar{\phi} = 0.560$ as shown in Fig. 1. Their experiment involved a hot-wire rotating in the relative frame to obtain data inside and at the exit of the rotor passage. The objective of their experiment was to discern the effect of the annulus and hub-wall boundary layer, secondary flow, tip leakage, and turbulence on the wake structure. The present experiment is aimed at the investigation of the wake structure at peak pressure rise coefficient and the effects of loading. The comparison is focused at the radius of $R = 0.7297$ since the present rotor was operated at a larger tip clearance and the most complete data available for comparison were at $R = 0.7297$. Figure 1 shows the performance map of the PSU Axial Flow Compressor (AFC). The difference in tip clearance between the two data sets is assumed to have little or no effect on the rotor wake characteristics at this and lower radii.

The curve shows the operating point for both the present and earlier data. The average efficiency and pressure rise for Ravindranath and Lakshminarayana's (1980) experiment is shown in Fig. 1. Again, note that the two sets of data were obtained at different tip clearances as well as different loading and flow coefficients. Ravindranath and Lakshminarayana (1980) obtained data at a tip clearance of $\tau = 1.10$ percent whereas only a single point is shown on an undetermined curve for the present data with $\tau = 1.52$ percent. First a presentation of the velocity and pressure profiles, decay, and growth characteristics of the present data will be given, followed by a comparison and discussion of the wake behavior under different loading.

Experimental Facility, Procedure, and Instrumentation

The measurements reported in this paper were obtained using the Axial Flow Compressor Facility (AFC) at the Turbomachinery Laboratory of The Pennsylvania State University. The inlet guide vane (IGV) of the single-stage compressor, consisting of 43 blades, is followed by the rotor. The rotor has 21 cambered, twisted double-circular-arc blades. The blade elements are of modified NACA 65-010 basic profile on a circular-arc camber. The hub/annulus wall diameter ratio of the facility is 0.5, with the diameter of the annulus wall being 0.939 m and the blade tip diameter of 0.932 m. All radii are nondimensionalized by the tip radius ($R = 1$ at the annulus wall). The average tip clearance of the rotor is 3.5 mm, or $\tau = 1.52$ percent (based on blade height). At the rotor blade tip ($R = 0.9925$), blade spacing is 14.12 cm, stagger angle is 45.0 deg, maximum thickness of 5 percent tip chord, and a maximum camber 8 percent tip chord. Additional information on the compressor facility, blading, and flow path is given by Lakshminarayana (1980).

The compressor facility has provisions for flow measurements to be taken in the relative frame of reference. This capability is achieved by means of a probe traversing mechanism rotating with the compressor rotor. The circumferential stepping is 0.0166 deg/step, which represents 1032 steps per blade passage. The probe is traversed across the passage, at

Nomenclature

c = blade chord length
c_p = static-pressure rise coefficient $= (p_2 - p_1)/1/2\rho U_t^2$
H = wake shape factor $= \delta^*/\theta^*$
h = height of the blade
L_s, L_p = wake width at half the depth on rotor blade suction and pressure-surface of the wake, respectively, normalized by the blade spacing
L = $(L_s + L_p)/S$ = semi-wake width normalized by the blade spacing
P_o = stagnation pressure
PS = pressure surface
p = static pressure
R = radius ratio = local radius/tip radius = r/rt
Re = Reynolds number
r = local radius, radial direction
(r, θ, z) = rotating cylindrical coordinate system
S = blade spacing
SS = suction surface
t = tip clearance height
U = rotor speed
V = local absolute velocity
W = local relative velocity
y = tangential distance
(y/S) = tangential distance normalized by the blade spacing ($y = 0$ at wake center)
Z = axial distance from blade trailing edge normalized by rotor chord (at a given radius)
β_o = blade outlet angle
β = air outlet angle
δ = boundary layer thickness
δ^* = displacement thickness = $\frac{1}{S}\int_0^S \left(1 - \frac{W}{W_o}\right) r d\theta$
η = rotor efficiency
θ^* = momentum thickness = $\frac{1}{S}\int_0^S \frac{W}{W_o}\left(1 - \frac{W}{W_o}\right) r d\theta$
τ = $100t/h$
$\bar{\phi}$ = mass-averaged flow coefficient $= \bar{W}_z/U_t = \bar{V}_z/U_t$
$\bar{\psi}$ = mass-averaged stagnation pressure rise coefficient $= 2(\overline{P_{02}} - \overline{P_{01}})/\rho U_t^2$
ω = rotation speed of the rotor blade

Subscripts

a = ambient condition
c = defect (difference between the free-stream value and the value at the wake center)
max = maximum value
o = value at the edge/free-stream value/stagnation property
p = pressure side
(r, θ, z) = values in the radial, tangential, and axial coordinate directions, respectively
s = suction side
h, t = value at the rotor hub, tip
$t.e.$ = value at the trailing edge
1 = value at the inlet
2 = value at the exit

Superscripts

$-$ = mass averaged

the trailing edge, and downstream of the rotor blade row, while the rotor is in motion. The shaft from the rotor to the data transmission system is hollow to accommodate pneumatic and electrical lines from the probe and traversing mechanism to the slip-ring units. The output signals from the transducer are transferred from the rotating to the stationary frame through the mercury slip-ring unit, while input signals are sent to the scanivalve and tangential stepping motor via a brush slip-ring assembly mounted on a tripod upstream of the compressor inlet. The flow field was surveyed at four radial locations at approximately ten axial stations downstream. Each rotor wake was discretized using 27 tangential locations from midpassage to midpassage of the rotor. Data point clustering was employed with the smallest tangential steps (corresponding to approximately 1 mm of arc length at $R = 0.8615$) taken across the wake center to resolve the wake structure finely. All present measurements have been carried out at a rotor speed of 1020 rpm, inlet axial velocity of 25.4 m/s, at the peak operating flow coefficient (based on tip speed) $\bar{\phi}$ of 0.510 and loading coefficient $\bar{\psi}$ of 0.513. The Reynolds number based on the axial chord and inlet axial velocity was 2.6×10^5.

A five-hole probe was rotated with the compressor rotor and stepped tangentially with respect to the rotor to obtain the rotor wake measurements in the trailing-edge, near-wake, and far-wake regions. The probe was of miniature scale with a probe diameter of 1.67 mm. The five-hole probe data reduction technique due to Treaster and Yocum (1979) allowed the relative velocity vector to be oriented at ±30 deg to the probe tip in the yaw and pitch planes and still remain within the calibration map. Data are presented showing typical profiles of mean velocity and pressure. The variations of overall wake characteristics with streamwise and spanwise positions are also given. Since the flow field was assumed to be statistically steady in the mean (the mean is steady in the rotating frame), it is assumed that the pressure sensed by the transducer (both the total and static pressure) was a time-averaged pressure. The average velocity was then derived from incompressible flow relations. All velocities discussed in this section are relative velocities (relative to the rotating rotor) and are normalized with respect to the corresponding maximum axial velocity, unless otherwise specified. Only typical data are presented in this paper. The comprehensive data are presented and interpreted by Prato (1990).

Sources of error in the five-hole probe are given by Sitaram and Lakshminarayana (1983) and are as follows: Misalignment in the reference direction, wall and blade vicinity effects, finite dimension of the probe tip in a velocity and/or pressure gradient, effects of probe blockage, turbulence effects, Reynolds and Mach number effects. The probe was calibrated in the same range of Reynolds number encountered in the flow field and, furthermore, corrections for static pressure and yaw angle coefficients with Reynolds number have been employed; therefore, Reynolds number effects have been incorporated. The error due to probe blockage was minimized in two ways; the probe was calibrated in its supporting structure, the ratio of the probe diameter (1.67 mm) to the average blade spacing (200 mm) was 0.8 percent. Thus errors due to probe blockage were neglected. The error due to pressure and velocity gradients (based on typical data) is estimated to be less than 1 percent on the pressure and velocity. The estimated inaccuracies in positioning the probe are as follows: axial position, ±1.0 mm; tangential position $\pm 2.4 \times 10^{-3}$ rad; radial position, ±1.0 mm. The probe alignment is accurate to within ±1deg, the probe calibration technique by Treaster and Houtz (1986) is accurate to −0.5 deg, therefore, the yaw and pitch angle accuracy is about ±2 deg. The error due to the turbulence effect is estimated to be 0.33 percent on the total velocity based on an estimated 10 percent turbulence intensity. Therefore the (maximum) cumulative error on the total velocity is estimated to be ±1.33 percent.

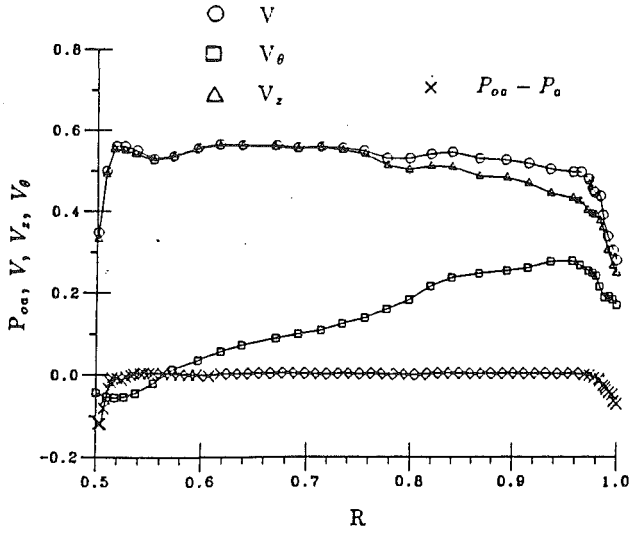

Fig. 2 Radial distribution of velocity and pressures at inlet ($Z = -0.73$)

Figure 2 shows the radial distribution of velocity and pressures at the inlet to the rotor ($Z = -0.73$). The inlet guide vane is located far upstream of the rotor (about 3.25 chord lengths of the rotor chord at midspan), hence the flow is nearly axisymmetric upstream of the rotor. The radial velocity is not shown since it is nearly zero everywhere from hub to tip. Therefore the total velocity is comprised of the axial and tangential components. As can be seen in Fig. 2, the tangential velocity increases from hub to tip due to the radial variation of the outlet angle of the inlet guide vanes, which were designed to guide the inlet flow to the rotor at the correct incidence angle at all radii. The boundary layer at the hub is approximately 4 percent of the span while it approaches 8 percent at the tip. The boundary layer at the tip is larger due to the secondary flow induced by larger turning of the flow at the tip by the inlet guide vane. This turning of the flow by the inlet guide vane increases with radius to keep the rotor design incidence angle at all radii.

Mean Velocity and Static Pressure Profiles

Axial Mean Velocity. Figures 3–6 show the variation of the axial mean velocity across the rotor wake at various axial and radial locations. The axial mean velocity is normalized by the maximum axial velocity in the wake at its respective axial and radial locations. The tangential distance is normalized by the blade spacing (y/S). *PS* and *SS* stand for the pressure and suction sides of the blade, respectively. It is clear (considering Figs. 4 and 5) that the wake profiles are asymmetric about the wake center. Also, the edge velocity is higher on the suction surface. This effect is due to the existence of pressure gradients (inviscid effects) across the passage immediately downstream of the blade trailing edge as reported by Ravindranath and Lakshminarayana (1980) and confirmed by the present author. This asymmetry is maintained to 0.3540 chords at $R = 0.7297$ (Fig. 4) and to 0.9220 chords at $R = 0.8615$ (Fig. 5).

All the wake profiles, except $R = 0.9595$, are outside the annulus and hub-wall boundary layer regions. Wake profiles and decay are fairly well behaved in these regions, again with the exception of $R = 0.9595$. Because of wake spreading and mixing with the free stream, as well as the exchange of mass, momentum, and energy on either side of the wake, the wake shows a tendency to become symmetric at far downstream locations. In the trailing-edge region, for the radius $R = 0.5676$ (Fig. 3), the wake defect W_z/W_{zo} is 0.95, which reduces to 0.25 at $Z = 0.6560$. For the wake at $R = 0.8615$ (Fig. 5), a defect of 0.69 at $Z = 0.0104$ reduces to 0.18 at $Z = 0.6250$. It appears

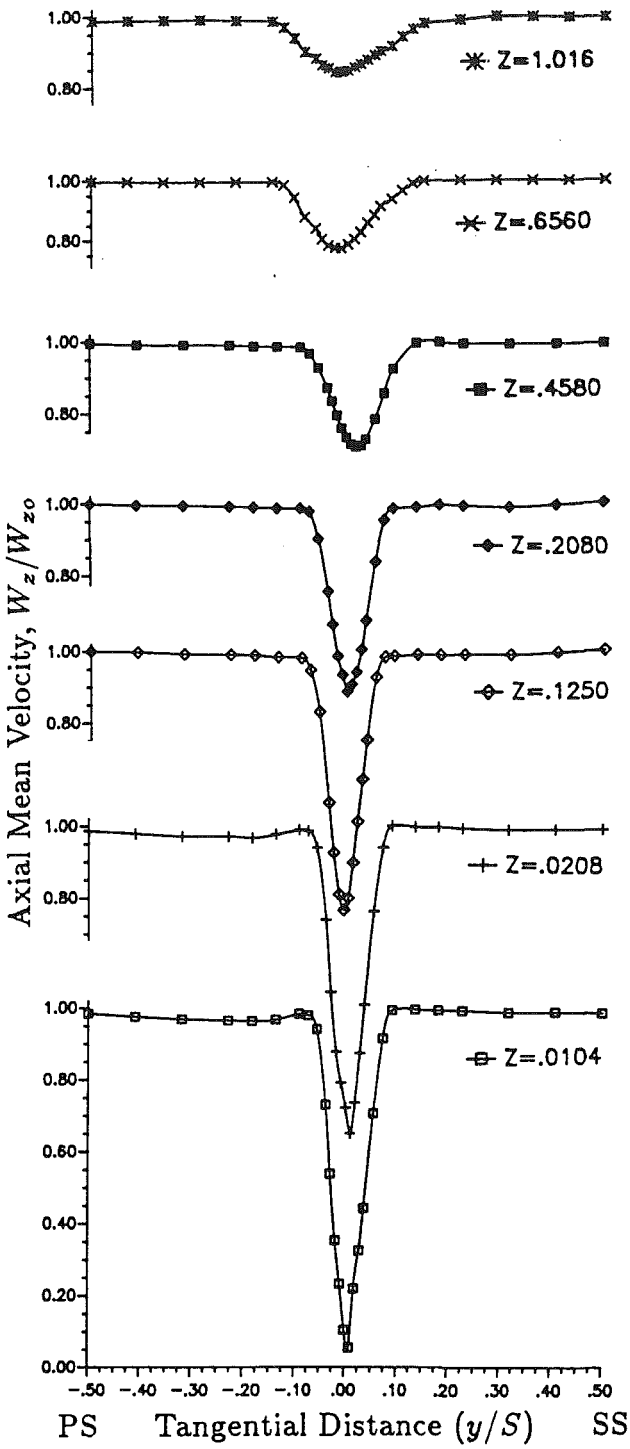

Fig. 3 Axial mean velocity profiles, $R = 0.5676$

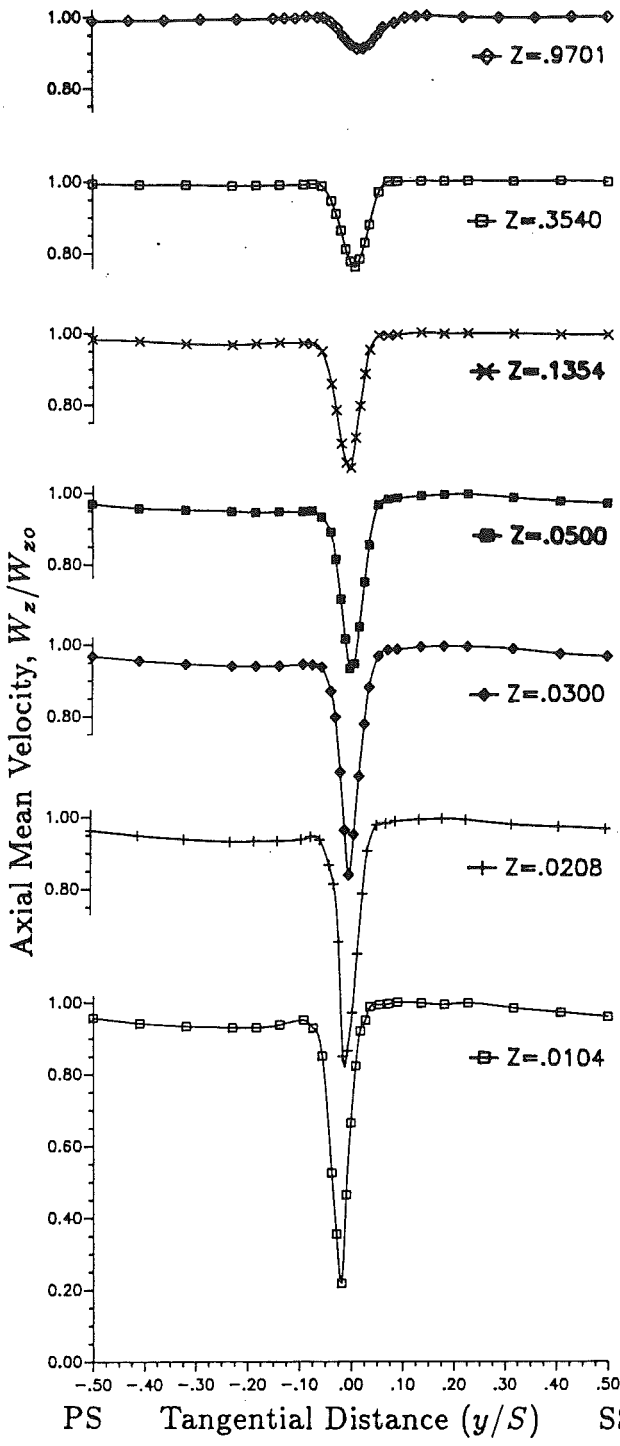

Fig. 4 Axial mean velocity profiles, $R = 0.7297$

that the velocity defect decay is faster in the tip region ($R = 0.8615$, 0.9595) even though the wake defect is larger at the trailing edge in the hub-wall region. However, the decay in the streamwise direction $Z/\cos\beta_o$ must be considered (since the blade outlet angle β_o and the blade chord length c, on which the parameter Z is based, vary in the radial direction) before any conclusions can be drawn considering the decay rates. This will be discussed later.

The wakes at $R = 0.9595$ (Fig. 6) are influenced greatly by the tip leakage flow and show some unusual behavior. The wake edge velocities are much higher on the suction side than on the pressure side; this may have been caused by large pressure gradients that exist in the blade-to-blade direction. The leakage flow tends to increase the blade suction pressures and move the blade suction peak toward the trailing edge. This behavior is confirmed from the wake data shown in Fig. 6. The leakage flow has not interacted with the wake in the near-wake region. The leakage flow tends to move farther into the passage due to blade rotation and roll up or mix with the mainstream. Such a phenomenon is clear from Fig. 6. The interaction region is located near the midpassage; hence, the leakage interaction region and wake are distinct in the near wake region. The leakage interaction region decays more slowly than the wake (as can be seen in Fig. 6). At $Z = 0.24$, the wake is almost totally decayed, whereas the leakage flow effects are still significant. This is a significant factor in design consid-

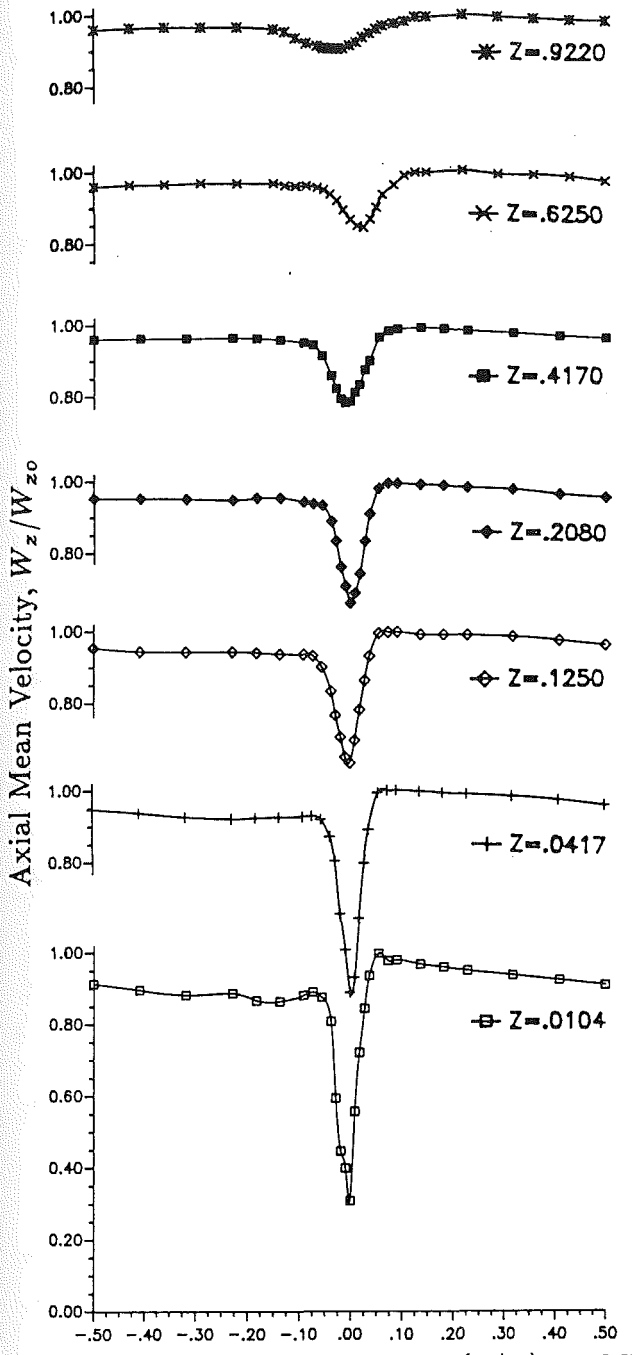

Fig. 5 Axial mean velocity profiles, $R = 0.8615$

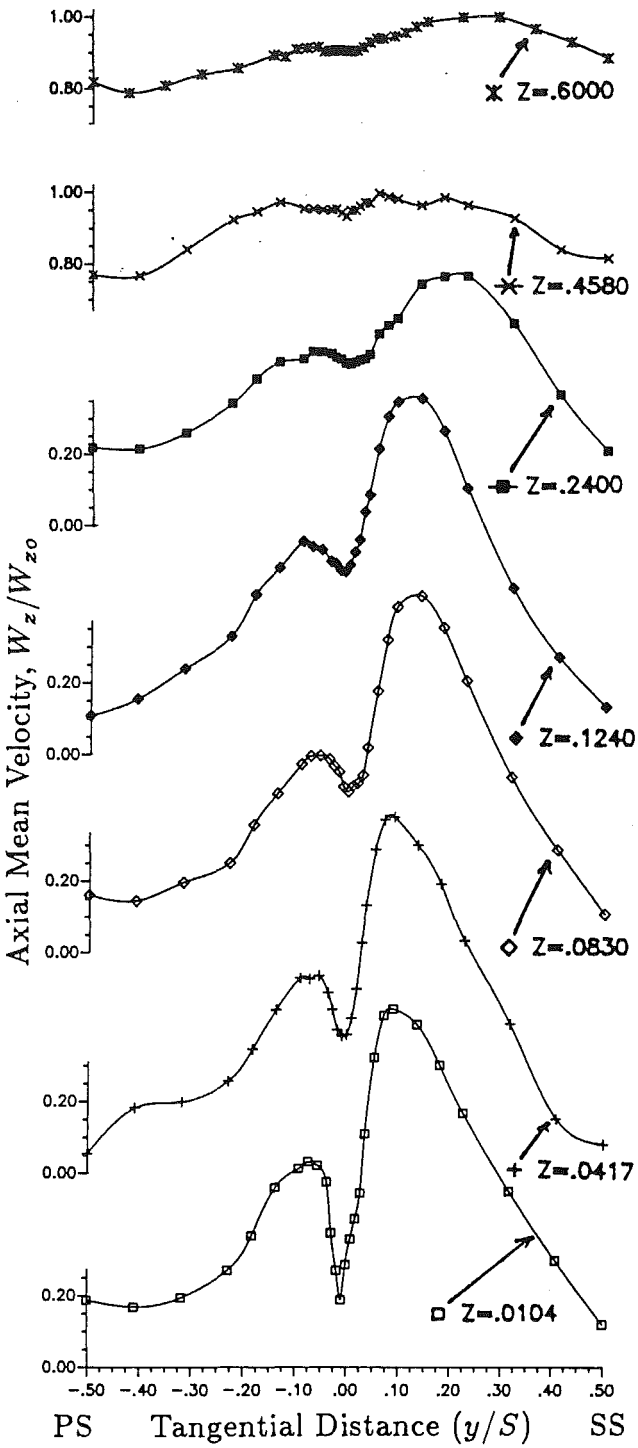

Fig. 6 Axial mean velocity profiles, $R = 0.9595$

erations, rotor-stator interaction effects, noise, flutter, and vibration effects. The tip leakage effects persist longer than the wake effects in the tip region.

Tangential Mean Velocity. Figures 7–10 show the variation of the tangential mean velocity across the wake at various axial and radial locations. The tangential velocity profiles in the near-wake region ($Z = 0.0104$ to 0.208) at all radii (except $R = 0.9595$) show some unusual trends never measured or observed before near the wake center; the tangential velocities show not only negative values (reversed direction) but also reveal peak values near the pressure surfaces. One possible reason is the separation of the flow near the trailing edge and formation of a steady separation bubble at the trailing edge as shown in Fig. 11, derived from the Navier–Stokes computation of a turbine cascade flow field by Hobson and Lakshminarayana (1990). The separation bubble for a compressor rotor blade used in this investigation is likely to be much smaller than that shown in Fig. 11. The presence of a separation bubble such as that shown in Fig. 11 is confirmed by the tangential velocity profiles in the near wake (Fig. 7–9). High tangential velocities occur in the wake edge region (marked A in Figs. 7–9), while reversed tangential velocities occur in the separated or reversed flow region (marked B in Figs. 7–9). This separation bubble is observed at $R = 0.5676$ and 0.7297 up to about 10–12 percent of chord downstream. It persists only up to about 4 percent chord at $R = 0.8615$ and no such phenomena is observed in the tip region. One possible reason for the absence

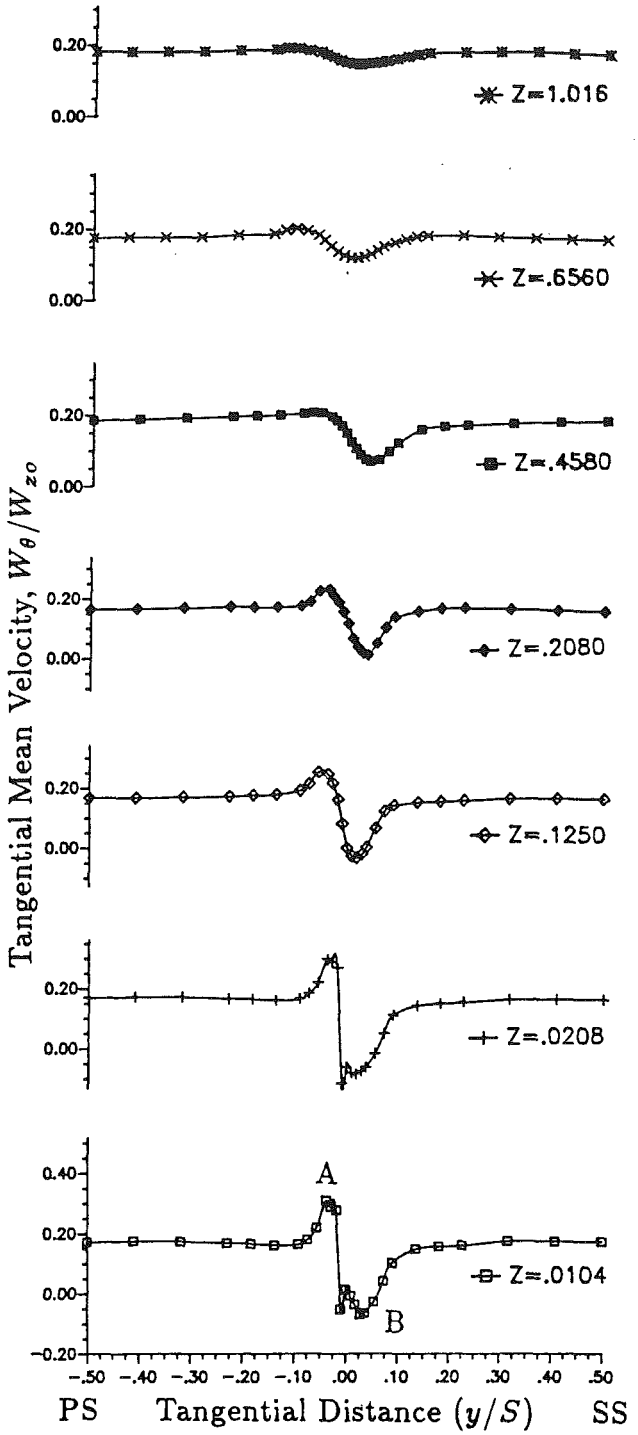

Fig. 7 Tangential mean velocity profiles, $R = 0.5676$

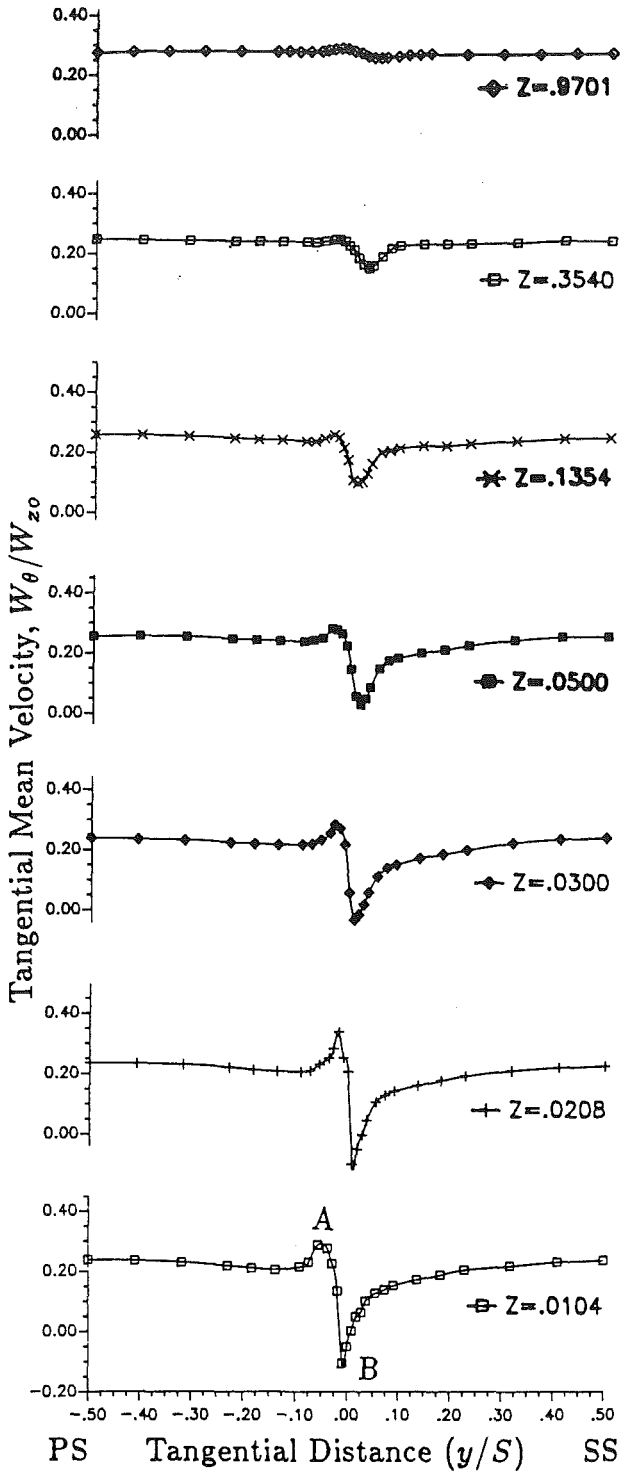

Fig. 8 Tangential mean velocity profiles, $R = 0.7297$

of such separated flow in the tip region is that the flow moves radially outward in the separated region at the trailing edge, caused by the imbalance between the centrifugal forces (which are high) and the radial pressure gradient. This can be demonstrated by the approximate radial equilibrium equation

$$\frac{\partial p}{\partial r} = \frac{\rho V_\theta^2}{r}$$

Inside the separation zone, V_θ is much higher than the free-stream value but $\partial p/\partial r$ is nearly the same as the free-stream value. This imbalance results in the radial motion inside the separation zone at the trailing edge. Dring et al. (1982) observed this in their rotor. Therefore as the outer radius is approached, the radial flow has a tendency to reduce or eliminate the separation zone. This explains the observed early diffusion of the separation region at $R = 0.8615$ and 0.9595. Moreover, the tip clearance flow overshadows the wake flow at $R = 0.9595$.

For the wake in the tip region, $R = 0.9595$ (Fig. 10), the tangential velocity profiles resemble the axial profiles except they are smaller in magnitude. The profiles in this region show the effect of the complex interactions in the tip region. As discussed in the case of the axial velocities, the leakage flow, secondary flow, and the annulus-wall boundary layer contribute significantly to the overall shape of the velocity profile and its shape in this region. The wake decays much more rapidly in this region and disappears before $Z = 0.24$. Up to this region,

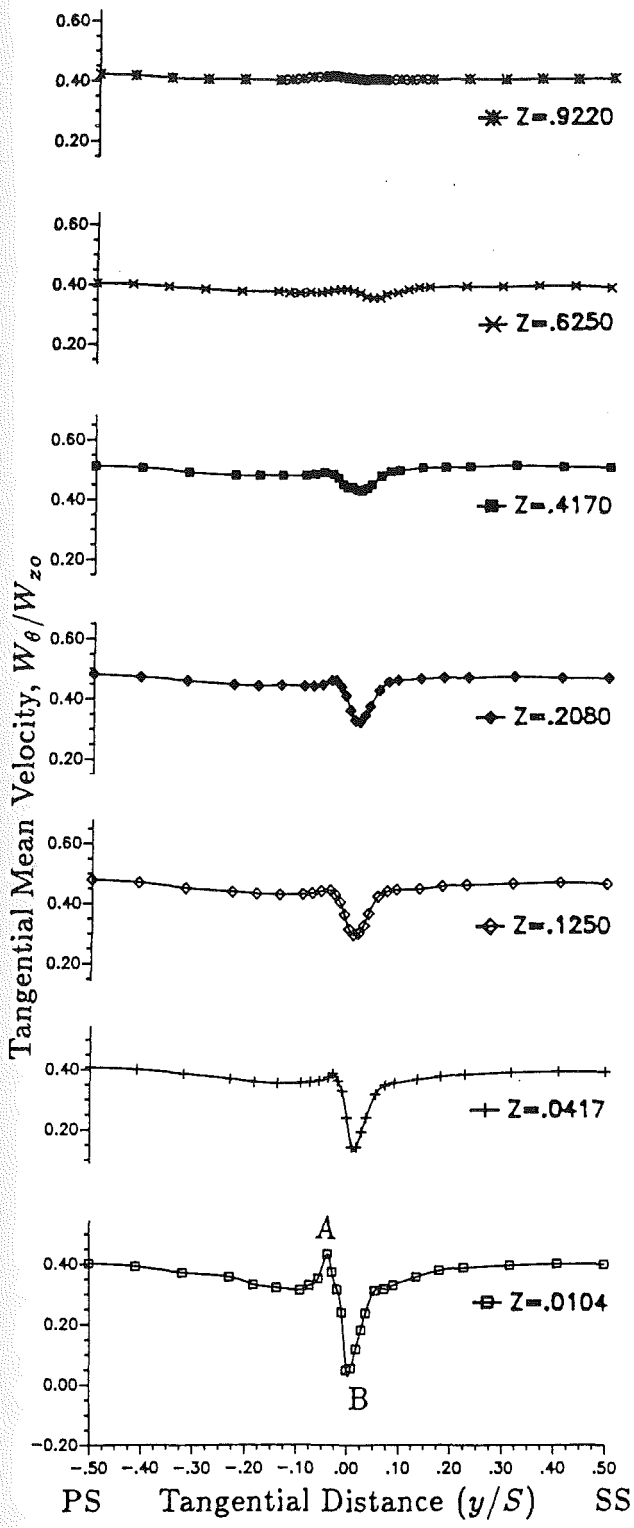

Fig. 9 Tangential mean velocity profiles, $R=0.8615$

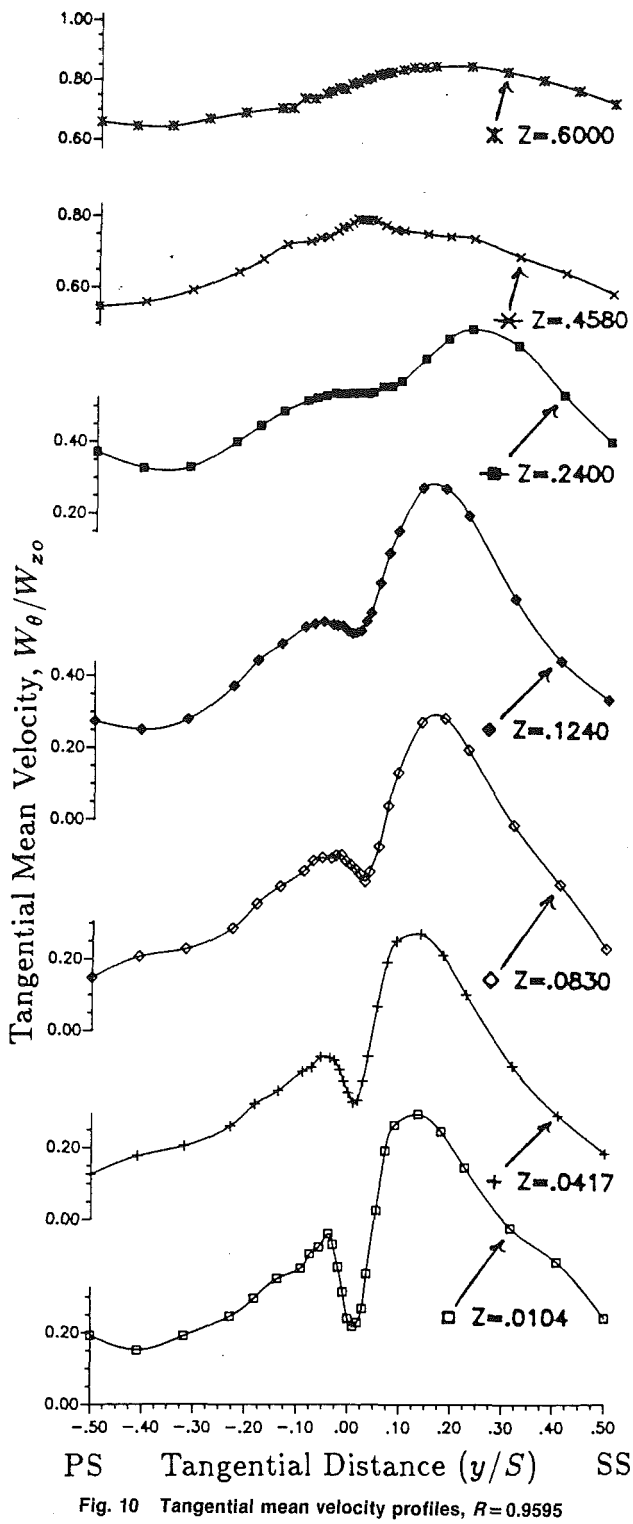

Fig. 10 Tangential mean velocity profiles, $R=0.9595$

the leakage flow and the wake regions are distinct, with no noticeable interaction. Beyond $Z=0.24$, the leakage flow and its interaction with the main flow dominate the flow field. Intense mixing of the flow in this region give rise to smooth velocity profile at $Z=0.6$. The mixing of the leakage flow is intense from the trailing edge to $Z=0.6$.

Radial Mean Velocity. The radial velocity profiles are shown in Figs. 12–15 for $R=0.5676$, 0.7297, 0.8615, and 0.9595, respectively. The radial velocities are appreciable at the wake centerline near the trailing edge away from the tip region. The peak values are close to 20 percent of the axial velocity near the trailing edge, decreasing to nearly zero in the free stream. The radial velocities show the slowest decay of all the velocity components, maintaining almost constant peak values up to about half a chord at $R=0.5676$, 0.7297, and 0.8615, noticeable decrease is observed only at one chord downstream. Figure 13 shows the radial mean velocity profiles for $R=0.7297$. Note that at almost a full chord downstream the maximum radial velocity is still well over 50 percent of its value in the trailing-edge region. The maximum radial velocity has the slowest decay rate of the three components of the total velocity vector.

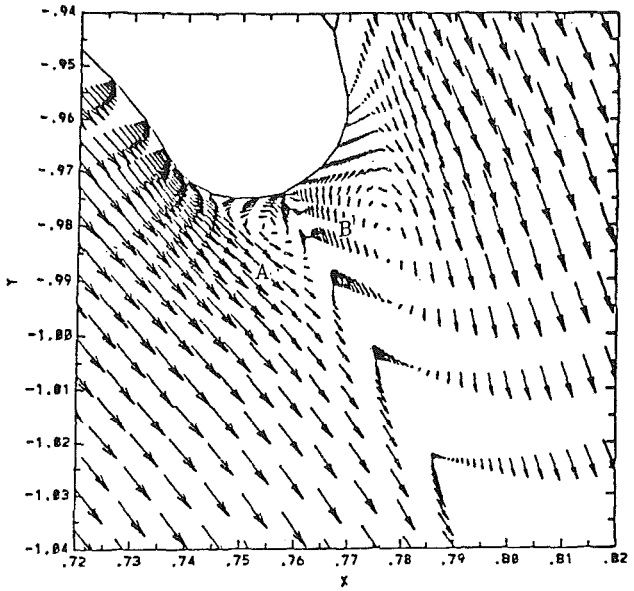

Fig. 11 Navier-Stokes simulation of the blade training edge region in a turbine cascade (Hobson and Lakshminarayana, 1990)

Some interesting results are shown in Fig. 15 where the radial velocity profile across the wake at $R=0.9595$ is shown. Again the radial flow due to the boundary layer is evident and dominates in the near and far-wake regions. Note that the radial velocity spans the entire passage. This is believed to be the effect of tip leakage flow. The blade undergoes high unloading in the tip region, accompanied by a strong tip leakage flow, which spans the entire passage resulting in the observed velocity distribution. The radial velocity in the tip region shows an unusual distribution. The radial velocities in the wake region are outward and nearly constant across the wake. Consistent with the axial (Fig. 6) and the tangential velocity (Fig. 10) distributions at this radial location, the wake decay is very rapid. However, the radial velocity due to the leakage flow is consistently high across the entire passage, and the peak values near the trailing edge are located close to 30 percent of the passage from the pressure surface. The radial velocities are small from suction surface to midpassage, and large from midpassage to pressure surface. The leakage flow, due to blade motion, tends to move toward the pressure side of the blade and interacts with the main flow to produce a "wake"-like region as observed by Lakshminarayana et al. (1991). The outer edge of this interaction region is located close to $R=0.9595$. Large radially outward velocities in this region ($y/S=-0.5$ to -0.10) represent entrainment of the main flow (through radial migration) by the mixing region. Unlike other regions, the radial velocities decrease rapidly from $Z=0.4580$ to 0.6.

Pressure Variation Across the Wake. Figure 16 shows the variation of the static pressure rise coefficient across the rotor wake at $R=0.7297$. The data at other locations can be found from Prato (1990). The static pressure varies not only across the wake, but also at the wake edge due to inviscid effects. The static pressure variation across the wake is as large as 30 percent in the trailing-edge region and drops off to about 8 percent at $Z=0.354$ downstream. The measurement seems to confirm the trend observed by Thompkins and Kerrebrock (1975) who have reported a 25 percent variation in static pressure across the wake at 10 percent of an axial chord downstream of a transonic rotor. In the present case the first measurement station is very close to the trailing edge and, consequently, very large static pressure gradients were measured. However, the data at the trailing edge must be viewed with some caution. As mentioned earlier, the pressure probes are subject to wall vicinity effects and also the large angle variations within the

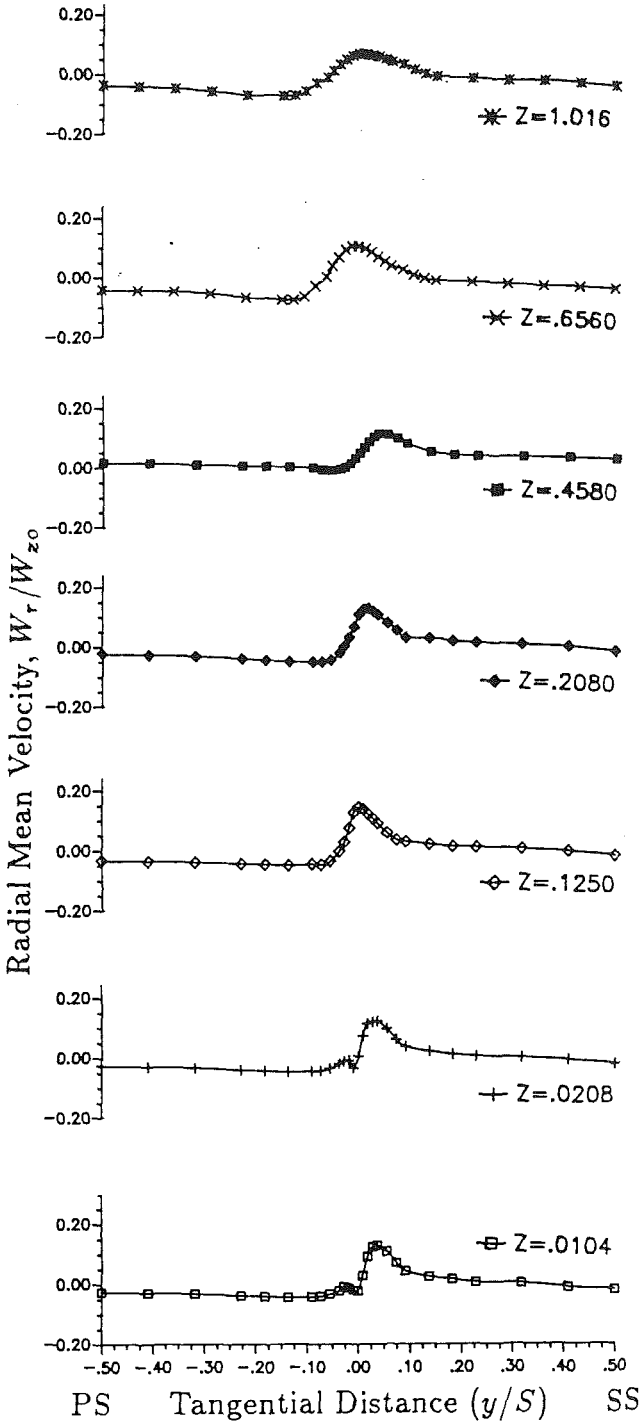

Fig. 12 Radial mean velocity profiles, $R=0.5676$

wake could affect the values of the static pressure in the trailing-edge region.

The static pressure distribution in the near-wake region clearly shows the presence of a separation bubble at the trailing edge region and this persists up to $Z=0.354$. Paterson and Weingold (1985) reported that the wake static pressures were strongly influenced by the presence of vortex shedding from the trailing edge of a simulated compressor rotor. In Fig. 16, the locations marked A and B are the edges and C is the core of the bubble. This corresponds to A and B in Fig. 8, where the tangential velocity gradients are very large. The size of the bubble is small, its size decaying very rapidly, with only a trace at $Z=0.354$. The pressure coefficient C_p distribution in the free stream indicated that the inviscid effect on the pressure

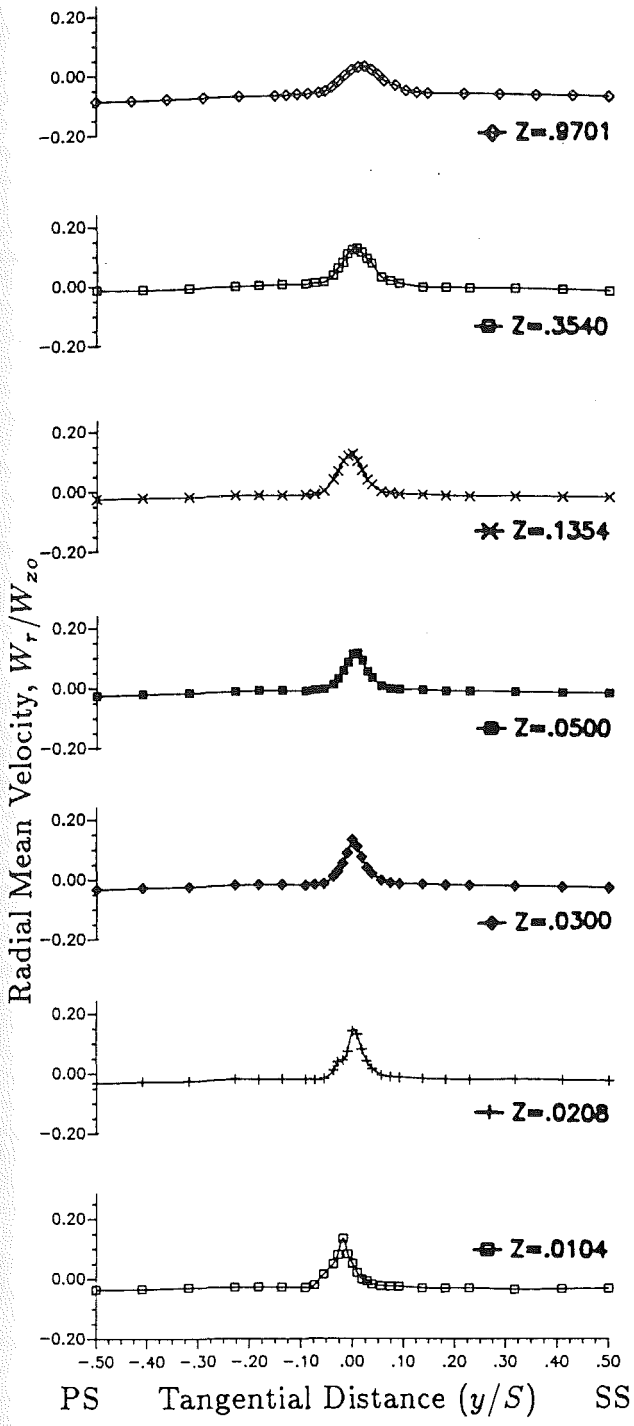

Fig. 13 Radial mean velocity profiles, $R = 0.7297$

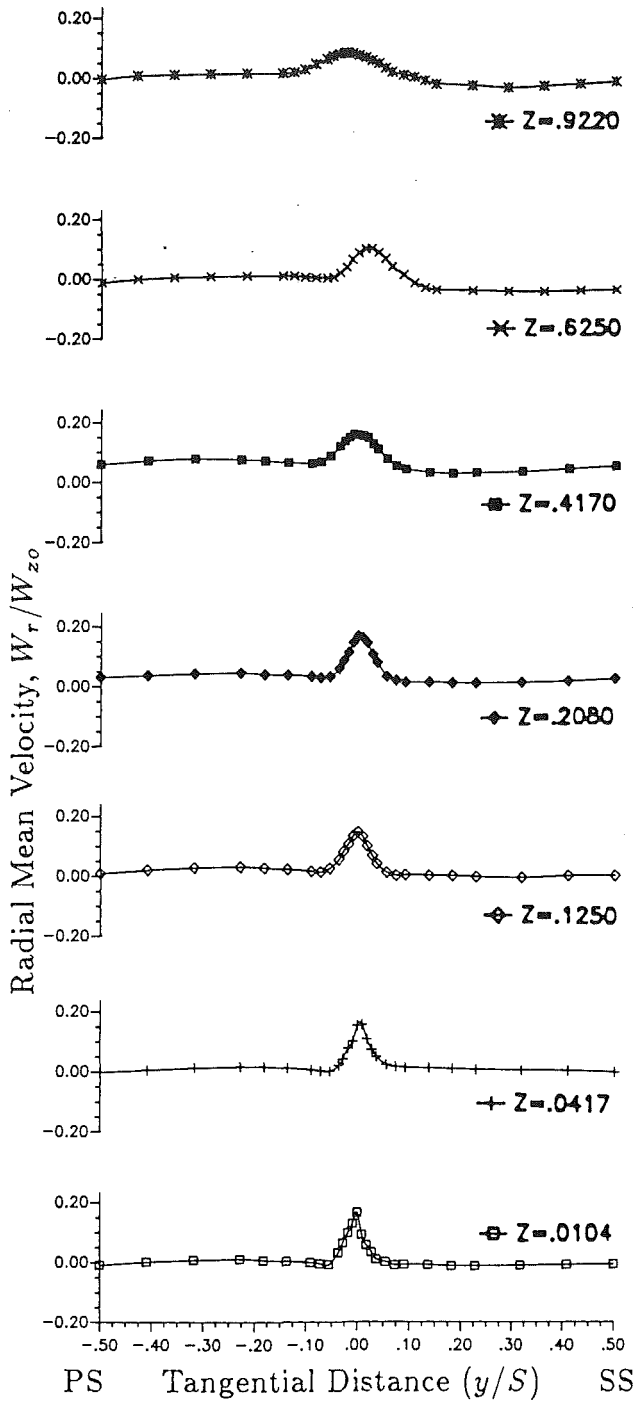

Fig. 14 Radial mean velocity profiles, $R = 0.8615$

distribution is still present. Note that the widely assumed equalization of pressure (even in inviscid flows) on either side of the blade surfaces at the trailing edge is not valid in the trailing-edge and near-wake regions. Considerable blade-to-blade static pressure gradients exist in the inviscid region at $Z = 0.0104$, $R = 0.7297$, and these persist up to even 5 percent chord from the trailing edge, becoming nearly uniform at $Z = 0.2190$. The static pressure differences decays more rapidly than the velocity defect. As expected, the static pressures near the trailing edge are lower on the suction surface at the edge of the wake (e.g., point D in Fig. 16) and increase continuously toward the pressure surface until the outer edge of the wake is reached (e.g., point E in Fig. 16). The static pressure decreases from this point through the separated region, increasing again as the wake center is approached. Hence the separated region is located closer to the pressure side away from the wake center. This phenomenon, in a rotor, has never been measured or reported earlier and shows complex features of the flow field in the vicinity of the trailing edge.

Experimental data (Fig. 16) indicate that the static pressure increases at the wake center and as the wake travels downstream this difference decreases. For the data presented at $R = 0.7297$, the ratio of the static pressure at the wake center to the corresponding static pressure in the free-stream decays rapidly in the trailing-edge region, and the decay is slower in the near and far-wake regions. This very rapid decay in the trailing-edge region is attributed to the rapid decay in the velocity defect and turbulence intensity as reported by Ravindranath

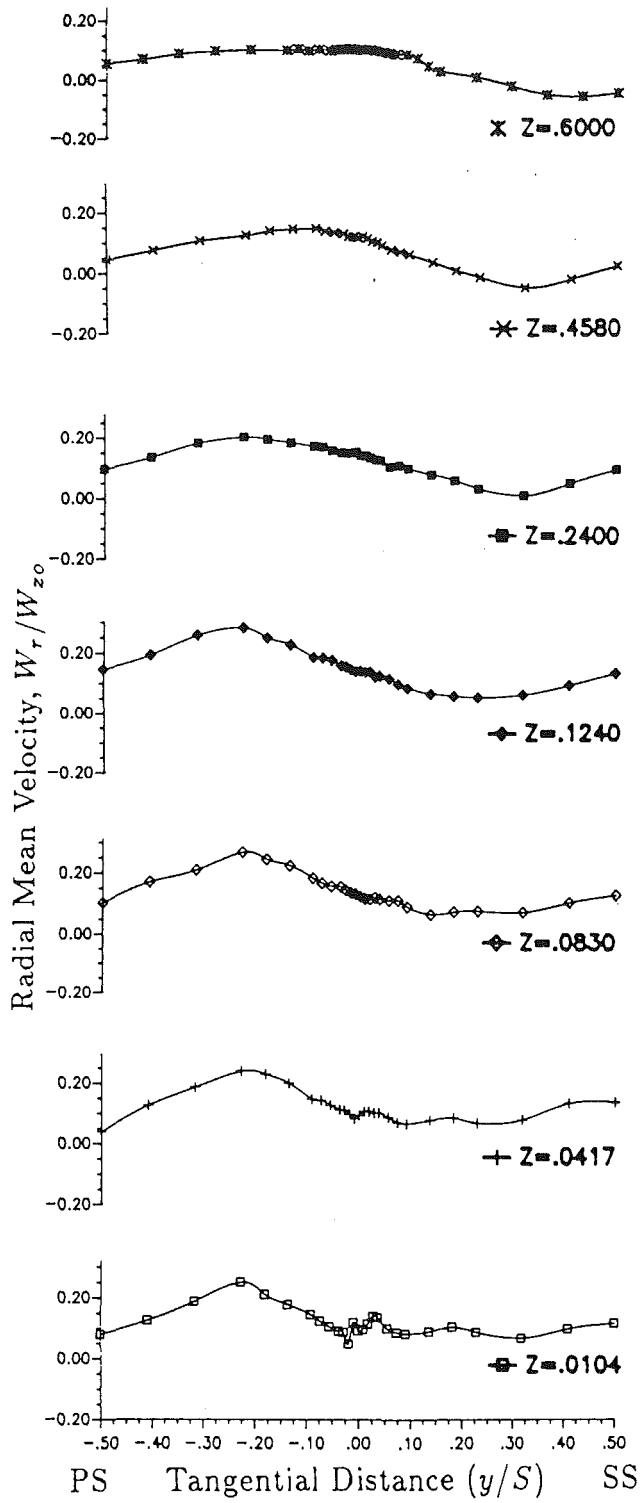

Fig. 15 Radial mean velocity profiles, $R = 0.9595$

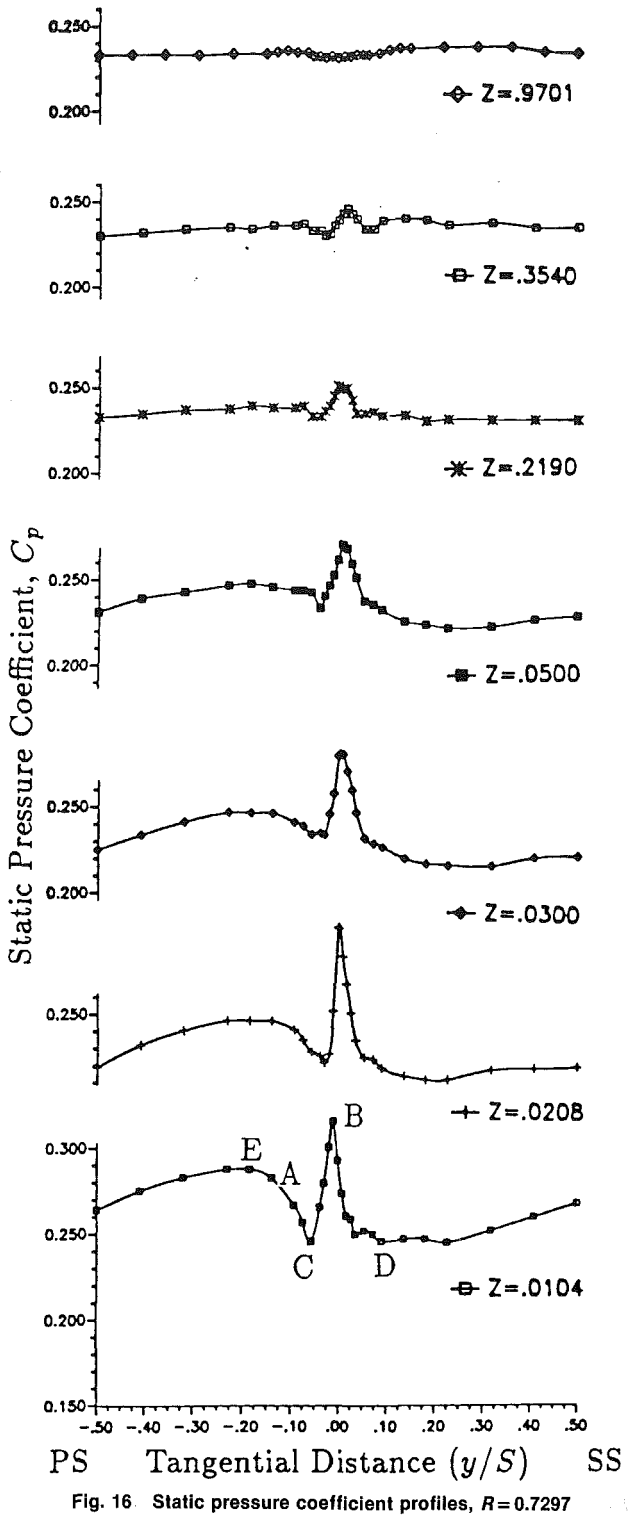

Fig. 16 Static pressure coefficient profiles, $R = 0.7297$

and Lakshminarayana (1980). The existence of pressure gradients across the wake has been explained by Ravindranath and Lakshminarayana (1980) and can be understood by examining the equation of motion of the fluid in the rotating coordinate system in a direction normal (n) to the streamline(s). The equation can be approximately written (neglecting the viscous terms as well as some of the inertial terms)

$$\frac{-1}{\rho}\frac{\partial p}{\partial n} \simeq 2\omega W_r \cos\beta - \frac{W_s^2}{R_c} - \frac{\partial \overline{(w')^2}}{\partial n}$$

where n is the direction normal to the streamlines, W_s is the streamwise velocity, R_c is the radius of curvature of the streamline and $\overline{(w')^2}$ is the turbulent fluctuation in the (n) direction and ρ is the density. It is evident from the above equation that, in addition to Coriolis and centrifugal forces, the gradients of the turbulent intensity in the (n) direction have an appreciable effect on the pressure gradient $\partial p/\partial n$. At the wake center, near the trailing-edge region, the turbulence intensity terms dominate (as reported by Ravindranath and Lakshminarayana, 1980) and hence the static pressure gradients can exist even in the absence of curvature R_c. Qualitative analysis of this effect is given by Reynolds et al. (1979).

Rotor-Wake Decay Characteristics

Decay of Maximum Defect in Mean Velocities. The decay of the wake centerline is important in understanding the decay of the wake. Therefore, the decay of the wake centerline is interpreted and discussed in this section. The decay of the defects (or maximum velocity in the case of the radial velocity) in velocity is plotted versus $Z/\cos\beta_o$, where Z is the axial distance measured from the trailing edge and β_o is the local value of the blade outlet angle. The downstream streamwise distance is the appropriate coordinate system to use in the interpretation of the wake decay characteristics. Decay of the mean velocity defect is affected by pressure gradients, turbulence structure, Reynolds number, rotation, and curvature and by the viscous effects that exist near the blade trailing edge. The secondary flow that exists near the hub wall as well as the secondary flow and the tip-leakage flow in the annulus-wall region also contribute to the decay of the defect in velocity near the annulus and hub wall.

The decays of the defects of the axial and tangential velocities are shown in Fig. 17. The defect is based on the minimum and the maximum velocity in the wake, the latter of which usually occurs near the suction surface. The decay of the axial and tangential defects is very rapid in the trailing-edge region and becomes less rapid in the near and far-wake regions. Again the trailing edge region is up to about 5 percent chord from trailing edge. The near-wake extends to nearly 40 percent chord and the far-wake region is beyond this region. The very large decay rate in the trailing-edge region is attributed to high turbulence intensities (reported by Ravindranath and Lakshminarayana, 1980), pressure gradients, and three-dimensional and near-wake regions. The rate of decay of the axial and the tangential velocity defects are about the same in the far-wake region.

In an earlier paper (Ravindranath and Lakshminarayana, 1980), three regions of the wake were identified. The trailing-edge region, where flow separation, the presence of vortices and mixing of the boundary layers on either surfaces produce intense mixing, resulting in a rapid decay of the wake centerline and rapid increase in the wake width (as shown later). In this region the axial velocity defect (Fig. 17) decreases from 1.0 to nearly 0.5 in a distance of 5 percent chord from the trailing edge (except at $R=0.9595$ and 0.5676). Tangential velocity defect also decreases very rapidly in this trailing-edge region. In the near-wake region (extending from approximately 0.05 to 0.4 chord), the decay slows down considerably. For example, the axial velocity defect near the midspan decreases from nearly 0.5 to almost 0.2 in the near-wake region. Beyond $Z/\cos\beta_o > 0.4$, the decay is very slow.

The centerline velocity defects in the trailing-edge and near-wake regions (both axial and tangential) decay more rapidly in regions away from the endwall, much less rapidly in the hubwall (influenced by secondary flow) and tip (influenced by leakage flow) regions. However, in the far-wake region, the wake near the tip shows the fastest decay. These results clearly show that extremely small rotor/stator spacing (say 10–20 percent, which is common in aircraft engines) results in highly unsteady flow in subsequent blade rows due to upstream rotor wakes. This highly unsteady flow influences rotor/stator noise, blade and endwall heat transfer, vibration and flutter characteristics as well as overall performance of gas turbine engines. These phenomena are directly related to the rotor wake width as well as the defect in velocity.

Figure 18 shows the decay of the maximum radial velocity in the wake. The distribution shows an unusual trend. Unlike the axial and tangential defect decay the decay of $W_{r_{\max}}$ is very slow. At $R=0.7297$ and 0.8615 there is an appreciable decrease in $W_{r_{\max}}$ in the trailing-edge region, beyond which the decay is very slow. The rapid decay in the trailing-edge region is caused by the intense mixing in the flow field and dissipation

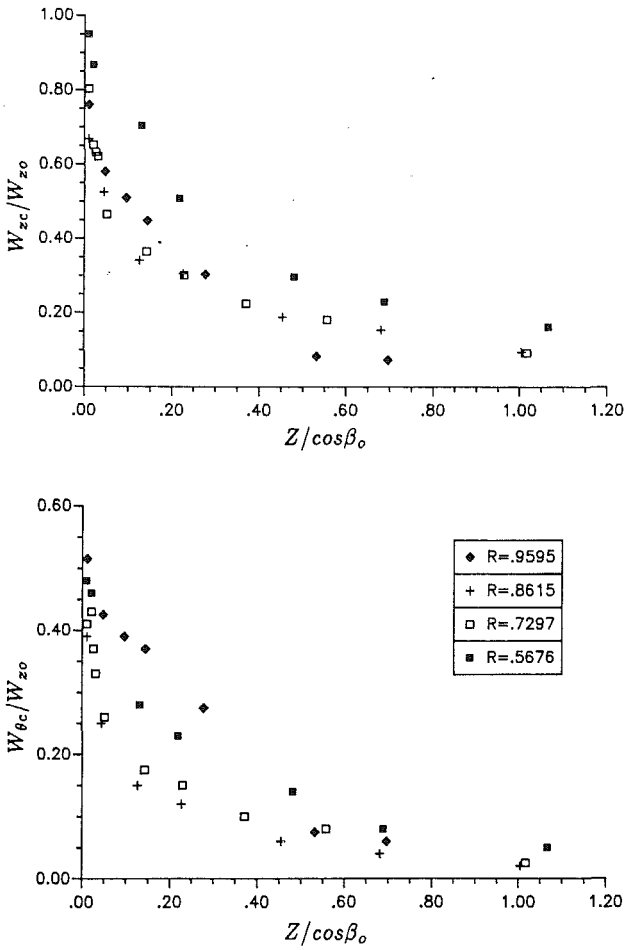

Fig. 17 Decay of axial and tangential mean velocity defects with streamwise distance

of the separation bubble discussed earlier. At $R=0.8615$, $W_{r_{\max}}$ has actually increased at $Z/\cos\beta_o=0.2$ due to the radial migration caused by the imbalance between the static pressure gradient and the centrifugal forces acting on the fluid, as explained earlier. Near the hub ($R=0.5676$), the radial velocity increases initially partly due to the secondary flow in this region before decreasing downstream. The radial velocity at the tip shows the effect of the interaction between the leakage and the main flow, which tends to entrain fluid from other regions (and hence increase radial velocities) initially up to $Z/\cos\beta_o=0.2$. This behavior seems to persist up to $Z/\cos\beta_o=0.5$, beyond which this interaction region mixes out resulting in low radial velocities.

Figure 18 also shows the decay of the total mean velocity. The decay of the total mean velocity follows almost exactly the trend of the axial velocity. The decay rate of the total velocity defect in the tip region is slightly lower than the decay rate of the axial velocity defect since the total velocity has smaller velocity gradients in this region. The slowest decay rate seems to be (again influenced by secondary flow) at the radius $R=0.5676$ for the trailing-edge, near and far-wake regions. The decay rate at $R=0.9595$ is, again, slower than those at $R=0.7297$ and 0.8615 in the trailing-edge and near-wake regions. The maximum decay rates occur in the midspan regions.

Decay of Static Pressure Difference Across the Wake. The variation of the maximum static pressure difference across the rotor wake for $R=0.7297$ is shown versus streamwise distance in Fig. 19. The static pressure decay is referenced to the maximum static pressure in the wake minus the free-stream value

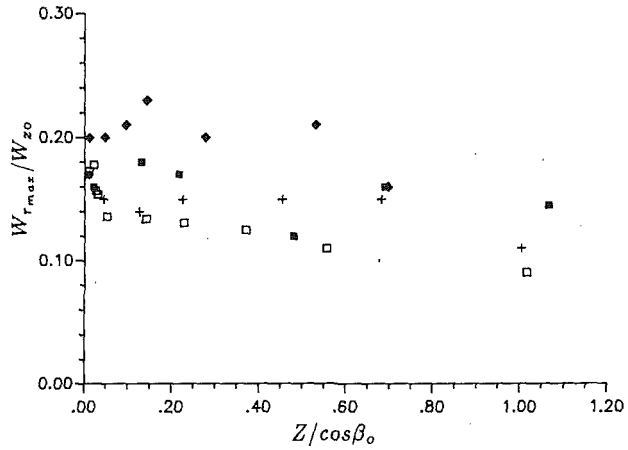

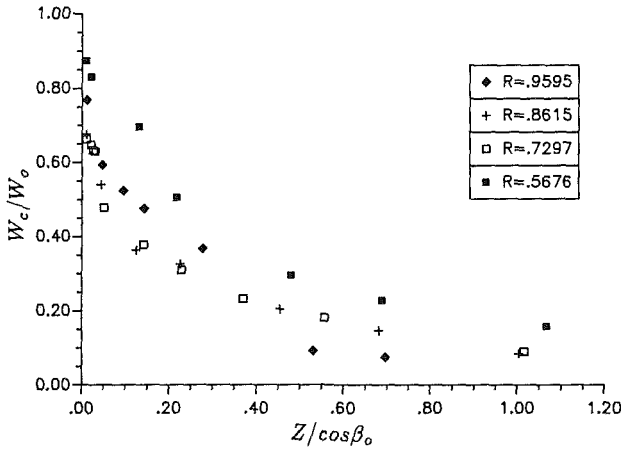

Fig. 18 Decay of maximum radial velocity and total mean velocity defect with streamwise distance

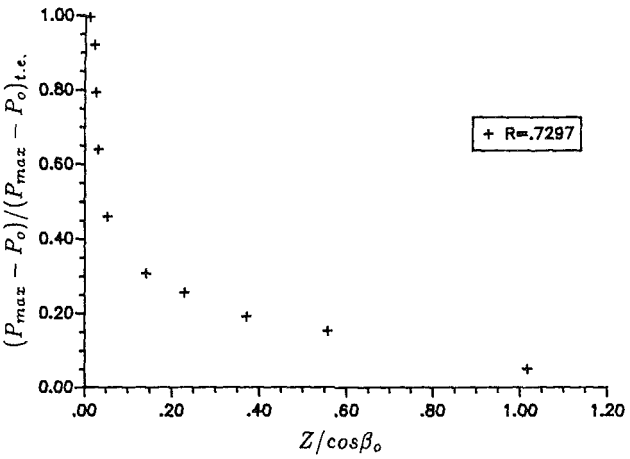

Fig. 19 Decay of maximum static pressure with streamwise distance

at the trailing edge of the rotor blade. Therefore at the trailing edge of the blade the referenced value of the static pressure is equal to unity. Note the very rapid decay of the maximum static pressure in the trailing-edge region. The value of the maximum static pressure drops by over 50 percent in about 5 percent chord in the streamwise direction and to nearly 70 percent of its value at the trailing edge in about 13 percent of the chord in the streamwise direction. The slope of the static pressure decay rate is almost a vertical line (approaching an infinite rate of decrease) in the trailing-edge region. This rapid decrease is caused by the intense mixing and high turbulence

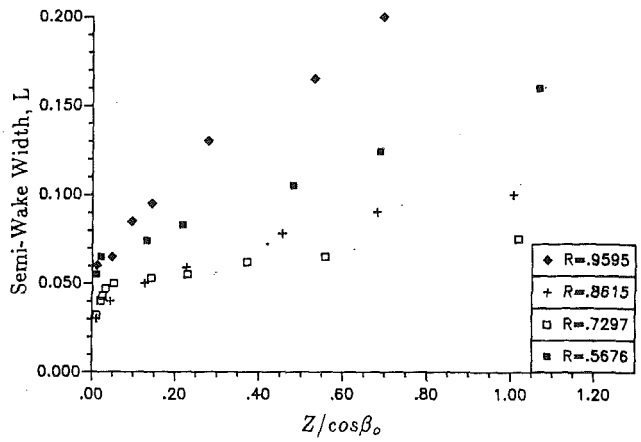

Fig. 20 Variation of semi-wake width with streamwise distance

intensities (Ravindranath and Lakshminarayana, 1980). Furthermore, the higher the blade loading, the larger the decay rate in the trailing-edge region becomes. The decay is less rapid in the near and far-wake regions and asymptotically approaches the value of 0.10 in the far-wake region. Most analysts assume that the static pressure is uniform at the trailing edge, both inside the wake and in the free stream. This assumption is not valid, as can be clearly seen from Fig. 19. Substantial pressure gradients exist across the wake, even up to half a chord downstream, and its decay in the wake is expected to be considerably influenced by the blade loading and three dimensionality of the flow field. The streamwise and cross-stream gradients in static pressure will influence the wake decay characteristics considerably.

Semi-Wake Width Variation. The semi-wake width is defined as the width of the wake at half the defect of total velocity. The variation of this semi-wake width with streamwise distance is shown in Fig. 20. The wake width increases rapidly in the trailing-edge region and the growth becomes more gradual in the near and far-wake regions. The growth is due to exchange of momentum and energy on each side of the wake. In the region ($0 < Z/\cos\beta_o < 0.1$) the growth rate is to some fractional power (usually 1/2) of the streamwise distance. For $0.1 < Z\cos\beta_o < \infty$) the wake width growth is approximately linear with the streamwise distance. The rate of growth of the wake width in the trailing-edge region at $R = 0.7297$ and 0.8615 is higher compared to those near the hub and tip regions. The wake width increases rapidly in the trailing-edge region ($Z/\cos\beta_o = 0$ to 0.04), almost doubling in value for $R = 0.7297$. The initial wake width is highest near the hub and the tip due to larger boundary layer growth and complex interaction of secondary flow and/or leakage flow. This trend persists even far downstream. The rate of growth of the wake width in the near and far wake region is slowest in the midspan regions ($R = 0.7297$ and 0.8615), and higher in the hub region ($R = 0.5676$), and highest in the tip region ($R = 0.9595$).

Comparison of Rotor Wake Decay Characteristics

In this section the effect of blade loading on the wake characteristics of the present rotor is considered. The present data will be compared with data by Ravindranath and Lakshminarayana (1980) who used a hot-wire to capture the wake at a design flow coefficient of 0.56 in the same compressor rotor. The data will be referred to as the "design data," and the data by the author will simply be referred to as the "present data."

Comparison of the total mean velocity defects are shown in Fig. 21 for $R = 0.7297$. The top plot shows similar magnitudes and decay rates for both sets of data. Small discrepancies in agreement occur in the near-wake region but are within the

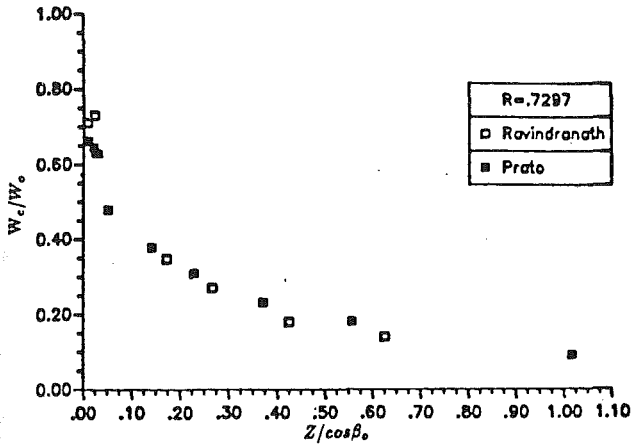

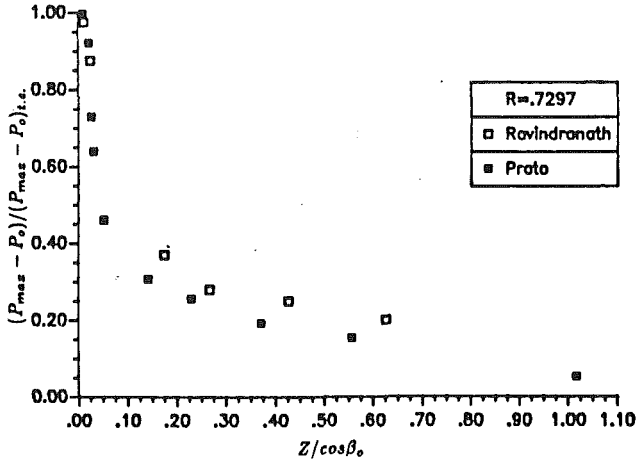

Fig. 22 Comparison of static pressure difference decay

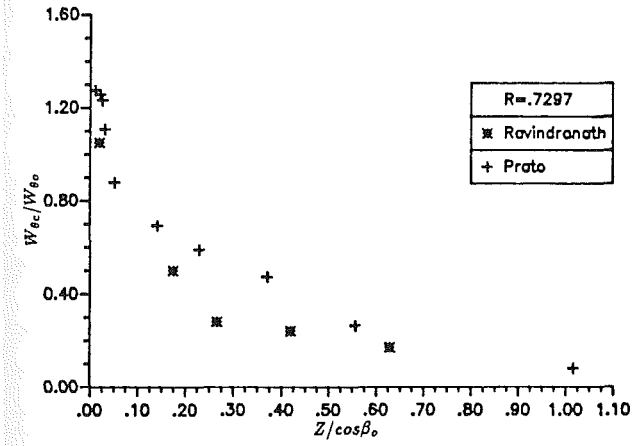

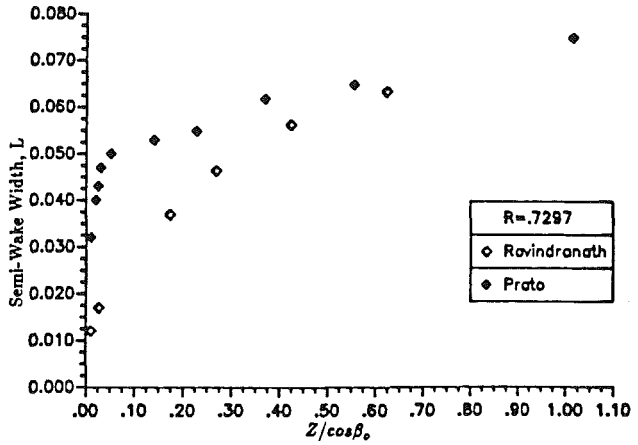

Fig. 21 Comparison of total and tangential mean velocity defects

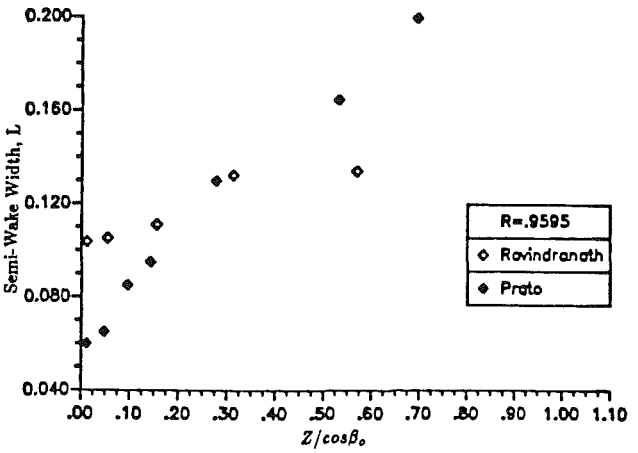

Fig. 23 Comparison of semi-wake width variation

scatter due to experimental uncertainty. At $R = 0.7297$ the two sets of data have equal magnitudes and decay rates and are in fact nearly coincident everywhere. It is assumed that the difference in tip clearance between the two data sets has very little or not effect on the wake characteristics at this location. Large variations in the total relative velocity defect due to blade loading was not expected. The axial velocity defect and its decay were also identical in both cases (Prato, 1990). Hence, the loading effect on the total and axial velocity defect and their decay rates is not significant.

The decay of the tangential velocity defect is also shown in Fig. 21. The tangential velocity defect in the present case is found to be higher than the lower loading case everywhere, equalizing only in the far-wake region. The loading has a major effect on the flow turning and the tangential velocities. This is clear from Fig. 21. The rate of decay of defect in tangential velocity with streamwise distance is nearly the same in both cases.

Figure 22 shows the comparison of the decay of the static pressure difference across the wake for $R = 0.7297$. Both data support the existence of very strong static pressure gradients and associated high decay rates in the trailing-edge region. Through the near-wake and into the far wake both decay rates remain smooth and asymptotic. The present data suggests a lower static pressure in the near and far-wake regions. Again, the scatter due to experimental uncertainty rules out any interpretation of the differences due to loading so the magnitudes and decay rates will be considered equivalent. Therefore the loading effect on the nondimensional tangential pressure gradient is not significant.

A comparison of the semi-wake width variation for $R = 0.7297$ is shown in Fig. 23. Very large wake width and growth rates are evident at the peak pressure rise condition (present data). This growth rate quickly becomes linear with downstream distance in the near-wake region. Data at design condition (top graph for $R = 0.7297$) suggests a lower semi-wake width everywhere and this is expected due to smaller blade boundary layer growth at design conditions. The wake width and growth rate in the far-wake region are almost identical for both cases.

The semi-wake width comparison at $R = 0.9595$ is shown plotted in Fig. 23. Caution must be exercised in the interpre-

tation of this data due to the larger tip clearance of the present case. The blade undergoes higher unloading in the tip region due to larger tip clearance in the present case. This is accompanied by a decreased adverse pressure gradient which leads to a smaller semi-wake width. Both wakes seem to spread monotonically even in the trailing-edge region. However, the present data maintain a larger growth rate in all wake regions. Again the flow in the tip region is very complex and large mixing occurs there. Increased tip clearance allows even stronger mixing of the fluid and results in rapid spreading of the wake.

Conclusions

Some of the important conclusions that can be drawn on the basis of the results of the present investigation are as follows:

1 The asymmetric velocity profiles in the trailing-edge and near-wake regions tend to become symmetric in the far-wake region due to mixing and the exchange of mass, momentum, and energy.

2 The decay of the maximum radial velocity was the slowest compared to the axial and tangential velocity defects in the near and far-wake regions.

3 The wakes at $R = 0.9595$ are greatly influenced by the leakage flow and show unconventional behavior. The leakage flow interaction region (with the main flow) and the wakes are distinct in this region. The leakage flow interaction region decays more slowly than the wake.

4 The radial velocity profile is substantially different in the tip region ($R = 0.9595$) from that at lower radii. Because of the large tip clearance of the present rotor, the radial velocity profiles show the effects of the leakage flow, which spans the entire blade passage. These radial velocities are very large and represent entrainment of the main flow (through radial migration) by the mixing region.

5 Strong static pressure gradients exist across the wake in the trailing-edge and near-wake regions. The static pressure increases (the total velocity decreases) as the wake center is approached. This static pressure decays very rapidly in the trailing-edge region and the decay rate is very gradual in the far-wake region.

6 Wake width in the near and far-wake regions is largest in the tip region due to the complex flow mixing caused by the interaction of the leakage flow, the wake, and the annulus-wall boundary layer. The wake width is also high in the hub region due to secondary flow.

7 An increase in the blade loading has an insignificant effect on the decay rate of the axial and the total velocity defect.

8 An increase in the blade loading increases the tangential velocity defect, but the decay rate of the velocity defect is very similar.

9 An increase in the blade loading has no significant effect on the decay rate of the static pressure difference across the wake.

10 In the trailing-edge and near-wake regions, increases in blade loading increases the wake width (due to larger boundary layer growth) and growth rates significantly. The wake width and growth rate in the far-wake region are almost identical for both cases.

References

Dring, R. P., Joslyn, H. D., and Hardin, R., 1982, "An Investigation of Compressor Rotor Aerodynamics," ASME *Journal of Engineering for Power*, Vol. 104, p. 84.

Gallus, H., Grollius, H., and Lambertz, J., 1982, "The Influence of Blade Number Ratio and Blade Row Spacing on Axial Flow Compressor Stator Blade Dynamic Load and Stage Sound Pressure Level," ASME *Journal of Engineering for Power*, Vol. 104, p. 633.

Hirsch, C. H., Kool, P., and DeRuyck, J., 1978, "The Three-Dimensional Flow and Blade Wake in an Axial Plane Downstream of an Axial Flow Compressor Rotor," ASME Paper No. 78-GT-66.

Hobson, G. V., and Lakshminarayana, B., 1990, "Computation of Turbine Flow Fields With a Navier-Stokes Code," AIAA Paper No. 90-2122.

Lakshminarayana, B., 1980, "An Axial Flow Research Compressor Facility Designed for Flow Measurement in Rotor Passages," ASME *Journal of Fluids Engineering*, Vol. 102, pp. 402-411.

Lakshminarayana, B., Zaccaria, M., and Marathe, B., 1991, "Structure of Tip Clearance Flows in Axial Flow Compressors," *Proc. Tenth International Symposium on Air Breathing Engines*, Nottingham, United Kingdom, Sept. 6; ASME JOURNAL OF TURBOMACHINERY, in press.

Paterson, R. W., and Weingold, H. D., 1985, "Experimental Investigation of a Simulated Compressor Airfoil Trailing-Edge Flowfield," *AIAA Journal*, Vol. 23, No. 5. p. 768.

Prato, J., 1990, "Effects of Blade Loading on the Wake Characteristics of a Compressor Rotor Blade," M.S. Thesis, Department of Aerospace Engineering, Pennsylvania State University, University Park, PA.

Raj, R., and Lakshminarayana, B., 1973, "Characteristics of the Wake Behind a Cascade of Airfoils," *Journal of Fluid Mechanics*, Vol. 61, p. 707.

Ravindranath, A., and Lakshminarayana, B., 1980, "Mean Velocity and Decay Characteristics of the Near- and Far-Wake of a Compressor Rotor Blade of Moderate Loading," ASME *Journal of Engineering for Power*, Vol. 102, pp. 535-548.

Reynolds, B., Lakshminarayana, B., and Ravindranath, A., 1979, "Characteristics of the Near Wake of a Compressor or Fan Rotor Blade," *AIAA Journal*, Vol. 17, p. 959.

Sitaram, N., and Lakshminarayana, B., 1983, "Endwall Flow Characteristics and Overall Performance of an Axial Flow Compressor Stage," NASA CR-3671.

Strasizar, A., et al., 1989, "Laser Anemometer Measurements in a Transonic Axial Flow Fan Rotor," NASA TP-2879.

Thompkins, W. T., and Kerrebrock, J. L., 1975, "Exit Flow From a Transonic Compressor Rotor," AGARD CP-177.

Treaster, A. L., and Yocum, A. M., 1979, "The Calibration and Application of Five-Hole Probes," *ISA Transactions*, Vol. 18, No. 3, p. 23.

Treaster, A. L., and Houtz, H. E., 1986, "Fabricating and Calibrating Five-Hole Probes," in: *Fluid Measurements and Instrumentation*, ASME FED Vol. 34.

Numerical Simulation of Compressor Endwall and Casing Treatment Flow Phenomena

A. J. Crook
Allison Gas Turbine Division,
Indianapolis, IN 46206

E. M. Greitzer

C. S. Tan

Massachusetts Institute of Technology,
Cambridge, MA 02139

J. J. Adamczyk
NASA Lewis Research Center,
Cleveland, OH 44135

A numerical study is presented of the flow in the endwall region of a compressor blade row, in conditions of operation with both smooth and grooved endwalls. The computations are first compared to velocity field measurements in a cantilevered stator/rotating hub configuration to confirm that the salient features are captured. Computations are then interrogated to examine the tip leakage flow structure since this is a dominant feature of the endwall region. In particular, the high blockage that can exist near the endwalls at the rear of a compressor blade passage appears to be directly linked to low total pressure fluid associated with the leakage flow. The fluid dynamic action of the grooved endwall, representative of the casing treatments that have been most successful in suppressing stall, is then simulated computationally and two principal effects are identified. One is suction of the low total pressure, high blockage fluid at the rear of the passage. The second is energizing of the tip leakage flow, most notably in the core of the leakage vortex, thereby suppressing the blockage at its source.

Introduction

It is well known that the use of grooves or slots in the endwall of a compressor can substantially increase the stable flow range of the machine, although generally with some penalty in efficiency (e.g., Prince et al., 1977; Fujita and Takata, 1984; Smith and Cumpsty, 1985). Such grooves have been successfully employed in a variety of different geometries and flow regimes: over rotor tips in both high and low Mach number axial compressors, on a rotating hub under a cantilevered stator, in an axial compressor, and over the impeller, as well as on a rotating shroud under a vaned diffuser in a centrifugal compressor. Several current engines, in fact, make use of this "casing treatment."

There have been a number of investigations to assess performance of compressors with grooved endwalls, but the basic fluid mechanics underlying the increased ability of the blade row to withstand stall is still not well understood. One reason is that, even with a smooth shroud or hub, the flow in the endwall region of a compressor blade is complex. More precisely, simplifying approaches that have worked well in other realms of fluid dynamics (e.g., secondary flow, boundary layer analyses) have not been helpful in providing the required insight.

As will be argued below, although our original interest was in the mechanism of operating of casing treatment, it became evident that better understanding of the flow with a smooth endwall was a prerequisite for dealing with grooved endwall configurations. The paper thus presents an examination of both of these situations, with the central focus on flow structure in the endwall region with a tip, or hub, clearance. From considerations of this structure, possible mechanisms are presented not only for compressor stall but for its delay when a grooved endwall is used.

Background of Research on Casing Treatment

As background, we present a brief description of the features of compressor casing treatment that are relevant to the investigation reported herein. First, it has been shown that casing treatment is effective only in situations in which the flow in the endwall region sets the stall limit, i.e., wall stall or endwall stall (Greitzer et al., 1979; McDougall, 1988); this is the case in the configuration studied here. In addition, we concentrate on those treatments that have had the most success in suppressing stall, namely the so-called "axial skewed grooves," which have been examined by other investigators, most notably Smith and Cumpsty (1985), and Takata and co-workers (Takata and Tsukuda, 1977; Fujita and Takata, 1974). The axial skewed grooves used in the experiments to be discussed are depicted in Fig. 1. An important aspect of the flow in these grooves is the recirculation, from the rear of the passage to the front, driven by the mean pressure rise of the compressor. Although the recirculation is unsteady (because a given groove sweeps through the pressure field of the blades), the unsteady effects have been shown by Smith and Cumpsty (1985) to be of secondary importance, so that it is the mean back-to-front motion that is critical.

The recirculation through the groove has two main consequences for the flow in the passage: removal of fluid at the

Contributed by the International Gas Turbine Institute and presented at the 37th International Gas Turbine and Aeroengine Congress and Exposition, Cologne, Germany, June 1-4, 1992. Manuscript received by the International Gas Turbine Institute February 24, 1992. Paper No. 92-GT-300. Associate Technical Editor: L. S. Langston.

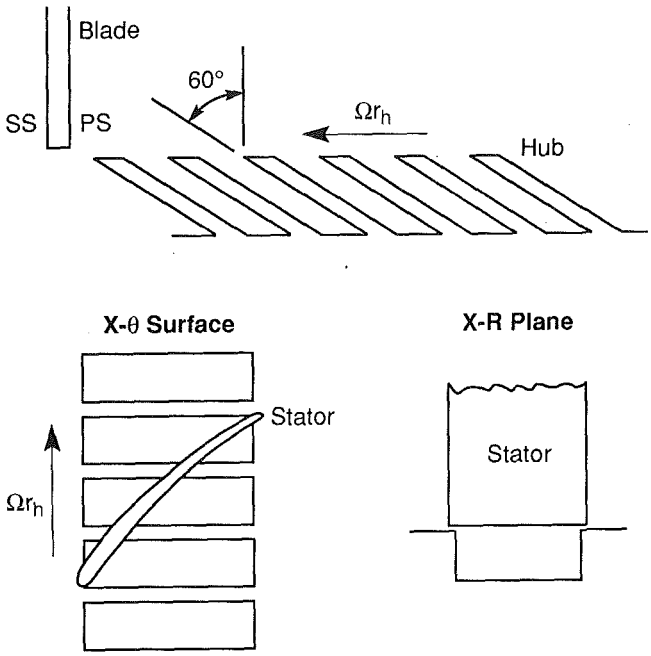

Fig. 1 Detail of hub treatment used in experiment (geometry similar to rotor casing treatment)

rear, and injection of fluid at the front. Because of the relative motion of the groove and the blade, there is work done as the fluid passes through the groove and the injected fluid usually enters with a higher than free-stream total pressure in the blade relative frame.

Lee (1990) has assessed the influence of injection and removal on stall inception by independently varying the rate and the position of the two. In this manner, the effect of each could be examined separately. Both injection and removal were found to be useful in delaying stall, although neither was as effective by itself as the casing treatment in which they both act in combination. For injection, a strong correlation was found between change in stalling pressure rise capability and streamwise component of momentum of the injected flow.

While one might infer that *removal* is analogous to boundary layer suction, i.e., sucking off the low-velocity flow near the endwall, there are differences between the flow with a moving endwall (even a smooth one) and a conventional boundary layer. In particular, as pointed out by Smith and Cumpsty (1985), Lee (1990), and Johnson (1985), the fluid that exists at locations toward the rear of the passage has a relative dynamic pressure that is a sizable fraction of the free-stream dynamic pressure. In fan rotors, for example, where much of the high-speed work on casing treatment has been carried out, the stagger angles may be 65 deg or more. For these geometries, the relative dynamic pressure of the fluid *on* the wall is over 80 percent of the free-stream value at inlet. Since the relative velocity decreases through the rotor along a streamline away from the wall, this ratio is even higher at exit, and it is not obvious why removing this high dynamic pressure fluid would delay stall.

The situation with *injection* at the front of the blade passage is even less resolved. A link between increase in pressure rise capability and streamwise momentum addition certainly seems plausible. However, even a qualitative description of the interaction between the injected and the blade passage flow responsible for this link was lacking when this study was initiated.

With the foregoing as background, we pose the two fluid dynamic issues to be addressed in this paper:

1 What is the mechanism of stall with a smooth wall, i.e., what features of the flow in the endwall region set the limit on pressure rise capability?
2 How does casing or hub treatment act to alleviate these consequences?

Motivation and Scope of the Paper

It is useful to discuss briefly the objectives of the present investigation, since these determined the underlying approach. Although a number of different approximate approaches to the compressor endwall problem have been tried and found wanting, in the past few years, numerical procedures have been developed that can capture the basic "flow physics" of realistic configurations (e.g., Hah, 1986; Pouagare and Delaney, 1986; Dawes, 1987; Adamczyk et al., 1990). We have used one such procedure (Adamczyk et al., 1990) to examine the endwall region flow structure, for smooth and grooved endwalls. The emphasis of the study is not on precise prediction of loss levels or deviation for a specific geometry, but rather on using computations to develop understanding of phenomena that occur in a broad class of turbomachines that use casing treatment. The question to be asked of the numerical procedures is therefore whether they are able to capture those features of the endwall/tip clearance flow that have a major impact of these phenomena. As seen below, our position is that the answer to the question is yes, and that one can derive considerable physical insight from interrogation of the computational results.

The organization of the paper, which reflects these views, is thus somewhat unconventional in that comparison with experiment is presented at an early stage, essentially as part of the methodology rather than the results. We first summarize the computational procedure. The experimental configuration is then described, and a discussion is given of the modifications made to the computation to simulate the grooved endwall. Comparison of the numerical solutions with measurements is then presented, as illustration of the ability of the computations to reproduce experimental results for endwall flow, with a smooth wall and with an axial skewed groove configuration. The degree to which salient features are captured gives confidence that the computation can be used to probe other key aspects of the flow. We therefore examine in more detail the tip clearance velocity and total pressure fields, and the streamlines at various locations in the endwall region, for both smooth and grooved walls. From the computational results, it will be seen that there is a close link between the tip leakage flow and the high-loss, high-blockage region at the rear of the blade passage, and that the action of the casing or hub treatment decreases this blockage through energizing of the leakage vortex core region.

Brief Description of the Computational Procedure

The computational scheme is based on a finite volume-time marching procedure, originally developed by Jameson et al. (1981). The scheme is finite volume-cell centered and is second-order accurate in space for a smooth uniform mesh. The time-stepping scheme is a four-stage Runge–Kutta integration, with local time stepping for each cell used to accelerate convergence. Further description of the scheme is given in the appendix.

The boundary conditions at upstream and downstream ends of the computational domain, as well as on the blade and the smooth endwall, are standard for these types of three-dimensional codes. The total pressure profile used at inlet was the one measured in the experiment. Additional information on the computational procedure and boundary conditions can be found from Crook (1989).

Experimental Configuration Used to Assess the Computational Results

The experimental measurements were made in a single-stage low-speed compressor facility. The endwall region examined was at the *rotating hub* of a *cantilevered stator*. The stagger

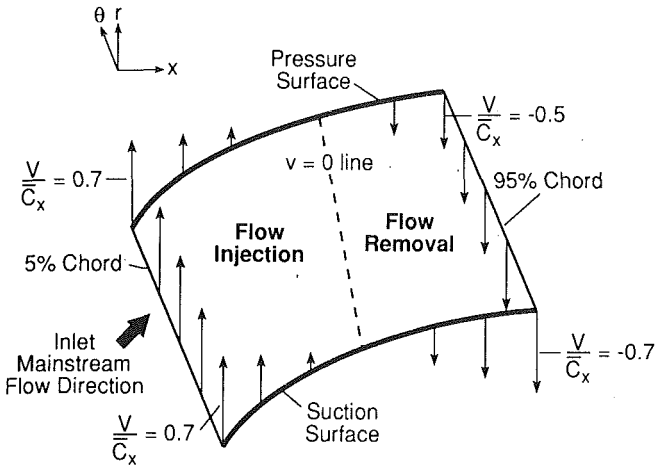

Fig. 2 Hub treatment radial velocity profile; V denotes radial velocity

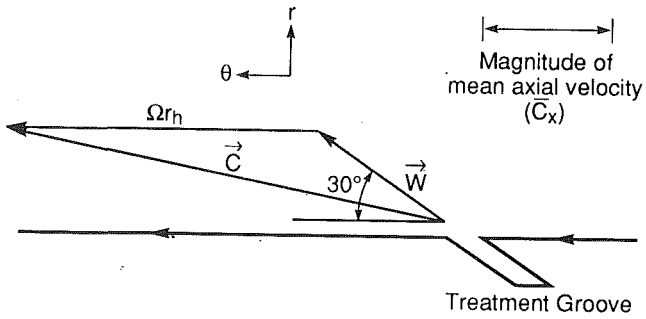

Fig. 3 Relative and absolute velocity vectors at treatment exit

of the rotor and the stator, and the stator hub clearance, were chosen so that the stator hub would be the stalling section and the flow at this section would be similar to that at the tip of a compressor rotor. The overall performance, as well as the detailed measurements, show that this is the case and that the stator/rotating hub configuration gives a useful simulation of the flow phenomena occurring at rotor tips. This last point should be stressed, since it is the generic aspects of the measurements (and of the computations) that are of most interest. The stator operating point was at a high loading condition, close to the peak pressure rise point. Further information on the overall performance (pressure rise versus flow) of the stator row with and without the grooved hub is given by Cheng et al. (1984), and Lee (1990). Detailed measurements were also carried out on the three-dimensional flow in the stator passage using hot wires, and these are described in the latter of the above references and by Johnson (1985).

Simulation of Hub Treatment in the Computations

The hub treatment grooves in the experiments extended from 5 to 95 percent axial chord, as illustrated in Fig. 1. The groove design was taken from geometries that have shown large stall margin increases when used as rotor casing treatment. The flow from the grooves is unsteady, but the measurements of Johnson (1985) indicate that the discrete jets out of the grooves mix rapidly. In particular, except in the first 10 percent of chord and the bottom several percent of the span, time-resolved measurements showed little deviation from time-averaged data. Based on these experiments, steady-state simulation of the hub treatment was adopted.

Hub or casing treatments have an area of flow removal over the downstream portion, and an area of flow injection over the upstream portion, of the treatment area, as indicated in Fig. 2, which shows the radial component of velocity, V, nondimensionalized by the stator mean axial velocity, $\bar{C}_x$. This combination of flow removal and injection can be simulated numerically by modeling the treatment area as a second inlet/exit to the flowfield domain. The four conditions specified at the boundary of the hub treatment (see Fig. 3) were the r–z flow angle, the r–θ flow angle, the stagnation temperature, and the radial mass flow (density and radial velocity). The r–z flow angle was set at zero and the r–θ angle was calculated assuming that the flow in the grooves had a relative angle equal to the angle of the treatment, as shown in Fig. 3. From the data of Johnson (1985) and Smith and Cumpsty (1982), the shape of the radial velocity near the hub is roughly a saw-tooth as a function of axial distance. The magnitude of the radial velocity was set by prescribing the amount of flow injected (or removed, since the two must balance) to be 3.5 percent of the inlet mass flow, which was the measured value.

Comparison of Numerical Solutions to Experiments

Velocity measurements were taken at seven radial locations in the hub region of the blade passage. The first station was at two percent span, the location corresponding to the end of the blade, i.e., the top of the clearance, and the outermost was at 27 percent. Each radial station had 76 data points spaced evenly between the blades. For the comparisons to be presented, the velocities from the numerical solution grid were interpolated to the experimental locations unless otherwise specified.

The velocity data are organized in two types of surfaces, one at constant radius and one at constant axial station. For the latter, the angle at which the velocity vectors are viewed is important in extracting the flow structure. The view angle used, unless stated, is the stagger angle of the blades. Although no one angle is totally satisfactory because of the variation in flow angle with radius, and although more elaborate schemes can be used for bringing out the "secondary flow" aspects, viewing along the stagger angle can be thought of as roughly viewing along the free-stream direction. The effect of viewing angle on the observed flow pattern is shown by Crook (1989); it is analogous to the imposition of a constant (crossflow) velocity. If the latter is large, information about any circulatory or vortical structure tend to be submerged, so that the flow appears roughly unidirectional.

Comparison of Smooth Wall Results

Velocity vectors at 2 percent span, the radial measurement location closest to the endwall, are shown in Fig. 4 for the smooth endwall. Experimental measurements and viscous and inviscid computations are presented to illustrate several points. First, the strong crossflow, which is evident in the rear of the passage, is the result of the tip leakage. Second, both of the numerical solutions can be seen to reproduce the measured magnitude of the crossflow as well as the axial extent, although the viscous solution gives better representation. Similarity between experiment and (the two) numerical solutions is also seen for the line demarcating the passage throughflow and the leakage crossflow. We include the inviscid results to emphasize that the leakage flow is pressure driven and the computations are insensitive to details of the turbulence modeling used. Further evidence on the minor role played by turbulence modeling considerations in this problem can be found from Crook (1989) and Storer (1991).

Good correspondence between experiment and numerical solution was also seen at other radial stations, but the clearance flow has the greatest effect at the 2 percent span location, and subsequent comparisons will focus on this station. In addition, because the viscous code was used in the hub treatment studies,

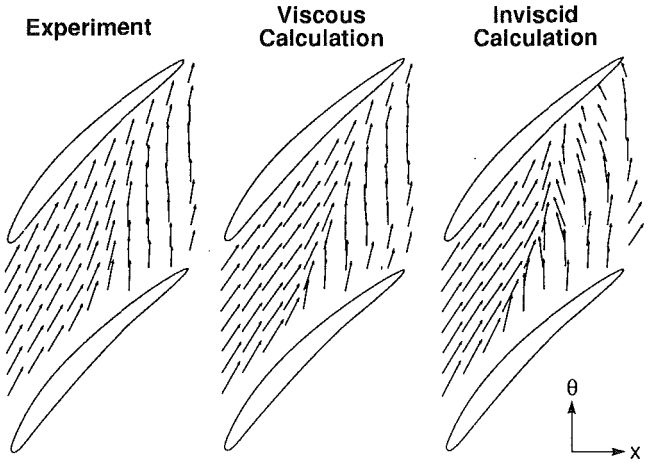

Fig. 4 Velocity vectors on surfaces of constant radius at 2 percent span from hub, for smooth wall

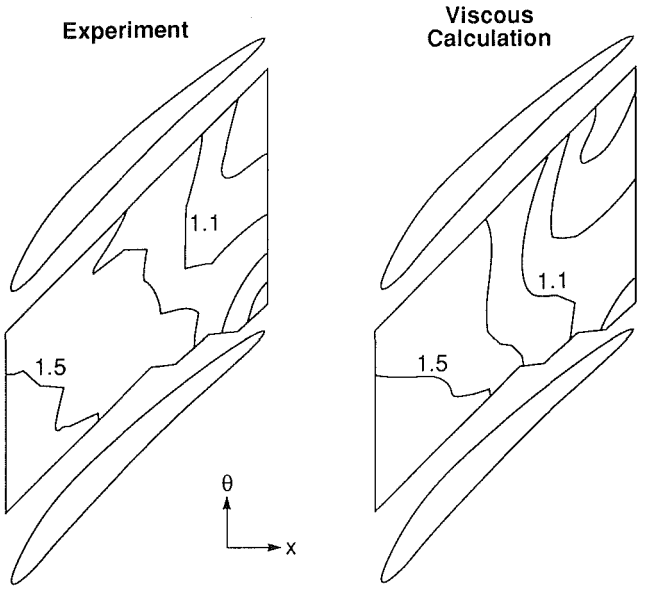

Fig. 5 Contours of $C/\overline{C}_x$ on constant radius surface at 2 percent span, for smooth wall

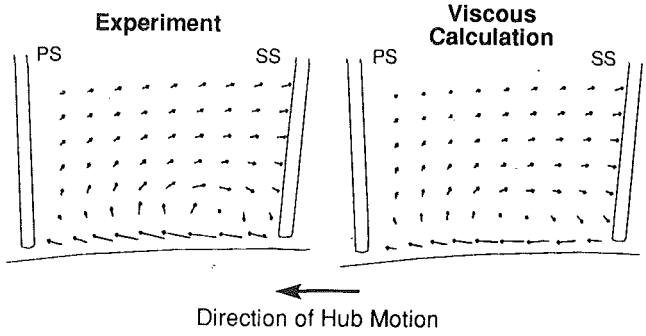

Fig. 6 Velocity vectors at 90 percent chord axial station for smooth wall

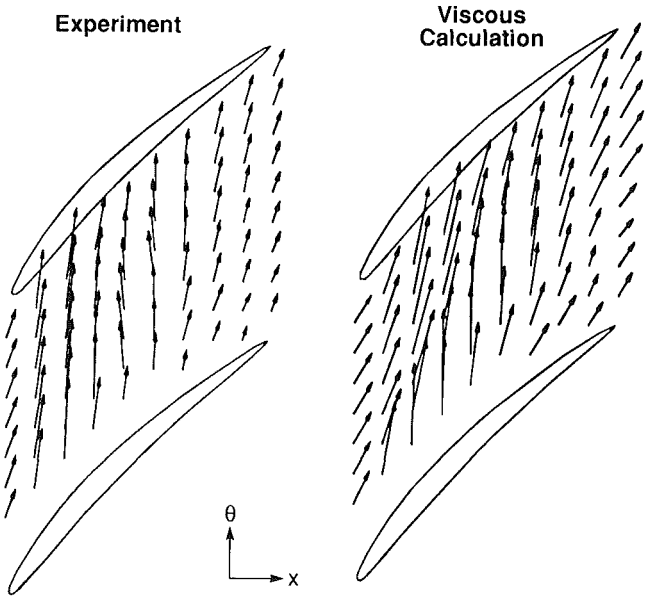

Fig. 7 Velocity vectors on constant radius surface at 2 percent span with hub treatment

we will show comparisions with viscous computations only from now on.

Velocity vector data are useful for showing overall similarity between computation and experiment, but numerical comparisons are more readily made if the data are displayed as contour plots. Figure 5 thus shows contour plots of velocity magnitude, C, referenced to the average inlet axial velocity, $\overline{C}_x$, for experiment and computations, again at the 2 percent span radial location. Agreement is seen between calculation and experiment in both magnitude and pattern.

Figure 6 shows velocity vectors on axial planes at 90 percent chord, from experiment and from the numerical solution. The tip leakage flow from the blade at the right of the passage is evident. The leakage flow and its roll-up into a vortex are major features in the endwall region, and the numerical solution captures these features. Although only viscous results are shown, the strength of the clearance vortex in both viscous and inviscid numerical solutions is similar to experiment; the nondimensional circulation (circulation divided by blade chord times mean axial velocity) was 0.68 in the experiment, 0.58 in the viscous calculation, and 0.79 in the inviscid calculation, again demonstrating the essentially inviscid nature of the leakage flow. The main difference between the three is the position of the vortex in the inviscid solution (Crook, 1989).

Comparison With Hub Treatment Experiments

Velocity vectors on the radial surface at 2 percent span with hub treatment are shown in Fig. 7 for experiment and computation. In both, the jet flow from the forward portions of the treatment is considerably stronger than the clearance flow with the smooth wall. Representative velocities with the hub treatment are roughly twice those associated with the smooth wall clearance flow, i.e., the dynamic pressure is roughly four times as high.

Contour plots of the normalized velocity magnitude ($C/\overline{C}_x$) for experiment and for computation show similar patterns as seen in Fig. 8. The contour with magnitude greater than three, which outlines the hub treatment flow in the forward portion of the passage, can be compared with the values of one to one-and-a-half that existed with the smooth wall (Fig. 5).

Velocity vectors on an axial plane at 90 percent chord are displayed in Fig. 9. A downward velocity into the treatment exists in both experiment and numerical solution. A vortical structure is also seen in the left portion of the passage in both experiment and computation, although it is not precisely in the same place. (Note the slight shift in the positions of the

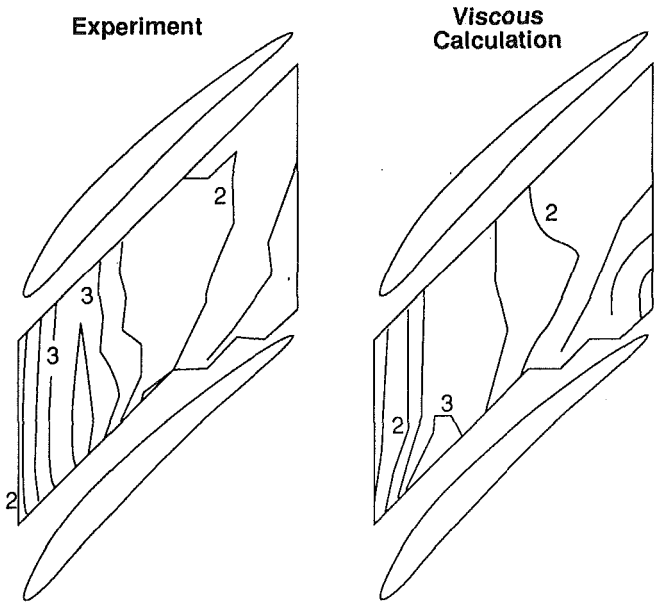

Fig. 8 Contours of velocity magnitude ($C/\overline{C}_x$) on constant radius surface at 2 percent span with hub treatment

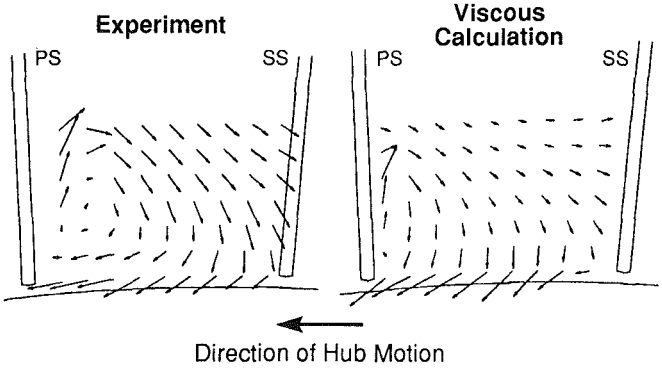

Fig. 9 Velocity vectors at 90 percent chord axial station with hub treatment

interpolated calculation points.) The experimentally measured circulation was approximately twice that of the smooth wall; the computational value was 1.8 times that of the smooth wall. The changes in circulation compared to the smooth wall situation result from the vorticity in the treatment jet.

We can summarize the comparisons shown in Figs. 4–9 by stating that the major features in the endwall region, namely the clearance leakage crossflow, the vortex associated with this leakage, and the large change in velocity field due to the high velocity jet emerging out of the treatment grooves, are well captured. (Crook (1989) shows that this was also true for the inviscid calculations, implying, as stated previously, that turbulence modeling plays little role in determining the degree to which the computations describe the principal flow features.) In addition, it should be emphasized that differences between experiment and computation are significantly less than those between smooth wall and hub treatment flows, and it is this latter comparison upon which we focus. The evidence, therefore, is that the computations can be used to examine aspects of the flow field other than those which can be measured experimentally. This is the main theme of the paper, and the one to which we now turn.

Analysis of Numerical Solutions

The numerical solutions generated to investigate the endwall and hub treatment flow fields are listed in Table 1. The first two have no clearance and were carried out to illustrate the different effects of (*a*) moving endwall, and (*b*) clearance, separately.

Table 1 Descriptions of numerical solutions

Solution No.	Description
1	No clearance, smooth wall, stationary hub
2	No clearance, smooth wall, moving hub
3	Clearance, smooth wall, moving hub
4	Clearance, hub treatment

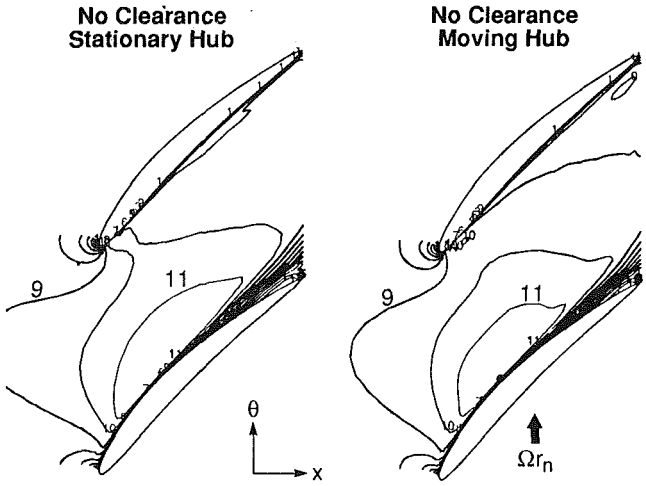

Fig. 10 Axial velocity ($C_x/\overline{C}_x$) on constant radius surface at 2.4 percent span for smooth wall (contour 1 = 0.0, contour 11 = 1.0, contour increment = 0.1)

No Clearance/Smooth Wall/Stationary Hub. A feature of the flow with no clearance is a suction surface-hub corner separation. Figure 10(*a*), which is a contour plot of the axial velocity normalized by inlet average axial velocity at 2.4 percent span, shows this. The conditions are that the endwall is stationary and there is no clearance. The increment between contour lines is 0.1 $\overline{C}_x$. A corner separation can be seen with a region of negative axial velocity near the trailing edge; the separation is similar to that found by Dong et al. (1987), although smaller in extent.

Figure 11, also for the no clearance, stationary hub, shows the total pressure coefficient at two axial situations, 50 and 78 percent of blade chord. The quantity plotted is the difference between the local total pressure and the total pressure averaged over the entire inlet, divided by the average inlet dynamic pressure ($(P_t - t_{tin})/q_{in}$), with each contour one tenth the mean dynamic pressure. The lower 25 percent of the span and roughly 90 percent of a blade pitch are shown.

The figure indicates the axial development of the endwall corner flow and the build-up of low total pressure fluid on the suction surface near the hub due, in part, to the migration of boundary layer fluid on the hub to the suction surface. (For reference, the hub boundary layer thickness at inlet is roughly 2 percent span.) Examination of the streamlines near the blade surface showed little migration of boundary layer fluid down the span, with the larger part of the accumulation of low-momentum fluid in the suction corner from the endwall flow across the passage.

No Clearance/Smooth Wall/Moving Hub. The solution for no clearance and a *moving* endwall at the hub was also examined to assess the effects of wall motion on the flow in the endwall region. Figure 10(*b*), which presents contours of axial velocity ($C_x/\overline{C}_x$) at the 2.4 percent span radial location,

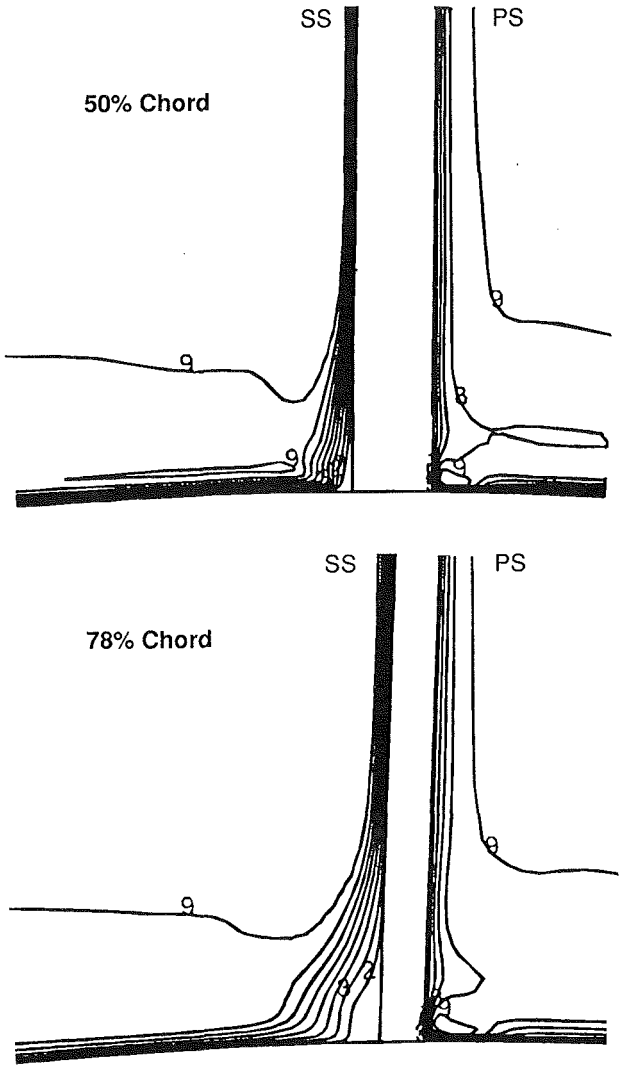

Fig. 11 No clearance/stationary hub: contours of total pressure (($P_t - P_{tin}$)/q_{in}) at different axial stations for smooth wall (contour 1 = −1.0, contour 9 = −0.2, contour increment = 0.1)

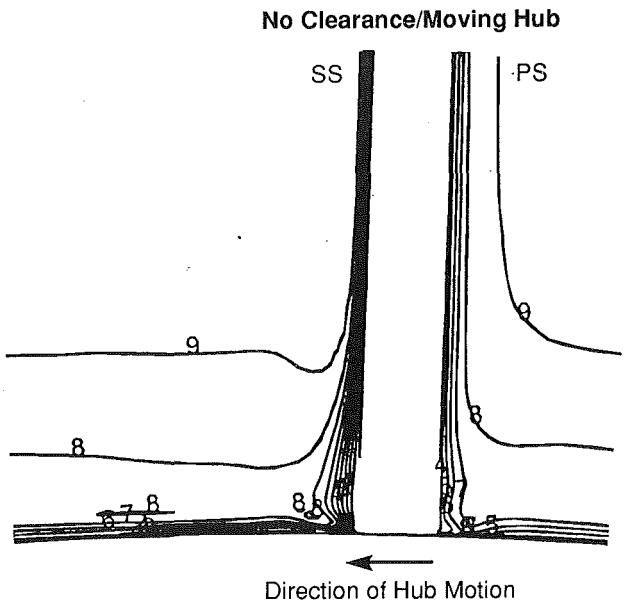

Fig. 12 No clearance/moving hub: contours of total pressure (($P_t - P_{tin}$)/q_{in}) at 50 percent chord for smooth wall (contour 1 = −1.0, contour 9 = −0.2, contour increment = 0.1)

can be compared directly to Fig. 10(*a*) for a stationary wall. Figure 12 presents contours of total pressure at the 50 percent chord location and can be compared to the results for this location in Fig. 11. The comparisons show that the moving wall causes little change in overall flow features. More specifically, the changes that occur between moving and stationary walls will be demonstrated to be small compared to those due to clearance (to be discussed below). The principal change with a moving wall is the existence of a small region near the hub with higher energy fluid, presumably resulting from the work done by the moving hub, but the low-velocity region near the suction surface corner is still present.

Hub Clearance/Smooth Wall/Moving Hub

Axial Velocity Contours. With clearance, the flow in the endwall region changes markedly. Figure 13, which presents axial velocity normalized by average inlet velocity ($C_x/\overline{C}_x$) on a radial surface at 2.4 percent span, can be compred directly to the no clearance results in Fig. 10. Higher axial velocities associated with the clearance flow are seen in the midchord region near the blade suction surface. More importantly, the low-velocity contours at the rear of the passage are not near the blade but are rather clustered near midpitch, and there is no obvious suction surface separation. As shown in more detail subsequently, we identify these features with the clearance vortex.

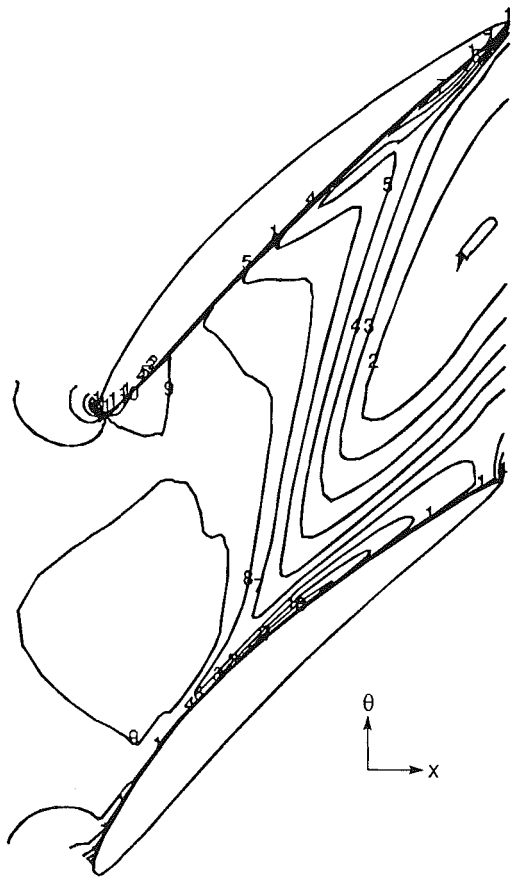

Fig. 13 Contours of axial velocity ($C_x/\overline{C}_x$) on 2.4 percent span constant radius surface, with clearance/smooth wall/moving hub (contour 1 = 0.0, contour 11 = 1.0, contour increment = 0.1)

Total Pressure Contours. Figure 14 shows the total pressure coefficient for two axial planes at 50 and 78 percent chord, and can be compared directly with Fig. 11 (or 12). At 50 percent chord, the suction surface boundary layer near the clearance is thinned due to the clearance flow. Further, the fluid at the

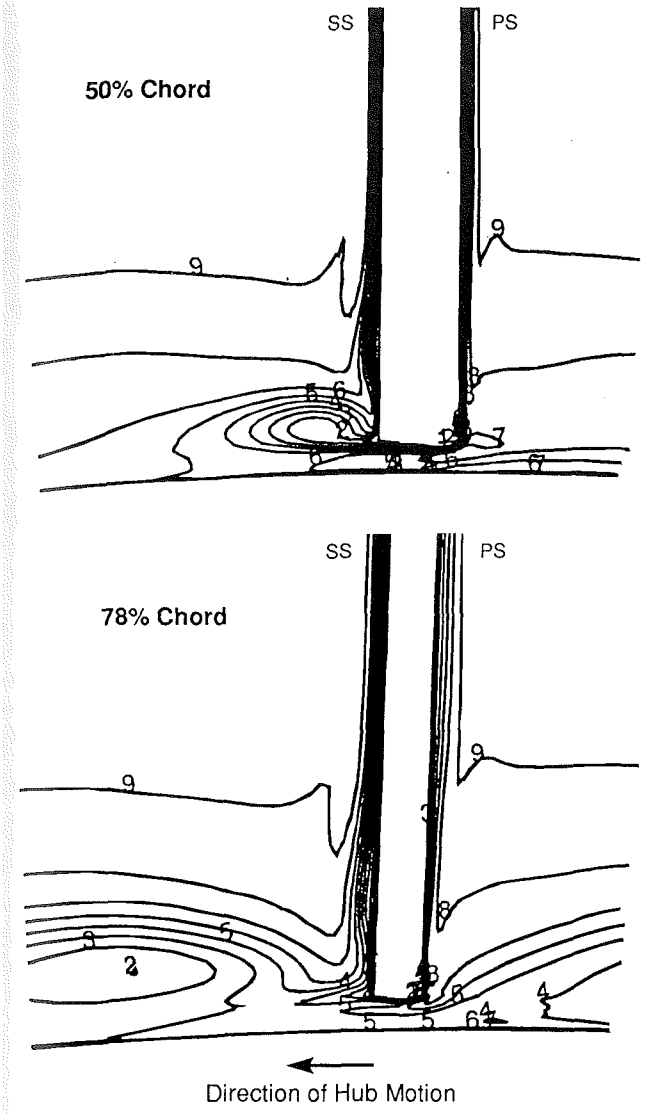

Fig. 14 Clearance/moving hub: contours of total pressure ($(P_t - P_{tin})/q_{in}$) at different axial stations (contour 1 = −1.0, contour 9 = −0.2, contour increment = 0.1)

edge of the jet, which flows through the clearance, forms the core of a vortex, which can be seen at the left of the blade tip. This core travels away from the blade surface (compare with the total pressure region at 78 percent chord in the lower figure), as can be inferred from basic considerations of vortex kinematics (Chen et al., 1991). In addition to motion across the passage, the presence of the vortex implies that higher total pressure fluid from outside the blade surface boundary layer moves down near the suction surface. Evidence of this motion can be seen at both the 50 and 78 percent locations.

From the calculations, one can see not only that flow through the clearance is the major agent in preventing corner separation (as has been known for some time), but also several other points. One, which was made initially by Storer (1991), is that the leakage jet boundary is the main region of high dissipation, as might be expected because of the high shear. Another point that relates more to the issue of blockage is that the low total pressure fluid appears in the core of a vortex, which grows in size as one proceeds downstream. Finally, although corner separation is suppressed with clearance, fluid with high loss and low momentum is still present across much of the passage near the hub.

This last feature may be more apparent in Fig. 15. In this figure, the grey surface in the upper right corner is the suction

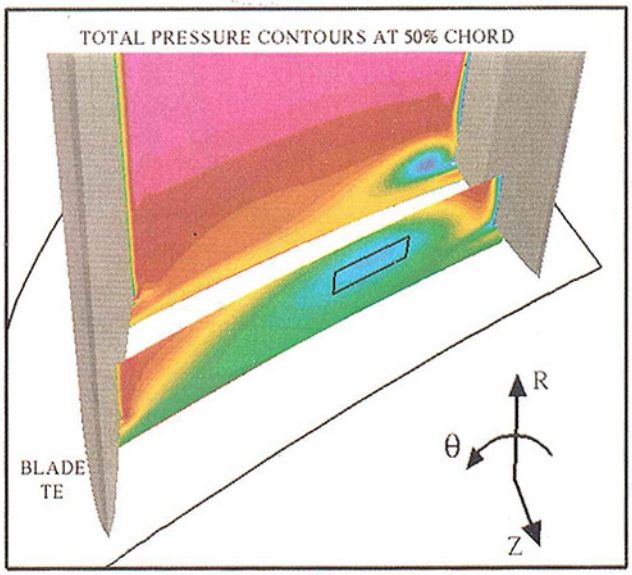

Fig. 15 Total pressure contours in the passage with smooth wall; contour planes at axial locations of 50 and 78 percent chord, view from rear of passage

surface of the blade from midchord to trailing edge. A neighboring blade is shown to the left. The trailing edges of the blades are in the foreground and the hub is outlined in black. Roughly the lower 25 percent of the passage (at the exit) is shown. The view is looking at the exit plane of the passage from downstream.

The large surface in the upper portion of the figure is an axial station at 50 percent chord on which are displayed levels of total pressure. The color scale in terms of the total pressure loss coefficient ranges from red ($(P_t - \overline{P}_{tin})/q_{in} \sim 0$) to blue ($(P_t - \overline{P}_{tin})/q_{in} \sim -0.8$). The other colored plane surface is at 78 percent chord, and includes only the lower 8 percent of the blade span. The low total pressure region associated with the clearance flow is seen even at 50 percent chord, but at 78 percent chord this has grown to occupy much of the endwall region. In the figure, the lowest total pressure fluid is outlined somewhat arbitrarily by a rectangle, which will be referred to as the "high-loss rectangle" in what follows. At both these planes, the lowest total pressure is not on the wall but rather at the center of the leakage vortex.

Particle Paths. To examine the source of the high-loss fluid, particles were released in the lowest total pressure region at 50 percent chord and tracked forward and backward along streamlines. The paths integrated forward intersected the high-loss rectangle at 78 percent chord, verifying that the particle paths tracked the regions of low total pressure. Particle paths integrated backward came from the region where the tip leakage jet left the clearance gap.

To illustrate the last point, particle paths originating from a position two computational cells (0.2 percent span) underneath the blade are displayed in Fig. 16. The orientation of the view into the blade passage is similar to Fig. 15 and the particle paths have been followed past the axial position of the high-loss rectangle at 78 percent chord to the blade trailing edge plane. The blue paths, which originate from the first 40 percent of the blade chord, show helical trajectories because these particles spiral around the vortex core before passing through the high loss rectangle. The red paths, which originate from 50 to 78 percent of the chord, encircle the loss rectangle. Particles released from two cells below the blade tip over the last 20 percent of the chord are colored green in the figure. These convect across the passage, ending up at radial positions higher than the blade gap. The boundary that the green and

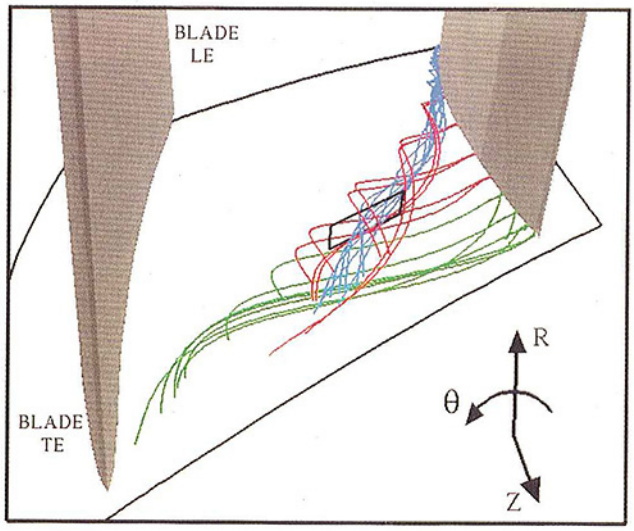

Fig. 16 Particles released from the blade tip, smooth wall; view from rear of passage

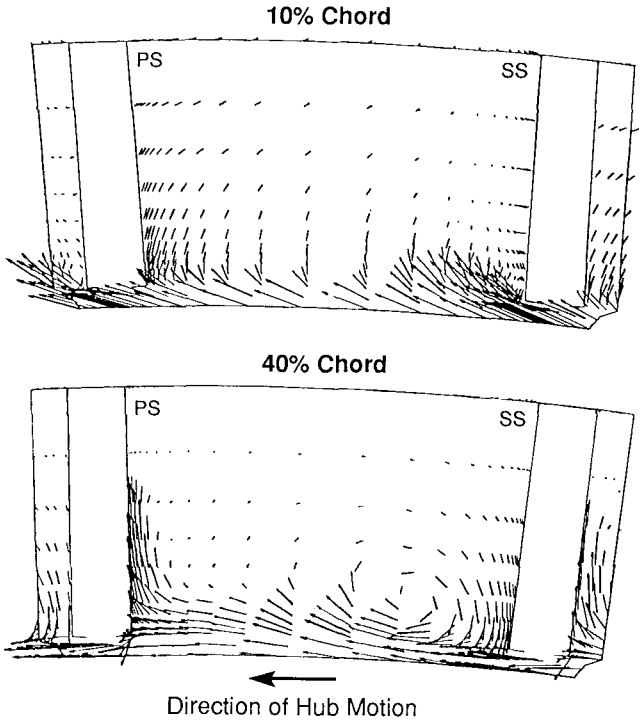

Fig. 17 Hub treatment: velocity vectors at different axial stations; view angle = 55 deg

red particles make at blade row exit has a shape similar to the boundary of the low total pressure fluid at that axial location (shown in Fig. 15 by the plane of data at 78 percent chord).

These particle paths indicate that the low total pressure has not been removed from the flow, but rather transported by the clearance flow and vortex across the endwall region. Moreover, the computations show that loss has been generated by the shear flow emerging from the blade tip and, to a smaller extent, by mixing in the vortical region, and the overall loss in the endwall region is more than that of the no-clearance case. The particle tracking showed that the high-loss fluid is located in the vortex core. Further, the high-loss region is near the suction side of the blade where the jet exists; particles that end up in the central part of the core come principally from the edge of the clearance jet, as seen in Fig. 15.

The clearance flow is thus a primary contributor to loss and the existence of low total pressure fluid in the passage. Further, although the discussion so far is in terms of loss, it is not much of a stretch to connect the regions of high loss with high blockage as well. While these regions can be linked to low streamwise and axial velocity in the endwall, they have not been determined conclusively to be the cause of the stall in the experiment. It is observed, however, that as incidence is increased, the high-loss, low-velocity region, which is located in the vortex core, grows substantially. Also, the clearance flow velocity increases in the direction perpendicular to the blade stagger line, resulting in larger regions of negative axial velocity in the endwall region, and thus larger blockage.

Hub Treatment

Velocity Vectors. With hub treatment, the flow is qualitatively different as to both streamline pattern and momentum content. Figure 17 displays velocity vectors at two axial stations. The vectors are viewed at an angle 55 deg from axial; this is roughly the angle that the vortex has as it crosses the passage. The difference in the incoming jet flow angle (in the r–θ plane) at the two stations arises because of the difference in hub outflow velocity; at the 40 percent location the absolute velocity is almost wholly the hub velocity, whereas at the 10 percent location the relative outflow velocity from the grooves is near its maximum value. At the 10 percent chord location, the jet enters from the hub treatment, with a vortex forming near the blade tip at the right of the passage. The vortex center moves away from the blade and the vortex enlarges as it proceeds downstream, as shown in the 40 percent chord results. At this location, a high-velocity flow moves up the pressure surface of the blade at the left of the passage; this originated from the jet shown at the 10 percent location.

Vorticity Contours. To examine the strength and size of the vortex in a more quantitative fashion, Fig. 18 displays contours of streamwise vorticity at the 40 percent chord axial station, for both smooth wall and hub treatment. The magnitude of the streamwise vorticity has been nondimensionalized by the ideal leakage velocity for the smooth wall, $C_{leakage}$, as defined using the mean blade loading, $C_{leakage} = \sqrt{2 \bullet \text{Mean Blade Pressure Difference}/\rho}$ (Chen et al., 1991) and the tip clearance, τ[1]. The figure indicates increased secondary circulation with hub treatment compared to smooth wall clearance flow, as one might expect from the high dynamic pressure of the jet. The circulation magnitude obtained from the calculations as well as from the velocity measurements confirm this. Although not shown, at the rear of the passage, the vortex is drawn to the hub and much of the high-vorticity fluid is sucked into the treatment.

Total Pressure Contours. To demonstrate the effect of hub treatment on the endwall flowfield in a different manner, plots of total pressure loss coefficient at two axial stations are shown for the smooth wall and the hub treatment in Figs. 19 and 20. The station at 10 percent chord is displayed in Fig. 19. A high total pressure jet emanates from the hub treatment with total pressure several q_{in} higher than the total pressure near the endwall in the smooth wall case.

Figure 20 shows the axial station at 40 percent chord. With hub treatment, high total pressure fluid from the jet fills the endwall region. The high total pressure fluid from the jet is also found near the pressure surface, moving away from the endwall. With the smooth wall, the high loss (and high blockage) area associated with the clearance vortex has started to

[1]This choice of parameters is not totally unequivocal; it amounts to basing the vorticity on a circulation of magnitude, $C^2_{leakage}\, t$, where t is the time during which vorticity is produced, spread over an area $(C_{leakage}\, t)\, \tau$.

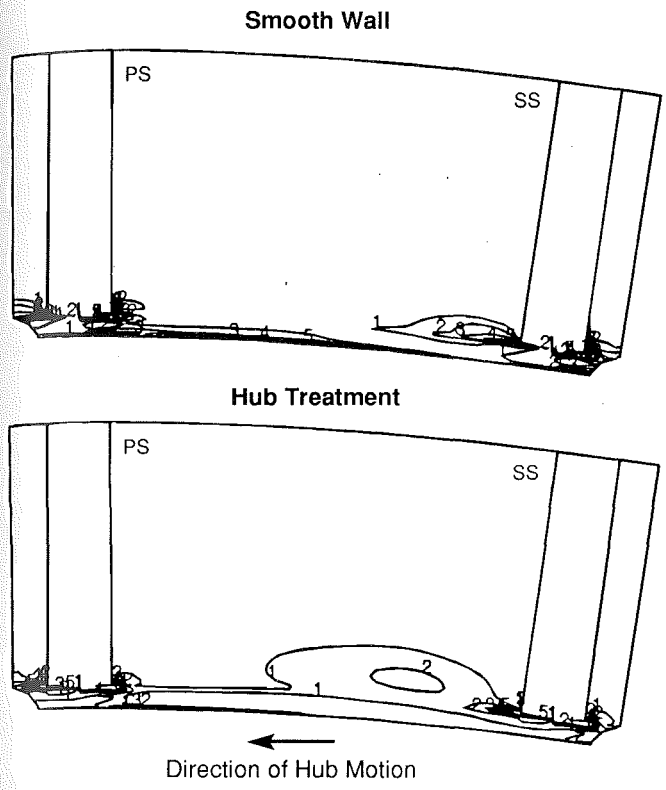

Fig. 18 Contours of streamwise vorticity (ω_s × clearance/$C_{leakage}$) at 40 percent chord (contour 1 = 0.2, contour 5 = 1.0, contour increment = 0.2)

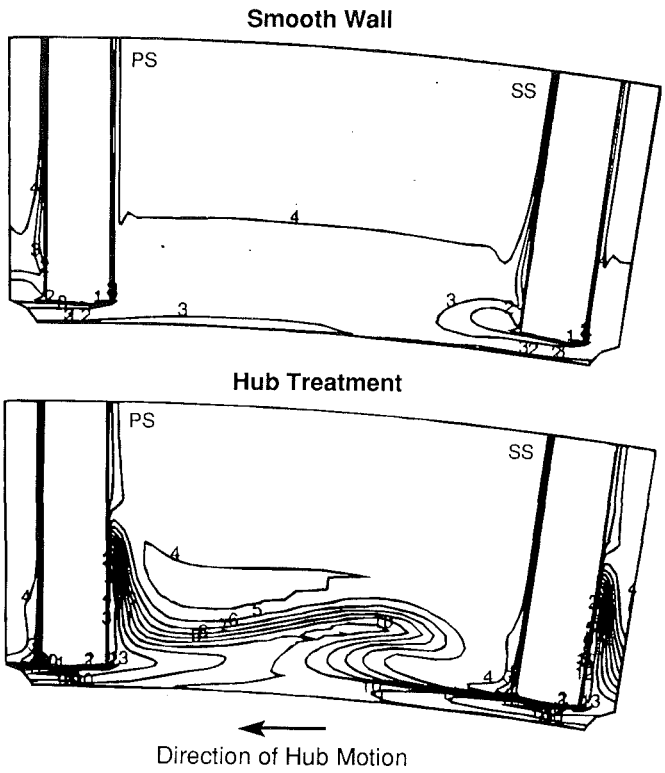

Fig. 20 Total pressure ($(P_t - P_{tin})/q_{in}$) contours at 40 percent chord (contour 1 = −1.0, contour 13 = 2.0, contour increment = 0.25)

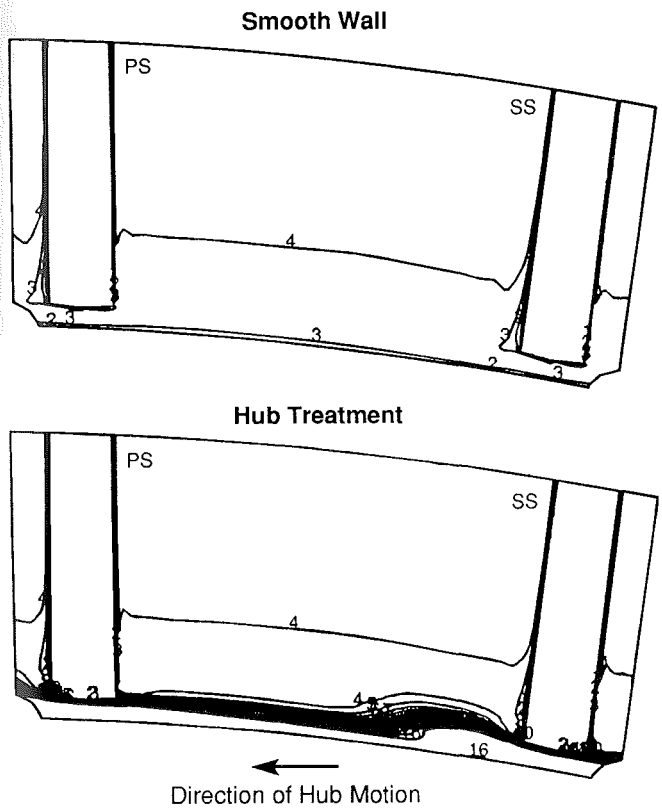

Fig. 19 Total pressure ($(P_t - P_{tin})/q_{in}$) contours at 10 percent chord (contour 1 = −1.0, contour 16 = 2.75, contour increment = 0.25)

form. With the hub treatment, there is no low total pressure vortex core because the high-pressure jet emerging from the hub treatment upstream of this axial station has washed the blade tip and removed (through mixing) the low total pressure fluid.

The total pressure loss coefficient at 78 percent chord is displayed in Fig. 21. For the smooth wall, the region with appreciable loss (say greater than 0.5 q_{in}) takes up much of the passage in the endwall region. With the hub treatment, however, this area is occupied by fluid with an excess of total pressure. The suction at the rear of the treatment draws this high total pressure fluid down to the hub. At the right of the passage, the suction also draws low total pressure fluid from the suction side of the blade into the treatment. At the left of the passage, high total pressure fluid that originated from the treatment jet at the front of the passage can be seen near the pressure surface of the blade moving away from the endwall. This fluid emerges as a jet at the rear of the passage (Cheng et al., 1984) and contributes little to the elimination of the blockage.

To examine the roles of treatment jet, suction, and leakage flow from another perspective, particle paths in the three-dimensional flowfield are displayed in Fig. 22. The particles are released on the hub roughly bounding the region of higher total pressure fluid coming from the treatment at 10 to 15 percent axial chord. The view is looking down the blade passage with the leading edge of one blade at the center of the figure, the neighboring blades invisible, and approximately the lower 40 percent of the blade span shown. A contour plot of total pressure is shown on a plane at the trailing edge location with low total pressure indicated by blue and high total pressure by red. The particles are marked with two different colors to show the release position; red particles were released over the central 50 percent of the pitch and blue particles over the rest. The computations show that the groups follow quantitatively different trajectories. Most of the red particles cross the passage, impact the pressure surface of the blade, and move up this surface away from the endwall. The blue particles, however, take helical paths, moving back toward the endwall. The hub

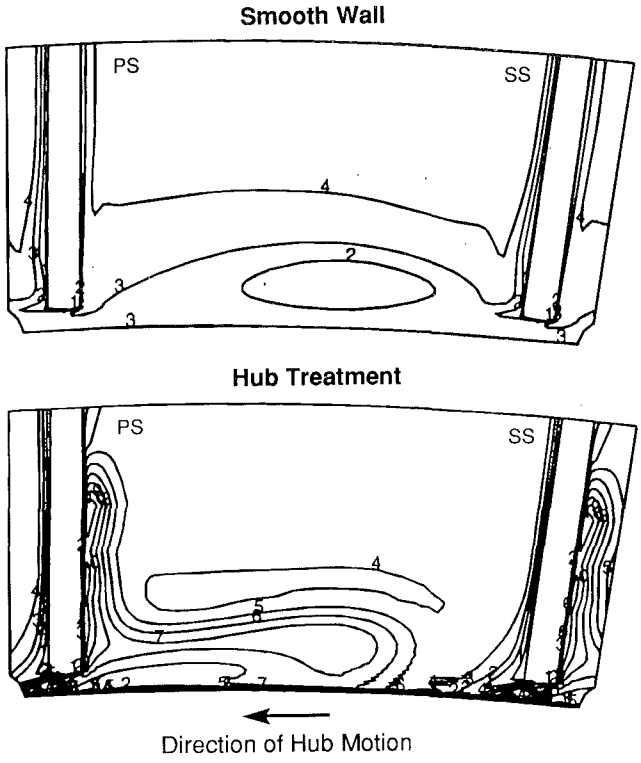

Fig. 21 Total pressure ($(P_t - P_{tin})/q_{in}$) contours at 78 percent chord (contour 1 = −1.0, contour 10 = 1.25, contour increment = 0.25)

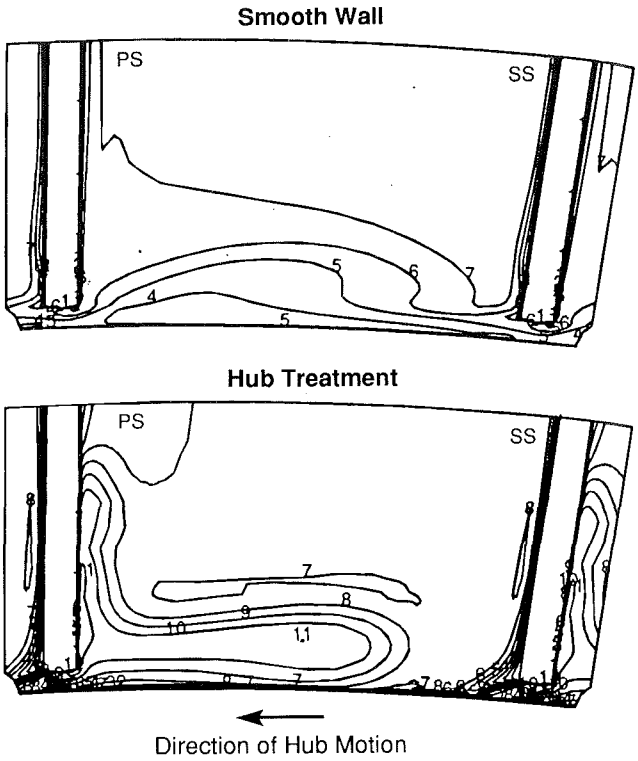

Fig. 23 Contours of velocity along stagger line ($C_{stagger}/\bar{C}_x$) at 78 percent chord (contour 1 = 0.0, contour 11 = 2.0, contour increment = 0.2)

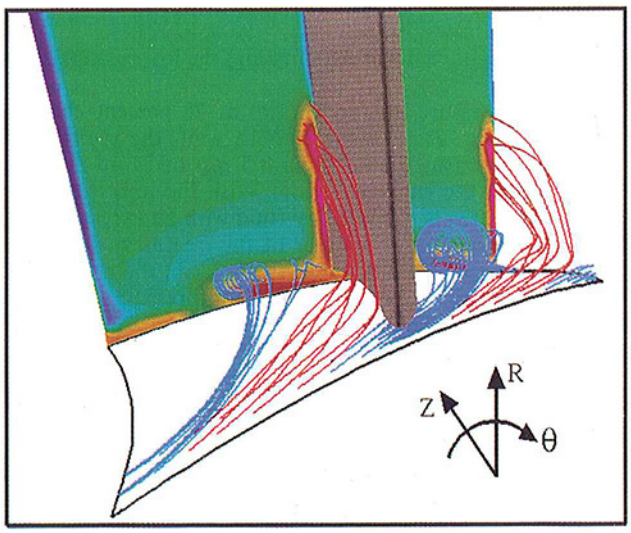

Fig. 22 Hub treatment: particles released in treatment jet; view from upstream looking downstream

treatment, therefore, does not suppress the vortex, but its core is now a region of high, rather than low, total pressure fluid.

Blockage. The action of the treatment has been described so far in terms of the streamlines and total pressure, but a quantity more directly related to endwall stall is blockage. The effect of the hub treatment on blockage in the passage is illustrated by Fig. 23, which presents contour plots of the component of velocity along the blade stagger line (velocity component along the (45 deg) stagger line/$\bar{C}_x$), at the 78 percent chord location for smooth wall and for hub treatment. The velocity component in the stagger direction is used as a crude indication of the flow "along" the blade passage; other components can also be examined, but the message is similar.

The velocity plots are similar to those of total pressure. For the smooth wall they show a midpassage region of low velocity (all contours with number less than 6 have velocity less than the mean axial velocity) and consequently large stream tube area increase. For the hub treatment, this low-velocity, high-blockage region does not exist. In fact the highest velocity occurs roughly in the region that was occupied by the low-velocity fluid with the smooth wall, but is now occupied by high total pressure fluid that emerged from the front of the treatment grooves. Again, on the right side of the passage the treatment suction can be seen to be removing low-velocity fluid.

Figure 23 is a demonstration of the combined effects of the casing treatment. There is a region of high velocity due to the injection. In the aft part of the passage, this high-velocity region is moved closer to the endwall by the suction that occurs there; this suction is also capable of removing high blockage fluid from the rear of the passage.

As a final note on the operation of hub and casing treatment portrayed here, we can make some comments on the relation of this work to high speed compressors. The computations of Adamczyk et al. (1993) strongly suggest that the leakage flow is also an important feature of stall onset in high-speed machines, i.e., compressors in which the pressure rise due to a shock is appreciable. In particular, that study showed a buildup of low total pressure fluid along the endwall due to the interaction of the leakage vortex and the passage shock. It thus appears that many features of the stall problem may carry over from low speed to high speed and that, in particular, injection of high-energy fluid in the forward part of the blade passage endwall to reduce or eliminate the growth of the regions of low total pressure would have a beneficial effect on flow range.

Summary and Conclusions

1 Computations have been carried out of the flow in the endwall region of a compressor blade row, with a smooth and a grooved endwall.

2 Comparison with velocity field measurements in a highly loaded cantilevered stator/rotating hub configuration shows that the computations provide a description that is useful for obtaining insight into the general features of the flow structure.

3 The computations show that the tip leakage and resulting vortex are dominant features of the endwall flow. The region of high loss and high blockage found near midpitch (rather than near the blades) is associated directly with the leakage flow.

4 First-of-a-kind computations have been carried out with blowing and suction through the hub to simulate the types of casing treatment that have been most successful in suppressing stall.

5 The computations show that there are two main actions of hub or casing treatment on the leakage flow: (1) suction of the low total pressure fluid at the rear of the passage, and (2) suppression of the blockage in the core of the leakage vortex due to the energizing of the leakage flow by high velocity injection at the front of the passage. In the latter, it is also shown that 50 percent or less of the treatment flow is useful in accomplishing this, the rest being dissipated with little effect on the endwall characteristics.

Acknowledgments

Support for the part of this work carried out at MIT was provided by Allison Gas Turbine Division of General Motors. This support, and the interest, strong encouragement, and helpful comments of Dr. R. A. Delaney and Mr. P. C. Tramm of Allison, are gratefully acknowledged. In addition, the authors express their appreciation for the many useful discussions with Mr. A. Khalid, the constructive critiques of Professor N. A. Cumpsty, and the efforts of Ms. D. I. Park in the preparation of the manuscript. We also wish to acknowledge the help given by T. A. Beach, M. L. Celestina, K. Kirtley, and R. A. Mulac in carrying out the computations.

References

Adamczyk, J. J., Celestina, M. L., Beach, T. A., and Barnett, M., 1990, "Simulation of Three-Dimensional Viscous Flow Within a Multi-stage Turbine," ASME JOURNAL OF TURBOMACHINERY, Vol. 112, pp. 370–376.

Adamczyk, J. J., Celestina, M. L., and Greitzer, E. M., 1993, "The Role of Tip Clearance in High-Speed Fan Stall," ASME JOURNAL OF TURBOMACHINERY, Vol. 155, pp. 28–39.

Baldwin, B., and Lomax, H., 1978, "Thin Layer Approximation and Algebraic Model for Separated Turbulent Flows," AIAA Paper No. 78-257.

Chen, G.-T., Greitzer, E. M., Tan, C. S., and Marble, F. E., 1991, "Similarity Analysis of Compressor Tip Clearance Flow Structure," ASME JOURNAL OF TURBOMACHINERY, Vol. 113, pp. 260–271.

Cheng, P., Prell, M. E., Greitzer, E. M., and Tan, C. S., 1984, "Effects of Compressor Hub Treatment on Stator Stall Margin and Performance," *Journal of Aircraft*, Vol. 21, No. 7, pp. 469–475.

Crook, A., 1989, "Numerical Investigation of Endwall/Casing Treatment Flow Phenomena," MIT GTL Report No. 200.

Dawes, W. N., 1987, "A Numerical Analysis of the Three-Dimensional Viscous Flow in a Transonic Compressor Rotor and Comparison With Experiment," ASME JOURNAL OF TURBOMACHINERY, Vol. 109, pp. 83–90.

Dong, Y., Gallimore, S. J., and Hodson, H. P., 1987, "Three-Dimensional Flows and Loss Reduction in Axial Compressors," ASME JOURNAL OF TURBOMACHINERY, Vol. 109, pp. 354–361.

Fujita, H., and Takata, H., 1984, "A Study of Configurations of Casing Treatment for Axial Flow Compressors," *Bulletin of the JSME*, Vol.27, No. 230, pp. 1675–1681.

Greitzer, E. M., Nikkanen, J. P., Haddad, D. E., Mazzawy, R. S., and Joslyn, H. D., 1979, "A Fundamental Criterion for the Application of Rotor Casing Treatment," ASME *Journal of Fluids Engineering*, Vol. 101, pp. 237–243.

Hah, C., 1986, "A Numerical Modeling of Endwall and Tip Clearance Flow of an Isolated Compressor Rotor," ASME *Journal of Engineering for Power*, Vol. 108, pp. 15–21.

Jameson, A., Schmidt, W., Turkel, E., 1981, "Numerical Solutions of the Euler Equations by Finite Volume Methods Using Runge-Kutta Time-Stepping Schemes," Paper No. AIAA-81-1259.

Johnson, M. C., 1985, "The Effects of Hub Treatment on Compressor Endwall Flowfields," M.S. Thesis, Dept. of Aeronautics and Astronautics, MIT, Cambridge, MA.

Lee, N. K. W., 1990, "Effects of Compressor Endwall Suction and Blowing on Stability Enhancement," MIT GTL Report No. 192, Jan. 1988; ASME JOURNAL OF TURBOMACHINERY, Vol. 112, pp. 133–144.

McDougall, N. M., 1988, "Stall Inception in Axial Compressors," Ph.D. Thesis, Engineering Department, Cambridge University, United Kingdom.

Pouagare, M., and Delaney, R. A., 1986, "Study of Three-Dimensional Viscous Flows in an Axial Compressor Cascade Including Tip Leakage Effects Using a SIMPLE-Based Algorithm," ASME *Journal of Turbomachinery*, Vol. 108, pp. 51–58.

Prince, D. C., Jr., Wisler, D. C., and Hilvers, D. E., 1974, "Study of Casing Treatment Stall Margin Improvement Phenomena," NASA CR-134552.

Smith, G. D. J., and Cumpsty, N. A., 1985, "Flow Phenomena in Compressor Casing Treatment," ASME *Journal of Engineering for as Turbines and Power*, Vol. 107, pp. 532–541.

Storer, A., 1991, "Tip Clearance Flow in Axial Compressors," Ph.D. Thesis, Dept. of Engineering, Cambridge University, United Kingdom.

Takata, H., and Tsukuda, Y., 1977, "Stall Margin Improvement by Casing Treatment—Its Mechanism and Effectiveness," ASME *Journal of Engineering for Power*, Vol. 99, pp. 121–133.

APPENDIX

Computational Procedure

Governing Equations and Boundary Conditions. The equations that govern the steady viscous flow in three dimensions, along with the equation of state, form the system to be solved. The scheme used is finite volume-cell centered and second-order accurate in space for a smooth uniform mesh. The discretized system of equations has unstable properties and can exhibit odd-even point decoupling. To suppress these instabilities, artificial dissipation terms made up of second and fourth difference smoothing operators are added to the equations. The time-stepping scheme used to discretize the system fully is a four-stage Runge–Kutta integration. Local time stepping for each cell and residual averaging are used to accelerate the convergence. A solution was deemed convergent when the average of the density time derivative over the domain had fallen two to three orders of magnitude from the initial value. Turbulent stresses are simulated using the model of Baldwin and Lomax (1978). The artificial dissipation is modified by a Mach number scaling to remove its influence on the regions of the flowfield in which viscous effects are dominant.

With subsonic inlet and exit regions four conditions must be set at the upstream boundary and one at the downstream boundary. Stagnation pressure and temperature were specified at the inlet as well as the flow angles in the z–θ and r–θ planes. The inlet axial velocity is set with a characteristic equation as is usual in this procedure. For the downstream boundary, the static pressure at the hub is set and simple radial equilibrium

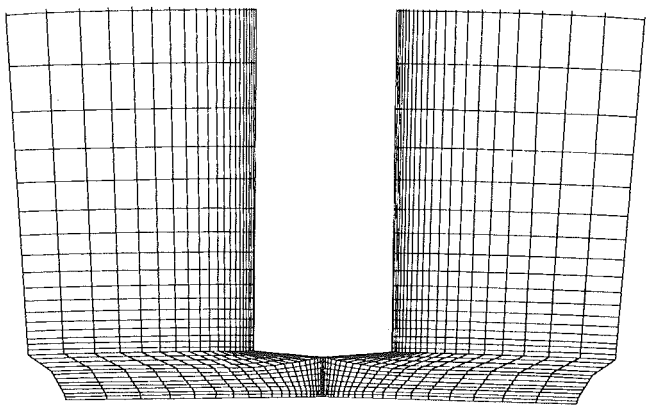

Fig. A.1 Viscous computation grid at midchord location; lower fifth of blade shown

Table A.1 Grid configuration

Number of grid points	Viscous grid	
	Hub clearance	No hub clearance
Blade to blade	49	41
Hub to tip	47	33
Hub to gap	9	---
Inlet to exit	111	89
L.E. to T.E.	56	44

is held. For solid wall boundaries, no-slip conditions were held at all surfaces.

Computational Grids. For both the viscous and inviscid solutions, an axisymmetric algebraic **H**-type mesh is generated. Table A.1 contains pertinent information about the grids.

Figure A.1 shows an r-θ plane at the midchord of the grid used in the calculations. The lower third of the blade passage is shown to emphasize the grid in the gap region underneath the tip of the blade. The grid was formed in this manner to resolve the flow in the gap region; however, grid distortion (shear) is introduced in the gap near the blade tip. Because of concern that grid shear might introduce errors in the flowfield solution, an investigation of the effect of grid shear on the solution was carried out. As reported by Crook (1989), the conclusion is that there is no strong effect of the shear on the tip flow solution.

An Investigation of Factors Influencing the Calibration of Five-Hole Probes for Three-Dimensional Flow Measurements

R. G. Dominy
School of Engineering and Computer Science, University of Durham, Durham, United Kingdom

H. P. Hodson
Whittle Laboratory, Cambridge University, Cambridge, United Kingdom

The effects of Reynolds number, Mach number, and turbulence on the calibrations of commonly used types of five-hole probe are discussed. The majority of the probes were calibrated at the exit from a transonic nozzle over a range of Reynolds numbers ($7\times10^3 < Re < 80\times10^3$ based on probe tip diameter) at subsonic and transonic Mach numbers. Additional information relating to the flow structure were obtained from a large-scale, low-speed wind tunnel. The results confirmed the existence of two distinct Reynolds number effects. Flow separation around the probe head affects the calibrations at relatively low Reynolds numbers while changes in the detailed structure of the flow around the sensing holes affects the calibrations even when the probe is nulled. Compressibility is shown to have little influence upon the general behavior of these probes in terms of Reynolds number sensitivity but turbulence can affect the reliability of probe calibrations at typical test Reynolds numbers.

Introduction

Five-hole probes of many different configurations are widely used in turbomachinery applications. The spatial confines of even the simplest machines and rigs invariably preclude the use of such probes in their nulled mode, and three-dimensional calibrations are therefore necessary. Where access to a measurement plane is relatively unrestricted, for example in the case of many linear cascades, two probe types are most commonly adopted, largely due to their relatively simple construction. The "Pyramid" probe generally consists of either five hypodermic tubes, which are bundled together and ground to form the head with forward facing pressure tappings (Fig. 1*a*), or a solid, ground pyramid with either forward facing or side facing (Fig. 1*b*) pressure tappings. The alternative "Cone" probe has a conical head with either forward or side facing pressure tappings (Figs. 1*c*, 1*d*). Variations on these basic probe geometries have been developed for specific applications such as the seven-hole probe developed by Gallington and Sisson (1980) for flow angle measurements at high angles of attack (±70 deg). A useful overview of multihole pressure probes and their application is provided by Bryer and Pankhurst (1971).

In order to maximize their spatial resolution, such probes are generally miniaturized. However, the flow conditions are dictated by the requirements of the blade row under investigation, so that the probe Reynolds number is determined solely by the relative length scales (d/c) of the probe and the blade row. The low probe Reynolds numbers that result may unfortunately fall within a region of significant Reynolds number sensitivity. Tables 1(*a*) and 1(*b*) give typical cascade and probe Reynolds numbers for both high-speed and low-speed cascade tests.

The individual characteristics of the two separate Reynolds number effects that appear to exist have never been formally

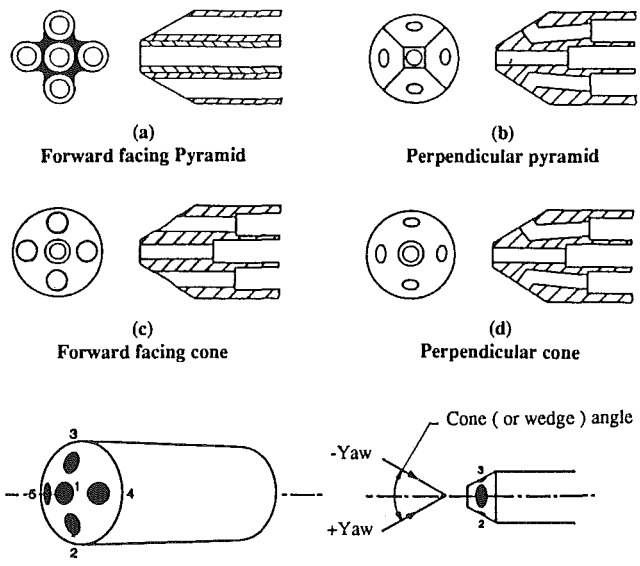

Fig. 1 Five-hole probe geometry

Contributed by the International Gas Turbine Institute and presented at the 37th International Gas Turbine and Aeroengine Congress and Exposition, Cologne, Germany, June 1–4, 1992. Manuscript received by the International Gas Turbine Institute February 20, 1992. Paper No. 92-GT-216. Associate Technical Editor: L. S. Langston.

Table 1(*a*) Reynolds numbers for a sonic cascade with a chord of 50 mm and a probe diameter of 2 mm at ambient temperature

Static Pressure	Re_c	Re_p
1/30 atm	0.35×10^5	1×10^3
1/3 atm	3.50×10^5	14×10^3
1 atm	11.0×10^5	42×10^3
2 atm	22.0×10^5	84×10^3

Table 1(*b*) Reynolds numbers for a low-speed cascade with a chord of 250 mm and a probe diameter of 2 mm

Static Pressure	Re_c	Re_p
1 atm	5×10^5	4×10^3

identified. The first is associated with the separation of the flow from the probe body when the probe is at incidence. Krause and Dudzinski (1969) examined the effects of Reynolds number upon the yaw and pitch sensitivity of a five-hole pyramid probe over a range of Reynolds numbers ($3 \times 10^3 < Re_p < 40 \times 10^3$). They found changes in the calibration coefficient that represented errors in the yaw and pitch of 1.5 deg and 3 deg, respectively, at a yaw angle of 10 deg and a pitch angle of 20 deg with the greatest variation at the lowest Reynolds numbers and negligible changes at the highest. Smith and Adcock (1986), using a broadly similar design of pyramid probe, also found the effects of Reynolds number to be limited to the lower end of the useful range of such probes ($Re_p < 100 \times 10^3$). Wallen (1983) found the yaw and pitch measurements from a conical probe to suffer from a similar degree of Reynolds number sensitivity and also demonstrated errors in the measurement of the stagnation and static pressures. Koschel and Pretzsch (1988) concluded that for a broadly similar design of five-hole cone probe, the effects of Reynolds number are negligible in the range from $Re_p = 37 \times 10^3$ to 82×10^3. However, a close examination of their data reveals indicated errors of approximately 0.8 deg at 15 deg yaw or pitch over the range investigated.

A second apparent Reynolds number effect is revealed by Novak (1983). At low Reynolds numbers ($2 \times 10^3 < Re_p < 20 \times 10^3$) it was observed that even for a nulled 90 deg cone probe there is still a sensitivity to Reynolds number that is indicated by static pressure variations of as much as 5 percent of the true dynamic pressure.

Huffman et al. (1980) provided some insight into the physical nature of the flow and they have derived a mathematical model to predict the flow over simple probe shapes. This achieved reasonable agreement with their own experimental data. Calibrations were obtained at Reynolds numbers from 10.5×10^3 to 35.6×10^3, which corresponded to Mach numbers from 0.6 to 0.9. However, their model was inviscid and their conclusions took no account of Reynolds number (referring only to Mach number dependence) despite their test Reynolds numbers lying within the most Reynolds number sensitive range.

The published literature clearly shows that the calibrations of five-hole cone probes are influenced by Reynolds number, with the greatest effects at the lowest Reynolds numbers, although little insight is given as to the physical nature of the phenomena. Surprisingly there has been relatively little investigation of the effect of probe head geometry upon the Reynolds number sensitivity of these probes. Comparisons made between data presented by different investigators for individual probes are of doubtful validity since discrepancies between calibrations in different facilities are notorious (e.g., Broichhausen and Fransson, 1984). With one exception, the discussion presented here relies upon data from a single facility. The present study focuses upon the Reynolds number sensitivity of a variety of five-hole cone and pyramid probe geometries. The effects of turbulence and compressibility upon Reynolds number sensitivity are also briefly discussed.

Experimental Facilities

Transonic Nozzle. The high-speed calibrations of the probes were carried out using the Transonic Cascade Test Facility of the Whittle Laboratory (Gostelow and Watson, 1976). This is a closed-circuit, variable density wind tunnel in which the Mach number and Reynolds number can be varied independently at ambient temperature.

The test section was fitted with a transonic nozzle similar to that developed by Baines (1983) in which the upper and lower walls were perforated to provide continuous acceleration over a range of subsonic and supersonic exit Mach numbers without requiring a change of geometry. The Mach number was defined by the pressure ratio across the nozzle. The stagnation pressure was measured in the upstream plenum and the static pressure variation through the nozzle was determined from a set of pressure tappings at midheight along one of the side walls. This wall was mirrored to allow double pass Schlieren photography. The Mach numbers that were derived from the wall static pressures were confirmed by a needle static probe at the nozzle axis and also by Schlieren photographs, which allowed the local Mach number to be determined from the angles of the Mach lines originating from the holes in the porous top and bottom walls. For equivalent conditions the maximum difference in Mach number obtained using these measurement methods was 0.006. The probe was positioned at the center of the nozzle exit plane and a computer-controlled traverse system rotated the probe about its tip during the calibration. Probe angles could be adjusted in steps of 0.02 deg in both pitch and yaw with an absolute accuracy of better than 0.1 deg.

Pressures were measured using a single transducer by means of a scanivalve-based system in order to minimize any errors arising from transducer calibrations. Individual pressure coefficients were estimated to be accurate to within 0.3 percent of the true dynamic pressure.

Low-Speed Nozzle. The low-speed measurements and flow visualization were performed using a conventional, atmospheric exit, low-speed wind tunnel fitted with a convergent nozzle at its exit. Observations were made using both surface oil flow visualization and smoke. The addition of a biplanar turbulence grid allowed measurements to be made at a higher turbulence level. The grid consisted of 6 mm bars spaced at 32 mm intervals.

Probe Geometries

The cone and pyramid probes used for this study are identified in Table 2.

The terms *forward facing* and *perpendicular* refer to whether

Nomenclature

c = blade chord or characteristic length
d = probe diameter
M = Mach number
p = pressure
Re_c = chord-based Reynolds number
Re_p = probe-diameter-based Reynolds number

Subscripts

av = average of $p_i (i = 2\text{–}5)$
i = pressure hole identifying number
s = free-stream static
0 = free-stream stagnation

Table 2 Probe designs

Probe Number	Cone or Pyramid	Cone/Wedge Angle	Hole Configuration	Probe Diameter or Thickness (mm)
1	C	60	Forward facing	2.06
2	C	60	Perpendicular	3.29
3	C	90	Perpendicular	3.29
4	C	45	Perpendicular	3.29
5	C	60	Forward facing	34.5
6	P	90	Perpendicular	3.29

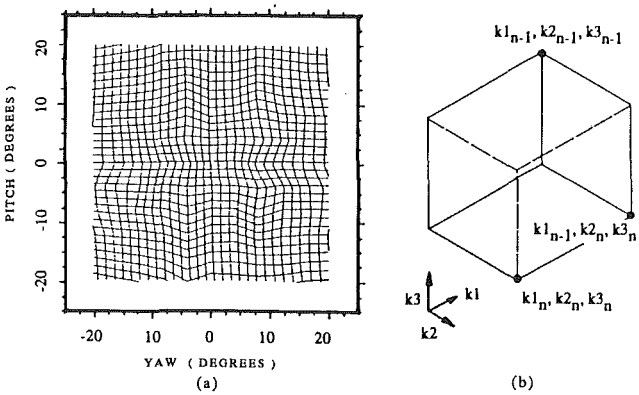

Fig. 2 Yaw and pitch calibration coefficient contours (probe No. 1, contour interval 0.1)

the axes of the yaw and pitch holes were parallel to the axis of the probe, thus facing forward into the flow, or perpendicular to the surface of the cone or pyramid (Fig. 1). The cone or wedge angle refers to the included angle at the probe tip. The largest probe (No. 5) was used to investigate the effect of turbulence on the Reynolds number sensitivity at low speed. The probes were mounted on stings to eliminate any influence from stem blockage and in each case the probe head blockage was less than 0.1 percent of the nozzle exit area.

Calibration and Pressure Coefficients

The convention used to number the five-hole pressure tubes is shown in Fig. 1 and the following widely adopted definitions are used for the calibration coefficients presented:

$$\textit{pitch angle coefficient } (k1) = \frac{p_4 - p_5}{p_1 - p_{av}}$$

$$\textit{yaw angle coefficient } (k2) = \frac{p_2 - p_3}{p_1 - p_{av}}$$

$$\textit{stagnation pressure coefficient} = \frac{p_0 - p_1}{p_1 - p_{av}}$$

$$\textit{dynamic pressure coefficient} = \frac{p_0 - p_s}{p_1 - p_{av}}$$

where p_{av} is the mean of the pressures measured by the side holes, that is:

$$p_{av} = \frac{(p_2 + p_3 + p_4 + p_5)}{4}$$

Numerous alternative calibration coefficients could have been chosen. For example, a static pressure coefficient $(p_{av} - p_s)/(p_1 - p_{av})$ is sometimes adopted in place of the dynamic pressure coefficient used here (e.g., Treaster and Yocum, 1979).

In addition to the calibration coefficients, the pressures from each hole are presented as nondimensional pressure coefficients of the form:

$$\text{pressure coefficient } i = \frac{p_i - p_0}{p_0 - p_s}$$

where i represents the identifier of a specific hole between 1 and 5. The use of these individual hole-based coefficients allows the flow phenomena to be investigated irrespective of the chosen calibration coefficient definitions.

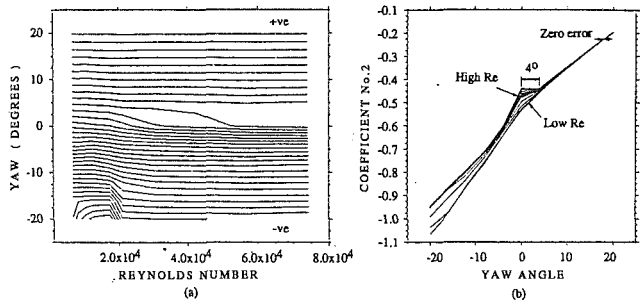

Fig. 3 Effect of Reynolds number and yaw angle upon pressure coefficient No. 2 of a 60 deg forward-facing cone probe (No. 1), M = 0.9: (*a*) contour interval = 0.025; (*b*) elevations plotted at Re intervals of 5×10^3 starting at 10×10^3

Using the Calibration Coefficients

When compressibility is not a consideration, it is usual to determine the actual flow angle at the probe tip from contours of pitch coefficient and yaw coefficient over the calibrated range of pitch and yaw angles (Fig. 2*a*). Once the flow direction has been established, the remaining pressure and hence velocity data may be determined from further coefficients. For compressible flows a third coefficient is required, which must be related to a third independent variable, i.e., Mach number, in order to determine the flow angle and other flow variables. An appropriate coefficient is the "pseudo Mach number," which is defined as:

$$\text{pseudo Mach number } (k3) = \frac{p_{av}}{p_1}$$

Any measured data point may be located within a cell bounded by adjacent contours of $k1$, $k2$, and $k3$ to find the pitch angle, yaw angle, and Mach number (Fig. 2*b*). The stagnation pressure and static pressure may then be found from their appropriate coefficients.

Results and Discussion

In this discussion, the effects of Reynolds number have generally been presented in terms of contoured surfaces where the contour height represents the value of the particular coefficient. The results have all been obtained at zero pitch angle, since the authors were mainly concerned with the determination of the mechanisms associated with the Reynolds number effects and the range over which they existed. The combined effects of pitch and yaw can easily be inferred from the results at zero pitch angle. For reasons that are discussed later, compressibility effects are assumed to have little influence on the basic flow mechanisms associated with the sensitivity of probes to Reynolds number and have not therefore been included in the initial discussion.

Effects of Reynolds Number. The results described here were obtained by calibrating the probes over a range of Reynolds numbers extending from approximately 7×10^3 to 80×10^3 at Mach 0.9.

The effects of Reynolds number are most graphically revealed by the *60 deg, forward-facing cone probe (No. 1)*. In Fig. 3, which demonstrates the sensitivity of a yaw hole (hole 2) to changes in Reynolds number, there are two regions of significant influence. The first is observed at large negative yaw angles below Reynolds numbers of approximately 21×10^3, when the measured pressure begins to fall with reducing Reynolds number. The low pressure is due to the influence of a separation bubble, which originates near the leading edge of

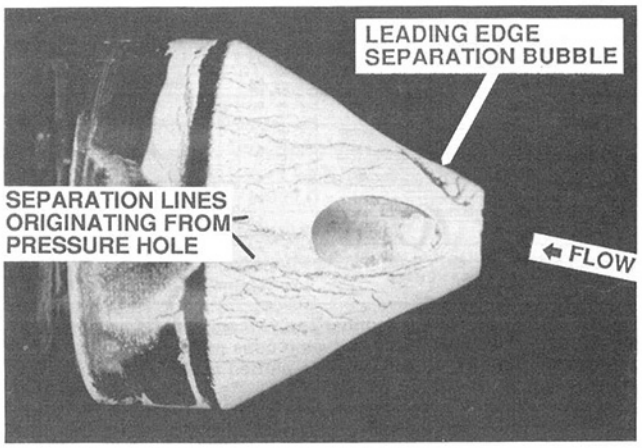

Fig. 4 Surface flow visualization on a large scale, 60 deg forward-facing cone probe; yaw = 8 deg, pitch = 0 deg, $Re_p = 13 \times 10^3$ (from Johnson, 1985)

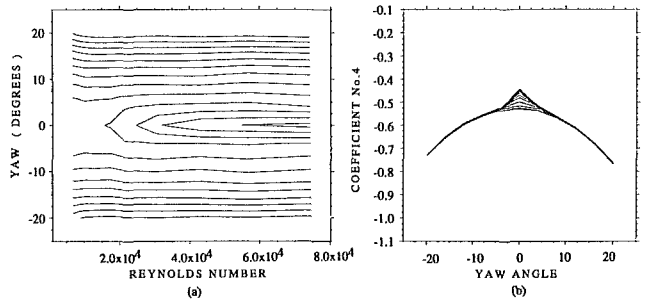

Fig. 5 Effect of Reynolds number and yaw angle upon pressure coefficient No. 4 of a 60 deg forward-facing cone probe (No. 1), M = 0.9: (*a*) contour interval = 0.025; (*b*) elevations plotted at Re intervals of 5×10^3 starting at 10×10^3

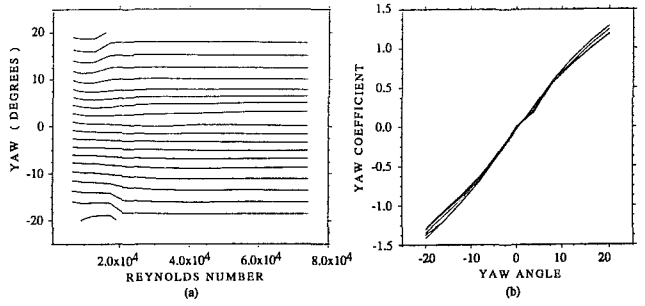

Fig. 6 Effect of Reynolds number and yaw angle upon yaw coefficient of a 60 deg forward facing cone probe (No. 1), M = 0.9: (*a*) contour interval = 0.136; (*b*) elevations plotted at Re intervals of 5×10^3 starting at 10×10^3

the probe and extends over the forward part of the yaw hole (Fig. 4). An apparent recovery of pressure at the lowest tested Reynolds numbers is thought to arise from the changing nature of the interaction of the separated flow with the pressure hole. Gaillard (1983) shows that although the pressure measured by the downwind yaw hole of a 45 deg probe at similar Reynolds numbers recovers when stall takes place, a 60 deg probe does not exhibit the same phenomena at the yaw angles encountered here. Hence it is unlikely that full separation is indicated.

The second observed region of significant Reynolds number influence occurs at yaw angles of less than 8 deg. Figure 3(*a*) shows that when $Re_p > 50 \times 10^3$ the pressure coefficient is insensitive to yaw between 0 and +4 deg while at small negative yaw angles the sensitivity to yaw is greatest. The asymmetry is less pronounced at lower Reynolds numbers and when $Re_p < 20 \times 10^3$ the effect has virtually disappeared. The response of the second yaw hole (hole 3) mirrors that described above.

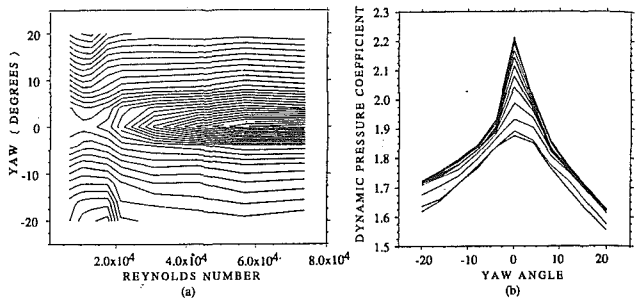

Fig. 7 Effect of Reynolds number and yaw angle upon dynamic pressure coefficient of a 60 deg forward-facing cone probe (No. 1), M = 0.9: (*a*) contour interval = 0.022; (*b*) elevations plotted at Re intervals of 5×10^3 starting at 10×10^3

The corresponding data from a pitch hole (hole 4) are presented in Fig. 5. At large positive or negative yaw angles, the influence of Reynolds number is only just discernible in either Fig. 5(*a*) or 5(*b*). However, Reynolds number effects are clearly evident at small yaw angles where the region of influence extends from $Re_p = 13 \times 10^3$ to the highest values tested. With the probe nulled, the pressure variation across the Reynolds number range is equivalent to 10 percent of the dynamic pressure and is therefore similar in magnitude to the changes observed for the yaw holes over the same range of Reynolds numbers. Thus, it might reasonably be concluded that the same mechanism is responsible in each case.

Although the study of the response of individual pressure holes is helpful to isolate and understand the flow phenomena, it is the coefficients of yaw, pitch, and dynamic pressure that are ultimately required for practical probe calibrations. The influence of Reynolds number upon the yaw coefficient is illustrated in Fig. 6. In Fig. 6(*a*) the effects of flow separation at high yaw angles are demonstrated for Reynolds numbers less than approximately 21×10^3, with the variation leading to a possible error of about 5 deg (the contour interval represents yaw angle changes of about 2 deg). This is the error that would occur if the probe were to be calibrated at $Re_p > 21 \times 10^3$ and used at a Reynolds number of say, 10×10^3. At small yaw angles the potential error is less than 2 deg, approximately half that indicated by Fig. 3. For probes that have more asymmetry than the present one, this may not be the case and errors may be substantially greater.

The dynamic pressure coefficient for the same probe is plotted in Fig. 7. At the largest yaw angles changes in the separated flow over a small range of Reynolds numbers may lead to errors of up to 6 percent in the measurement of dynamic pressure (in Fig. 7*a* the contour interval represents approximately 1 percent of the true dynamic head). In practice, the yaw angle will itself be in error by up to 5 deg, which will fortuitously reduce the error in dynamic pressure measurement to approximately 3 percent. With the probe nulled the dynamic pressure coefficient reflects the Reynolds number sensitivity of the yaw and pitch holes at small yaw angles (Figs. 3 and 5). This may lead to a potential error of 20 percent if dynamic pressure measurements are made at low Reynolds numbers using a calibration obtained at higher values. This is approximately four times that observed by Novak (1983) for a 90 deg, forward-facing cone probe.

Although the pressure measured by the center hole is essentially a function of the flow angle, the value of the correction $(p_o - p_1)$ to be applied to the measured value, p_1, in order to obtain the true stagnation pressure, p_o, will be subject to the same relative errors as the true dynamic pressure $(p_o - p_s)$. This is because the error lies in the accuracy of the denominator of the relevant coefficients, $(p_1 - p_{av})$.

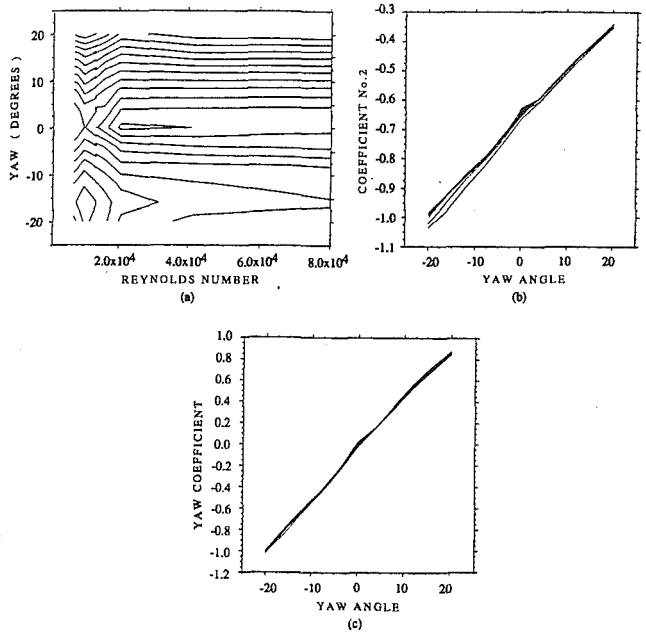

Fig. 8 Effect of Reynolds number and yaw angle upon (*a*) dynamic pressure coefficient, (*b*) pressure coefficient No. 2, and (*c*) yaw coefficient of a 60 deg perpendicular cone probe (No. 2), M = 0.9: (*a*) contour interval = 0.016; (*b*), (*c*) elevations plotted at Re intervals of 5 × 10^3 starting at 10 × 10^3

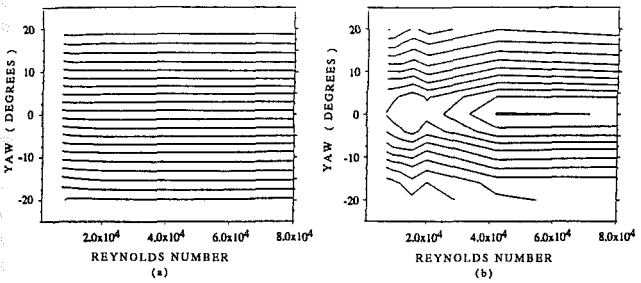

Fig. 9 Effect of Reynolds number and yaw angle upon (*a*) yaw coefficient and (*b*) dynamic pressure coefficient of a 90 deg perpendicular cone probe, M = 0.9: (*a*) contour interval 0.139; (*b*) contour interval 0.025

Effects of Hole Geometry. For a fixed hole center location, the most upstream edge of a pressure hole will lie further from the probe tip when the axis of the hole is perpendicular to the probe surface than is the case for the forward-facing holes of the probe described above. The holes will also occupy a smaller surface area. The *60 deg, perpendicular cone probe* incorporates such a hole arrangement, but is in all other respects similar to the 60 deg, forward-facing cone probe that has been discussed above.

The dynamic pressure coefficient for the new probe is presented in Fig. 8. The lower overall level of the coefficient (cf. Fig. 7*a*) indicates that the sensitivity to dynamic pressure has been improved by about 25 percent. (The contour interval in Fig. 8*a* represents approximately 1 percent of the true dynamic pressure.) However, the sensitivity to Reynolds number when nulled has been significantly reduced. Only when the probe is yawed at $Re_p < 20 \times 10^3$ does Reynolds number become influential due to the effects of the leading edge separation. A further benefit is the reduced sensitivity of the coefficient to yaw angle. However, some asymmetry can also be seen, though it does appear to be independent of Reynolds number.

The sensitivity of the yaw holes to yaw angle changes (Fig. 8*b*) is similar to that of the forward-facing probe, but the yaw coefficient would seem to be less sensitive to yaw angle because the measured pseudo-dynamic pressure ($p_1 - p_{av}$) is increased relative to the forward-facing probe. The influence of Reynolds

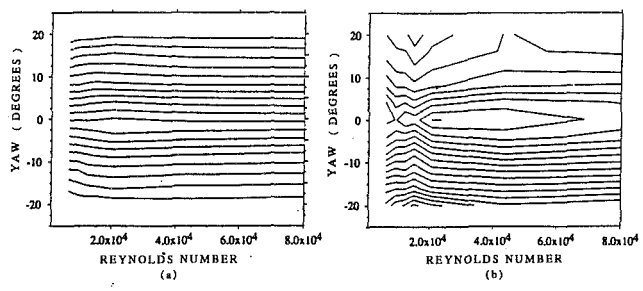

Fig. 10 Effect of Reynolds number and yaw angle upon (*a*) yaw coefficient and (*b*) dynamic pressure coefficient of a 45 deg perpendicular cone probe, M = 0.9: (*a*) contour interval 0.081; (*b*) contour interval 0.014

number at high yaw angles is also reduced, as confirmed by Fig. 8(*b*). The reduced sensitivity is believed to result from the position of the pressure tubes, which are located farther from the tip and are therefore less likely to be affected by leading edge separation bubbles. The maximum possible error in the measurement of yaw angle is less than 1 deg across the range of Reynolds numbers at all angles of attack (Fig. 8*c*, cf. Fig. 6*b*) but again, the pressure coefficients of the individual holes (Fig. 8*b*) imply a greater potential error. At 10 deg of yaw for Reynolds numbers between 25 × 10^3 and 72 × 10^3 the errors are similar to the value of 1.1 deg quoted by Wallen (1983) for a probe of identical design.

Figure 8(*a*) showed that the change in hole configuration significantly reduces the effect of changes in Reynolds number upon dynamic pressure measurement when the probe is nulled. This is confirmed by Fig. 8(*b*), which indicates a reduced sensitivity of the individual yaw tubes to changes in Reynolds number when the yaw angle is small.

Effects of Cone Angle. It has been shown that the Reynolds number sensitivity of a probe is influenced by the interaction between flow separations and the pressure holes. Since the degree of separation must be related to the cone angle, it was decided to calibrate two additional probes with *45 and 90 deg cone angles*. Both probes were of the perpendicular type.

Figure 9 presents the yaw coefficient and dynamic pressure coefficient results obtained for the 90 deg probe. The sensitivity of the yaw calibration to changes in Reynolds number is less than that observed for either of the 60 deg probes and there is only a hint of separation at high yaw angles even at the lowest Reynolds numbers (Fig. 9*a*, cf. Fig. 6*a*). The contours of dynamic pressure coefficient (Fig. 9*b*) suggest that separation actually exists up to Reynolds numbers of approximately 40 × 10^3. This apparent discrepancy arises because the effects of separation upon the dynamic pressure coefficient are not masked by the changes resulting from changes in the yaw angle. The variation represents an error of no more than 2.5 percent in the measurement of dynamic pressure.

The dynamic pressure coefficient contours (Fig. 9*b*) may be compared to those of the 60 deg probe with perpendicular holes (Fig. 8*a*). For the 90 deg probe, the sensitivity of the dynamic pressure coefficient to changes in Reynolds number extends over a wider range with the dependence being minimal only above a Reynolds number of 40 × 10^3. The maximum possible error over this wider range is, however, identical to that for the 60 deg probe, suggesting that the 90 deg probe is much better suited to measurements below a Reynolds number of 20 × 10^3. For the 60 deg probe, the variation of the coefficient is less rapid in the range of Reynolds numbers from 20 × 10^3 to 40 × 10^3, so that the converse appears to be true.

Figure 10 shows the effects of yaw and Reynolds number upon the yaw and dynamic pressure coefficients for the 45 deg cone probe. The influence of Reynolds number is most clearly evident in the dynamic pressure contours of Fig. 10(*b*). The effects of flow separation at large yaw angles extend to higher Reynolds numbers ($Re_p < 40 \times 10^3$) than for the less sharp

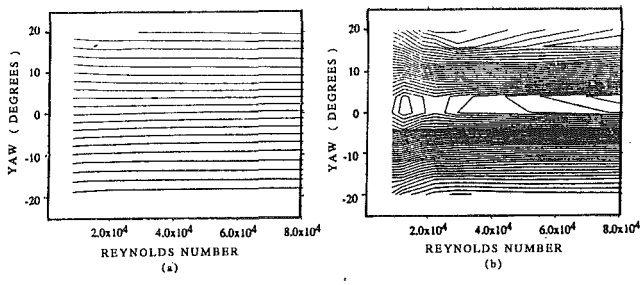

Fig. 11 Effect of Reynolds number and yaw angle upon (*a*) yaw coefficient and (*b*) dynamic pressure coefficient of a 90 deg perpendicular pyramid probe, M = 0.9: (*a*) contour interval 0.225; (*b*) contour interval 0.0125

probes. However, when nulled, the region of significant Reynolds number influence is similar to that for the 60 deg probe. The limit is again approximately 20×10^3, where the yaw coefficient contours are also distorted as a result of rapid variations in the pseudo-dynamic pressure $(p_1 - p_{av})$.

The sensitivities of the pressures measured by the individual yaw tubes of the 45 and 90 deg probes to changes in yaw angle were found to be respectively 10 percent less and 10 percent greater than that of the 60 deg, perpendicular probe. Therefore at higher Reynolds numbers it appears that there is little to choose between the three cone angles in terms of the true sensitivity of the probes to changes in flow angle. Selection must therefore be made according to the level of accuracy required for the measurement of the dynamic pressure. At the lower Reynolds numbers investigated, the required accuracies of flow angle and dynamic pressure measurements must be weighed against each other.

Pyramid Probes. Since the Reynolds number sensitivity of cone probes essentially results from interactions between pressure holes and separations, it may be expected that there may be some differences in the behavior of pyramid probes, since the separation points are defined by the sharp corners of the probe even in the event of the movement of the stagnation point. Yaw coefficient contours for a *90 deg, perpendicular pyramid probe* (probe 1, Fig. 1*b*) at a Mach number of 0.9 are shown in Fig. 11(*a*), and these may be compared directly with those from the 90 deg cone probe (Fig. 9*a*). No significant differences are observed, both probe types displaying typical errors in yaw coefficient of 0.5 deg in the sensitive range $(20 \times 10^3 < \mathrm{Re}_p < 80 \times 10^3)$. The poor calibration data at approximately +15 deg at low Reynolds numbers is due to minor imperfections in the probe construction and is seen more graphically in the dynamic pressure coefficient data of Fig. 11(*b*). Comparison with the dynamic pressure coefficient data from the cone probe (Fig. 9*b*) shows that when nulled there is very little difference in the performance of the two probes over the full range of Reynolds numbers. When the probes are yawed, the pyramid provides more linear dynamic pressure coefficient data in the sensitive range $(20 \times 10^3 < \mathrm{Re}_p < 50 \times 10^3)$ and the error resulting from Reynolds number effects typically corresponds to 1 percent of dynamic head compared with the 3 percent shown by the cone probe data. The positive yaw data have not been considered in this comparison for the reasons explained above.

These results have highlighted two separate Reynolds number effects. The first and simplest is associated with the separation of the flow from the probe tip when yawed even at relatively small flow angles. The effects of the separation appear only at relatively low Reynolds numbers. It is believed that the Reynolds number affects the transition process and therefore the overall size of the separation bubble. The greater the cone angle of the probe, the lower is the Reynolds number above which the effects of separation cease to be apparent. Similarly, the closer the pressure holes are to the tip of the probe, the more likely they are to be influenced by the flow separation.

The second Reynolds number effect is most pronounced when the probe is nulled. The effect extends over a greater Reynolds number range than the separation effect and, perhaps more significantly, to higher Reynolds numbers. The measurement of dynamic (or static) pressure is most influenced by this effect. A comparison of the 60 deg probes with the forward-facing holes and with perpendicular pressure holes has shown that the errors caused by operation over a range of Reynolds numbers are greatest in probes of the forward facing type. Although the errors and differences are much smaller, this conclusion is supported by a comparison between the results presented here for a 90 deg probe with perpendicular holes and the forward-facing 90 deg type of Novak (1983). The former exhibited a 3 percent error in dynamic pressure measurement while the latter produced a 5 percent variation over the same range of Reynolds numbers.

It is not known whether this second effect, which might appropriately be termed a "hole" effect, is due to the changes in the open area of the holes, the orientation of the hole axis, or both. Nor is the mechanism of the Reynolds number influence understood. However, it must be noted that the pressure holes in a probe such as the forward-facing type of Fig. 4 occupy a large proportion of the conical surface. For this reason, care has been taken not to refer to the holes as pressure tappings, since to do so would infer that the holes themselves do not influence the flow field around the probe. Clearly this is not the case. The holes might well permit flow patterns to develop on a scale that is not dissimilar to the scale of the probe; should this occur, the flow might be strongly dependent upon Reynolds number. The flow visualization of Fig. 4 provides evidence that the yaw and pitch holes influence the flow around the probe. Two separation lines can be seen extending from the rear of the pressure hole facing the camera. These separation lines are believed to begin where the flow separates as it moves rearward over the lip created by the forward part of the hole. With separation occurring at the edges of the holes, it is not unreasonable to assume that the flow would be sensitive to small changes in Reynolds number. Indeed, the hypothesis presented here is entirely consistent with the observations of Fransson and Sari (1981) who studied the flow around a two-dimensional model of a nulled, forward-facing probe. They found significant levels of unsteadiness in the pressure tubes connected to the yaw holes.

It has been noted that the yaw coefficient is less sensitive to changes in Reynolds number than might be expected from the pressure coefficient data alone. In a turbomachinery environment, where the flow vector may be continually changing, the nonlinear response of individual holes may prevent such a fortuitous combination of events.

Effects of Compressibility. In the above discussion the effects of compressibility are considered to have little bearing on the sensitivity of these probes to Reynolds number changes and all the results have been obtained at a Mach number of 0.9. This assumption is based upon a series of calibrations of the 45 deg, perpendicular cone probe at different Mach number. The yaw coefficient contours of this probe at the lower Mach number of 0.5 are shown in Fig. 12(*a*) and may be directly compared with those of Fig. 10(*a*). The difference between the yaw coefficient contours is only apparent at Reynolds numbers below 17×10^3. Thus, the yaw coefficient is insensitive to Mach number except at the lowest Reynolds numbers, a result that was later confirmed by the calibration of all of the cone probes over a range of Mach numbers up to Mach 1.2. In contrast and as might be expected, the dynamic pressure coefficient is not independent of Mach number. However, the general shapes of the contours of Figs. 10(*b*) and 12(*b*) are similar, suggesting that all of the Reynolds number effects so far encountered need not be studied again at high Mach numbers.

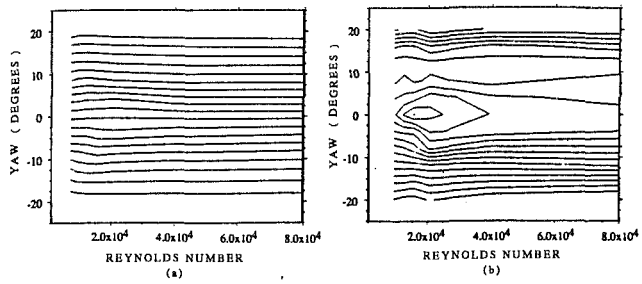

Fig. 12 Effect of Reynolds number and yaw angle upon (*a*) yaw coefficient and (*b*) dynamic pressure coefficient of a 45 deg forward-facing cone probe at low speed (M = 0.5)

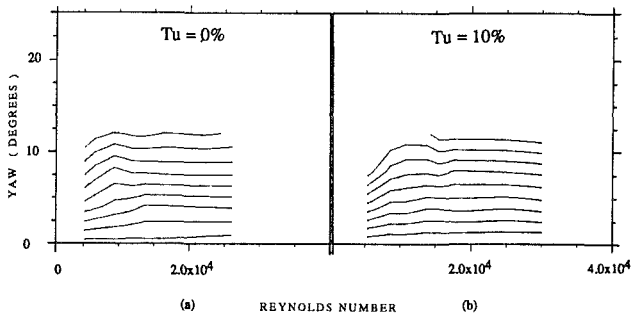

Fig. 13 Effect of Reynolds number and yaw angle upon yaw coefficient of a 60 deg forward-facing cone probe at low speed: (*a*) streamwise turbulence intensity < 0.01 percent, contour interval = 0.1; (*b*) streamwise turbulence intensity = 10 percent, contour interval = 0.1

Effect of Turbulence. It has been demonstrated that at least part of the influence of Reynolds number upon probe calibrations is due to the changing nature of the separations that exist at all flow angles; changes that stem from the influence that Reynolds number exerts upon the transition processes within the separation bubbles. Since free-stream turbulence is also known to influence transition processes, a brief study of the influence of free-stream turbulence was undertaken at low speed using a large-scale model of the 60 deg, forward-facing probe (probe 5). This model was calibrated in a low-turbulence stream and then again behind a biplanar turbulence grid with a mesh spacing equal to 85 percent of the probe diameter. The grid size was chosen so as to create turbulence of a similar relative scale to that occurring in practical environments and a free-stream turbulence intensity (streamwise component) of 10 percent was generated compared with < 0.1 percent without the grid fitted.

The yaw coefficient calibrations derived from these two test cases are shown in Fig. 13 and the results may also be compared with those of the geometrically similar, smaller scale probe (Fig. 6*a*). It is evident that the intensity of the turbulence does affect the probe calibration when $Re_p < 20 \times 10^3$ when, in the case of low turbulence, a separation bubble is known to exist (Fig. 4). Thus free-stream turbulence may influence the accuracy of probes that are sensitive to Reynolds number.

Conclusions

A number of different, commonly used five-hole probe designs have been calibrated over a range of Reynolds numbers that are typical of those encountered in turbomachinery, and the existence of two separate Reynolds number effects has been confirmed. The first results from separation of the flow from the probe head when the probe is at incidence. The effect of this upon the accuracy yaw measurements is limited to Reynolds numbers below 15×10^3 for a 90 deg cone probe, 20×10^3 for a 60 deg cone probe, and 35×10^3 for a 45 deg cone probe. The geometry of the pressure-sensing holes has little effect on these limits. However, the hole geometry does affect the magnitude of the Reynolds number sensitivity, and it has been shown that probes with their pressure holes set perpendicular to the probe surface were less sensitive to changes in Reynolds number.

The second Reynolds number effect is apparent when the probe is at small or zero yaw angles and the effect was found to occur over a large part of the investigated range of Reynolds numbers. This effect is therefore significant even when probes are used in their nulled mode. The dependence of the dynamic pressure coefficient upon Reynolds number under these conditions is such that probes with pressure holes perpendicular to the surface should be employed whenever possible in preference to forward-facing designs.

The 90 deg pyramid cone displays similar characteristics to the corresponding cone type but the magnitude of the error arising from Reynolds number effects is reduced at high yaw angles. When nulled, no difference is observed between the performances of equivalent cone and pyramid probes.

A comparison of three conical, perpendicular probes shows that the probe with the largest cone angle was least sensitive to changes in Reynolds number. For this 90 deg probe the variation in yaw coefficient was equivalent to a maximum error of 0.7 deg while the error in the measurement of dynamic pressure was limited to approximately 3 percent. However, the accuracy of dynamic pressure measurement is compromised over a greater range of Reynolds numbers.

An investigation of the effects of compressibility and free-stream turbulence upon the sensitivity to Reynolds number showed that the basic flow patterns are unaffected by compressibility, whereas changes in free-stream turbulence may have a significant effect due to the influence upon low Reynolds number separation bubbles.

References

Baines, N. C., 1983, "Development of a Perforated Nozzle for Calibrating Transonic Probes," *Proc. of 7th Symposium on Measuring Techniques in Transonic and Supersonic Flows in Cascade and Turbomachines*, Aachen, Germany.

Broichhausen, K.-D., and Fransson, T., ed., 1984, *Proc. of the European Workshop on Probe Calibrations (1984–1983)*, Aachen, Germany.

Bryer, D. W., and Pankhurst, R. C., 1971, "Pressure-Probe Methods for Determining Wind Speed and Flow Direction," Her Majesty's Stationery Office, London.

Fransson, T., and Sari, I., 1981, "Characteristics of Aerodynamic Five-Hole-Probes in Transonic and Supersonic Flow Regimes," *Proc. of 6th Symposium on Measuring Techniques in Transonic and Supersonic Flows in Cascade and Turbomachines*, Lyon, France.

Gaillard, R., 1983, "Calibration and Use of an ONERA Miniature Five Hole Probe," *Proc. of 7th Symposium on Measuring Techniques in Transonic and Supersonic Flows in Cascade and Turbomachines*, Aachen, Germany.

Gallington, R., and Sisson, G., 1980, "Flow Visualisation Using a Computerised Data Acquisition System," presented at the Second International Symposium on Flow Visualization, Bochum, Germany.

Gostelow, J. P., and Watson, P. J., 1976, "A Closed Circuit Variable Density Air Supply for Turbomachinery Research," ASME Paper No. 76-GT-62.

Huffman, G. D., Rabe, D. C., and Poti, N. D., 1980, "Flow Direction Probes From a Theoretical and Experimental Point of View," *J. Phys. E: Sci. Instrum.*, Vol. 13, pp. 751–760.

Johnson, A. B., 1985, "Reynolds Number Dependence of 5-Hole 3-Dimensional Truncated Cone Probes," Project report, Part II, Engineering Tripos, Cambridge University, United Kingdom.

Koschel, W., and Pretzsch, P., 1988, "Development and Investigation of Cone-Type Five-Hole Probes for Small Gas Turbines," *Proc. of 9th Symposium on Measuring Techniques in Transonic and Supersonic Flows in Cascade and Turbomachines*, Oxford, United Kingdom.

Krause, L. N., and Dudzinski, T. J., 1969, "Flow-Direction Measurement With Fixed Position Probes in Subsonic Flow Over a Range of Reynolds Numbers," *Proc. 15th Int. ISA Aerospace Instrumentation Symposium*, Las Vegas, NV, pp. 217–223.

Novak, O., 1983, "Investigation of the Reynolds Number Effect of Two Pressure Probes for Measurements in Turbomachines," *Proc. of 7th Symposium on Measuring Techniques in Transonic and Supersonic Flows in Cascade and Turbomachines*, Aachen, Germany.

Smith, A. L., and Adcock, J. B., 1986, "Effect of Reynolds Number and Mach Number on Flow Angularity Probe Sensitivity," NASA TM-87750.

Treaster, A. L., and Yocum, A. M., 1979, "The Calibration and Application of Five-Hole Probes," *ISA Transactions*, Vol. 18, No. 3.

Wallen, G., 1983, "Reynolds Number Effects of a Cone and a Wedge Type Pressure Probe," *Proc. of 7th Symposium on Measuring Techniques in Transonic and Supersonic Flows in Cascade and Turbomachines*, Aachen, Germany.

On the Conservation of Rothalpy in Turbomachines

F. A. Lyman
Department of Mechanical and Aerospace Engineering, Syracuse University, Syracuse, NY 13244-1240

The conditions under which rothalpy is conserved are investigated by means of the energy and moment-of-momentum equations for unsteady flow of a viscous, compressible fluid. Differential and integral equations are given for the total enthalpy and rothalpy in both stationary and rotating coordinates. From the equations in rotating coordinates it is shown that rothalpy may change due to: (1) pressure fluctuations caused by flow unsteadiness in the rotating frame; (2) angular acceleration of the rotor; (3) work done by viscous stresses on the relative flow in the rotating frame; (4) work done by body forces on the relative flow; (5) changes in entropy due to viscous dissipation and heat transfer. Conclusions of this investigation are compared with those of previous authors, some of whom have stated that rothalpy is conserved even in viscous flows. A modified Euler's turbomachine equation, which includes viscous effects, is derived and errors in previous derivations noted.

Introduction

It is well known that for steady adiabatic flow in stationary passages with negligible change in potential energy, the total or stagnation enthalpy

$$h_0 = h + \frac{V^2}{2} \tag{1}$$

is conserved. For steady, isentropic flow in rotating passages and negligible change in potential energy it is the *rothalpy* (Wu, 1953)

$$I = h + \frac{1}{2}(W^2 - U^2) \tag{2}$$

that is conserved. In Eq. (2) $\mathbf{W}$ is the velocity of the fluid relative to the frame rotating with the blade, and $\mathbf{U}$ is the blade velocity. Since the absolute velocity of the flow is

$$\mathbf{V} = \mathbf{U} + \mathbf{W} \tag{3}$$

and $\mathbf{U} = \omega r \mathbf{e}_\theta$, the rothalpy can also be written

$$I = \left(h + \frac{1}{2} V^2\right) - \mathbf{U} \cdot \mathbf{V} = h_0 - \omega r V_\theta \tag{4}$$

The turbomachinery textbooks of Vavra (1960), Dixon (1978), Cumpsty (1989), and Whitfield and Baines (1990) prove that rothalpy is conserved in adiabatic steady flows. The proofs rely on a simplified form of the energy equation, which does not include the work done on the relative flow by the viscous stresses. Since it is not always recognized that this work has been neglected, the books differ on whether rothalpy is conserved for *viscous* flows in impellers.

According to Cumpsty (1989), "In a moving passage the rothalpy is therefore constant provided:

(*a*) the flow is steady in the rotating frame;
(*b*) no work is done on the flow in the rotating frame (for example by friction from the casing);
(*c*) there is no heat flow to or from the flow."

This statement appears in Chap. 1 of Cumpsty's book, following the usual proof that rothalpy is constant in steady adiabatic flow. Although it is a clear and (as will be shown) accurate summary of the conditions under which rothalpy is conserved, it is contradicted later in the book (Chap. 6), where the equation I = const appears without comment among the equations governing the flow of a *viscous* compressible fluid relative to the impeller of a centrifugal compressor.

Dixon (1978) claims that the rothalpy "... is constant for an adiabatic irreversible flow process, relative to a rotating component." According to Vavra (1960) the rothalpy is constant along a relative streamline in adiabatic steady flows "... even though entropy changes occur because of frictional effects." Whitfield and Baines (1990) state that "... for any adiabatic flow in a turbomachine, I is constant, regardless of external work transfers or radius changes." Although the last authors had made it clear that their derivation was for steady adiabatic flow, they did not mention friction.

On the other hand, a few theoretical analyses have shown that rothalpy is *not* conserved when work is done on the relative flow by the viscous stresses. Csanady (1964) derived an integral (control volume) equation for the rothalpy, which included the viscous power dissipation.[1] Sehra (1979) derived a differential equation for the rate of change of the mean (pitchwise-averaged) rothalpy along the mean streamline. Sehra's result

Contributed by the International Gas Turbine Institute and presented at the 37th International Gas Turbine and Aeroengine Congress and Exposition, Cologne, Germany, June 1-4, 1992. Manuscript received by the International Gas Turbine Institute February 20, 1992. Paper No. 92-GT-217. Associate Technical Editor: L. S. Langston.

[1] Csanady's derivation contains an incorrect assumption, but as shown in Appendix A, this assumption can be removed without affecting the result.

is quite complicated (see Sehra and Kerrebrock, 1980), but it clearly shows that changes in the mean rothalpy are due to both molecular viscosity and the apparent stresses due to velocity fluctuations relative to the blade.

Urbach (1990) derived differential equations for the total enthalpy and rothalpy in the rotor-fixed frame. By integrating his equation for the total enthalpy, he obtained a result that he called the "Euler Turbomachinery Equation With Viscous Correction." Urbach's equation differs from Csanady's in that there are two terms instead of one representing the useful mechanical power. Each of these terms is the product of a mass flow rate in the radial or axial direction and the corresponding change of UV_θ in that direction. This discrepancy was not mentioned by Urbach, although he did cite Csanady's book.[2] Urbach did obtain the correct expression for the viscous correction term, which Vavra (1960) had omitted altogether in his form of Euler's turbine equation. Vavra argued that his equation nevertheless accounted for friction.

Computations of viscous flow in centrifugal impellers have been carried out by numerous authors. The results reported in a series of papers by J. Moore, J. G. Moore, and R. H. Timmins (1980, 1984, 1985) are of particular interest because they include rothalpy production at the wall of the stationary shroud. Work done by the viscous stress at the shroud wall was found to increase the rothalpy by about 1 or 2 percent of the total work input, depending on the impeller design and operating conditions.

The present investigation began as an attempt on the author's part to resolve the contradictions in the literature regarding conservation of rothalpy in *viscous* flow. The equation for the rate of change of rothalpy following the motion of a fluid particle relative to the impeller is derived by transforming the differential equations for the total enthalpy and moment of momentum of a viscous, compressible, heat-conducting fluid into coordinates rotating with the impeller. This approach is similar to that used previously by Urbach (1990), whose work was unknown to the author at the time this investigation was started. Urbach assumed a flow that was adiabatic and steady in coordinates fixed to an impeller rotating with constant angular velocity. The present analysis includes heat transfer and allows unsteadiness due to either velocity fluctuations within the rotor passage or angular acceleration of the rotor. It also provides a simple and rigorous derivation of the integral form of the rothalpy equation, resolving inconsistencies in prior analyses.

[2]It is shown in Appendix B that had the integration been performed correctly, Urbach's result would have agreed with both Csanady's and that obtained in the present paper.

Analysis

1 Equations for Total Enthalpy. The total enthalpy h_0 changes according to the following equation for a viscous, compressible fluid with heat conduction (Liepmann and Roshko, 1957):

$$\rho \frac{Dh_0}{Dt} = \frac{\partial p}{\partial t} + \nabla \cdot (\tau \cdot \mathbf{V}) + \rho \mathbf{f} \cdot \mathbf{V} - \nabla \cdot \mathbf{q} \tag{5}$$

If Eq. (5) is integrated over a region moving with the fluid and use is made of Reynolds' transport theorem (Aris, 1962) to transform to a fixed control volume, the result is

$$\frac{\partial}{\partial t} \int \rho h_0 d\forall + \int \rho h_0 \mathbf{V} \cdot \mathbf{n} dS = \int \frac{\partial p}{\partial t} d\forall + \int \mathbf{n} \cdot \tau \cdot \mathbf{V} dS + \int \rho \mathbf{f} \cdot \mathbf{V} d\forall - \int \mathbf{q} \cdot \mathbf{n} dS \tag{6}$$

The viscous stress-resultant $\mathbf{n} \cdot \tau$ does work only on moving boundaries, so that the second integral on the right of Eq. (6) is nonzero only on those boundaries. For a flow passage with all its boundaries stationary this integral vanishes completely. If the boundaries are also adiabatic and the flow steady, the only remaining term is the second on the left, which yields the familiar result that the net rate of efflux of total enthalpy from the control volume is zero.

Equation (5) is now transformed from a fixed system of cylindrical coordinates (r, θ, z) to a system (r', θ', z') rotating about the z axis by means of the relations

$$\left.\begin{aligned} r' &= r \\ \theta' &= \theta - \int \omega dt \\ z' &= z \\ t' &= t \end{aligned}\right\} \tag{7}$$

It follows that

$$\frac{\partial}{\partial r} = \frac{\partial}{\partial r'}, \quad \frac{\partial}{\partial \theta} = \frac{\partial}{\partial \theta'}, \quad \frac{\partial}{\partial z} = \frac{\partial}{\partial z'} \tag{8a}$$

or

$$\nabla = \nabla' \tag{8b}$$

and

$$\frac{\partial}{\partial t} = \frac{\partial}{\partial t'} - \omega \frac{\partial}{\partial \theta'} \tag{8c}$$

The substantial derivative of any scalar function $f(r, \theta, z, t)$ is therefore

Nomenclature

A = entrance or exit area of control volume
a = acceleration
$\mathbf{e}$ = unit vector
$\mathbf{F}$ = force per unit volume
$\mathbf{f}$ = body force per unit mass
h = enthalpy
I = rothalpy
$\mathbf{M}$ = moment acting on fluid in control volume
$\dot{m}$ = mass flow rate
$\mathbf{n}$ = unit normal vector
P = power
p = static pressure
p^* = rotary stagnation pressure, Eq. (23)
q = heat flux vector
r = radius in cylindrical coordinates
S = surface area
s = entropy
T = absolute temperature
$\mathbf{U}$ = blade velocity
$\mathbf{V}$ = absolute velocity vector
$\mathbf{W}$ = relative velocity vector
z = distance along axis of rotation
$\forall$ = volume
θ = angle in cylindrical coordinates
ρ = density
τ = viscous stress tensor
Φ = rate of viscous dissipation per unit volume
ω = angular velocity of rotor

Subscripts

c = centrifugal
f = frictional
in = into control volume
out = out of control volume
z = component along axis of rotation
0 = total or stagnation quantity
θ = component in tangential direction

Superscripts

$'$ = relative to rotor-fixed coordinates

$$\frac{Df}{Dt}\equiv\frac{\partial f}{\partial t}+\mathbf{V}\cdot\nabla f$$

$$=\frac{\partial f}{\partial t'}-\omega\frac{\partial f}{\partial\theta'}+(\mathbf{U}+\mathbf{W})\cdot\nabla' f$$

$$=\frac{\partial f}{\partial t'}+\mathbf{W}\cdot\nabla' f\equiv\frac{Df}{Dt'} \tag{9}$$

where D/Dt' means the substantial derivative in the rotating frame.[3] Letting $f = h_0$, combining Eqs. (5) and (9), and noting that the viscous stresses do no work of deformation in solid-body rotation (i.e., $\tau:\nabla\mathbf{U} = 0$), one obtains

$$\rho\frac{Dh_0}{Dt}=\frac{\partial p}{\partial t'}+\omega rF_\theta+\nabla\cdot(\tau\cdot\mathbf{W})+\rho f\cdot\mathbf{W}-\nabla\cdot\mathbf{q} \tag{10}$$

where

$$F_\theta\equiv-\frac{1}{r}\frac{\partial p}{\partial\theta}+(\nabla\cdot\tau)_\theta+\rho f_\theta \tag{11}$$

is the tangential component of the net force per unit volume of fluid. The second term on the right of Eq. (10) is the moment of this force about the z axis times the angular velocity ω of the rotor. That is, it is the power per unit volume that must be supplied by the surrounding fluid and ultimately the blades just to rotate a fluid particle with angular velocity ω against the tangential pressure, friction, and body forces acting on it. The third term on the right of Eq. (10) is the rate at which work is done on the relative motion of the fluid in the rotating frame by viscous stresses. The fourth term on the right is the rate at which work is done on the relative motion by the body force, and the fifth the net rate of heat addition.

Integrating Eq. (10) over a region moving with the fluid and using Reynolds' transport theorem to transform to a control volume that rotates with the impeller leads to the result

$$\frac{\partial}{\partial t'}\int\rho h_0 d\forall'+\int\rho h_0\mathbf{W}\cdot\mathbf{n}dS'=\int\left(\frac{\partial p}{\partial t'}+\omega rF_\theta+\rho\mathbf{f}\cdot\mathbf{W}\right)d\forall'+\int\mathbf{n}\cdot(\tau\cdot\mathbf{W}-\mathbf{q})dS' \tag{12}$$

On the rotating surfaces $\mathbf{W} = 0$, so the viscous stress-resultant $\mathbf{n}\cdot\tau$ does no work on these surfaces. Only the stresses on the fixed surfaces, which appear to rotate relative to the rotor frame, do work on the relative flow and change the total enthalpy.

Another form of the differential equation for the total enthalpy can be obtained by splitting the third term on the right of Eq. (10) as follows:

$$\nabla\cdot(\tau\cdot\mathbf{W})=(\nabla\cdot\tau)\cdot\mathbf{W}+\tau:\nabla\mathbf{W} \tag{13}$$

The first term on the right of Eq. (13) is the rate at which the net viscous force per unit volume $\nabla\cdot\tau$ does work on the relative flow, while the second term is the rate of viscous dissipation,

$$\Phi\equiv\tau:\nabla\mathbf{V}=\tau:\nabla\mathbf{W} \tag{14}$$

which is never negative. Since the rate of increase of entropy due to viscous dissipation and heat transfer is given by the equation (Liepmann and Roshko, 1957)

$$\rho T\frac{Ds}{Dt}=\Phi-\nabla\cdot\mathbf{q} \tag{15}$$

an alternate form of Eq. (10) is

$$\rho\frac{Dh_0}{Dt}=\frac{\partial p}{\partial t'}+\omega rF_\theta+(\nabla\cdot\tau+\rho\mathbf{f})\cdot\mathbf{W}+\rho T\frac{Ds}{Dt} \tag{16}$$

2 Moment-of-Momentum Equation. The differential and integral forms of the moment-of-momentum equation are derived in numerous references, e.g., Vavra (1960). All that is needed here is the z component of this equation, which is readily obtained by multiplying the θ component of the linear momentum equation, $F_\theta = \rho a_\theta$, by r. The tangential acceleration a_θ in cylindrical coordinates is

$$a_\theta=\left[\frac{\partial}{\partial t}+V_r\left(\frac{\partial}{\partial r}+\frac{1}{r}\right)+\frac{V_\theta}{r}\frac{\partial}{\partial\theta}+V_z\frac{\partial}{\partial z}\right]V_\theta$$

$$=\left(\frac{\partial}{\partial t'}+\mathbf{W}\cdot\nabla+\frac{1}{r}V_r\right)V_\theta$$

$$=\frac{1}{r}\left(\frac{\partial}{\partial t'}+\mathbf{W}\cdot\nabla\right)(rV_\theta)=\frac{1}{r}\frac{D}{Dt}(rV_\theta) \tag{17}$$

Hence the moment-of-momentum equation is

$$rF_\theta=\rho\frac{D}{Dt}(rV_\theta) \tag{18}$$

An even simpler derivation of this familiar result can be found in Cumpsty (1989). From Eq. (11) it is obvious that F_θ includes all the forces on the fluid particle, namely pressure, viscous, and body forces. Integration of Eq. (18) over the rotating control volume surrounding the fluid in the impeller gives what is perhaps the most familiar form of this equation, namely, the Euler turbomachinery equation[4]:

$$M_z\equiv\int rF_\theta d\forall'=\frac{\partial}{\partial t'}\int\rho rV_\theta d\forall'+\int\rho rV_\theta\mathbf{W}\cdot\mathbf{n}dS' \tag{19}$$

3 Differential Equation for Rothalpy. The following two forms of the differential equation for the rothalpy are readily obtained from Eqs. (4), (9), (10), (13)–(15), and (18):

$$\rho\frac{DI}{Dt}=\frac{\partial p}{\partial t'}-\rho rV_\theta\frac{d\omega}{dt}+\nabla\cdot(\tau\cdot\mathbf{W})+\rho\mathbf{f}\cdot\mathbf{W}-\nabla\cdot q \tag{20a}$$

$$\rho\frac{DI}{Dt}=\frac{\partial p}{\partial t'}-\rho rV_\theta\frac{d\omega}{dt}+(\nabla\cdot\tau+\rho\mathbf{f})\cdot\mathbf{W}+\rho T\frac{Ds}{Dt} \tag{20b}$$

From Eq. (20*b*) it is clear that changes in rothalpy of a fluid particle are caused by:

(1) pressure fluctuations due to flow unsteadiness in the rotating frame;
(2) angular acceleration of the rotor;
(3) work done by the net viscous force per unit volume $\nabla\cdot\tau$ on the relative flow in the rotor;
(4) work done by body forces on the relative flow;
(5) changes in entropy due to viscous dissipation and heat transfer.

Therefore the rothalpy of a fluid particle is conserved provided that the three conditions (*a*)–(*c*) of Cumpsty (1989) quoted in the introduction are satisfied, and in addition, pro-

[3]Equation (9) holds only for scalar functions. For vector functions the substantial derivatives in the fixed and rotating frames will be different because the unit vectors change direction. Because of Eqs. (8*b*) and (9) primes on ∇ and D/Dt are unnecessary and are dropped in subsequent equations, but by Eq. (8*c*) the prime is necessary to distinguish the partial time derivative $\partial/\partial t'$ in the rotating frame from the derivative $\partial/\partial t$ in the fixed frame.

[4]This term is unfortunately used for both the moment-of-momentum equation and the result of combining that equation with a simplified version of the energy equation which neglects unsteady and viscous effects. The latter usage is historically inaccurate, because Euler's mémoire on reaction turbines (1754), in which the torque was calculated from the rate of change of moment of momentum (see also Rouse and Ince, 1957), preceded the first law of thermodynamics by about 100 years. Moreover, as Cumpsty (1989) points out, "the Euler equation is valid no matter how the moment of momentum is produced, and even viscous drag on the blades can produce a positive work input." Calling the combined equation, which lacks the term for the work done by friction, the "Euler turbomachinery equation" may be responsible for some of the confusion as to whether friction affects rothalpy.

vided that the body force does no work on the relative motion in the rotating frame. The last condition, although not mentioned by Cumpsty, is not very important in most turbomachinery applications. If necessary, the work done by a conservative body force could always be accounted for by simply adding its potential energy to the total enthalpy or rothalpy on the left of Eqs. (10) and (20).

An equation similar to Eq. (20*b*) was derived by Wu (1952) for an *inviscid* flow without body forces or rotor angular acceleration (cf. his Eq. (20)). Equation (20*b*) includes the effects neglected by Wu, of which the most important is probably friction.

4 Rothalpy Equation for a Control Volume. Integration of Eq. (20*a*) over a control volume rotating with the impeller leads to

$$\frac{\partial}{\partial t'}\int \rho I d\forall' + \int \rho I \mathbf{W}\cdot\mathbf{n} dS' = \int\left(\frac{\partial p}{\partial t'} - \rho r V_\theta \frac{d\omega}{dt} + \rho \mathbf{f}\cdot\mathbf{W}\right) d\forall' + \int \mathbf{n}\cdot(\tau\cdot\mathbf{W} - \mathbf{q}) dS' \quad (21)$$

As mentioned above in connection with Eq. (12), the viscous stresses on the rotating surfaces do no work on the relative flow, so they affect neither the total enthalpy nor rothalpy. For an unshrouded rotor this means that only the casing friction and possibly the viscous stresses on the control surfaces at the rotor entrance and exit do work on the relative flow. On the casing $\mathbf{W} = -\mathbf{U}$, so if the stress resultant $\mathbf{n}\cdot\tau$ exerted on the fluid by the casing is opposite to the blade velocity the rothalpy would increase from inlet to outlet, as Moore et al. (1980, 1984, 1985) calculated. For a shrouded rotor no work is done by the viscous stresses on any of the internal rotor passages.

5 Alternate Form of Rothalpy Differential Equation. From the definition of I in Eq. (2) and the thermodynamic relation $dh = Tds + (1/\rho)dp$ it follows that

$$\rho\frac{DI}{Dt} = \rho T\frac{Ds}{Dt} + \frac{Dp}{Dt} + \frac{1}{2}\rho\frac{D}{Dt}(W^2 - U^2)$$

$$= \rho T\frac{Ds}{Dt} + \frac{Dp^*}{Dt} + \frac{1}{2}(U^2 - W^2)\frac{D\rho}{Dt} \quad (22)$$

where

$$p^* \equiv p + \frac{1}{2}\rho(W^2 - U^2) \quad (23)$$

is the rotary stagnation pressure introduced by Hawthorne (1974). It is interchangeable with the rothalpy in incompressible, isentropic flows, for then $p^* = \rho I$.

Equating the expressions for $\rho DI/Dt$ on the rights of Eqs. (20*b*) and (22) gives

$$\frac{Dp^*}{Dt} = \frac{\partial p}{\partial t'} - \rho r V_\theta \frac{d\omega}{dt} + \frac{1}{2}(W^2 - U^2)\frac{D\rho}{Dt} + (\nabla\cdot\tau + \rho\mathbf{f})\cdot\mathbf{W} \quad (24)$$

Note that the entropy production terms do not appear in this veresion of the equation. For steady incompressible flow only the net viscous and body forces affect p^*. If these forces were absent p^* would be conserved.

Special Cases

1 Unsteady and Steady Isentropic Flow. For an inviscid flow with no body forces or heat transfer Eqs. (10) and (20) for the total enthalpy and rothalpy reduce to

$$\rho\frac{Dh_0}{Dt} = \frac{\partial p}{\partial t'} - \omega\frac{\partial p}{\partial\theta} = \frac{\partial p}{\partial t} \quad (25)$$

$$\rho\frac{DI}{Dt} = \frac{\partial p}{\partial t'} - \rho r V_\theta \frac{d\omega}{dt} \quad (26)$$

Equation (25) shows that unsteadiness is necessary in order for an adiabatic turbomachine to do useful work on an inviscid flow (Dean, 1959). But this conclusion requires only unsteadiness in the laboratory frame. Assuming that the flow in the rotating frame is steady does not remove the possibility that the machine can do work, because the blade-to-blade pressure variation in the rotating frame does work at a fixed point in the laboratory frame. This comes from the term $\omega r F_\theta = -\omega(\partial p/\partial\theta)$. A nice physical explanation of this is given by Dean.

Equation (26) shows how unsteadiness affects the rothalpy. If the flow is steady in the rotating frame, $\partial p/\partial t' = d\omega/dt = 0$, and Eqs. (25) and (26) become

$$\rho\mathbf{W}\cdot\nabla h_0 = \omega r F_\theta \quad (27)$$

$$\rho\mathbf{W}\cdot\nabla I = 0 \quad (28)$$

In words, the rate of change of total enthalpy of a fluid particle as it moves along its relative streamline in the rotating frame is equal to the rate at which the net tangential pressure force per unit volume does work, and the rothalpy is constant along a streamline of the relative flow. Contrary to Vavra's (1960) statement quoted in the Introduction, rothalpy would *not* be constant along the streamline in the presence of friction.

2 Steady Viscous Flow in Rotor. If the flow is steady in coordinates rotating with a constant angular velocity ω, and there is no heat transfer or body forces, Eq. (21) reduces to

$$\int \rho I \mathbf{W}\cdot\mathbf{n} dS' = \int \mathbf{n}\cdot\tau\cdot\mathbf{W} dS' \quad (29)$$

The integral on the left is nonzero only on the portions of the control surface that form the entrance and exit sections. The integral on the right is nonzero only on the stationary surfaces, such as the casing of the turbomachine, and on the entrance and exit sections. Thus Eq. (29) can be written

$$\dot{m}(\bar{I}_{out} - \bar{I}_{in}) = P_f \quad (30)$$

where $\dot{m}$ is the mass flow rate through the rotor,

$$\bar{I} \equiv \frac{1}{\dot{m}}\int_A \rho I \mathbf{W}\cdot\mathbf{n} dS' \quad (31)$$

is the mass-averaged rothalpy over the entrance or exit area A, and

$$P_f = \int \mathbf{n}\cdot\tau\cdot\mathbf{W} dS' \quad (32)$$

is the power loss due to viscous friction. Although the integral in Eq. (32) is over both the casing and the entrance and exit sections, usually the viscous stresses on the latter sections could be neglected and only the friction from the casing considered. In some cases it may be possible to make simple engineering estimates of P_f and determine the change in average rothalpy from Eq. (30).

Setting $I = h_0 - \omega r V_\theta$ in Eq. (30), one obtains a more familiar-looking result

$$(\bar{h}_0)_{out} - (\bar{h}_0)_{in} = \omega[(\overline{rV_\theta})_{out} - (\overline{rV_\theta})_{in}] + (P_f/\dot{m}) \quad (33)$$

Different versions of this equation have appeared in the literature. Equation 11 (57) of Vavra (1960) is Eq. (33) *without* the frictional loss term. Vavra argued that his equation would be valid even if friction were present, because the effect of friction would be to increase the moment of momentum at exit above what would be obtained without friction. That seems a tacit acknowledgment of the missing frictional term.

A result equivalent to Eqs. (29) and (32) was derived by Csanady (1964), who erroneously assumed constant radial mass

flow rate. As shown in Appendix A, his result can be obtained without that assumption.

Urbach (1990) derived a different version of this equation, which has separate terms for the change in moment of momentum in the axial and radial directions. It is also based on the faulty assumption of constant axial and radial mass flow rates. In Appendix B the present results are compared with those of Urbach, and it is shown that Eq. (33) is the correct result.

Concluding Remarks

It has been shown that rothalpy is conserved only under five rather restrictive conditions. Two of these conditions are that the flow is steady in the rotor frame and that the rotor angular velocity is constant. Both pressure fluctuations in the relative flow and angular acceleration of the rotor can change the rothalpy. Rotor acceleration will not cause a significant change as long as the angular velocity variation is small during the residence time of a fluid particle in the rotor. The third and fourth conditions for constancy of rothalpy are that the net viscous and body forces do no work on the relative flow. The effect of body forces is usually of little consequence. The last condition is that the flow is isentropic, i.e., there is no heat transfer or viscous dissipation. The effect of heat transfer is probably negligible in most cases, although it might be important in the hot rotating sections of gas turbines or in interstage passages in cooled multistage centrifugal compressors.

Unsteadiness of the flow in the rotating passages and friction on the nonrotating surfaces will probably be the major factors affecting the rothalpy. It should be pointed out that even when the flow is adiabatic and steady in rotor-fixed coordinates, the rothalpy changes because the work of the viscous stresses affects the moment of momentum and total enthalpy differently. The reason for this is that the total enthalpy can be affected by nonisentropic processes in the rotor, whereas the change in moment of momentum is the same whether the mechanical work is done reversibly or irreversibly by the torque.

Finally, although rothalpy is in general *not* conserved in viscous flows, it has often been *assumed* constant in turbomachine throughflow calculations that incorporate loss models (Bosman and Marsh, 1974; Hirsch and Warzee, 1977). Such an assumption cannot be rigorously justified, but it does greatly simplify the calculations, in that it allows the differential energy equation to be replaced by the algebraic equation $I = \text{const}$ along streamlines. The cited analyses utilize a "consistent" loss model, in which the net viscous force $\nabla \cdot \tau$ is replaced by a "drag" force $\mathbf{D}$, so that for steady flow without external body forces the assumption $DI/Dt = 0$ reduces Eq. (20*b*) to $\rho TDs/Dt = -\mathbf{D}\cdot\mathbf{W}$. From Eq. (20*a*) it can be seen that this requires $\nabla \cdot (\mathbf{q} - \tau \cdot \mathbf{W}) = 0$, i.e., all the work done by the viscous stress is carried away by conduction. This is the special condition postulated by Denton (1986) to show that his viscous loss model implies conservation of rothalpy. Earlier, Hirsch and Warzee (1977) had concluded that the simple loss model conserves rothalpy, but without mentioning the heat transfer implications. Unfortunately, the simple loss models do not correctly account for entropy generation by viscous dissipation, so the fact that they conserve rothalpy is merely fortuitous.

Acknowledgments

The author is grateful to Drs. Thong Dang and Joost Brasz for reading previous versions of this paper and suggesting improvements. He also acknowledges the pertinent comments of an anonymous referee, who pointed out that conservation of rothalpy has been a vexed question even among turbomachinery experts and that the author should be aware of the work of Sehra and Kerrebrock.

References

Aris, R., 1962, *Vectors, Tensors, and the Basic Equations of Fluid Mechanics*, Prentice-Hall, Englewood Cliffs, NJ (reprinted 1989 by Dover, Mineola, NY), p. 84.

Bosman, C., and Marsh, H., 1974, "An Improved Method for Calculating the Flow in Turbomachines, Including a Consistent Loss Model," *Journal of Mechanical Engineering Science*, The Institution of Mechanical Engineers, Vol. 16, pp. 25–31.

Csanady, G. T., 1964, *Theory of Turbomachines*, McGraw-Hill, New York, pp. 107–108.

Cumpsty, N. A., 1989, *Compressor Aerodynamics*, Longman Scientific & Technical, Harlow, Essex, United Kingdom, pp. 5, 6, 237, 319.

Dean, R. C., Jr., 1959, "On the Necessity of Unsteadiness in Fluid Machines," ASME *Journal of Basic Engineering*, Vol. 81, pp. 24–28.

Denton, J. D., 1986, "The Use of a Distributed Body Force to Simulate Viscous Effects in 3D Flow Calculations," ASME Paper No. 86-GT-144.

Dixon, S. L., 1978, *Fluid Mechanics and Thermodynamics of Turbomachinery*, 3rd ed., Pergamon, Oxford, p. 226.

Euler, L., (1754), 1756, "Théorie plus complette des machines qui sont mises en mouvement par la réaction de l'eau," *Mémoires de l'academie des sciences de Berlin*, Vol. 10, pp. 227–295; reprinted in *Commentationes Mechanicae ad Theoriam Machinarum Pertinentes*, Vol. I, J. Ackeret, ed., *Leonhardi Euleri Opera Omnia*, Series 2, Vol. 15, Orell Füssli Turici, Lausanne, 1957, pp. 157–218.

Hawthorne, W. R., 1974, "Secondary Vorticity in Stratified Compressible Fluids in Rotating Systems," Report No. CUED/A-Turbo/TR 63, Cambridge University Engineering Department, Cambridge, United Kingdom.

Hirsch, Ch., and Warzee, G., 1977, "A Finite Element Method for Through Flow Calculations in Turbomachines," ASME *Journal of Fluids Engineering*, Vol. 98, No. 3, pp. 403–421.

Liepmann, H. W., and Roshko, A., 1957, *Elements of Gasdynamics*, Wiley, New York, pp. 337–338.

Moore, J., and Moore, J. G., 1980, "Three-Dimensional, Viscous Flow Calculations for Assessing the Thermodynamic Performance of Centrifugal Compressors—Study of the Eckardt Compressor," *AGARD Conference Proceedings No. 282, Centrifugal Compressors, Flow Phenomena and Performance*, pp. 9-1–9-19.

Moore, J., Moore, J. G., and Timmins, R. H., 1984, "Performance Evaluation of Centrifugal Compressor Impellers Using Three-Dimensional Viscous Flow Calculations," ASME *Journal of Engineering for Gas Turbines and Power*, Vol. 106, pp. 475–481.

Moore, J., 1985, "Performance Evaluation of Flow in Turbomachinery Blade Rows," *AGARD Lecture Series No. 140, 3-D Computation Techniques Applied to Internal Flows in Propulsion Systems*, pp. 6-1–6-26.

Rouse, H., and Ince, S., 1957, *History of Hydraulics*, Institute of Hydraulic Research, State University of Iowa, Ames, IA.

Sehra, A. K., 1979, "The Effect of Blade-to-Blade Flow Variations on the Mean Flowfield of a Transonic Rotor," Ph.D. Thesis, Massachusetts Institute of Technology, Cambridge, MA.

Sehra, A. K., and Kerrebrock, J. L., 1981, "Blade-to-Blade Flow Effects on Mean Flow in Transonic Compressors," *AIAA Journal*, Vol. 19, pp. 476–483.

Urbach, H. B., 1990, "A Differential Turbomachinery Equation With Viscous Correction," David Taylor Research Center Report DTRC-PAS-90-45, Bethesda, MD.

Vavra, M. H., 1960, *Aero- Thermodynamics and Flow in Turbomachines*, Wiley, New York (reprinted with corrections 1974 by Krieger, Melbourne, FL); p. 125; Chap. 6; p. 259.

Whitfield, A., and Baines, N. C., 1990, *Design of Radial Turbomachines*, Longman Scientific & Technical, Harlow, Essex, United Kingdom, p. 53.

Wu, C.-H., 1952, "A General Theory of Three-Dimensional Flow in Subsonic and Supersonic Turbomachines of Axial-, Radial-, and Mixed-Flow Types," NACA Technical Note 2604.

Wu, C.-H., 1953, Discussion of a paper by Smith, Traugott, and Wislicenus, ASME *Transactions*, Vol. 75, pp. 802–803.

APPENDIX A

Correction of Csanady's Derivation

Csanady (1964) derived an integral equation for the rothalpy by writing a steady-state power balance in the rotating frame as

$$P_c + P_f = \int \left(h + \frac{W^2}{2} + \phi \right) dG \tag{A1}$$

where P_f is the power developed by fluid friction, ϕ ($= gz$ in his notation) is the potential energy, $dG \equiv \rho \mathbf{W} \cdot \mathbf{n} dS'$ is the differential mass flow rate, and P_c is the power input due to the centrifugal force,

$$P_c = \int \rho \omega^2 r W_r d\forall' \tag{A2}$$

Csanady incorrectly assumed that the radial mass flow rate

$\int \rho W_r dS'$ was constant in order to reduce Eq. (A2) to the desired form. His result can be obtained without this assumption as follows:

Since $W_r = Dr/Dt = \mathbf{W} \cdot \nabla r$, Eq. (A2) can be written

$$P_c = \int \rho\omega^2 \mathbf{W} \cdot \nabla (r^2/2) d\forall'$$

$$= \frac{1}{2} \int \omega^2 [\nabla \cdot (\rho \mathbf{W} r^2) - r^2 \nabla \cdot (\rho \mathbf{W})] d\forall' \quad \text{(A3)}$$

But for steady flow in the rotor the continuity equation is $\nabla \cdot (\rho \mathbf{W}) = 0$, so the second term in the integrand on the right of Eq. (A3) vanishes. Since ω = const, applying Gauss's theorem to the remaining integral gives

$$P_c = \int \frac{\omega^2 r^2}{2} \rho \mathbf{W} \cdot \mathbf{n} dS' = \int \frac{U^2}{2} dG \quad \text{(A4)}$$

Combining Eqs. (A1) and (A4) gives Csanady's result,

$$P_f = \int (I + \phi) dG \quad \text{(A5)}$$

When there are no body forces this becomes the same as Eq. (29) of the present paper.

APPENDIX B

Comparison With Results of Urbach

Urbach's report (1990) covers much of the same ground as the present paper, and, as will be shown in this appendix, the differential equations derived here for the substantial rates of change of total enthalpy and rothalpy in the rotating frame reduce to Urbach's equations when one imposes the additional restrictions of steady relative flow, no angular acceleration of the rotor, and no body forces nor heat transfer. It is also shown here that Urbach's differential equation for total enthalpy, when properly integrated over the rotor control volume, leads to Eq. (33) of this paper rather than Urbach's result.

Urbach's Eq. (22) is the differential equation for the rothalpy. In the present notation it reads

$$\rho \frac{DI}{Dt} = \nabla \cdot (\tau \cdot \mathbf{W}) \quad \text{(B1)}$$

Equation (20) of this paper reduces to the same result under the conditions cited in the previous paragraph.

Urbach's Eq. (26) for the total enthalpy may be written

$$\rho \frac{Dh_0}{Dt} = \mathbf{U} \cdot (-\nabla p + \nabla \cdot \tau) + \nabla \cdot (\tau \cdot \mathbf{W}) \quad \text{(B2)}$$

Equation (10) of this paper reduces to the same result, because when there are no body forces the scalar product of $\mathbf{U}$ with the momentum equation gives

$$\mathbf{U} \cdot (-\nabla p + \nabla \cdot \tau) = \rho \mathbf{U} \cdot \frac{D\mathbf{V}}{Dt} = \omega r F_\theta \quad \text{(B3)}$$

Thus the differential equations for total enthalpy and rothalpy derived in this paper are in full agreement with the corresponding equations of Urbach (1990) under the stated conditions. The derivations differ mainly in the handling of the first term in the right of Eq. (B2). Here it was replaced by $\omega r F_\theta$, which by Eq. (18) is $\rho\omega$ times the rate of change of moment of momentum following the fluid particle. Urbach replaced it by $\rho \mathbf{U} \cdot D\mathbf{V}/Dt$, expressing $D\mathbf{V}/Dt$ as the sum of the relative acceleration in the rotating frame and the Coriolis and centripetal accelerations. Since $\partial \mathbf{W}/\partial t' = 0$ in the present case,

$$\frac{D\mathbf{V}}{Dt} = (\mathbf{W} \cdot \nabla)\mathbf{W} + 2\omega \times \mathbf{W} - \nabla \left(\frac{U^2}{2} \right) \quad \text{(B4)}$$

Urbach's Eq. (25) for the total enthalpy follows from Eqs. (B2)–(B4):

$$\rho \frac{Dh_0}{Dt} = \rho \mathbf{U} \cdot [(\mathbf{W} \cdot \nabla)\mathbf{W} + 2\omega \times \mathbf{W}] + \nabla \cdot (\tau \cdot \mathbf{W}) \quad \text{(B5)}$$

Although this equation is correct for steady flow in the rotor, the complexity of the first two terms on the right somewhat obscures their physical meanings, and it is easy to make errors when integrating these terms over the rotor control volume, as Urbach did. In integrating the first term on the right, which can be written

$$\rho \mathbf{U} \cdot (\mathbf{W} \cdot \nabla)\mathbf{W} = \rho U \left(W_r \frac{\partial W_\theta}{\partial r} + \frac{W_\theta}{r} \frac{\partial W_\theta}{\partial \theta} + W_z \frac{\partial W_\theta}{\partial z} + \frac{W_r W_\theta}{r} \right) \quad \text{(B6)}$$

Urbach split the moment-of-momentum transport terms into separate radial and axial components and assumed constant axial and radial mass flow rates. This is obviously untrue in a mixed-flow impeller, because the flow enters in a nearly axial direction and leaves in a direction which is neither radial nor axial.

The integration can be performed without these assumptions, however, by recognizing that Eq. (B6) can be rewritten as

$$\rho \mathbf{U} \cdot (\mathbf{W} \cdot \nabla)\mathbf{W} = \rho\omega \mathbf{W} \cdot \nabla (r W_\theta) = \nabla \cdot (\rho \mathbf{W} U W_\theta) \quad \text{(B7)}$$

where the steady-state continuity equation $\nabla \cdot (\rho \mathbf{W}) = 0$ was used to obtain the last equality.

The second term on the right of Eq. (B5) is just twice the integrand in Eq. (A2), so that

$$\rho \mathbf{U} \cdot (2\omega \times \mathbf{W}) = 2\rho\omega^2 r W_r = \rho \mathbf{W} \cdot \nabla (U^2) \quad \text{(B8)}$$

Therefore, substituting Eqs. (B7) and (B8) into Eq. (B5), integrating over the rotating control volume, and using Gauss's and Reynolds' theorems, one obtains

$$\int \rho I \mathbf{W} \cdot \mathbf{n} dS' = \int \mathbf{n} \cdot \tau \cdot \mathbf{W} dS' \quad \text{(B9)}$$

This is precisely the result derived in the body of this paper (cf. Eq. (29)). Thus Eq. (33) of this paper, which follows from it, is the correct form of the so-called "Euler turbomachinery equation with viscous correction," rather than Urbach's Eq. (40).

$\int \rho W_r dS'$ was constant in order to reduce Eq. (A2) to the desired form. His result can be obtained without this assumption as follows:

Since $W_r = Dr/Dt = \mathbf{W} \cdot \nabla r$, Eq. (A2) can be written

$$P_c = \int \rho\omega^2 \mathbf{W} \cdot \nabla (r^2/2) d\forall'$$

$$= \frac{1}{2} \int \omega^2 [\nabla \cdot (\rho \mathbf{W} r^2) - r^2 \nabla \cdot (\rho \mathbf{W})] d\forall' \quad \text{(A3)}$$

But for steady flow in the rotor the continuity equation is $\nabla \cdot (\rho \mathbf{W}) = 0$, so the second term in the integrand on the right of Eq. (A3) vanishes. Since ω = const, applying Gauss's theorem to the remaining integral gives

$$P_c = \int \frac{\omega^2 r^2}{2} \rho \mathbf{W} \cdot \mathbf{n} dS' = \int \frac{U^2}{2} dG \quad \text{(A4)}$$

Combining Eqs. (A1) and (A4) gives Csanady's result,

$$P_f = \int (I + \phi) dG \quad \text{(A5)}$$

When there are no body forces this becomes the same as Eq. (29) of the present paper.

APPENDIX B

Comparison With Results of Urbach

Urbach's report (1990) covers much of the same ground as the present paper, and, as will be shown in this appendix, the differential equations derived here for the substantial rates of change of total enthalpy and rothalpy in the rotating frame reduce to Urbach's equations when one imposes the additional restrictions of steady relative flow, no angular acceleration of the rotor, and no body forces nor heat transfer. It is also shown here that Urbach's differential equation for total enthalpy, when properly integrated over the rotor control volume, leads to Eq. (33) of this paper rather than Urbach's result.

Urbach's Eq. (22) is the differential equation for the rothalpy. In the present notation it reads

$$\rho \frac{DI}{Dt} = \nabla \cdot (\tau \cdot \mathbf{W}) \quad \text{(B1)}$$

Equation (20) of this paper reduces to the same result under the conditions cited in the previous paragraph.

Urbach's Eq. (26) for the total enthalpy may be written

$$\rho \frac{Dh_0}{Dt} = \mathbf{U} \cdot (-\nabla p + \nabla \cdot \tau) + \nabla \cdot (\tau \cdot \mathbf{W}) \quad \text{(B2)}$$

Equation (10) of this paper reduces to the same result, because when there are no body forces the scalar product of $\mathbf{U}$ with the momentum equation gives

$$\mathbf{U} \cdot (-\nabla p + \nabla \cdot \tau) = \rho \mathbf{U} \cdot \frac{D\mathbf{V}}{Dt} = \omega r F_\theta \quad \text{(B3)}$$

Thus the differential equations for total enthalpy and rothalpy derived in this paper are in full agreement with the corresponding equations of Urbach (1990) under the stated conditions. The derivations differ mainly in the handling of the first term in the right of Eq. (B2). Here it was replaced by $\omega r F_\theta$, which by Eq. (18) is $\rho\omega$ times the rate of change of moment of momentum following the fluid particle. Urbach replaced it by $\rho \mathbf{U} \cdot D\mathbf{V}/Dt$, expressing $D\mathbf{V}/Dt$ as the sum of the relative acceleration in the rotating frame and the Coriolis and centripetal accelerations. Since $\partial \mathbf{W}/\partial t' = 0$ in the present case,

$$\frac{D\mathbf{V}}{Dt} = (\mathbf{W} \cdot \nabla)\mathbf{W} + 2\omega \times \mathbf{W} - \nabla \left(\frac{U^2}{2}\right) \quad \text{(B4)}$$

Urbach's Eq. (25) for the total enthalpy follows from Eqs. (B2)–(B4):

$$\rho \frac{Dh_0}{Dt} = \rho \mathbf{U} \cdot [(\mathbf{W} \cdot \nabla)\mathbf{W} + 2\omega \times \mathbf{W}] + \nabla \cdot (\tau \cdot \mathbf{W}) \quad \text{(B5)}$$

Although this equation is correct for steady flow in the rotor, the complexity of the first two terms on the right somewhat obscures their physical meanings, and it is easy to make errors when integrating these terms over the rotor control volume, as Urbach did. In integrating the first term on the right, which can be written

$$\rho \mathbf{U} \cdot (\mathbf{W} \cdot \nabla)\mathbf{W} = \rho U \left(W_r \frac{\partial W_\theta}{\partial r} + \frac{W_\theta}{r} \frac{\partial W_\theta}{\partial \theta} + W_z \frac{\partial W_\theta}{\partial z} + \frac{W_r W_\theta}{r} \right) \quad \text{(B6)}$$

Urbach split the moment-of-momentum transport terms into separate radial and axial components and assumed constant axial and radial mass flow rates. This is obviously untrue in a mixed-flow impeller, because the flow enters in a nearly axial direction and leaves in a direction which is neither radial nor axial.

The integration can be performed without these assumptions, however, by recognizing that Eq. (B6) can be rewritten as

$$\rho \mathbf{U} \cdot (\mathbf{W} \cdot \nabla)\mathbf{W} = \rho\omega \mathbf{W} \cdot \nabla (r W_\theta) = \nabla \cdot (\rho \mathbf{W} U W_\theta) \quad \text{(B7)}$$

where the steady-state continuity equation $\nabla \cdot (\rho \mathbf{W}) = 0$ was used to obtain the last equality.

The second term on the right of Eq. (B5) is just twice the integrand in Eq. (A2), so that

$$\rho \mathbf{U} \cdot (2\omega \times \mathbf{W}) = 2\rho\omega^2 r W_r = \rho \mathbf{W} \cdot \nabla (U^2) \quad \text{(B8)}$$

Therefore, substituting Eqs. (B7) and (B8) into Eq. (B5), integrating over the rotating control volume, and using Gauss's and Reynolds' theorems, one obtains

$$\int \rho I \mathbf{W} \cdot \mathbf{n} dS' = \int \mathbf{n} \cdot \tau \cdot \mathbf{W} dS' \quad \text{(B9)}$$

This is precisely the result derived in the body of this paper (cf. Eq. (29)). Thus Eq. (33) of this paper, which follows from it, is the correct form of the so-called "Euler turbomachinery equation with viscous correction," rather than Urbach's Eq. (40).

DISCUSSION

J. Moore[5] and J. G. Moore[5]

The author is to be complimented on his thorough, careful, and rigorous review of the equations and physics governing rothalpy in turbomachinery rotor flows. Part of the apparent confusion concerning this that he found in recent literature stems from the fact that calculation methods for turbomachinery have been undergoing a transition from inviscid flow to viscous flow. Some of the intermediate methods involved approximations that were clearly not rigorous.

In our research on the thermodynamics and fluid mechanics of centrifugal compressor flows we discovered that our initial calculations did not give a correct evaluation of the absolute stagnation temperature at the stationary shroud wall. We traced the problem to an incorrect handling of the rothalpy boundary condition at the stationary wall where the source term for rothalpy, Eq. (32), had been omitted. As the author mentions, our subsequent calculations then showed a rothalpy production in the impellers of about 1 or 2 percent of the total work input. Physically, as Eqs. (30) and (33) in the paper show, not all the work done in an unshrouded turbomachinery rotor appears at

[5]Mechanical Engineering Department, Virginia Polytechnic Institute and State University, Blacksburg, VA 24061-0238.

the exit as an increase in moment of momentum; some appears as an increase in rothalpy. Moment of momentum is dissipated at the stationary shroud wall, giving a corresponding rothalpy production.

Has the author considered what percentage of the total work input might appear as rothalpy production in compressor rotors with casing treatment for enhanced compressor stability?

Author's Closure

As mentioned in the paper, the pioneering computation by John and Joan Moore of three-dimensional viscous flow in centrifugal compressor impellers showed that rothalpy was produced by the shear stresses at the stationary shroud wall. It was by reading John Moore's written discussion of a paper by Ng and Epstein (1985) soon after it appeared in the ASME *Transactions* that I first learned of this work. His statement, "... that moment of momentum is destroyed by shear stresses at the stationary shroud wall in rotors giving rise to production of rothalpy ...," came as a surprise, since it contradicted statements in the well-known textbooks of Vavra (1969) and Dixon (1978). The question lay dormant for several years, until the necessity of preparing lectures for a graduate course in turbomachinery forced me to rethink it. The present paper was written mainly to improve my own understanding of rothalpy and the conditions under which it is conserved. I am grateful that the reviewers thought it should be published. The Moores' comments are especially appreciated, because their work inspired this analysis, and I am honored to have their discussion appended to my paper.

The question regarding rothalpy production in compressors with casing treatment to improve the stability margin is an interesting one. It is, however, difficult to predict exactly how much the casing treatment would change the rothalpy, as compared with an untreated casing. This would require detailed calculation of the unsteady viscous flow in the vicinity of the blade tips and casing slots or grooves. I will nevertheless venture some observations to stimulate further discussion and research.

The careful experiments of Fujita and Takata (1984) on a low-speed axial compressor showed that casing treatment caused additional losses. If these losses were due to increased viscous dissipation alone, then assuming steady flow in rotor-fixed coordinates, one might conclude that the rothalpy increase would be greater in a treated compressor, because of the greater power loss due to viscous friction (P_f in Eq. (30) of this paper). But the flow in rotor-fixed coordinates *cannot* be steady if the casing is slotted in the axial-skewed or axial-radial configuration of Fujita and Taneka (see their Fig. 2). The circumferential motion of the blade tips relative to the slots causes pressure fluctuations, which in turn affect the rothalpy of a fluid particle passing through the tip region.[6] According to Eqs. (20), pressure fluctuations cause the rothalpy of such a particle to vary at the rate $(1/\rho)\partial p/\partial t'$; hence the change in rothalpy of a particle passing through the rotor will depend not only on how much and how fast the pressure changes with time at each point along its path, but also on how much time the particle spends in regions where the pressure fluctuations are significant. It will be necessary to calculate this change accurately for all particles passing through the rotor, a quite difficult undertaking. Smith and Cumpsty (1984) tentatively concluded from their detailed hot-wire measurements in the blade passage and in the casing slots that "... unsteady effects in the slots are of secondary importance." This statement evidently refers to the overall effects of the slotted casing on the flow (e.g., the effect on reduced endwall blockage) and not on the rothalpy, however. The effect of casing treatment on rothalpy remains to be determined, along with many other aspects of the flow in treated casings.

References

Fujita, H., and Takata, H., 1984, "A Study on Configurations of Casing Treatment for Axial Flow Compressors," *Bulletin of the JSME*, Vol. 27, No. 230, pp. 1675–1681.

Johnson, M. C., and Greitzer, E. M., 1987, "Effects of Slotted Hub and Casing Treatments on Compressor Endwall Flow Fields," ASME JOURNAL OF TURBOMACHINERY, Vol. 109, pp. 380–387.

Moore, J., 1985, Discussion of a paper by Ng and Epstein, ASME *Journal of Engineering for Gas Turbines and Power*, Vol. 107, p. 353.

Smith, G. D. J., and Cumpsty, N. A., 1984, "Flow Phenomena in Compressor Casing Treatment," ASME *Journal of Engineering for Gas Turbines and Power*, Vol. 106, pp. 532–541.

[6]This is not to imply that the tip flow is steady in rotor-fixed coordinates if the casing is untreated; it probably is not, due to tip vortex shedding, but Johnson and Greitzer (1987) found that the unsteady velocity component is small compared to the steady component for an untreated but not for a treated casing.

the exit as an increase in moment of momentum; some appears as an increase in rothalpy. Moment of momentum is dissipated at the stationary shroud wall, giving a corresponding rothalpy production.

Has the author considered what percentage of the total work input might appear as rothalpy production in compressor rotors with casing treatment for enhanced compressor stability?

Author's Closure

As mentioned in the paper, the pioneering computation by John and Joan Moore of three-dimensional viscous flow in centrifugal compressor impellers showed that rothalpy was produced by the shear stresses at the stationary shroud wall. It was by reading John Moore's written discussion of a paper by Ng and Epstein (1985) soon after it appeared in the ASME *Transactions* that I first learned of this work. His statement, "... that moment of momentum is destroyed by shear stresses at the stationary shroud wall in rotors giving rise to production of rothalpy ...," came as a surprise, since it contradicted statements in the well-known textbooks of Vavra (1969) and Dixon (1978). The question lay dormant for several years, until the necessity of preparing lectures for a graduate course in turbomachinery forced me to rethink it. The present paper was written mainly to improve my own understanding of rothalpy and the conditions under which it is conserved. I am grateful that the reviewers thought it should be published. The Moores' comments are especially appreciated, because their work inspired this analysis, and I am honored to have their discussion appended to my paper.

The question regarding rothalpy production in compressors with casing treatment to improve the stability margin is an interesting one. It is, however, difficult to predict exactly how much the casing treatment would change the rothalpy, as compared with an untreated casing. This would require detailed calculation of the unsteady viscous flow in the vicinity of the blade tips and casing slots or grooves. I will nevertheless venture some observations to stimulate further discussion and research.

The careful experiments of Fujita and Takata (1984) on a low-speed axial compressor showed that casing treatment caused additional losses. If these losses were due to increased viscous dissipation alone, then assuming steady flow in rotor-fixed coordinates, one might conclude that the rothalpy increase would be greater in a treated compressor, because of the greater power loss due to viscous friction (P_f in Eq. (30) of this paper). But the flow in rotor-fixed coordinates *cannot* be steady if the casing is slotted in the axial-skewed or axial-radial configuration of Fujita and Taneka (see their Fig. 2). The circumferential motion of the blade tips relative to the slots causes pressure fluctuations, which in turn affect the rothalpy of a fluid particle passing through the tip region.[6] According to Eqs. (20), pressure fluctuations cause the rothalpy of such a particle to vary at the rate $(1/\rho)\partial p/\partial t'$; hence the change in rothalpy of a particle passing through the rotor will depend not only on how much and how fast the pressure changes with time at each point along its path, but also on how much time the particle spends in regions where the pressure fluctuations are significant. It will be necessary to calculate this change accurately for all particles passing through the rotor, a quite difficult undertaking. Smith and Cumpsty (1984) tentatively concluded from their detailed hot-wire measurements in the blade passage and in the casing slots that "... unsteady effects in the slots are of secondary importance." This statement evidently refers to the overall effects of the slotted casing on the flow (e.g., the effect on reduced endwall blockage) and not on the rothalpy, however. The effect of casing treatment on rothalpy remains to be determined, along with many other aspects of the flow in treated casings.

References

Fujita, H., and Takata, H., 1984, "A Study on Configurations of Casing Treatment for Axial Flow Compressors," *Bulletin of the JSME*, Vol. 27, No. 230, pp. 1675–1681.

Johnson, M. C., and Greitzer, E. M., 1987, "Effects of Slotted Hub and Casing Treatments on Compressor Endwall Flow Fields," ASME JOURNAL OF TURBOMACHINERY, Vol. 109, pp. 380–387.

Moore, J., 1985, Discussion of a paper by Ng and Epstein, ASME *Journal of Engineering for Gas Turbines and Power*, Vol. 107, p. 353.

Smith, G. D. J., and Cumpsty, N. A., 1984, "Flow Phenomena in Compressor Casing Treatment," ASME *Journal of Engineering for Gas Turbines and Power*, Vol. 106, pp. 532–541.

[6]This is not to imply that the tip flow is steady in rotor-fixed coordinates if the casing is untreated; it probably is not, due to tip vortex shedding, but Johnson and Greitzer (1987) found that the unsteady velocity component is small compared to the steady component for an untreated but not for a treated casing.

Experimental and Computational Investigation of the NASA Low-Speed Centrifugal Compressor Flow Field

M. D. Hathaway
U. S. Army Research Laboratory,
Vehicle Propulsion Directorate,
Cleveland, OH 44135

R. M. Chriss

J. R. Wood

A. J. Strazisar

NASA Lewis Research Center,
Cleveland, OH 44135

An experimental and computational investigation of the NASA Low-Speed Centrifugal Compressor (LSCC) flow field has been conducted using laser anemometry and Dawes' three dimensional viscous code. The experimental configuration consists of a backswept impeller followed by a vaneless diffuser. Measurements of the three-dimensional velocity field were acquired at several measurement planes through the compressor. The measurements describe both the throughflow and secondary velocity field along each measurement plane. In several cases the measurements provide details of the flow within the blade boundary layers. Insight into the complex flow physics within centrifugal compressors is provided by the computational analysis, and assessment of the CFD predictions is provided by comparison with the measurements. Five-hole probe and hot-wire surveys at the inlet and exit to the rotor as well as surface flow visualization along the impeller blade surfaces provide independent confirmation of the laser measurement technique. The results clearly document the development of the throughflow velocity wake, which is characteristic of unshrouded centrifugal compressors.

Introduction

The complex curvature of centrifugal compressor impeller blade channels, coupled with strong rotational forces and clearance between the rotating impeller and stationary shroud, generates secondary flows in unshrouded impellers that transport low-momentum fluid into the mainstream of the impeller passage. The ability to reduce the resultant flow nonuniformities at the impeller exit by altering new impeller designs to control the secondary flow development may therefore lead to improved performance. In order to succeed, such a design activity must be guided by an improved understanding of the flow physics within the impeller and by reliable numerical flow field predictions.

Several previous investigators have provided flow field measurements within unshrouded centrifugal compressor impellers. Eckardt's laser anemometer measurements in a radial-outflow impeller provided the first experimental evidence in high-speed impellers of the development of a "wake" of low-momentum fluid near the suction surface/shroud corner of the blade passage (Eckardt, 1976). Krain (1988), Krain and Hoffman (1990), Ahmed and Elder (1990), Sipos (1991), and Rohne and Banzhaf (1990) have acquired laser anemometer measurements in backswept impellers that indicate that the wake develops near the shroud at midpitch.

Due to the small passage size and optical access limitations in these previous investigations, few experimental details of the secondary flow development inside high-speed impeller passages are available. Krain (1988) and Sipos (1991) have therefore used vortex models to infer the vortical nature of the secondary flow from the flow angle measurements, which they were able to acquire on blade-to-blade streamsurfaces.

Several low-speed investigations have also provided some insight into secondary flows. Senoo et al. (1986) used dye in a water-flow experiment to visualize the tip clearance flow. Farge et al. (1989) performed five-hole pressure measurements in a 1-m dia shrouded impeller, which rotated at 500 rpm. A clearance gap was left between the blade tip and the impeller shroud in order to generate a tip clearance flow. However, as the authors point out, there is no relative motion between the blade and the shroud, so the physics of the tip clearance flow in this investigation is not the same as it would be in an unshrouded impeller. Fagan and Fleeter (1991) used laser anemometry to measure all three velocity components in a low-speed, shrouded, mixed-flow compressor.

In lieu of detailed experimental measurements of the secondary flow fields in ushrouded impellers, several investigators have recently shown secondary flow details generated using three-dimensional Navier–Stokes numerical simulations (Krain and Hoffman, 1989, 1990; Hah and Krain, 1990; Bansod and Rhie, 1990; Moore and and Moore, 1990a). Fagan and Fleeter (1991) have also shown calculated secondary flow field results for their shrouded impeller.

The purpose of the present investigation is to provide a detailed experimental study of primary and secondary flow development within an unshrouded centrifugal compressor impeller. A Low-Speed Centrifugal Compressor (LSCC), which

Contributed by the International Gas Turbine Institute and presented at the 37th International Gas Turbine and Aeroengine Congress and Exposition, Cologne, Germany, June 1-4, 1992. Manuscript received by the International Gas Turbine Institute February 20, 1992. Paper No. 92-GT-213. Associate Technical Editor: L. S. Langston.

has an exit diameter of 1.52 m, has been specifically designed and commissioned to meet this objective. The LSCC was designed to generate a flow field that is aerodynamically similar to that found in high-speed subsonic centrifugal compressors. The large size of the impeller enables the measurement of all three velocity components throughout the impeller blade passage.

Laser anemometer measurements and surface flow visualization results are presented and compared to a prediction of the flow field generated using Dawes' three-dimensional Navier–Stokes code (Dawes, 1988). The processes that lead to the formation of the throughflow momentum wake characteristics of unshrouded centrifugal compressor impellers are clearly explained using results from both the CFD and experimental effort. The results indicate that low-momentum fluid near the blade surfaces migrates outward toward the tip of the blade and becomes entrained into the tip clearance jet. In addition, low-momentum fluid near the blade tip is transported to the pressure side/shroud corner of the blade passage where it accumulates to form the wake.

Measurements acquired downstream of the impeller are also presented to illustrate how the flow field nonuniformities, which exist at the impeller exit, mix out through the vaneless diffuser. Finally, the flow field measurements obtained in the LSCC are compared to those measured in high-speed impellers by Krain and Hoffman (1989, 1990) to assess the degree to which the flow physics in the LSCC simulates the flow physics within a high-speed centrifugal impeller.

Test Compressor

The NASA Low-Speed Centrifugal Compressor (LSCC) is an experimental facility designed to duplicate the essential flow physics of high-speed subsonic centrifugal compressor flow fields in a large low-speed machine in which very detailed investigations of the flow field can be made. A complete description of the facility is provided by Wood et al. (1983) and Hathaway et al. (1992).

The test compressor is a backswept impeller with a design tip speed of 153 m/s. The impeller is followed by a vaneless diffuser in order to generate an axisymmetric outflow boundary condition, which is desirable for CFD analysis of an isolated blade row. The impeller has 20 full blades with a backsweep of 55 degs. The inlet diameter is 0.870 m and the inlet blade height is 0.218 m. The exit diameter is 1.524 m and the exit blade height is 0.141 m. The tip clearance between the impeller blade and the shroud is 2.54 mm, and is constant from the impeller inlet to the impeller exit. This tip clearance is 1.8 percent of the blade height at the exit of the impeller.

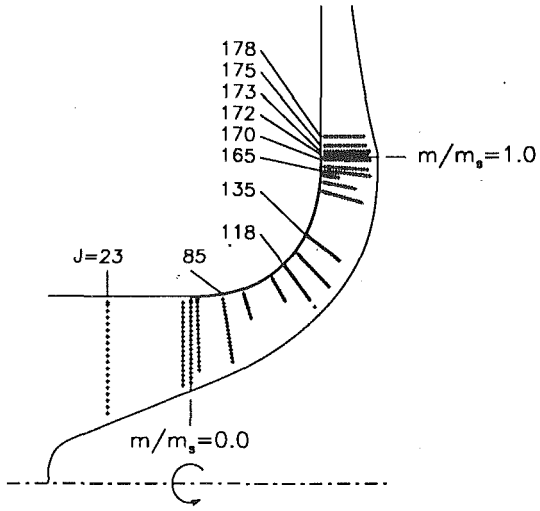

Fig. 1 Meridional view of LSCC rotor showing laser anemometer measurement locations

The blade surfaces are composed of straight-line elements from hub to tip. This feature enabled fabrication of the impeller by a flank-milling process on a five-axis milling machine. This feature also facilitates acquisition of laser anemometer measurement of velocities close to the blade surfaces by enabling the laser anemometer optical axis to be directed parallel to the blade surface.

The research operating point selected for both computational and experimental investigations of the LSCC flow field was set at standard-day corrected conditions of 30 kg/s and 1862 rpm, which is near peak efficiency, for all data presented herein.

Instrumentation and Measurement Technique

Separate laser windows provide optical access to the impeller in each of three regions: the impeller inlet, knee, and exit. Each window has compound curvature and matches the shroud contour in both the streamwise and circumferential direction in order to maintain the proper impeller tip clearance throughout the compressor. A meridional view of the LSCC, see Fig. 1, shows the spanwise and streamwise locations at which laser anemometer data have been acquired. The numbered cross-channel measurement stations denote the stations from which data will be presented. The station numbers are the streamwise indices of a body-fitted measurement grid, which was used to

Nomenclature

$\hat{c}$ = unit vector in the measured velocity component direction
$\mathbf{g}$ = local streamwise grid direction vector
$\hat{g}_m$ = unit vector in local meridional grid direction
$\hat{g}_p$ = unit vector in local pitchwise grid direction
$\hat{g}_s$ = unit vector in local spanwise grid direction
$\mathbf{J}$ = streamwise measurement grid index
m/m_s = nondimensional shroud meridional distance
N_{cpp} = number of encoder counts per blade pitch
N_p = number of impeller blade passages
PS = pressure surface
r/r_t = radius nondimensionalized by exit tip radius
SS = suction surface
U_t = impeller tip speed, m/s
$\mathbf{V}$ = absolute total velocity vector, m/s
V_c = mean velocity component measured in direction $\hat{c}$, m/s
V_m = meridional velocity component, m/s
V_p = pitchwise secondary velocity component, m/s
V_{qm} = quasi-meridional velocity component, m/s
V_r = radial velocity component, m/s
V_s = spanwise secondary velocity component, positive toward the shroud, m/s
V_{st} = velocity component tangent to the shroud meridional direction, m/s
V_T = total relative velocity, m/s
V_z = axial velocity component, m/s
V_θ = relative tangential velocity component, m/s
α = flow pitch angle, deg, $\alpha = \tan^{-1}(V_r/V_z)$
β = absolute flow angle, deg, $\beta = \tan^{-1}[(\mathbf{V}\cdot\hat{g}_p)/V_{qm}]$
θ = tangential coordinate, rad

Superscripts

$\bar{}$ = passage average

position the the laser measurement point within the impeller. The measurement grid used in this investigation divides the streamwise blade length into a series of "quasi-orthogonal," or near-normal, cross-channel planes. Stations 23, 85, 118, 135, 165, and 170 are located at -40, 14, 47, 64, 94, and 99 percent of meridional shroud length. The four measurement stations in the vaneless diffuser (172, 173, 175, and 178) are at impeller tip radius ratios of 1.01, 1.02, 1.04, and 1.06.

Laser Anemometer and Data Acquisition. A two-component laser fringe anemometer operating in on-axis backscatter mode was used in this investigation. Frequency shifting was used for both fringe systems to provide directional sensitivity for all velocity measurements.

Two digital shaft angle encoders (one for each laser anemometer channel) were used to generate a fixed number of pulses for each rotor revolution. When a laser velocity measurement occurred, the current encoder count was recorded along with the velocity data. The encoder count indicates the circumferential location of the velocity measurement relative to a once-per-rev timing mark on the impeller. In the present investigation, the encoders were set to generate $N_{\text{cpp}} = 200$ counts per pitch across each of the 20 impeller blade channels. Futher details of the encoding technique are described by Strazisar et al. (1989) and Wood et al. (1990).

The velocity component measurements acquired at each encoder count are first arithmetically averaged to determine the mean of each measured velocity component, V_c, where subscript c denotes that the velocity was measured in the direction of the unit vector $\hat{c}$. The mean velocities are then averaged across the 20 blade channels as shown in Eq. (1), to yield a single "passage-averaged" velocity profile for each velocity component, which is representative of the profile across each individual blade passage:

$$\overline{V}_c(i) = \frac{1}{N_p} \sum_{j=1}^{N_p} V_c(i + N_{\text{cpp}} * (j-1)), \quad i = 1, N_{\text{cpp}} \tag{1}$$

The normalized difference

$$\frac{\overline{V}_c(i) - V_c(i + N_{\text{cpp}} * (j-1))}{\overline{V}_c(i)} \tag{2}$$

where $\overline{V}_c(i)$ is the passage-averaged velocity component at any pitch-wise location i and $V_c\ (i + N_{\text{cpp}} * (j-1))$ is the mean velocity component in blade passage j at the same pitchwise location, has been checked and the difference is generally less than 1 percent. This indicates that the passage-averaging process does not appreciably alter any of the blade-to-blade velocity profile details. All the data presented in this report are based on passage-averaged velocity distributions.

In most regions of the flow field, 50,000 velocity measurements were acquired at each (axial, radial) measurement point shown in Fig. 1. This would yield an average of 250 measurements at each of the 200 points in the passage-averaged velocity distribution if the measurements were evenly distributed across the blade pitch. However, in general the number of measurements were not evenly distributed across the pitch. Therefore, the total number of measurements had to be adjusted in order to maintain a reasonable number of measurements in regions across the pitch where the data rate was low.

Seeding Technique. Polystyrene latex (PSL) spheres, manufactured using the process developed by Nichols (1987), were used as the seed material. Due to limitations in the manufacturing tolerance, the mean size of the seed particles produced for a given batch of seed varied from batch to batch, although the standard deviation of the particle sizes for a given batch of seed was generally less than 0.01–0.03 μm. The mean size of the seed particles used during the course of this investigation varied from 0.8 μm to 0.95 μm.

The seed material manufactured by Nichols' technique consists of a dilute suspension of PSL spheres in water. This mixture is further diluted in pure ethyl alcohol. The seed/water/alcohol mixture is injected into the airstream approximately 3 m upstream of the impeller leading edge using air-driven atomizing nozzles. The alcohol and water quickly evaporate, leaving individual PSL particles suspended in the airstream.

Extensive in-situ particle size measurements were made with an aerodynamic particle sizer prior to making laser anemometer measurements to insure that the seeding scheme was operating properly (Wasserbauer and Hathaway, 1993). The sizer was used to analyze samples of the airstream, which were extracted through a pitot tube located at measurement station 23 ahead of the impeller. No particles could be detected ahead of the impeller when pure alcohol was injected through the spray nozzles. The sizer was also used to analyze air samples when seed particles were added to the alcohol carrier to insure that individual seed particles did not agglomerate into groups of larger particles.

Three-Dimensional Velocity Measurement Technique. In order to determine all three components of the total velocity vector at a point in the flow field, two velocity components are measured at each of two different orientations of the laser anemometer optical axis. The two orientations of the optical axis were selected to minimize the amount of the blade passage that is optically blocked by the blade while maintaining a 20–30 deg included angle between the two orientations in order to minimize propagation of uncertainty of the measured velocity components into the calculated components. The resultant four measured components are combined using a least-squares fit (Eq. (3)) to yield the total three-dimensional velocity vector,

$$\frac{\partial \left[\sum_{k=1}^{4} (\mathbf{V} \cdot \hat{c}_k - (\overline{V}_c)_k)^2 \right]}{\partial \mathbf{V}} = 0 \tag{3}$$

where $\hat{c}_k$ is the unit vector in the kth measurement direction, $\mathbf{V}$ is the absolute total velocity vector, which is to be determined, and $(\overline{V}_c)_k$ is the measured passage-averaged velocity component in the direction of $\hat{c}_k$. As a check, the projection of the calculated total vector in the direction of each of the four measured components is compared to the measured component. The difference is generally less than 2 percent of the measured component.

The emphasis in the measurement technique described above was in obtaining the spanwise velocity component since this component has not been measured by most previous laser anemometer investigations in centrifugal compressors and is by far the most difficult component to resolve in most turbomachinery applications. The ability to measure the spanwise velocity component was verified upstream of the impeller at station 23 (shown in Fig. 1) by comparing the pitch angle, α, derived from the laser anemometer measurements to the pitch angle measured by a five-hole probe. The results of this exercise, shown in Fig. 2, indicate that the laser measurement technique is capable of accurately measuring the relatively small pitch angles which exist near the shroud. The agreement between the laser and five-hole probe measurements of the pitch angle is better than 2 deg over the outer 70 percent of span (0.20 m immersion). The laser measurements tend to depart from the five-hole probe measurements at lower spans, which is probably due to the effect of window curvature, which distorts the laser measurement volume.

Measurement Uncertainty

The uncertainty of the individual velocity component measurements was estimated from the least-squares calculation to be on the average approximately ± 1.5 m/s throughout most of the impeller passage. Through much of the impeller passage,

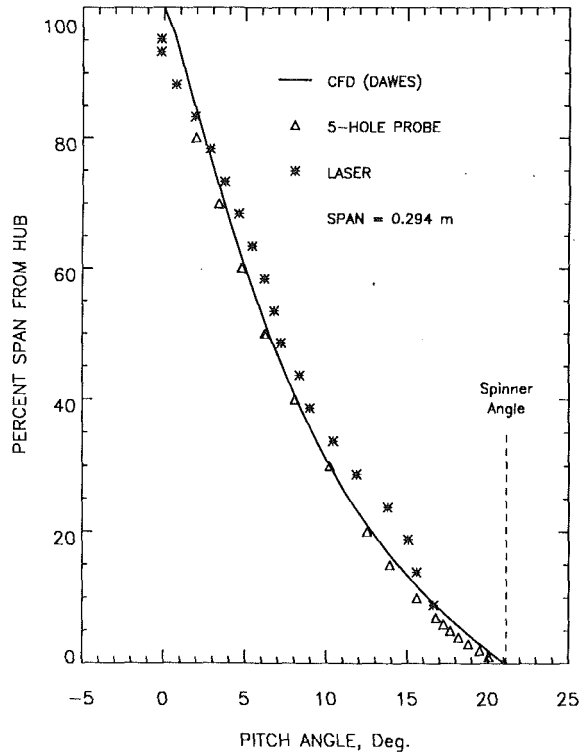

Fig. 2 Measured and predicted pitch angle distribution at rotor inlet station $J = 23$

the throughflow velocity magnitude is on the order of 75 m/s. Thus, the uncertainty of the measured velocity components is less than 2 percent of the throughflow component.

In addition to the propagation of uncertainties of the measured velocity components into the calculated velocity components, the measured velocity components are subject to the uncertainties arising from window curvature effects, which distort the laser anemometer probe volume. The spanwise velocity component and flow pitch angle are most susceptible to uncertainty propagation and are therefore most sensitive to window curvature effects. Based on the results shown in Fig. 2, the uncertainty in pitch angle, which directly indicates the ability to resolve the spanwise velocity component, is estimated to be less than ± 2 deg for measurement locations in the outer 70 percent of blade span for all measurement stations up to and including station 135. Because window curvature and blade span both decrease in the rear of the impeller, the uncertainty in the pitch angle for measurement stations 165–178 should be less than ± 2 deg over the entire blade span.

Computational Analysis

The computational results for the LSCC flow field were obtained using the Reynolds-averaged Navier–Stokes code developed by Dawes (1988). The code solves the equations of motion in cylindrical coordinates in integral conservation form using six-sided control volumes formed by a simple **H**-mesh. The basic algorithm as described by Dawes (1988) is similar to a two-step Runge–Kutta method plus residual smoothing. A combined second and fourth derivative artificial viscosity model with pressure gradient switching is used to eliminate spurious "wiggles" and to control shock capturing. The eddy viscosity is obtained using the Baldwin–Lomax (1970) mixing length model. Tip clearance is handled by gradually decreasing the thickness of the blade to zero in the tip clearance and enforcing periodicity. Since this simple treatment of the tip clearance does not solve for the details in the tip clearance gap, the actual tip clearance used in the code was reduced to 60 percent of the physical tip clearance to simulate the "vena-contracta" formed by the tip clearance jet.

The solution grid has 137 streamwise points (75 points are within the blade) with clustering around the leading edge, 71 points spanwise with 4 volumes in the tip clearance, and 41 points pitchwise. The pitchwise spacing at midpitch is about 5 percent of pitch and the nearest points away from the blade surfaces are at about 1 percent of pitch (however, the cell centers are 0.5 percent pitch from the surfaces). The spanwise spacing varies from a maximum of about 5 percent of span at midspan to 0.15 percent of span for the grid nodes nearest the hub and shroud (the cell centers are about 0.07 percent away from the endwalls). The maximum streamwise spacing is about 2.5 percent of meridional chord at midchord.

The actual spinner geometry was modeled by fitting a small-diameter cylindrical section to the spinner at a radius of 107 mm. In the calculation the spinner rotation was started at grid line 8, which is 54 percent of shroud meridional chord upstream of the blade leading edge and about 12 percent chord upstream of measurement station 23. Impeller hub rotation was stopped just downstream of the trailing edge.

Convergence was determined when the mass flow error throughout the domain was deemed acceptable and the losses through the compressor stabilized. Also, velocity components at selected points in the grid were monitored to insure that the velocity field was not changing. The maximum mass flow error was 0.56 percent of the inlet flow and occurred near the downstream boundary. The maximum mass flow error in the compressor blade passage was 0.38 percent and occurred near the trailing edge.

Results and Discussion

CFD analysis has been used in a synergistic fashion with the experimental effort throughout the course of the LSCC research program and this investigation is no exception. A coarse-grid flow field prediction was first generated prior to the experiment using Dawes' three dimensional Navier–Stokes code (Hathaway et al., 1992) to help develop an understanding for the flow field characteristics and to aid in planning the location of laser anemometer measurements. The final CFD solution, presented herein, was used to further our understanding of flow physics phenomena, such as the tip clearance flow, which were not completely captured during the experimental effort.

The results presented below consist of laser anemometer measurements of the velocity field along several quasi-orthogonal planes through the impeller. Ammonia-ozalid surface flow visualization results within the impeller and hot-wire anemometer results obtained in the vaneless diffuser will also be presented. The main objective of the data and computational analysis presented herein is to describe the complex flow physics within a subsonic centrifugal compressor and to demonstrate the fidelity of the three-dimensional Navier–Stokes flow field analysis.

The laser anemometer and CFD results that document the development of the throughflow velocity distribution through the impeller will be presented first. Secondary velocity vector plots will then be presented in order to illustrate the migration of low-momentum fluid through the impeller blade passage. Blade-to-blade distributions of the throughflow and secondary velocity components and flow pitch angles will also be presented at a few points of interest within the impeller. Finally, pitchwise distributions of the absolute flow angle will be presented in order to illustrate the mixing of the impeller exit flow in the vaneless diffuser.

Throughflow Development. The streamwise development of the throughflow velocity will be illustrated through the use of "wire-frame" plots of the quasi-meridional velocity nor-

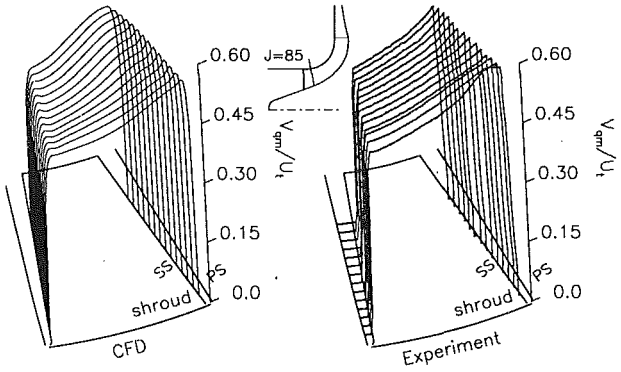

Fig. 3(*a*) Distribution of quasi-meridional velocity at station 85 (m/m_s = 0.149) at intervals of 5 percent span starting at 95 percent span

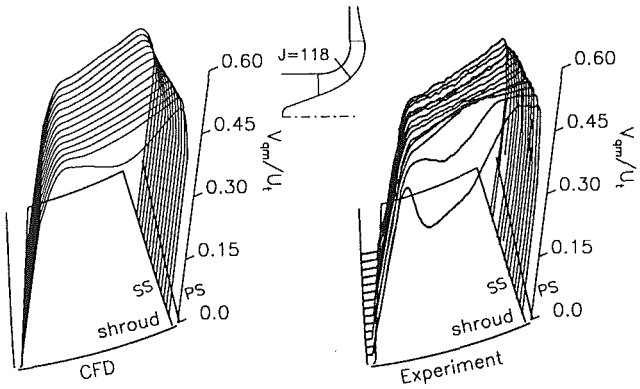

Fig. 3(*b*) Distribution of quasi-meridional velocity at station 118 (m/m_s = 0.475) at intervals of 5 percent span starting at 95 percent span

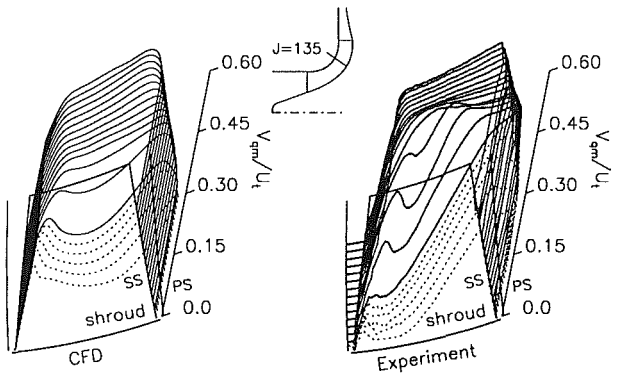

Fig. 3(*c*) Distribution of quasi-meridional velocity at station 135 (m/m_s = 0.644); solid lines at intervals of 5 percent span starting at 95 percent span; broken lines at intervals of 1 percent span starting at 100 percent span

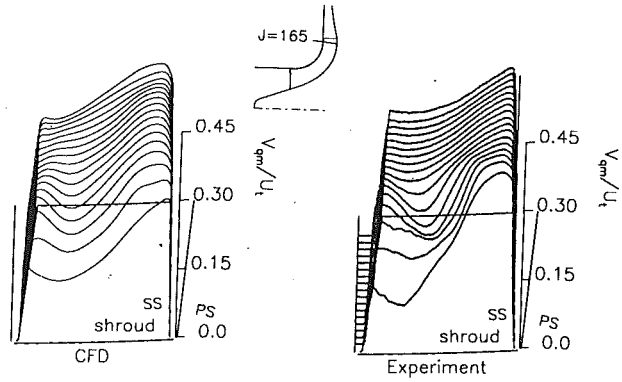

Fig. 3(*d*) Distribution of quasi-meridional velocity at station 165 (m/m_s = 0.941) at intervals of 5 percent span starting at 95 percent span

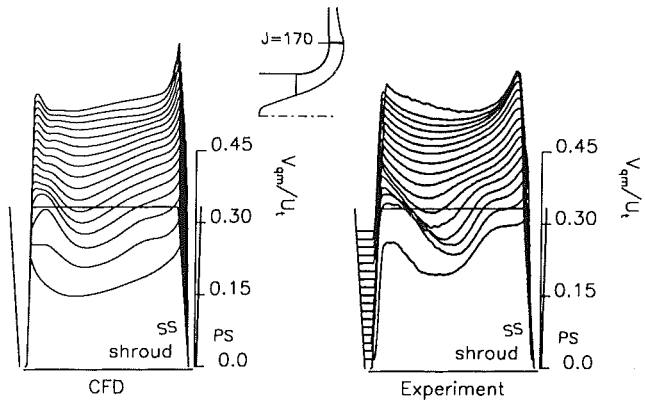

Fig. 3(*e*) Distribution of quasi-meridional velocity at station 170 (m/m_s = 0.990) at intervals of 5 percent span starting at 95 percent span

malized by the rotor tip speed, V_{qm}/U_t. As described in the appendix, the quasi-meridional velocity V_{qm} approximates the throughflow velocity component at any cross-channel station in the impeller. In order to compare the CFD solution directly to the laser data, the CFD solution was first interpolated in the streamwise direction to obtain predicted values of the velocity components V_r, V_θ, V_z at the experimental measurement planes shown in Fig. 1. On each plane the CFD solution was then interpolated to the same spanwise locations as the laser data. The velocity components V_{qm}, V_s, V_p, defined in the appendix, were then determined in the same manner for both experiment and CFD relative to the experimental measurement grid. There is therefore a one-to-one correspondence between the blade-to-blade velocity profiles in the CFD and experimental wire-frame plots. The results in each plot are shown at every 5 percent of span, with the results nearest the shroud located at 95 percent of blade span from the hub, where 100 percent span denotes the blade tip.

The complex nature of the flow field can lead to concern over the impact of interpolating the CFD results to the laser measurement locations. Therefore, for each measurement station presented in this paper, we compared the CFD results on the two quasi-orthogonal CFD calulation planes that lie on either side of the laser measurement plane to the CFD results that were interpolated to the measurement plane. In all cases we found that the interpolation process did not alter the predicted flow field characteristics.

Favorable agreement between CFD predictions and the laser anemometer measurements is obtained at station 85 (m/m_s = 0.14), as shown in Fig. 3(*a*). Both the CFD and experimental results indicate an almost linear velocity distribution across the blade passage. The results obtained at station 118 (m/m_s = 0.47) are shown in Fig. 3(*b*). At this station, a region of low streamwise momentum appears near the shroud at about midpitch. This region has been referred to as the "wake" region by previous investigators (Eckardt, 1976; Krain, 1988). The wake is evident in the experimental data at both 90 and 95 percent span, but is only evident in the CFD solution at 95 percent span. Inspection of data not presented here indicates that the wake first begins to develop at midpitch at m/m_s = 0.40.

The results obtained at station 135 (m/m_s = 0.64) are shown in Fig. 3(*c*). The broken lines indicate additional results obtained at 1 percent span intervals from 96 to 100 percent span. The momentum deficit near the shroud in both the measurements and the CFD results continues to grow in magnitude. The wake centerline also moves toward the pressure side of the passage. The measured wake occupies the outer 25 percent of the span. Note that the CFD solution underpredicts both the maximum velocity deficit in the wake and the spanwise

extent of the wake. Also note from Figs. 3(*a*, *b*, *c*) that both the measured and predicted throughflow momentum in the portion of the passage that is outside the wake is nearly constant from stations 85–135.

At station 165 ($m/m_s = 0.94$), shown in Fig. 3(*d*), the measured throughflow velocity deficit in the wake is less severe than it was at station 135. However, the minimum wake velocity at 95 percent span is nearly unchanged between stations 135 and 165. A detailed inspection of the blade-to-blade distributions of the throughflow velocity, plotted at individual spanwise locations, indicates that the streamwise velocity throughout the lower half of the passage and near the suction surface in the upper half of the passage has dropped significantly relative to its level at station 135. This behavior makes the wake appear less severe at station 165 than at station 135. The CFD solution indicates the wake has grown to occupy a larger spanwise extent than at station 135 and that the predicted minimum wake velocity is now comparable to the measured wake minimum velocity. Station 165 is in the region of the impeller blade passage where the pressure surface is not "covered" by the suction surface. This region begins at $m/m_s = 0.85$. The observed increase in pressure surface velocity and decrease in suction surface velocity is expected as a result of unloading of the blade. There is also a shift of the wake centerline toward midpitch.

The results obtained at station 170, which is a radius ratio of 0.99, are shown in Fig. 3(*e*). The CFD results agree qualitatively with the measurements. As we move from station 165 to station 170 we also note a continued unloading of the blade, as well as a continued shift of the wake centerline toward midpitch. The shift in wake centerline location near the exit of the impeller results from a continuing increase in the throughflow velocity near the pressure surface with increasing downstream distance. This behavior can be seen more clearly in Fig. 4, where the measured blade-to-blade distributions of throughflow velocity at 90 percent span for stations 135–170 are plotted.

In summary, the results shown in Fig. 3 indicate that the classic throughflow momentum deficit, or wake, which has been observed in centrifugal compressors by many other investigators occurs in the outer 25–35 percent of the span at the blade exit for this compressor. The wake is initially detected near midpitch, moves to the pressure surface/shroud corner of the passage, and then moves toward midpitch due to a continued increase in momentum in the pressure surface/shroud corner of the blade passage near the exit of the impeller.

The CFD solution predicts the location and strength of the wake near the impeller exit quite well, but underpredicts the maximum velocity deficit in the wake and the spanwise extent of the wake at stations 118 and 135. These features of the CFD solution are quite sensitive to the tip clearance model used in the code. The code models the vena-contracta formed by the clearance jet crossing the sharp blade edge by using a tip clearance value that is less than the physical tip clearance. The value used in the present solution is 60 percent of the physical tip clearance. The effect of increasing the tip clearance used in the code from 60 to 100 percent of the actual clearance has been studied using a slightly coarser grid (75 streamwise points in the blade, 41 points spanwise, 41 points pitchwise). The results indicate that increasing the tip clearance in the CFD solution does indeed result in an increase in the spanwise extent of the wake and moves the wake minimum velocity closer to the pressure surface at a given station. Inspection of the impeller blade tips at the conclusion of testing indicated that the blade tip corners were not sharp. A contraction coefficient of 0.6 is therefore too small. Calculations using a larger contraction coefficient will be pursued in a future analysis of this impeller.

Secondary Velocity Development. The objective of this section is to illustrate how the secondary velocity field within the impeller contributes to the formation and movement of the throughflow wake within the impeller. The development of the secondary velocity field will be documented by presenting secondary velocity vector plots on the cross-channel measurement planes. "Secondary velocity" as used in this paper is defined as that component of the total relative velocity vector not aligned with streamwise CFD grid lines. A detailed definition of the spanwise and pitchwise secondary velocity components is given in the appendix. Measured and predicted secondary velocity vectors are calculated in the same way.

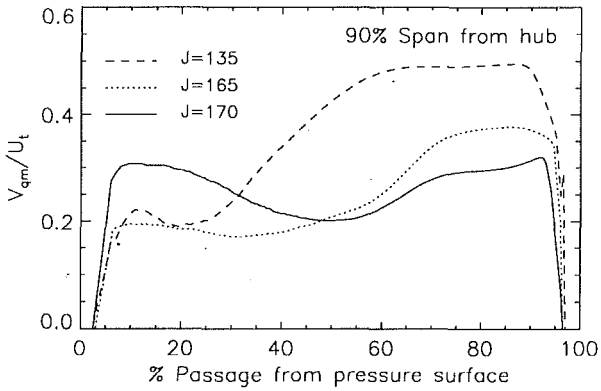

Fig. 4 Blade-to-blade distribution of measured quasi-meridional velocity at 90 percent span for several stations near the exit of the impeller

As in the previous section, the CFD results were interpolated to the streamwise and spanwise location of the laser measurements. In order to provide more details of the tip clearance flow, CFD results are also shown at 98 percent of blade span and at 101 percent of blade span, which lies inside the tip clearance gap. The pitchwise location of each vector in the CFD results is fixed by the pitchwise location of the CFD grid nodes. Although the laser measurements were made at 200 points across the pitch, only the data at every third point are presented for the sake of clarity. The predicted and measured vectors are drawn to the same scale with a reference vector of length $0.5*U_t$ shown in each plot. The streamwise momentum outside of the wake region for measurement stations up to and including station 135 is on the order of $0.5*U_t$. The strength of the secondary flow relative to the throughflow can therefore be approximated by comparing the secondary velocity vector magnitudes to the reference vector magnitude in each plot.

Also shown on the predicted secondary velocity vector plots are the locations of CFD tracer particles that were released along the blade leading edge from hub to tip on either side of the leading edge stagnation line. The CFD trace locations illustrate how low-momentum fluid along the blade surface migrates toward the blade tip and becomes entrained in the tip clearance flow.

The secondary flow at station 85 near the impeller inlet is shown in Fig. 5(*a*). The CFD results shows a spanwise flow of fluid along the pressure surface in the outer 50 percent of the blade span. A fairly weak vortical flow is predicted at this station and the experiment is just beginning to indicate some vortical flow near the shroud. Some of the CFD tracer particles released on the suction surface at the leading edge, denoted by *'s, have already migrated to the tip of the blade, have been entrained in the tip clearance jet, and have begun to move toward the pressure side of the passage. Some of the CFD tracer particles released on the pressure surface at the leading edge, denoted by ◇'s, have migrated to the tip of the blade, have crossed over the tip, and are also beginning to move toward the pressure side of the passage.

At station 118, shown in Fig. 5(*b*), both the CFD and experimental results indicate that the low-momentum fluid near the blade suction surface is migrating outward toward the blade

tip. The CFD solution also indicates a continuing migration of fluid toward the tip along the pressure surface. However, the experimental results indicate that the fluid moving outward along the blade pressure surface is met and turned by fluid from the vortical flow near the shroud, which is moving inward toward the hub near the pressure surface/shroud corner. The vortical flow near the shroud resides in approximately the same location as the low-momentum throughflow wake region indicated in Fig. 3(*b*). The CFD and experimental results do not provide a clear indication of the origin of the inward flow, which is measured in the pressure surface/shroud corner. However, the CFD tracer locations indicate that the blade leading edge particles, which are now entrained with the tip clearance flow, are migrating toward the pressure surface. The inward flow in the blade pressure surface/shroud corner may therefore be a result of the tip clearance flow impinging on the blade pressure surface.

The secondary flow results obtained at station 135 are shown in Fig. 5(*c*). Both the CFD and experimental results indicate a continuing migration of fluid outward toward the tip near the blade surfaces. However, the CFD results indicate that the fluid migrating outward along the blade pressure surface is now being met and turned inward by fluid moving downward near the blade pressure surface/shroud corner, just as was shown in the experimental results at station 118. In addition, the CFD tracers show further migration toward the blade pressure surface and the tracers appear to be rolling up into a vortical flow. The experimental results now show a stronger vortical flow near the shroud than indicated at station 118.

The insets in Fig. 5(*c*) show additional details of the measured and predicted flows in the tip region, which, for the sake of clarity, are not provided in the full-size passage view. The vector scale is different for each inset and is chosen so as to minimize overlap among vectors. Details of the predicted results in the blade pressure surface/shroud corner are shown in the left inset of Fig. 5(*c*), which is a magnified view of the full-size passage results. The results show that the inward flow in the pressure surface/shroud corner of the passage is caused by the roll-up of endwall fluid near the tip of the blade. The middle inset of Fig. 5(*c*) provides further details of the measured flow field from 95–100 percent span at the full pitchwise resolution of the laser anemometer measurements. The results verify the roll-up of fluid predicted by the CFD solution in the pressure surface/shroud corner and show the movement of fluid near the suction surface into the tip clearance gap. Finally, the right inset provides details measured within the blade suction surface boundary layer at 85, 90, and 95 percent span at the full pitchwise resolution of the laser anemometer measurements. The data clearly show the migration of the suction surface boundary layer fluid toward the shroud.

A comparison of Fig. 3(*c*) and Fig. 5(*c*) indicates that there is once again a strong correlation between the location of the throughflow velocity deficit and the location of strong secondary flow. As shown in Fig. 3(*c*), the magnitude of the measured normalized throughflow velocity in the pressure surface/shroud corner of the passage is $V_{qm}/U_t = 0.10–0.15$. In this region the magnitude of the secondary flow is on a par with the throughflow velocity.

At station 165, shown in Fig. 5(*d*), the CFD solution indicates a continued migration of flow outward along the blade surfaces and a well-behaved roll-up of flow in the pressure surface/shroud corner of the passage. The experimental results do not indicate outflow along the suction surface of the blade as predicted by the CFD result. We also note that a weak but discernible outward flow appears in the measurements toward the pressure-side half of the passage below about 70 percent span. However, the most dominant measured flow features are the strong spanwise flows in the pressure surface/shroud

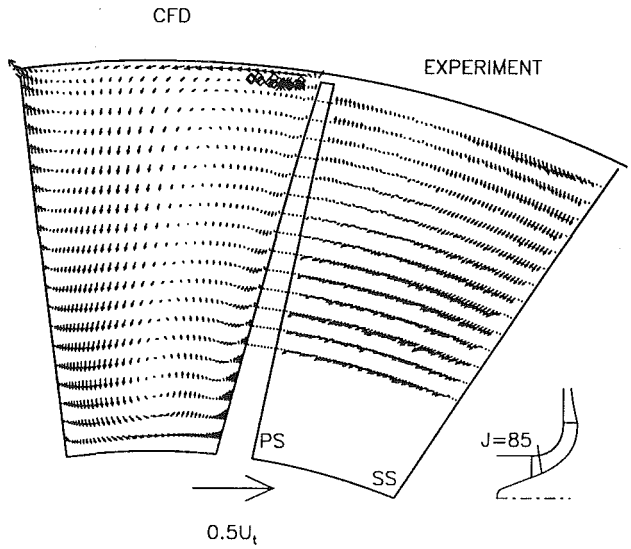

Fig. 5(*a*) Secondary flow velocity vector plots at station 85 (m/m_s = 0.149). Both CFD and experimental results shown at intervals of 5 percent span starting at 95 percent span with additional CFD results at 98 percent and 101 percent span. ◇ and ∗ denote CFD tracers released along the blade leading edge on the pressure and suction surfaces, respectively.

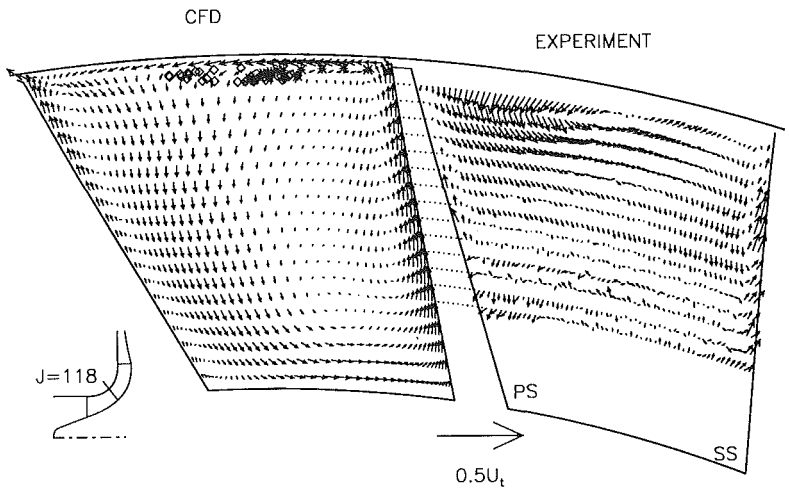

5(*b*) Secondary flow velocity vector plots at station 118 (m/m_s = 0.475). Both CFD and experimental results shown at intervals of 5 percent span staring at 95 percent span with additional CFD results at 98 and 101 percent span. ◇ and ∗ denote CFD tracers released along the blade leading edge on the pressure and suction surfaces, respectively.

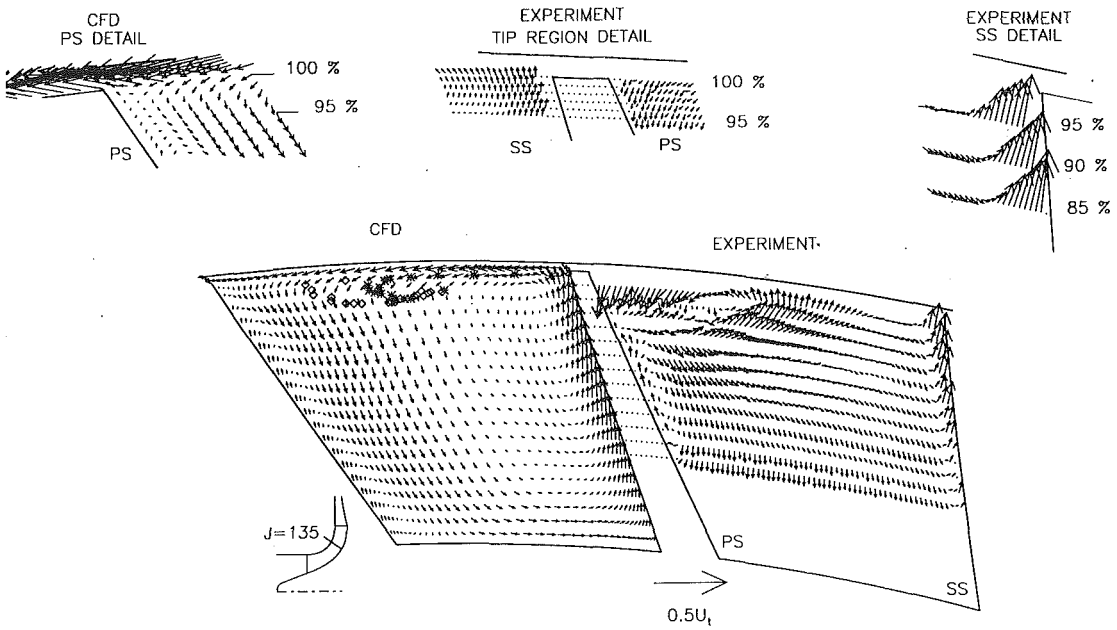

5(c) Secondary flow velocity vector plots at station 135 (m/m_s = 0.644). Both CFD and experimental results shown at intervals of 5 percent span starting at 95 percent span with additional CFD results at 98 and 101 percent span. ◇ and ∗ denote CFD tracers released along the blade leading edge on the pressure and suction surfaces, respectively. Insets show additional details of the tip region flow using the actual CFD grid and full laser measurement resolution.

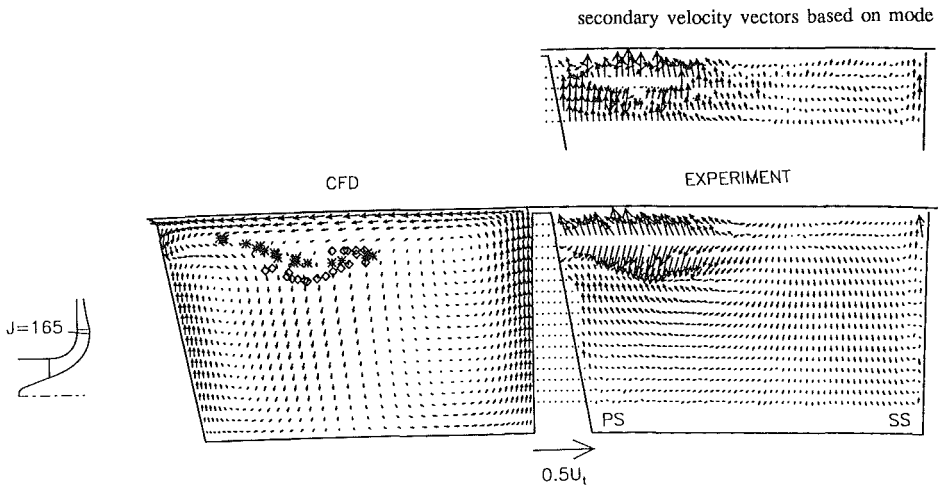

5((d) Secondary flow velocity vector plots at station 165 (m/m_s = 0.941). Both CFD and experimental results shown at intervals of 5 percent span starting at 95 percent span with additional CFD results at 98 and 101 percent span. ◇ and ∗ denote CFD tracers released along the blade leading edge on the pressure and suction surfaces, respectively.

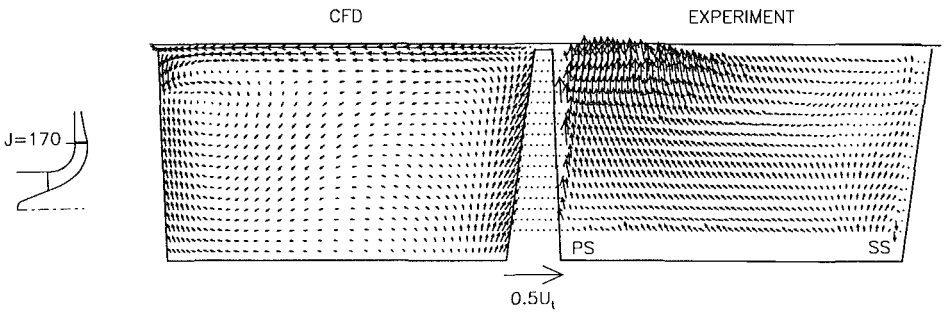

5(e) Secondary flow velocity vector plots at station 170 (m/m_s = 0.990). Both CFD and experimental results shown at intervals of 5 percent span starting at 95 percent span with additional CFD results at 98 and 101 span. ◇ and ∗ denote CFD tracers released along the blade leading edge on the pressure and suction surfaces, respectively.

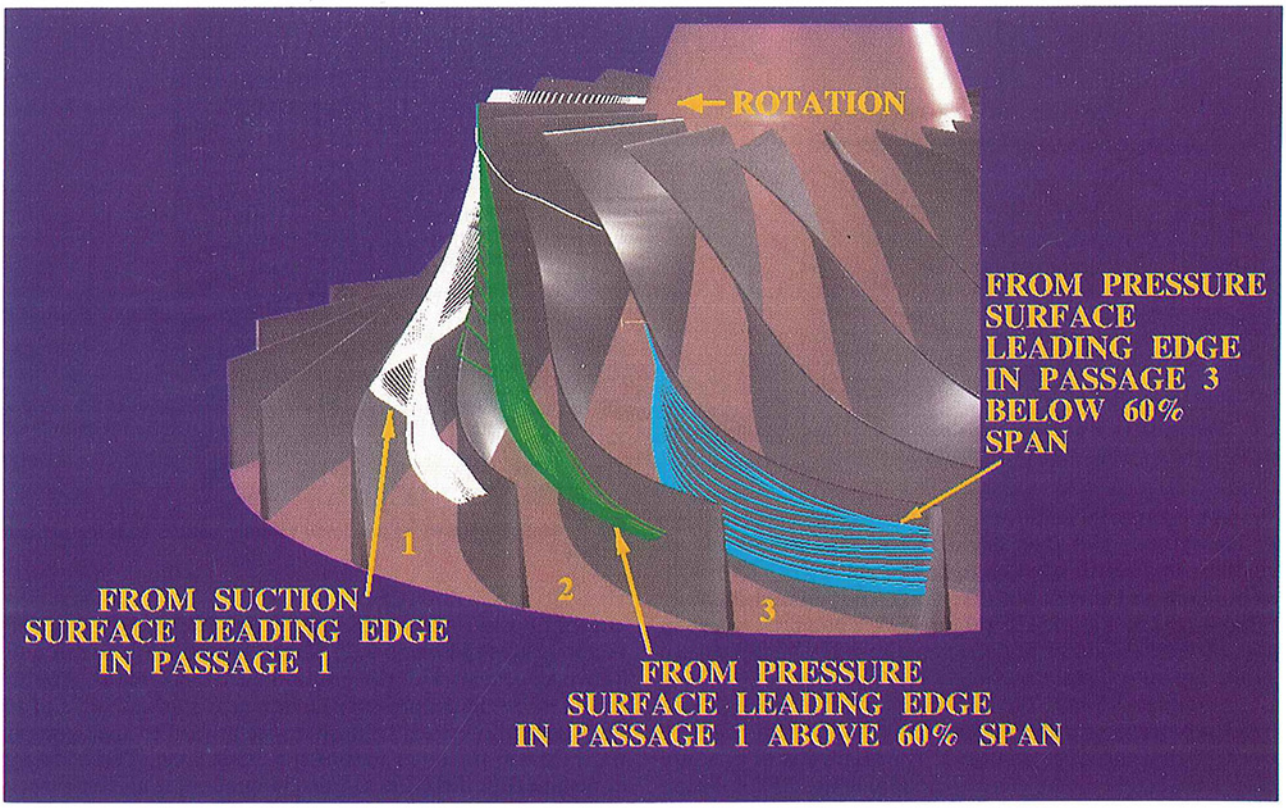

Fig. 6 Perspective view of the paths of CFD tracers released on the blade surfaces near the impeller leading edge

corner with an apparent strong reversal in spanwise flow direction (to be addressed subsequently) at about 87 percent span. The measurements in this region were repeated on three separate occasions and each measurement session yielded identical results.

At station 170, shown in Fig. 5(*e*), we see a dramatic change in the measured secondary flow relative to that just shown at station 165. The outward flow near the blade pressure surface, which was located below about 70 percent span and was quite weak at station 165, now dominates the secondary flow field in the pressure surface/shroud corner.

In order to investigate the cause of the secondary flow results shown in Fig. 5(*d*), we inspected the statistics of the individual laser anemometer measurements acquired at each of the 200 measurement points across the blade pitch. At each point a probability density distribution (p.d.d.) was constructed for all the measurements that occurred at that point. Throughout most of the flow field, these p.d.d.'s are Gaussian in character, which is to be expected for a turbulent flow. However, for points in the pressure surface/shroud corner at station 165, the p.d.d.'s are skewed, with long "tails," which result from the occurrence of velocities that are well below the mean velocity. The averaging method used to process all of the laser anemometer data essentially calculates the mean of each p.d.d. For Gaussian p.d.d's the mode, defined as the velocity that occurs most often, is close to or identical to the mean. However, for the p.d.d.'s that are skewed toward lower velocities, the mean occurs at a lower velocity than the mode.

The secondary velocity vectors shown in the inset in Fig. 5(*d*) are calculated using the mode of each p.d.d. rather than the mean. The mode results yield a secondary velocity field that has no vortical structure and is more similar to that measured at station 170. Since the mode is by definition the velocity that occurs most often, the mode results are felt to be more representative of the secondary velocity field in the pressure surface/shroud corner at station 165.

The skewed p.d.d.'s in the pressure surface/shroud corner suggest that the flow is quasi-steady in this region. This might be caused by a "meandering" of the throughflow wake at station 165. The secondary velocity vectors at stations 135 and 170 were also calculated based on the mode of the p.d.d.'s. The results, which are not included here, indicate that there is no appreciable difference between the vectors calculated using the mode and those calculated using the mean. These results indicate that the flow is steady at stations 135 and 170.

The results at station 135 indicate the development of a vortex that does not appear at stations 165 and 170. The ability to "see" a vortex is highly dependent on the viewing direction used when creating the secondary velocity vectors. The fact that a vortex appears at station 135 indicates that the vortex core is well aligned with the streamwise grid lines at that station. The results shown in Fig. 3 indicate that the throughflow velocity wake drifts from a location near the pressure surface toward midpitch as we move from station 135 to stations 165 and 170. If the vortex is associated with the wake, then the vortex core might also drift toward midpitch in the rear of the rotor. The vortex might therefore still be present at stations 165 and 170 but is no longer evident in the secondary velocity vector plots because the core is no longer aligned with the streamwise grid lines.

The secondary velocity results and CFD particle tracers presented in Fig. 5 illustrate that low-momentum fluid near the blade surface migrates toward the blade tip throughout most of the impeller passage, becomes entrained in the tip clearance flow, and then migrates toward the blade pressure surface/shroud corner. A perspective view of the process is presented in Fig. 6, which shows the predicted trajectories of particles that are released from hub to tip along the blade leading edge on either side of the leading edge stagnation line. The view in Fig. 6 is as viewed looking upstream into the impeller blade passage from a viewpoint near the impeller exit.

The white traces in passage 1 are the trajectories of particles released on the suction surface in blade passage 1. These particles migrate up the blade surface toward the tip, are entrained

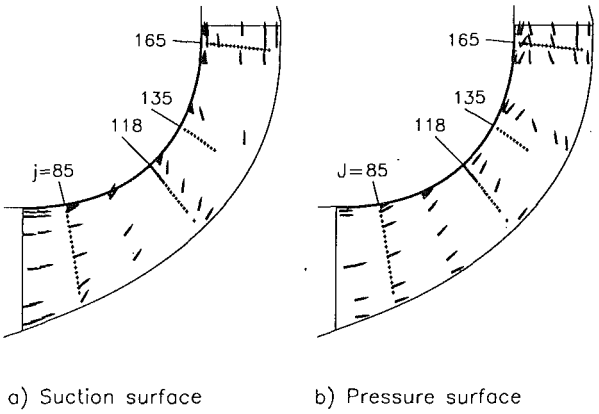

Fig. 7 Meridional view of suction and pressure surface flow directions measured using ammonia/ozalid flow visualization

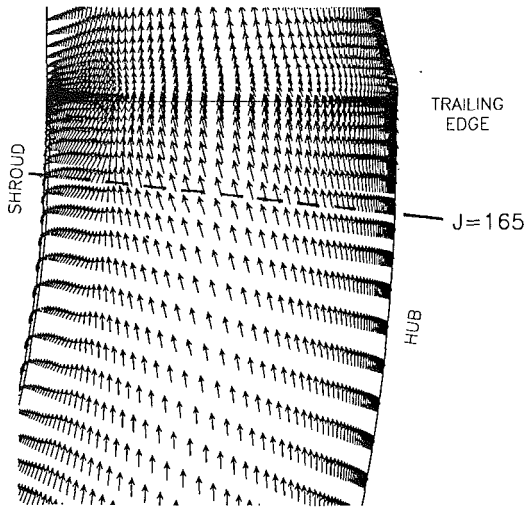

Fig. 8 Meridional view of predicted velocity vectors near the pressure surface

in the tip clearance jet and transported across the blade passage near the shroud, and then begin to roll up in the pressure surface/shroud corner of passage 1. This roll-up can be clearly seen in Fig. 6 and also in both the CFD solution and the laser measurements at station 135 (Figure 5*c*). The green traces in Fig. 6 are the trajectories of particles released in blade passage 1 on the pressure surface outboard of 60 percent span. These particles migrate toward the tip, cross over the blade, move across the passage near the shroud, and roll up in the pressure surface/shroud corner in passage 2. The migration of pressure surface fluid across the tip can also be seen in the CFD solution at stations 85 and 118 (Fig. 5*a*, *b*). The blue traces in passage 3 in Fig. 6 are the trajectories of particles released in blade passage 3 on the pressure surface inboard of 60 percent span. These particles begin to migrate toward the tip but are met and turned inward by the fluid that rolls up in the pressure surface/shroud corner. This behavior can also be seen in the CFD results shown in Figs. 5(*c*, *d*) at stations 135 and 165. Comparison of the particle trajectories in Fig. 6 with the throughflow velocity results of Fig. 3 clearly demonstrates that the throughflow velocity wake is formed by the migration of low-momentum fluid near the blade surfaces toward the shroud where it is entrained by the tip clearance flow and transported toward the pressure surface.

We have studied the trajectories of additional CFD tracers released all along the blade chord on the blade surfaces near the tip. These trajectories, which are not shown here, indicate that all of the fluid outboard of the tracers shown in Fig. 5 originated on the blade surfaces. The tracer locations shown in Fig. 5 therefore define the lower bound of the tip clearance flow.

In order to supplement the laser anemometer secondary flow measurements near the blade surfaces, the ammonia/ozalid surface flow visualization technique described by Joslyn and Dring (1986) was used to measure the flow direction along the impeller blade suction and pressure surfaces. The uncertainty in the surface flow angles measured with this technique is on the order of ± 2 deg.

The results of the ammonia/ozalid technique are shown in Fig. 7. The suction surface flow traces show a significant spanwise flow toward the tip in the area between stations 85 and 135. The ammonia traces at station 85 ($m/m_s = 0.14$) indicate that fluid is already entering the tip clearance gap at this station. An appreciable accumulation of seed particles was observed on the shroud windows in the region $m/m_s = 0.20$–0.30, which provides further evidence that the clearance jet develops to an appreciable strength in this region.

The ammonia traces near station 118 indicate a strong outward flow along the entire suction surface. The ammonia traces along the pressure surface indicate an outward flow below midspan, which diminishes in strength and then becomes an inward flow as we move toward the tip. The measured velocity vector results at station 118, shown in Fig. 5(*b*), are in qualitative agreement with these ammonia/ozalid results. The ammonia traces on the pressure surface near stations 135 and 165 show several reversals from spanwise inward to spanwise outward flow in the outer half of the blade span. These changes in surface flow direction are also in qualitative agreement with the measured velocity vector results shown in Figs. 5(*c*) and 5(*d*), which indicate the presence of a strong secondary flow in the pressure surface/shroud corner of the blade passage. The velocity vector results at station 170 (Fig. 5*e*) do not seem to agree with the ammonia trace results on the pressure surface near the shroud. The ammonia results show that the flow near the shroud is moving inward, while the velocity vector results seem to indicate that the flow is moving outward at all spanwise locations near the pressure surface. This apparent discrepancy arises from the fact that we were not able to measure the velocity near the pressure surface at station 170 due to an optical blockage problem.

The predicted flow directions near the blade pressure surface in the rear of the impeller are shown in Fig. 8, which is a meridional view of the CFD results on the first grid plane from the blade surface. A demarcation line, which separates flow moving toward the hub from that moving toward the tip, can be seen at about 80 percent span near the impeller exit. This demarcation line can also be seen in Fig. 6 for the CFD tracer results near the pressure surface in passage 3. The CFD results are in excellent qualitative agreement with the pressure surface ammonia/ozalid results shown in Fig. 7(*b*) at the impeller exit near the tip, which also indicate the presence of a distinct change in spanwise flow at about 80 percent span.

The secondary flow field results presented thus far have qualitatively illustrated the features of the secondary flow field and the comparison between CFD and experimental results. A more quantitative comparison between CFD and experimental results will now be provided by presenting blade-to-blade distributions of velocity and pitch angle at selected measurement locations at stations 118 and 165.

The measured and predicted distributions of the normalized quasi-meridional velocity, normalized spanwise secondary velocity, and pitch angle at 65 percent span at station 118 are shown in Fig. 9. The comparison between predicted and measured values of V_{qm}/U_t, which approximates the throughflow velocity, are excellent. The extents of the suction and pressure surface boundary layers are clearly shown. The laser anemometer measurements of the normalized spanwise secondary velocity, V_s/U_t (see Fig. 9*b*), indicate appreciable outflow near

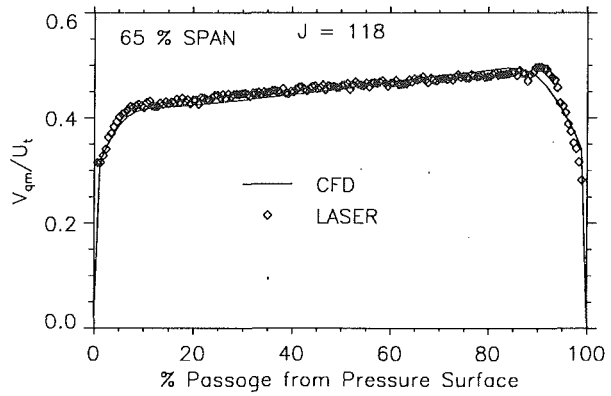

Fig. 9(*a*) Blade-to-blade distribution of quasi-meridional velocity at 65 percent span for station 118 (m/m_s = 0.475)

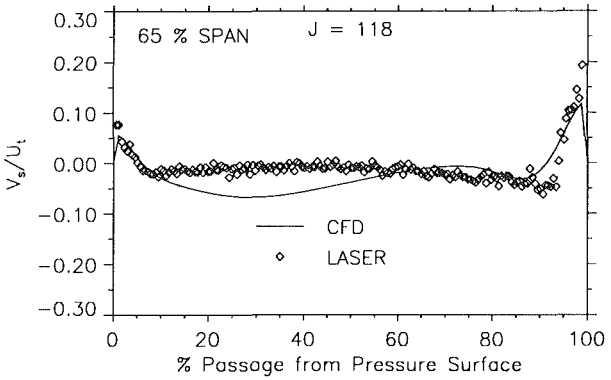

Fig. 9(*b*) Blade-to-blade distribution of spanwise secondary velocity at 65 percent span for station 118 (m/m_s = 0.475)

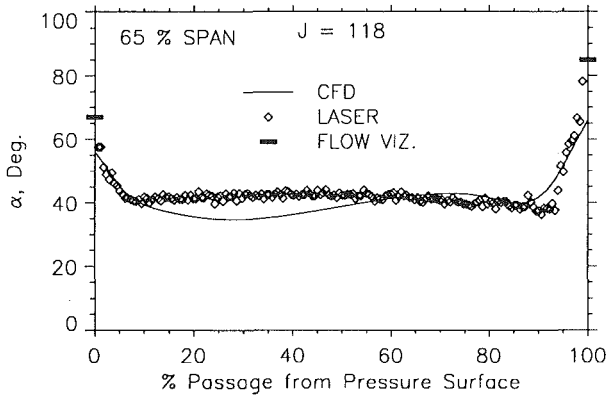

Fig. 9(*c*) Blade-to-blade distribution of pitch angle at 65 percent span for station 118 (m/m_s = 0.475)

both the pressure and suction surfaces and a weak inflow across the remainder of the passage. Note that the outflow regions shown in Fig. 9(*b*) closely correspond to the blade boundary layers shown in Fig. 9(*a*). The ability of the laser measurements to resolve the spanwise velocity component accurately is illustrated in Fig. 9(*c*) where we see that the pitch angles, α, measured on the blade surfaces with the ammonia/ozalid flow visualization technique are in close agreement with the near-surface pitch angles measured with the laser anemometer.

Measured and predicted pitch angle distributions, as well as the ammonia/ozalid surface flow angle results at 20, 80, and 95 percent span for station 165, are shown in Fig. 10. At 80 and 95 percent span the pitch angle distributions derived from both the mean and mode of the laser measurements are shown. As discussed previously, the mode results are considered to be more representative of the flow in this region than are the

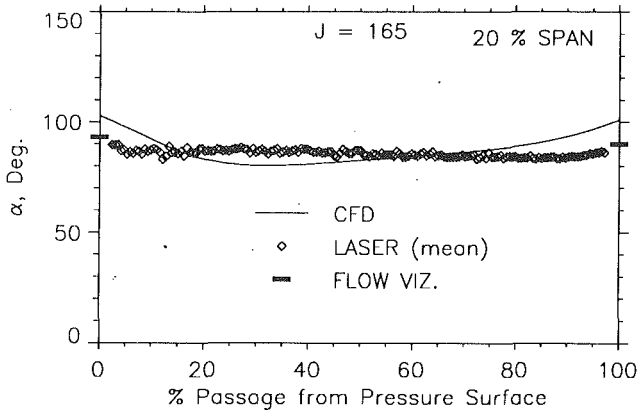

Fig. 10(*a*) Blade-to-blade distribution of pitch angle at 20 percent span for station 165 (m/m_s = 0.941)

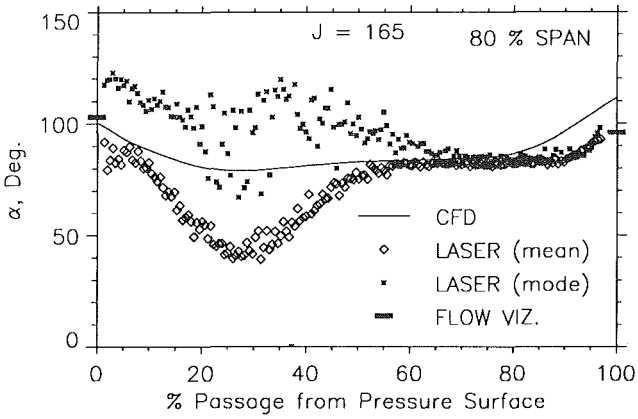

Fig. 10(*b*) Blade-to-blade distribution of pitch angle at 80 percent span for station 165 (m/m_s = 09.41)

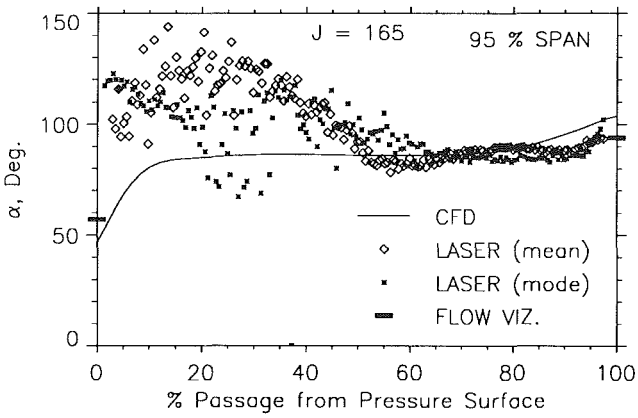

Fig. 10(*c*) Blade-to-blade distribution of pitch angle at 95 percent span for station 165 (m/m_s = 09.41)

mean results. The grid normal at station 165 has a pitch angle of 85 deg. Therefore, a flow pitch angle greater than 85 deg indicates a spanwise flow toward the shroud, while a flow pitch angle less than 85 degrees indicates a spanwise flow toward the hub.

There is no appreciable spanwise flow across the entire passage at the 20 percent span location. The laser measurements do not indicate a large change in flow angle near the pressure surface between 80 and 95 percent span. However, the CFD and ammonia/ozalid results indicate a change in pitch angle on the pressure surface on the order of 50 deg between these two spanwise locations. Note that all three techniques also indicate a relatively weak spanwise flow along the suction surface at all immersions.

Impeller Wake Mixing. Mixing phenomena downstream of centrifugal impellers are quite complex. At the impeller exit a viscous blade wake is present at all spans and a throughflow velocity wake is present near midpitch in the outer 30 percent of the blade span. In order to study wake mixing phenomena, laser anemometer measurements were acquired at four measurement stations in the vaneless diffuser at radius ratios of 1.01, 1.02, 1.04, and 1.06. The absolute flow angle distributions acquired at these stations will be used to illustrate the mixing in the LSCC vaneless space. The results provide an indication of the incidence angle variation into the diffuser vanes if a vaned diffuser were present.

The blade-to-blade variation in absolute flow angle at 50 percent span is shown in Fig. 11(*a*) for the four measurement stations in the vaneless diffuser. The results are shown across two complete blade pitches, with the blade centered at 0 percent blade pitch. For each radius ratio, the flow angle variation is presented as the difference between the local flow angle, β, and the minimum flow angle at that radius ratio, β_{min}. At radius ratios of 1.01 and 1.02 the flow angle variation across the viscous blade wake is more than 30 deg. This angle variation decreases rapidly to levels below 10 deg at radius ratios of 1.04 and 1.06. The flow angle variation across the remainder of the blade passage is less than 6 deg at all radius ratios.

The pitchwise variation in flow angle at 90 percent span is shown in Fig. 11(*b*). At this spanwise location, the flow exiting the impeller contains a throughflow velocity wake as well as a viscous blade wake. The blade is thinner at 90 percent span than at 50 percent span, which contributes to a weaker viscous blade wake than at 50 percent span. At a radius ratio of 1.01, the absolute angle variation across the viscous wake is on the order of 20 deg, while the angle variation across the throughflow velocity wake is on the order of 10 deg. As we move downstream, the flow angle variation across the viscous wake decreases rapidly. However, the angle variation across the throughflow wake decreases much more slowly. As a result, the variation in absolute angle across the viscous and throughflow velocity wakes is almost equal at radius ratios of 1.04 and 1.06.

Hot-wire anemometer surveys of the flow field were acquired at a radius ratio of 1.06 using a slanted hot wire measurement technique described by Hanson et al. (1992). The primary purpose of this exercise was to provide an independent check on the accuracy of the laser anemometer measurement technique. The hot-wire and laser anemometer results are shown in Fig. 12. Both measurements indicate flow migrating toward the shroud in the viscous wake region (toward the right-hand side of each plot) and in the throughflow wake region (toward the left-hand side of each plot over the upper 50 percent immersion).

Fidelity of the Low-Speed Compressor Flow Field Simulation

The LSCC was designed to generate a flow field that is aerodynamically similar to that found in high-speed subsonic centrifugal compressors, as described by Wood et al. (1983) and Hathaway et al. (1992). If the flow field that has been investigated in the LSCC can be shown indeed to be similar to that found in actual subsonic centrifugal compressors, then the results presented here can be used to assess the accuracy of Navier–Stokes analyses and the lessons learned can be used with confidence when analyzing actual high-speed impellers. In order to determine how well the LSCC flow field simulates that found in a high-speed subsonic compressor, the throughflow velocity in the LSCC will be compared with the throughflow velocity measured in two 4:1 pressure ratio, 30 deg backswept, impellers as reported by Krain and Hoffman (1989, 1990). These impellers will be denoted as Rotor I and Rotor II. Rotor II is similar to Rotor I, but features a reduction in exit blade height of approximately 30 percent. The tip speed of Rotor I is 470 m/s and the tip clearance is 0.2 mm at the exit and 0.5 mm at the inlet. The exit blade span of the impeller is 14.7 mm, which yields a tip clearance based on exit blade

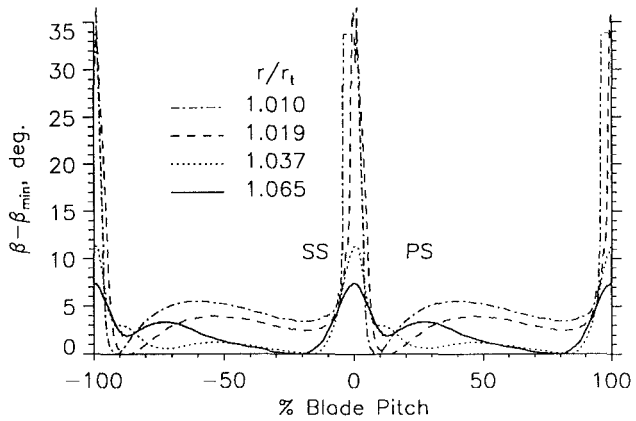

Fig. 11(*a*) Pitchwise distribution of absolute flow angle difference, $\beta - \beta_{min}$, in the vaneless diffuser at 50 percent span

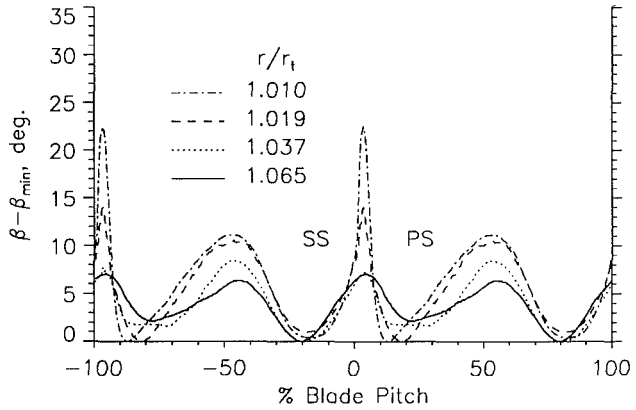

Fig. 11(*b*) Pitchwise distribution of absolute flow angle difference, $\beta - \beta_{min}$, in the vaneless diffuser at 90 percent span

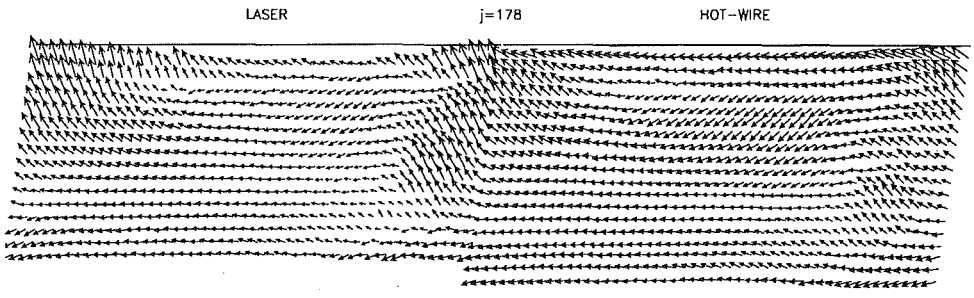

Fig. 12 Comparison of laser and hot-wire anemometer measurements of secondary velocity vectors at station 178 (r/r_t = 1.065)

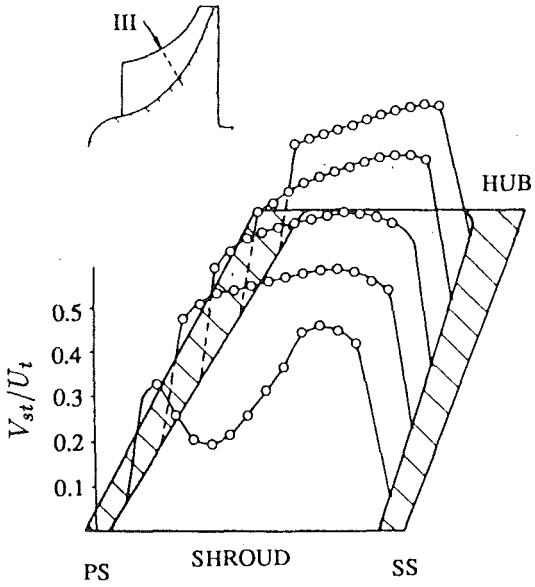

Fig. 13(*a*) Rotor I, measurement plane III (m/m_s = 0.4)

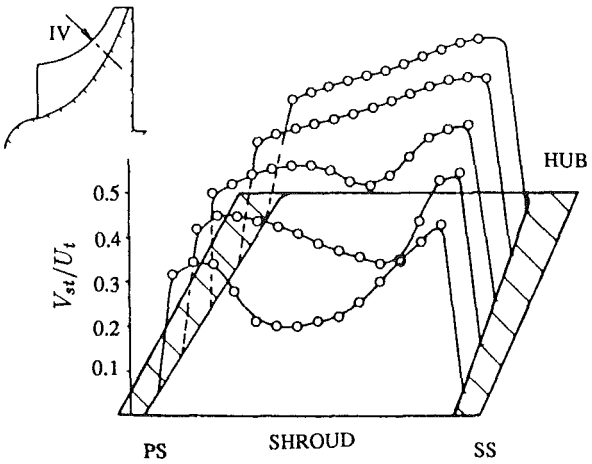

Fig. 13(*b*) Rotor I, measurement plane IV (m/m_s = 0.6)

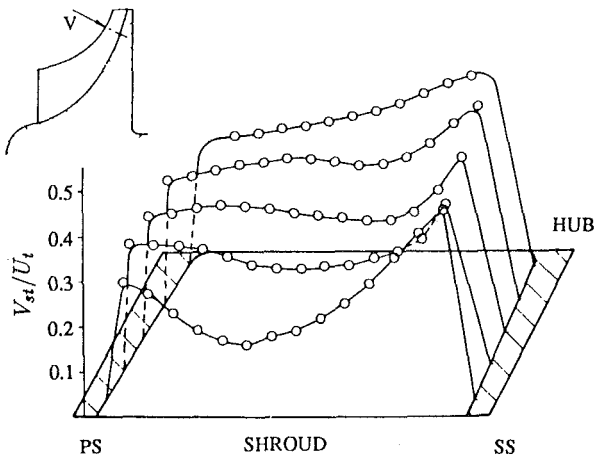

Fig. 13(*c*) Rotor I, measurement plane V (m/m_s = 0.8)

span of 1.4 percent (0.2 mm) at the exit and 3.4 percent (0.5 mm) at the inlet. The tip clearance of the LSCC based on exit blade span is 1.8 percent (2.54 mm) and is constant from inlet to exit.

The LSCC results are shown in Fig. 3 and Rotor I and II results are shown in Fig. 13. Rotor I & II results are shown at

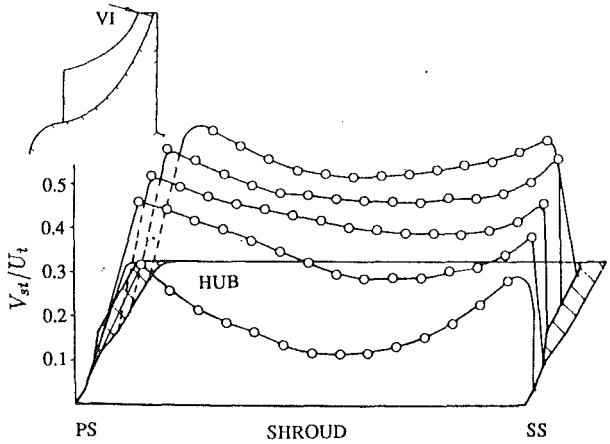

Fig. 13(*d*) Rotor I, measurement plane VI (m/m_s = 1.004)

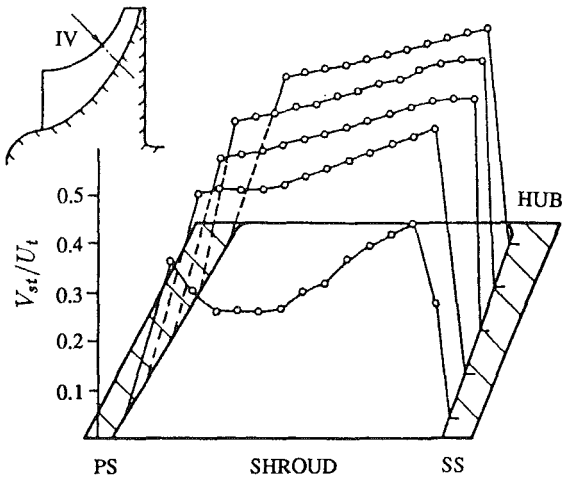

Fig. 13(*e*) Rotor II, measurement plane IV (m/m_s = 0.6)

10, 30, 50, 70, and 90 percent span at each station, while the LSCC results presented in Fig. 3 are shown every 5 percent of span starting at 95 percent span. The velocity component measured by Krain and Hoffman, denoted herein as V_{st}, is the velocity component that is tangent to the shroud in the meridional direction. The velocity component measured in the LSCC, V_{qm}, is tangent to the local streamwise grid lines, which are tangent to the shroud at 100 percent blade span and tangent to the hub at 0 percent blade span. While V_{st} and V_{qm} are not identical velocity components, they are very similar.

The throughflow velocity wake first appears in the Rotor I results near the pressure surface at station III and occupies at least 10 percent of span at this station. This result compares favorably to that measured in the LSCC at station 118, shown in Fig. 3(*b*). The LSCC results at station 135, however, do not agree with Rotor I results at station IV. The wake in the LSCC is close to the blade pressure surface at this station, while the wake in Rotor I remains near midpitch. The wake in Rotor I penetrates to 50 percent span while that in the LSCC only penetrates to 75 percent span, which is probably due to the fact that the tip clearance in the inlet region of Rotor I is more than double that of the LSCC. In moving from station V to VI in Rotor I, the velocity near the pressure surface rises while the velocity near the suction surface falls, indicating a reduction in blade loading. This behavior is similar to that found in the LSCC as we proceed from station 165–170.

The movement of the Rotor I wake toward midpitch at station IV might result from the low-momentum fluid in the wake being subjected to a larger cross-passage pressure gradient than in the LSCC. This may indeed be what is occurring

if the results from rotor II (Krain and Hoffman, 1990) are considered. Since the throughflow velocity in Rotor II is somewhat higher than in Rotor I, while the cross-passage pressure gradient is similar for both rotors (the overall pressure ratio for both rotors is similar), it would seem reasonable to expect that the low-momentum wake fluid in Rotor II would remain closer to the pressure side of the passage than the wake fluid in Rotor I. The plane IV results measured in Rotor II, shown in Fig. 13(*e*), confirm that the wake is located closer to the pressure surface than it is in Rotor I. In addition, the wake in Rotor II does not penetrate below 70 percent span, which agrees favorably with the wake penetration to 75 percent span in the LSCC at station 135.

Analysis of Rotor I, Rotor II, and the LSCC with a one-dimensional centrifugal compressor performance prediction code shows that the relative velocity ratio (exit velocity/inlet tip velocity) of the LSCC falls between that of Rotor I and Rotor II.

In summary, the throughflow development in the LSCC impeller is similar to that in Krain's impellers. Differences between the LSCC throughflow characteristics and those in Rotors I and II are on the same order as the differences between the two high-speed rotors. Since the throughflow development is tightly coupled to the secondary flow development, the secondary flow field characteristics in the LSCC should indeed be similar to those that exist in high-speed subsonic centrifugal impellers.

Summary and Conclusions

The results presented herein represent an extensive computational and experimental effort to document the velocity field within the NASA Low-Speed Centrifugal Compressor (LSCC). The large impeller passage size provides considerable optical access to the flow field and enables measurements of the three-dimensional velocity field throughout the impeller blade passage. In several cases the measurements provide details within the blade boundary layers. Independent validation of the laser measurements via five-hole probe and hot-wire anemometer surveys as well as ammonia/ozalid surface flow visualization results provides a high degree of confidence in the laser anemometer results.

The laser anemometer measurements and the CFD solution complement one another in illustrating the flow physics within the impeller. Laser anemometer measurements confirm that the low-momentum fluid near the blade surfaces migrates outward toward the tip of the blade, as predicted by the CFD solution. Particle traces done on the CFD solution indicate that the fluid that moves up the blade pressure and suction surfaces is entrained into the tip clearance jet. The particle traces also show that this fluid is then transported toward the pressure side/shroud corner of the passage, where it contributes to the formation of the characteristic throughflow momentum wake that is found in unshrouded centrifugal compressor impellers.

The throughflow momentum wake region generated as a result of the tip clearance flow mixes out more slowly than does the viscous blade wake as the flow moves through the vaneless diffuser. The flow field in the vaneless space near the shroud surface is therefore composed of low-momentum regions: one from the viscous blade wake and one from the throughflow momentum wake.

The development of the throughflow velocity field within the LSCC is shown to be qualitatively similar to that measured in a high-speed 4:1 pressure ratio centrifugal compressor. The experimental results presented provide a representative view of the flow physics within unshrouded centrifugal compressor impellers and should be useful in assessing the ability of viscous flow codes to predict the flow physics within centrifugal compressors accurately.

Acknowledgments

The authors would like to acknowledge the innumerable personnel without whose support this research endeavor would not have been possible. In particular the authors would like to thank Bill Darby, Bob Davis, John DeArmon, Marty Pietrasz, Rick Senyitko, Charles Wasserbauer, and Hal Weaver for their support of the LSCC experiment; Glenn Christman, Tim Hepner, and Mark Wernet for their support and advice relative to laser anemometer hardware and software; and Bruce Reichert, Kurt Hansen, and Andy Hiedinger for acquiring the hot-wire anemometer results.

References

Ahmed, N. A., and Elder, R. L., 1990, "Flow Investigation in a Small High Speed Impeller Passage Using Laser Anemometry," ASME Paper No. 90-GT-233.

Baldwin, B., and Lomax, H., 1970, "Thin Layer Approximation and Algebraic Model for Separated Turbulent Flows," AIAA Paper No. 78-257.

Bansod, P., and Rhie, C. M., 1990, "Computation of Flow Through a Centrifugal Impeller With Tip Leakage, AIAA Paper No. 90-2021.

Dawes, W. N., 1988, "Development of a 3-D Navier Stokes Solver for Application to all Types of Turbomachinery," ASME Paper No. 88-GT-70.

Eckardt, D., 1976, "Detailed Flow Investigations Within a High-Speed Centrifugal Compressor Impeller," ASME *Journal of Fluids Engineering*, Vol. 98, pp. 390-402.

Fagan, J. R., and Fleeter, S., 1991, "Impeller Flow Field Measurement and Analysis," ASME JOURNAL OF TURBOMACHINERY, Vol. 113, No. 4, pp. 670-679.

Farge, T. Z., Johnson, M. W., and Maksoud, T. M. A., 1989, "Tip Leakage in a Centrifugal Impeller," ASME JOURNAL OF TURBOMACHINERY, Vol. 111, pp. 244-249.

Hah, C., and Krain, H., 1990, "Secondary Flows and Vortex Motion in a High-Efficiency Backswept Impeller at Design and Off-Design Conditions," ASME JOURNAL OF TURBOMACHINERY, Vol. 112, pp. 7-13.

Hanson, K. A., Heidinger, A. K., Holder, C. M., and Reichert, B. A., 1992, "A Three-Dimensional Unsteady Hot-Wire Technique for the NASA Low-Speed Centrifugal Compressor," NASA TM-105339.

Hathaway, M. D., Wood, J. R., and Wasserbauer, C. W., 1992, "NASA Low-Speed Centrifugal Compressor for 3-D Viscous Code Assessment and Fundamental Flow Physics Research," ASME JOURNAL OF TURBOMACHINERY, Vol. 114, pp. 295-303.

Joslyn, H. D., and Dring, R. P., 1986, "Surface Indicator and Smoke Flow Visualization Techniques in Rotating Machinery," in: *Heat Transfer and Fluid Flow in Rotating Machinery*, Hemisphere Publishing Corp., pp. 156-169.

Krain, H., 1988, "Swirling Impeller Flow," ASME JOURNAL OF TURBOMACHINERY, Vol. 119, pp. 122-128.

Krain, H., and Hoffman, W., 1989, "Verification of an Impeller Design by Laser Measurements and 3D-Viscous Flow Calculations," ASME Paper No. 89-GT-159.

Krain, H., and Hoffman, W., 1990, "Centrifugal Impeller Geometry and Its Influence on Secondary Flows," in: *AGARD Secondary Flows in Turbomachines.*

Moore, J., and Moore, J. G., 1990a, "A Prediction of 3-D Viscous Flow and Performance of the NASA Low-Speed Centrifugal Compressor, ASME Paper No. 90-GT-234.

Nichols, C. E., Jr., 1987, "Preparation of Polystyrene Microspheres for Laser Velocimetry in Wind Tunnels," NASA TM 89163.

Rohne, K. H., and Banzhaf, M., 1990, "Investigation of the Flow at the Exit of an Unshrouded Centrifugal Impeller and Comparison With the 'Classical' Jet-Wake Theory," ASME JOURNAL OF TURBOMACHINERY, Vol. 113, pp. 654-659.

Senoo, Y., Yamaguchi, M., and Nishi, M., 1968, "A Photographic Study of Three-Dimensional Flow in a Radial Compressor," ASME Paper No. 68-GT-2.

Sipos, G., 1991, "Secondary Flow Loss Distribution in a Radial Compressor With Untwisted Backswept Vanes," ASME JOURNAL OF TURBOMACHINERY, Vol. 113, No. 4, pp. 686-695.

Strazisar, A. J., Wood, J. R., Hathaway, M. D., and Suder, K. L., 1989, "Laser Anemometer Measurements in a Transonic Axial-Flow Fan Rotor," NASA TP-2879.

Wasserbauer, C. W., and Hathaway, M. D., 1993, "Development of the Seeding System Used for Laser Velocimeter Surveys in the NASA Low-Speed Centrifugal Compressor Facility," NASA TM-106046.

Wood, J. R., Adam, P. W., and Buggele, A. E., 1983, "NASA Low-Speed Centrifugal Compressor for Fundamental Research," NASA TM 83398.

Wood, J. R., Strazisar, A. J., and Hathaway, M. D., 1990, "E/C0-2 Single Transonic Fan Rotor," AGARD-AR-275.

APPENDIX

Definition of Velocity Components

In order to visualize secondary flow, the total relative velocity vector must be viewed along the streamwise direction.

However, in a geometrically complex channel such as a centrifugal impeller blade passage, the streamwise direction can be defined in several different ways, and each definition will yield a slightly different result for the secondary flow. This problem has been pointed out by many previous authors. The purpose of the following discussion is to document the procedure used to generate the secondary flow field results presented in this paper. The same procedure is applied to both the computational and experimental results.

The secondary flows presented in this paper are defined as the departure of the local relative velocity vector from the local streamwise grid direction. The secondary velocity vector is given by $\mathbf{V}_T - \mathbf{V}_g$, where $\mathbf{V}_T$ is the relative velocity vector and $\mathbf{V}_g$ is the projection of $\mathbf{V}_T$ in the local streamwise grid direction, $\mathbf{g}(r, \theta, z)$. The spanwise and pitchwise components of the secondary velocity vector, V_s and V_p are the projections of the secondary velocity vector in the local spanwise and pitchwise grid directions, as given by the two dot products

$$V_s = (\mathbf{V}_T - \mathbf{V}_g) \cdot \hat{g}_s$$

$$V_p = (\mathbf{V}_T - \mathbf{V}_g) \cdot \hat{g}_p \tag{4}$$

where $\hat{g}_s$ and $\hat{g}_p$ are unit vectors in the local spanwise and pitchwise grid directions. When secondary flow results are presented in the form of vector plots in a quasi-orthogonal plane, V_s and V_p are used to determine the magnitude and direction of the plotted secondary velocity vectors.

The procedure described above is applied at each measurement grid node when processing experimental data and at each CFD grid node when processing CFD results. Thus a flow field with no secondary flow components will appear as a point at each grid node, indicating that the flow is following the streamwise grid direction. Since the local streamwise grid direction is parallel to the blade, hub, and shroud surfaces, the definition of secondary flow presented above also insures that the secondary velocity is zero at all solid surfaces.

The quasi-meridional velocity component, V_{qm}, is the vector projection of the meridional velocity vector, $\mathbf{V}_m$, in the local streamwise grid direction, $V_{qm} = \mathbf{V}_m \cdot \hat{g}_m$. Since a quasi-orthogonal plane is nearly normal to the streamwise grid direction in the meridional plane at any station in the impeller, V_{qm} is a close approximation to the throughflow velocity that crosses a quasi-orthogonal plane. V_{qm} is also a close approximation to the streamwise velocity component measured in laser anemometer investigations published by previous authors (Krain, 1988; Ahmed and Elder, 1990; Fagan and Fleeter, 1991). In these investigations, the streamwise velocity component was defined as the velocity component in the direction tangent to the shroud meridional direction at each measurement station.

However, in a geometrically complex channel such as a centrifugal impeller blade passage, the streamwise direction can be defined in several different ways, and each definition will yield a slightly different result for the secondary flow. This problem has been pointed out by many previous authors. The purpose of the following discussion is to document the procedure used to generate the secondary flow field results presented in this paper. The same procedure is applied to both the computational and experimental results.

The secondary flows presented in this paper are defined as the departure of the local relative velocity vector from the local streamwise grid direction. The secondary velocity vector is given by $\mathbf{V}_T - \mathbf{V}_g$, where $\mathbf{V}_T$ is the relative velocity vector and $\mathbf{V}_g$ is the projection of $\mathbf{V}_T$ in the local streamwise grid direction, $\mathbf{g}(r, \theta, z)$. The spanwise and pitchwise components of the secondary velocity vector, V_s and V_p are the projections of the secondary velocity vector in the local spanwise and pitchwise grid directions, as given by the two dot products

$$V_s = (\mathbf{V}_T - \mathbf{V}_g) \cdot \hat{g}_s$$

$$V_p = (\mathbf{V}_T - \mathbf{V}_g) \cdot \hat{g}_p \tag{4}$$

where $\hat{g}_s$ and $\hat{g}_p$ are unit vectors in the local spanwise and pitchwise grid directions. When secondary flow results are presented in the form of vector plots in a quasi-orthogonal plane, V_s and V_p are used to determine the magnitude and direction of the plotted secondary velocity vectors.

The procedure described above is applied at each measurement grid node when processing experimental data and at each CFD grid node when processing CFD results. Thus a flow field with no secondary flow components will appear as a point at each grid node, indicating that the flow is following the streamwise grid direction. Since the local streamwise grid direction is parallel to the blade, hub, and shroud surfaces, the definition of secondary flow presented above also insures that the secondary velocity is zero at all solid surfaces.

The quasi-meridional velocity component, V_{qm}, is the vector projection of the meridional velocity vector, $\mathbf{V}_m$, in the local streamwise grid direction, $V_{qm} = \mathbf{V}_m \cdot \hat{g}_m$. Since a quasi-orthogonal plane is nearly normal to the streamwise grid direction in the meridional plane at any station in the impeller, V_{qm} is a close approximation to the throughflow velocity that crosses a quasi-orthogonal plane. V_{qm} is also a close approximation to the streamwise velocity component measured in laser anemometer investigations published by previous authors (Krain, 1988; Ahmed and Elder, 1990; Fagan and Fleeter, 1991). In these investigations, the streamwise velocity component was defined as the velocity component in the direction tangent to the shroud meridional direction at each measurement station.

DISCUSSION

J. Moore[1] and J. G. Moore[1]

This paper is a welcome milestone in NACA/NASA studies of large-scale centrifugal compressor impeller flows. These experimental measurements in the Low-Speed Centrifugal Compressor Facility were made to provide "benchmark" data for the verification of three-dimensional viscous flow codes and to aid in the development of more sophisticated models of the various physical phenomena occurring in centrifugal compressors. This study with a 60-in. diameter wheel is the modern equivalent of the earlier NACA study with the 48-in. wheel (Hamrick, 1956).

To aid this study we performed a series of three computational investigations (Moore and Moore, 1988, 1990a, 1990b). First, we calculated the flow and performance of the NACA 48-in. impeller at design and off-design conditions. Next, we predicted the flow in the NASA 60-in. wheel at design conditions with a tip clearance gap varying from 2.6 percent of the hub–shroud blade height at the impeller inlet to 4.0 percent of the blade height at the exit. Then we made a computational prediction of the possible effects of curvature and rotation on turbulence and thus on the flow development in the NASA wheel.

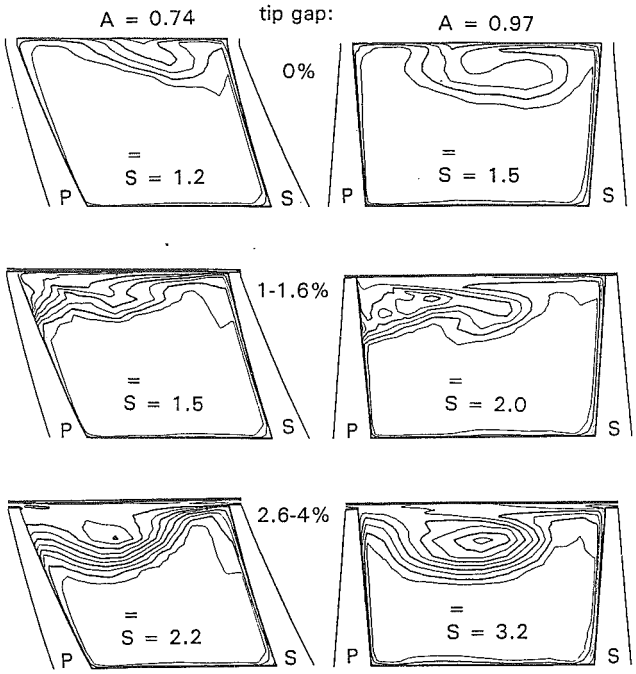

Fig. 14 Calculated entropy contours in the NASA 60-in. impeller for three tip gap heights; results at 74 percent of meridional distance and near the impeller exit; contour interval σs = 2J/kgK

Partly as a result of our predictions, the tip clearance gap for the tests in the present paper was reduced; it varies from 1.2 to 1.8 percent of local blade height, approximately one half of the clearance gap we used. Figure 14 shows results of our prediction of the effect of varying the tip clearance gap on the flow in the 60-in. impeller. The calculation method was the same as described by Moore and Moore (1990a). With tip leakage flow, the entropy contours show the high loss or wake fluid to be spread from the pressure-side/shroud corner to midshroud. Without tip leakage, the high loss fluid accumulates near the shroud toward the suction side. The tip leakage flow produces higher losses and convects them toward the pressure side.

To predict the effects of curvature and rotation on turbulence in the NASA wheel, one can calculate a gradient Richardson number based on rotation and local flow curvature and modify a mixing length for the turbulent flow. We used the following model, which applies a mean modification factor $\overline{F}$ in shear layers and the outer regions of boundary layers:

$$\mu_t = \rho L^2 \frac{"du"}{dy}$$

$$L = \text{smaller of} \quad 0.41"y"$$

$$0.08\delta\,\overline{F}$$

Van Driest correction used in $0.41y$ region

$$F = 1 - \beta\,\text{Ri} \qquad \text{for Ri} < 0$$

$$F = 1/(1 + \beta\,\text{Ri}) \qquad \text{for Ri} > 0$$

$$\beta = 4$$

[1]Mechanical Engineering Department Virginia Polytechnic Institute and State University, Blacksburg, VA 24061-0238.

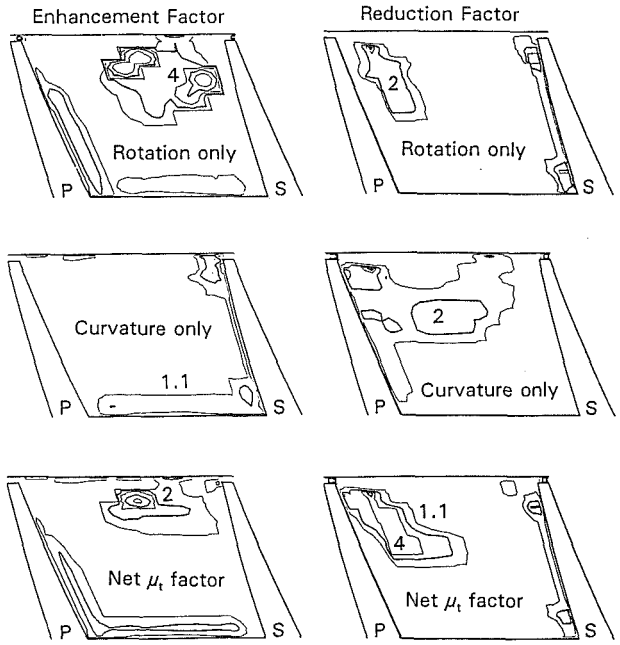

Fig. 15 Rotation/curvature modification factors, $\bar{F}^2$, for the turbulent viscosity 74 percent of the way through the impeller: left: enchancement factor contours, $\bar{F}^2$ = 1.1, 2, 4, 8, 16; right: reduction factor contours, $\bar{F}^2$ = 1/1.1, 1/2, 1/4, 1/8, 1/16

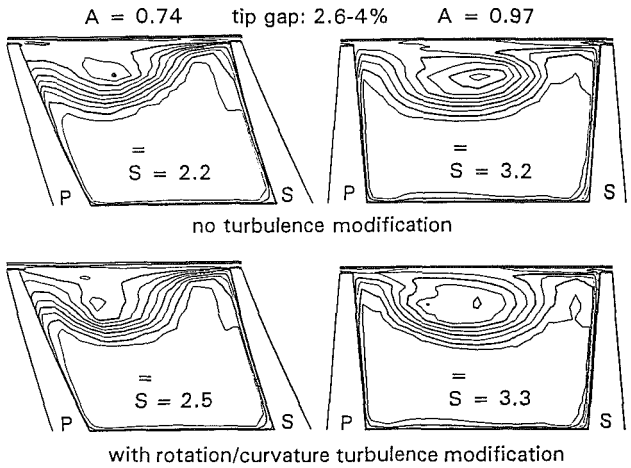

Fig. 16 Entropy contours for calculations without and with the rotation/curvature turbulent viscosity modification

$$\mathrm{Ri} = \frac{[2\mathbf{u}\times(\mathbf{u}\cdot\nabla\mathbf{u} - \Omega\times\mathbf{u})]\cdot[\mathbf{u}\times\mathbf{u}\times(\nabla\times\mathbf{u} + 2\Omega)}{[\mathbf{u}\times\mathbf{u}\cdot(\nabla\mathbf{u}^T + \nabla\mathbf{u})]^2}$$

$$\mathrm{Ri} = \frac{\text{(curv-rot) (abs vorticity)}}{\text{deformation squared}}$$

Figures 15 and 16 show results from this analysis for the NASA impeller flow with the original large tip gap (2.6–4.0 percent). In Fig. 15, the modification factors $\bar{F}^2$ for the turbulent viscosity are shown on a plane 74 percent of the meridional distance through the impeller, together with the individual contributions from rotation and curvature. The classical two-dimensional boundary layer modifications can be seen with enhancement due to rotation in the pressure side boundary layer, reduction due to rotation in the suction side boundary layer, and enhancement due to curvature on the concave hub wall. In the wake there are enhancements and reductions due to rotation where the entropy gradients are in the same sense as in the blade boundary layers. The wake also sees a reduction due to curvature near midheight where the entropy gradient is in the same sense as for a shroud wall (convex wall) boundary layer.

Overall, in Fig. 16, we see that the character of the flow development was the same with and without the turbulence modifications. The shape of the wake was slighty modified by changes in the turbulent mixing at the jet/wake boundary. There was increased mixing on the suction side of the wake leading to smaller entropy gradients, and reduced mixing on the hub and pressure sides of the wake resulting in larger entropy gradients.

We would expect these turbulence modifications, giving changes of the order of factors of two to four in turbulent viscosity, to be present and measurable in the large-scale NASA wheel. In addition, since there is significant backflow in the meridional direction along most of the shroud wall, especially with the large tip gap, we would expect enhanced turbulence near the shroud as this flow mixes to exit from the impeller. We encourage the authors and their NASA colleagues to study this interesting flow physics further.

References

Hamrick, J. T., 1956, "Some Aerodynamic Investigations in Centrifugal Impellers," *Trans. ASME*, Apr., pp. 591–602.

Moore, J., and Moore, J. G., 1988, "Secondary Flow, Separation and Losses in the NACA 48-Inch Centrifugal Impeller at Design and Off-Design Conditions," ASME Paper No. 88-GT-101.

Moore, J. G., and Moore, J., 1990b, "Effects of Curvature and Rotation on Turbulence in the NASA Low-Speed Centrifugal Compressor Impeller," *Proceedings of the 4th Annual Review Meeting of the Center for Turbomachinery and Propulsion Research*, Virginia Polytechnic Institute and State University, Blacksburg, VA, Apr.

Authors' Closure

The authors would like to thank the Moores for their continued interest in this research program and for their kind remarks regarding this paper. As previously reported (Hathaway et al., 1992), the Moores were awarded a NASA grant prior to initiation of the Low-Speed Centrifugal Compressor (LSCC) research program. This grant was to provide a calculation of the impeller flow field to determine whether any modifications might be required that would enhance the worth of the experiment to the turbomachinery community. Their predictions, together with experimental measurements, resulted in reduction of the LCSS tip clearance to avoid a shroud wall separation.

Due to the manner in which the LSCC laser anemometer data have been acquired to date, details of the three-dimensional turbulence field cannot be determined. Therefore, it is not currently possible to assess the validity of the Moores' predictions of the effects of curvature and rotation on turbulence. However, further research is planned in the LSCC that will include measurements of the level of unsteadiness of the three-dimensional velocity field. Furthermore, the authors believe that the throughflow velocity wake, which largely dominates the flow field, is an instationary vortical structure that requires further study.

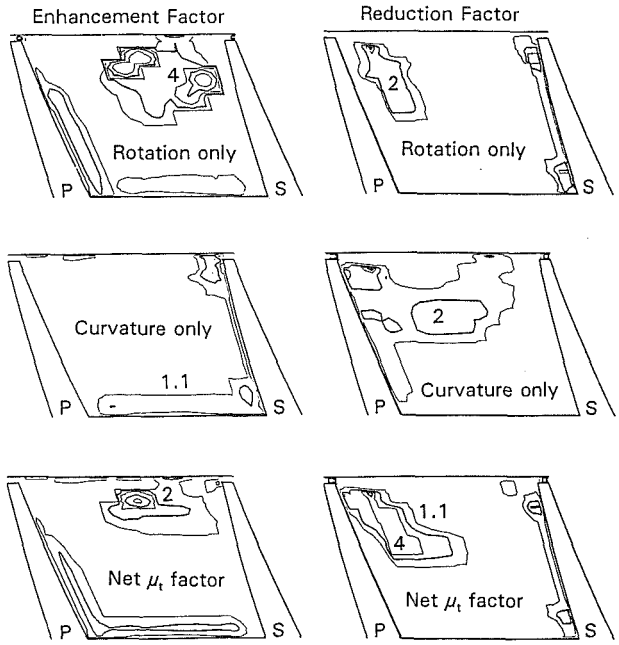

Fig. 15 Rotation/curvature modification factors, $\bar{F}^2$, for the turbulent viscosity 74 percent of the way through the impeller: left: enchancement factor contours, $\bar{F}^2$ = 1.1, 2, 4, 8, 16; right: reduction factor contours, $\bar{F}^2$ = 1/1.1, 1/2, 1/4, 1/8, 1/16

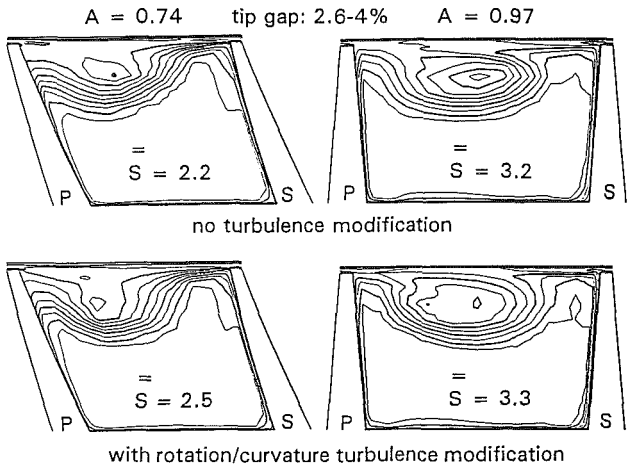

Fig. 16 Entropy contours for calculations without and with the rotation/curvature turbulent viscosity modification

$$\mathrm{Ri} = \frac{[2\mathbf{u}\times(\mathbf{u}\cdot\nabla\mathbf{u} - \Omega\times\mathbf{u})]\cdot[\mathbf{u}\times\mathbf{u}\times(\nabla\times\mathbf{u} + 2\Omega)}{[\mathbf{u}\times\mathbf{u}\cdot(\nabla\mathbf{u}^T + \nabla\mathbf{u})]^2}$$

$$\mathrm{Ri} = \frac{\text{(curv-rot) (abs vorticity)}}{\text{deformation squared}}$$

Figures 15 and 16 show results from this analysis for the NASA impeller flow with the original large tip gap (2.6–4.0 percent). In Fig. 15, the modification factors $\bar{F}^2$ for the turbulent viscosity are shown on a plane 74 percent of the meridional distance through the impeller, together with the individual contributions from rotation and curvature. The classical two-dimensional boundary layer modifications can be seen with enhancement due to rotation in the pressure side boundary layer, reduction due to rotation in the suction side boundary layer, and enhancement due to curvature on the concave hub wall. In the wake there are enhancements and reductions due to rotation where the entropy gradients are in the same sense as in the blade boundary layers. The wake also sees a reduction due to curvature near midheight where the entropy gradient is in the same sense as for a shroud wall (convex wall) boundary layer.

Overall, in Fig. 16, we see that the character of the flow development was the same with and without the turbulence modifications. The shape of the wake was slighty modified by changes in the turbulent mixing at the jet/wake boundary. There was increased mixing on the suction side of the wake leading to smaller entropy gradients, and reduced mixing on the hub and pressure sides of the wake resulting in larger entropy gradients.

We would expect these turbulence modifications, giving changes of the order of factors of two to four in turbulent viscosity, to be present and measurable in the large-scale NASA wheel. In addition, since there is significant backflow in the meridional direction along most of the shroud wall, especially with the large tip gap, we would expect enhanced turbulence near the shroud as this flow mixes to exit from the impeller. We encourage the authors and their NASA colleagues to study this interesting flow physics further.

References

Hamrick, J. T., 1956, "Some Aerodynamic Investigations in Centrifugal Impellers," *Trans. ASME*, Apr., pp. 591–602.

Moore, J., and Moore, J. G., 1988, "Secondary Flow, Separation and Losses in the NACA 48-Inch Centrifugal Impeller at Design and Off-Design Conditions," ASME Paper No. 88-GT-101.

Moore, J. G., and Moore, J., 1990b, "Effects of Curvature and Rotation on Turbulence in the NASA Low-Speed Centrifugal Compressor Impeller," *Proceedings of the 4th Annual Review Meeting of the Center for Turbomachinery and Propulsion Research*, Virginia Polytechnic Institute and State University, Blacksburg, VA, Apr.

Authors' Closure

The authors would like to thank the Moores for their continued interest in this research program and for their kind remarks regarding this paper. As previously reported (Hathaway et al., 1992), the Moores were awarded a NASA grant prior to initiation of the Low-Speed Centrifugal Compressor (LSCC) research program. This grant was to provide a calculation of the impeller flow field to determine whether any modifications might be required that would enhance the worth of the experiment to the turbomachinery community. Their predictions, together with experimental measurements, resulted in reduction of the LCSS tip clearance to avoid a shroud wall separation.

Due to the manner in which the LSCC laser anemometer data have been acquired to date, details of the three-dimensional turbulence field cannot be determined. Therefore, it is not currently possible to assess the validity of the Moores' predictions of the effects of curvature and rotation on turbulence. However, further research is planned in the LSCC that will include measurements of the level of unsteadiness of the three-dimensional velocity field. Furthermore, the authors believe that the throughflow velocity wake, which largely dominates the flow field, is an instationary vortical structure that requires further study.

Relative Flow and Turbulence Measurements Downstream of a Backward Centrifugal Impeller

M. Ubaldi

P. Zunino

A. Cattanei

Dipartimento di Ingegneria Energetica,
Universitá di Genova,
Genova, Italy

The paper presents the results of an experimental investigation on the three-dimensional relative flow at the exit of the backward bladed centrifugal impeller of the high-pressure stage of a two-stage biregulating pump-turbine model, operating at the pump nominal point. Mean velocity, Reynolds stress tensor, and total pressure of the relative flow have been measured with stationary hot-wire probes and fast response miniature pressure transducers, by means of a phase-locked ensemble-average technique. The results, shown in terms of secondary vector plots and contours of mean flow characteristics and Reynolds stress components, give a detailed picture of the flow kinematic structure and of the complex relative total pressure loss and turbulence distributions. In spite of strongly backswept blades, the flow leaving the impeller presents a jet and wake structure and an intense secondary flow activity. Large relative total pressure losses affect the wake and the region where secondary vortices interact. The turbulence data analysis provides information about the effects of the impeller rotation on the turbulence structure and about the mechanisms of the flow mixing process and of the secondary flow decay downstream of the impeller.

1 Introduction

Real flow that develops in centrifugal impellers, under the combined effects of deceleration, Coriolis force and meridional curvature acting on endwall and blade boundary layers, is very complex. The Coriolis force component perpendicular to the rotating blade surfaces also influences the boundary layer stability: On the blade suction side the turbulence production is inhibited and the boundary layer becomes prone to separation.

Comprehensive experimental and theoretical studies were done to study the physical aspects of these phenomena and to determine their effects on the impeller flow structure (Bradshaw, 1973; Moore, 1973; Johnston, 1974; Howard and Kittmer, 1975).

Experimental investigations carried out at the outlet and within radial bladed impellers showed that the above combined effects result in the typical flow configuration made of a jet and a wake, the position and extension of these two zones depending on the amount of flow deceleration and on the relative importance of Coriolis and centrifugal forces (Johnson, 1978; Johnson and Moore, 1980). The consequent circumferential disuniformity of the impeller outflow influences the flow stability in the diffuser and the efficiency of the diffusion process (Dean and Senoo, 1960; Senoo and Ishida, 1975). Backward curvature of the blades can eliminate or reduce the extent of the jet and wake flow configuration (Krain, 1988).

Most of the investigations on the impeller flow deal with centrifugal compressors (see, for example: Eckardt, 1975, 1976; Johnson and Moore, 1980, 1983; Inoue and Cumpsty, 1984; Krain, 1981, 1988), fewer concern pumps (Murakami et al., 1980; Tanabe et al., 1986, Jaberg and Hergt, 1989) or fans (Raj and Swim, 1981; Cau et al., 1987). This paper presents results of mean flow and turbulence measurements in the impeller outflow of the high-pressure stage of a pump-turbine model, operating in air as a pump. The investigation is part of an experimental research program on the performance of advanced regulating two-stage pump-turbines for high heads (Ubaldi and Zunino, 1990a, 1990b).

In this type of machine real flow phenomena are often carried to extremes, because of the design choices adopted to match opposite aerodynamic requirements of the two different operating conditions (as pump and as turbine). The impeller blades are strongly backswept as in pumps, but the outlet blade span is higher to allow for a better flow incidence in turbine operating mode. That results in a higher blade loading in pumping mode. This tendency is enhanced when the machine must operate under very high heads. In this case the designer tries to increase further the pressure rise in the impeller, in order to reduce the amount of pressure recovery in the diffuser, where very thick blades, required for structural reasons, affect the diffuser efficiency. The flow investigated, therefore, presents some analogies with that of the highly loaded radial bladed compressor impellers, and a number of relevant real flow features come out from the analysis of the experimental results.

Contributed by the International Gas Turbine Institute and presented at the 37th International Gas Turbine and Aeroengine Congress and Exposition, Cologne, Germany, June 1–4, 1992. Manuscript received by the International Gas Turbine Institute February 20, 1992. Paper No. 92-GT-212. Associate Technical Editor: L. S. Langston.

Because of the large amount of data processed and the dense distribution of points in the measuring station (one blade passage and half is described by 160×19 measuring points), the results reveal the picture of the outflow with a high degree of detail.

While systematic experimental analyses of turbulence properties were carried out in the field of axial compressors (e.g., Raj and Lakshminarayana, 1976; Ravindranath and Lakshminarayana, 1981; Inoue and Kuromaru, 1984), measurements of Reynolds stress components are not common in the literature on centrifugal machines. Examples of turbulence measurements in these machines, often concerning only the turbulence intensity, are those of Fowler (1968), Eckardt (1976), and Olivari and Salaspini (1975). Recently, Japikse and Karon (1989) have presented detailed turbulence intensity measurements in a high-speed centrifugal compressor. Kjörk and Löfdahl (1989) were able to measure five Reynolds stress components inside a centrifugal fan impeller, but their measurements regard the case of a low-speed impeller, and data at the impeller outlet are not available.

It is believed that there is still need of data on turbulence and Reynolds stress components associated with the complex flow from highly loaded centrifugal impellers. These data can be useful for a thorough understanding of the physical aspects of the flow and can give practical confirmations of theoretical hypotheses or numerical results about the phenomena that take place inside and downstream of a centrifugal impeller (rotation effects on turbulence, mechanism of jet and wake mixing, secondary flows decay). In the present investigation, efforts were spent to determine all the Reynolds stress components in the impeller outflow. The results are discussed in the paper.

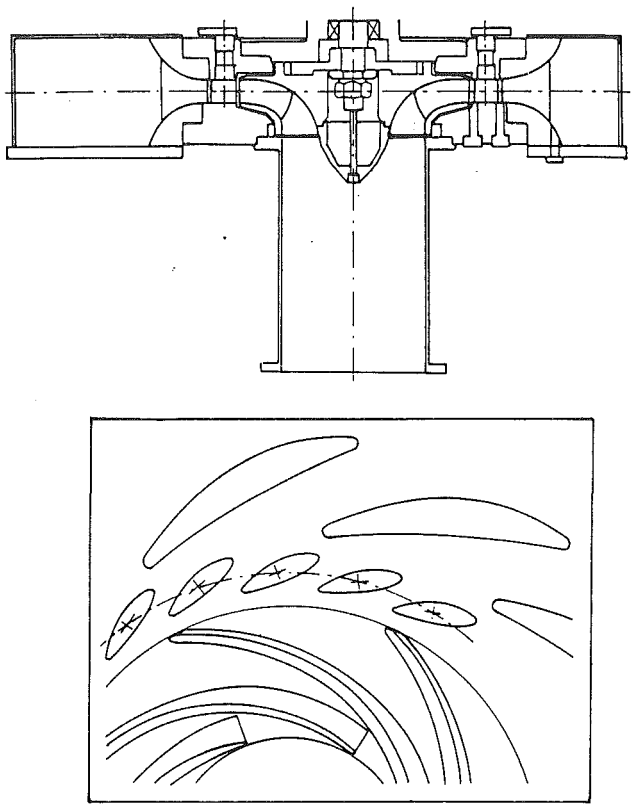

Fig. 1 Pump-turbine model

2 Experimental Procedure

2.1 Test Rig and Operating Conditions. Experiments were carried out at the University of Genoa in the high-pressure stage model of a two-stage regulating pump-turbine for high heads.

The model, shown in Fig. 1 and described in detail by Satta et al. (1988), consists of a shrouded impeller, a double vaned radial diffuser, and a rectangular scroll. The impeller, made of aluminum, has a diameter of 400 mm and seven backward blades, with an outlet blade span of 40 mm. The diffuser consists of a double row of 22 guide vanes and 11 stay vanes. The blades and the front cover of the diffuser, made of plexiglass, are instrumented with static pressure taps and inserts for probe positioning at different radial and circumferential locations. The details of the impeller design are proprietary, but the main geometric data including inlet and outlet blade angles are given in Table 1.

The rig is operated in an open circuit: The air flow enters the model through an axial inlet pipe; mass flow rate is measured by an orifice flowmeter and controlled by a throttling valve at the end of the discharge pipe. The impeller is driven at a rotational speed of 4000 rpm by a d-c electric motor and a gear box. The resulting outlet Reynolds number, based on the impeller tip speed and the diffuser width, is 2.2×10^5. The present experiment was conducted at a fixed flow rate coefficient $\varphi = 0.037$, corresponding to the nominal operating point of the pump model. The main geometric data of the model and the operating conditions are summarized in Table 1.

Nomenclature

b = outlet impeller blade span
c = absolute velocity
C_{ps} = static pressure coefficient $= 2(p_s - p_{ti})/(\rho U^2)$
C_{ptr} = relative total pressure coefficient $= 2(p_{tr} - p_{tri})/(\rho U^2)$
g = acceleration of gravity
G = circumferential pitch at the measuring station
H = pump head
k = isentropic exponent
p_s = static pressure
p_t = total pressure
p_{tr} = relative total pressure
q = turbulence kinetic energy $= (\overline{w_s'^2} + \overline{w_n'^2} + \overline{w_z'^2})/2$
Q = flow rate
r = radial coordinate
R = air constant
R_n = meridional curvature radius
R_2 = impeller outlet radius
T = temperature
Tu = turbulence intensity $= (2/3q)^{1/2}/w$
U = peripheral velocity at the impeller outlet
w = relative velocity
w' = fluctuating relative velocity
y = circumferential coordinate
z = axial coordinate
β = angle between the blade-to-blade velocity and the radial direction
β' = impeller blade angle with radial direction
γ = angle between the relative velocity and the blade to blade velocity
ν = kinematic viscosity
ρ = flow density
φ = flow rate coefficient $= Q/(U\pi R_2^2)$
ψ = head coefficient $= 2gH/U^2$

Subscripts

i = pump inlet
n = in transverse direction, from the pressure side to the suction side of the passage
r = in radial direction
s = of the primary flow
u = in circumferential direction
z = in axial direction, from hub to shroud

Superscripts

$^-$ = time average

Table 1 Geometric data and operating conditions

Impeller		
- inlet blade radius at the hub	R_{1h}	= 90 mm
- inlet blade radius at the shroud	R_{1s}	= 122 mm
- outlet radius	R_2	= 200 mm
- number of blades	N	= 7
- inlet blade angle at the hub	β'_{1h}	= -72 deg
- inlet blade angle at the shroud	β'_{1s}	= -78 deg
- outlet blade angle	β'_2	= -67 deg
- outlet blade span	b	= 40 mm
Diffuser		
Guide vane		
- chord	l_g	= 67 mm
- inlet radius	R_{gi}	= 211 mm
- outlet radius	R_{go}	= 242 mm
- number of blades	N_g	= 22
- blade span	b_g	= 40 mm
Stay vane		
- chord	l_s	= 195 mm
- inlet radius	R_{si}	= 255 mm
- outlet radius	R_{so}	= 335 mm
- number of blades	N_s	= 11
- inlet blade span	b_{si}	= 40 mm
- outlet blade span	b_{so}	= 150 mm
Operating conditions		
- rotational speed	n	= 4000 rpm
- nominal operating point	φ	= 0.037
- outlet Reynolds number	Re	$= Ub/\nu = 2.2\ 10^5$
- outlet Mach number	M	$= U/(kRT)^{1/2} = 0.24$
Inlet air reference conditions		
- temperature	T	= 298 K
- air density	ρ	= 1.2 kg/m³

2.2 Instrumentation and Measuring Techniques. Constant-temperature hot-wire anemometer and fast response semi-conductor pressure transducers were used to measure the unsteady velocity and total pressure at the impeller outlet. A phase-locked sampling and ensemble-averaging technique (Lakshminarayana, 1981) was applied to reconstruct the rotor flow field from the instantaneous signals of the stationary probes. This procedure allows separating the periodic component at the blade passing frequency from the random components due to turbulence, vortex shedding, and other fluctuations not correlated with rotor speed. The reference signal required for the phase-locked procedure was provided by a reflecting element glued on the shaft and a receiving photo cell.

Seven hundred records, each of 160 data corresponding to the circumferential positions, were digitized at a frequency rate of 50 kHz by means of a 12 bit A/D converter board and a trigger-alarm module (Burr Brown PCI-20019M, 20020M), mounted on a personal computer. The frequency rate was selected in order to cover a blade passage with a number of about 100 points, sufficient to describe the details of the impeller outflow and to resolve the wakes behind the blades. In order to produce statistically accurate results for mean and root mean square fluctuating cooling velocity, the number of data records used for the ensemble-averaging procedure was selected as the maximum allowable by the data acquisition software.

The measurement position was located at $r/R_2 = 1.03$ and the probes were circumferentially centered over the diffuser passage, to reduce the upstream influence of the vane leading edges on the impeller outflow. Detailed measurements on the effect of a vaned diffuser on the impeller flow are given by Krain (1981) and Inoue and Cumpsty (1984). The study of this phenomenon is beyond the scope of the present paper, but preliminary instantaneous velocity measurements have been performed at the impeller outlet for various circumferential positions between two adjacent diffuser vanes. The time traces of relative velocity and flow angle were similar to each other for large part of the diffuser passage, but near the suction side of the vane they varied markedly with strong depression of the relative velocity and large variations of the relative flow angle within the impeller blade circumferential pitch.

The probes were introduced from the front cover, perpendicularly to the diffuser wall, and traversed in axial direction from hub to shroud. Data were acquired for 19 axial locations and 160 circumferential sampling points.

A standard hot-wire unit (Dantec 55M10 and 55M17), a low pass filter, and miniature single sensor slanted and normal probes (models 55P11 and 55P12) were used for the measurement of the instantaneous velocity. Sensors were tungsten wires, of 5 μm diameter and 1.25 mm length. The frequency response of the system, deduced from a square wave test, exceeded 100 kHz. The hot-wire probes were accurately calibrated for velocity magnitude and direction, before and after each measuring session (typically two axial transverses).

Instantaneous cooling velocities were numerically obtained from the hot-wire outputs, sampled, and stored in the memory of the computer, by inversion of the calibration curve, before the ensemble-averaging procedure was applied.

For each measuring point, twelve ensemble-averaged cooling velocities and twelve rms values (nine for the slanted probe and three for the normal probe) were obtained by rotating the hot-wire probes about their stems at different angular positions. This set of data was used to determine the three velocity components and the six Reynolds stress components, by solving two overdetermined systems of algebraic equations. This hot-wire analysis technique, similar to that used by Inoue and Kuroumaru (1984) to investigate the flow field and the turbulence behind an axial rotor, is described in detail by Perdichizzi et al. (1990). They showed that the use of a normal probe, in addition to the slanted one, improves considerably the accuracy of the analysis, leading to better conditioned systems of equations.

Instantaneous total pressure distributions at the impeller outlet were obtained by combination of stationary and dynamic pressure measuring systems. The true time-averaged total pressure was obtained by a miniature Kiel probe and a pneumatic system, designed according to the recommendations of Johnson (1955), while the total pressure fluctuations were measured with a miniature probe equipped with a semiconductor transducer (Entran Epil-203-013G), mounted as shown by Eckardt (1975). The use of the combined measuring technique avoids the errors on the pressure level that affect the direct pressure measurement with semi-conductor transducers, due to the relevant thermal zero shift effects.

To get circumferential total pressure distributions at the rotor exit, the instantaneous pressure data were ensemble averaged with the same procedure applied to the hot wire data. Then, from these absolute total pressure results and from the mean velocity components given by the hot wire measurements, the static and relative total pressure distributions were also calculated.

The following experimental uncertainties for the hot-wire results, obtained by the ensemble-averaging procedure, are expected:

- mean velocity ±2 percent
- flow angles ±2 deg
- streamwise and transverse normal Reynolds stress components ±5 percent
- spanwise normal Reynolds stress component ±20 percent
- shear stress components ±15 percent

These values are deduced from the detailed analysis of the error sensitivity and from the verification tests of the hot-wire technique, presented by Perdichizzi et al. (1990).

The uncertainty of total pressure measurements was estimated as ±2 percent and the probe axial position was achieved with an accuracy of ±0.2 mm.

3 Experimental Results and Discussion

3.1 Mean Flow Characteristics. A detailed picture of the mean impeller outflow is given by the area plots of Figs. 2–7. These contour plots show the lines of constant primary kinetic energy of the relative flow, the lines of constant relative flow angle, radial and circumferential absolute velocity components, static and relative total pressure coefficients. All these quantities are made nondimensional by the impeller tip speed or by the kinetic energy based on this speed. In addition, in Fig. 8, the secondary flow vectors are pictured on the measuring domain. The abscissa of these diagrams is the circumferential coordinate, normalized with the circumferential blade pitch at $r/R_2 = 1.03$; the ordinate is the axial distance from the hub, divided by the impeller blade span. The physical scale of the frame is modified such that the vertical scale is 2.6 times the horizontal one. Primary and secondary flow components are those in the directions tangential and normal to the undisturbed flow in the core near the center of the passage ($\beta = -70$ deg, $\gamma = 0$ deg).

In Fig. 2 there is evidence of a region of low primary kinetic energy (wake), that extends on the suction side of the passage, from about 0.25 of the span toward the shroud. In this zone the primary kinetic energy coefficient is reduced to less than 0.08, while on the pressure side it rises with steep gradient and reaches values larger than 0.17, configuring a jet region.

The classic jet and wake flow structure (Dean and Senoo, 1960), typical of radial bladed impellers, is also not uncommon for highly loaded backward impellers (Japikse and Karon, 1989; Ahmed and Elder, 1990; Sipos, 1991). In the present case, in spite of a strong backward curvature ($\beta_2' = -67$ deg), the blades are highly loaded, because of the large outlet blade span. The inlet to outlet area ratio and the rotation number are such to set the operating point in the region of transition from corner to two-dimensional stall in the Rothe and Johnston (1976) performance plot for two-dimensional rotating diffusers.

The wake region is characterized by the presence of two distinct minima that are associated with the action of the two passage vortices, induced by the Coriolis force defect. These secondary flow vortices can be clearly observed in Fig. 8, going from the pressure to the suction side of the passage, near the hub and shroud endwalls.

The wake is located near the blade suction side and its tendency toward the shroud is moderate, compared with most of the investigated centrifugal impellers. This behavior can be explained considering the secondary flow development in the impeller in terms by Rossby number $\mathrm{Ro} = w/\omega R_n$, as suggested by Johnson (1978) and Johnson and Moore (1980). In the present case the Rossby number is low, because the blade extends mainly in the radial part of the meridional channel. Therefore, in the blade boundary layer, the defect of the centrifugal force, due to the meridional curvature, that drives low-momentum fluid toward the shroud, is weak, and the location of the wake is determined mainly by the effects of the Coriolis force, acting on the endwall boundary layers in the radial part of the impeller.

Near the hub (z/b lower than 0.2), the circumferential distribution of the kinetic energy is more uniform, with contours that tend to become parallel to the hub, showing the presence of the endwall boundary layer, except in the blade wake region, where a dip of kinetic energy is localized on the suction side, very close to the hub.

Figure 3 shows a nonuniform distribution of the relative flow angle. In the middle of the passage, there is an extended

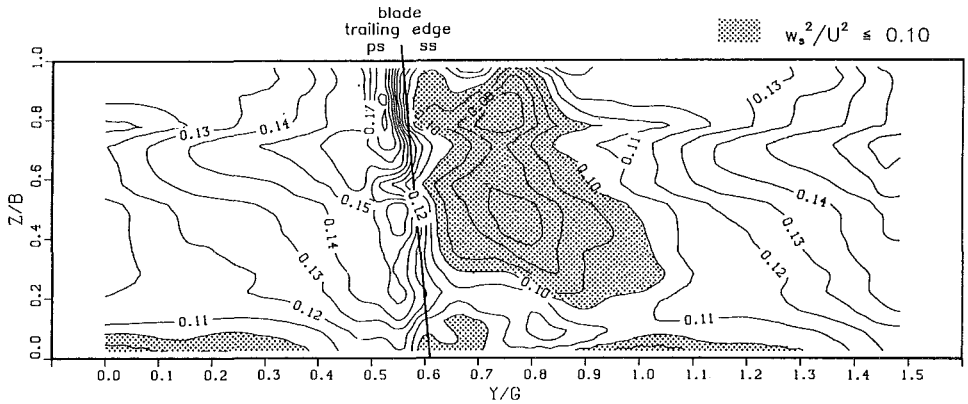

Fig. 2 Contour plot of primary kinetic energy of the relative flow w_s^2/U^2

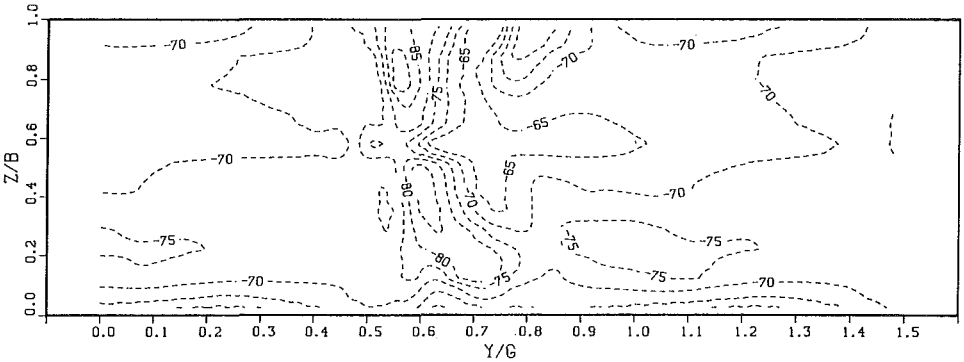

Fig. 3 Contour plot of relative flow angle β (deg)

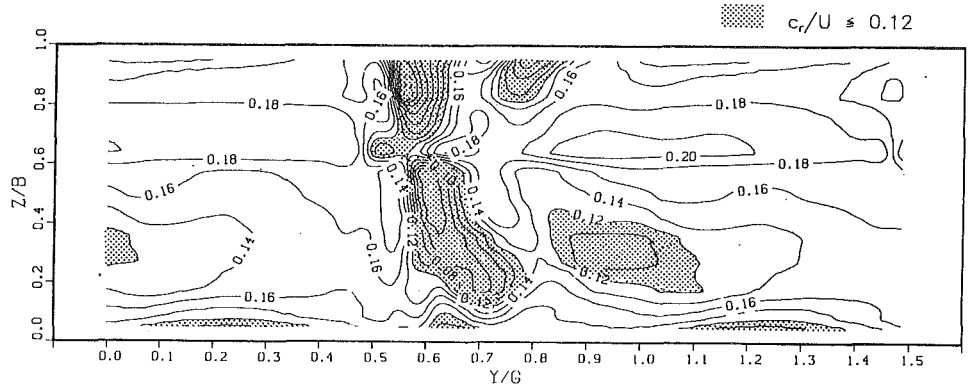

Fig. 4 Contour plot of radial velocity component c_r/U

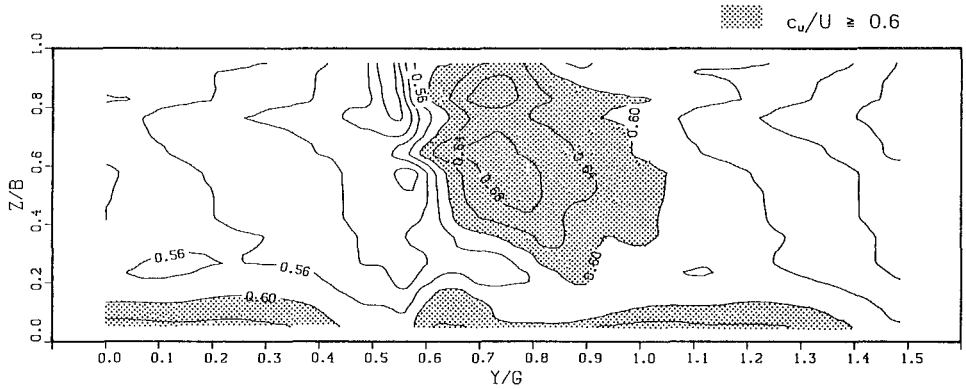

Fig. 5 Contour plot of circumferential absolute velocity component c_u/U

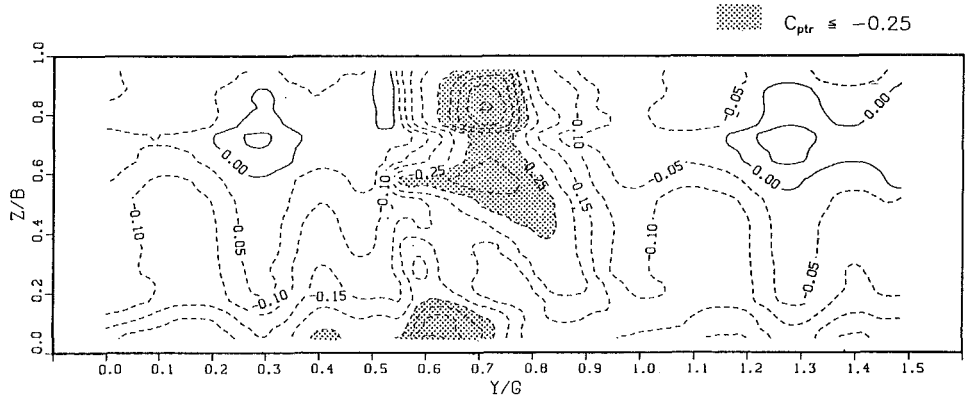

Fig. 6 Contour plot of relative total pressure coefficient C_{ptr}

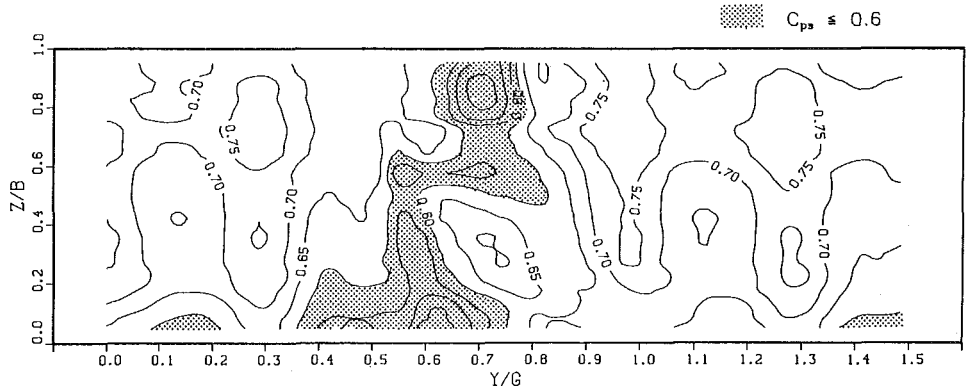

Fig. 7 Contour plot of static pressure coefficient C_{ps}

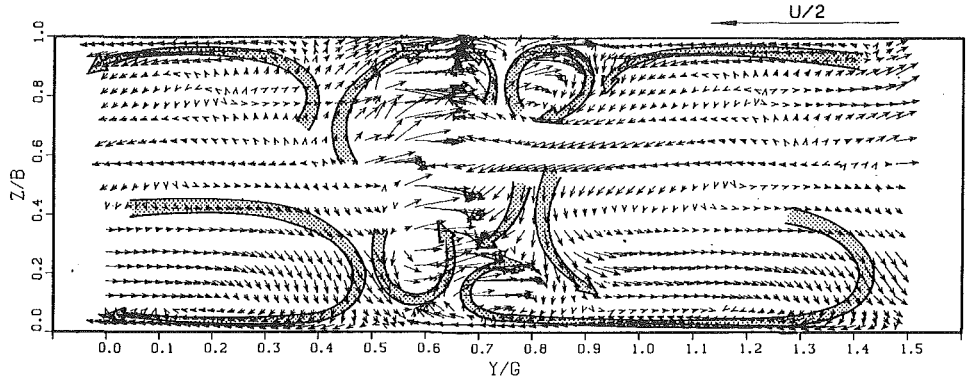

Fig. 8 Secondary flow vector plot

zone where the β angle is constant ($\beta = -70$ deg), but the jet and wake regions and the endwalls are affected by large secondary flow movements (Fig. 8) and, therefore, by large relative flow angle variations.

While the wake region tends to hold the relative flow angle close to the blade angle, the flow in the jet, on the blade pressure side, is turned against the rotation direction. The jet flow points toward the suction side, through the blade trailing edge region, and enters the wake region, enhancing the mixing process between the two zones. This behavior is in close agreement with the measurements of Japikse and Karon (1989) at the outlet of a high speed centrifugal compressor and with the secondary vector field in the section just before the outlet of the centrifugal impeller of Johnson and Moore (1983).

Near the hub endwall, the passage vortex results in changes of the relative flow angle. Going toward the endwall, first the relative flow becomes more tangential than the undisturbed one (β reaches -75 deg), then it becomes more radial (β equals -60 deg at the station nearest to the endwall).

These large variations of the relative flow angle are reflected in a distribution of the radial velocity component (Fig. 4) that is rather dissimilar to the one of the primary kinetic energy. In fact the relative velocity defect in the wake is due to the circumferential component rather than to the radial one. The defect of radial velocity is less extended and is more concentrated in a first region near the suction side of the passage and in two other regions located a little apart, toward the midpassage (one, more intense, very close to the shroud and the second, more extended, toward the hub). Furthermore, a rather thick boundary layer is present on the hub endwall. In the jet, because of the large relative flow deviations, the radial velocity is reduced, while the maximum values are shifted in a large region located in the middle of the passage.

Large flow deviations and high relative velocities reduce considerably the circumferential component of the absolute velocity (Fig. 5) and, therefore, the work exchange in the jet flow. On the contrary, for the opposite reason, a large amount of work is exchanged in the wake and near the hub endwall, where the overturning effect of the passage vortex on the absolute velocity is important. Of course, not all the work exchanged results in an increase of the absolute total pressure, because the regions of large work exchange are also those where a large loss production has taken place. Therefore the maximum absolute total pressure increase occurs in the center of the blade channel, where the loss of relative total pressure is minimum (Fig. 6).

Relative total pressure losses are mostly concentrated in the wake, especially in a well-defined core near the shroud, where the dissipation reaches about 40 percent of the dynamic pressure based on the impeller tip speed. The hub endwall region presents distributed losses, with a loss concentration on the suction side of the blade wake, where the passage vortex and the counterrotating trailing vortex interact.

Due to the additional presence of the distinct blade wake and a rather thick hub endwall boundary layer, the total relative pressure loss pattern appears more complicated than those shown in the papers of Eckardt (1975) and Johnson and Moore (1983); nevertheless, the assumptions of isentropic flow in the core and in the jet regions, and of entropy accumulation in the wake are also supported by the present results.

Figure 7 shows that the static pressure also is circumferentially not uniform. In spite of its large relative velocity, the undisturbed flow, located near the center of the passage, possesses the highest pressure. Also the jet region in the pressure side shroud corner has a rather high static pressure, because of the nondissipative nature of this flow.

The static pressure coefficient C_{ps}, which is defined as the difference between the local static pressure and the inlet total pressure, normalized by the dynamic pressure based on the impeller tip speed, can be directly compared with the head coefficient ψ, that is nearly equal to one at the nominal operating point. As shown in Fig. 7, about 70 percent of the flow pressure rise is achieved in the impeller, where losses are expected to be lower than in the high-pressure diffuser, which has very thick blades and narrow flow channels.

The secondary flow pattern of Fig. 8 appears to be very complicated. Besides the abovementioned presence of passage and trailing shed vortices and the large flow migration from the jet, other secondary flow structures may be recognized in the wake near the two minima of the primary kinetic energy. The origin of these secondary flows is not clear to the authors. Only one of these flow structures, located near the shroud, appears as a complete flow loop, which rotates against the passage vortex, like a trailing shed vortex. Between this vortex and the jet region, another secondary flow points toward the endwall and the blade wake region. Near the hub, two legs of secondary flow are direct toward the endwall, one feeding flow to the passage vortex and the other toward the low-pressure region in the blade wake.

3.2 Turbulence Characteristics. Contour plots of turbulence kinetic energy and Reynolds shear stress components of the relative flow, normalized with the squared impeller tip speed, are given in Figs. 9–12. These plots, as those of mean flow characteristics above shown, also present a good periodicity.

As shown in Fig. 9, the undisturbed flow, in the center of two adjacent blade passages, is characterized by a low turbulence kinetic energy level, while the region constituted by the jet and wake and by the blade wake presents a complicated high turbulence distribution. Comparing these turbulence contours with the diagrams of the mean flow characteristics, it is apparent that the turbulence pattern is strictly related to the mean flow field, but it does not directly reflect the jet and wake structure.

The blade wake trace, which in the contours of the kinetic

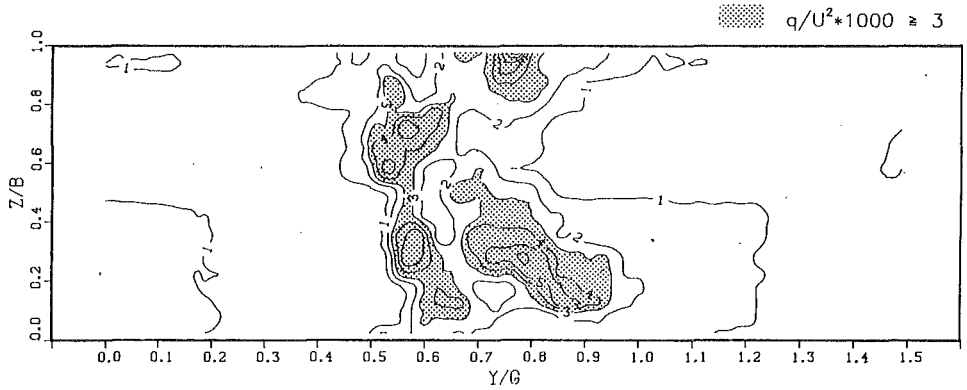

Fig. 9 Contour plot of turbulence kinetic energy $q/U^2 \times 10^3$

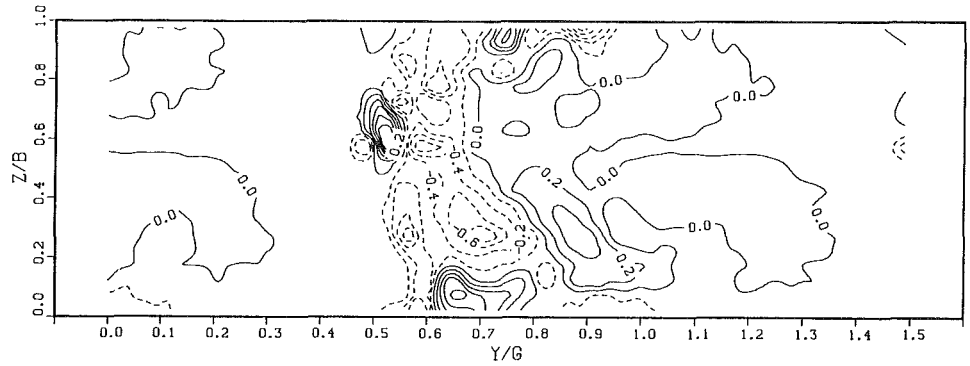

Fig. 10 Contour plot of Reynolds shear stress $\overline{w_s' w_n'}/U^2 \times 10^3$

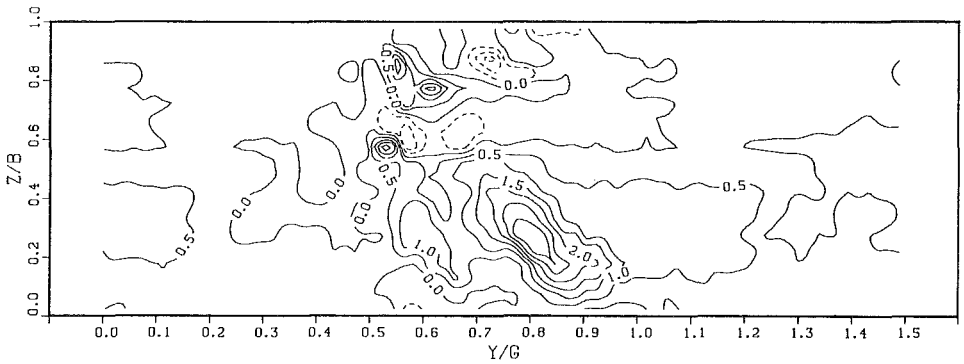

Fig. 11 Contour plot of Reynolds shear stress $\overline{w_s' w_z'}/U^2 \times 10^3$

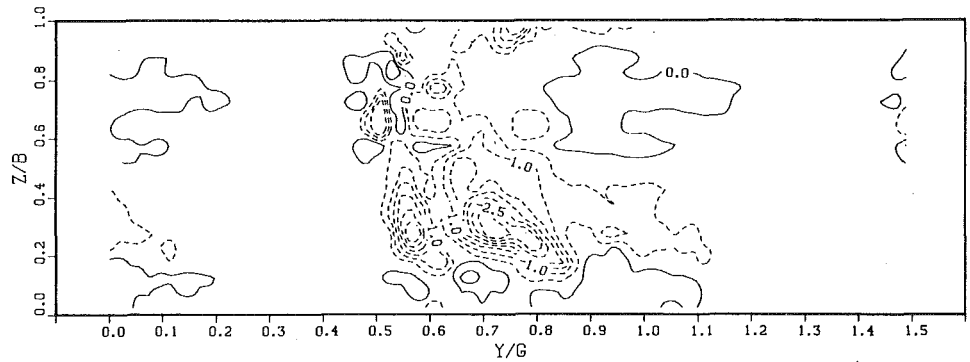

Fig. 12 Contour plot of Reynolds shear stress $\overline{w_n' w_z'}/U^2 \times 10^3$

energy of the relative flow was obscured by the jet and wake flow, is now more clear. High turbulence kinetic energy is present on the pressure side of the blade wake, which, especially near the shroud, is characterized by the high-velocity jet flow. On the contrary, the suction side of the blade wake, which is partly occupied by the wake flow, presents a lower level of turbulence kinetic energy. This feature, which is also in agreement with the hot-wire measurements of Olivari and Salaspini (1975), is a consequence of the Coriolis force effects on the blade boundary layer turbulence structure. As explained by Bradshaw (1973) and Johnston (1974) by means of stability considerations, the Coriolis force, operating perpendicularly to the blade surface, depresses the turbulence on the suction side and enhances it on the pressure side. This action, preventing pressure side boundary layer separation and reducing the capability of the suction side boundary layer to resist deceleration, is one of the principal mechanisms that determine the jet and wake flow, together with flow deceleration and secondary flow development.

High-turbulence kinetic energy is also present in two distinct cores, pertaining to the wake, that correspond to the regions of interaction of the two counterrotating secondary flow structures observed in the wake near the hub and the shroud. Probably the turbulence is in part convected here by the action of the passage vortices and by the meridional curvature effects and, partly, has been generated by the vortex interactions. From the analysis of the single normal Reynolds stress components (not shown in the paper) it appears that the turbulence is not isotropic and that the normal Reynolds stress components in transverse and axial directions are, generally, larger than the component in streamwise direction. For example, in the core close to the shroud, the high turbulence level is mainly due to the normal Reynolds stress component in transverse direction, which is probably produced by dissipation of the corresponding secondary mean velocity component, very high near this position.

The turbulence intensity of the relative flow differs from the turbulence kinetic energy coefficient, because the turbulence kinetic energy is made nondimensional with the local relative velocity, instead of the rotor tip speed. The contours of these two quantities show some local differences due to the different velocity levels of the jet and wake flows, but the general trend is mostly unchanged and, therefore, the turbulence intensity contour plot is not shown. Values of turbulence intensity between 3 and 4 percent are characteristic of the undisturbed flow core, located near the center of the passage. In the region of high turbulence, peaks larger than 14 percent are present. These levels are in very close agreement with the ones observed in the measurements of Japikse and Karon (1989).

The Reynolds shear stress components, shown in Figs. 10–12, complete the picture giving information on the development of the turbulence properties in the impeller, as well as on the mechanisms of dissipation acting on the distorted impeller discharge flow. Solid and dashed lines are used to represent contours of constant positive and negative shear stresses, respectively.

At a first impression, the shear stress contours show a very complicated pattern. However, the overall trends seem to be explainable qualitatively in terms of the eddy viscosity concept: The shear stresses are high in the regions where also the corresponding normal stresses are and, therefore, the kinetic energy is high; the changes of sign are generally correlated with those of the velocity gradients.

The $w_s' w_n'$ stress component (Fig. 10) presents a change of sign from negative to positive approximately along a line that passes through the central region of the wake and in the relative kinetic energy dip, observed near the hub endwall. This shear stress component is much less intense (about a quarter) than the other two components. This rather surprising result agrees with some conclusions about the experiments of Senoo and Ishida (1975), who investigated the evolution of the absolute velocity distributions associated with the jet and wake structure, in a vaneless diffuser. They noticed that the velocity gradient between the wake and the jet did not change much and, therefore, concluded that the shear forces along the boundary should not give a large contribution for equalizing the velocities in the wake and jet zones. The mixing process at the impeller outlet is, therefore, mainly produced by the reversible energy exchange mechanism explained in the classic paper of Dean and Senoo (1960).

In the meridional plane, the shear stress mixing action is expected to be more intense, since the $w_s' w_z'$ stress component, mainly associated with the spanwise variations of the streamwise velocity, is rather large and is widely extended, especially in the wake region near the hub. In Fig. 11, from hub to shroud, zones of positive and negative values alternate, approximately in accord with reduction and increase of streamwise velocity in the wake region.

The $w_n' w_z'$ component (Fig. 12), which acts in the plane perpendicular to the primary flow and is associated with the secondary flow development, is the largest of the three shear stresses. The same trend was also observed in turbine blade cascades. Moore et al. (1987) showed that the work of deformation associated with this stress component causes the secondary vortices to decay, giving the largest contribution to the mixing loss production downstream of the cascade. Also downstream of this centrifugal impeller, an important dissipative effect associated with this shear stress component is expected.

The weak positive values of the $w_n' w_z'$ component observed near the hub endwall are correlated with the development of the passage vortex, which induces negative spanwise gradients of the transverse velocity in this region. It must be noticed that, in the adopted reference system, the transverse velocity is positive when directed from the pressure to the suction side of the passage.

The $\overline{w_n' w_z'}$ shear stress component is negative in the jet zone and in the regions of the wake where the vortical structures identified by means of the secondary vector plot, cause large positive transverse gradients of the spanwise velocity component.

4 Conclusions

Mean flow and turbulence measurements have been performed at the impeller outlet of a pump-turbine model with hot-wire anemometry and fast response miniature pressure transducers.

A large amount of data has been processed by means of a phase-locked and ensemble-average technique, to reconstruct kinematic and dynamic properties of the relative flow. The results show the details of the flow structure and their analysis puts in evidence some relevant features of the impeller outflow and leads to the following conclusions.

The relative velocity distribution indicates that the flow is characterized by an extended wake on the suction side of the passage and a jet on the pressure side. The flow in the wake tends to hold the direction imposed by the blade, but the jet deviates against the impeller speed and points towards the wake through the trailing edge region.

Intense secondary flows occupy the transverse plane at the impeller outlet, with evidence of the passage and trailing shed vortices and secondary flow structures localized in the wake.

Relative total pressure losses are mainly concentrated in the wake near the shroud, in the blade wake, and in the endwall boundary layer near the hub.

Turbulence kinetic energy is very high on the pressure side of the blade wake, where the jet has originated, and is lower on the suction side. The wake flow does not possess large

turbulence kinetic energy, except in those zones where secondary flow structures are observed to interact. As expected, low turbulence intensity characterizes the undisturbed flow core near the center of the passage.

Reynolds stress components are large in the meridional and crossflow planes, but rather low in the blade-to-blade plane. These results support the hypothesis that downstream of the impeller a large dissipative action of the turbulence acts against the secondary velocities and that the flow mixing process in the circumferential direction is nearly isentropic.

Acknowledgments

This work has been carried out with the support of C.N.R. and M.U.R.S.T. The authors are also grateful to Riva-Hydroart S.p.A., Milan, for having supplied the pump-turbine model within a national research program on reversible hydraulic machines for high heads.

References

Ahmed, N. A., and Elder, R. L., 1990, "Flow Investigation in a Small High Speed Impeller Passage Using Laser Anemometry," ASME Paper No. 90-GT-233.

Bradshaw, P., 1973, "Effects of Streamline Curvature on Turbulent Flow," AGARDograph 169.

Cau, G., Mandas, N., Manfrida, G., and Nurzia, F., 1987, "Measurements of Primary and Secondary Flows in an Industrial Forward-Curved Centrifugal Fan," ASME Paper No. 87-FE-4.

Dean, R. C., and Senoo, Y., 1960, "Rotating Wakes in Vaneless Diffusers," ASME *Journal of Basic Engineering*, Vol. 82, pp. 563–574.

Eckardt, D., 1975, "Instantaneous Measurements in the Jet-Wake Discharge Flow of a Centrifugal Compressor Impeller," ASME *Journal of Engineering for Power*, Vol. 97, pp. 337–345.

Eckardt, D., 1976, "Detailed Flow Investigations Within a High-Speed Centrifugal Compressor Impeller," ASME *Journal of Fluids Engineering*, Vol. 98, pp. 390–402.

Fowler, H. S., 1968, "The Distribution and Stability of Flow in a Rotating Channel," ASME *Journal of Engineering for Power*, Vol. 90, pp. 229–236.

Howard, J. H. G., and Kittmer, C. W., 1975, "Measured Passage Velocities in a Radial Impeller With Shrouded and Unshrouded Configurations," ASME *Journal of Engineering for Power*, Vol. 97, pp. 207–213.

Inoue, M., and Cumpsty, N. A., 1984, "Experimental Study of Centrifugal Impeller Discharge Flow in Vaneless and Vaned Diffusers," ASME *Journal of Engineering for Gas Turbines and Power*, Vol. 106, pp. 455–467.

Inoue, M., and Kuroumaru, M., 1984, "Three-Dimensional Structure and Decay of Vortices Behind an Axial Flow Rotating Blade Row," ASME *Journal of Engineering for Gas Turbines and Power*, Vol. 106, pp. 561–569.

Jaberg, H., and Hergt, P., 1989, "Flow Patterns at Exit of Radial Impellers at Part Load and Their Relation to Head Curve Stability," *Proceedings 3rd ASCE/ASME Conference*, San Diego, CA, pp. 213–225.

Japikse, D., and Karon, D. M., 1989, "Laser Transit Anemometry of a High Speed Centrifugal Compressor," ASME Paper No. 89-GT-155.

Johnson, M. W., 1978, "Secondary Flows in Rotating Bends," ASME *Journal of Engineering for Power*, Vol. 100, pp. 553–560.

Johnson, M. W., and Moore, J., 1980, "The Development of Wake Flow in a Centrifugal Impeller," ASME *Journal of Engineering for Power*, Vol. 102, pp. 382–390.

Johnson, M. W., and Moore, J., 1983, "Secondary Flow Mixing Losses in a Centrifugal Impeller," ASME *Journal of Engineering for Power*, Vol. 105, pp. 24–32.

Johnson, R. C., 1955, "Averaging of Periodic Pressure Pulsations by a Total Pressure Probe," NACA TN 3568.

Johnston, J. P., 1974, "The Suppression of Shear Layer Turbulence in Rotating Systems," NASA SP-304, pp. 207–250.

Kjörk, A., and Löfdahl, L., 1989, "Hot Wire Measurements Inside a Centrifugal Fan Impeller," ASME *Journal of Fluids Engineering*, Vol. 111, pp. 363–368.

Krain, H., 1981, "A Study of Centrifugal Impeller and Diffuser Flow," ASME *Journal of Engineering for Power*, Vol. 103, pp. 688–697.

Krain, H., 1988, "Swirling Impeller Flow," ASME JOURNAL OF TURBOMACHINERY, Vol. 110, pp. 122–128.

Lakshminarayana, B., 1981, "Techniques for Aerodynamic and Turbulence Measurements in Turbomachinery Rotors," ASME *Journal of Engineering for Power*, Vol. 103, pp. 374–392.

Moore, J., 1973, "A Wake and a Eddy in a Rotating, Radial-Flow Passage," ASME Papers Nos. 73-GT-57 and 73-GT-58.

Moore, J., Shaffer, D. M., and Moore, J. G., 1987, "Reynolds Stresses and Dissipation Mechanisms Downstream of a Turbine Cascade," ASME JOURNAL OF TURBOMACHINERY, Vol. 109, pp. 258–267.

Murakami, M., Kikuyama, K., and Asakura, E., 1980, "Velocity and Pressure Distributions in the Impeller Passages of Centrifugal Pumps," ASME *Journal of Fluids Engineering*, Vol. 102, pp. 420–426.

Olivari, D., and Salaspini, A., 1975, "Measurement of Velocity Distribution at the Impeller Exit of a Radial Compressor," VKI Technical Note No. 106.

Perdichizzi, A., Ubaldi, M., and Zunino, P., 1990, "A Hot Wire Measuring Technique for Mean Velocity and Reynolds Stress Components in Compressible Flow," *Proceedings of the 10th Symposium on Measuring Techniques for Transonic and Supersonic Flows in Cascades and Turbomachines*, VKI, Bruxelles, Belgium, Paper 8.

Raj, R., and Lakshminarayana, B., 1976, "Three Dimensional Characteristics of Turbulent Wakes Behind Rotors of Axial Flow Turbomachinery," ASME *Journal of Engineering for Power*, Vol. 98, pp. 218–228.

Raj, D., and Swim, W. B., 1981, "Measurements of the Mean Flow Velocity and Velocity Fluctuations of an FC Centrifugal Fan Rotor," ASME *Journal of Engineering for Power*, Vol. 103, pp. 393–399.

Ravindranath, A., and Lakshminarayana, B., 1981, "Structure and Decay Characteristics of Turbulence in the Near and Far-Wake of a Moderately Loaded Compressor Rotor-Blade," ASME *Journal of Engineering for Power*, Vol. 103, pp. 131–140.

Rothe, P. H., and Johnston, J. P., 1976, "Effects of System Rotation on the Performance of Two-Dimensional Diffusers," ASME *Journal of Fluids Engineering*, Vol. 98, pp. 422–430.

Satta, A., Ubaldi, M., and Zunino, P., 1988, "An Experimental Investigation of the Flow in a Pump-Turbine Model Operating as a Pump," *L'Energia Elettrica*, Vol. LXV, No. 6, pp. 259–270 [in Italian].

Senoo, Y., and Ishida, M., 1975, "Behavior of Severely Asymmetric Flow in a Vaneless Diffuser," ASME *Journal of Engineering for Power*, Vol. 97, pp. 375–387.

Sipos, G., 1991, "Secondary Flow and Loss Distribution in a Radial Compressor With Untwisted Backswept Vanes," ASME JOURNAL OF TURBOMACHINERY, Vol. 113, pp. 686–695.

Tanabe, S., Ikegawa, M., Tanaka, Y., Yoshinaga, Y., and Yokogama, T., 1986, "A Study on Internal Flow of a Centrifugal Runner," *Proceedings of IAHR*, Montréal, Canada, Vol. 2, Paper No. 49.

Ubaldi, M., and Zunino, P., 1990a, "Experimental Study of the Flow Diffusion in a Pump-Turbine at Different Operating Points," *Proceedings of ISROMAC-3*, Honolulu, HI, Vol. 1.

Ubaldi, M., and Zunino, P., 1990b, "Experimental Investigation of the Stalled Flow in a Centrifugal Pump-Turbine With Vaned Diffuser," ASME Paper No. 90-GT-216.

Investigations on a Radial Compressor Tandem-Rotor Stage With Adjustable Geometry

B. Josuhn-Kadner
Lehrstuhl für Fluidenergiemaschinen,
Ruhr-Universität Bochum,
Bochum, Federal Republic of Germany

B. Hoffmann
Institut für Antriebstechnik,
DLR Köln,
Federal Republic of Germany

A radial compressor stage has been investigated mainly experimentally for aerodynamic stage optimization. The rotor ($\pi_t = 3.9$) consists of a profiled axial inducer and a conventionally designed radial impeller. Inducer and impeller can be locked at different circumferential positions relative to each other, thus forming a tandem wheel with adjustable geometry. Conventional and Laser-2-Focus system measurements for the tandem rotor and the stage were performed at different operating points to study the influence of the circumferential clearance geometry between inducer and impeller with respect to compressor characteristics and performance. Furthermore, three-dimensional Navier–Stokes calculations are being developed at design point condition to analyze the flow field. A small influence of the inducer adjustment on the rotor characteristics is observed. The maximum rotor efficiency of 93.5 percent varies in a range of less than 1 percent depending on the different inducer positions.

Introduction

Two decelerating blade profiles placed one after the other with an axial clearance x_s and a circumferential displacement y_s are called tandem blades. For example, a tandem-bladed axial compressor rotor is shown in Fig. 1. In general with such an arrangement a separation and new start of the blade boundary layer can be achieved and higher blade loading are possible.

Many publications dealing with tandem blades in axial turbomachines and cascades used as a medium of aerodynamic optimization were published in the past. For radial turbomachines only a few were presented up to now and will be discussed below.

A very detailed study of the influence of different tandem-blade configurations on the characteristics of a radial pump was presented by Gostelow and Watson (1972). Improvements of the operating range, efficiency, and cavitation were observed for different inducer positions. A much better suction performance with a tandem-bladed pump was found by Takamatsu et al. (1980). For centrifugal compressors such systematic variations of the rotor geometry have not been published up to now.

Reported studies of centrifugal rotors with tandem blades were given by Klassen (1977) and Reeves and Schweitzer (1974) with the objective of carrying out a reduction of a supersonic flow at inducer inlet to a subsonic one at inducer exit with minimum loss. The separation and new start of the boundary layer at the inducer trailing edge was judged as an advantage, but no circumferential displacement of the inducer was investigated.

Studies have been made by Knapp (1979) and Boyce and Nishida (1977) with modified conventionally designed radial compressor rotors, which were cut into an inducer and impeller part and were locked relative to each other with circumferential displacement. The influence of the varied rotor geometry on the rotor performance is judged as negligible by Knapp (1979) and effective for avoiding impeller flow separation by Boyce and Nishida (1977). Other investigations of tandem-bladed radial turbomachines were carried out by Lindner and Kramer (1985) and Gui et al. (1989) at very low Mach numbers with the result of an improved efficiency and balanced impeller flow field.

Comparing all published papers on tandem-bladed centrifugal compressor rotors, there are very contradictory statements

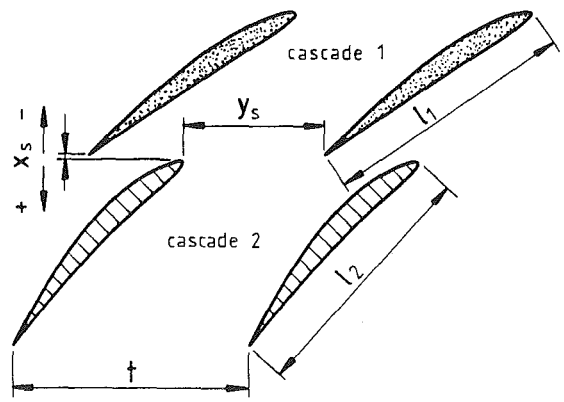

Fig. 1 Blade profiles of a tandem cascade (modified from Turanskyi, 1985

Contributed by the International Gas Turbine Institute and presented at the 37th International Gas Turbine and Aeroengine Congress and Exposition, Cologne, Germany, June 1–4, 1992. Manuscript received by the International Gas Turbine Institute February 20, 1992. Paper No. 92-GT-218. Associate Technical Editor: L. S. Langston.

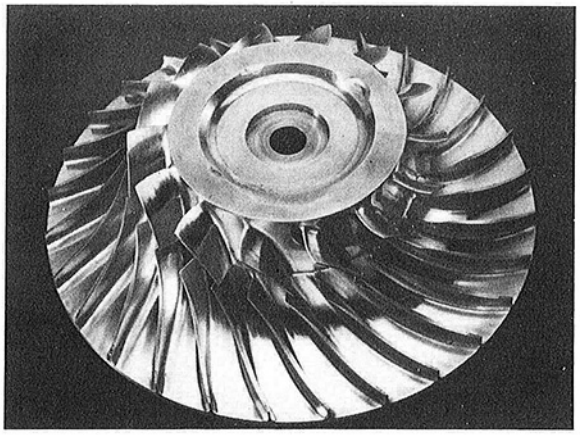

Fig. 2 Radial compressor rotor with axial inducer and radial impeller

of the attainable improvements of such a blade arrangement so that no design rules are available. In contrast to this knowledge, the present paper gives additional information for the rotor and stage characteristics and impeller flow field of a new tandem-bladed rotor with the following combination of main features:

- High subsonic Mach number ($M_{rel,1,T} = 0.95$) and medium rotor pressure ratio ($\pi_{t,12} = 3.9$) with a high rotor efficiency level ($\eta_{t,12} = 93.3$ percent).
- Profile and aerodynamically optimized inducer.
- Systematic investigations with different circumferential inducer positions for different operating points.

Tandem-Bladed Rotor

The centrifugal compressor stage is equipped with a backswept tandem-bladed rotor (Fig. 2) and a vaneless diffuser with parallel side walls. The complete rotor consists of an axial inducer part with 14 blades designed by means of five radially profile cuts and a radial impeller part with 28 blades.

Inducer and impeller can be locked at different circumferential positions relative to each other by using Voith–Hirth serrations. The necessary boreholes and steps cause the permitted strain level to be exceeded, so that the maximum speed has to be limited to 88 percent of design speed.

The rotor was designed for an end stage of a combined axial-radial compressor with medium pressure ratio and a high efficiency level. Splitting the complete rotor into a separate inducer and an impeller (tandem rotor) will offer a better facility to influence the blade loading in the front part of the rotor (Fig. 3).

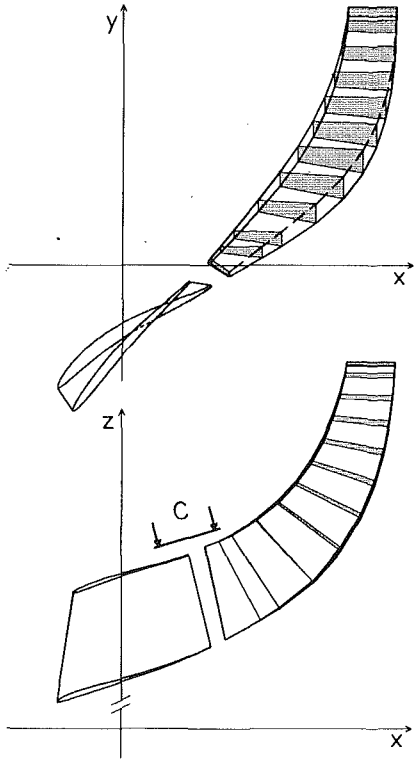

Fig. 3 Blade geometry of inducer and impeller in reference position

The inducer design of a conventional centrifugal compressor rotor is limited by geometric conditions. In contrast to these limits, a separate inducer part will facilitate a more balanced blade loading from hub to tip and a better adaption of the velocity profiles at the rotor inlet.

The work input at the hub can be increased, whereas the velocity at the shroud will be reduced. This will lead to lower deceleration losses due to the lower velocity level and the possibility to optimize the inducer blade design comparable to a profiled axial rotor with different profile cuts from hub to tip.

As a consequence of the tandem-blade design, the boundary

Nomenclature

b = channel depth
c = absolute velocity
c_p = specific heat capacity
D = diameter
DS = pressure side
k = blockage factor
$\dot{m}$ = corrected mass flow rate
M = Mach number
n = shaft speed
OP = operating point (see Fig. 7)
p = static pressure
p_t = total pressure
R = gas constant
s = parameter of clearance geometry (see Fig. 4)
s_m = meridional shroud length (= 0 at inducer leading edge)
SS = suction side
t = pitch
T = temperature
u = circumferential velocity
w = relative velocity
x, y, z = Cartesian coordinates
x_s, y_s = parameter of clearance geometry
$\bar{y}$ = dimensionless pitch
z/b = dimensionless channel depth (normal to shroud, $z/b = 1$)
β = relative blade angle (with reference to the negative circumferential direction)
η = efficiency
κ = isentropic exponent
π_s = $p/p_{t,0}$ = shroud pressure ratio
π_t = pressure ratio (total-to-total)
ρ = density
ω = angular velocity

Subscripts

0–5 = measuring planes (see Fig. 6)
12 = rotor (from plane 1 to 2)
14 = stage (from plane 1 to 4)
05 = compressor (from plane 0 to 5)
Imp = impeller
Ind = inducer
m = meridional
rel = relative
t = total or total to total
T = tip
u = circumferential velocity or direction

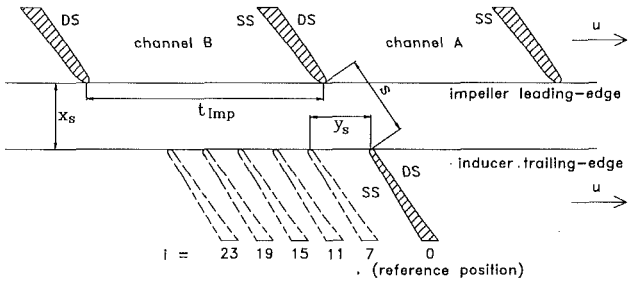

Fig. 4 Geometry of the clearance between inducer trailing edge and impeller leading edge at the shroud (see site C in Fig. 3)

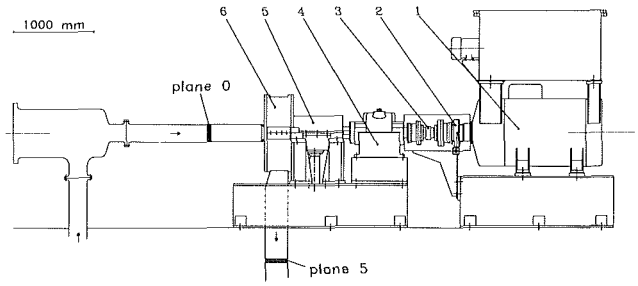

Fig. 5 Compressor test rig with inlet duct and driving equipment for closed cycle operation

layer will separate at the inducer trailing edge and will affect the impeller flow field. Furthermore, the velocity level at the impeller suction side might be increased.

The question is, whether there is any circumferential inducer position improving the rotor efficiency or balancing the impeller flow field.

Figure 3 shows the blade profiles at inducer hub and tip in reference position to the impeller. The impeller blade surfaces are constructed by straight line elements.

To reach an exact adjustment in positioning the inducer with respect to the impeller, there must be a serration with pitch angles of about one degree, which are not available for the existing diameters. Choosing the serration pitch a little bit larger than the blade pitch of the impeller allows a sufficient positioning of the inducer in steps of 0.4 deg.

Turning the inducer by one step of the serration moves the trailing edge of the inducer by one impeller pitch plus the difference of serration and impeller blade pitch (Δt).

$$\Delta t = t_{\text{Serration}} - t_{\text{Imp}} = \frac{360 \text{ deg}}{27} - \frac{360 \text{ deg}}{28} = 0.48 \text{ deg}$$

$$y_s = i \cdot \Delta t \quad (i = 0..26)$$

$$\bar{y} = \frac{y_s}{t_{\text{Imp}}} = i \cdot 3.7 \text{ [percent]}$$

In addition to the reference position, 26 more inducer positions are possible. This requires a very accurate balancing of the rotor for all inducer-to-impeller positions, especially for the maximum shaft speed.

Figure 4 shows the geometry of the effective clearance between inducer and impeller in the direction of view C in Fig. 3 with all inducer positions (i = 0, 7, 11, 15, 19, 23) investigated for the present paper. The impeller channel, which follows the trailing edge of the inducer, is always named channel B.

The distance s between inducer trailing edge and impeller leading edge is s = 3.4 mm at the hub and s = 4.4 mm at the shroud.

Table 1 Design data of centrifugal impeller

Inducer:			
tip diameter at inlet	$D_{1,T}$	=146.2	[mm]
tip diameter at exit	D_T	=151.3	[mm]
rel. Mach number	$Ma_{rel,1,T}$	= 0.95	[-]
number of blades	z	= 14	[-]
Impeller:			
diameter at exit	D_2	= 233.1	[mm]
channel width at exit	b_2	= 8.1	[mm]
Mach number (referred to the circumferential velocity at rotor exit)	$Ma_{u,2}$	= 1.29	[-]
number of blades	z	= 28	[-]
relative blade angle at exit (with reference to the negative circumferential direction)	b_2	= 58	[°]
Rotor:			
pressure ratio (total-total)	$\pi_{t,12}$	= 3.9	[-]
polytropic efficiency (total-total)	$\eta_{p,t,12}$	= 93.3	[%]
shaft speed	n	= 600	[s^{-1}]
mass flow	$\dot{m}$	= 1.2	[kg/s]

Table 2 Instrumentation of the compressor

Measuring plane:	Index	P	P_t	T_t
compressor inlet	0	4	2	3
rotor inlet	1	4	-	-
rotor	-	9	-	-
rotor exit	2	8	-	-
diffuser inlet	3	16	-	-
diffuser	-	28	-	-
diffuser exit	4	16	-	-
collecting chamber	4a	-	-	4
compressor exit	5	4	2	3

Test Rig and Instrumentation

For the experimental investigations on the centrifugal compressor stage, the test rig shown in Fig. 5 was built.

The compressor is driven by a variable speed synchronous motor (1) with a power input of 75–750 kW and a speed range of 150–1500 min^{-1}. A spur gear (4) with a gear ratio of 28 is connected with the motor by a curved teeth coupling (2) and a torque metering shaft with wire strain gages. The compressor shaft is supported by an axial/radial sliding bearing (5) and sealed with a special shaft packing of solid carbon rings (Fig. 6*a*) for low leakage losses.

The compressor itself (6) is shown in detail in Fig. 6. The inducer (c) and impeller (d) part of the rotor are locked together by a front serration (e) and the complete rotor with the compressor shaft by a rear serration (b). The diffuser (g) has parallel side walls.

The complete test rig is driven in a closed cycle by an electronic control equipment operated by light-pen on a monitor. This automatic controlling causes an accurate adjustment of compressor inlet temperature ($T_{t,0}$ = 288.1 K), inlet pressure ($P_{t,0} = 0.98 \times 10^5$ Pa), and shaft speed, respectively.

For the present investigations, the following measured variables of measuring plane 0 up to 5 (Figs. 5 and 6), given in Table 2, have been analyzed.

Wall pressure taps are used to measure the static pressure, Kiel probes are used for total pressure measurements, and

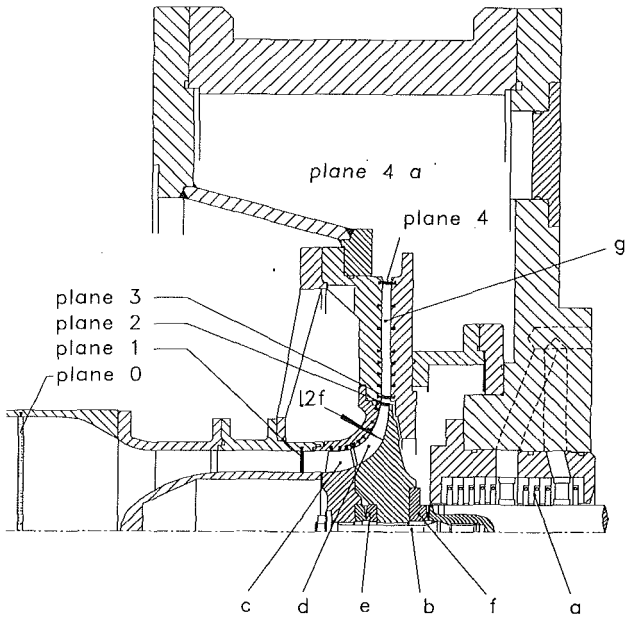

Fig. 6 Cross section of the centrifugal compressor stage with measuring planes, pressure taps (▾), and the L2F-measuring location (planes 0 and 5, see Fig. 5)

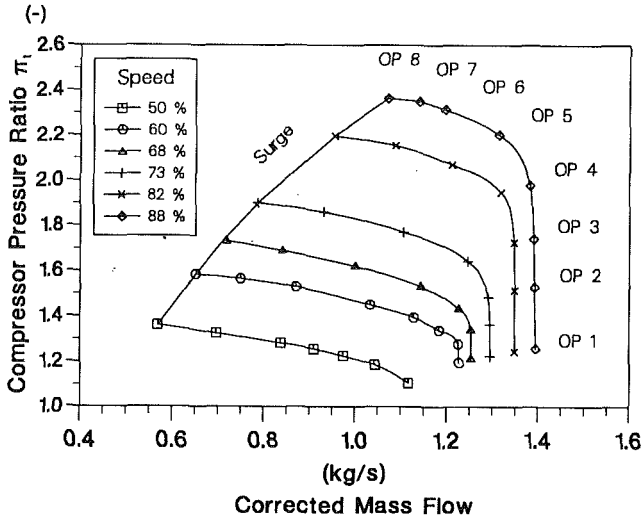

Fig. 7 Performance map of the centrifugal compressor (05) with backswept impeller and vaneless diffuser

resistance thermometers are employed to measure total temperature.

The stage mass flow is measured by an orifice in the pressure connection with regard to the leakage losses at the rotor exit.

Due to constructive reasons for this first investigation, no total pressure measurements could be carried out at the exit of the rotor and diffuser.

Therefore the following calculation is used to determine the pressure ratio and the efficiency of the rotor and the stage.

Assumptions:

one-dimensional calculation

$T_{t,0} = T_{t,1}$ and $T_{t,2} = T_{t,4}$ (adiabatic system)

$\dot{m}_0 = \dot{m}_1$ and $\dot{m}_2 = \dot{m}_4 = \dot{m}_0 - \dot{m}_{\text{leakage}}$

Calculation Procedure (iterative):

$\rho = \frac{p}{RT}$	(density)
$\dot{m} = \rho \cdot c_m \cdot k \cdot A$	(continuity equation)
$k = 1$	(full area, zero blockage)
$c_{u,1} = 0$	(no prewhirl)
$c_{u,2} = \frac{c_p(T) \cdot (T_{t,2} - T_{t,1})}{u_2}$	(tangential velocity with Euler equation)
$c_{u,3} = f(c_{u,2})$	(see note below)
$c = (c_u^2 + c_m^2)^{0.5}$	(velocity triangle)
$T = T_t - \frac{c^2}{2c_p}$	(total temperature)
$p_t = p \cdot \left(\frac{T_t}{T}\right)^{\frac{\kappa}{\kappa-1}}$	(isentropic stagnation)

Polytropic efficiency (adiabatic, total-to-total):

$$\eta = \frac{\int \frac{dp}{\rho} + \frac{\Delta c^2}{2}}{c_p(T) \cdot (T_{t,2} - T_{t,1})}$$

The flow conditions of diffuser exit have been approximated from a one-dimensional solution of the viscous, compressible flow within the diffuser taking into account the known static pressure. A description of the numerical code used can be found from Traupel (1962).

The declarations for the coefficient of wall friction (Mager, 1958) and those for the displacement thickness (Schlichting, 1965) have been incorporated.

Experimental Results

Measurements With Inducer in Reference Position. The first step in experimental investigations was to establish the compressor map with the inducer in reference position up to a maximum speed of 88 percent of design speed (Fig. 7).

At this rotational speed the compressor surges at 75 percent of the mass flow rate of choke condition. The choke conditions for the different speed lines were measured at fully opened throttle. The position of the surge line could be identified by a distinct hissing sound at a frequency of about 1 Hz. This effect could be reproduced for all speed lines. No rotating stall effect was observed by the stationary measurement technique for the last stable operating point near surge (*OP*8).

Figures 8(*a*) and 8(*b*) show, versus reduced mass flow, the ratio of total pressure and the polytropic efficiency of the compressor (05), the stage (14), and the rotor (12), respectively.

There is a remarkable drop of the lines in Fig. 8(*b*) near *OP*-1, indicating that the rotor has been choked. The lines of pressure and the laser measurements described later on show that, at choke, the impeller flow accelerates strongly up to sonic speed. Near surge, the rotor efficiency reaches 93.5 percent. This high value at low mass flow is due to the fact that the stage has been designed for a bladed diffuser with lower mass flow than the one without vanes and with parallel side walls, which is discussed here. Thus, the drop of the stage and compressor efficiency toward the surge line is due to the increase in diffuser loss.

The uncertainty of calculating the total pressure at diffuser exit explains the stronger decrease in stage efficiency compared with the compressor efficiency at low mass flow.

Figure 9 shows the stage pressure rise along a representative shroud streamline for four different operating points. At choke (*OP*1), there is an abrupt decrease of pressure at the inlet of the inducer. This is accompanied by a strongly accelerated flow. Downstream of the rotor, the splitter blade blocking

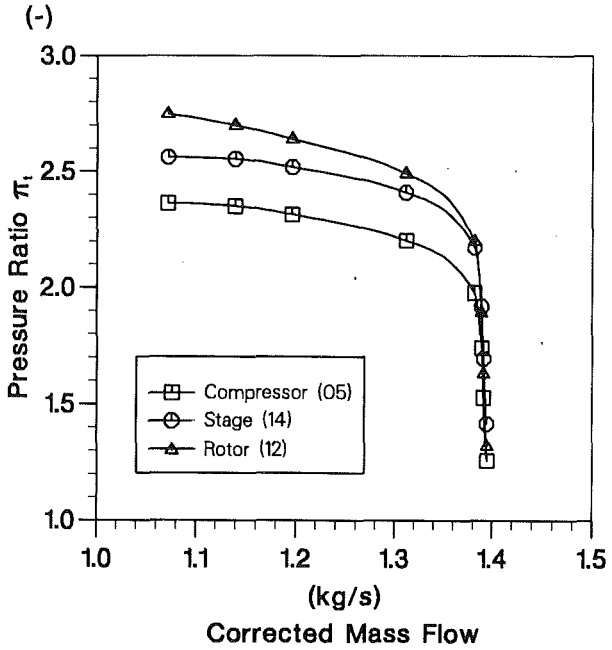

Fig. 8(*a*) Pressure ratio (total-total)

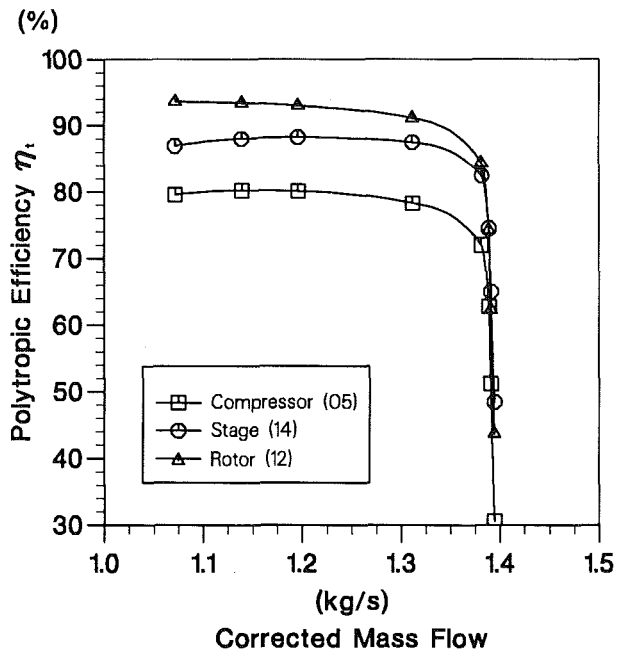

Fig. 8(*b*) Polytropic efficiency (total-total)

Fig. 8 Characteristics of the compressor (05), the stage (14), and the impeller (12) (reference position (see Fig. 4), speed: 88 percent)

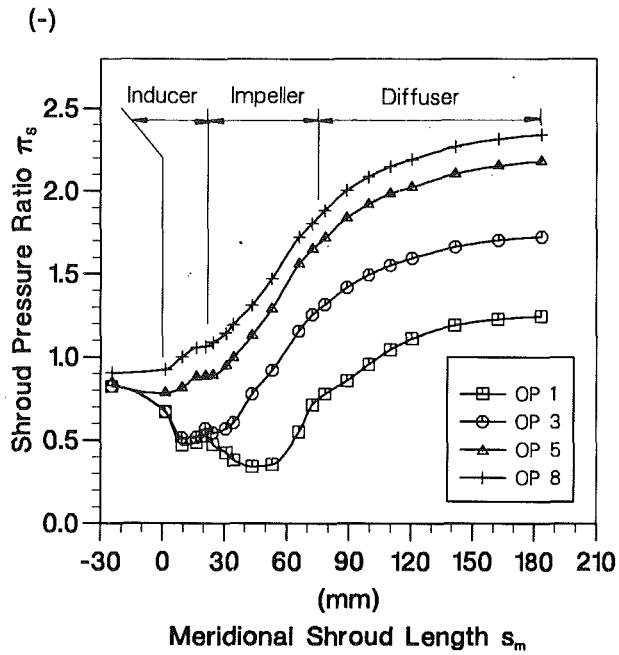

Fig. 9 Stage pressure rise for different operating points (see Fig. 7) (reference position (see Fig. 4), speed: 88 percent)

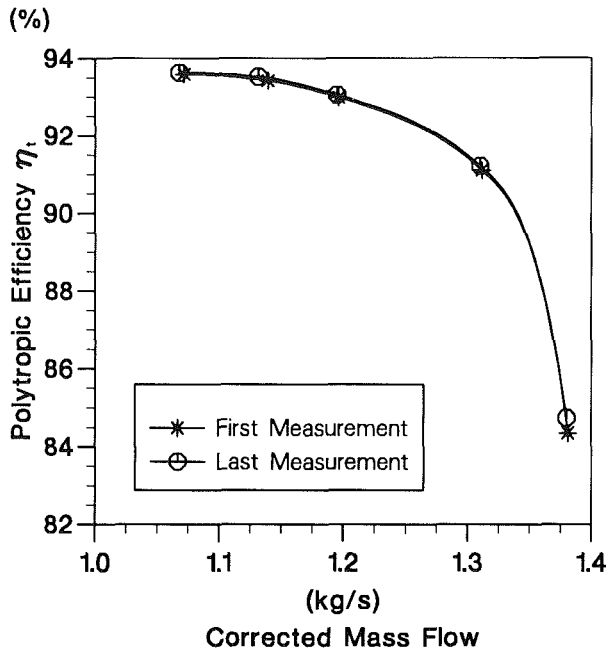

Fig. 10 Comparison of rotor efficiencies as an example of the consistency of the measuring values

induces another strong pressure drop. The corresponding accelerated flow region spreads into the radial part of the impeller (s_m = 53 mm) reaching sonic speed locally.

Assuming constant rothalpy and isentropic flow, the relative velocity may be calculated from the pressure measured at the wall. At this position, the relative velocity is w = 440 m/s and consequently it is supersonic. The corresponding laser measurements show a mean value of w = 460 m/s.

Measuring point *OP*8 near the surge line and best rotor efficiency shows a continuous pressure rise that is not decisively influenced by the pass between inducer and impeller. The deceleration ratio at the shroud for the abovementioned operating point is $w_2/w_{1,T}$=0.59.

Measurements With Different Inducer Positions

In addition to the reference position of the inducer, the circumferential positions (i = 7, 11, 15, 19, 23) sketched in Fig. 4 have been examined with regard to their influence on the characteristics of rotor and stage at the rotational speed n/n_A = 0.88.

To validate the calibrated measurement technique, the speed lines for the reference position have been measured once more. As an example for all lines, Figure 10 shows the rotor efficiency of the first and the second measurement of the reference position. They are in very good agreement. Thus, even minor deviations of the curves discussed in the following results can

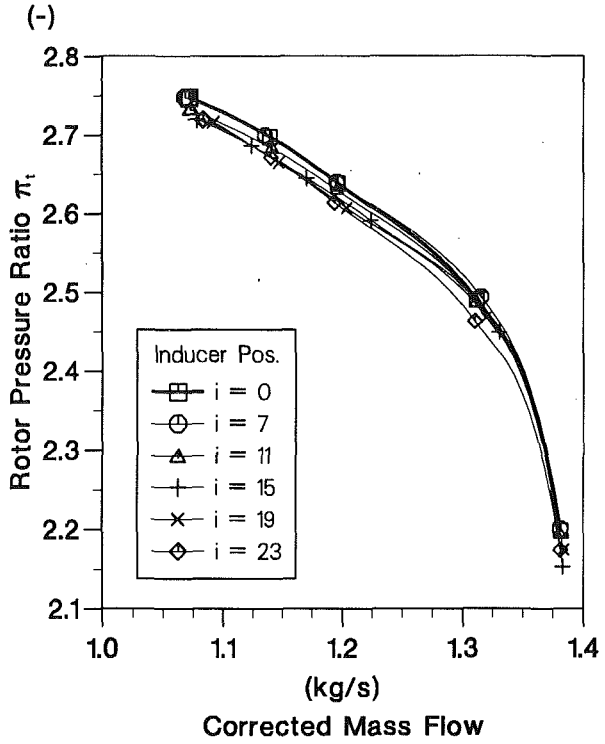

Fig. 11(*a*) Pressure ratio (total-total)

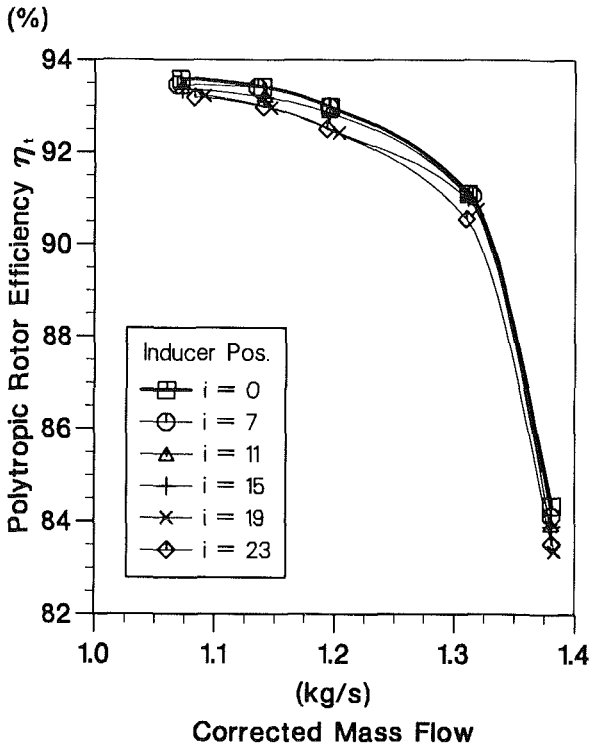

Fig. 11(*b*) Polytropic efficiency (total-total)

Fig. 11 Characteristics of the impeller (12) for different inducer positions; see Fig. 4 (speed: 88 percent)

be assumed to be certain with respect to the accuracy of measurement.

Figures 11(*a*) and 11(*b*) show the pressure ratio and polytropic efficiency for all investigated different inducer positions. All in all there is little influence of the different circumferential

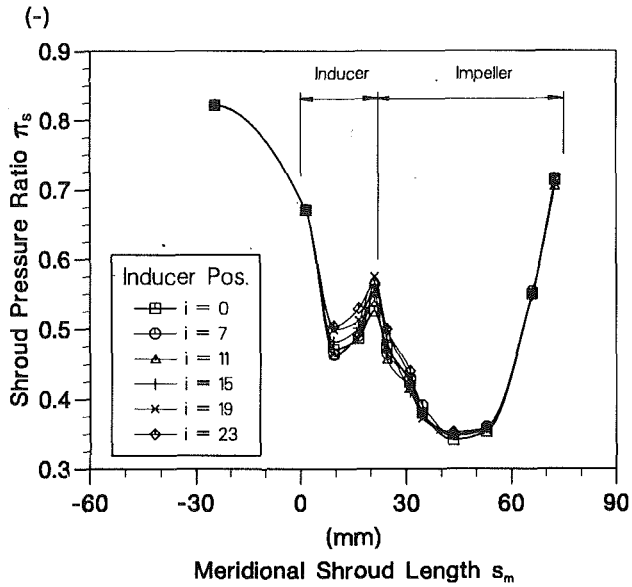

Fig. 12 Rotor pressure rise for different inducer positions (see Fig. 4) (*OP*1 (see Fig. 7), speed: 88 percent)

clearances on the characteristics due to the variable adjustment of the inducer relative to the impeller. The largest deviation in rotor efficiency is about 0.5 percent, in rotor pressure ratio 2 percent (in relation to the maximum pressure ratio of 2.75). But it is remarkable that the optimum inducer position is identically with its reference position. The adjustment of the trailing edge of the inducer toward the pressure side of the impeller ($i = 23$, $\bar{y} = 0.85$) changes for the worse. In this case choking and surge line remain nearly unchanged.

Further information of the influence on the rotor characteristics by changing the inducer-to-impeller position can be obtained from the stage pressure rise. There are only small differences for all operating points of the 88 percent speed line, especially for those with lower mass flow (*OP*4 to *OP*8). For example, the rotor pressure rise along the shroud is plotted for operating point (*OP*1) (choke) in Fig. 12. By moving the inducer trailing edge toward the pressure side of the impeller blade the pressure increases mainly within the inducer and at the inlet of the impeller.

These differences diminish toward the impeller exit and cause no remarkable change in rotor pressure ratio. Yet it must be kept in mind that the averaging stationary pressure measurement at the shroud is not able to distinguish between impeller channel A and channel B; see Fig. 4.

A more detailed insight into the rotor flow field at different inducer positions is gained from the Laser-Two-Focus (L2F) measurements inside the impeller ($s_m = 43$ mm, Fig. 6).

Figure 13 shows the velocity distribution inside channels A and B of the impeller measured with the L2F system. Despite the supersonic flow near *OP*1, the meridional velocity component c_m increases nearly linearly from the pressure to the suction side of the impeller. Minor differences between both the impeller channels sketched here are only visible at the shroud ($z/b = 1$).

A similar flow field has been depicted for operating point *OP*7. Near the shroud pressure side ($\bar{y} = 0.7$), however, a distinct minimum occurs. This effect is more pronounced within channel B and is due to the superposition of secondary flow with the tip clearance flow. Comparable velocity distributions have been observed in other rotors (Krain and Hoffmann, 1989).

Adjusting the inducer toward the pressure side of the impeller ($i = 7$, 11, Fig. 4), channel A of the impeller is not

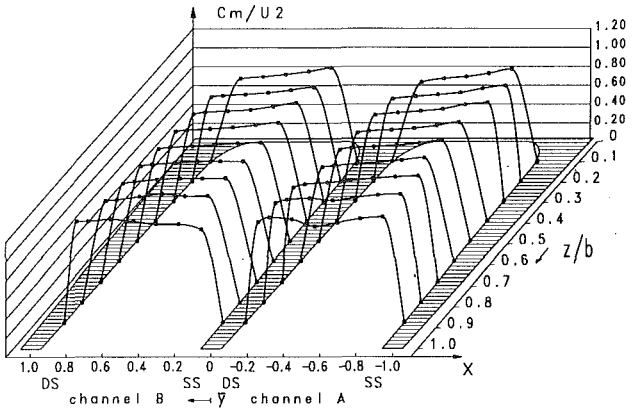

Fig. 13(*a*) Choked flow *OP*1 (see Fig. 7)

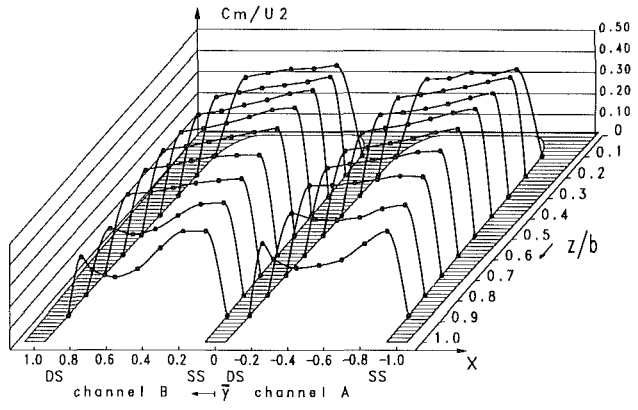

Fig. 13(*b*) Near-Surge *OP* 7 (see Fig. 7)

Fig. 13 Dimensionless meridional velocity profiles of impeller channels A and B (see Fig. 4) (reference position, speed: 88 percent)

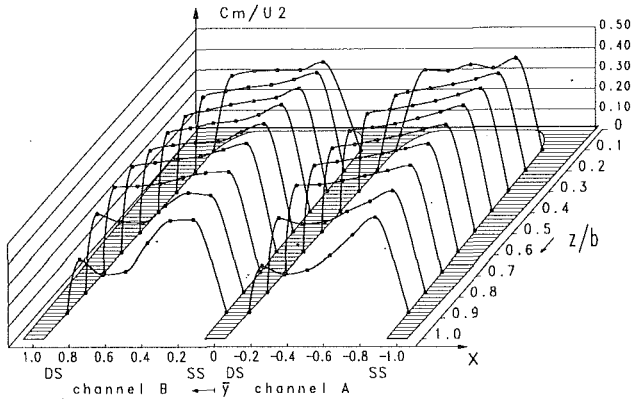

Fig. 14(*a*) Inducer position *i* = 7 (see Fig. 4)

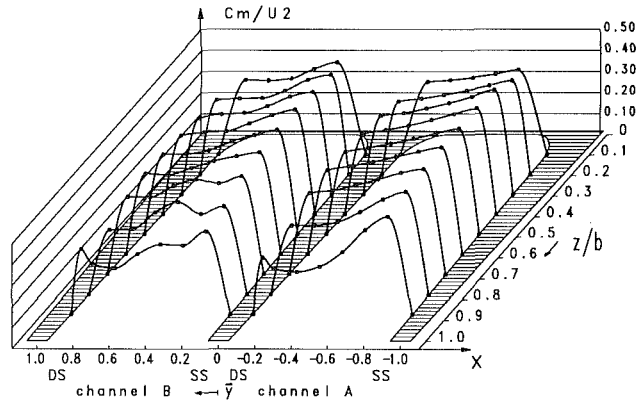

Fig. 14(*b*) Inducer position *i* = 11 (see Fig. 4)

Fig. 14 Dimensionless meridional velocity profiles of impeller channels A and B (see Fig. 4) (near surge (*OP* 7, see Fig. 7), speed: 88 percent)

influenced very much. The abovementioned minimum of the velocity is visible more or less clearly at all inducer positions. Near the shroud and in the middle of impeller channel B ($\bar{y}$ = 0.4 to 0.6), a small increase of the velocity profile is achieved by adjusting the trailing edge of the inducer. However, the overall velocities are not balanced near the shroud at inducer position i = 11.

Numerical Flow Field Analysis

Besides the experimental investigations, a numerical procedure is being developed that will be able to solve the three-dimensional viscous flow field of the tandem rotor configuration. Inducer and impeller rotate with the same angular speed, thus having the same relative system for both rotor computing grids. The numerical solution for this single relative system needs no unsteady solution of the Navier–Stokes equations, as this would be necessary in the case of two rotors moving relative to each other. The tandem rotor configuration discussed here performs a good basis to advance an existing numerical three-dimensional Naiver–Stokes flow simulation program system for three-dimensional Navier–Stokes equations (Hoffmann, 1989). The intermediate steps in this development are:

- Development of a numerical grid generator for combinations of rotors of any geometry including blade clearance, blade root radii, and splitter blades.
- Simulation of the flow field within both rotors having the same number of blades each and axial clearance zero in between. This case can be calculated with the already existing code.
- Development of the Navier–Stokes code to calculate splitter and axial clearances in between two rotors.
- Extention to calculate two different rotors that move relative to one another.

With the first three of these steps, the experimentally investigated tandem rotor flow of this study can be simulated numerically. Up to now, the first two steps have been worked out.

Conclusions

A radial compressor stage with medium pressure ratio and high efficiency level equipped with a tandem rotor of adjustable geometry has been investigated experimentally. The operating range, the pressure ratio, and the efficiency are satisfactory, although they are not comparable to the design data because of the limited speed (88 percent). The observed results of the measurements with different inducer positions can be summarized as follows:

- The influence of the inducer shift on the rotor and stage characteristics is small for the investigated tandem constellations.
- The optimum inducer position is identical with its reference position (see Fig. 4).
- L2F-system measurements show a similar velocity distribution in the impeller channels A and B, which are not influenced substantially by the inducer shift.

The further development of this project will contain the following main features:

- Manufacturing of a new rotor of titanium alloy for design speed with modifications in the clearance geometry (s = 0, see Fig. 4). This work is completed.
- Detailed conventional measurements of the characteristics and the rotor flow field by L2F-system measurements at seven more stations.
- Development of the numerical analysis to calculate the viscous flow field within the real tandem-rotor geometry with splitter-tape blades and axial clearance in between inducer and impeller.

Acknowledgments

The authors gratefully acknowledge the Motoren- und Turbinen-Union (MTU) Munich for cooperation and support as well as for placing the compressor blade design at our disposal. Furthermore, thanks are due to Dr. R. Schodl and T. Klemmer (DLR, Cologne) for the cooperation on taking the L2F system measurements.

References

Boyce, M., and Nishida, A., 1977, "Investigation of Flow in Centrifugal Impeller With Tandem Inducer," *Tokyo Joint Gas Turbine Congress*, p. 353.

Gostelow, J. P., and Watson, P. J., 1972, "Experimental Investigation of Staggered Tandem Vane Pump Impellers," University of Cambridge CUEDIA-Turbo/Tr. 38.

Gui, L., Gu, C., and Chang, H., 1989, "Influences of Splitter Blades on the Centrifugal Fan Performances," ASME Paper No. 89-GT-33.

Hoffmann, W., 1989, "A Computer Program System for the Analysis of 3-d Steady Flows in Turbomachinery Components," Thesis, University of Bochum, Federal Republic of Germany.

Klassen, H. A., Wood, J. R., and Schumann, L. F., 1977, "Experimental Performance of a 13.65 cm-Tip-Diameter Tandem Bladed Sweptback Centrifugal Compressor Designed for a Pressure Ratio of 6," NASA TP-1091.

Knapp, P., 1979, "Einfluß der Gestaltung des Vorsatzläufers auf die Energieumsetzung im Radialverdichter," Universität Hannover, Sonderforschungsbereich SFB 61, Bericht No. 31.

Krain, H., and Hoffmann, W., 1989, "Verification of an Impeller Design by Laser Measurements and 3D-Viscous Flow Calculations," ASME Paper No. 89-GT-159.

Lindner, E., and Kramer, U., 1985, "Strömungsuntersuchungen an diagonalen Verdichterlaufrädern mit Spaltgitterbeschaufelung," *Maschinenbautechnik*, Berlin, Vol. 34, No. 11, p. 507.

Mager, A., 1958, "Transformation of the Compressible Turbulent Boundary Layer," *Journal of the Aeronautical Sciences*.

Reeves, G. B., and Schweitzer, J. K., 1974, "Modified Centrifugal Compressor," Eustis Directorate, U.S. Army Air Mobility Research and Development Laboratory USAAMRDL-TR-74-96.

Schlichting, H., 1965, *Grenzschicht-Theorie*, G. Braun Verlag, Karlsruhe, Federal Republic of Germany.

Schodl, R., 1980, "A Laser-Two-Focus (L2F) Velocimeter for Automatic Flow Vector Measurements in the Rotating Components of Turbomachines," ASME *Journal of Fluids Engineering*, Vol. 102, pp. 412.

Takamatsu, Y., Ookuma, K., Nakamura, R., and Furukawa, A., 1980, "Improvement of Suction Performance of Centrifugal Pump Impeller," *Bulletin of the JSME*, Vol. 23, No. 177, p. 361.

Traupel, W., 1962, *Die Theorie der Strömung durch Radialmaschinen*, G. Braun Verlag, Karlsuhe, Federal Republic of Germany.

Turanskyi, L., 1985, "Über die Entwicklungsarbeiten an Tandemgitterstufen für Industrie-Axialkompressoren," Verein Deutscher Ingenieure VDI-Bericht 572.1, p. 403.

H. Hayami
Institute of Advanced Material Study,
Kyushu University 86,
Kasuga 816, Japan

M. Sawae
Nikko Kyodo Co., Ltd.,
Chita 478, Japan

T. Nakamura
Toshiba Co.,
Yokohama 230, Japan

N. Kawaguchi
Institute of Advanced Material Study,
Kyushu University 86,
Kasuga 816, Japan

Blade Loading and Shock Wave in a Transonic Circular Cascade Diffuser

A low-solidity circular cascade, conformally transformed from a high-stagger linear cascade of double-circular-arc vanes with solidity 0.69, was tested as a part of diffuser systems of a transonic centrifugal compressor and the static pressures were measured around a vane of the cascade and on the side wall between cascade vanes in detail. The blade loading of cascade vane was discussed by integrating the pressure distribution around the vane. The experimental data for lift-coefficient of vane were almost on a single straight line with positive gradient against angle-of-attack over a wide range of inflow Mach number and inflow angle. The maximum lift coefficient reached about 1.5 and the vane worked well to the surge condition of the compressor. The structure of shock wave was also discussed by drawing a contour map of the flow Mach number between cascade vanes. The normal shock wave was observed on the suction surface of vane and it moved upstream along the suction surface with the decrease in inflow angle. The vane did not fall in stall even though the Mach number upstream of the shock wave was over 1.4.

Introduction

If the pressure ratio of a single-stage centrifugal compressor is larger than four, the velocity relative to the inducer and the diffuser usually exceeds the velocity of sound. Since a conventional vaned diffuser is sensitive to the angle of incidence, especially at a supersonic condition, the flow range of high pressure ratio compressors with a vaned diffuser is very narrow.

In the preceding paper (Hayami et al., 1990), low-solidity circular cascades, conformally transformed from linear cascades of double-circular-arc vanes with solidity 0.69, were successfully applied as a part of diffuser system to a transonic centrifugal compressor. That is, good compressor performance, a wider flow range as well as a higher pressure ratio and a higher efficiency, superior to those with a vaneless diffuser, were obtained, although the maximum flow rate was limited by choke of the impeller. The test cascade diffusers demonstrated a good pressure recovery over a wide range of inflow angle, and furthermore the pressure recovery was improved a little by an increase in inlet Mach number up to 1.1.

In the present paper, the static pressures were measured around a vane of the cascade and on the side wall between cascade vanes in detail. The blade loading of cascade vane or the lift coefficient of vane against angle-of-attack was discussed by integrating the pressure distribution around the vane. The structure of the shock wave was also discussed by drawing a contour map of the flow Mach number between cascade vanes.

Contributed by the International Gas Turbine Institute and presented at the 37th International Gas Turbine and Aeroengine Congress and Exposition, Cologne, Germany, June 1-4, 1992. Manuscript received by the International Gas Turbine Institute January 28, 1992. Paper No. 92-GT-34. Associate Technical Editor: L. S. Langston.

Experimental Apparatus

A high-pressure-ratio centrifugal compressor was tested in a closed loop with Freon R-12 gas at four speeds between

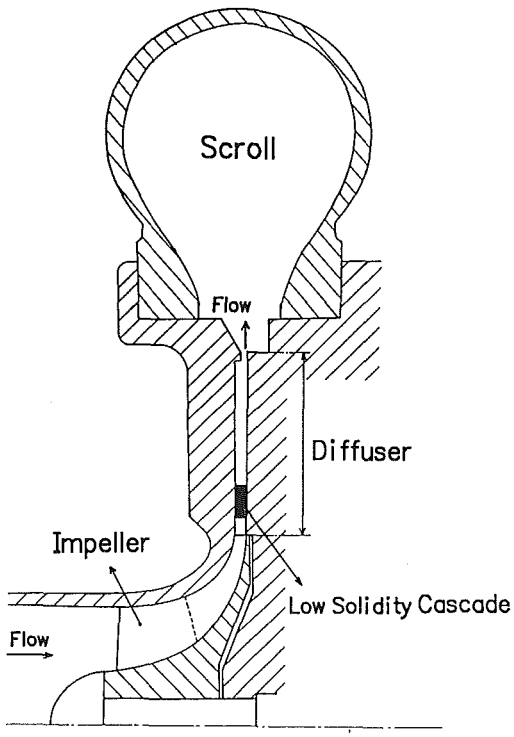

Fig. 1 Meridional profile of test compressor

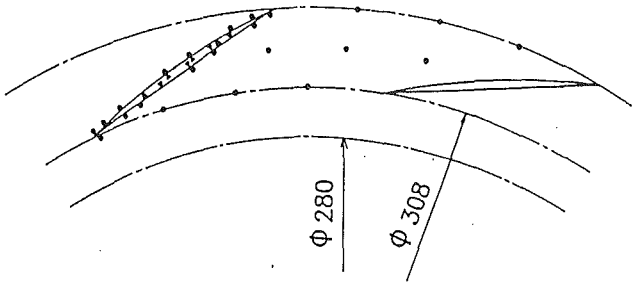

Fig. 2 Circular cascade, SVD69

15,000 and 19,000 rpm. The meridional profile of the test compressor is shown in Fig. 1. The diameter of the impeller was 280 mm, the exit blade width was 8.9 mm, and the inducer diameter was 172 mm. The open shroud impeller had 15 main blades and 15 splitter blades with a backward sweep angle of 40 deg at the exit.

The circular cascade of interest was installed between the two parallel walls, perpendicular to the impeller axis and 9.4 mm apart, so that the leading edges of vanes were located at 308 mm in diameter or 1.1 in radius ratio to the impeller exit. A double-circular-arc vane, with 10 deg blade turning angle and 4 percent thickness, was adopted as the original airfoil section of the reference linear cascades. The solidity of the linear cascades was 0.69 and the stagger angles were 69 deg and 72 deg, respectively. The linear cascades were conformally transformed to circular cascades with eleven blades. They are identified as the SVD69 cascade and the SVD72 cascade, respectively. The SVD69 cascade is shown in Fig. 2.

In addition to securing conventional test data for compressor characteristics, static pressure was measured at eight positions along a vane at the midspan line, at 14 positions along the root of the same vane, and at nine positions on the side wall between cascade vanes as shown in Fig. 2, and at three positions on the side wall downstream of the cascade. The diameter of the pressure taps was 0.7 mm.

Compressor Characteristics and Test Range

Characteristics of Compressor. The characteristic curves of the compressor with different diffusers are presented in Fig. 3. The ordinate P_4/P_0 is the total pressure ratio and the abscissa G/G^* is the ratio of the mass flow rate to the choking flow rate in the suction pipe. The parameter M_t is the inducer tip Mach number based on inducer tip speed and inlet stagnation temperature. The total pressure at the compressor exit is the sum of the static pressure and the dynamic pressure in the delivery pipe of the compressor. The dynamic pressure was less than 1 percent of the inlet total pressure.

The minimum flow conditions at different shaft speeds are connected by thin lines in the graph. The lines, including inducer stall points, are called surge lines. For the case of M_t = 0.940, the inducer fell into stall but the compressor was not in surge. For comparison, the stall limit conditions of the isolated impeller (Hayami et al., 1986) are indicated as four arrows.

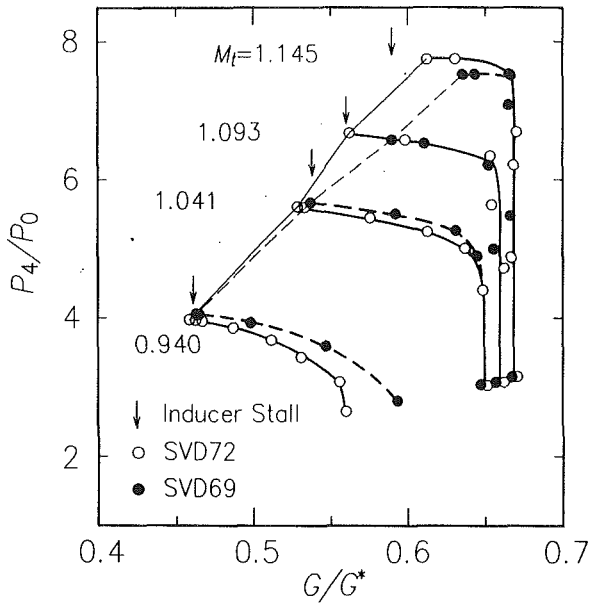

Fig. 3 Characteristics of compressor; G^* = choking flow rate in suction pipe

In the case of $M_t \leq 1.041$, the critical flow rates for surge were almost identical regardless of the type of diffuser. Furthermore, the flow rate was equal to the critical flow rate for inducer stall in the test of the isolated impeller. That is, the surge was caused by stall of the impeller. On the other hand, in the case of $M_t \geq 1.093$, the critical flow rates for surge with SVD69 and SVD72 diffusers were larger than that of inducer stall, and they depended on the type of diffuser. That is, the surge was induced by diffuser stall.

Flow at Upstream of Cascade. The test range of the inflow angle α and the inflow Mach number M at the impeller exit (R = 1.0) and at the cascade inlet (R = 1.1) are presented in Fig. 4. At the impeller exit, the flow velocity and the flow angle were estimated using the tangential velocity evaluated from the work factor and the radial velocity calculated from the measured pressure and the flow rate assuming that there was no preswirl at the impeller inlet. The impeller work factor was estimated from the measured stagnation temperature difference between the inlet and the exit of the compressor after subtracting the disk friction power, which was 0.02 to 0.05 of the input power and was estimated.

The flow in the vaneless diffuser zone upstream of the cascade was analyzed by a one-dimensional method assuming frictional, steady, and compressible flow, where the skin friction coefficient was a function of Mach number M and was assumed to be 0.04 for M = 0. The Mach number is certainly smaller than that at the diffuser inlet, but it is still supersonic except at a low-speed operation, and the maximum inflow Mach number tested was 1.17. At the same time, the flow angle becomes a little smaller due to the increase in gas density. The minimum inflow angle was 10.6 deg for SVD69 and 9.7 deg

Nomenclature

b = width of diffuser
C_L = lift coefficient
C_p = pressure coefficient = $(p - p_2)/(P_2 - p_2)$
G = mass flow rate
M = Mach number
M_t = inducer tip Mach number
P = stagnation pressure
p = static pressure
R = radius ratio = r/r_2 or $(r - r_{3i})/(r_{3e} - r_{3i})$
r = radius
α = absolute flow angle from the tangent
α^* = angle of attack

Subscripts

0 = compressor inlet
1 = impeller inlet
2 = impeller exit
$3i$ = cascade inlet
$3e$ = cascade exit
4 = compressor exit

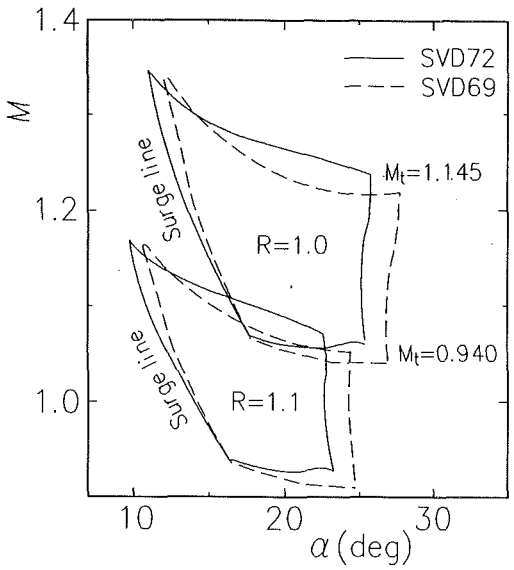

Fig. 4 Flow conditions at impeller exit and at cascade inlet

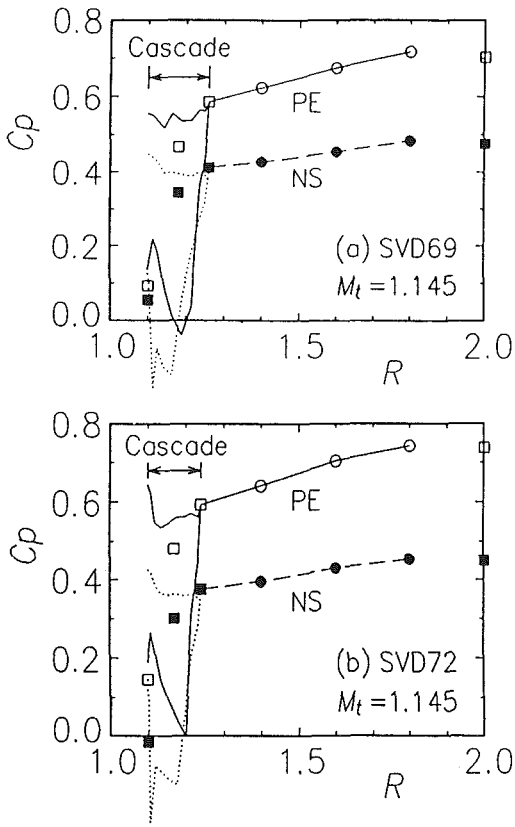

Fig. 5 Radial distribution of pressure

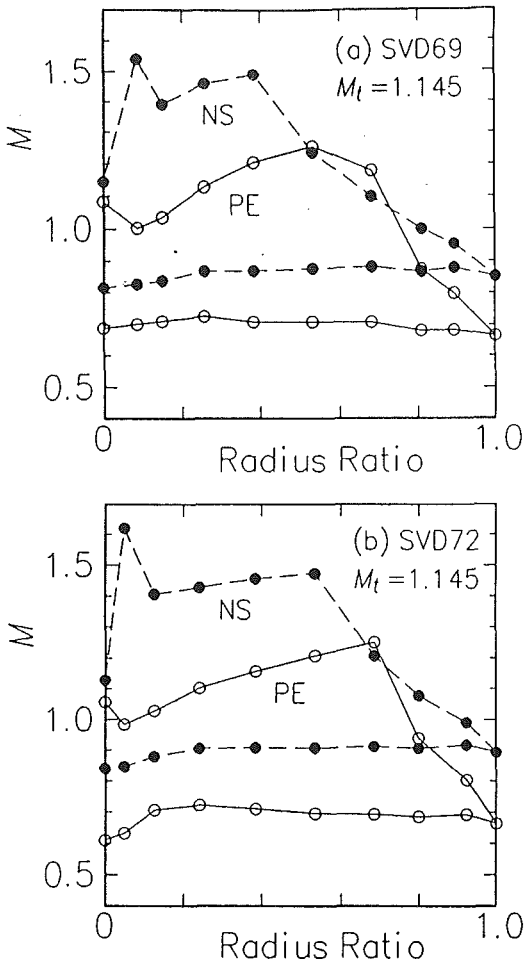

Fig. 6 Distribution of Mach number along cascade vane

for SVD72. The inlet vane angle of the cascade was 16 deg for SVD69 and 13 deg for SVD72, that is, the maximum incidence angle was 5.4 deg for SVD69 and 3.3 deg for SVD72, respectively.

Experimental Results and Discussion

Radial Distribution of Static Pressure in Diffuser. The radial distribution of static pressure between the impeller exit (R = 1) and the diffuser exit (R = 2) is shown in Fig. 5, where PE represents the peak efficiency condition of the diffuser and NS represents the critical condition of compressor surge. The ordinate Cp is the pressure coefficient, that is, the ratio of the static pressure rise to the nominal dynamic pressure ($P_2 - p_2$) including a blockage factor of 0.15 at the impeller exit (Senoo and Ishida, 1987). The square symbols at the right-hand edge show the delivery static pressure of the compressor and the square symbols in the cascade are the mean wall static pressure between cascade vanes. The pressure coefficient along the pressure surface of vane and that along the suction surface of vane are also plotted. The pressure coefficient at the cascade exit is smoothly connected to the three sets of data downstream of the cascade. Although the pressure coefficient for NS is lower than that for PE as a whole, the pressure rise in the cascade is sufficiently high on the basis of either average pressures or pressure distributions around a vane.

Distribution of Mach Number Along Vane Surface. The measured static pressure on the vane surface was converted to the Mach number using an isentropic assumption. The total pressure at the impeller exit was estimated using the static pressure at the impeller exit, the orifice flow, and the measured stagnation temperature at the compressor exit. The Mach number calculated in this manner for cases PE and NS are plotted in Fig. 6(a) for SVD69 and 6(b) for SVD72, respectively. The abscissa is the radius ratio based on the inlet/exit radius of the cascade. The Mach number at the cascade exit was evaluated from the mean value of three wall static pressures between cascade vanes.

The Mach number was nearly constant along the pressure surface of vane and the flow was subsonic. With the decrease in flow from PE to NS, the level of Mach number increased

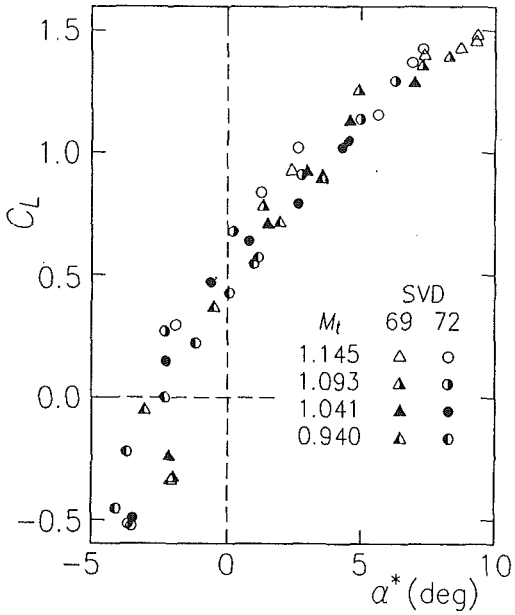

Fig. 7 Lift characteristics of cascade vane

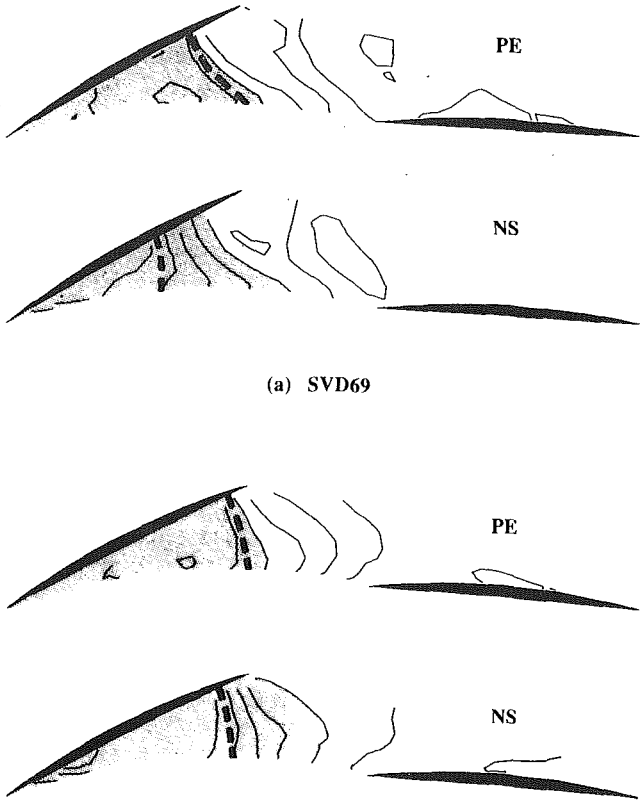

Fig. 8 Contour map of Mach number in cascade, M_t = 1.145

as a whole, and the position with high blade loading moved upstream from the midchord and the peak Mach number increased from 1.2 to 1.6. As a result, the blade loading was significantly changed with the flow rate.

The steep deceleration at the rear half of the suction surface of vane was due to the existence of a normal shock, which will be discussed later, and the shock wave moved upstream with the decrease in flow rate. In the case of interaction between the normal shock wave and the boundary layer in the duct flow with constant area, the flow separation of turbulent boundary layer occurs when the upstream Mach number is beyond about 1.2 (Gadd, 1962). In the present cascade, the Mach number is beyond 1.4 so that the boundary layer along the suction surface of vane is just near the critical condition of flow separation. In comparison with the duct flow, the separation would be delayed owing to the effect of boundary layer suction along the suction surface of the vane by a secondary flow on the side wall (Senoo et al., 1983) and/or the effect of the three-dimensional structure of flow by the interaction between the shock wave and the side wall boundary layer. The total pressure should be decreased due to the pressure loss in reality so that the Mach number in Fig. 6 was a little overestimated.

Blade Circulation and Lift Coefficient. The blade circulation was evaluated from the following angular momentum equation using the measured pressure distribution around a vane (Hayami et al., 1985):

$$\Gamma = 2\pi b \int r\Delta p \, dr/G \tag{1}$$

where Δp is the pressure difference between the pressure surface and the suction surface of vane at radius r. The circulation was calculated using the midspan pressure referring to the root pressure. The difference between the midspan pressure and the root pressure was less than 3 percent of the nominal dynamic pressure $(P_2 - p_2)$.

The lift coefficient of the vane was evaluated using the circulation of the vane and the vector mean flow velocity at inlet and exit of the cascade, where the flow at the cascade exit was predicted using a one-dimensional flow analysis assuming the compressible flow in the cascade. In the calculation, the drag-lift ratio was assumed to be 0.04 and the effect of friction on the side wall was considered. The results of the relationship between the lift coefficient of the blade C_L and the angle of attack α^* are plotted in Fig. 7.

All data of the present experiments are included for the whole flow rate between the choking flow condition and the critical surge condition, for four impeller speeds and for two different stagger angles of the cascade, SVD69 and SVD72. The data are on a straight line with a positive gradient over a wide range of inflow Mach numbers and inflow angles regardless of the stagger angle of cascade, considering the low number of pressure taps along the blade surface and the generation of shock waves. The maximum lift coefficient reached 1.5, that is, the vane worked well with high blade loading to the surge condition even though the diffuser was the cause of the compressor surge.

Flow Pattern in Cascade and Behavior of Shock Wave. Contour maps of flow Mach number in the cascade are drawn in Fig. 8, which are calculated using the measured static pressures at 31 locations in the cascade and the isentropic flow assumption. The interval of contour lines is 0.1 in Mach number. The area with a screen tone shows a region where the flow was supersonic. Even though the inflow Mach number to the cascade was beyond unity in this case, the flow was subsonic along the pressure surface of vane. Along the suction surface of vane, on the other hand, the fluid was further accelerated from the leading edge, and a step in Mach number was observed just downstream of the maximum Mach number zone, as shown by a fat broken stripe, which would be recognized as a normal shock wave. With decrease in flow rate, the normal shock wave moved upstream keeping its shape and the inflow Mach number upstream of the shock wave was increased.

The Mach number change measured across the shock was less than that observed in an ordinary normal shock. This may be caused by the effect of the side wall boundary layer and/or by the insufficient number of pressure taps. Furthermore,

in cases of surge condition, the supersonic area was spread downstream of the shock. There may be a possibility of the shock wave moving back and forth near stall condition. At the supersonic inflow condition, generation of shock waves is expected. In cases of a channel-type diffuser, shock waves generated near the leading edge of a vane reach the suction surface of the adjacent vane, and the flow in the boundary layer on the suction surface may be separated and the vane stalled. In the present low-solidity cascade, however, the shock wave was generated on the suction surface of vane due to the expansion wave without a shock wave just upstream of the leading edge of vane.

Conclusions

The pressure distributions around a vane and between cascade vanes of a transonic low-solidity circular cascade were measured to investigate the blade loading and the behavior of a shock wave being generated in the cascade.

1 The relationship of lift coefficient of vane against angle-of-attack was on a single straight line with positive gradient over a wide range of inflow Mach numbers and inflow angles regardless of the stagger angle of cascade.

2 The maximum lift coefficient reached about 1.5 and the cascade vane worked well to the surge condition even though the diffuser was the cause of the compressor surge.

3 In cases of supersonic inflow conditions, normal shock waves were observed on the suction surface of vanes without a shock wave just in front of the leading edges of vane.

4 The normal shock wave moved upstream along the suction surface of vane with the decrease in flow rate.

5 The vane did not fall in stall even though the Mach number upstream of the shock wave was over 1.4.

Acknowledgments

The authors are grateful to Dr. Senoo, the former director of our laboratory, who originated the idea of a low-solidity cascade diffuser and gave various discussions. This study has been carried on partly under a Grant-in-Aid from the Ministry of Education, Science and Culture of Japan in 1988 (No. 01550151).

References

Gadd, G. E., 1962, "Interactions Between Normal Shock Waves and Turbulent Boundary Layers," ARC Report and Memorandum, No. 3262.

Hayami, H., Senoo, Y., and Kitayama, F., 1985, "Correction of Lift Coefficient for Tandem Circular-Cascade Diffusers," *Bulletin of JSME*, Vol. 28, No. 241, pp. 1354–1358.

Hayami, H., Senoo, Y., and Nakashima, K., 1986, "On the Stall and Choke Limits of Supersonic Centrifugal Impellers," *Trans. JSME*, Ser. B, Vol. 53, No. 486, pp. 489–495 [in Japanese].

Hayami, H., Senoo, Y., and Utsunomiya, K., 1990, "Application of a Low-Solidity Cascade Diffuser to Transonic Centrifugal Compressor," ASME JOURNAL OF TURBOMACHINERY, Vol. 112, pp. 25–29.

Senoo, Y., Hayami, H., and Ueki, H., 1983, "Low Solidity Cascade Diffusers for Wide-Flow-Range Centrifugal Blowers," ASME Paper No. 83-GT-3.

Senoo,Y., and Ishida, M., 1987, "Deterioration of Compressor Performance Due to Tip Clearance of Centrifugal Impellers," ASME JOURNAL OF TURBOMACHINERY, Vol. 109, pp. 55–61.

Design and Rotor Performance of a 5:1 Mixed-Flow Supersonic Compressor

R. Mönig
Siemens AG, KWU Group,
Gas Turbine Technology,
Mülheim a.d. Ruhr,
Federal Republic of Germany

W. Elmendorf

H. E. Gallus

Institut für Strahlantriebe und
Turboarbeitsmaschinen,
Rheinisch-Westfälische
Technische Hochschule,
Aachen, Federal Republic of Germany

In consideration of further jet-engine developments required by applications for supersonic travel aircraft, airbreathing propulsion of space vehicles, or only the improvement of conventional high-performance turbo-engines, highly loaded supersonic compressors seem to meet the future demands. Particularly mixed-flow compressor stages with moderate supersonic rotor and stator inlet flow reveal the potential of high pressure rise and mass flow as well as favorable performance characteristics and efficiency. The first part of this paper presents analytical considerations for mixed-flow supersonic compressors with strong shock waves. This theoretical approach proves to be essential besides established design tools in order to ensure safe rotor and stage operation in accordance with the design objectives. In this context, the conditions for shock wave stabilization within a diagonal rotor passage are discussed in detail for design and off-design rotational speeds. The main part of this paper, however, presents the results and flow analysis obtained by extensive experimental investigations of the designed mixed-flow compressor rotor. The investigations were restricted to operation without stator in order to strictly separate rotor performance from rotor–stator interactions. The results reveal the design goals to be met in general. Mass flow, total pressure rise, and efficiency in particular show a good agreement with the design properties for near-surge operation at design and off-design conditions.

1 Introduction

The continued improvement of civil and military jet engines has led to a remarkable technological standard of multistage axial-flow compressors with fan stages operating at transonic or even supersonic speeds. In the field of small gas turbines and helicopter engines, high-performance centrifugal compressors with extremely high total pressure ratios have been developed, taking advantage of the increased circumferential speed at the rotor exit.

An early development of a highly loaded mixed-flow compressor stage was presented by Wilcox and Robbins (1951). The investigated single-stage compressor provided a high corrected mass flow of 8.48 kg/s and a rotor total pressure ratio of 3.7:1 (Fig. 1). The rotor efficiency of 0.78, however, did not meet the standards established by axial flow and centrifugal compressors.

In 1986 another design of a mixed-flow compressor was published by Dodge (1986). At this time, more sophisticated design tools were available and the experience with high-performance axial flow compressors provided an improved understanding of characteristic flow phenomena in turbomachines. The experimental investigations of the compressor revealed an overall pressure ratio of 3.36:1 in combination with a corrected mass flow of 9.1 kg/s and a total efficiency of 0.866. These data demonstrated the capabilities of adequate mixed-flow compressor designs.

One year later, a further mixed-flow compressor develop-

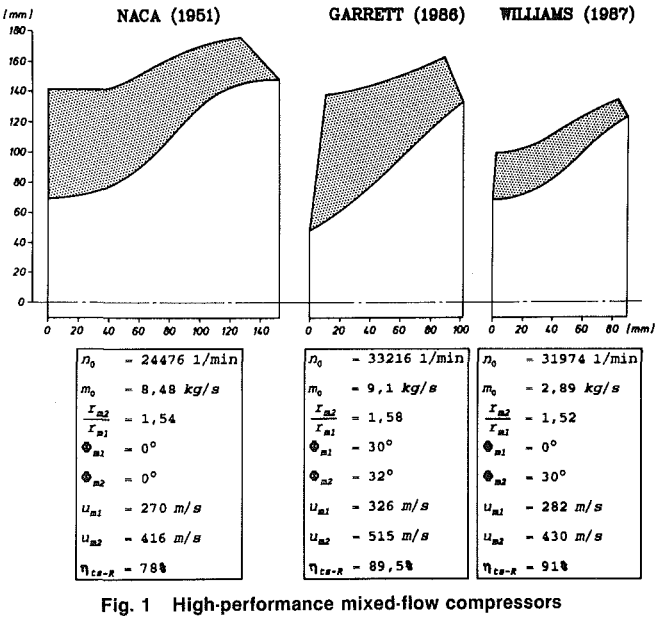

Fig. 1 High-performance mixed-flow compressors

Contributed by the International Gas Turbine Institute and presented at the 37th International Gas Turbine and Aeroengine Congress and Exposition, Cologne, Germany, June 1–4, 1992. Manuscript received by the International Gas Turbine Institute February 4, 1992. Paper No. 92-GT-73. Associate Technical Editor: L. S. Langston.

ment was published by Musgrave and Plehn (1987). In spite of a lower rotor aspect ratio, the design rotor efficiency of 0.91 exceeded the data of the most recently presented mixed-flow compressor. The overall total pressure ratio was measured to be 3.02:1 at a total efficiency of 0.84. Nevertheless, the corrected mass flow of 2.89 kg/s was considerably lower compared to the other compressor stages under discussion.

The development of a mixed-flow supersonic compressor at the Technical University of Aachen was initiated by an internal feasibility study in 1984, covering possible improvements of small jet-engine compressors. As a fundamental result of this study, an appropriate single-stage compressor should produce a total pressure ratio of 5:1 at a mass flow of at least 8.2 kg/s (Mönig et al., 1987).

The presented compressor was designed for an axial rotor inlet Mach number of 0.7 and a swirl free stator exit flow at Mach 0.5. The design was carried out with respect to basic results of prior investigated supersonic axial-flow compressor stages (Simon and Bohn, 1974; Broichhausen and Gallus, 1982). Thus, the compressor stage to be developed was specified by the following main design data:

- absolute inlet Mach number: $M_{1-abs} = 0.7$
- mean relative inlet Mach number: $M_{1-rel} = 1.4$
- absolute inlet flow angle: $\alpha_1 = 90$ deg
- mean relative inlet flow angle: $\beta_1 = 30$ deg

Additionally, the rotor exit conditions were determined by a meanline flow analysis incorporating loss correlations as:

- ratio of circumferential speed: $u_2/u_1 = 1.335$
- mean exit relative flow angle: $\beta_2 = 72$ deg

2 Rotor Design

Due to the promising stage data and favorable performance characteristics of a supersonic axial-flow compressor consisting of shock rotor and tandem stator, a corresponding conception has been selected for the mixed-flow jet-engine compressor.

The rotor geometry was developed by means of mainly four different computer programs:

- Geometry generator with input of desired blade data
- Streamline-curvature code for throughflow calculations and loss prediction
- Meanline code for prediction of off-design performance and stage characteristics
- Three dimensional-Euler solver for detailed flow analysis

The compressor rotor is characterized by a strong shock wave positioned at the inlet section in order to achieve a considerable static pressure rise within the rotor. Thus, the necessary "unstart" of the rotor has to be ensured by adequate aerodynamic conditions. The stabilization of the shock wave may principally be controlled by

- an adequate backpressure adjustment,
- a critical rotor exit section, or
- a suitable stator inlet cross section and blade angle.

For stage operation at meridional subsonic but absolute supersonic stator inlet flow, the correct rotor shock position can only be controlled by a critical rotor exit or an adequate stator design (Broichhausen et al., 1988). In the present case a rotor controlled shock wave stabilization ($M_{2-rel} = 1$) was preferred in order to maintain a higher flexibility with regard to the stator design.

In this context it has to be considered that the area of the critical cross section depends on the performed rotor massflow, the relative flow turning angle, the ratio of circumferential speed u_2/u_1, and the total rotor efficiency. Thus, the rotor exit geometry has to be designed very carefully. In the present case the final rotor passage geometry and blade shape was determined by means of streamline curvature calculations incorporating correlations for shock losses, wall and profile boundary layers, and separation. The design goal was specified as follows:

- mass flow (Freon op.): 16.8 kg/s
- total pressure ratio: 5.97
- total efficiency: 0.837

The corresponding rotor geometry data are presented in Table 1; the rotor blade geometry is shown in Figs. 2 and 3. A straight inlet section has been chosen for the suction side surface in order to avoid a flow acceleration upstream of the strong inlet shock wave.

The design rotational speed in freon is 14,000 rpm. This value corresponds to 29,737 rpm for air operation. The mixed-flow rotor consists of 22 blades. For mechanical reasons, a comparatively large tip clearance of 0.7 mm had to be accepted. The machined compressor rotor is shown in Fig. 4.

Table 1 Rotor geometry

	HUB	MIDSPAN	TIP
inlet radius	105.0 mm	131.5 mm	158.0 mm
exit radius	168.0 mm	175.5 mm	183.0 mm
inlet pitch angle	0.0°	0.0°	0.0°
exit pitch angle	25.4°	23.1°	20.8°
inlet s.s. angle	35.9°	30.0°	25.7°
inlet p.s. angle	40.9°	33.0°	28.7°
exit s.s. angle	65.9°	60.0°	55.7°
exit p.s. angle	77.9°	72.0°	67.7°
lead. edge angle	8.0°	8.0°	8.0°
trail. edge angle	-8.0°	-8.0°	-8.0°
axial length	85.0 mm	80.2 mm	75.4 mm
lead. edge radius	0.6 mm	0.5 mm	0.4 mm
trail. edge radius	0.4 mm	0.33 mm	0.25 mm

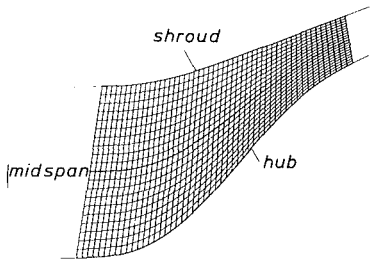

Fig. 2 Meridional view of the mixed-flow compressor rotor

Nomenclature

A = area
c_p = specific heat
M = Mach number
p = static pressure
T = temperature
u = circumferential speed
α = absolute flow angle
β = relative flow angle
η = total efficiency
κ = ratio of specific heats
∂ = partial differential

Subscripts

abs = absolute
m = mean
R = rotor
rel = relative
rot = related to rotating system
s = isentropic
t = total
0 = design
1 = rotor inlet
2 = rotor exit

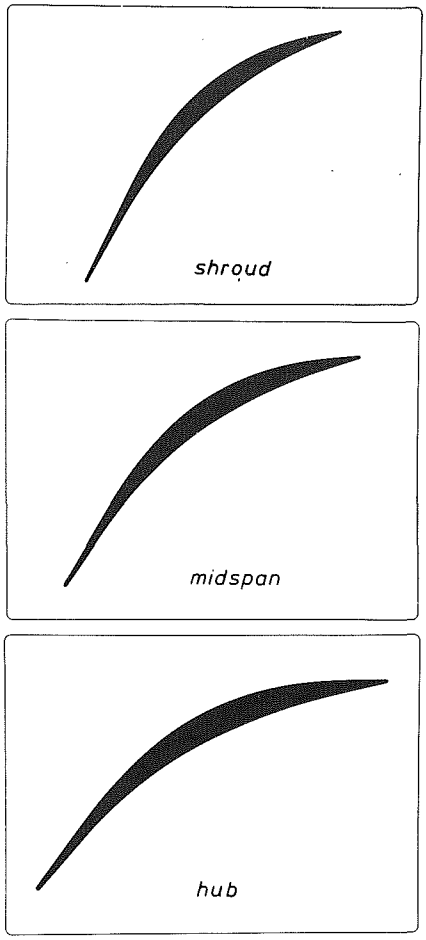

Fig. 3 Blade design for shroud, midspan, and hub

3 Compressor Test Rig

A view of the closed-loop supersonic compressor test rig and the measuring section is given in Fig. 5. In the first phase, presented in this paper, the mixed-flow rotor was tested without stator.

The rotor inlet data were measured by means of a five-hole ball probe, installed 15 mm upstream of the rotor inlet. The time-averaged static pressure distribution was recorded by means of 56 static pressure taps inserted at the compressor casing. In order to determine the rotor exit flow data, a specially manufactured three-hole wedge probe (Fig. 6) has been installed downstream of the compressor rotor. The unsteady wall pressure distribution was measured by means of 12 Kulite-semiconductor transducers.

4 Shock Wave Stabilization Within the Rotor

Concerning a supersonic compressor rotor of the proposed type, a strong shock wave has to be stabilized within the rotor inlet section, as specified above. The anticipated shock position and structure may be generally predicted by means of extremely time-consuming three-dimensional Euler or even Navier-Stokes solutions.

During the iterative phase of rotor design, however, fast prediction methods are required in order to decide immediately whether strong shock waves are stable at a particular speed and a particular rotor cross section. For this reason, a simple analytical method is described below, yielding positions of stable strong shock waves at design and off-design operation for mixed-flow rotors.

As is well known for one-dimensional flow without energy transfer, normal shock waves may only be stabilized within a

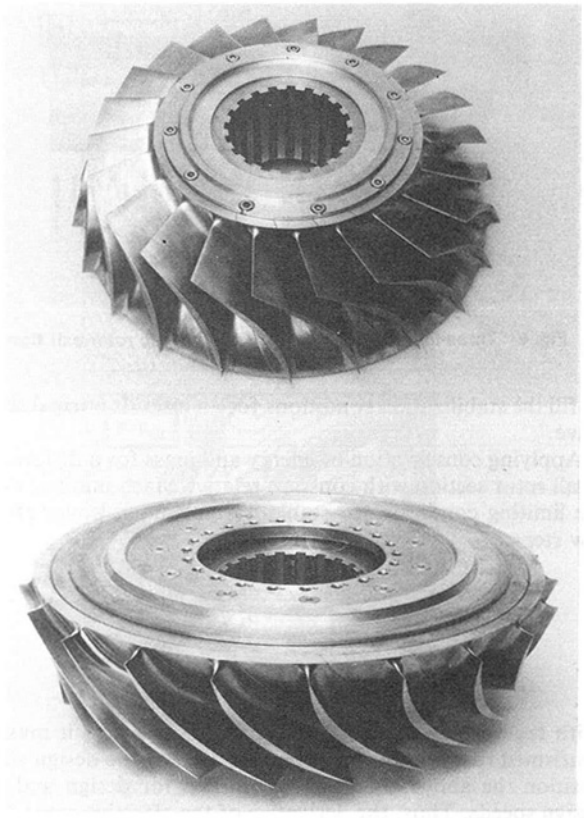

Fig. 4 Machined mixed-flow compressor rotor

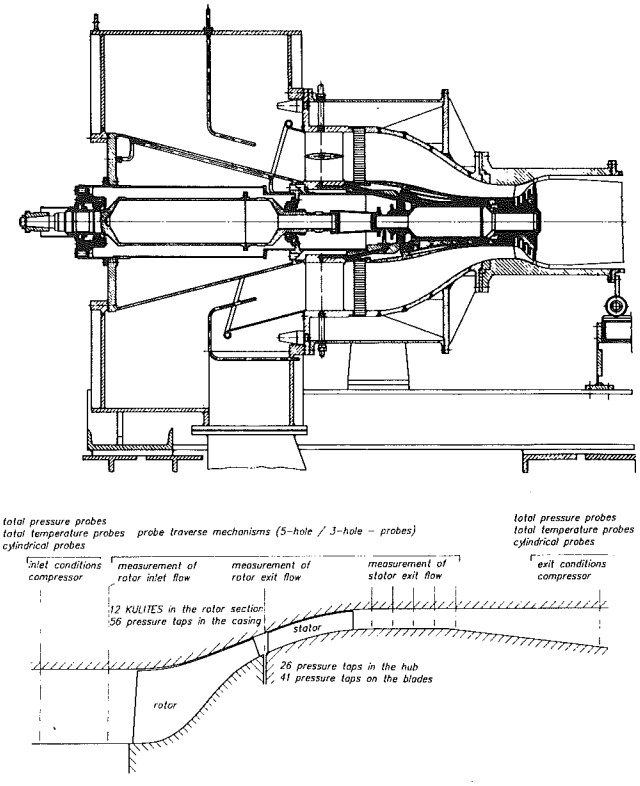

Fig. 5 Supersonic compressor test rig and measuring section

cross section with constant or increasing supersonic Mach number (e.g., Shapiro). Regarding a meanline computation for a mixed-flow rotor, it can be shown that the supersonic relative Mach number has to increase or remain constant in order to

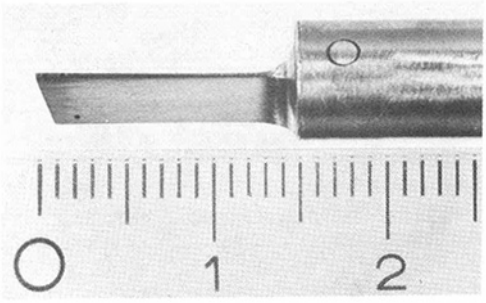

Fig. 6 Three-hole wedge probe for supersonic rotor exit flow

fulfill the stabilization conditions for an interior normal shock wave.

Applying conservation of energy and mass for a differential small rotor section with constant relative Mach number yields the limiting condition for stable normal shock waves after a few steps:

$$\frac{\partial}{\partial z}\left(\frac{A}{A_1}\right) \geq \frac{\partial}{\partial z}\left[\frac{\frac{2C_pT_{\text{rot}}}{u_1^2}+1}{\frac{2C_pT_{\text{rot}}}{u_1^2}+\left(\frac{u}{u_1}\right)^2}\right]^{\frac{\kappa+1}{2(\kappa-1)}} \tag{1}$$

With regard to the mixed-flow compressor rotor, it must be confirmed that within the passage section of the design shock position the above condition is fulfilled for design and off-design speeds. Thus, the derivative of the effective rotor cross section (perpendicular to the rotor meanline) was calculated for several axial locations within the rotor and plotted in Fig. 7. Additionally, the right-hand side of condition (1) was computed for the same axial locations at midspan.

A strong shock wave may be stabilized at those locations, where the particular speed line derivative (right-hand side of condition (1)) is essentially smaller than the area derivative (left-hand side of condition (1)). Thus, a particular speedline derivative has to meet the dark shaded area in Fig. 7 in order to allow the stabilization of a normal shock wave for the considered rotor speed and location.

A shock wave is basically unstable at all those locations, where the area derivative is distinctly smaller than the considered speed line derivative. If both terms are of similar order, however, three-dimensional flow-computation methods are inevitable in order to determine the correct shock position and structure.

Figure 7 shows that for all considered speeds the most forward stable shock position within the blade passage occurs at about 18 percent of the rotor length (A), due to the straight suction side region. Downstream of this location a very stable shock position even for low-speed operation is found to exist (B), as can be determined from the increased distance between area and speed line derivative.

The range between 35 percent (C) and about 90 percent (D) of the axial rotor length, however, turned out to be important with regard to the operating characteristics of the compressor rotor. At off-design speeds up to approximately 93 percent of the design speed, normal shock waves appear to be unstable within this rotor section. At design speed, however, strong shock waves seem to be stable even within the extremely converging rotor portion.

The rotor exit is designed to consist of a nearly constant cross section ($\partial A/\partial z \approx 0$). The geometry derivative, however, diverges considerably with respect to the speed-line derivative due to the mixed-flow design. As a result, strong shock waves may be also positioned within the rotor exit section at all considered rotational speeds.

The predicted locations of stable shock waves were con-

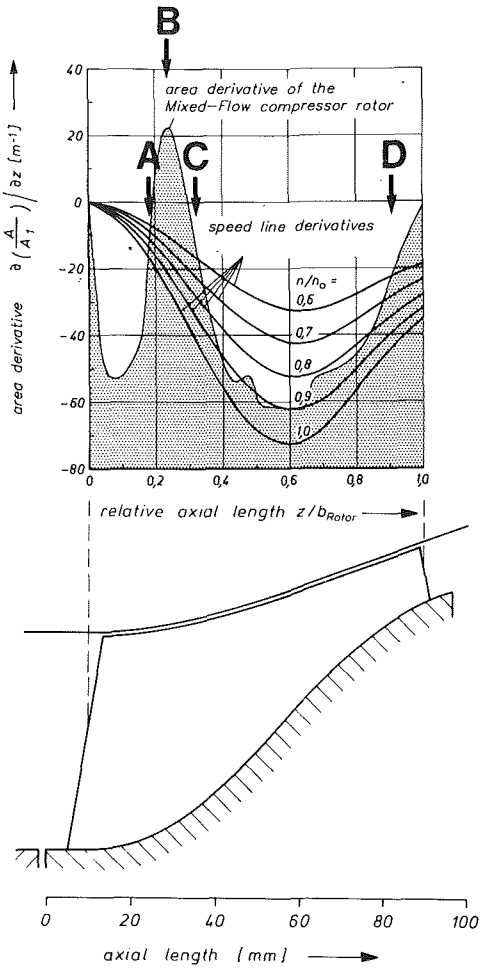

Fig. 7 Shock wave stabilization within the compressor rotor

trolled experimentally by means of wall-pressure measurements.

The time-average wall-pressure distribution at 84 percent corrected speed is shown in Fig. 8(*a*) for various operating conditions. Two corresponding blade-to-blade loadings are plotted additionally in Figs. 8(*b*) and 8(*c*).

For all loading conditions, a steep pressure rise is recorded at the rotor inlet section. The significantly increased density of isopressure lines immediately upstream of the rotor blading indicates this pressure rise to be caused by a strong shock wave (Figs. 8*b* and 8*c*). The shock wave appears to be extended to nearly two blade passages and is likely being caused by rotor choking. As a result, each streamline has to pass two strong inlet shock waves at this particular rotor speed.

At the rotor exit a distinct pressure drop is found to occur for unthrottled operation (meridional supersonic exit flow). The critical cross section within the rotor is apparently located at the maximum of pressure. Subsequently, the rotor flow is accelerated to supersonic speed, leading to the observed pressure drop.

At increasing back pressure a strong shock wave is forced to move upstream and enter the rotor exit. This shock wave is also indicated by a considerable pressure rise. At moderate back pressure (Fig. 8*b*) the shock wave is located immediately behind the rotor. At near surge operation (Fig. 8*c*) the shock wave is stabilized within the rear rotor section as predicted by the theoretical approach (Fig. 7).

The rotor performance at design speed is found to deviate significantly with respect to the off-design behavior. The time-averaged pressure recordings are plotted in Fig. 9(*a*). The cor-

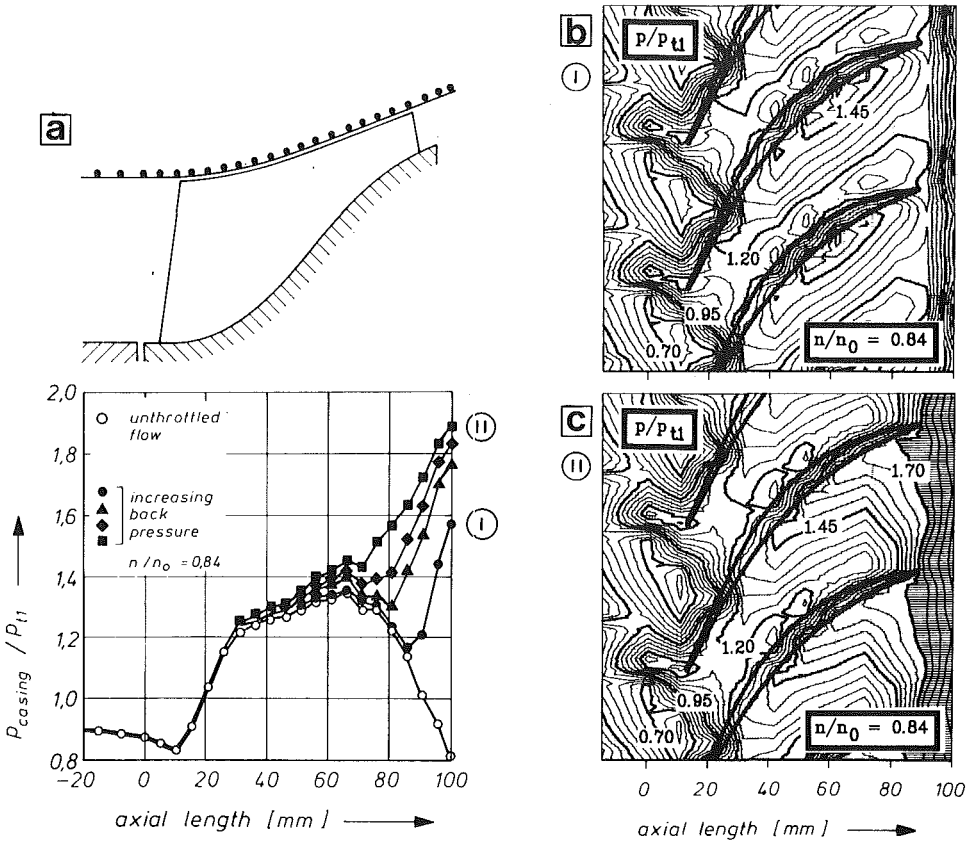

Fig. 8 Pressure distributions at 84 percent corrected speed

responding iso-pressure lines near the casing are shown in Figs. 9(*b*)–9(*d*) for low, moderate, and maximum back pressure.

For unthrottled operation, the significant pressure rise at the rotor inlet has completely disappeared (Fig. 9*a*). Instead of this, a first remarkable pressure rise is now observed at midchord. This phenomenon is attributed to a downstream movement of the strong inlet shock wave, indicating that rotor choking disappears at design speed. The shock stabilization near midchord is in close agreement with the theoretical approach. It is attributed to significantly increasing shock losses and blockage by subsequent boundary layer separation, leading to critical flow conditions again. Acceleration to supersonic flow is again indicated by the pressure drop near the rotor exit.

The presumed shock wave at midchord, however, can not be clearly identified by means of the blade-to-blade loadings (Fig. 9*b*). The shock-induced boundary layer separation and distinct secondary flow effects may be responsible for this deficiency.

At increased loading, a second strong shock wave is stabilized with the rotor exit section (Fig. 9 *c*). This effect was already observed at off-design speed and is in agreement with the prediction.

For high back pressure operation the pressure rise at midchord can be continuously moved in the upstream direction. Thus, the strong shock wave is stabilized within the rotor inlet section again at near surge operation (Fig. 9*d*).

Thus, it can be stated for design speed that a strong shock wave is obviously stable within the whole rotor passage as was predicted by the rather simple theoretical approach.

Rotor Performance

The flow data obtained at the rotor inlet are presented in Fig. 10 together with the predicted performance characteristics. The corresponding rotor exit data are shown in Fig. 11. In order to illustrate the effect of loss variation on the operating behavior of the supersonic mixed-flow rotor, the calculations were performed for a rotor total efficiency of 0.80 and 0.90.

Beyond 38 percent corrected speed the mass flow increase is significantly reduced. At the same time, a sudden increase of the average incidence angle is observed as is also predicted by the computation. These effects are obviously caused by rotor choking, as was already indicated by the wall pressure distributions (chapter 4, Fig. 8 and 9).

Downstream of the critical cross section (at approximately 85 percent of the chord length), the rotor flow is accelerated to supersonic velocity at low back pressure operation. Consequently, the absolute rotor exit Mach numbers are considerably higher in this case compared to the prediction for critical rotor exit flow (Fig. 11).

For an increase of back-pressure (near-surge operation) the relative rotor exit flow is again decelerated to subsonic velocity by the abovementioned upstream movement of a strong shock wave at the rotor exit (Fig. 11). Due to the deviations of the rotor exit Mach number from its design value ($M_{2-rel} = 1$), the absolute flow angle is higher for unthrottled operation and lower for near-surge operation than predicted by the calculation.

The obtained total and static pressure rise of the compressor rotor is in fairly good agreement with the prediction for the entire speed range. Due to the subsonic rotor exit relative velocity at near-surge operation, the measured total pressure is even higher in this case compared to the calculation.

The experimentally determined rotor performance map is given in Fig. 12. For all considered rotor speeds the corrected mass flow is independent on loading. The design goal is met with regard to total pressure rise and efficiency. The corrected mass flow at design speed, however, is slightly lower than predicted by the meanline and streamline-curvature computation.

Significant differences regarding rotor performance were detected for low and high-speed operation.

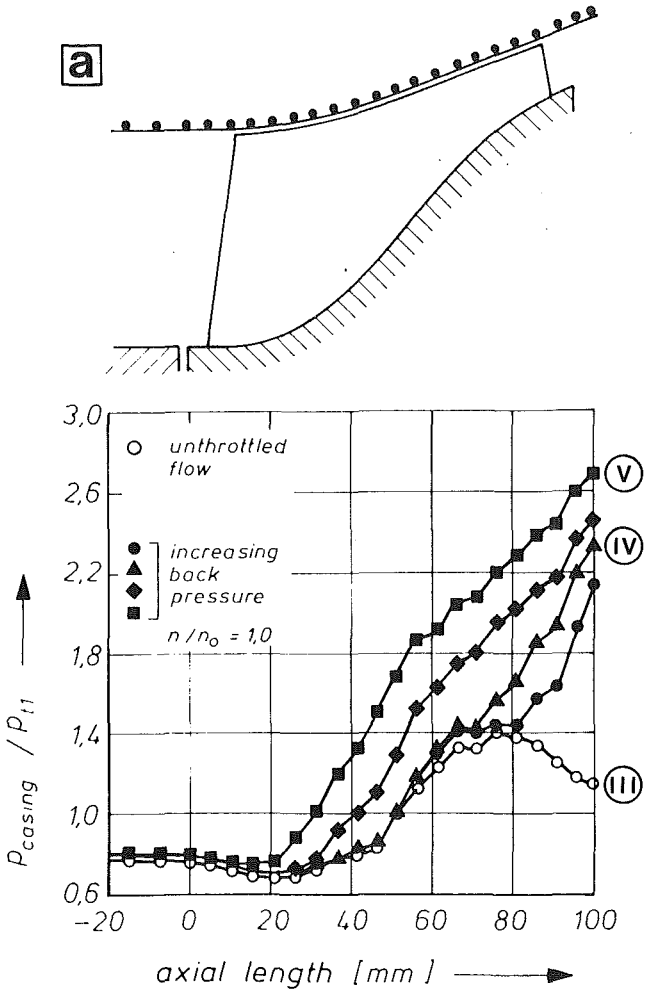

At low-speed operation (79 and 84 percent corrected speed) rotor efficiency and total pressure ratio increase with increasing back pressure (measurement I at 84 percent corrected speed, corresponding to the equally signed wall-pressure distribution in Fig. 8) until the throttling shock wave is stabilized immediately downstream of the critical cross section. Nevertheless, the rotor efficiency is comparatively low in this speed range, due to the two shock waves to be passed by the flow at the rotor inlet and one throttling shock within the rotor exit region (compare Fig. 8).

At 79 percent corrected speed, efficiency and total pressure decrease significantly with further increasing backpressure. At 84 percent rotor speed only the efficiency is found to decrease (measurement II). These effects are attributed to distinct separation effects, occurring within the highly loaded rear rotor section.

At high-speed operation (93 and 96 percent corrected speed), the worst efficiency and total pressure are measured at moderate loading. At near-surge operation total pressure ratio and efficiency are found to increase again. Decreasing shock losses are apparently being responsible for this behavior.

At design speed, efficiency and total pressure ratio drop continuously with loading until the rear shock wave has entered the critical cross section (measurements III and IV). Apparently, the extremely high aerodynamic loading for subsonic rotor exit flow causes serious flow separation at design speed.

At higher rotor loading the forward shock wave is moved upstream, leading to increasing efficiency and total pressure. At near-surge operation (design operation, measurement V) the shock losses reach their minimum value due to the most forward shock position.

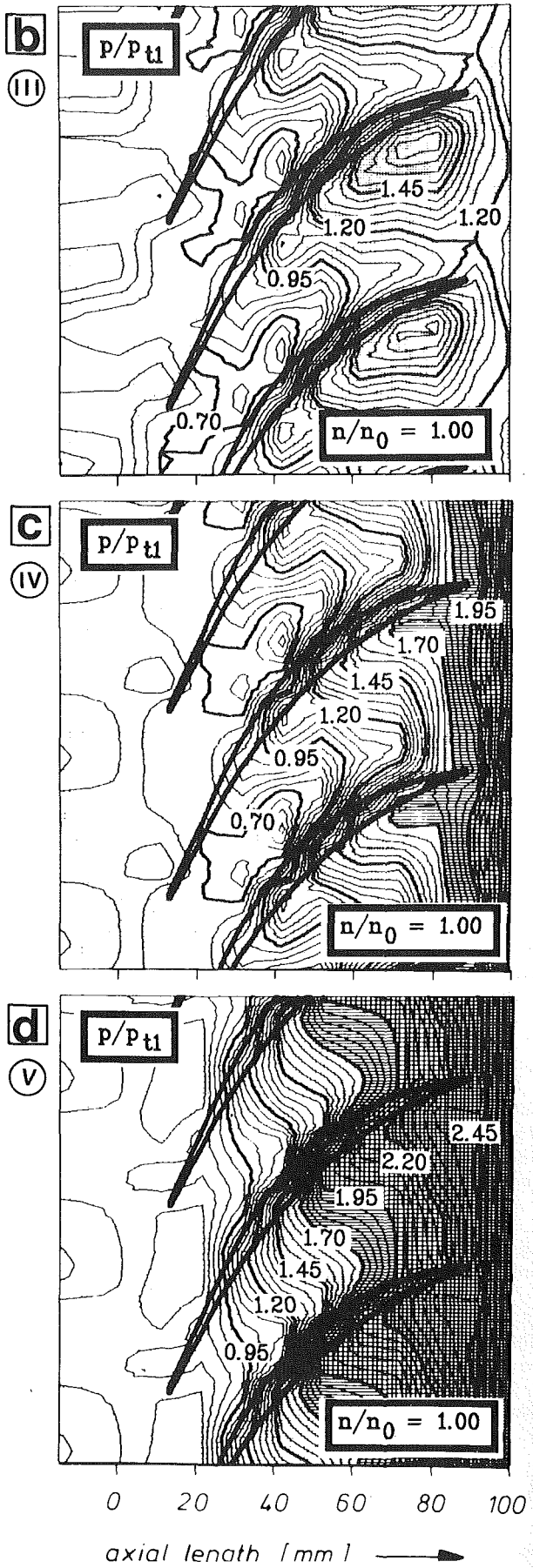

Fig. 9 Pressure distributions at design speed

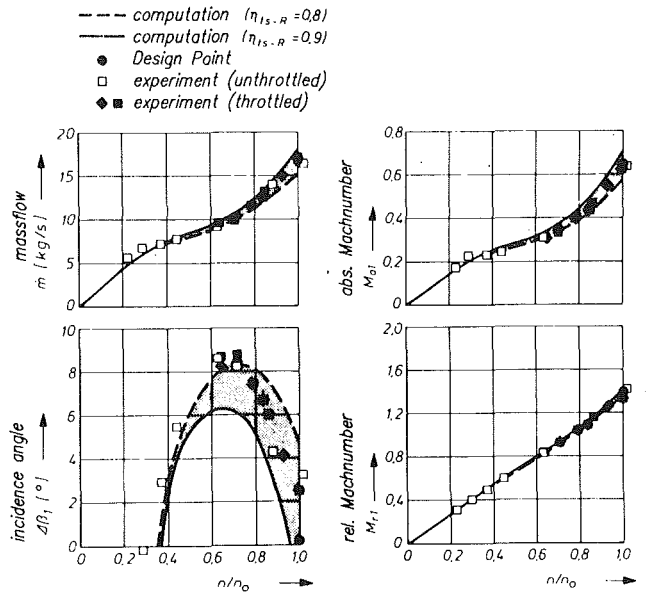

Fig. 10 Measured and predicted rotor inlet data

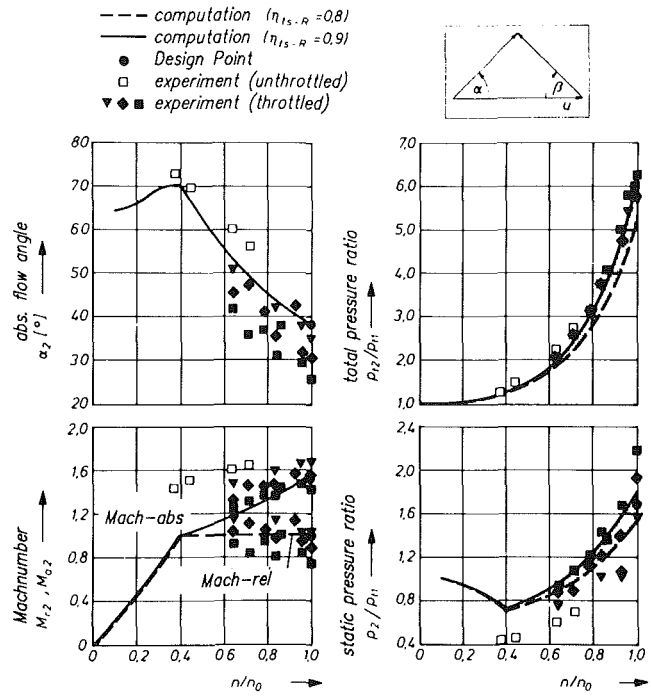

Fig. 11 Measured and predicted rotor exit data

Summarizing the performance characteristics of the mixed-flow compressor rotor, it is found that:

- A good compromise with regard to efficiency and total pressure rise is obtained at high off-design speeds, being important for the cruise capability of jet engines (96 percent corrected speed: peak total pressure ratio 5.79, total isentropic efficiency 0.869).
- A significant drop of efficiency has to be accepted for design operation due to extremely high loading. Nevertheless, the high total pressure rise at design speed is desirable for take-off and the acceleration capability of jet engines.

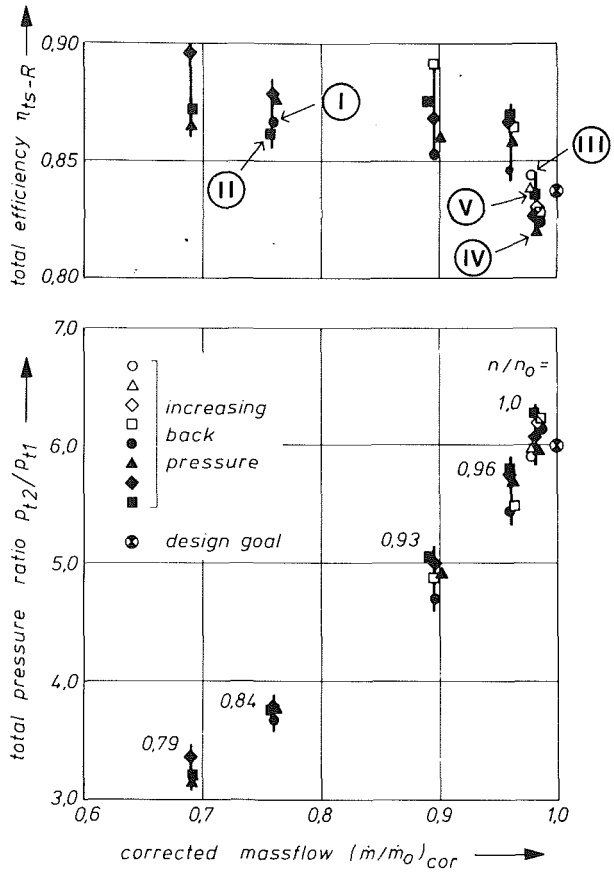

Fig. 12 Performance map of supersonic mixed-flow compressor rotor

6 Conclusions

This paper presents the design and experimental investigation of a highly loaded supersonic mixed-flow compressor rotor.

Concerning shock stabilization within a mixed-flow rotor, an efficient analytical method is presented, yielding stable shock positions for the entire operating range. As a result, a strong shock is indicated to be stable within the entire diagonal blade passage at design speed. At off-design speed, however, the positioning of strong shock waves is restricted to the rotor inlet and exit section. The predicted locations of stable shock waves are verified experimentally.

The further experimental investigations reveal rotor choking occurring at off-design speed and leading to a normal shock-wave immediately upstream of the rotor.

For low back-pressure operation at design speed, however, the shock wave moves downstream until both increasing shock losses and incipient boundary layer separation again lead to critical conditions within the rotor.

At design operation the strong shock wave is moved upstream to the rotor inlet section, leading to considerably increasing rotor efficiency and total pressure ratio.

The relative rotor exit flow is supersonic beyond 38 percent rotor speed for unthrottled operation. At near-surge operation, however, subsonic relative exit flow is provided even at design speed. The absolute rotor exit flow is supersonic for all operating conditions beyond 38 percent rotor speed.

The design goal is met with respect to both total pressure ratio and efficiency. The corrected mass flow at design speed reaches 98 percent of the design value.

Acknowledgments

The investigations presented in this paper were supported by the German government. The researching "Institut für

Strahlantriebe und Turboarbeitsmaschinen" and the authors gratefully acknowledge this promotion.

References

Broichhausen, K. D., and Gallus, H. E., 1982, "Theoretical and Experimental Analysis of the Flow Through Supersonic Compressor Rotors," *AIAA Journal*, Vol. 20, No. 8.

Broichhausen, K.-D., Gallus, H. E., and Mönig R., 1988, "Off-Design Performance of Supersonic Compressors With Fixed and Variable Geometry," ASME JOURNAL OF TURBOMACHINERY, Vol. 110, pp. 312–322.

Dodge, J. L., Bush, D. B., Pechuzal, G. A., and Ravindranath, A., 1986, "High Efficiency Transonic Mixed-Flow Compressor Method and Apparatus," European Patent Application, Publication No. 0201318.

Mönig, R., Broichhausen, K. D., and Gallus, H. E., 1987, "Application of Highly Loaded Single-Stage Mixed-Flow Compressors in Small Jet-Engines," AGARD CP 421.

Musgrave, D. S., and Plehn, N. J., 1987, "Mixed-Flow Compressor Stage Design and Test Results With a Pressure Ratio of 3:1," ASME JOURNAL OF TURBOMACHINERY, Vol. 109, pp. 513–519.

Shapiro, A. H., 1953/54, *The Dynamics and Thermodynamics of Compressible Fluid Flow*, The Ronald Press Company, New York, Vol. I/II.

Simon, H., and Bohn, D., "Experimental Investigation of a Recently Developed Supersonic Compressor Stage (Rotor and Stage Performance)," ASME Paper No. 74-GT-116.

Wilcox, W. W., and Robbins, W., 1951, "Design and Performance of Experimental Axial-Discharge Mixed-Flow Compressor. III—Overall Performance of Impeller and Supersonic-Diffuser Combination," NACA RM E51 A02.

Aerodesign and Performance Analysis of a Radial Transonic Impeller for a 9:1 Pressure Ratio Compressor

S. Colantuoni

A. Colella

Alfa Romeo Avio,
Società Aeromotoristica p.A.,
Research and Development,
Napoli, Italy

The aerodynamic design of a centrifugal compressor for technologically advanced small aeroengines requires more and more the use of sophisticated computational tools in order to meet the goals successfully at minimum cost development. The objective of the present work is the description of the procedure adopted to design a transonic impeller having 1.31 relative Mach number at the inducer tip, 45 deg back-swept exit blade angle, and a tip speed of 636 m/s. The optimization of the blade shape has been done by analyzing the aerodynamic flowfield by extensive use of a quasi-three-dimensional code and a fully three-dimensional Euler solver based on a time-marching approach and a finite volume discretization. Testing has been done on the impeller-only configuration, using a compressor rig that simulates real engine hardware, i.e., having an S-shaped air-intake. The overall performance of the impeller is presented and discussed.

Introduction

The requirements of small gas turbine engines for advanced helicopter propulsion and for auxiliary power units has renewed interest in centrifugal compressors, where high pressure ratios are required in a single stage. In an era dominated by fuel costs, the demand for efficient and high loaded machines has never been greater. A research program on high pressure ratio centrifugal compressors was initiated at the Alfa Romeo Avio in 1987. Here we describe the impeller design, the testing, and the analysis of the results. One-dimensional calculations, using semi-empirical correlations, for the losses, slip factor, and blockages have been performed to define the preliminary design of impeller.

The aerodynamic design is carried out in two steps:

- In the first step a quasi-three-dimensional approach has been used, so that the definition of the channel portion of blade has been performed at a relatively low cpu charge.
- The second step has been the optimization of the blade shape principally in the inducer portion, where the transonic flow behavior can be simulated only by means of transonic codes. A fully three-dimensional Euler code has been used.

The impeller was tested in ARA in autumn 1990. The overall performance was tested, and information was gathered on the impeller static pressure along the shroud. The following theoretical–experimental comparisons show the interesting capability of the three-dimensional Euler code to predict the transonic flow in the inducer region and the flow margin of the impeller.

Preliminary Design

The function of the preliminary design is to compute, on an essentially "one-dimensional" flow basis, the skeletal geometry of the impeller and a rough description of the flow at inlet and outlet.

Calculation Code. The code used is based on the evaluation of the theoretical head and all of the losses for any operating condition, from which the pressure ratio and efficiency can be determined.

The basic equations for the determination of the pressure ratio and efficiency are extremely simple. The pressure ratio is determined by:

$$PR = [1 + ETA_{is} * U^{2} * \Delta Q_{th}/cpT1]^{(T/T-1)}$$

where ETA_{is} is the isentropic efficiency and Q_{th} is the theoretical head nondimensionalized with respect to the tip speed squared.

The isentropic efficiency is defined in terms of the theoretical head and the internal losses occurring in the compressor:

$$ETA_{is} = 1 - \Sigma\Delta Q_{internal}/\Delta Q_{th}$$

while the overall efficiency is defined as:

$$ETA_{ov} = (\Delta Q_{th} - \Sigma\Delta Q_{internal})/(\Delta Q_{th} + \Sigma\Delta Q_{external})$$

The internal losses are defined as those that reduce the total pressure from that which is theoretically obtainable from the

Contributed by the International Gas Turbine Institute and presented at the 37th International Gas Turbine and Aeroengine Congress and Exposition, Cologne, Germany, June 1–4, 1992. Manuscript received by the International Gas Turbine Institute February 11, 1992. Paper No. 92-GT-183. Associate Technical Editor: L. S. Langston.

work input to the fluid imparted by the impeller, and the external losses are defined as those that necessitate a work input to the impeller in excess of the theoretical head produced.

The theoretical head is evaluated from Euler's equation with introduction of slip factor. The problem of determining the pressure ratio and efficiency of compressor is reduced to the evaluation of the slip factor and the internal and external losses occurring within the machine.

The losses evaluated in the impeller are those due to skin friction, blade loading, blade-wake mixing, impeller shroud clearance, and throat blockage. The effects of shock waves are included in terms of a Mach number correction, while the secondary flows are indirectly incorporated in the blade-loading losses.

Preliminary Design Output. The target requirements for the preliminary design are:

Total pressure ratio	9.8:1
Total efficiency	89 percent
Mass flow	3.35 kg/s

Due to economic reasons and rig layout, there are the following geometric constraints:

Exit tip radius	$\leq$ 139.5 mm
Inlet shroud radius	= 82.65 mm
Inlet hub radius	$\geq$ 29.2 mm
Use of an available shroud contour	

Moreover, another design constraint is to design an impeller with full blades.

Table 1 lists the output of the preliminary design. The parameters marked with an asterisk have been taken as constraints. The constraints on tip radius and inducer tip radius, together with the maximum tip speed to reach the target pressure ratio and the high value of mass flow, lead to a relative Mach number of 1.3 at the inducer tip. The aerodynamic design of the impeller is without any doubt quite critical.

To control the blade loading, the optimum blade number is 29, but reasons of manufacturing cost set the blade number at 23, due to difficulties to machine the hub vane sections.

To reduce the shock strength the inducer tip thickness at the leading edge was originally set to 0.2, but for the reasons above it has been increased to 0.4 mm.

The backsweep angle is set to 45 deg, which seems a better compromise between the target of pressure ratio, stress levels, and the absolute tip Mach number.

Blade Geometry Definition

Having obtained, from the preliminary design, the impeller geometry scantlings in the form of inlet and outlet diameters and blade angles, the next step is to define the three-dimensional blade geometry, specifying hub and casing meridional profiles and distributions of blade camber angle and thickness.

Table 1 Impeller design data

Rotational speed	43,500 rpm
NREC specific speed	0.096
BALIE specific speed	77.8
Efficiency $T - T$	89 percent
Mass flow	3.35 kg/s
Pressure ratio $T - T$	9.8
Prewhirl angle	0.0 deg
Number of blades	23
Inlet hub radius*	31.8 mm
Inlet shroud radius*	82.65 mm
Inlet shroud relative Mach number	1.31
Inlet hub blade angle	35.00 deg
Inlet shroud blade angle	60.00 deg
Inlet hub incidence	6.2 deg
Inlet shroud incidence	1.8 deg
Tip radius*	139.5 mm
Exit blade height	8.4 mm
Exit blade angle	45.00 deg
Blade tip speed	635.5 m/s
Exit absolute Mach number	1.13
Work input parameter ($DH/U^{**}2$)	0.719

*Design constraints.

The method is based on the application of Bezier polynomial patches (Casey, 1983; Qinghuan, 1988). The meridional channel is divided by means of five patches, three of them inside the blade and two respectively upstream and downstream of impeller. Continuity between the patches is obtained by equality of the first and second derivatives at corner points. The camber angles are defined at hub and shroud contour of the patches and hub-to-shroud straight-line elements interpolation is chosen because it is easier to machine, even if it is not always aerodynamically acceptable.

This approach has the great advantage of defining the whole geometry by analytic expressions; therefore, it is particularly suitable to be used in computer-aided design (CAD) methods, where input shape information is given efficiently and overcame the limitation of the past years, where the geometry was given by an array of points.

Aerodynamic Design

The aerodynamic design was carried out in two steps. During the first one a quasi-three-dimensional approach with meridional loss distribution model has been used (Katsanis and McNally, 1977), to have a very quick aerodynamic tool suitable to be integrated into the geometric generation procedure of the impeller blade.

Moreover, even if the flow is highly three dimensional and transonic, the quasi-three-dimensional codes give realistic distributions on blade loading and meridional velocity (Came and Herbert, 1980), therefore the blading shape and meridional contour should need few modifications.

Nomenclature

ALFA3 = exit absolute flow angle
CL = loading coefficient = $(V_{ss} - V_{ps})/V_{av}$
DH = enthalpy rise
ETA = efficiency
MACH3 = exit absolute Mach number
M = Mach number
PR = pressure ratio
PS = shroud local static pressure
PSIE = impeller exit static pressure
PT1 = impeller inlet total pressure
Q = head rise
S = normalized meridional distance
SLIP = slip factor
TLE = total temperature at leading edge
TPLEN = total temperature in the plenum of test rig
U = tip speed
V = relative velocity
VM = meridional velocity
W = mass flow
Υ = specific heat ratio

Subscripts

av = average
is = isentropic
ov = overall
ps = pressure side
ss = suction side
th = theoretical
tt = total-to-total

Figures 1(A, B, C) show the results obtained. The blade loading seems acceptable, although the design choice of a full-blade impeller and blade number is not the optimum.

The final aerodynamic design has been performed by means of a fully three-dimensional Euler code, widely used since large-scale digital computers have become available. The method used here is based on a time-marching technique and finite volume discretization procedure (Arts, 1988). The computational domain (Fig. 2) consists of 77 spanwise (51 of them between leading and trailing edge), 13 streamwise surface, and 7 bladewise surfaces.

The inlet conditions are purely axial flow and constant total pressure and temperature profiles. Downstream of the blade row, the static pressure has been imposed at the hub, although the code can be able to accept this condition at any spanwise position of the exit boundary.

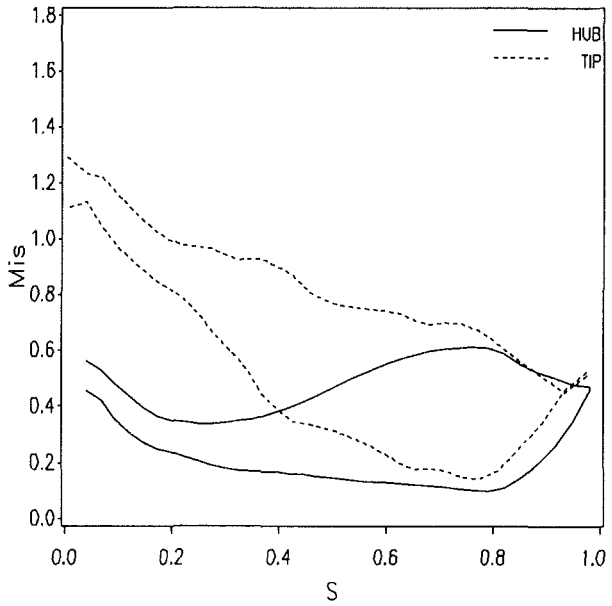

Fig. 1(A) Quasi-three-dimensional analysis at the design point: isentropic Mach number

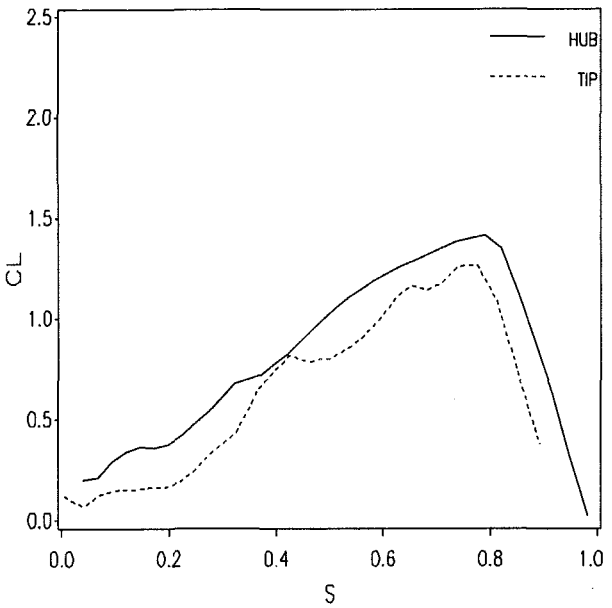

Fig. 1(B) Quasi-three-dimensional analysis at the design point: loading coefficient

The results of three-dimensional analysis are shown in Fig. 3 for the hub, mid, and tip sections. The solution obtained shows smooth velocity distribution with high diffusion gradient at the shroud pressure side. In reality this gradient should be less, because of the blockage effect of boundary layer buildup. The impeller inducer has good behavior, with smooth diffusion of the transonic flow.

The three-dimensional investigation has also been performed at the off-design conditions. The analysis has been limited to design rotation speed, and has been performed changing the value of static pressure at the discretization exit. The impeller speedline, in terms of exit pressure ratio versus mass flow, obtained during this analysis is shown in Fig. 4.

Figure 5 shows the velocity distribution for the near-surge condition. Here a strong deceleration is detected just downstream of the leading edge, with maximum pressure recovery of the inducer. For this flow condition the code still gives a numerically stable solution; in fact, a further small increase of exit static pressure make the solution unstable. Therefore we can define this condition as "near-surge condition."

The results for the incipient choke are presented in Fig. 6. The flow is extremely critical with a strong shock deep in the inducer. This type of flow field is responsible for the low values of efficiency for these operating conditions.

Performance Test

Test Facility. The impeller has been tested in the ARA's compressor test plant. The layout of test facility is shown in Fig. 7(A). The compressor is driven by a 2000 kW electrical engine through a speed variator and a gearbox (Fig. 7B).

Test Rig. In Fig. 7(C) the test rig is shown. The air enters into the impeller from the intake and it is discharged in a radial vaneless diffuser. A deswirl is used to have an axial flow at exit instrumentation plane. A balance piston is used to reduce the axial thrust on the front bearing.

The intake has an asymmetric shape and became axisymmetric just upstream of the impeller.

The radial vaneless diffuser has a long radial extension, which could reduce the flow range of impeller. The availability of this vaneless diffuser, together with the few modifications needed in the next full-stage test, justifies the choice.

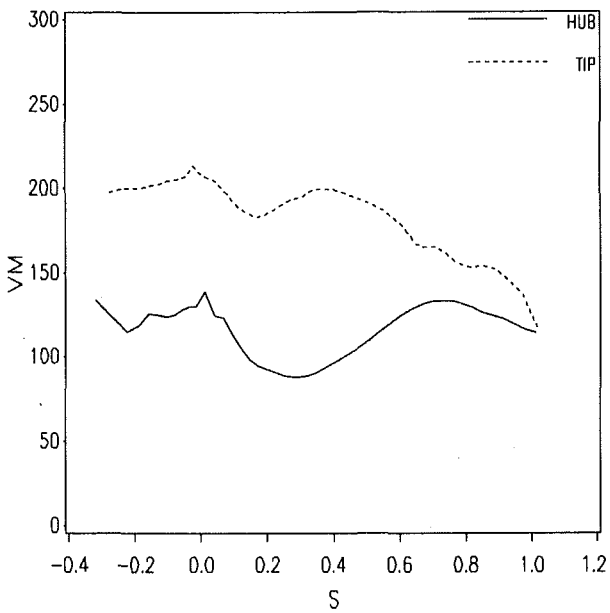

Fig. 1(C) Quasi-three-dimensional analysis at the design point: meridional velocity

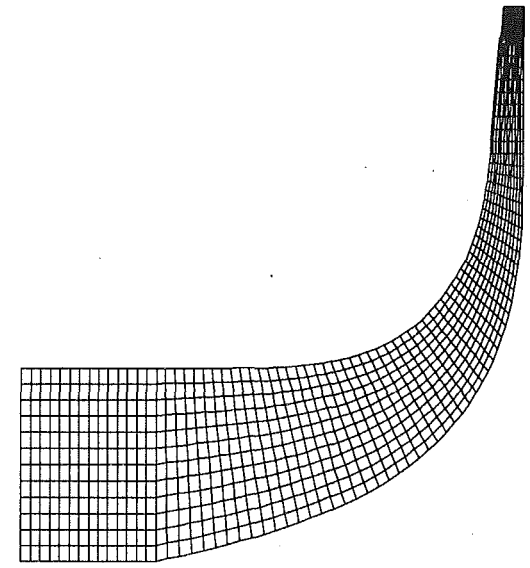

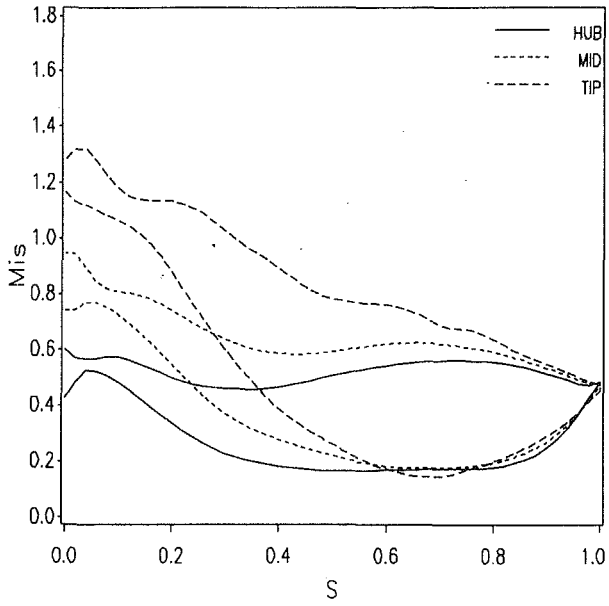

Fig. 3 Result of transonic three-dimensional analysis at the design point

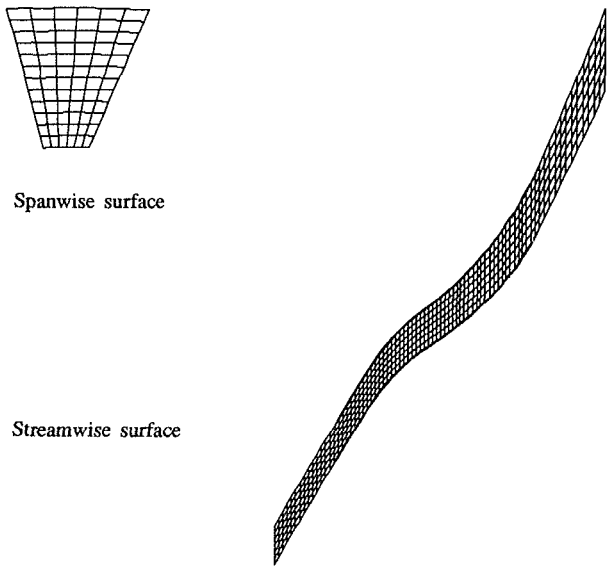

Fig. 2 Computational domain

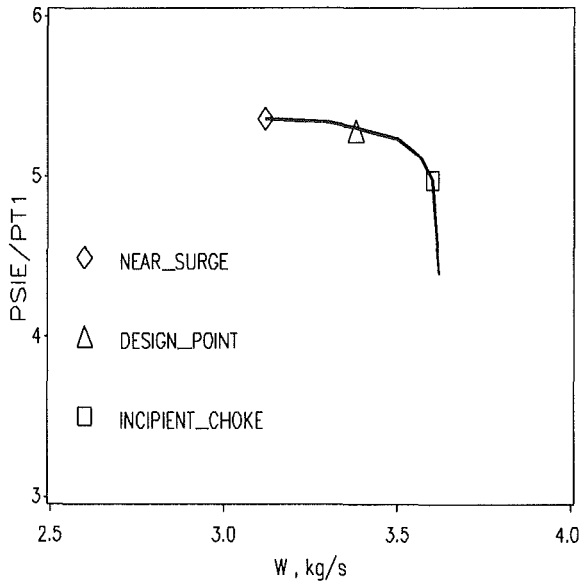

Fig. 4 Result of transonic three-dimensional analysis: impeller design speedline

Instrumentation. The instrumentation is the classic one used in performance evaluation tests, with total pressure probe and thermocouple in the plenum, and static pressure taps at inlet and exit plane of the impeller. The exit impeller temperature is obtained by means of total-temperature rakes located at the exit plane of compressor. The mass flow has been measured at inlet by a venturi nozzle located upstream of the plenum chamber and at exit by an orifice plate situated in the outlet duct.

To get information on impeller behavior, two rows of static taps on the shroud, at the top and bottom positions, have been used. Moreover four thermocouples, equally spaced over the circumference, are located just upstream of the impeller leading edge.

Test Results

The performance of the impeller have been carried out for the speedlines 70, 80, 85, 90, 95, and 100 percent of design speed.

The rig has been assembled with an axial tip clearance of 1.51 mm. This leads to 0.7 mm of measured running clearance at design speed, quite large with respect to the design value of 0.32 mm.

Since inlet/exit stagnation pressure has not been directly measured, one-dimensional analysis, based on mass flow continuity, using the measured static pressure and total temperature, has been used. Moreover, in accordance with the design hypothesis, 12 and 2 percent of aerodynamic blockage have been applied at exit and inlet of impeller, respectively.

The performances of the impeller have been presented in Figs. 8(A–F). A summary of comparison between target and measured performance values is presented in Table 2 for the design speed. The experimental data are referred to 3.2 kg/s of mass flow, where the peak efficiency is detected.

As we can see, at the design speed and pressure ratio the target efficiency of 89 percent is quite well achieved, but the flow is 4.48 percent lower than design value. The absolute flow

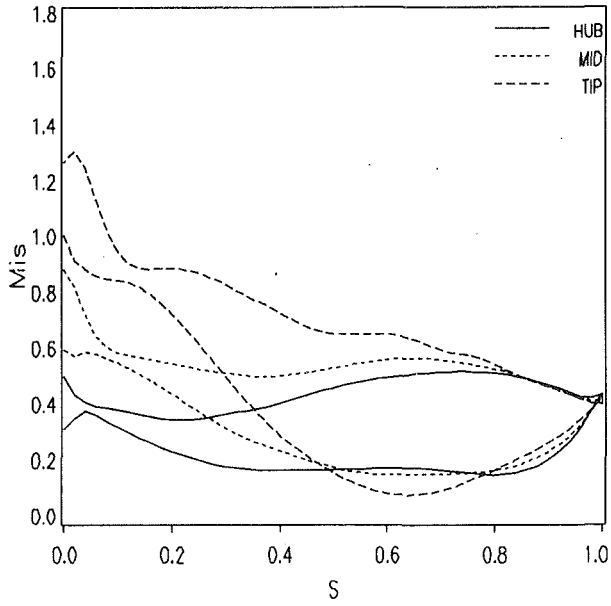

Fig. 5 Result of transonic three-dimensional analysis for the near-surge condition

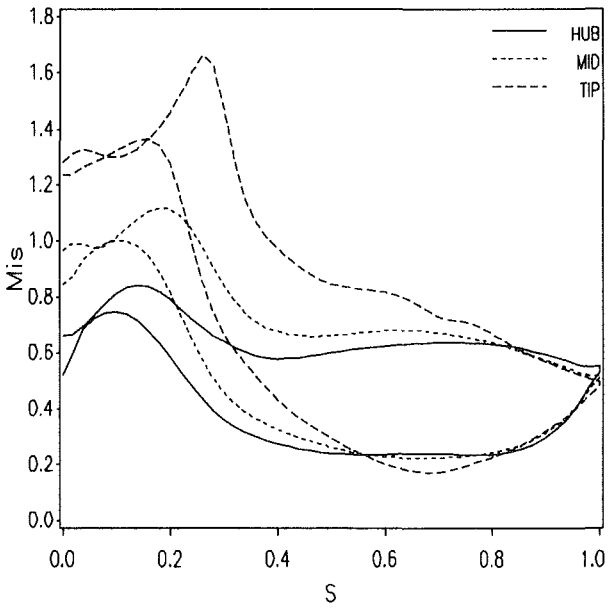

Fig. 6 Result of transonic three-dimensional analysis for the incipient choke condition

angle results 2.2 deg greater than design; therefore, an increase in work parameter is detected, since the Mach number is the same as design.

Unfortunately the analysis of the measures has shown a failure of mass flow measure at the venturi nozzle; therefore we cannot evaluate the exact mass flow deficiency. The mass flow through the impeller is without doubt greater than the one measured from the orifice plate, since there is the same leakage flow from backplate through the balance piston seal. (A study of the rig air system has showed that this amount of air can be up to 80 g/s at choke condition.)

The level of efficiency reached is a positive result, taking into account that the impeller works with high values of inlet relative Mach number, high blade loading, a value of running clearance double with respect to the design one and, last but not least, has been coupled to an asymmetric intake.

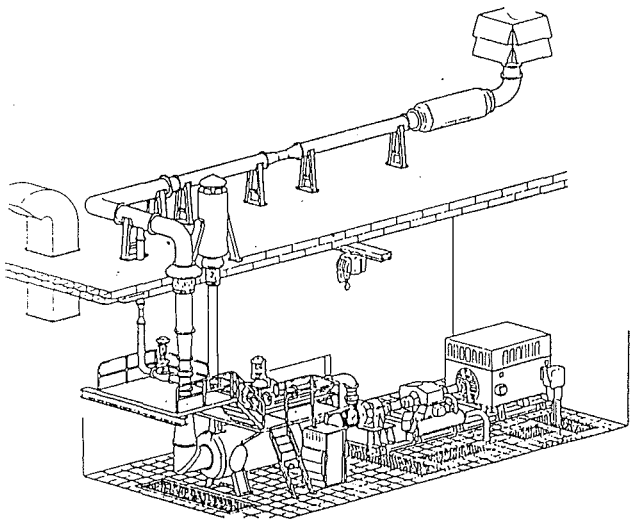

Fig. 7(A) Compressor test plant

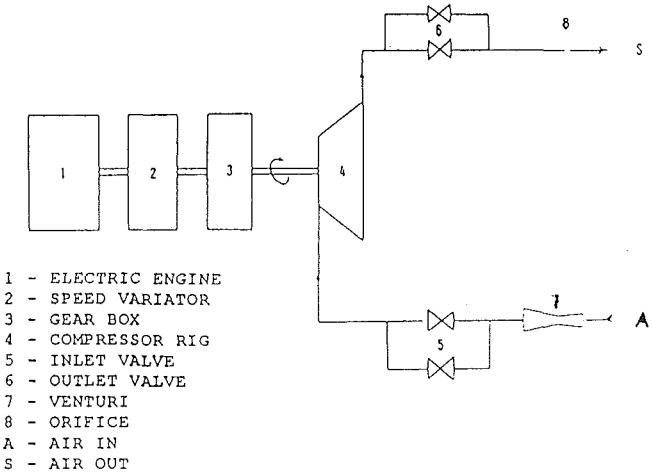

Fig. 7(B) Test facility layout

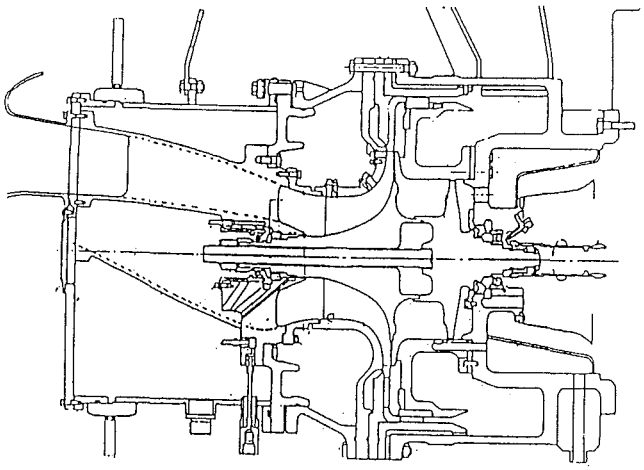

Fig. 7(C) Compressor rig

Impeller Aerodynamic Behavior and Theoretical Comparison With Results of Three-Dimensional Transonic Analysis

Figures 9(A) and 9(B) show, for the near-top (42–49 deg) and near-bottom position (222–229 deg) the static pressure ratio measured along the impeller shroud, in all the conditions, from choke to surge of design speed.

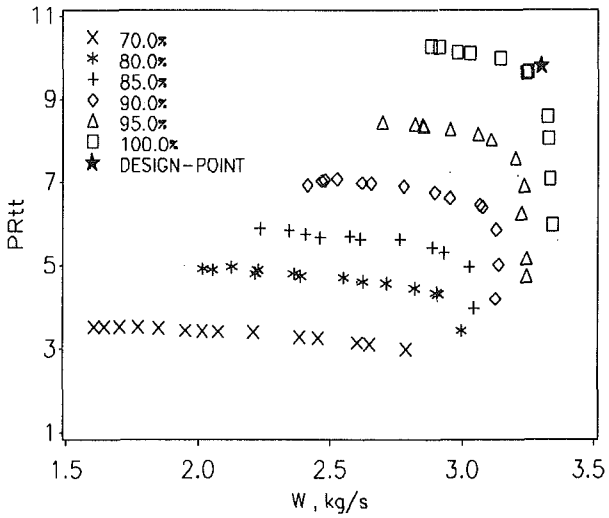

Fig. 8(A) Test results: total-to-total pressure ratio versus mass flow

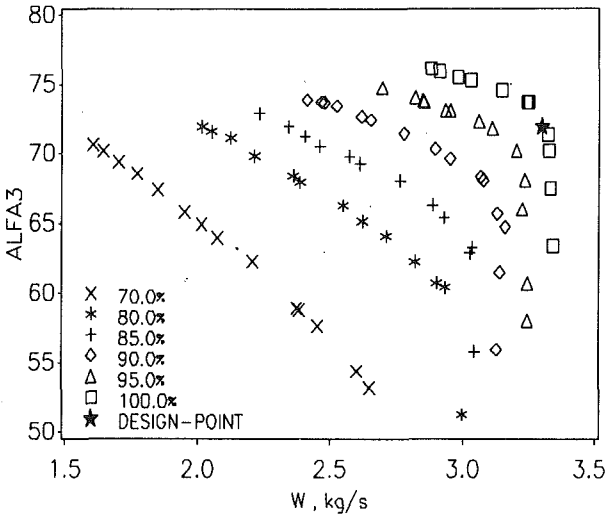

Fig. 8(D) Test results: absolute exit flow angle versus mass flow

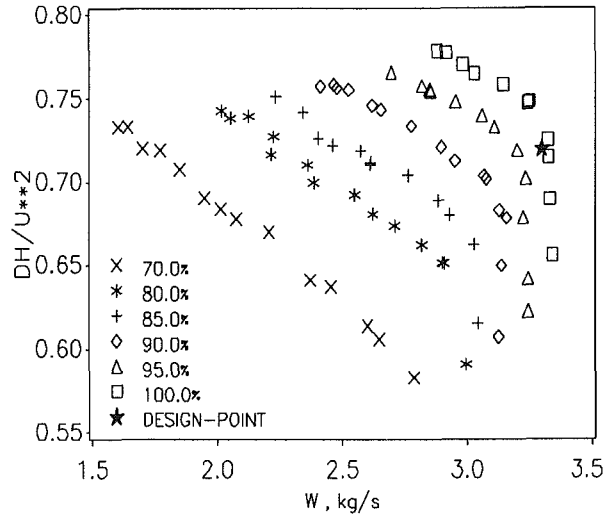

Fig. 8(B) Test results: work parameter versus mass flow

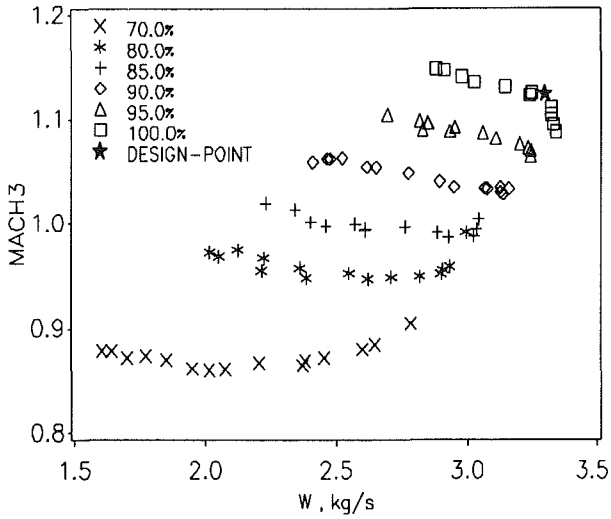

Fig. 8(E) Test results: absolute exit Mach number versus mass flow

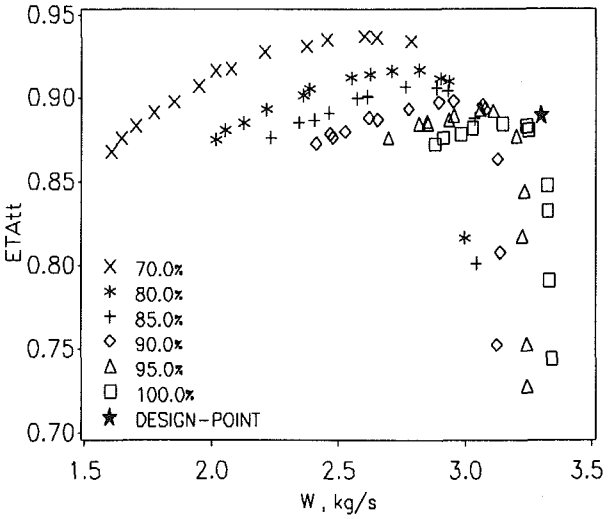

Fig. 8(C) Test results: total-to-total efficiency versus mass flow

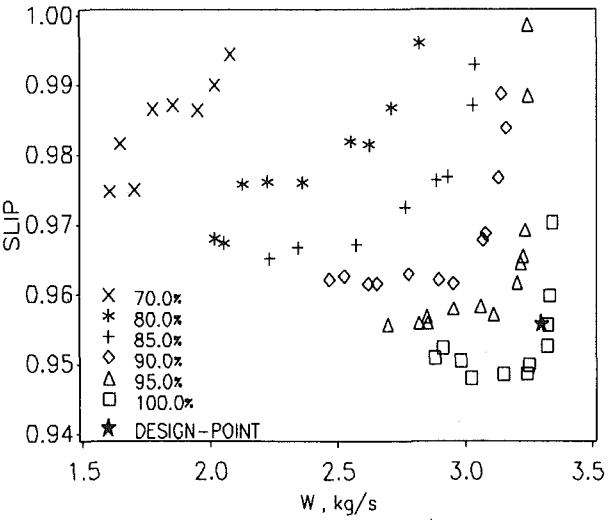

Fig. 8(F) Test results: slip factor versus mass flow

From the comparison between the static pressure distributions, the different behavior from the top and bottom positions of the impeller is clear. This is due to the shape of the intake, which is responsible for the circumferential distortion of the flow coming into the impeller. Therefore, as we can see from the figures above, the impeller is forced to work with different values of incidence angles, with top values greater than bottom.

Table 2 Experimental results

Parameter	Target	Exper.	Percent
W, kg/s	3.35	3.20	−4.48
PR_{tt}	9.8	9.8	0.0
ETA_{tt}, percent	89	88.5	−0.67
DH/U**2	0.72	0.75	4.17
ALFA3, DEG	71.8	74.0	3.06
MACH3	1.13	1.13	0.0
Slip	0.956	0.949	−0.73

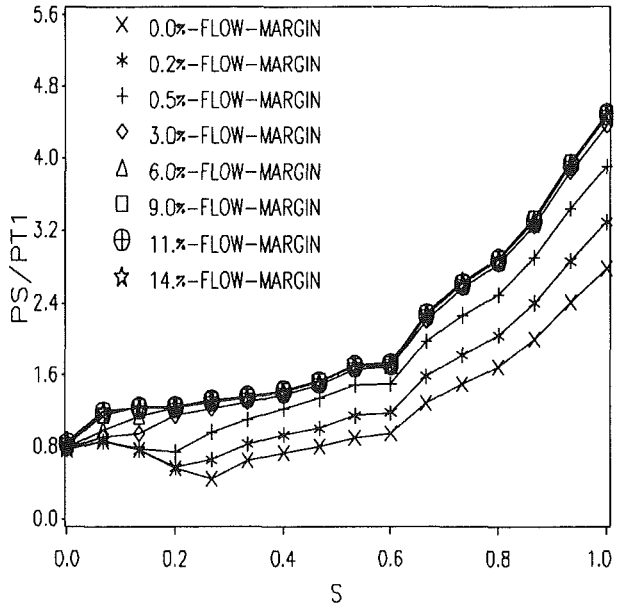

Fig. 9(A) Test results: static pressure ratio at top position of the impeller shroud

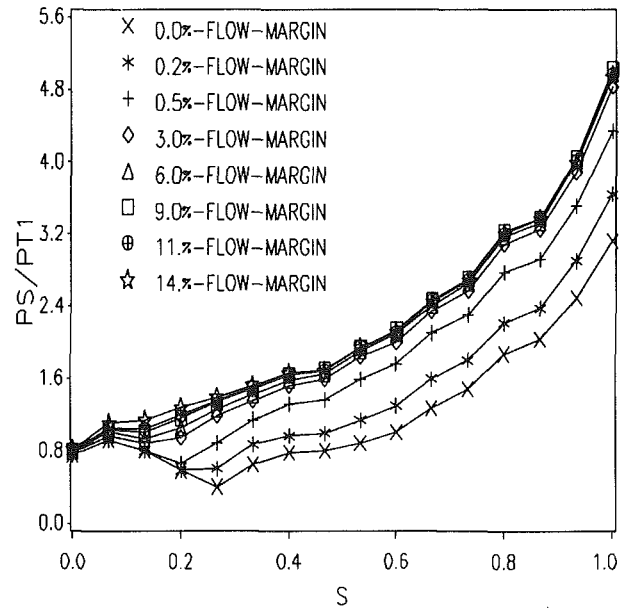

Fig. 9(B) Test results: static pressure ratio at bottom position of the impeller shroud

For this reason the top of the inducer is already stalled at 9 percent of flow margin ($1 - W_{surge}/W_{choke}$) while the bottom region doesn't seem to be on stall in the whole flow range.

To confirm what was said above, Fig. 9(C) shows the circumferential distribution of measured temperatures just upstream of the impeller leading edge. Values of temperature ratio ~0.5 at the 0 deg position are indicative of recirculation flow region and therefore stall. It is clear that the shape of the intake has a negative influence on the impeller performances, with reduction of flow margin and pressure ratio, and therefore efficiency.

Figure 10(A) shows for the design speed the static pressure ratio of the impeller derived from measurements relatively at top and bottom positions versus mass flow. Moreover, in the same figure, the theoretical speedline, obtained from the three-dimensional transonic analysis for the off-design conditions, is also plotted.

The symbols are relative to the operating conditions chosen for the comparison. For the reasons discussed above there are differences between top and bottom impeller static pressure ratios. Besides, as expected, the theoretical speedline presents higher pressure ratio and mass flow, because of the viscous effects on the flow that the Euler code cannot take into account.

What we found interesting is plotted in Fig. 10(B) from which we can see that the stability range, calculated by three-dimensional code, is very close to the measured one. Therefore it should seem that numerical flow field instability, detected for mass flow values less than the point called "near surge," is related to a physical phenomenon.

In Figs. 11(A–D), the results of the static pressure distribution along the impeller shroud are presented. The experimental-theoretical results are relative to four flow conditions at design speed: incipient choke, peak efficiency, 9 percent flow margin, and near surge, which are represented by different symbols in Figs. 10(A, B). In all the conditions the comparison between predictions and experimental data, derived from static taps at bottom, relative to the inducer region are very good.

Conclusion

The aerodynamic design and experimental evaluation of an impeller for a single-stage high pressure ratio compressor have been described.

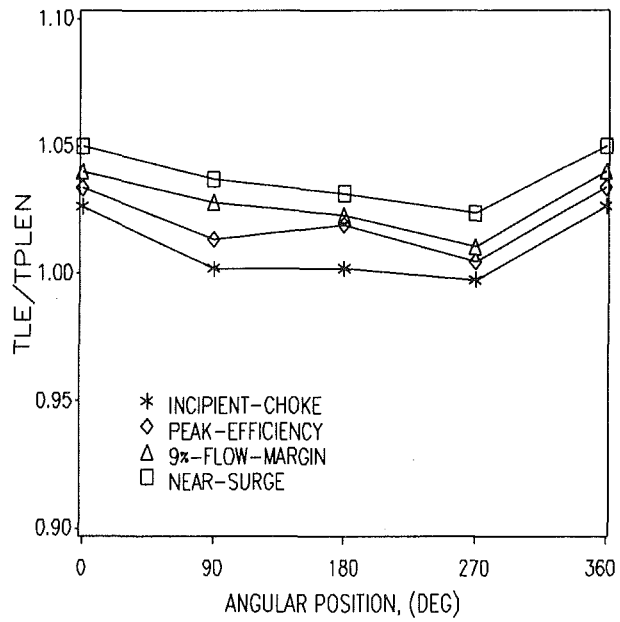

Fig. 9(C) Test results: total temperature at impeller leading edge

The preliminary design has been carried out under severe geometric limitations:

- Shroud contour fixed
- Inducer shroud diameter fixed
- Limitation on maximum tip diameter
- Full blade

These constraints, together with the target requirements (9.8:1 total pressure ratio, 89 percent of total efficiency, and 3.35 kg/s), have forced the design versus a transonic impeller (inlet relative Mach number 1.3) with high tip speed and exducer blade loading.

The preliminary aerodynamic design has been performed using a fast procedure obtained coupling an aerodynamic solver, based on a quasi-three-dimensional approach, together with a geometric tool, based on the use of the Bezier polynomial patches.

The final aerodynamic design has been performed using a fully three-dimensional Euler code, which has also been used to analyze the fluid-dynamic behavior of the impeller in the off-design conditions relatively to the design speed.

The preliminary tests have been carried out on this impeller, and sufficient data have been obtained to indicate its potential development.

In fact, although the first impeller only test has been carried out with quite a large running clearance (measured value of 0.7 mm against design value of 0.32 mm), the efficiency level is near the expected value.

The impeller has been forced to work with different inlet flow conditions from design, because it has been coupled with asymmetric air-intake; therefore nonuniform inlet flow conditions have produced more inlet blockage and nonuniform velocity profile in radial and tangential directions, impacting negatively on the impeller performances.

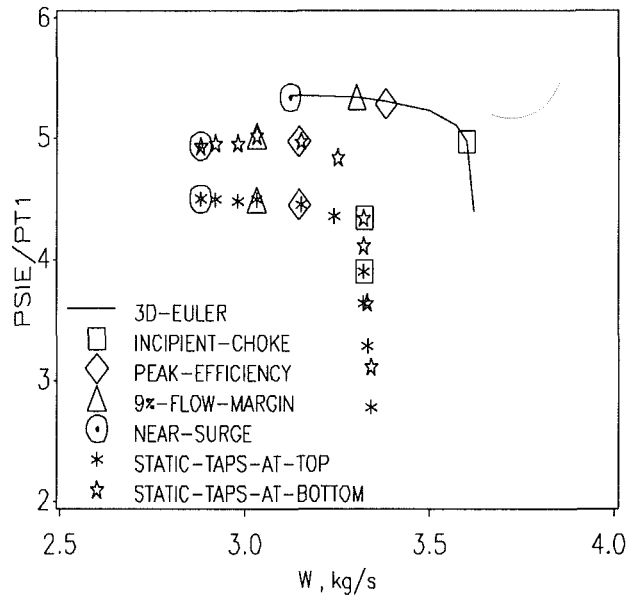

Fig. 10(A) Experimental-theoretical comparison: impeller static pressure ratio versus mass flow

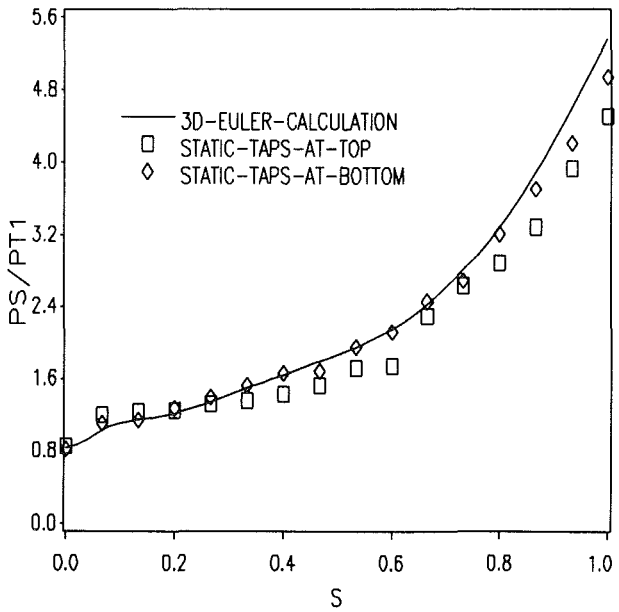

Fig. 11(A) Experimental-theoretical comparison: impeller shroud static pressure ratio for near-surge condition

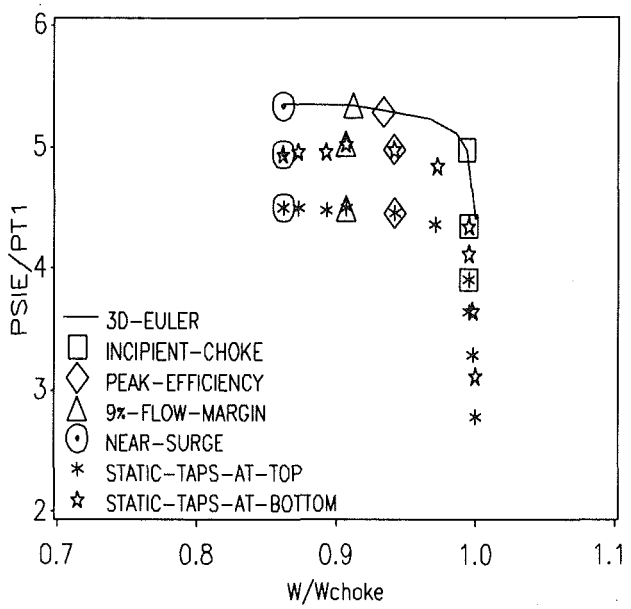

Fig. 10(B) Experimental-theoretical comparison: impeller static pressure ratio versus nondimensional mass flow

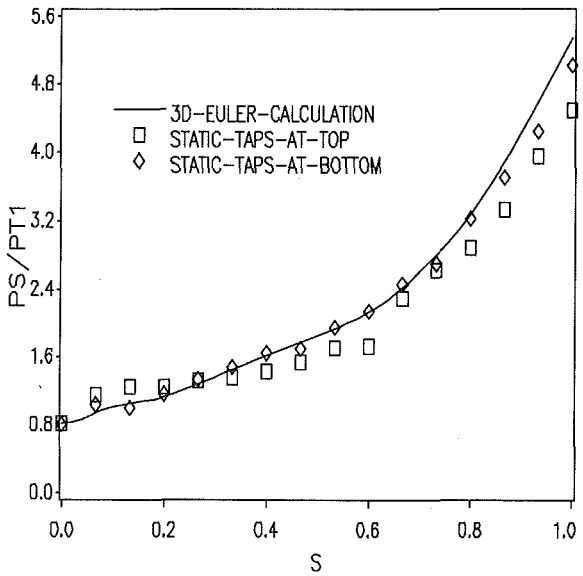

Fig. 11(B) Experimental-theoretical comparison: impeller shroud static pressure ratio near 9 percent flow margin condition

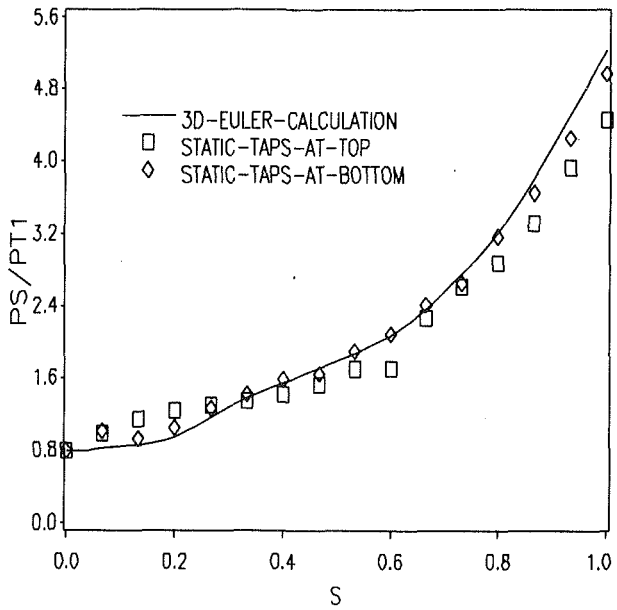

Fig. 11(C) Experimental-theoretical comparison: impeller shroud static pressure ratio for peak efficiency condition

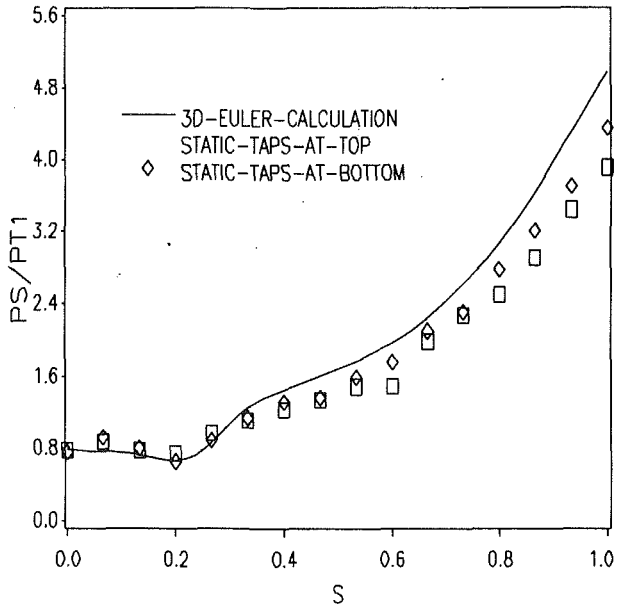

Fig. 11(D) Experimental-theoretical comparison: impeller shroud static pressure ratio for incipient choke condition

Nevertheless, the comparison between the results of aerodynamic analysis by the three-dimensional Euler code and experimental results is satisfactory. Finally the tool's capability to design a transonic, highly loaded impeller for high-pressure single-stage centrifugal compressors has been confirmed.

References

Arts, T., 1988, "Three Dimensional Inviscid Flow Calculations in Turbomachinery Components," presented at the 16th ICAS Congress.

Came, P. M., and Herbert, M. V., 1980, "Design and Experimental Performance of Some High Pressure Ratio Centrifugal Compressors," AGARD-CP-282.

Casey, M. V., 1983, "A Computational Geometry for the Blades and Internal Flow Channels of Centrifugal Compressors," ASME *Journal of Engineering for Power*, Vol. 105, pp. 288-295.

Katsanis, T., and McNally, W. D., 1977, "Revised Fortran Program for Calculating Velocities and Streamlines on the Hub-Shroud Midchannel Stream Surface on an Axial, Radial, or Mixed-Flow Turbomachine or Annular Duct," NASA TN D-8431.

Qinghuan, W., and Xiayan, H., 1988, "The Use of Bezier Polynomial Patches to Define the Geometrical Shape of the Flow Channels of Compressors," ASME Paper No. 88-GT-60.

E. Ayder

R. Van den Braembussche

von Karman Institute for Fluid Dynamics,
Rhode Saint Genese, Belgium

J. J. Brasz
Carrier Corporation,
Syracuse, NY 13221

Experimental and Theoretical Analysis of the Flow in a Centrifugal Compressor Volute

Detailed measurements of the swirling flow in a centrifugal compressor volute with elliptical cross section are presented. They show important variations of the swirl and throughflow velocity, total and static pressure distribution at the different volute cross sections and at the diffuser exit. The basic mechanisms defining the complex three dimensional flow structure are clarified. The different sources of pressure loss have been investigated and used to improve the prediction capability of one-dimensional mean streamline analysis correlations. The tangential flow loss model under decelerating flow conditions and the friction loss model are confirmed. New empirical loss coefficients are proposed for the exit cone loss model and the tangential flow loss model for the case of accelerating flow in the volute.

Introduction

The highly three-dimensional flow field inside centrifugal compressor and pump volutes has been measured by Peck (1951), Muller (1973), Van den Braembussche and Hande (1990), Elholm et al. (1992), and Ayder and Van den Braembussche (1991).

Most prediction methods presented in the literature, however, assume a uniform flow distribution over the cross section of the volute (Iversen et al., 1960; Japikse, 1982; Weber and Koronowski, 1986), or calculate the flow inside a simplified two-dimensional model of the volute by transforming it into a divergent or convergent channel (Kurokawa, 1980). Volute losses are obtained by adding friction losses and tangential and meridional velocity dump losses. None of these methods accounts for the three-dimensional swirling flow.

These simplifications cause errors on the predicted volute-impeller matching mass flow. The predicted circumferential pressure variation is different from the experimental one (Stiefel, 1972). This leads to incorrect prediction of variable blade loadings and of the radial forces on the shaft and bearings. Improvements can be made only by a better understanding of the flow structure in the volute.

Only two prediction methods of volute flow that account for the three-dimensional flow effects have been found in the literature: Muller (1973), and Van den Braembussche and Hande (1990). Total pressure losses due to the boundary layer on the walls and internal friction because of swirl are accounted for by means of a nondimensional total pressure variation over the cross section. The static pressure variation over the cross section results from a nondimensional swirl distribution and volute inlet flow conditions.

The purpose of the present study is to give a better insight into the three-dimensional flow structure in a centrifugal compressor volute with elliptical cross section: in order to verify the assumptions used in the three-dimensional analytical models, to investigate the sources of losses, and to evaluate and improve the prediction capability of a simple one-dimensional model.

Experimental Facility

The measurements have been performed on the R6 test facility at the von Karman Institute. This facility has been described by Ayder and Van den Braembussche (1991). A low specific speed impeller is combined with a narrow vaneless diffuser of radius ratio 2.24, and a commercial volute with elliptic cross-sectional shape (Fig. 1). The circumferential var-

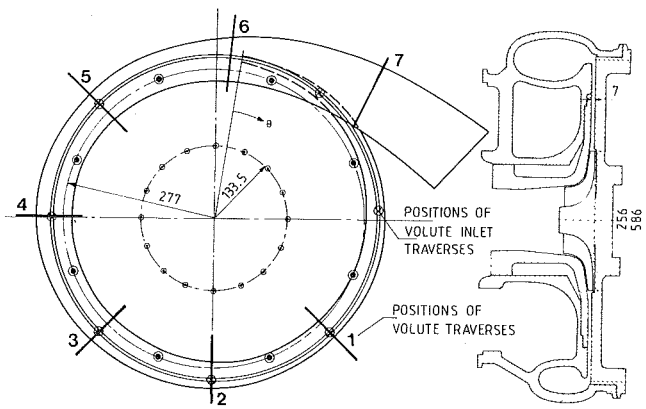

Fig. 1 Geometry of the centrifugal compressor; positions of diffuser outlet and volute traverses

Contributed by the International Gas Turbine Institute and presented at the 37th International Gas Turbine and Aeroengine Congress and Exposition, Cologne, Germany, June 1–4, 1992. Manuscript received by the International Gas Turbine Institute January 28, 1992. Paper No. 92-GT-30. Associate Technical Editor: L. S. Langston.

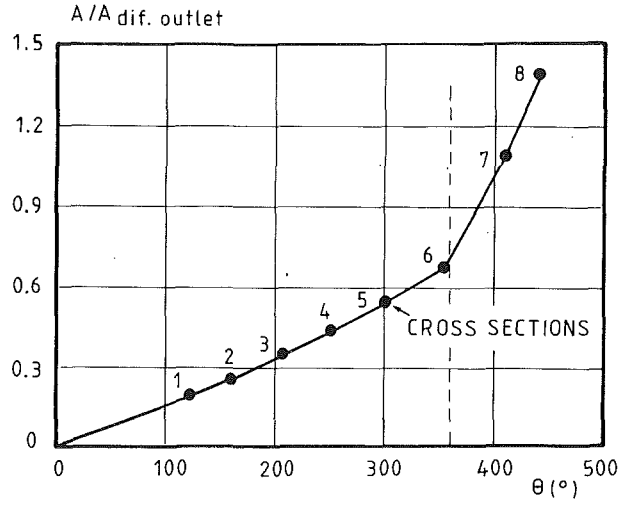

Fig. 2 Circumferential variation of cross-sectional area

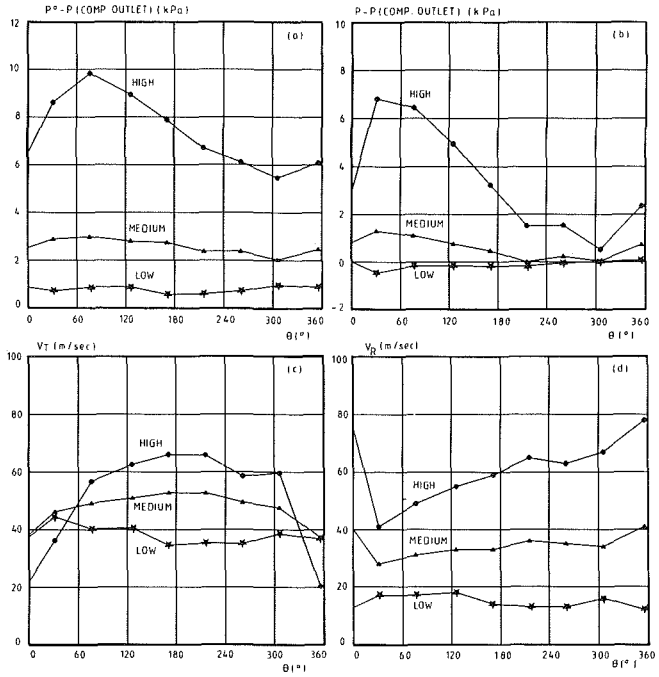

Fig. 3 Circumferential variation of diffuser outlet mass-averaged total pressure (*a*), static pressure (*b*), throughflow velocity (*c*), and radial velocity (*d*) for three mass flows

iation of cross-sectional area nondimensionalized by the diffuser outlet area is shown in Fig. 2.

The detailed volute measurements have been made at 14,364 rpm for three different mass flows called high (0.933 kg/s), medium (0.575 kg/s), and low (0.255 kg/s).

All pressures are measured relative to the compressor outlet static pressure. As the flow was controlled by the throttling valve upstream of the impeller, this was constant and equal to the atmospheric pressure during all tests.

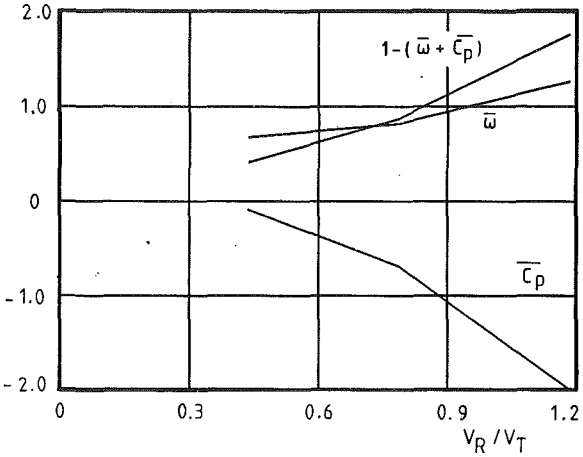

Fig. 4 Variation of the volute loss coefficient $\bar{\omega}_v$ and static pressure recovery coefficient $\bar{C}_p$ as a function of diffuser outlet swirl

Experimental Results

Volute Inlet Conditions. A three-hole United Sensor probe has been used to measure the diffuser outlet flow at the eight circumferential positions shown in Fig. 1. The probe stem is placed in the axial direction (R = 293 mm) to assure minimum blockage when traversing the diffuser from hub to shroud. The circumferential variation of the spanwise mass-averaged total pressure, static pressure, tangential velocity and radial velocity are shown in Fig. 3 for the three mass flows specified previously.

The flow quantities indicate, at high mass flow, a decreasing static pressure along the volute periphery (Fig. 3*b*) causing an increase of radial velocity at the diffuser outlet (Fig. 3*d*). The incoming mass into the volute increases from the volute tongue to the outlet. The nearly constant tangential velocity at the volute inlet indicates that the amount of the work per unit mass transferred from the impeller to the fluid is nearly constant (Fig. 3*c*). Although the work input is nearly constant, a large variation of total pressure is observed (Fig. 3*a*). This can be explained by the circumferential variation of impeller efficiency. Due to the mass flow variation along the circumference of the impeller, blades are operating at different conditions.

The amount of distortion at medium mass flow is not as large as for high mass flow and results in a much smaller variation of the volute inlet flow conditions.

Nomenclature

C_p = volute static pressure recovery coefficient
D_{hyd} = hydraulic diameter of the volute channel
P = pressure
ΔP^o = losses in total pressure, Pas
Q = dynamic pressure
R = radius
r = distance from the swirl center
r_c = curvature radius of swirling component of velocity
V = velocity
ϵ = surface roughness
θ = circumferential position (Fig. 1)
ρ = density
ω = loss coefficient

Subscripts

c = exit cone
ex = exit
f = friction
in = inlet
m = meridional
R = radial
S = swirl component
T = throughflow component
TO = total
v = volute
1...8 = cross sections

Superscripts

o = stagnation conditions
$-$ = mass-averaged value

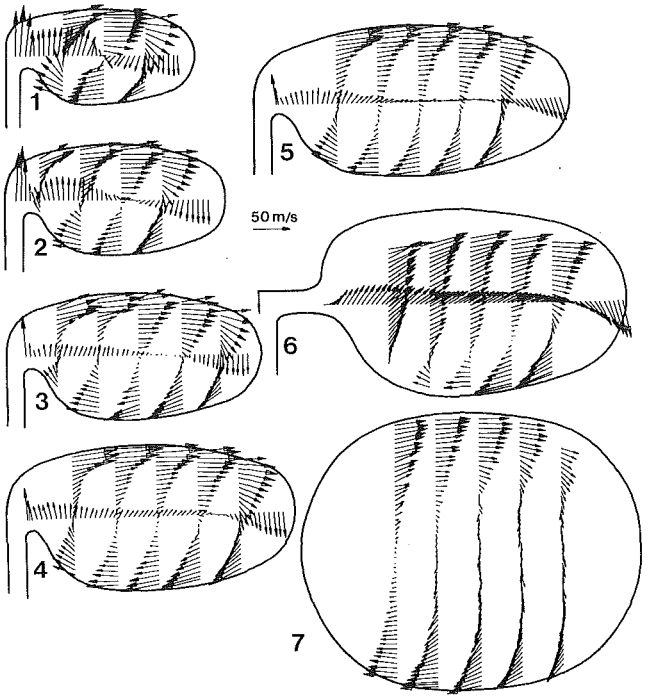

Fig. 5(*a*) Swirl velocities over the volute cross sections at high mass flow

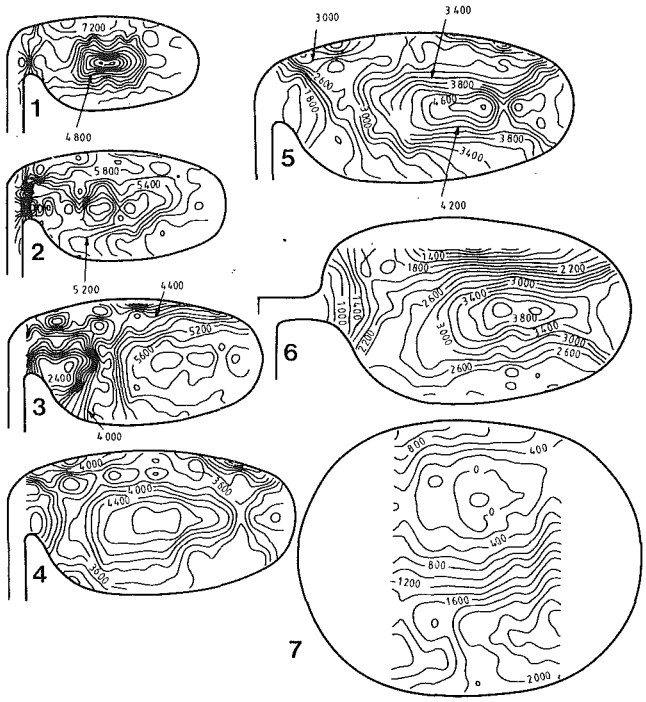

Fig. 5(*c*) Total pressure variations over the volute cross sections at high mass flow (Pa)

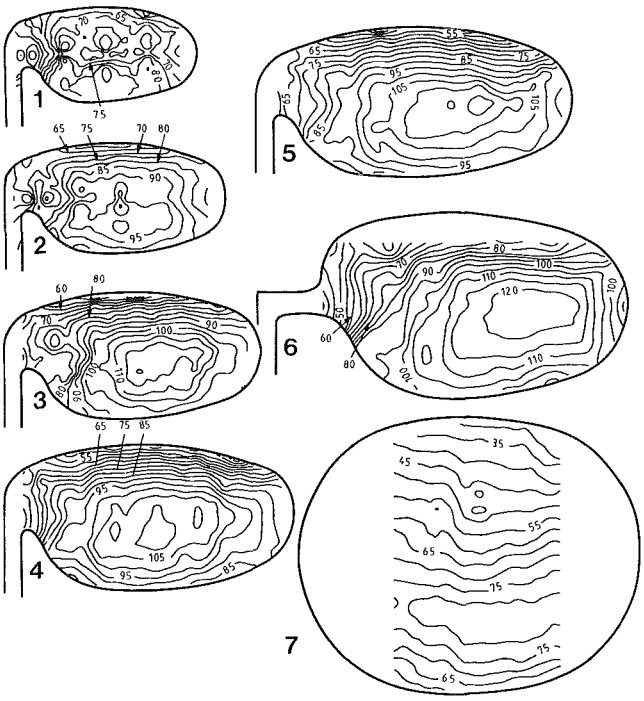

Fig. 5(*b*) Throughflow velocities over the volute cross sections at high mass flow (m/s)

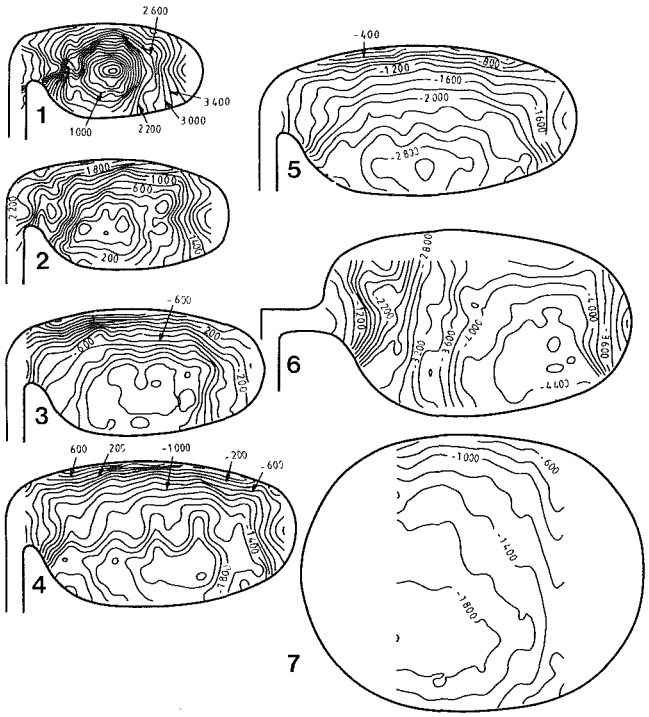

Fig. 5(*d*) Static pressure variations over the volute cross sections at high mass flow (Pa)

In the case of low mass flow, nearly uniform static pressure distribution is observed at the volute inlet, indicating that this is the optimum impeller-volute matching mass flow (Fig. 3*b*).

Volute Overall Performance. The overall performance of the volute and exit duct can be defined by means of a static pressure recovery coefficient

$$\overline{C}_p = \frac{\overline{P}_6 - \overline{P}_{in}}{\overline{P}^o_{in} - \overline{P}_{in}}$$

and loss coefficient

$$\overline{\omega} = \frac{\overline{P}^o_{in} - \overline{P}^o_6}{\overline{P}^o_{in} - \overline{P}_{in}}$$

calculated as a function of the mass-averaged flow quantities at the volute inlet and cross section 6. The variation in terms of the inlet swirl coefficient (V_R/V_T) is shown in Fig. 4.

The ratio of volute outlet kinetic energy to inlet kinetic energy is defined by

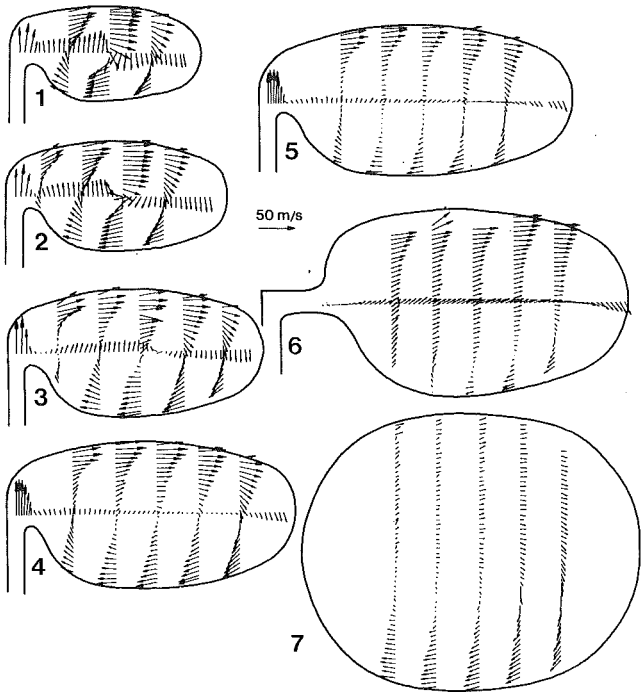

Fig. 6(*a*) Swirl velocities over the volute cross sections at medium mass flow

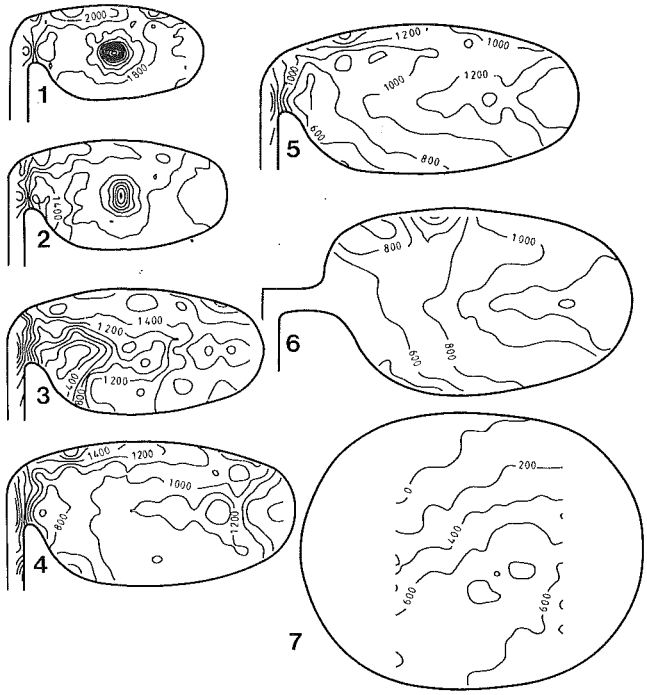

Fig. 6(*c*) Total pressure variations over the volute cross sections at medium mass flow (Pa)

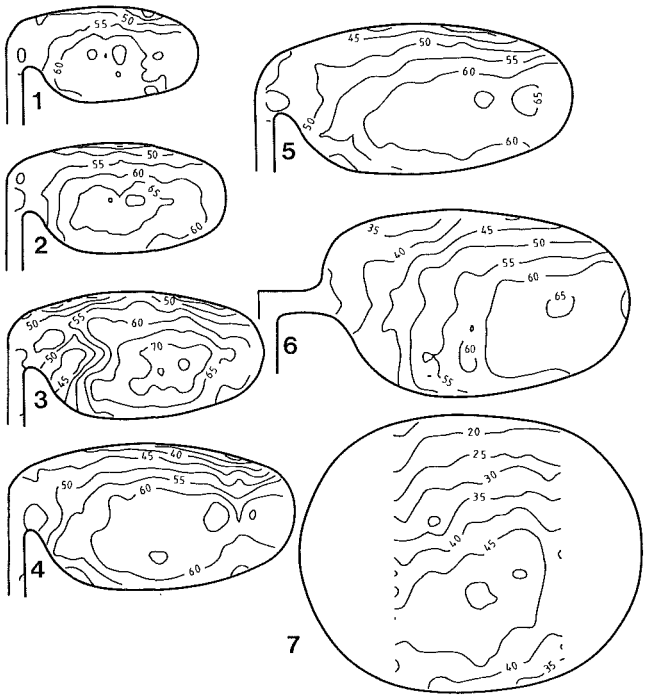

Fig. 6(*b*) Throughflow velocities over the volute cross sections at medium mass flow (m/s)

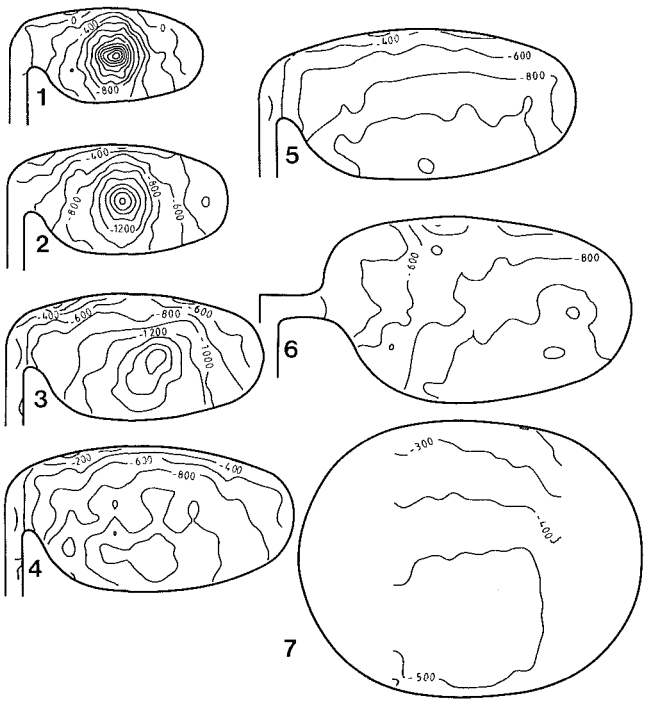

Fig. 6(*d*) Static pressure variations over the volute cross sections at medium mass flow (Pa)

$$\frac{\overline{P}_6^o - \overline{P}_6}{\overline{P}_{in}^o - \overline{P}_{in}} = 1 - (\overline{\omega} + \overline{C}_p)$$

It is smaller than 1 at low and medium mass flows, indicating a deceleration of the fluid between diffuser outlet and cross section 6. However this diffusion does not create any static pressure rise because of the high total pressure losses between the diffuser outlet (Fig. 3*a*) and the volute outlet (Fig. 7*c*). For high mass flow, the volute outlet kinetic energy is higher than at the inlet, indicating an accelerating flow in the volute. Together with the high total pressure losses in the volute at maximum mass flow ($\overline{\omega} = 1.26$), this results in a large negative static pressure recovery coefficient ($\overline{C}_p = -2$). The mechanism of these high losses will become clear when discussing the detailed flow measurements.

Detailed Flow Measurements. The three-dimensional volute flow field is measured by means of a five hole probe, which has a diameter of 3 mm, at seven cross sections (Fig. 1). In each cross section 3 to 5 radial traverses are made at different axial positions depending upon the size of the section.

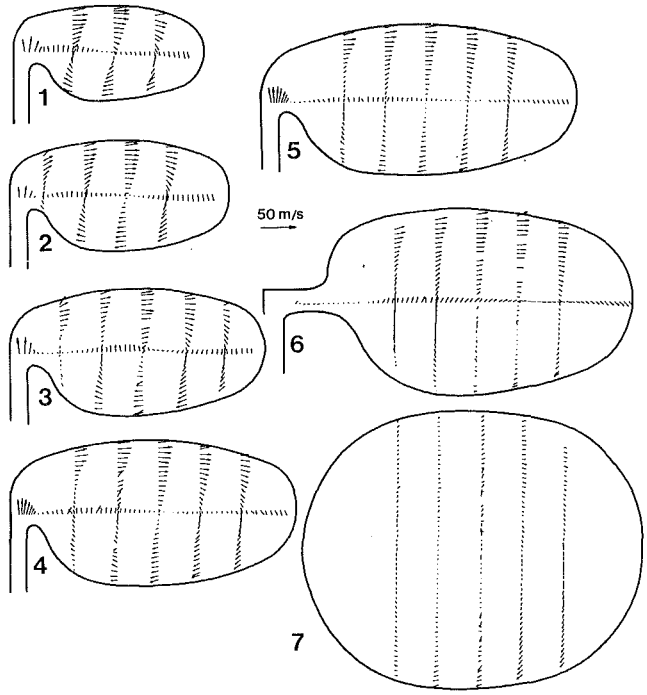

Fig. 7(*a*) Swirl velocities over the volute cross sections at low mass flow

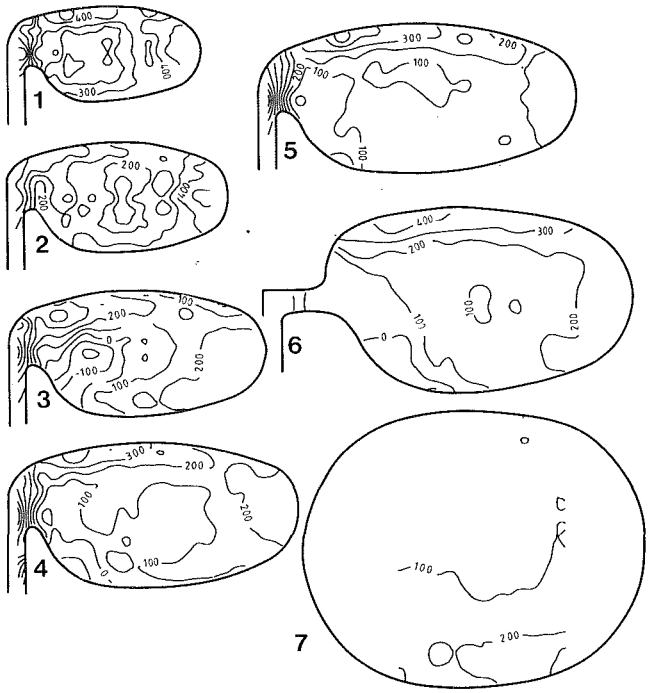

Fig. 7(*c*) Total pressure variations over the volute cross sections at low mass flow (Pa)

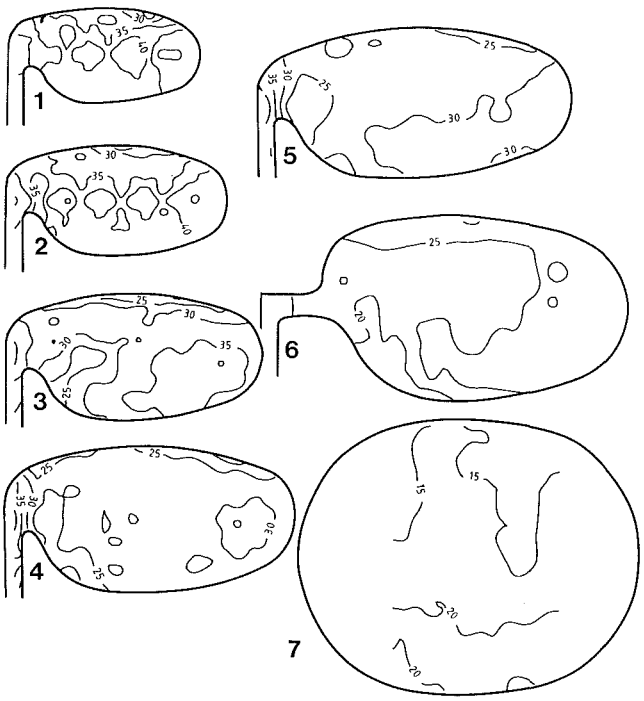

Fig. 7(*b*) Throughflow velocities over the volute cross sections at low mass flow (m/s)

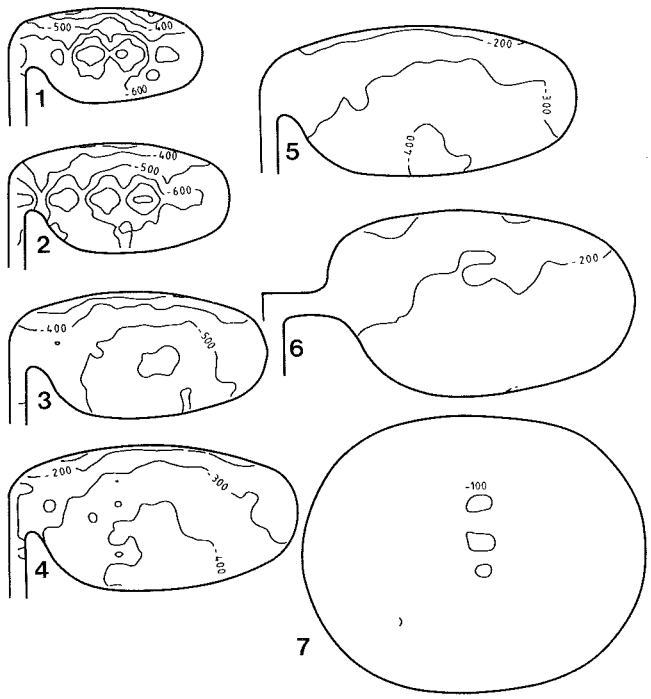

Fig. 7(*d*) Static pressure variations over the volute cross sections at low mass flow (Pa)

One axial traverse is made along the centerline. The results are shown in Figs. 5, 6, and 7. The swirl velocity V_S in the cross-sectional plane, and the throughflow velocity V_T perpendicular to the cross section, are shown in Figs. (*a*) and (*b*). Isopressure lines, at 200 Pa intervals, are shown in Figs. (*c*) and (*d*).

The fluid entering the volute close to the tongue starts swirling around the center of the cross section, giving rise to large velocity gradients and shear stresses. The swirl kinetic energy at the center is dissipated rapidly until a forced vortex or solid body rotation occurs. A well-defined spot of concentrated total pressure losses resulting from this dissipation is clearly observed in the center of the first cross section (Figs. 5*c* and 6*c*).

The model of Van den Braembussche and Hande (1990) describes how new fluid entering the volute further downstream wraps around the previous one and defines the swirl velocity distribution in the downstream direction. The increase of radial velocity at the volute inlet from the tongue to the volute outlet observed at high mass flow (Fig. 3*d*) results in an increase of the swirl velocity with the cross-sectional radius. The solid

body rotation in the downstream sections of the volute (Fig. 5*a*) therefore results from the particular volute inlet flow velocity distribution and not from the energy dissipation due to the internal shear stresses. The decreasing total pressure along the volute inlet from the tongue to the volute outlet results in a decrease of total pressure from the volute center to the outer radius at the downstream sections of volute (Fig. 5*c*). The total pressure distribution is no longer a consequence of the swirl shear losses but results also from the way the volute is filled with fluid. The internal shear stresses are zero in a solid body rotation so that any further decrease of the swirl is only possible by the friction on the volute walls or by an increase of radius in the exit diffuser.

Figure 5(*a*) shows lower swirl velocities perpendicular to the longer horizontal axis and larger swirl velocities perpendicular to the short vertical axis of the elliptic cross section. This results from the conservation of angular momentum of the flow on elliptic streamsurfaces

$$rV_s = \text{const} \tag{1}$$

The periodic increase and decrease of swirl velocity V_s during each rotation around the volute cross-sectional periphery results in extra diffusion and mixing losses. Increased turbulence mixing between the low-energy fluid in the boundary layers and the high-energy fluid at the center due to the curvature of the walls (Johnston, 1970), and the fact that after each rotation the boundary layer is absorbed by new fluid coming out of the diffuser, further contribute to a distribution of total pressure losses over the volute cross section. The total pressure over the volute cross section is lower than that of the incoming fluid and gradually decreases toward the volute outlet (Figs. 5*c* and 6*c*).

The change in location of the vortex center between section 5 and section 6 is due to an axial change of the volute centerline and an increase of center radius. As the measurements are made in axial planes, the probe measures an additional axial and radial velocity component and an apparent shift of the vortex center toward the lower right corner (Figs. 5*a* and 6*a*).

The measured static pressure variation over the cross section results from the swirl and the circumferential curvature of the volute channel. The centrifugal forces due to swirl are in equilibrium with the static pressure increase from the center toward the walls:

$$\frac{dP}{dr} = \rho \frac{V_S^2}{r_c} \tag{2}$$

The throughflow velocity and circumferential curvature create a pressure gradient between the inner and outer wall:

$$\frac{dP}{dR} = \rho \frac{V_T^2}{R} \tag{3}$$

The measurements (Figs. 5*d* and 6*d*) indicate that the static pressure variation over the small volute cross sections near the tongue is mainly determined by Eq. (2). This results from the large swirl velocity and low throughflow velocities. This gradually changes into a more radial pressure variation between inner and outer wall at the downstream cross sections. This is a consequence of the increasing throughflow velocity and decreasing swirl velocity.

Van den Braembussche and Hande (1990) show how the variation of throughflow velocity over the cross section results from the static and total pressure distribution

$$P^o - P = \frac{\rho}{2}(V_T^2 + V_S^2) \tag{4}$$

At the volute inlet sections both P^o and P decrease from the volute wall toward the center resulting in a nearly uniform throughflow distribution. At the downstream volute sections, the total pressure increases toward the center where the static pressure is decreasing toward the center. This results in a throughflow velocity at the center that is twice as large as the one at the volute inlet. The corresponding kinetic energy, which is four times bigger than the inlet kinetic energy, is partially dissipated between sections 6 and 7 and responsible for the high exit cone losses. One-dimensional volute models require large loss coefficients to account for this.

The volute flow field for medium mass flow is similar to the one at high mass flow. The results are given in order to complete the data set.

Only small swirl velocities are observed at low mass flow, resulting from the small radial velocities at the volute inlet (Fig. 7*a*). The constant velocity swirl near the walls results from the uniform radial velocity at the volute inlet. The forced vortex distribution at the center is due to the internal shear stresses. The corresponding energy dissipation is responsible for the zone of low total pressure at the center of the cross section. The extension of this forced vortex core gradually increases to cover the whole cross section at the downstream measurement planes, resulting in a more uniform distribution of total pressure losses.

The variation of the throughflow velocity and static pressure are determined by the circumferential curvature of the volute channel. The throughflow velocity increases toward the inner radius because of the momentum conservation. The static pressure distribution is mainly defined by Eq. (3).

Mean Streamline Volute Loss Modeling

The detailed flow measurements have been used to qualify an existing mean streamline volute loss model, which is similar to the model used by Japikse (1982) and improved by Weber and Koronowski (1986). The modified mean streamline volute and exit cone model has four loss mechanisms:

The *meridional dump loss* model assumes that all swirl is dissipated in the volute:

$$\Delta P_m^o = \frac{1}{2}\rho V_{R\ in}^2 \tag{5}$$

In the case of process conditions resulting in a circumferentially diffusing flow beyond the diffusion/acceleration corresponding to a conservation of angular momentum, the following equation is used for the *tangential flow loss*:

$$\Delta P_{T,\text{dec}}^o = \omega_{T,\text{dec}} \frac{1}{2}\rho(V_{T\ in}^2 - V_{T6}^2)\left(V_{T6} < \frac{R_{in}}{\overline{R}_6} V_{T\ in}\right) \tag{6a}$$

where $\omega_{T,\text{dec}} = 0.5$ is proposed by other investigators.

In the case of a circumferentially accelerating flow beyond the acceleration/diffusion corresponding to conservation of angular momentum, it is common to compare the volute to an accelerating nozzle and assume zero loss, e.g., Japikse (1982). However, the test data indicate that strong nonuniformities arise in the throughflow component in case of an accelerating flow. They result in shear stresses and corresponding mixing losses. It seems therefore reasonable to identify a loss mechanism when the tangential flow is accelerating. Weber and Koronowski (1986) introduced, without giving a physical explanation, a loss proportional to $(V_{T\,in} - V_{T\,\text{out}})^2$. Somewhat arbitrarily, we have assumed a similar functional dependence:

$$\Delta P_{T,\text{acc}}^o = \omega_{T,\text{acc}} \frac{1}{2}\rho(v_{T\ in} - V_{T6})^2\left(V_{T6} > \frac{R_{in}}{\overline{R}_6} V_{T\ in}\right) \tag{6b}$$

We will explain later how the volute flow measurements have been used to determine the loss coefficient $\omega_{T,\text{acc}}$.

The model adopted for *friction losses* is that of pipe friction flow, which is defined as follows:

$$\Delta P_f^o = \omega_f \frac{L}{D_{\text{hyd}}} \frac{1}{2}\rho \overline{V}_T^2 \tag{7}$$

Only the throughflow component is considered for the friction

Table 1 Summary of measured and calculated volute and exit cone losses in total pressure (in Pa)

	High Mass Flow			Medium Mass Fl.			Low Mass Flow		
	Calculated		Meas.	Calculated		Meas.	Calculated		Meas.
	1D	Data	Meas.	1D	Data	Meas.	1D	Data	Meas.
ΔP^o_f	2483			982			281		
ΔP^o_m	1453	2486	1939	492	791	674	94	157.5	126
ΔP^o_T	98			9			215		
ω_T	0.2			0.2			0.5		
ΔP^o_v	4034	5067	4520	1478	1777	1660	590	653	622
ΔP^o_{mc}			547			117			31
ΔP^o_c	2414	1381	1381	696	397	397	89	26	26
$Q_6 - Q_8$	2230	2230	5654	754	754	1517	145	145	329
ω_c	1.1	.62	.24	.92	.53	.26	.61	.18	.08
ΔP^o_{TO}	6448	6448	6448	2174	2174	2174	679	679	679
C_{p_c}			.578			.483			.55

losses since complete dissipation of the swirl velocity is already accounted for by Eq. (5).

The *exit cone losses* are quantified by a sudden expansion loss model

$$\Delta P^o_C = \omega_C \frac{1}{2} \rho (V^2_{T6} - V^2_{T8}) \tag{8}$$

However, in view of the strong inlet distortion, the theoretical value of ω_C is too low, and a more accurate realistic value will be defined as a function of the experimental results.

The detailed experimental data shown previously have been used to better quantify the empirical loss coefficients in Eqs. (5)–(8). Results are shown in Table 1.

The losses shown in the first column are the ones calculated as functions of the velocity components predicted by a one-dimensional analysis model, assuming uniform flow at the inlet and outlet sections. The results in the second column are calculated as functions of the velocities and pressures obtained by mass averaging the detailed experimental data. The average velocity at the volute outlet is evidently the same as that for the one-dimensional model. The mass-averaged pressure, however, is different from the one calculated by the one-dimensional model. The third column contains the measured losses.

The nonuniformity of the radial velocity at the volute inlet results in a higher swirl. The corresponding meridional dump losses (column 2) are therefore higher than the ones predicted by the one-dimensional model (column 1). The real volute swirl losses (column 3), however, are lower by the amount of residual swirl measured at cross section 6.

The volute total pressure losses obtained by comparing the mass-averaged P^o_6 and P^o_{in} (column 3) can be used to quantify the friction and tangential flow losses.

The loss coefficients for tangential flow loss under accelerating and decelerating flow conditions in the volute can be determined by requiring consistency of the friction loss model, i.e., a constant friction loss coefficient under all three flow conditions. The average Reynolds number under the operating conditions tested is approximately equal to 3×10^5. For this Reynolds number, the pipe friction factor is mainly dependent on the relative surface roughness. For the investigated volute the relative surface roughness $\epsilon/D_{\text{hyd}} = 0.001$, resulting in a ω_f value of 0.019.

Friction losses calculated as functions of the average throughflow velocity in the volute and mean hydraulic diameter are given in Table 1. The remaining tangential velocity flow losses can now be calculated by elimination.

Since the volute inlet velocity is almost equal to the volute outlet velocity, no tangential flow losses should occur at medium mass flow. This is in agreement with the very low value of ΔP^o_T given in Table 1. In case of decelerating flows (low mass flow) the resulting tangential flow losses are well predicted by a coefficient $\omega_T = 0.5$. This is the same value as the one proposed in previous investigations (Japikse, 1982; Weber and Koronowski, 1986). A value of $\omega_T = 0.2$ is required in Eq. (6*b*) to predict the tangential flow losses for accelerating flows correctly. This value is lower than that for decelerating flows as can be expected.

Exit cone losses are obtained by subtracting the volute losses from the total losses. Different values are obtained depending on the value of the volute losses. The real exit cone losses are the sum of the cone diffusion losses (ΔP^o_c) and the remaining swirl losses (ΔP^o_{mc}). Loss prediction (Eq. (8)) concerns only for cone diffusion losses. Use of the measured inlet kinetic energy, which takes into account the nonuniformity of the meridional velocity, results in the ω_c coefficient shown in column 3. This value is much larger at high and medium mass flow, as can be expected from the nonuniformity of the inlet flow.

In spite of the high losses at high and medium mass flow, relatively large values of static pressure rise coefficient C_{p_c} are observed. This is due to the stabilizing effect of the swirling flow on the exit cone diffuser (Japikse, 1982).

Very high loss coefficients (column 1) are needed to predict the exit cone losses by the one-dimensional model. This results from an overestimation of the cone losses (because of an underestimation of the volute losses), and an underestimation of the inlet dynamic pressure, by the one-dimensional model, neglecting the inlet nonuniformity at high and medium mass flow.

Calculating the real exit cone losses as a function of the inlet dynamic pressure, predicted by the one-dimensional model, requires a loss coefficient between 0.18 and 0.62 (column 2). These values are already much closer to the conventional values. A variation of the loss coefficient ω_c is required to account for the inlet distortion, whichever model is used to calculate the exit cone losses.

Conclusions

The detailed flow measurements presented in this paper provide a clear picture of the three-dimensional swirling flow inside an elliptic volute.

It has been shown how the forced vortex distribution of the swirl velocity can result from internal friction or from a particular radial velocity distribution at the volute inlet. The first mechanism results in high losses and low total pressure in the center of the cross sections. The total pressure distribution over the latter one is function of the total pressure distribution at the volute inlet and has much smaller losses.

The static pressure distribution depends on the relative importance of the centrifugal forces due to the swirl velocity in the cross section, compared to the centrifugal forces due to the throughflow velocity on the volute periphery.

The throughflow velocity results from the total and static pressure variation over a cross section and can be very large at the cross section center.

The detailed flow measurements have also been used to analyze the validity and shortcomings of existing mean streamline volute loss models.

Future benchmarking of this volute loss model against other volute test data of the same detail could further enhance its confidence level.

References

Ayder, E., and Van den Braembussche, R., 1991, "Experimental Study of the Swirling Flow in the Internal Volute of a Centrifugal Compressor," ASME Paper No. 91-GT-7.

Elholm, T., Ayder, E,. and Van den Braembussche, R., 1992, "Experimental Study of the Swirling Flow in the Volute of a Centrifugal Pump," ASME JOURNAL OF TURBOMACHINERY, Vol. 114, pp. 366–372.

Iversen, H., Rolling, R., and Carlson, J., 1960, "Volute Pressure Distribution, Radial Force on the Impeller and Volute Mixing Losses of a Radial Flow Centrifugal Pump," ASME *Journal of Engineering for Power*, Vol. 82, pp. 136–144.

Japikse, D., 1982, "Advanced Diffusion Levels in Turbocharger Compressors and Component Matching," *Proc. First Int. Conference on Turbocharging and Turbochargers*, IMechE, London, pp. 143–155.

Johnston, J. P., 1970, "The Effects of Rotation on Boundary Layers in Turbomachine Rotors," *Fluid Mechanics, Acoustics and Design of Turbomachinery, Part I*, NASA SP 304, pp. 207–249.

Kurokawa, J., 1980, "Theoretical Determinations of the Flow Characteristics in Volutes," *1980 IAHR-AIRH Symposium*, Tokyo, pp. 623–634.

Muller, K. J., 1973, "Bemessung und Betriebsverhalten von Spiralgehausen Radialer Stromungsarbeitsmachinen," VDI-Berichte, No. 93.

Peck, J. F., 1951, "Investigations Concerning Flow Conditions in a Centrifugal Pump, and the Effect of Blade Loading on Head Slip," *Proc. IMechE*, Vol. 164.

Stiefel, W., 1972, "Experiences in the Development of Radial Compressors," *Advanced Radial Compressors*, von Karman Institute Lecture Series 50, May.

Van den Braembussche, R., and Hande, B. M., 1990, "Experimental and Theoretical Study of the Swirling Flow in a Centrifugal Compressor Volutes," ASME JOURNAL OF TURBOMACHINERY, Vol. 112, pp. 38–43.

Weber, C. R., and Koronowski, M. E., 1986, "Meanline Performance Prediction of Volutes in Centrifugal Compressors," ASME Paper No. 86-GT-216.

Aeroloads and Secondary Flows in a Transonic Mixed-Flow Turbine Stage

K. R. Kirtley

T. A. Beach

Sverdrup Technology, Inc.,
LeRC Group,
Cleveland, OH 44135

C. Rogo

Teledyne CAE,
Toledo, OH 43612

A numerical simulation of a transonic mixed-flow turbine stage has been carried out using an average passage Navier–Stokes analysis. The mixed-flow turbine stage considered here consists of a transonic nozzle vane and a highly loaded rotor. The simulation was run at the design pressure ratio and is assessed by comparing results with those of an established throughflow design system. The three-dimensional aerodynamic loads are studied as well as the development and migration of secondary flows and their contribution to the total pressure loss. The numerical results indicate that strong passage vortices develop in the nozzle vane, mix out quickly, and have little impact on the rotor flow. The rotor is highly loaded near the leading edge. Within the rotor passage, strong spanwise flows and other secondary flows exist along with the tip leakage vortex. The rotor exit loss distribution is similar in character to that found in radial inflow turbines. The secondary flows and nonuniform work extraction also tend to redistribute a nonuniform inlet total temperature profile significantly by the exit of the stage.

Introduction

For small gas turbine engine applications, mixed-flow turbines (MFT) have the potential to provide greater specific work at higher efficiency than axial turbines for the given work requirements. In addition, single-stage axial flow turbines may reach their limit loading before achieving the design work requirements. Adding more stages can remove this limitation, but may not be an option in a small engine due to other constraints. Radial inflow turbines are an option; however, their space requirements may be prohibitive. Moreover, according to Civinskas (1985), tip speed limitations impose rotor incidence penalties on high work radial inflow turbines. Backsweeping the leading edges can improve the incidence. Unfortunately, such backsweep can lead to unacceptable blade stresses because the blade elements must be nonradial. By using a mixed flow turbine, sweep can be added to the rotor blades while maintaining radial blade elements. Specific work can then be increased without as great a performance penalty. Thus, the increased work capacity of the radial inflow turbine and the reduced incidence loss found in backswept designs can be achieved in a confined space by using a mixed-flow turbine.

Okapuu (1987) outlines many other reasons why MFTs are desirable. MFTs can provide greater work factors at lower tip speeds than axial turbines by virtue of the radius change along the flow path. The radius change also allows taller blades and a greater pitch at the trailing edge, thereby reducing tip gap to span and trailing edge thickness to pitch ratios at the rotor exit. Reducing these ratios can provide improved efficiencies over axial turbines designed for the same work requirements.

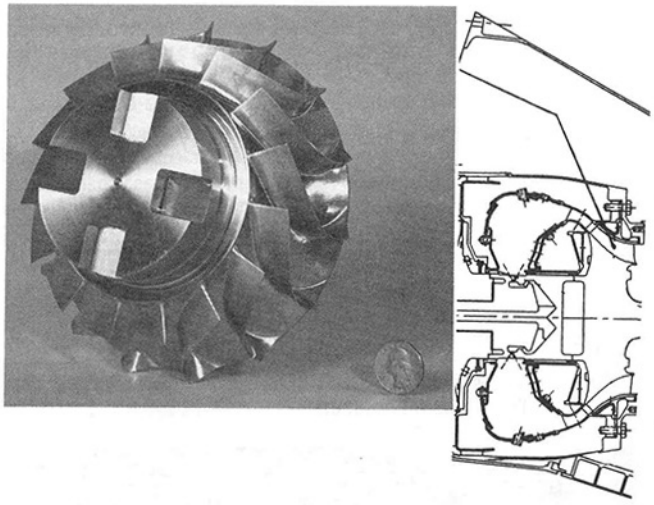

Fig. 1 TCAE propfan engine and gas generator mixed-flow turbine

The increased work capacity and potentially higher efficiencies make the mixed-flow turbine ideal for small engine applications. Unfortunately, knowledge of the flow details in the MFT is woefully lacking due to a dearth of experimental and computational analyses in the literature. To fill this need, a Space Act Agreement was entered into by Teledyne CAE and NASA Lewis Research Center to apply a three-dimensional average passage Navier–Stokes flow code to analyze mixed flow turbines. The MFT, shown in Fig. 1, serves as a practical baseline analysis configuration designed for an actual engine installation. This MFT, built and run in a TCAE core gas

Contributed by the International Gas Turbine Institute and presented at the 37th International Gas Turbine and Aeroengine Congress and Exposition, Cologne, Germany, June 1–4, 1992. Manuscript received by the International Gas Turbine Institute February 4, 1992. Paper No. 92-GT-72. Associate Technical Editor: L. S. Langston.

generator, was designed for a turboprop application with an engine thrust of 3336 Newtons at a flight Mach number of 0.7 at standard sea level conditions. The goal of this paper is to present the three-dimensional numerical analysis of the viscous flow in this generic MFT. The results are used to investigate blade loadings and secondary flows. Attempts are made to identify and quantify potential sources of loss.

Method of Analysis

The three-dimensional flow in the mixed-flow turbine stage was computed using the average passage Navier–Stokes equations derived by Adamczyk (1985). These equations represent the time-mean, spatially periodic, three-dimensional flow in a representative passage of each blade row embedded in a multistage environment. The analysis captures the development of secondary flows and their impact on neighboring blade rows. The effect of deterministic unsteadiness on the time-mean is included through correlations that augment the Reynolds stress. The numerical method used to solve the average passage equations is described by Kirtley et al. (1990) and is outlined here.

The equations are discretized using a cell-centered, finite volume scheme. The solution is advanced in time to a steady state using a four-step Runge–Kutta integration with local time stepping and implicit residual smoothing. Artificial dissipation is added to ensure a unique solution, but it is removed within boundary layers so as not to mask the physical dissipation. A multigrid scheme is employed to accelerate the convergence of the method. For multiple blade row calculations, the first blade row flow is calculated for a few hundred iterations. The average passage stress, blade body forces, and energy sources are computed for that blade row by comparing the three-dimensional and axisymmetric flow fields. The next blade row flow is computed using the aforementioned source terms, which represent the influence of the upstream blade row. The average passage stress, body forces, and energy sources for the second blade row are computed and used in a repeat calculation of the first blade row flow. The process is repeated until the axisymmetric averages of each blade row flow are identical. A common axisymmetric flow is the compatibility condition, which links the individual three-dimensional average passage flow for each blade row.

The deterministic stress component of the average passage stress is assumed to be axisymmetric, which allows for direct calculation by comparing the three-dimensional flow with its axisymmetric average. Additional modeling of this stress is included, which is essentially a correction to the eddy viscosity in the wake region in order to mix streamwise vortical flows at a rate seen experimentally in axial flow turbomachinery. The mixing rate for MFT's is assumed to be the same since no mixing data are available to confirm or contradict it. The spatial aperiodic stress is assumed to be very small as suggested by data (see Kirtley et al., 1990). The random unsteadiness, i.e., turbulence, is modeled using an algebraic eddy viscosity model based on the work of Baldwin and Lomax (1978). Within the blade passages, the length scale used in the model is based on the distance to the nearest wall. In the wake region, the length scale is determined from a correlation for the wake width developed by Raj and Lakshminarayana (1973); as a result, the wake centerline does not need to be found.

The accuracy of mean flow predictions using such a simple model in complicated flows like the MFT flow now comes into question. Two recent studies have attempted to quantify the effect of using different turbulence models in complex turbomachinery flows. Zunino et al. (1988) and Cleak and Gregory-Smith (1992), using different geometries and different numerical techniques, came to essentially the same conclusion, i.e., higher order turbulence models do not necessarily improve the prediction of mean flow quantities. In fact, Cleak and Gregory-Smith find that the best prediction of the mean flow came using an algebraic turbulence model with an empirically determined transition zone. The algebraic model used here fixes a transition point at roughly 10 percent chord along the span of the suction side of the first blade row and assumes the flow to be fully turbulent in downstream blade rows. The modeling of boundary layer transition is a pacing item in CFD research for gas turbine components (see Mayle, 1991) and can be critical in the accurate prediction of secondary flow vortex strength and location.

The rotor tip clearance flow is modeled as described by Kirtley et al. (1990), i.e., the flow is assumed to be periodic in the tip gap across control volumes that span the thickness of the blade. As a result, the flow within the tip gap is not resolved; however, a tip leakage jet forms and its strength and eventual rollup into a tip leakage vortex are governed by the Navier–Stokes equations and boundary conditions. In practice, the blade tip gap is set to the actual running clearance times an appropriate discharge factor based on the tip geometry. In this way, round, flat, knife edge, and squealer tips can all be modeled easily.

Familiar compressible flow boundary conditions are used for the simulation. At the stage inlet, flow angles are fixed and total pressure and temperature distributions are held at their design values but modified slightly to include the incoming shear layers. The axial velocity is then determined by extrapolating the upstream running Reimann invariant. At the stage exit, the whirl, axial, and radial velocities, and entropy are extrapolated and the static pressure is fixed. This boundary condition allows flow nonuniformities to pass unrestricted. The exit static pressure is fixed at the hub at the design value and varies from hub to tip according to the simplified radial equilibrium equation. The periodicity condition is applied outside of the blade passages and the adiabatic no-slip boundary condition is applied at solid walls.

The computational mesh used here, generated using the interactive program of Beach (1990), contains 36 cells each in the spanwise and blade-to-blade directions and 152 cells in the streamwise direction with 40 and 60 cells along the vane and blade chords, respectively. Six cells are used in the tip clearance region. On average, the first cell from the wall lies within a y^+ of 5 to 10.

Results and Discussion

The generic transonic MFT stage simulated here consists of 23 nozzle vanes and 15 rotor blades with a leading edge rotor tip diameter of 0.168 m. The stage was designed to operate at a weight flow of 1.82 kg/s with an inlet total temperature of 1232 K and an inlet to exit total pressure ratio of 4.69. At a design rotational speed of 62,158 rpm the device should extract 393 kJ/kg, which gives a work factor of 1.31 and a stage-specific speed N_s of 0.46 based on turbine exit volume flow and total-to-static adiabatic head. The low specific speed is more characteristic of radial than axial turbines.

The flow path and midspan vane and blade sections are given in Fig. 2. The rotor flow path was defined by a Teledyne Advanced Aerodynamic Design System (TAADS) streamline curvature computer code, which is a variant of the A. J. Wennerstrom compressor design program (see Law and Puterbaugh, 1982). Inlet mass flow, tangential velocity, and rotor geometry govern the rotor flow solution, whereas the nozzle was designed *a posteriori* to meet the rotor requirements. A subsequent computer-aided design (CAD) layout of the nozzle showed the throat area to be 8 percent larger than design intent. The average passage flow simulation passed roughly 9 percent more flow, which verifies the increased flow capacity of the nozzle.

Table 1 shows the stage mass-averaged total pressures and temperatures from the average passage simulation versus the design intent. It is clear that the average passage simulation provides similar specific work output; however, the total pres-

Table 1 Comparison of design intent and results of the simulation

	$\frac{\Delta T_o}{T_{o\,in}}$		$\frac{P_{o\,in}}{P_{o\,out}}$	
	TAADS	APC	TAADS	APC
Vane	0.0	0.0	1.0586	1.0443
Blade	0.267	0.265	4.432	4.246
Total	0.267	0.265	4.691	4.433

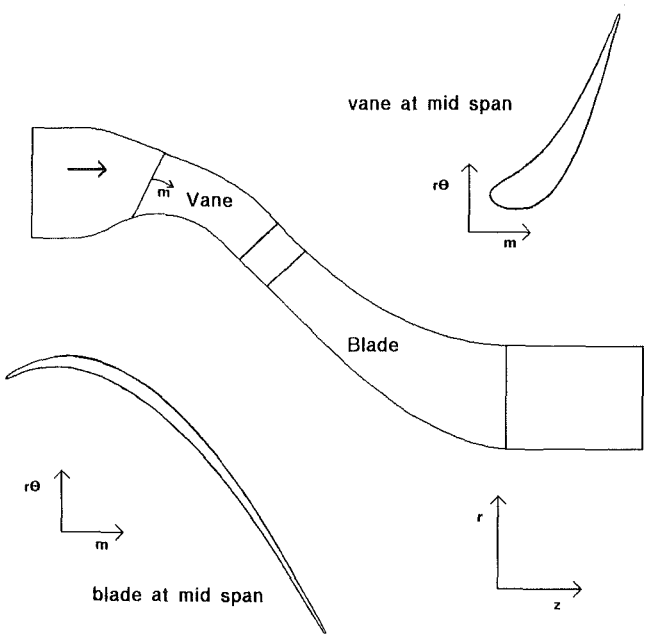

Fig. 2 MFT stage geometry

sure losses, which are built into the TAADS via empirical correlations, are not similar. The average passage simulation yields slightly higher efficiencies in both the vane and blade. Of course, comparisons between a numerical simulation and design intent can only be qualitative in nature. Quantitative validation of the average passage flow code has come in the form of data matches for various multistage turbomachinery, including a compact radial turbine by Heidmann and Beach (1990) and a simulation of a second proprietary Teledyne MFT whose accuracy is similar to Heidmann and Beach's in comparison with measurements of shroud static pressure and turbine exit total pressure.

With this validation, the average passage flow code is considered the equivalent of a calibrated experimental probe, accurate for applications for which it was calibrated but subject to errors when applied outside its calibration space. As indicated by Cleak and Gregory-Smith (1992), it is believed that the largest error in flow prediction will occur for flows with large regions of laminar-to-turbulent transitional flow. Unfortunately, no data exist to indicate the transitional nature of the MFT flow presented here.

Nozzle Vane. The nozzle vane was designed to generate a free vortex velocity distribution at the vane exit and the design is three-dimensional in this way only. The vane surface pressure distribution in Fig. 3 attests to this fact. The nozzle flow is transonic and fully expanded, i.e., the suction surface pressure in the uncovered region continues to decrease. In Fig. 4, Mach number contours show that the nozzle flow accelerates to Mach 1.25, then shocks down below the sonic speed. The high-frequency oscillations in the contours near the trailing edge are due to the highly sheared mesh, which is unavoidable when using **H**-type meshes with large blade angles. The interesting detail of this flow is that, while the flow is choked, the sonic line does not reside near the two-dimensional geometric throat, but actually lies in the uncovered region and spans the wake. With the reduction of flow path radius near the trailing edge, it is difficult to determine how close the aerodynamic throat is to the three-dimensional geometric throat.

The physical location of the rotor blade leading edge is indicated in Fig. 4 and it is clear that the shocks are smeared

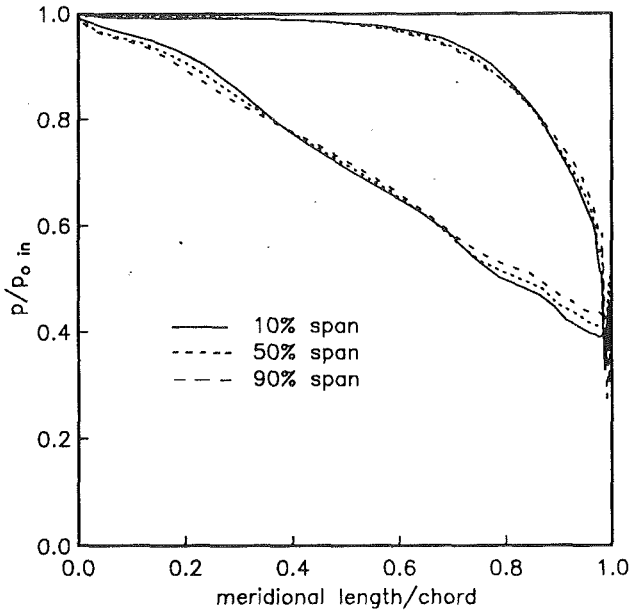

Fig. 3 Nozzle vane surface pressure distribution

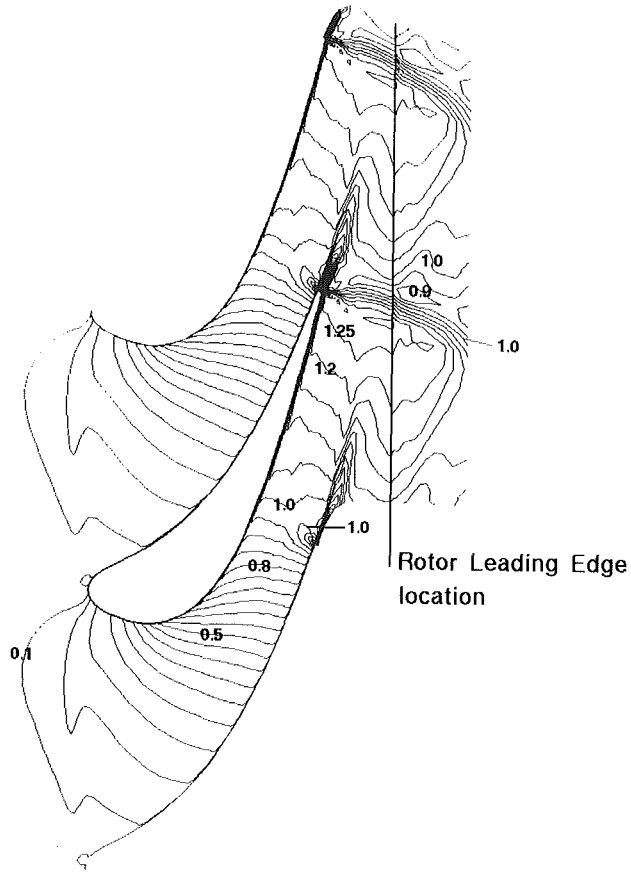

Fig. 4 Vane midspan Mach number contours

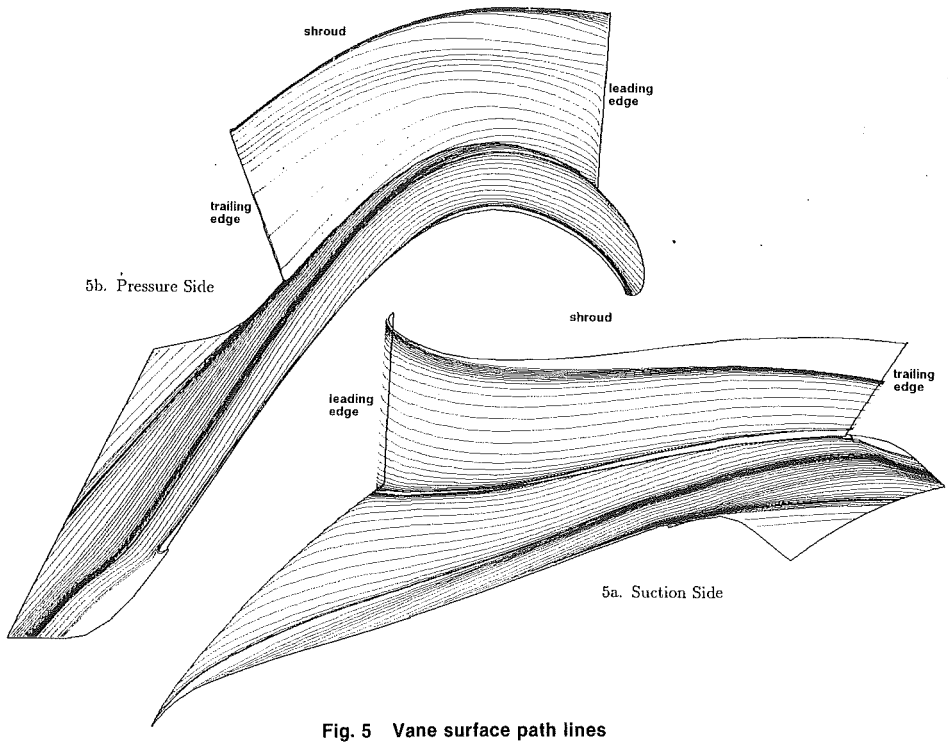

Fig. 5 Vane surface path lines

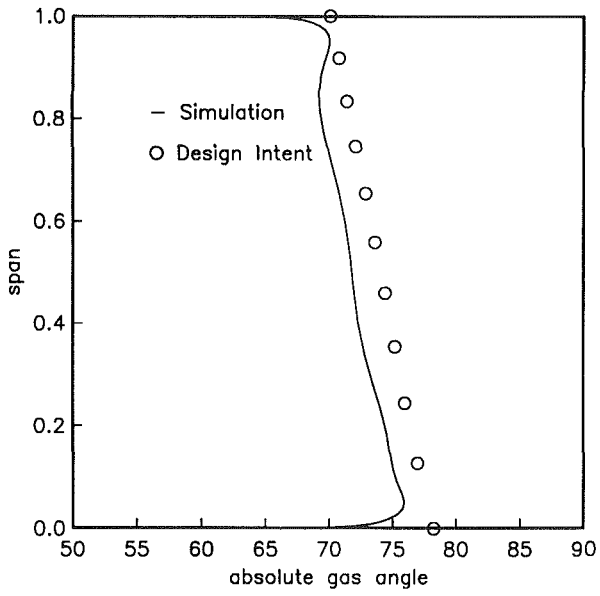

Fig. 6 Vane exit absolute flow angle

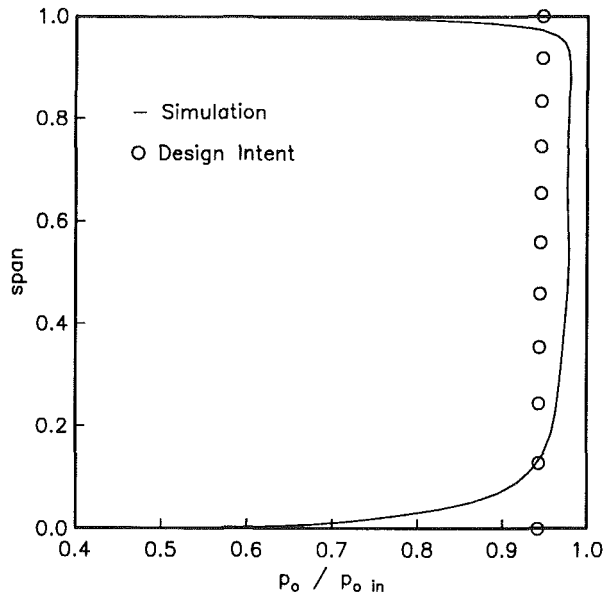

Fig. 7 Vane exit mass-averaged total pressure ratio

out by the chopping of the passing blade and the energy extraction near the rotor blade leading edge. This view is, of course, the time average of a very complicated unsteady interaction. In the vane frame of reference, the flow field relaxes to an axisymmetric state by rotor blade midchord.

Path lines confined to very near the suction and pressure sides in Fig. 5 indicate the large degree of secondary flow in the nozzle. The inlet boundary layers are rather thin, giving rise to a weak horseshoe vortex system. The large degree of flow turning, nearly 78 deg in the hub, and the growth of the hub boundary layer produce a large passage vortex on the hub. The suction surface path lines seem to indicate that the shroud passage vortex is larger, but this is merely an artifact of the overall spanwise downward flow from the radial pressure gradient unbalanced by the diminishing momentum close to the vane surface. The passage vortices are only slightly apparent in the vane exit gas angle in Fig. 6, indicating that these vortices have mixed out midway between the vane and blade and will not strongly impact the blade flow. Within 3 percent span of each endwall, underturning is present. This underturning is due to separation from shock boundary layer interaction on the suction side at the trailing edge, which is not present outside of the endwall region. The local flow separation causes the deviation of flow toward axial. The overall deviation from design intent is due to the high Mach numbers of the vane exit flow. The additional expansion turns the flow toward axial.

The vane exit mass-averaged total pressure distribution is presented in Fig. 7. The spanwise average is close to the design intent (see Table 1), and the spanwise variation in the simulation shows the largest loss to be generated by the large boundary layers on the endwalls. The hub boundary layer is much larger than the shroud boundary layer. Since the exit gas angle

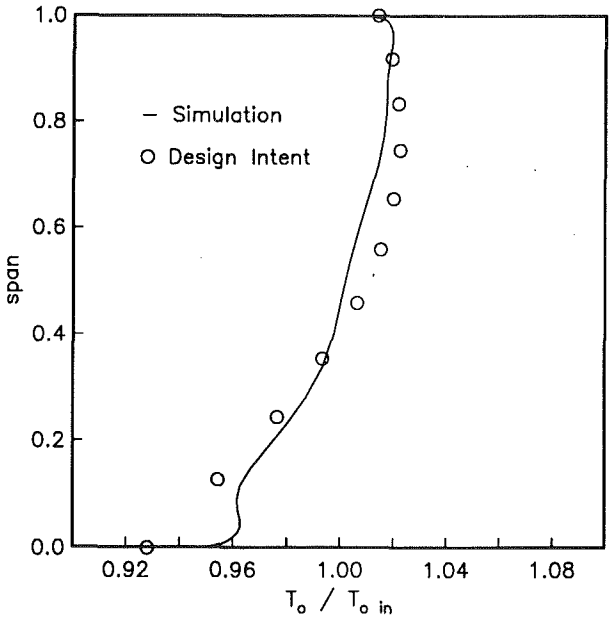

Fig. 8 Vane exit mass-averaged total temperature ratio

is so large, the difference is due to the different wall curvature that each near-wall flow encounters. Near the shroud, the flow encounters a concave curvature, which physically destabilizes the turbulence and enhances mixing, giving a thin boundary layer. Numerically, the algebraic model simulates this effect to first order through the increased rate of strain. On the hub, the opposite is true and the boundary layer thickens. The quickly growing boundary layer on the hub in the vaneless space is a large source of total pressure loss.

The mixing in the endwall region is also evident from the vane exit total temperature distribution in Fig. 8. The TAADS results show the vane exit temperature distribution to be very similar to the inlet while the average passage simulation gives a result that is mixed across the entire span.

Stage Axisymmetric Flow. As a prelude to a description of the rotor blade flow, it is instructive to view the axisymmetric average of the three-dimensional flow for the entire stage in Fig. 9. The total temperature variation through the stage is presented in Fig. 9(*a*). It is apparent from the abrupt spreading of contours that most of the mixing of total temperature in the neighborhood of the vane occurs very near the vane trailing edge. The work extraction in the blade is also visible. Near the hub, the wide gap between temperature contours indicates a low level of loading and reduced work extraction, particularly

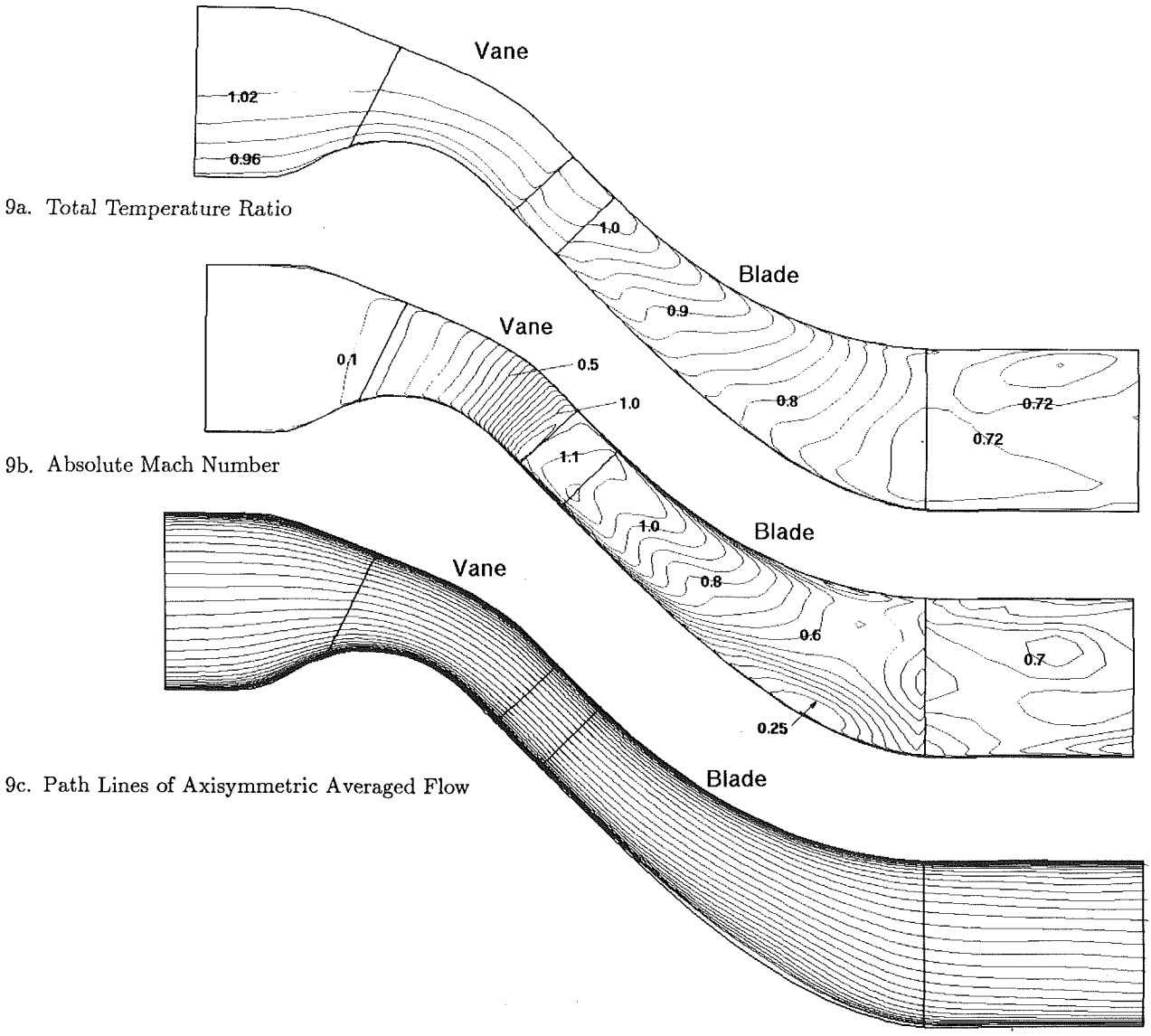

Fig. 9 Stage axisymmetric averaged flow field

near the trailing edge. In addition, the absolute Mach numbers in Fig. 9(*b*) show very low momentum flow in this same area. Such pictures might lead designers to recontour the hub to remove these low Mach numbers and low loadings as has been done by Civinskas (1985). Indeed, such recontouring in preliminary design studies gives small efficiency gains. However, these regions are not necessarily high loss zones, as details of the three-dimensional blade flow will indicate. The Mach contours also give some indication of the trajectory of the blade tip leakage vortex and associated secondary flows. Aft of the blade trailing edge, the leakage vortex does not remain near the shroud but migrates toward the midspan region. This effect will be discussed in the next section.

The path lines of the axisymmetric averaged flow are presented in Fig. 9(*c*). These path lines show that the only significant deviation from the mean flow path is in the hub region of the blade corresponding to the low Mach numbers in Fig. 9(*b*). This path line pattern hides the true complexity of the three-dimensional blade flow.

Turbine Rotor Blade. The blade surface pressure loading is given at three spanwise locations in Fig. 10. As suspected, from 20 percent chord on, the hub loading is greatly reduced from the midspan and tip regions. Near the hub, some diffusion is taking place; however, the suction side flow does not separate in the face of the increasing pressure. As compared to midspan, the tip region also shows reduced loading aft of 60 percent chord due to the tip leakage effect. The leading edge regions, however, are still highly loaded and produce very low relative Mach numbers on the pressure side and strong acceleration on the suction side as seen in Fig. 11.

At midspan, Fig. 11(*a*), the relative flow accelerates to supersonic in a small region on the suction side, then decelerates shock-free as the flow path opens up from the radius variation of the hub and shroud. Finally, the rotor chokes more or less near the geometric throat. But, due to the fixed exit static pressure, the flow on the uncovered side accelerates little and culminates in a very weak shock, which is confined to very near the trailing edge and is destroyed by three-dimensional secondary flows passing through this spanwise location. In the tip region, Fig. 11(*b*), the picture is similar except for the strong influence of the tip leakage vortex. The sonic line follows a rather convoluted path due to the large velocity defect associated with the leakage vortex. Near the hub, Fig. 11(*c*), the relative Mach contours have a similar appearance to those at midspan with low Mach numbers near the pressure side and strong acceleration on the suction side but without choking near the trailing edge. Unfortunately, the Mach numbers do not reveal the complexity and severity of the hub flow.

The path lines confined to near the hub surface, Fig. 12, show that the Coriolis force, which is responsible for the high

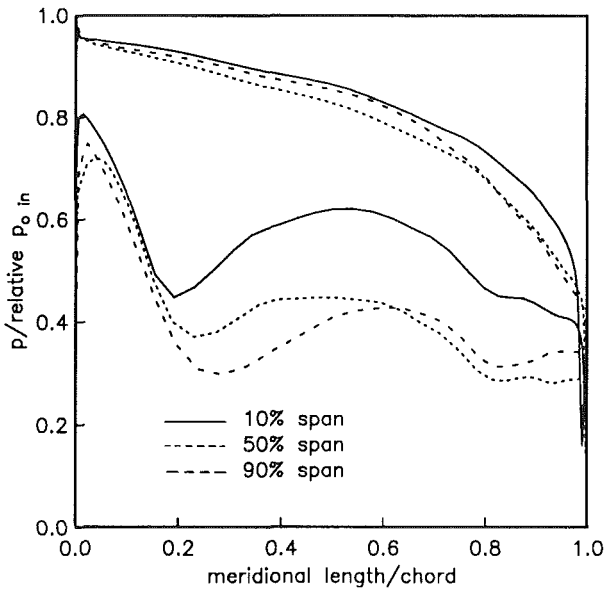

Fig. 10 Rotor blade surface pressure distribution

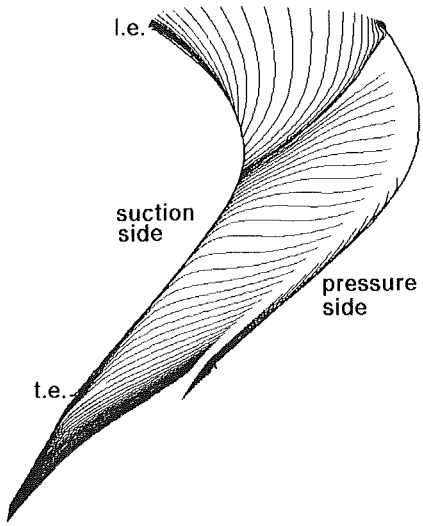

Fig. 12 Blade hub surface path lines

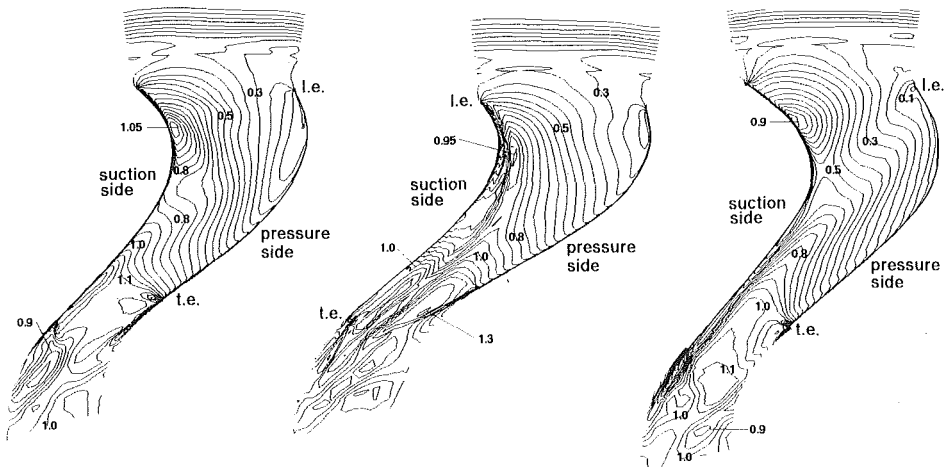

11a. Midspan 11b. Near Shroud, 95% Span 11c. Near Hub, 3% Span

Fig. 11 Blade relative Mach number contours

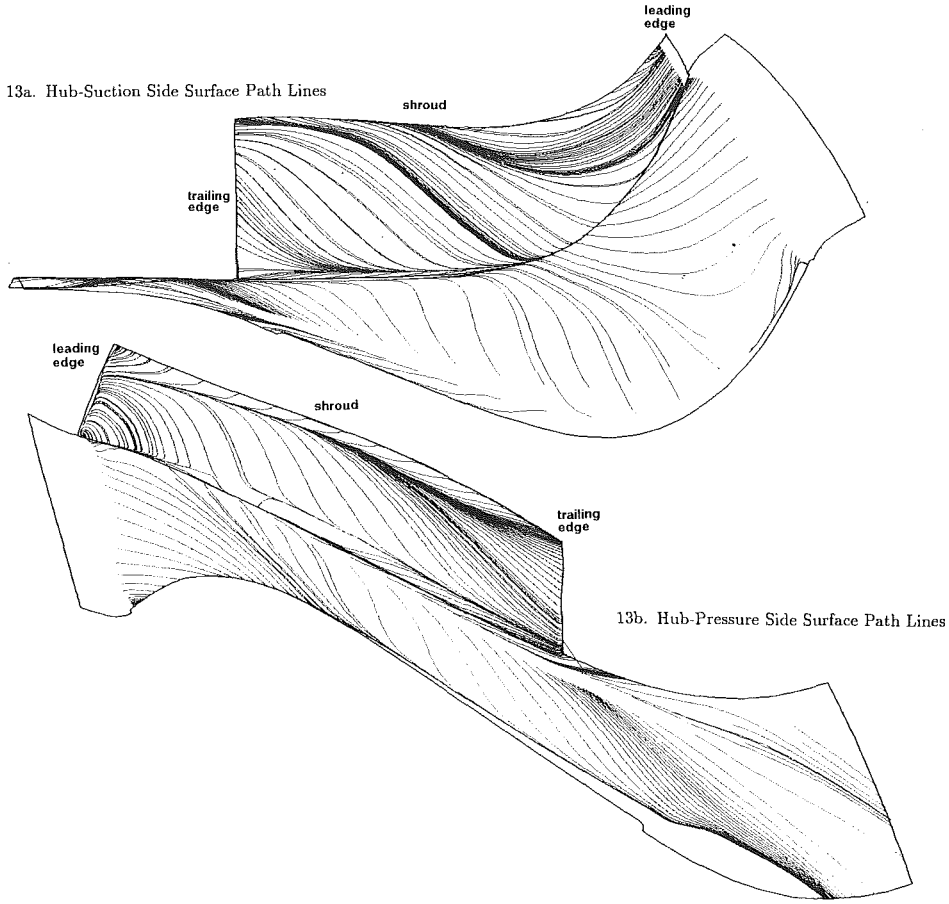

Fig. 13 Blade pressure and suction side surface path lines

degree of loading near the leading edge, combined with the low-momentum near-hub flow, produces a significant migration of flow from pressure side to suction side. The path lines indicate that nearly all of the high loss hub boundary layer flow, roughly 15 percent span thick (see Fig. 7) from within the vaneless space, is being accelerated toward the minimum suction side pressure, which will increase the loss further. A troubling picture indeed. Subsequent figures will show that from this point, the high loss flow migrates up the span and merges with the tip leakage vortex. Another interesting feature of the hub path line pattern is the two corner vortices, one along the pressure side and one on the suction side, which arise from the strong migration of flow down the pressure side, across the hub, and up the suction side.

Path lines along the suction side and hub and the pressure side and hub are plotted in Fig. 13. Figure 13(*a*) shows the very strong spanwise outward flow on the blade suction side from the hub passage and pressure side horseshoe vortices as well as the spanwise flow within the boundary layer due to the meridional curvature of the flow path.

With the hub boundary layer flow swept across to the suction side and up the span, the low Mach number flow from the pressure side flows down the span and into the hub region to fill the void. This flow from the pressure side with its nearly tangential motion and low absolute Mach numbers (see the axisymmetric flow in Fig. 9*b*) does not appear to be associated with high total pressure loss. Therefore, recontouring the hub in this region may not greatly increase efficiency. The movement of low Mach number flow from pressure to suction side leaves a large region of low-momentum flow along the hub-suction side corner, which is consistent with the blade loading diagram presented in Fig. 10. Because this large redistribution of flow tends to pull the hot shroud flow down, replacing the cold hub flow, it is a major convective mixing mechanism in the blade passage.

Path lines on the pressure side, Fig. 13(*b*), show the effect of the hub passage vortex and the corner vortex, which converge to a stagnation line. Okapuu's (1987) inviscid calculation of a mixed-flow turbine shows a spanwise outward flow as interpreted from lines of constant rothalpy. This outward motion along the pressure side follows formally from the relative eddy concept of rotating irrotational flow. The relative eddy in the MFT is overwhelmed by viscous generated secondary flows and so does not appear. The spanwise outward flow along the upper section of the blade pressure side is that entrained by the shroud passage vortex, which is roughly equal in strength to the hub passage vortex. Similar disagreement appears on the suction side where Okapuu's rothalpy lines indicate little spanwise flow, while Fig. 13(*a*) shows a large degree of spanwise outward flow in the present viscous simulation. The hub passage vortex generated by the thick blade inlet boundary layer and the low-momentum flow within the suction side boundary layer centrifuging out are the main mechanisms behind the spanwise motion here.

The complex secondary flow motion in the blade can be studied further by using plots of relative helicity, which is the inner product of the relative velocity and vorticity vectors, normalized by the velocity magnitude. The helicity is then the vorticity along individual streamlines rather than along a mean streamline. Figure 14 shows the relative helicity at various streamwise locations in the blade passage. In the average passage framework, secondary flows generated by the upstream vane appear as axisymmetric bands of helicity in the blade frame of reference. The axisymmetry is disturbed only through blade-generated potential influences. Such is the case upstream of the blade leading edge in Fig. 14(*a*). The underturning near

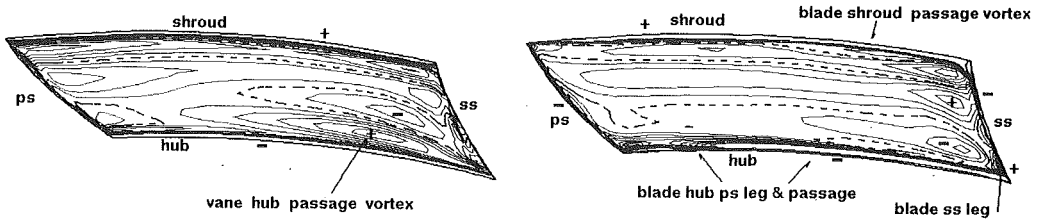

14a. Upstream of Blade Leading Edge

14b. 5% chord

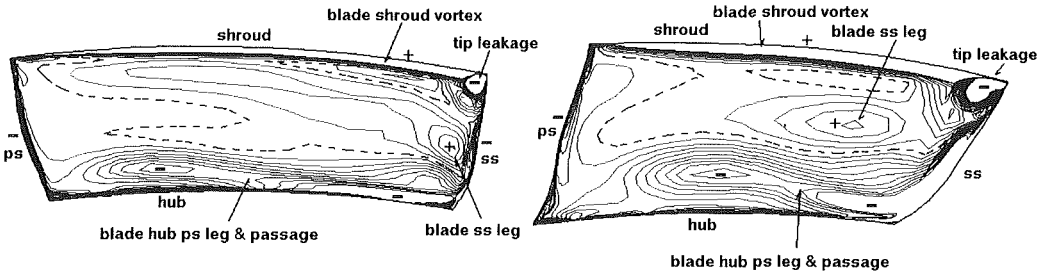

14c. 20% chord

14d. 40% chord

------ zero contour

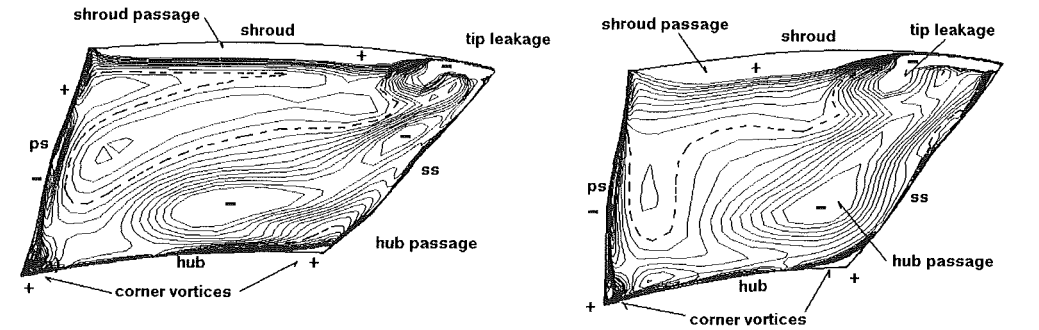

14e. 55% chord

14f. 75% chord

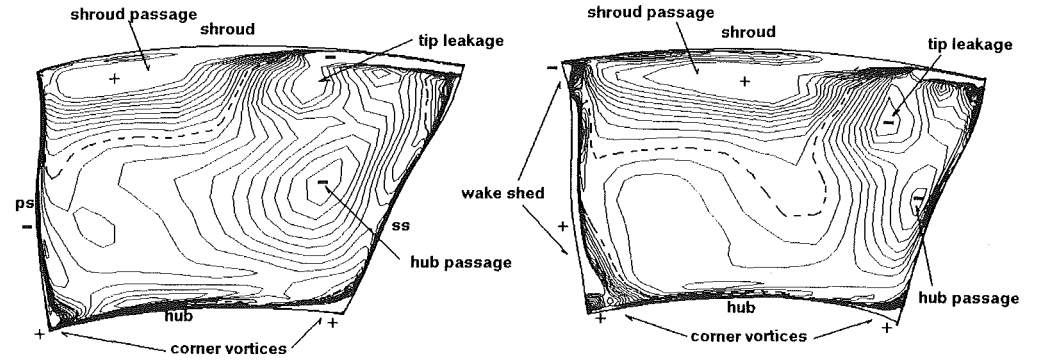

14g. 90% chord

14h. Near-Wake

Fig. 14 Relative helicity in the blade passage

the endwalls of the vane exit flow appears as thin regions of helicity of negative and positive sense on the hub and shroud, respectively. The small region of positive helicity near the hub indicates the location and strength of the vane-hub passage vortex. Just aft of the leading edge, Fig. 14(*b*) the vane-generated endwall vortices augment quickly growing blade passage vortices; however, the vane-hub passage vortex has dissipated and no longer appears in the contours. Near the hub, the legs of a horseshoe vortex system are visible. In contrast, the shroud horseshoe vortex system is not easily visible.

At roughly 20 percent chord, Fig. 14(*c*), several prominent features of the blade flow become more apparent. The synchronous development of the hub passage vortex and the pressure side leg of the hub horseshoe vortex are very similar to that in axial turbines as described by Sieverding (1985). The strong spanwise outward flow along the suction side is evident, as is some radial migration of the suction side leg of the hub horseshoe vortex. The shroud passage vortex grows in intensity and the negative helicity corresponding to the emerging tip leakage vortex is discernible in the shroud-suction side corner.

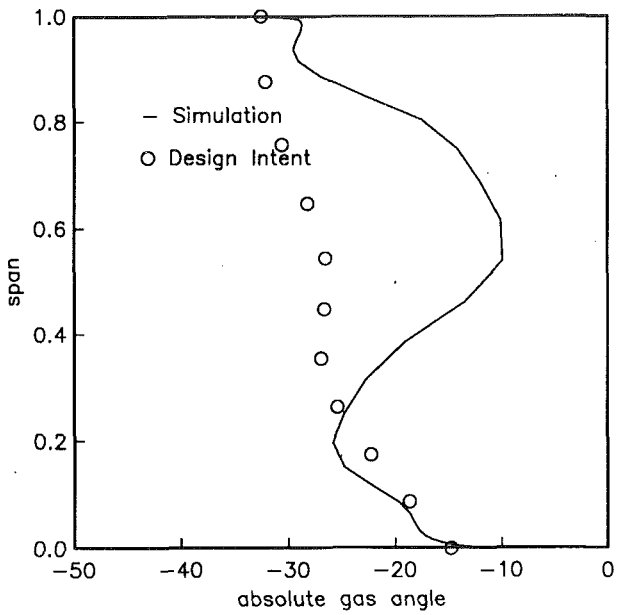

Fig. 15 Blade exit absolute flow angle

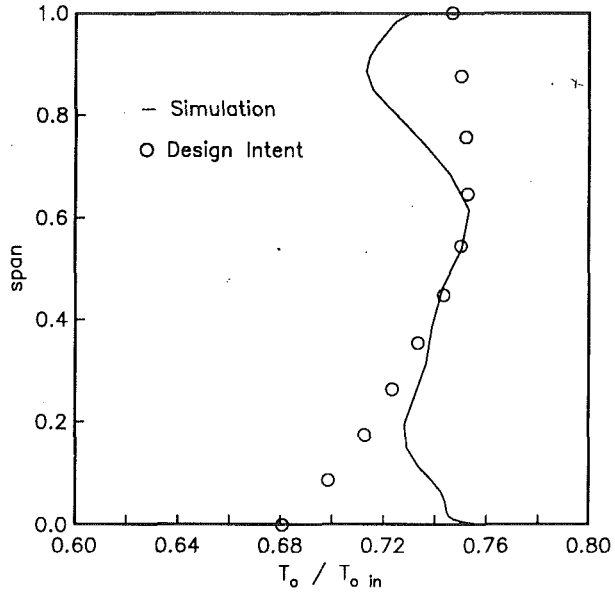

Fig. 16 Blade exit mass-averaged total temperature

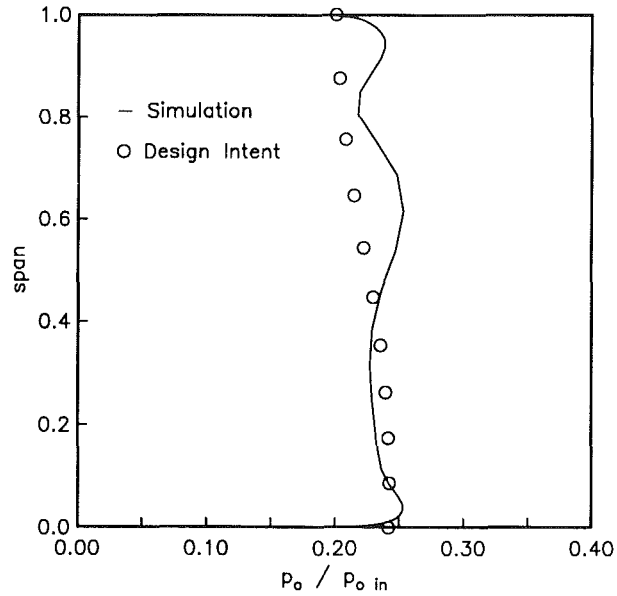

Fig. 17 Blade exit mass-averaged total pressure

All these features intensify by the 40 percent chord location, Fig. 14(*d*), except the suction side leg of the hub horseshoe vortex, which decays and is pushed toward the pressure side by both the hub and shroud passage vortices. The hub passage vortex also begins to diffuse somewhat.

By 55 percent chord, Fig. 14(*e*), the hub passage vortex continues to spread as the flow path opens and migrates spanwise outward under the influence of a radial pressure gradient, see Fig. 10. The tip leakage vortex is much stronger and has begun to merge with the suction side flow, whereas previously the two flows were distinct. The hub corner vortices are also clearly visible at this location.

In the exducer section at 75 percent chord and near the trailing edge, Figs. 14(*f*) and 14(*g*), respectively, the helicity plots show a complicated arrangement of three primary vortices under mutual interaction. The shroud passage vortex and the tip leakage vortex tend to induce a spanwise downward motion on each other that moves them well away from the shroud, which persists into the wake region in Fig. 14(*h*). The core of the hub passage vortex remains near the suction side at midspan and seems to tighten up as it passes along the uncovered portion of the blade. The corner vortices persist in all of these views.

The resulting blade discharge flow gives absolute gas angles much different from the design intent, see Fig. 15. The large secondary flows, particularly the shroud and hub passage vortices, produce a significant amount of underturning at the 60 percent span location. The corner vortices also tend to underturn the flow in the hub region. There is also a slight overall deviation from design intent from the flow rate mismatch.

The mass-averaged total temperatures are plotted in Fig. 16 versus design intent. Once again the design intent is essentially unmixed from the inlet temperature distribution; however, the average passage simulation gives a more uniform exit total temperature distribution due to significant mixing and nonuniform work extraction within the blade passage.

Also, the mass-averaged blade exit total pressure distribution is compared to design intent in Fig. 17 and shows a slightly greater exit total pressure commensurate with the fixed design exit static pressure and the increased flow capacity of the nozzle vane. The defect from the tip leakage vortex near 80 percent span is visible, as are the thin endwall boundary layers.

With all the complicated secondary flows present within the blade, the path lines of the axisymmetric average flow still follow the flow path in a more or less regular fashion except for a slight spreading from the hub surface in the low Mach number region (see Fig. 9*c*). With reasonable confidence we can examine the blade exit total pressure loss distribution by comparing (along meridional mesh lines) the inlet and exit mass averaged rotary total pressures as computed from rothalpy, which is a better indicator of loss than relative total pressure. Rothalpy, defined as:

$$I = H_o - \omega r V_\theta \tag{1}$$

where H_o is the stagnation enthalpy and ω is the blade rotation rate, is constant along a streamline in a rotor with adiabatic walls. A rotary total pressure computed from the rothalpy should then be constant along a streamline for ideal flow. Such is not the case for the relative total pressure.

Thus the change in rotary total pressure normalized by inlet rotary total pressure is presented in Fig. 18 to indicate total pressure loss. The surprising result is that the hub region, where Mach numbers and work extraction are low, is not an area of high loss. The greatest loss occurs near 80 percent span where the loss from the tip leakage vortex and the loss from the

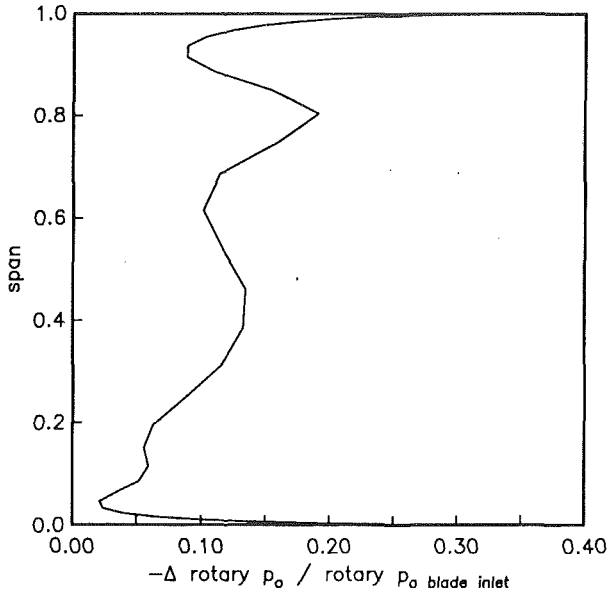

Fig. 18 Blade exit rotary total pressure loss

accelerated upstream hub boundary layer flow have merged. The shroud passage vortex also contributes to the loss there. A second peak occurs at midspan and is associated with the hub passage vortex, which has spread and migrated outward. Even with the high loss at the tip, Fig. 16 implies that the efficiency is high there as well.

Comparison With Radial and Axial Turbines

It is useful now to compare the secondary flows in the MFT with those commonly found in radial and axial turbines.

The predominant feature of the MFT flow, the strong radial migration, is much more pronounced than in axial machines. Also, the effect of the Coriolis force on blade loading is greater in the MFT due to larger radial velocities. Similar horseshoe vortex/passage vortex systems develop in the axial and mixed turbines except in the MFT, with its thin blade leading edges, the hub-pressure side leg of the horseshoe vortex is not as pronounced and so the passage vortex controls the flow pattern toward the trailing edge. The hub streamline pattern is very similar to annular and rectilinear turbine cascade flows with thick inlet boundary layers, including the strong pressure-to-suction side migration and hub-suction side corner vortex (cf. Choi and Knight, 1988). Axials, however, tend to have a more symmetric total pressure loss distribution along the span with large loss cores associated with the distinct endwall vortices and the tip vortex. Typically, the tip leakage vortex produces the greatest loss, e.g., Yamamoto and Yanagi's (1985) results, which is also the case in the MFT.

However, the MFT flow pattern is more like that in a radial turbine. The compact radial turbine (CRT) analyzed by Heidmann and Beach (1990) shows flow properties similar to those in the MFT, namely highly loaded blades with low-momentum flow near the hub and large radial migration of the flow on the suction side. However, the nonuniform work extraction and mixing found in the MFT either do not exist or counteract each other to produce an exit total temperature profile similar in shape to the inlet profile in the CRT. As with the MFT, the CRT exit loss distribution shows a very asymmetric distribution along the span with most of the loss accumulated in the shroud-suction side corner from the collection of high loss near wall flows and the tip leakage flow. The leakage vortex in the MFT also migrates down into the passage under the influence of a strong shroud passage vortex. In the CRT, the tip vortex remains near the shroud. A more generic radial turbine analyzed by Zangeneh-Kazemi et al. (1988) exhibits very similar characteristics, including a pressure side flow, which migrates toward the hub near the exducer section except for the near shroud flow, which is entrained by the shroud passage vortex and the tip leakage jet. This bifurcation of pressure side flow is very similar to that found in the MFT.

Conclusions

The flow in the generic mixed-flow turbine stage, simulated using the average passage Navier–Stokes equations, is highly three-dimensional and very complex. The passage vortices generated in the transonic nozzle vane are strong and tend to mix the inlet total temperature distribution. The nozzle trailing edge shock does interact with the rotor blade, but the character of this interaction cannot be illustrated with the average passage technique and is left for analysis by a fully unsteady technique.

The vane-generated secondary flow has little impact on the blade flow, which undergoes strong loading in the leading edge region. This loading engenders a strong pressure-to-suction side migration, which is most acute near the leading edge. At this location, the high loss hub boundary layer flow is entirely swept across the passage and is accelerated near the suction side and up the span. This fluid then merges with a quickly growing tip leakage vortex to produce a region of significant total pressure loss.

Large passage vortex systems develop in the MFT. The hub passage vortex is very strong and moves toward the shroud under the influence of a radial pressure gradient. The hub vortex and the shroud vortex then produce significant underturning of the turbine exit flow near 60 percent span. The shroud passage vortex also induces a radial downward migration of the tip leakage vortex.

While characteristics of both axial and radial machines can be seen in the MFT flow, the secondary flow pattern is more similar to that in a radial than an axial turbine, particularly the collection of high loss flow in the shroud-suction side corner. Although the present numerical simulation provides a detailed picture of the MFT flow, a good experimental data base is needed to understand more fully the complex phenomena found in the mixed flow turbine.

Acknowledgments

The lead authors were supported by the NASA Lewis Research Center under contract No. NAS3-25266 with Dr. J. Adamczyk as monitor. The joint development effort was conducted under the NASA Space Act Agreement. Thanks are given to all those who support and administer the NASA Space Act as this has been a most enjoyable and enlightening project. Special thanks are given to R. Roelke and J. Adamczyk of NASA Lewis for many helpful discussions, and to K. Dugas for editing this manuscript. The Cray Y-MP computer resources were provided by the NAS at NASA Ames Research Center.

References

Adamczyk, J. J., 1985, "Model Equation for Simulating Flows in Multistage Turbomachinery," ASME Paper No. 85-GT-226; NASA TM 86869.

Baldwin, B. S., and Lomax, H., 1978, "Thin Layer Approximation and Algebraic Model for Separated Turbulent Flows," AIAA Paper No. 78-257.

Beach, T. A., 1990, "An Interactive Grid Generation Procedure for Axial and Radial Flow Turbomachinery," AIAA Paper No. 90-0344.

Choi, D., and Knight, C. J., 1988, "Computation of Three-Dimensional Viscous Cascade Flows," AIAA Paper No. 88-0363.

Civinskas, K. C., 1985, "Aerodynamic Design Analysis of a Mixed-Flow, High Specific Work Turbine," presented as AIAA Oral Presentation No. 85-1275 at the 21st AIAA Joint Propulsion Conference, Monterey, CA, July 8–11.

Cleak, J. G. E., and Gregory-Smith, D. G., 1992, "Turbulence Modeling for Secondary Flow Prediction in a Turbine Cascade," ASME Journal of Turbomachinery, Vol. 114, pp. 590–598.

Heidmann, J. D., and Beach, T. A., 1990, "An Analysis of the Viscous Flow Through a Compact Radial Turbine by the Average Passage Approach," ASME Paper No. 90-GT-64; NASA TM 102471.

Kirtley, K. R., Beach, T. A., and Adamczyk, J. J., 1990, "Numerical Analysis of Secondary Flow in a Two-Stage Turbine," AIAA Paper No. 90-2356.

Law, H. C., and Puterbaugh, S. L., 1982, "A Computer Program for Axial Compressor Design (UDO300M)," Aero Propulsion Report No. AFWAL-TR-82-2074.

Mayle, R. E., 1991, "The Role of Laminar-Turbulent Transition in Gas Turbine Engines," ASME JOURNAL OF TURBOMACHINERY, Vol. 113, pp. 509–537.

Okapuu, Ü, 1987, "Design and Aerodynamic Performance of a Small Mixed-Flow Gas Generator Turbine," AGARD CP-421, pp. 16-1–16-11.

Raj, R., and Lakshminarayana, B., 1973, "Characteristics of the Wake Behind a Cascade of Airfoils," *J. Fluid Mech.*, Vol. 61, Part 4, pp. 707–730.

Sieverding, C. H., 1985, "Recent Progress in the Understanding of Basic Aspects of Secondary Flows in Turbine Blade Passages," ASME *Journal of Engineering for Gas Turbines and Power*, Vol. 107, pp. 248–257.

Yamamoto, A., and Yanagi, R., 1985, "Production and Development of Secondary Flows and Losses Within a Three-Dimensional Turbine Stator Cascade," ASME Paper No. 85-GT-217.

Zangeneh-Kazemi, M., Dawes, W. N., and Hawthorne, W. R., 1988, "Three-Dimensional Flow in Radial-Inflow Turbines," ASME Paper No. 88-GT-103.

Zunino, P., Ubaldi, M., Satta, A., and Peisino, E., 1988, "A Comparison Between Measurements and Turbulence Models in a Turbine Cascade Passage," ASME Paper No. 88-GT-226.

Kirtley, K. R., Beach, T. A., and Adamczyk, J. J., 1990, "Numerical Analysis of Secondary Flow in a Two-Stage Turbine," AIAA Paper No. 90-2356.

Law, H. C., and Puterbaugh, S. L., 1982, "A Computer Program for Axial Compressor Design (UDO300M)," Aero Propulsion Report No. AFWAL-TR-82-2074.

Mayle, R. E., 1991, "The Role of Laminar-Turbulent Transition in Gas Turbine Engines," ASME JOURNAL OF TURBOMACHINERY, Vol. 113, pp. 509–537.

Okapuu, Ü, 1987, "Design and Aerodynamic Performance of a Small Mixed-Flow Gas Generator Turbine," AGARD CP-421, pp. 16-1–16-11.

Raj, R., and Lakshminarayana, B., 1973, "Characteristics of the Wake Behind a Cascade of Airfoils," *J. Fluid Mech.*, Vol. 61, Part 4, pp. 707–730.

Sieverding, C. H., 1985, "Recent Progress in the Understanding of Basic Aspects of Secondary Flows in Turbine Blade Passages," ASME *Journal of Engineering for Gas Turbines and Power*, Vol. 107, pp. 248–257.

Yamamoto, A., and Yanagi, R., 1985, "Production and Development of Secondary Flows and Losses Within a Three-Dimensional Turbine Stator Cascade," ASME Paper No. 85-GT-217.

Zangeneh-Kazemi, M., Dawes, W. N., and Hawthorne, W. R., 1988, "Three-Dimensional Flow in Radial-Inflow Turbines," ASME Paper No. 88-GT-103.

Zunino, P., Ubaldi, M., Satta, A., and Peisino, E., 1988, "A Comparison Between Measurements and Turbulence Models in a Turbine Cascade Passage," ASME Paper No. 88-GT-226.

DISCUSSION

M. Zangeneh[1]

The average passage approach to the solution of the N–S equations in multistage turbomachines, as suggested by Adamczyk (1985), can make an important contribution to modeling of flow through turbomachines, where strong blade row interactions are present that significantly affect the *mean* flow field in the machine. However, this approach is quite expensive computationally compared to single blade row calculations. Therefore in applying this method to a particular problem it is important to establish clearly whether strong blade row interactions do have a significant effect on the mean flow field in the machine. If such interactions are not present, then designers can continue to use the more efficient single blade row calculations. There is some evidence that the interaction between the nozzle vanes and the rotor in radial turbines does not have a significant effect on the mean flow field. In the absence of experimental results, it would perhaps help to clarify the above point if the authors compare the predicted exit flow distribution of the rotor only calculation (on the same grid as the stage calculation) with the results obtained from the stage calculation.

The authors correctly state that the secondary flow patterns in the mixed flow impeller are quite similar to that found in radial-inflow turbines. The secondary flow effects tend to accumulate low-momentum fluids in the impeller toward the location of maximum Mach number on the shroud suction corner. The effect of tip leakage flows, as shown by Zangeneh et al. (1988), is to move the "wake" region toward the midpassage near the tip. In the predicted results, however, the location of maximum underturning occurs at 60 percent of span rather near the tip region. For most conventional radial turbines the location of maximum underturning moves down toward the midspan location only at low flow coefficients (Zangeneh, 1992). One possible explanation for this predicted flow pattern is the use of larger than normal tip clearance gap in the calculation. Could the authors indicate what the tip gap used for the calculation was and what in their opinion is the reason for this predicted exit flow pattern?

References

Zangeneh, M., 1992, "Numerical Methods for Inviscid and Viscous Flow Analysis," VKI lecture series, Radial Turbines, 1992-5, Belgium.

[1]Department of Mechanical Engineering, University College London, United Kingdom.

Authors' Closure

Dr. Zengeneh brings up a question that many of our colleagues have, i.e., how important is deterministic unsteadiness on the performance of multistage turbomachinery and should it be included in time-mean numerical simulations? As modeled in the average passage Navier–Stokes equations used in this paper, the deterministic unsteadiness is a function of the three dimensionality of the neighboring blade row flows rotating relative to the blade row in question. Therefore, designs or operating points that give rise to strong three dimensionality yield large levels of deterministic unsteadiness, which must be accounted for in any steady multistage simulation. Good designs operating near their design point or machines whose blade rows are far apart may not need such accounting. The importance of the deterministic unsteadiness can be quantified by interrogating experimental data and average passage numerical simulations, which removes the need for an isolated rotor simulation comparison. Li and Cumpsty (1990), in their Fig. 6, show total unsteadiness intensities in the stationary frame downstream of an axial compressor rotor for two tip gap heights. When the data were filtered to remove unsteadiness that correlated with blade passing frequency, i.e., deterministic unsteadiness, only the random unsteadiness or turbulence was left. The difference between the filtered and unfiltered intensities is small for the small tip gap but large for the large tip gap. So clearly, for large gaps, the deterministic unsteadiness is as important if not more important than the turbulence. Similarly, the mixed flow turbine stage simulation can be interrogated and the divergence of the deterministic unsteady stress, which is unique to the average passage equation set, can be compared to the divergence of the turbulence stress as in Fig. 19. From these two points one can draw the conclusion that if turbulence is important, then the deterministic unsteadiness is important for many turbomachinery at design and off-design points and plays a strong role in mixing across axisymmetric streamsheets. One may not know how important *a priori*; therefore we consider it worth the added expense to solve the average passage equations rather than treat the system as a series of isolated blade rows. In addition, the average passage equation set is the only time-averaged system that conserves all flow quantities including streamwise vorticity from one blade row to another (see Adamczyk, 1991).

Regarding the secondary flow pattern at the exit, the tip gap

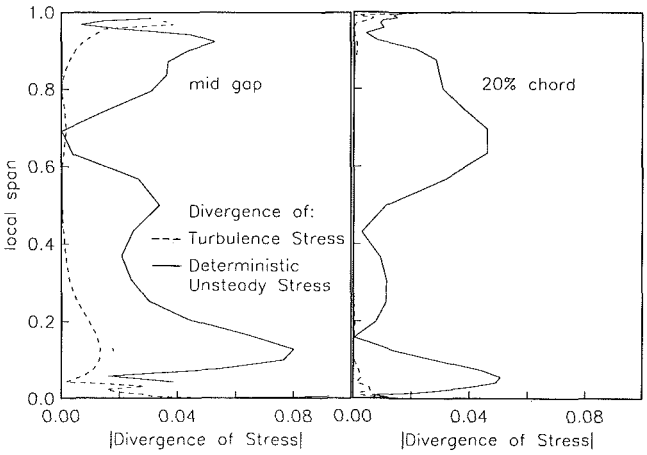

Fig. 19 Absolute value of the divergence of the deterministic unsteady stress versus turbulence stress from vane-generated flow plotted at midgap and 20 percent rotor chord downstream of rotor leading edge. Turbulence is mostly due to end wall boundary layers while deterministic unsteadiness comes from three-dimensional vane-generated flow as well as the vane trailing edge shock.

Aerodynamic Design of Turbomachinery Blading in Three-Dimensional Flow: An Application to Radial Inflow Turbines

Y. L. Yang

C. S. Tan

W. R. Hawthorne

Gas Turbine Laboratory,
Massachusetts Institute of Technology,
Cambridge, MA 02139

A computational method based on a theory for turbomachinery blading design in three-dimensional inviscid flow is applied to a parametric design study of a radial inflow turbine wheel. As the method requires the specification of swirl distribution, a technique for its smooth generation within the blade region is proposed. Excellent agreements have been obtained between the computed results from this design method and those from direct Euler computations, demonstrating the correspondence and consistency between the two. The computed results indicate the sensitivity of the pressure distribution to a lean in the stacking axis and a minor alteration in the hub/shroud profiles. Analysis based on a Navier-Stokes solver shows no breakdown of flow within the designed blade passage and agreement with that from a design calculation; thus the flow in the designed turbine rotor closely approximates that of an inviscid one. These calculations illustrate the use of a design method coupled to an analysis tool for establishing guidelines and criteria for designing turbomachinery blading.

1 Introduction

In the two papers on the "Theory of Blade Design for Large Deflections" published in 1984 [11], a new technique was presented for designing the shape of turbomachinery blades in three-dimensional flow. Applications of this theory to the design of radial turbomachinery have been reported in [1, 4, 5, 15, 14]. The experimental data in [1, 15] showed that the radial inflow turbines designed by the new technique gave an improvement in efficiency over a rather wide operating range. Studies on the influence of the loading distribution, stacking position, etc., upon the resulting blade shape and pressure distribution were reported in [4]. A concise but general exposition of the theoretical basis for the present design technique was presented in [5]. In this paper, we describe: (1) a numerical technique based on finite-element/Fourier collocation method for computation of blade shape in radial inflow turbine wheels; (2) the development of a proposed method for generating the loading distribution within the blade region; and (3) the results of further studies of the design of blades for radial inflow turbines. The present study is solely concentrated on exploring the aerodynamic factors affecting the blade shape without compromising them by structural or manufacturing considerations. We will first present a summary of the theoretical formulation.

Contributed by the International Gas Turbine Institute and presented at the 37th International Gas Turbine and Aeroengine Congress and Exposition, Cologne, Germany, June 1-4, 1992. Manuscript received by the International Gas Turbine Institute February 4, 1992. Paper No. 92-GT-74. Associate Technical Editor: L. S. Langston.

2 A Summary of Theoretical Formulation

2.1 Design Specification. In inverse design methods for two-dimensional flow, it is convenient to prescribe the surface velocity or pressure (or a mixture of thickness and velocity on one surface). However, flow deflection and work distribution must be compatible at all radii in three-dimensional flows; as it is difficult to satisfy this constraint in terms of surface velocities, the two-dimensional techniques cannot be easily adapted to three-dimensional flow.

A useful design specification for the inverse design of blading in three-dimensional flow is the mean swirl distribution $r\bar{V}_\theta$ (V_θ is the tangential absolute velocity); it is given by:

$$r\bar{V}_\theta(r, z) = \frac{B}{2\pi} \int_0^{\frac{2\pi}{B}} rV_\theta(r, \theta, z)d\theta \tag{1}$$

where the overbar defines a tangential mean, B is the number of blades, and (r, θ, z) is the right-handed cylindrical coordinate system. We will use subscript (r, θ, z) to denote vector component in the radial, tangential, and axial directions, respectively. As $2\pi r\bar{V}_\theta$ is the circulation around the axis, the swirl distribution is thus related to the bound circulation Γ on the blade. In particular, for uniform upstream flow and free vortex design, Γ on the blade is given by:

$$\Gamma B = 2\pi r\bar{V}_\theta \tag{2}$$

Design specification based on $r\bar{V}_\theta$ has been reported by Theodorsen [13] for aircraft propellers, Smith [10] for unducted fan, and Kerwin [7] for marine propellers.

2.2 Inverse Design Theory. A design specification based on circulation distribution leads to the natural use of surfaces of singularities (in this case a bound vortex sheet) to represent blade surfaces. In contrast to other singularity methods, as will be seen below, use is made of Clebsch's transformation [8].

The blade surfaces may be represented by

$$\alpha(r, \theta, z) \equiv \theta - f(r, z) = \pm \frac{n2\pi}{B} \tag{3}$$

where n is zero or an integer. Assuming the flow is steady and that far upstream the approaching flow is axisymmetric, irrotational, and reversible (i.e., a homenthalpic and homentropic flow), then the absolute vorticity bound to the blades can be written in the form

$$\Omega = (\nabla r\overline{V}_\theta \times \nabla\alpha)\delta_p(\alpha) \tag{4}$$

where $\delta_p(\alpha)$ is the periodic delta function [9] given as

$$\delta_p(\alpha) = \frac{2\pi}{B} \sum_{n=-\infty}^{\infty} \delta\left(\alpha - \frac{n2\pi}{B}\right) = \sum_{n=-\infty}^{\infty} e^{inB\alpha} \tag{5}$$

A compelling attraction of Clebsch's transformation [8] is that, if it is possible to represent the vorticity as the vector product of the gradient of two scalars, i.e.,

$$\Omega = \nabla\lambda \times \nabla\mu, \tag{6}$$

then one may immediately express the velocity in the form

$$\mathbf{V} = \nabla\Phi + \lambda\nabla\mu \tag{7}$$

Inspection of Eq. (4) shows that the choice of Clebsch's transformation is a natural one in this case, and it yields

$$\mathbf{V} = \nabla\Phi + r\overline{V}_\theta\nabla\alpha - S(\alpha)\nabla r\overline{V}_\theta \tag{8}$$

where $S(\alpha)$ is the periodic sawtooth function [9], given as

$$S(\alpha) = \sum_{n=-\infty}^{\infty} \frac{e^{inB\alpha}}{inB} \tag{9}$$

The jump in velocity across the blades may be derived by applying Stokes' theorem to a circuit enclosing the boundary vorticity [11] in the form

$$(\mathbf{W}^+ - \mathbf{W}^-) = \frac{2\pi}{B}\frac{\overline{\Omega}\times\nabla\alpha}{|\nabla\alpha|^2}$$

$$= \frac{2\pi}{B}\left(\frac{\nabla\alpha\cdot\nabla r\overline{V}_\theta}{|\nabla\alpha|^2}\nabla\alpha - \nabla r\overline{V}_\theta\right) \tag{10}$$

where the relative velocity $\mathbf{W} = \mathbf{V} - \mathbf{r}\times\omega$ with ω as the angular velocity of the rotor; the superscript $+/-$ refers to blade pressure/suction side respectively. It can be shown [4, 5, 15] that in compressible, irrotational, and reversible flow, the enthalpy jump across the blades is

$$H^+ - H^- = \frac{2\pi}{B}[\mathbf{W}_{bl}\cdot\nabla r\overline{V}_\theta] \tag{11}$$

where $\mathbf{W}_{bl}$ denotes the velocity at the blade. This useful equation offers an elegant method of satisfying the Kutta condition at the trailing edge by setting the right-hand side to zero so that the pressure is continuous at the trailing edge. It should also be pointed out that Eq. (4) may also describe the vorticity in a trailing vortex sheet [12], which will sustain no static pressure difference, for which therefore

$$\mathbf{W}_{bl}\cdot\nabla r\overline{V}_\theta = 0 \tag{12}$$

It is convenient to separate the velocity into a mean part $\overline{V}$ and a periodic part $\tilde{V}$, as

$$\overline{\mathbf{V}} = \nabla\overline{\Phi} + r\overline{V}_\theta\nabla\alpha \tag{13}$$

$$\tilde{\mathbf{V}} = \nabla\tilde{\Phi} - S(\alpha)\nabla r\overline{V}_\theta \tag{14}$$

The formulation has made use of a Fourier series to represent the θ dependence of the flow variables. As such, the mean flow can be regarded as the zeroth mode of this Fourier series representation.

The continuity equation for compressible flow can be written as

$$\nabla\cdot\mathbf{W} = -\mathbf{W}\cdot\nabla\ln\rho \tag{15}$$

the tangential average of which is

$$\nabla\cdot\overline{\mathbf{W}} = -\overline{\mathbf{W}\cdot\nabla\ln\rho} \tag{16}$$

2.3 The Mean Flow and the Bladed Actuator Duct. The mean velocity may either be formulated using the Clebsch expression in Eq. (13) or in terms of the more familiar Stokes stream function, which has often found application in throughflow and actuator disk calculations. Here we will adopt the use of Stokes' streamfunction, ψ, for the description of the mean flow. We note that, while the blade has been represented as surfaces of singularities, the blockage effect due to the finite thickness of the blade could be partially accounted for through the use of a blockage parameter, b. With the introduction of this parameter b, the mean velocity is obtained from the stream function ψ using

$$rb\rho_{av}\overline{W}_r = -\frac{\partial\psi}{\partial z} \tag{17}$$

and

$$rb\rho_{av}\overline{W}_z = \frac{\partial\psi}{\partial r} \tag{18}$$

In the above equations, ρ_{av} is defined to satisfy

$$\overline{\mathbf{W}}\cdot\nabla\ln(b\rho_{av}) = -\nabla\cdot\overline{\mathbf{W}} \tag{19}$$

A rational modification of the continuity equation, Eq. (15), to approximate the blockage effect of the blade thickness is

$$\nabla\cdot\mathbf{W} = -\mathbf{W}\cdot\nabla\ln b\rho \tag{20}$$

(see discussion in appendix).

By taking the pitchwise average of Eq. (20) and substituting for $\nabla\cdot\overline{\mathbf{W}}$ in Eq. (19), we obtain

$$\overline{\mathbf{W}}\cdot\nabla\ln(\rho)_{av} = \overline{\mathbf{W}\cdot\nabla\ln(\rho)} \tag{21}$$

which can be integrated to give ρ_{av} for a known mean flow and a known periodic flow.

Use of the expression for $\overline{\Omega}_\theta$ (mean tangential vorticity component) allows one to derive a governing equation for ψ as

$$L\psi = rb\rho_{av}\left[\frac{\partial r\overline{V}_\theta}{\partial z}\frac{\partial f}{\partial r} - \frac{\partial_r\overline{V}_\theta}{\partial r}\frac{\partial f}{\partial z}\right] \tag{22}$$

where the differential operator L is given by

$$L = \left[\frac{\partial^2}{\partial r^2} - \frac{1}{r}\frac{\partial}{\partial r} + \frac{\partial^2}{\partial z^2}\right] - \left[\frac{\partial\ln(b\rho_{av})}{\partial r}\frac{\partial}{\partial r} + \frac{\partial\ln(b\rho_{av})}{\partial z}\frac{\partial}{\partial z}\right]$$

As the number of blades becomes infinite in the limit, keeping $r\overline{V}_\theta$ fixed, we obtain a useful flow model referred to as the bladed actuator duct [11]. In this flow model, the periodic terms vanish and the streamlines are at the intersection of the ψ and α surfaces. The governing equation for the Stokes streamfunction ψ is Eq. (22) with ρ_{av} replaced by the mean density, $\overline{\rho}$.

2.4 Periodic Flow Equation. A continuity equation for the periodic flow is obtained by subtracting from Eq. (20) its pitchwise mean value to give

$$\nabla\cdot\tilde{\mathbf{V}} = -[\mathbf{W}\cdot\nabla\ln(b\rho) - \overline{\mathbf{W}\cdot\nabla\ln(b\rho)}] \tag{23}$$

Substituting for $\tilde{\mathbf{V}}$ from Eq. (14) in Eq. (23), we have

$$\nabla^2\phi = \nabla\cdot[S(\alpha)\nabla r\overline{V}_\theta] - [\mathbf{W}\cdot\nabla\ln(b\rho) - \overline{\mathbf{W}\cdot\nabla\ln(b\rho)}] \tag{24}$$

As the flow is spatially periodic from blade to blade, the periodic velocity potential $\tilde{\Phi}$ can be expressed as

$$\tilde{\Phi} = \sum_{n=-\infty, \neq 0}^{+\infty} \tilde{\phi}_n(r, z) e^{inB\theta}, \tag{25}$$

This gives a governing equation for $\tilde{\phi}_n$ as

$$\nabla^2_{2D}\tilde{\phi}_n = \frac{e^{-inBf}}{inB}\nabla^2 r\overline{V}_\theta - e^{inBf}\left(\frac{\partial f}{\partial r}\frac{\partial r\overline{V}_\theta}{\partial r} + \frac{\partial f}{\partial z}\frac{\partial r\overline{V}_\theta}{\partial z}\right) + [-\mathbf{W}\cdot\nabla\ln(b\rho) + \overline{\mathbf{W}\cdot\nabla\ln(b\rho)}]_{FT(n)} \tag{26}$$

where

$$\nabla^2_{2D} = \frac{1}{r}\frac{\partial}{\partial r}\left(r\frac{\partial}{\partial r}\right) + \frac{\partial^2}{\partial z^2} - \frac{n^2B^2}{r^2}$$

and subscript $FT(n)$ denotes the Fourier coefficients of the nth mode.

Since it is assumed that the specified $\overline{rV}_\theta$ distribution is such that no trailing vorticity appears downstream of the blade row, and that the upstream flow is irrotational, the first two terms on the right-hand side of Eq. (26) vanish identically upstream and downstream of the blade. The energy equation reduces to the statement that the rothalpy.

$$H_t^* = H + \frac{1}{2}V^2 - \omega\overline{rV}_\theta \tag{27}$$

remains constant throughout the flow field.

2.5 Blade Boundary Condition. The procedure for determining the blade shape is an iterative one. A first guess for the blade shape is used to compute the velocities, and the blade shape is updated by using the blade boundary condition in the form:

$$\mathbf{W}_{bl}\cdot\nabla\alpha = 0 \tag{28}$$

The above equation may be expanded to give

$$\overline{W}_r\frac{\partial f}{\partial r} + \overline{W}_z\frac{\partial f}{\partial z} = \frac{r\overline{V}_\theta}{r^2} - \omega + (\tilde{\mathbf{V}})_{bl}\cdot\nabla\alpha \tag{29}$$

The solution for Eq. (29) requires the specification of an integration constant for f, which implies that values of f have to be specified along a line on the surface stretching from the hub to the shroud. This specification is called the "stacking condition." The camber distribution f in the bladed actuator duct is similarly determined but with the periodic term omitted. Once $\overline{rV}_\theta$ and a stacking condition for f are prescribed, the method gives all the other velocities. Note that the actuator duct offers rapid solutions, which are useful in the preliminary stages of a design when assessing the effectiveness of various specifications of $\overline{rV}_\theta$ and the stacking condition.

2.6 Boundary Conditions. When the relative flow is subsonic, both the governing equations for the mean and the periodic flow are of the elliptic type. Thus, their solution requires the specification of a boundary condition at: (*a*) an upstream boundary; (*b*) a downstream boundary; (*c*) the shroud and the hub surface; and (*d*) the blade surface.

3 Numerical Solution Procedure

The use of Fourier series representation for θ dependence has enabled us to reduce the governing equations in three dimensions (r, θ, z) to a set of equations in two dimensions (r, z). For practical implementation, we will have to truncate the Fourier series by taking a finite n in Eq. (25). Spatial discretization on the (r, z) plane is based on the finite-element technique. Figure 3 shows a typical finite element mesh and Fourier collocation grid used for solving Eqs. (21), (22), (26), and (29), and hence the inverse design calculation. A four-node isoparametric element for interpolation is used. With each element mapped into a square element with the natural coordinate system (ξ, η), the coordinates (r, z) are expressed in terms of the coordinates of the four corner nodes by

$$\begin{Bmatrix} r \\ z \end{Bmatrix} = \sum_{i=1}^{4}(1+\xi_i\xi)(1+\eta_i\eta)\begin{Bmatrix} r_i \\ z_i \end{Bmatrix} = \underline{N}^T\begin{Bmatrix} r_i \\ z_i \end{Bmatrix} \tag{30}$$

where $\underline{N}^T$ is the transpose of the shape function vector. The Jacobian, in terms of the coordinates (r_i, z_i), is

$$[\underline{J}] = \begin{bmatrix} \frac{\partial r}{\partial \xi} & \frac{\partial z}{\partial \xi} \\ \frac{\partial r}{\partial \eta} & \frac{\partial z}{\partial \eta} \end{bmatrix} \tag{31}$$

The derivative of variables in the physical plane is thus related to those in the computational plane by

$$\begin{Bmatrix} \frac{\partial}{\partial r} \\ \frac{\partial}{\partial z} \end{Bmatrix} = [\underline{J}]^{-1}\begin{Bmatrix} \frac{\partial}{\partial \xi} \\ \frac{\partial}{\partial \eta} \end{Bmatrix} = \begin{bmatrix} I_{11} & I_{12} \\ I_{21} & I_{22} \end{bmatrix}\begin{Bmatrix} \frac{\partial}{\partial \xi} \\ \frac{\partial}{\partial \eta} \end{Bmatrix} \tag{32}$$

where matric elements I_{ij} are those of the inverse of the Jacobian. Extremization of the variational form of Eq. (22):

$$I = \frac{1}{2}\int\int \underline{\psi}^T\left[\frac{1}{r}\left(\frac{\partial N^T}{\partial r}\right)\left(\frac{\partial N}{\partial r}\right) + \frac{1}{r}\left(\frac{\partial N^T}{\partial z}\right)\left(\frac{\partial N}{\partial z}\right)\right]\underline{\psi}dA + \int\int \underline{\psi}^T\underline{N}^T\underline{N}\underline{q}dA = \frac{1}{2}\underline{\psi}^T[k]\underline{\psi} + \underline{\psi}^T\underline{q} \tag{33}$$

leads to, for each element,

$$[k]\underline{\psi} = -\underline{q} \tag{34}$$

with the corresponding boundary conditions; q is the nodal value of

$$\left[\frac{1}{r}\frac{\partial \ln b\rho_{av}}{\partial r}\frac{\partial \psi}{\partial r} + \frac{1}{r}\frac{\partial \ln b\rho_{av}}{\partial z}\frac{\partial \psi}{\partial z} + b\rho_{av}\frac{\partial r\overline{V}_\theta}{\partial z}\frac{\partial f}{\partial r} - b\rho_{av}\frac{\partial r\overline{V}_\theta}{\partial r}\frac{\partial f}{\partial z}\right].$$

The evaluation of $[k]$ and $\underline{q}$ is done by Gaussian Quadrature. The direct stiffness technique is applied to derive the global matrix over the whole domain as

$$[K]\underline{\psi} = -\underline{Q} \tag{35}$$

The same procedure is applied to the periodic velocity potential in Eq. (26). The above matrix equations are solved iteratively via the preconditioned conjugate gradient method (including use of multigrid scheme).

In the numerical solution of fictitious density from Eq. (21) and camber distribution f from Eq. (29) by finite element method, we form the discrete approximation to differential operator using Eq. (32) for each element. The determination of f is implemented on an element-by-element basis, proceeding upstream and downstream from the elements adjacent to the stacking line on which appropriate initial values have been prescribed. Likewise, the determination of fictitious density would proceed downstream but using prescribed values at the inflow boundary.

4 Mean Swirl Distribution $\overline{rV}_\theta$.

The aerodynamic design of the blades was implemented by specifying a distribution of the mean swirl $\overline{rV}_\theta$ (which is an important quantity, as can be seen from the above) throughout the blade region, in addition to the overall geometry, number of blades, and mass flow rate. The overall stagnation enthalpy change across a rotating blade row is approximately related to the overall change in $\overline{rV}_\theta$ between the leading edge and the trailing edge. As the angular momentum is proportional to the mass flow weighted mean of the tangential velocity and not

$\overline{V_\theta}$, when the mass flow distribution becomes more circumferentially uniform, the above approximation becomes more accurate. However, there could be many $\overline{rV_\theta}$ distributions within the blade region to give this same overall change in $\overline{rV_\theta}$ across the blade row. It is conjectured that there would be an optimum $\overline{rV_\theta}$ distribution that results in a flow field with minimum loss, be it due to skin friction or to the secondary flow and resulting boundary layer behavior.

The specified $\overline{rV_\theta}$ distribution must satisfy the following boundary conditions:

1 The trailing edge where the Kutta condition must be specified,

$$\mathbf{W}_{bl} \cdot \nabla \overline{rV_\theta} = 0 \tag{36}$$

and where we have assumed $\overline{rV_\theta}$ = const. Hence,

$$\frac{\partial \overline{rV_\theta}}{\partial s} = 0 \tag{37}$$

where s is the meridional distance along the quasi-streamline coordinate. In the numerical calculations reported below the second derivative was also set to zero.

2 At the leading edge $\overline{rV_\theta}$ = const, and if we assume a zero local incidence there, i.e.,

$$\mathbf{W}_{bl} \cdot \nabla \overline{rV_\theta} = 0 \tag{38}$$

Hence, again

$$\frac{\partial \overline{rV_\theta}}{\partial s} = 0 \tag{39}$$

In the numerical calculations reported below the second derivative was also set to zero.

3 For irrotational flow, the $\overline{rV_\theta}$ distribution must satisfy

$$\frac{\partial \overline{rV_\theta}}{\partial n} = 0 \tag{40}$$

on the hub and shroud surfaces. In Eq. (40), n is the distance normal to the hub and shroud surfaces. The justification for this is given in [11, 12].

The swirl schedules used in this study were obtained by first specifying an $\overline{rV_\theta}$ distribution or a distribution of the derivative of $\overline{rV_\theta}$ with respect to the meridional distance s along the hub and shroud. A typical plot of the derivative of $\overline{rV_\theta}$ with respect to meridional distance along the hub is shown in Fig. 1. Away from the leading and trailing edges, the derivative of $\overline{rV_\theta}$ was assumed to vary linearly with s. The main portion of the curve is a straight line with a prescribed slope, and at the leading and trailing edges the required values of $\overline{rV_\theta}$ and its derivatives are obtained by using curves that are quartic or quintic polynomials in s for $\overline{rV_\theta}$ and that are fitted to give an appropriate slope of $\overline{rV_\theta}$ and its derivatives at the points shown as A and B in Fig. 1, along the abscissa (the meridional distance). The value of the derivative of $\overline{rV_\theta}$ at point A is also specified. The area under the curve gives a value of change of $\overline{rV_\theta}$ across the wheel. Additional specifications include the setting of the first derivative of $\overline{rV_\theta}$ at the leading and trailing edges to zero to satisfy boundary conditions (1) and (2) above; in the latter, as noted above the second derivative at these points is also set to zero. At points A and B, the values of $\overline{rV_\theta}$ and its first two derivatives are matched. These specifications are applied both at the hub and the shroud with the additional note that the change in $\overline{rV_\theta}$ across the wheel has to be the same to give constant circulation. In the parametric study to be presented later, an important restriction has been applied in which the maximum derivative of $\overline{rV_\theta}$ with respect to meridional distance must be the same on the hub and the shroud. This is done to minimize the variation in flow parameters between the hub and the shroud in the first portion of the flow path. By altering the value of the slope of the linear portion, the location of A and B, and the values of the derivative of $\overline{rV_\theta}$ at A, a variety of distributions of $\overline{rV_\theta}$ can be obtained. In many instances,

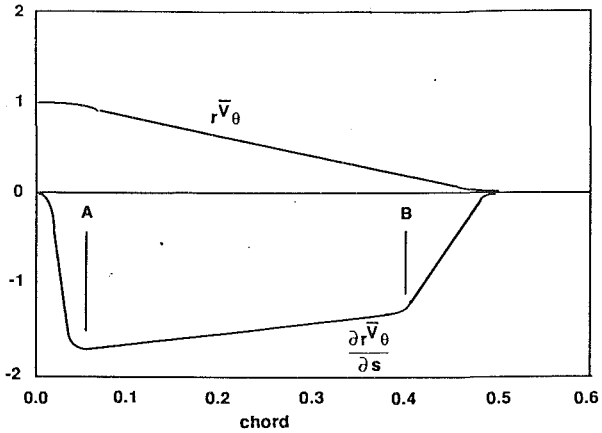

Fig. 1 A typical distribution of $\overline{rV_\theta}$ and $\partial \overline{rV_\theta}/\partial s$ along hub/shroud

the meridional distance to A on the hub and the shroud has been made the same and the value of $\overline{rV_\theta}$ made equal on the hub and the shroud; this latter prescription implies that the loading on the hub and the shroud over the outer portion of the wheel is approximately the same.

The above prescription of the $\overline{rV_\theta}$ along the hub and the shroud provides only a limited class of $\overline{rV_\theta}$ distributions. By varying the parameters within these limits, we obtained some indication of the effects of $\overline{rV_\theta}$ distribution on blade shape, pressure distribution, and other flow parameters, which, as we shall see later, led to some conclusions about $\overline{rV_\theta}$ that may offer useful design approaches.

Having specified the $\overline{rV_\theta}$ distribution along the hub and the shroud, we need to interpolate to obtain the interior values. There are various ways in which this can be done to satisfy boundary conditions (1), (2), and (3) and the required values of $\overline{rV_\theta}$ along the hub and shroud boundaries, as well as the leading and trailing edges. It is possible to use polynomial expressions to specify the distribution along quasi-orthogonal of the hub and the shroud. However, a mathematically more elegant method based on the solution of biharmonic equation

$$\nabla^4(\overline{rV_\theta}) = R(r, z) \tag{41}$$

where

$$\nabla^4 = \left(\frac{\partial^2}{\partial r^2} + \frac{1}{r}\frac{\partial}{\partial r} + \frac{\partial^2}{\partial z^2}\right)^2$$

is used to obtain a smooth continuous distribution of $\overline{rV_\theta}$ within the blade region. The source term $R(r, z)$ can be used as a mean to control/tailor the $\overline{rV_\theta}$ distribution in a desirable way. Here, $R(r, z)$ is set to zero for simplicity.

5 Numerical Results From a Design Study

We now present a sample of results from a parametric design study of a radial inflow turbine; this turbine has been proposed for application to a helicopter power plant [3]. All the results in this paper assume infinitely thin blades, i.e., b = 0. The design specifications for the turbine are: mass flow rate of 2.37 kg/s, power of 1105 kW, inlet stagnation pressure of 1.637×10^6 N/m^2, inlet stagnation temperature of 1607 K, wheel speed 64,000 rpm, rotor tip diameter of 0.2038 m. The absolute flow angle at the inlet is about 75 deg and the corresponding absolute Mach number was computed to be about 0.98. The radial inflow turbine wheel will be designed to yield a blade camber distribution that will result in the complete removal of swirl at the outlet. Thus, the flow will leave the turbine wheel axially at the exit.

With a blade number of 14 and a specified $\overline{rV_\theta}$ distribution of Fig. 2, the three-dimensional inverse design method was

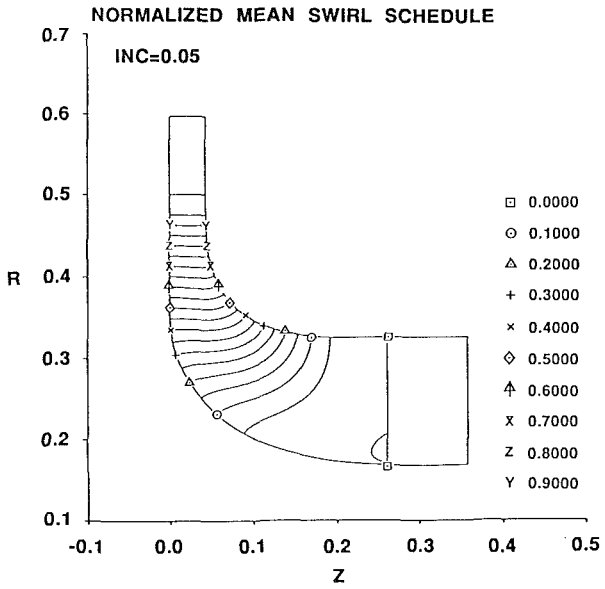

Fig. 2 Specified mean swirl $\overline{rV_\theta}$ for the design calculation

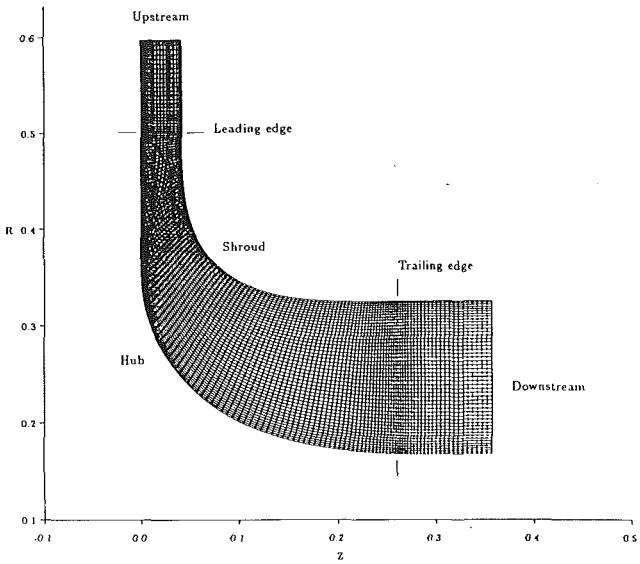

Fig. 3(*a*) Computational mesh on meridional plane

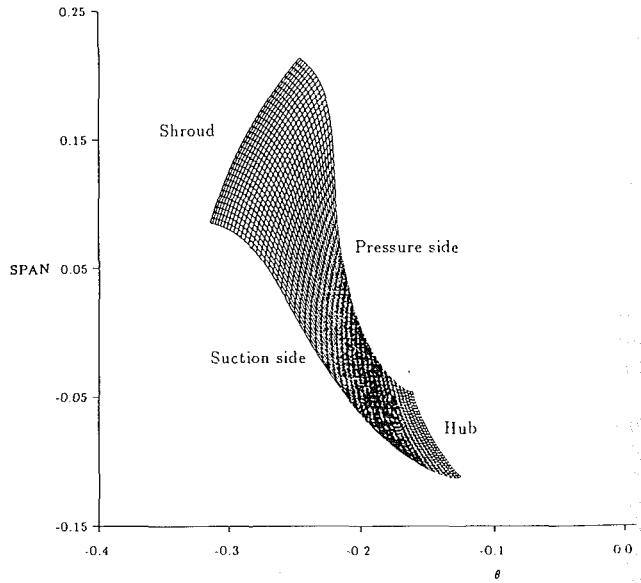

Fig. 3(*b*) Fourier collocation points on blade-to-blade plane

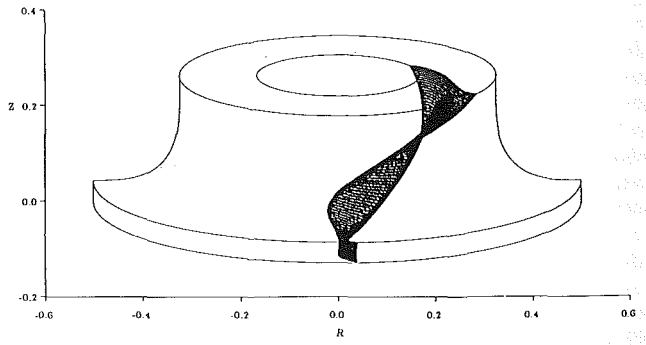

Fig. 4 Blade shape from design calculation with 14 blades and stacking at quarter chord

applied to the determination of the blade shape. The calculation is implemented with a grid resolution of 49 elements spanning the hub-to-shroud region, 33 Fourier collocation points between adjacent blades, and 145 elements extending from inflow to outflow boundary (Fig. 3). With stacking $f = 0$ at the quarter chord position of the wheel, the computed blade shape was obtained and is shown in Fig. 4.

To check the consistency and accuracy of this design calculation with the geometry of the turbine wheel now completely defined, we can proceed to use a standard Euler code to compute the flow in the designed impeller [2]. This computed flow field is then used to determine the swirl and its distribution within the blade region is shown as a contour plot in Fig. 5. Upon comparing the specified swirl in Fig. 2 to the computed swirl in Fig. 5, the agreement is observed to lie within 2 percent of the value at the blade leading edge. Excellent agreements have also been obtained between the computed flow quantities from the present inverse design calculation and those from direct inviscid computations based on the Euler solver.

Having demonstrated the agreement of the computed results from the inverse design code with those from a direct Euler code, we now present results from a parametric design study of the turbine wheel. We examined the influence of the following parameters on the turbine wheel design: (*i*) the loading distribution characterized in terms of $\overline{rV_\theta}$; (*ii*) the stacking position; (*iii*) the specification of f at the stacking position; (*iv*) the hub and shroud profiles; and (*v*) the number of blades.

It has been shown in [11, 4] that the pressure distribution within the blade passage is quite sensitive to variations in the swirl distribution and the stacking specification through its influence on the mean velocity at the blade. As the pressure distribution controls the behavior of the boundary layer and the development of the secondary flow, it is important to understand fully the influence of the swirl distribution on the pressure distribution, and hence the blade loading and the secondary flow.

An examination of the computed results (not shown here) from the design calculations based on the actuator duct approximation for a wide variety of $\overline{rV_\theta}$ distributions and various choices of stacking specifications shows that: (*a*) the specification of a stacking $f = 0$ in the neighborhood of the maximum loading would yield a design with an improved reduced static pressure field and a more reasonable blade wrap angle; and (*b*) the mean tangential velocity distribution should be such that the maximum loading occurs near the leading edge to achieve an improved reduced static pressure field and a smoother blade wrap angle. When the position of maximum loading is chosen to be near the blade trailing edge, the resulting

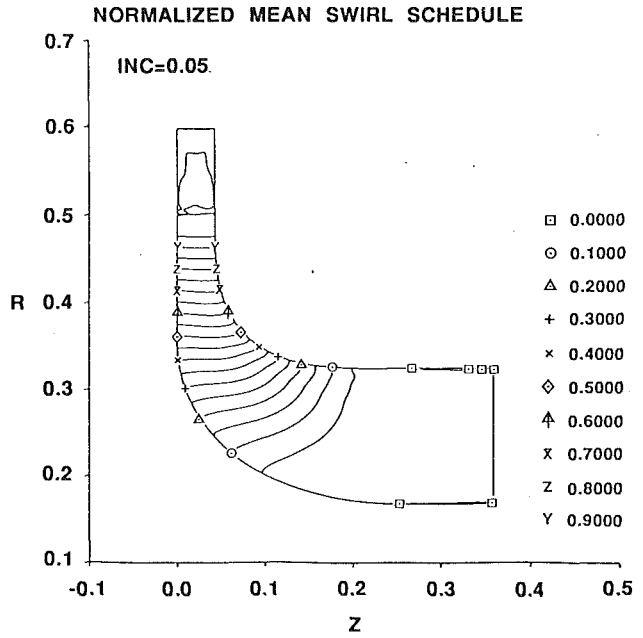

Fig. 5 Computed mean swirl $\overline{rV_\theta}$ from Euler code using geometry of Fig. 4

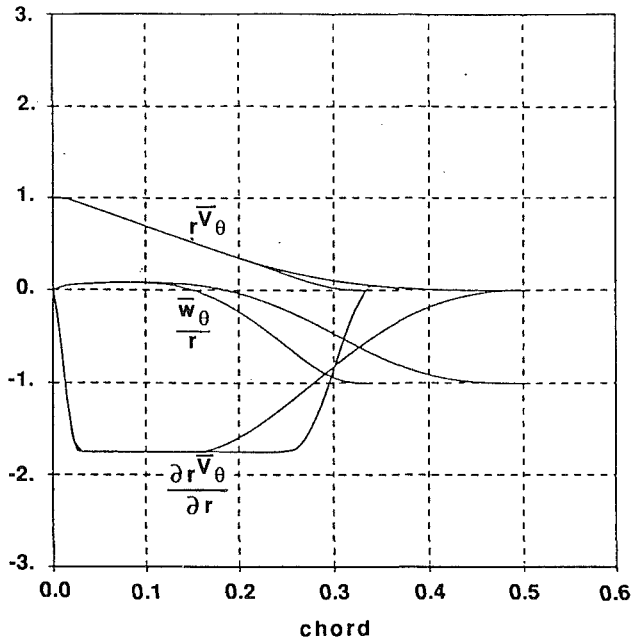

Fig. 6(*a*) Distribution of $\overline{rV_\theta}$, $\overline{W_\theta}/r$, and $\partial \overline{rV_\theta}/\partial s$ along the hub and shroud for flat loading

reduced static pressure distribution is seen to be highly irregular. In these design calculations, when the stacking is specified at a position away from the point of maximum loading, the resulting flow field is such that the mean velocity at the blade can approach zero. This can only result in the formation of a region of strong adverse reduced static pressure gradient in the meridional direction, which is undesirable from the point of view of a well-behaved boundary layer in the blade passage. It is this observation of the computed results based on actuator duct design calculations that leads to the point made in (*a*) above. The point made in (*b*) above has also been examined with the three-dimensional inverse design calculations assuming a blade number of 14. The computed results, shown in Figs. 6 and 7, serve to illustrate the point made in (*b*) above. These two designs have been done with stacking ($f = 0$) at the leading edge. The results in Fig. 6 show that when the mean position of maximum loading is farther away from the leading edge, there is a lack of smoothness in the relative Mach number (denoted by M_{rel}) distribution and hence the reduced static pressure distribution. However, when the point of maximum loading is near the leading edge, the resulting relative Mach number distribution is rather smooth. Upon comparing the computed results of Fig. 7(*c*) with those of Fig. 6(*c*), it is seen that the inviscid region of reverse flow on the pressure side is reduced somewhat.

It was found that the inclusion of three-dimensional effects in the design restricts the choice of the $\overline{rV_\theta}$ distribution and the stacking specifications. The restriction on these choices arises from the failure of the solution to converge, which occurs whenever the magnitude of the reverse velocity on the blade surface (usually the blade pressure surface) becomes so large that the mean velocity at the blade approaches zero.

For the present impeller with 14 blades, the three-dimensional design calculations based on a wide variety of $\overline{rV_\theta}$ distributions and various choices of stacking specifications indicate there always exists a region of reverse flow on the pressure side of the blade. A typical result is shown in Fig. 9 with the $\overline{rV_\theta}$ distribution of Fig. 8; the relative Mach number distribution on the pressure side indicates the regions of reverse flow. Occurrence of reverse flow regions on the blade surface implies the presence of a strong adverse pressure gradient,

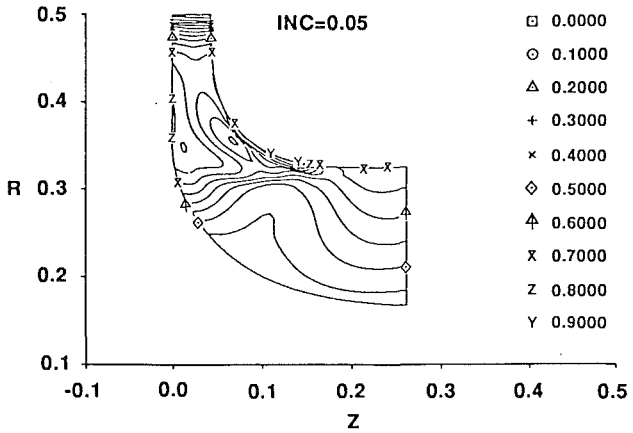

Fig. 6(*b*) M_{rel} on suction surface for flat loading

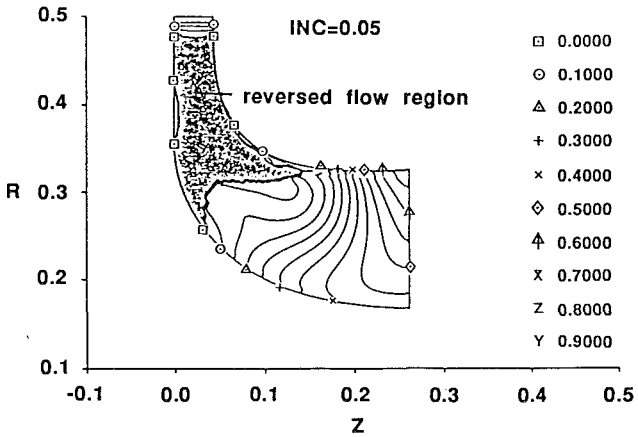

Fig. 6(*c*) M_{rel} on pressure surface for flat loading

which in a viscous flow may result in boundary layer separation. Designs with such a flow feature may not constitute a good design in aerodynamic terms. The presence of a reverse

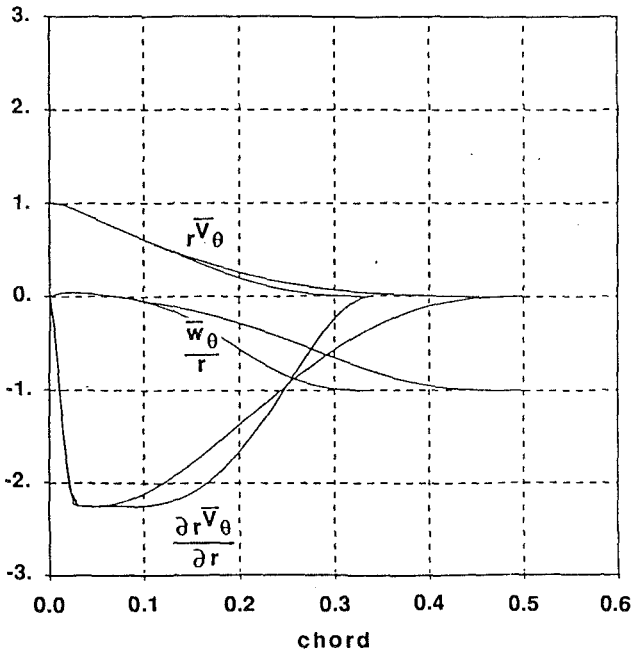

Fig. 7(*a*) Distribution of $\overline{rV_\theta}$, $\overline{W_\theta}/r$, and $\partial\overline{rV_\theta}/\partial s$ along the hub and shroud for triangular loading

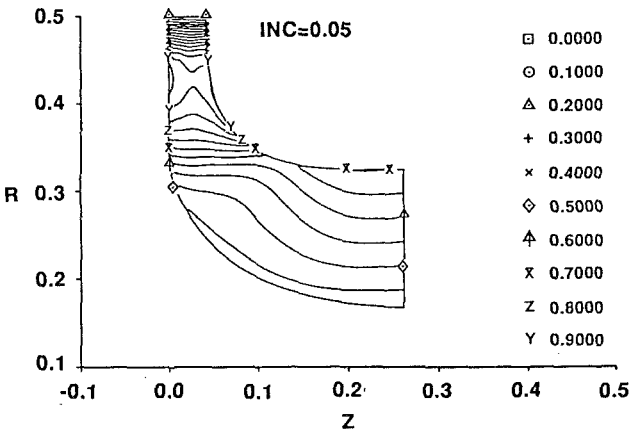

Fig. 7(*b*) M_{rel} on suction surface for triangular loading

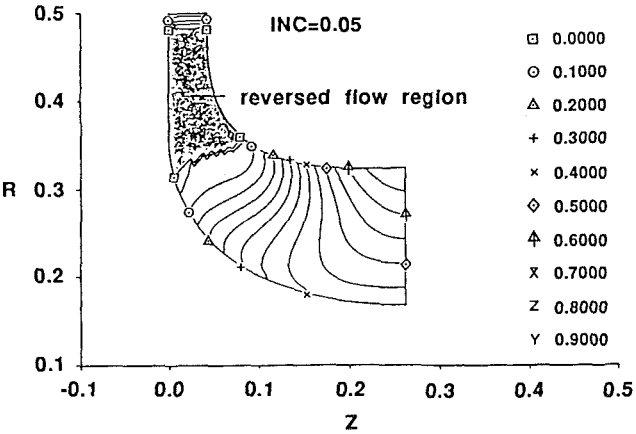

Fig. 7(*c*) M_{rel} on pressure surface for triangular loading

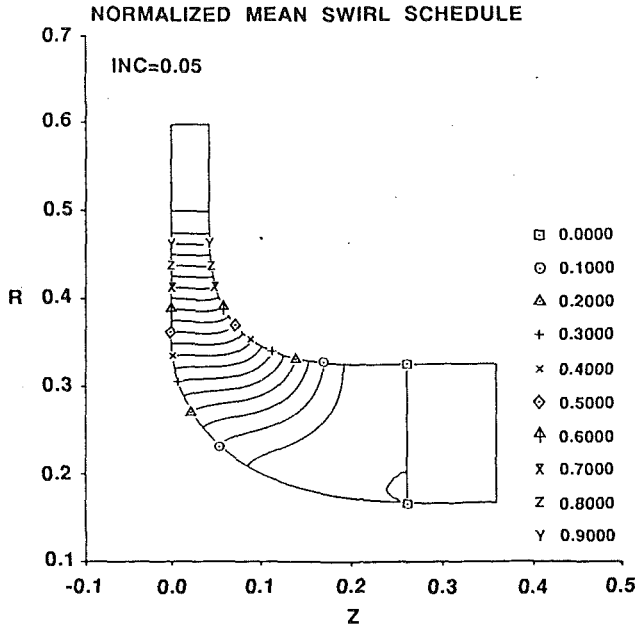

Fig. 8 Distribution of $\overline{rV_\theta}$ for computed results in Figs. 9 and 10

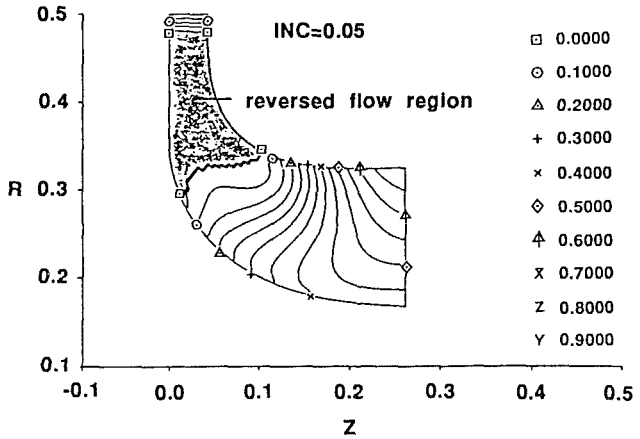

Fig. 9 M_{rel} on pressure surface with 14 blades

flow region on the blade surface of this turbine wheel is not so surprising since it is a very highly loaded radial inflow turbine. The number of blades needed to eliminate the reverse flow region on the blade pressure surface can be obtained as follows: The flow velocity associated with the relative eddy in the impeller passage is approximately $2\pi r\omega/B$ on the pressure surface of the blade and is in a direction opposite to the oncoming flow $\overline{W}_r$; thus the number of blades B needed should be at least equal to or more than $2\pi r\omega/\overline{W}_r$. For the radial inflow turbine considered here, the required blade number is about 21. It is therefore not surprising that when the number of blades is increased to 21, the results of the design calculation show that in most cases the region of reverse flow on the blade surface can be eliminated (Fig. 10). This is to be expected since the aerodynamic loading per blade decreases with an increase in the number of blades.

Another parameter that was examined for its influence on the reduced static pressure distribution of the resulting design is the specification of f at the stacking position. Figure 11 shows three stacking configurations when the stacking position coincides with the tip of the impeller. In position (*a*), $f = 0$; in (*b*) and (*c*) the radial section of the blade camber surface is straight but leaned in and opposite to the direction of rotation. Figure 12 shows the reduced static pressure distribution at the hub, midspan, and shroud sections for the three stacking con-

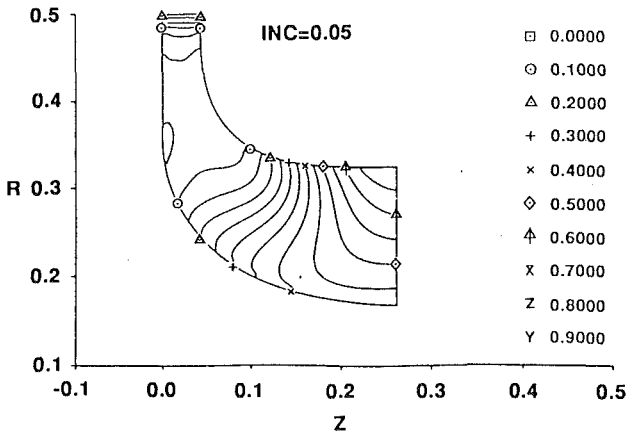

Fig. 10 M_{rel} on pressure surface with 21 blades

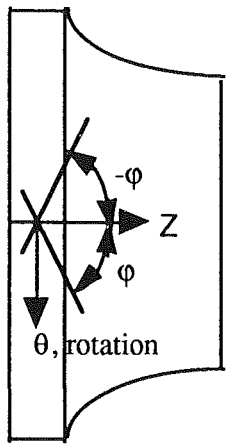

Fig. 11 Definition of lean angle φ

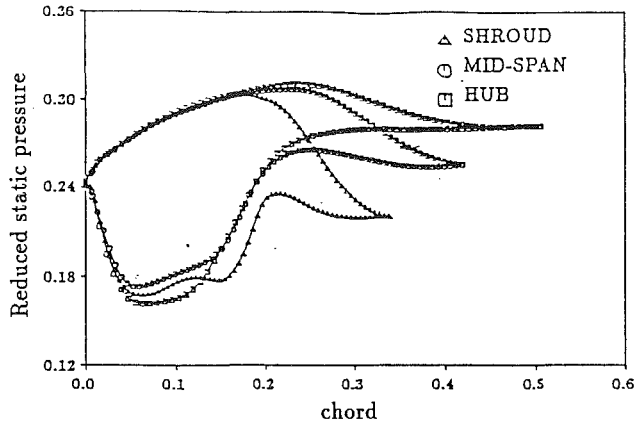

Fig. 12(*a*) Reduced static pressure distribution with lean angle φ = 0 deg

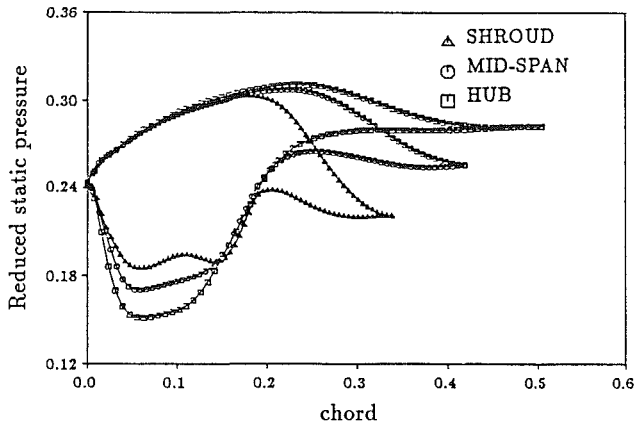

Fig. 12(*b*) Reduced static pressure distribution with lean angle φ = 6.65 deg

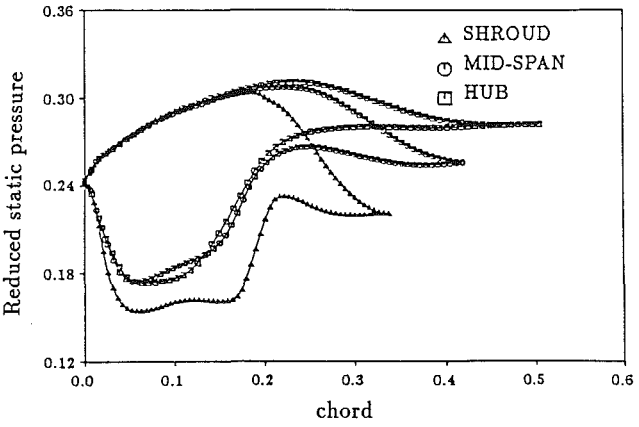

Fig. 12(*c*) Reduced static pressure distribution with lean angle φ = −6.65 deg

figurations shown in Fig. 11, the $\overline{rV_\theta}$ distribution of Fig. 2, the hub and shroud profile of Fig. 3. The results in Fig. 12 show that, with configuration (*b*) in Fig. 11 (leaning in the direction of rotation), the blade loading near the shroud at the tip of the impeller is reduced compared to configuration (*a*), and with configuration (*c*), the region of reduced blade loading is at the hub. The influence of the lean in the stacking axis on the design can be further explained in terms of the equation for the tangential component of the bound vorticity:

$$\Omega_\theta = \frac{\partial r\overline{V}_\theta}{\partial r}\frac{\partial f}{\partial z} - \frac{\partial r\overline{V}_\theta}{\partial z}\frac{\partial f}{\partial r} \tag{42}$$

This equation shows the dependence of the tangential component of bound vorticity on $\overline{rV_\theta}$ distribution and the camber distribution. A nonzero $\partial f/\partial z$ can materially alter the strength of Ω_θ and hence the associated flow field and the reduced static pressure distribution as well. Although the $\overline{rV_\theta}$ distribution is maintained the same for all three stacking configurations, this effect of the Ω_θ change alters the value of $\mathbf{W}_{bl}$ in Eq. (11) and hence the blade loading.

The effect of altering the hub/shroud profile from that shown in Fig. 3 on the pressure distribution within the blade passage was examined next. The hub and shroud profile geometries used for this study are as shown in Fig. 13, which also shows the contours of the $\overline{rV_\theta}$ distribution. In order to obtain a meaningful comparison with the results obtained with the hub/shroud profile of Fig. 3, we assume the same stacking position and, as nearly as possible, the same $\overline{rV_\theta}$ distribution as Fig. 8. The results of the design calculation with the profile of Fig. 3 are shown in Fig. 14 while those with the new profile are shown in Fig. 15. The changes in the blade camber distribution in response to the modification in the hub and shroud profile are shown in Fig. 16. From these results, the sensitivity of the pressure distribution and the blade geometry to a variation in hub/shroud profile is apparent. The blade camber distribution in the tip section for the radial inflow turbine with the modified hub/shroud profile can be seen to differ considerably from that of an impeller with the hub/shroud profile of Fig. 3. Comparing the reduced static pressure distributions shown in

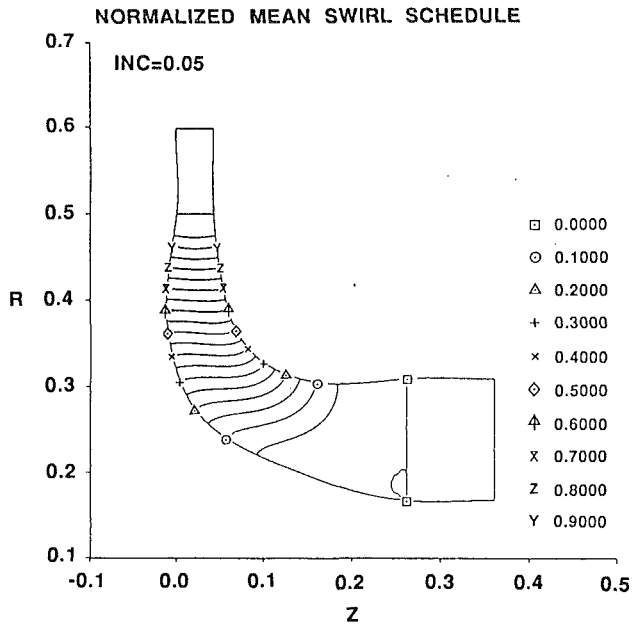

Fig. 13 Distribution of $\overline{rV_\theta}$ for modified hub and shroud profiles

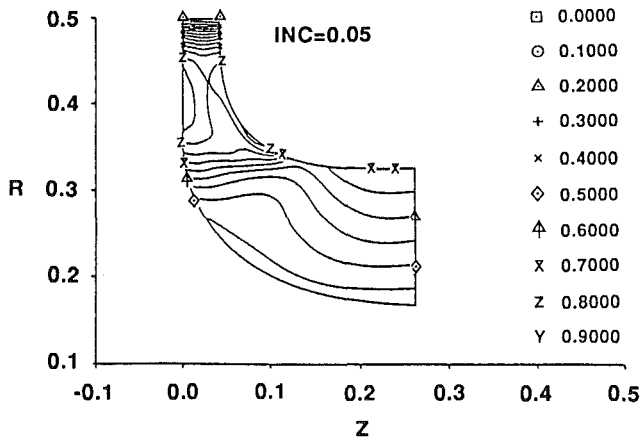

Fig. 14 M_{rel} on suction surface with $\overline{rV_\theta}$ distribution and hub-shroud profile on Fig. 8

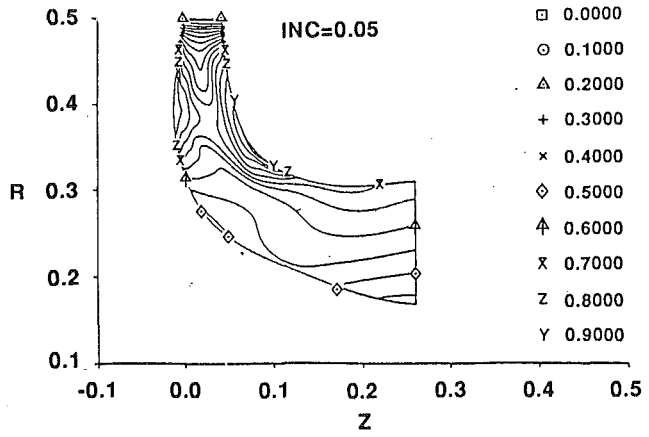

Fig. 15 M_{rel} on suction surface with $\overline{rV_\theta}$ distribution and hub-shroud profile on Fig. 13

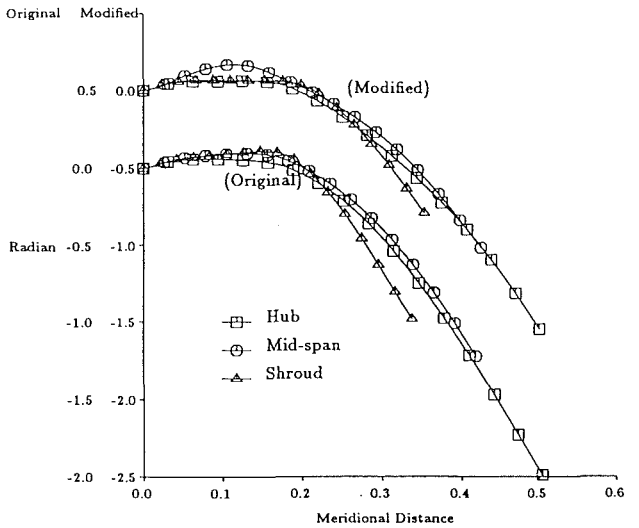

Fig. 16 Blade camber versus meridional distance for original and modified hub-shroud profiles

Figs. 14 and 15, we observed a considerable spanwise pressure gradient in the tip section of the impeller with the modified hub/shroud profile when compared to that with the original hub/shroud profile. This effect can be explained in terms of one of the results of inverse design theory, which shows that the pressure difference across the blade is directly related to the product of the rate of change of $\overline{rV_\theta}$ along the mean streamline at the blade and the mean velocity at the blade. With nearly identical $\overline{rV_\theta}$ distribution in both cases, a change in the hub/shroud profile could have a strong influence on the magnitude and distribution of the mean blade velocity, with a resulting change in pressure distribution. This effect is not unlike that which we have observed when a change is made in the choice of stacking position. The modification of the hub and shroud profiles did not affect the extent of the reverse flow region on the pressure surface of the blade. It did, however, limit the range over which the stacking position could be varied without failure to converge. We have already noted that, with 14 blades, this turbine rotor is too heavily loaded to avoid reverse flow on the pressure surface. To reduce this high loading level, we can: (*i*) increase the number of blades (splitter blade could be used to avoid choking at the exducer); (*ii*) reduce the tip speed and the pressure ratio; (*iii*) reduce the inlet swirl; (*iv*) increase the outlet swirl; and (*v*) increase the radial velocity at the tip through alteration of the hub/shroud profile in the tip section. Note that all but (*i*) and (*v*) will result in the reduction of work output.

Finally, we present results from a three-dimensional viscous analysis of the flow through the designed radial inflow turbine wheel with 14 blades and with a specified $\overline{rV_\theta}$ distribution, as shown in Fig. 2. As we have seen in the above, computed values for this radial inflow turbine wheel from inverse design calculations (based on a wide variety of $\overline{rV_\theta}$ distribution and various choices of stacking specifications) indicate that there exists an inviscid region of reverse flow on the pressure side of the blade. Because of the inviscid assumption in the present inverse design technique, there is thus a need to address the issues of boundary layer behavior and secondary flow formation in the designed turbine wheel. This can be done through the use of a Navier–Stokes solver to analyze the flow in the blade passage [6]. The results from this viscous analysis indicate the existence of reverse flow on the pressure side of the blade and the absence of flow breakdown within the blade passage. Furthermore the computed values of swirl distribution (shown in Fig. 17) and reduced static pressure distribution (not shown) from the Navier–Stokes calculation agree fairly well with those from the inverse design calculation (except for values at the

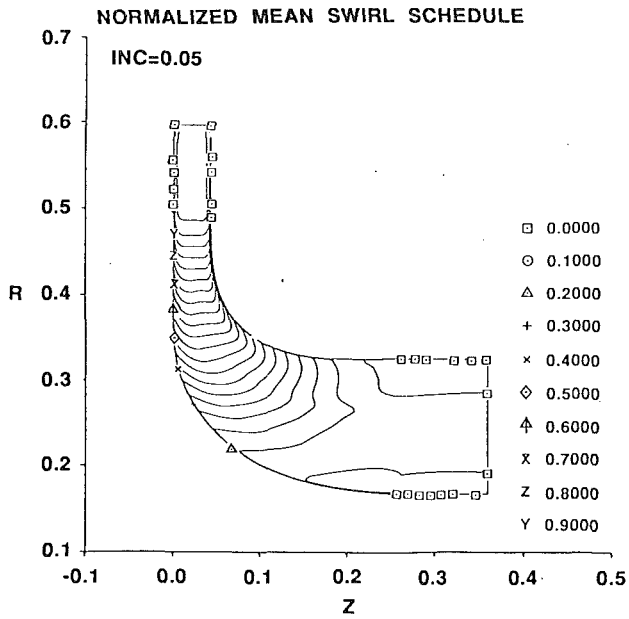

Fig. 17 Computed mean swirl $\overline{rV_\theta}$ from Navier-Stokes code using geometry in Fig. 4

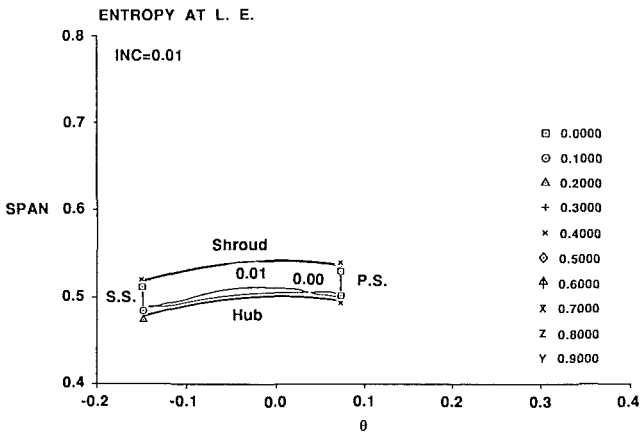

Fig. 18(*a*) Distribution of entropy on leading edge plane

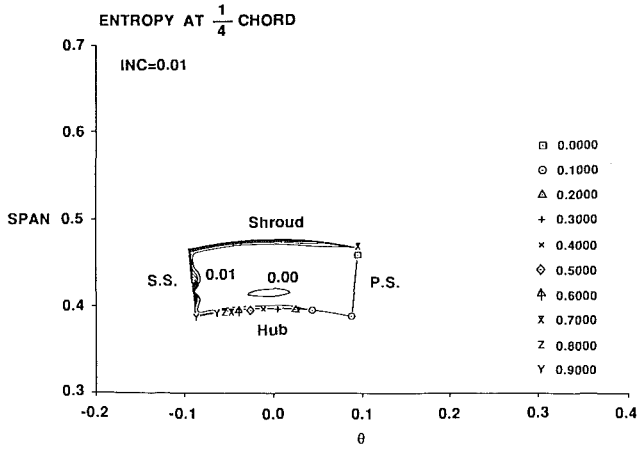

Fig. 18(*b*) Distribution of entropy on quarter chord plane

wheel exit and at the solid surfaces along the hub and shroud). These results are rather surprising for, as we noted above, we anticipated a different flow behavior due to the observation

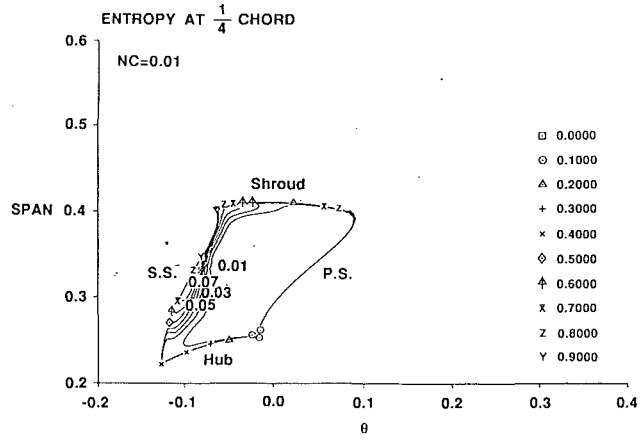

Fig. 18(*c*) Distribution of entropy on half-chord plane

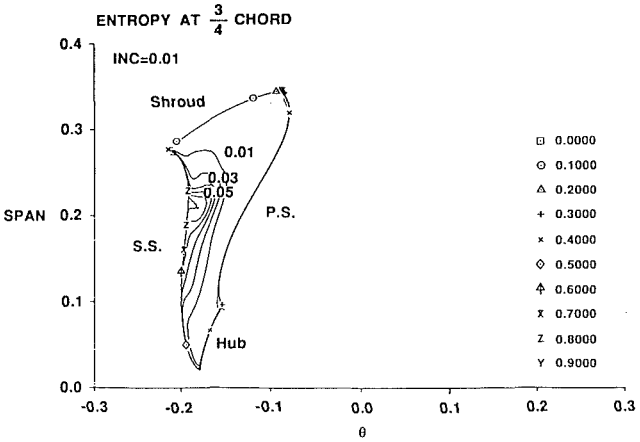

Fig. 18(*d*) Distribution of entropy on three-quarter chord plane

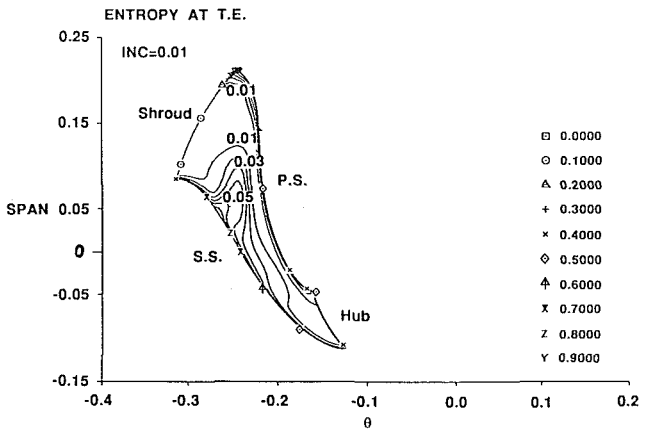

Fig. 18(*e*) Distribution of entropy on trailing edge plane

of the presence of an inviscid region of reverse flow on the pressure surface of the blade. The viscous calculations indicate that the region of reverse flow does not necessarily lead to flow breakdown and substantial losses as feared in the above. To sum up, we deduce that the specified swirl distribution leads to a designed turbine rotor for which the flow field of a real fluid will closely approximate that of an inviscid one.

The evolution of viscous layers on the solid surfaces within the blade passage from the leading edge plane to the trailing edge plane is shown as a region of increased entropy in Fig. 18. The pressure distribution in the blade passage acts to trans-

port the low-momentum fluid within the viscous layer to the suction side of the blade; at the trailing edge plane, this low-momentum fluid appears to collect in the lower corner on the suction side of the blade passage, forming a wake-like region. This observation agrees qualitatively with that of [15].

6 Summary and Conclusions

In this paper, we have shown again how the new approach can be used to design turbomachinery blading in three-dimensional flow. The computed results illustrate the use of the technique to implement design studies in which one can isolate the influence of each design parameter, for example stacking position, loading distribution, lean in stacking axis, and hub and shroud profile geometry. Further, excellent agreement was obtained between the prescribed $\overline{rV_\theta}$ distribution and that obtained from a direct Euler calculation of the flow through the designed rotor. This serves to establish the correspondence and consistency between a technique that computes the blade geometry from a specified aerodynamic loading (i.e., the inverse problem) and one that computes the flow from a specified blade geometry (i.e., the direct problem).

A three-dimensional viscous computation program can also be used to analyze the flow in the rotor designed using the present technique; this allows one to assess the extent of the viscous effects (e.g., boundary behavior and formation of secondary flow). In the cases that we have analyzed with the Navier–Stokes solver, the viscous effects do not appear to distort the prescribed $\overline{rV_\theta}$ distribution materially, even with a strong reverse flow over part of the blade surface. This implies that the presence of an inviscid region of reverse flow does not necessarily lead to flow breakdown and substantial losses when we allow for real fluid effects. Such observations lead us to deduce that it is not unrealistic to use an inviscid design program coupled with a viscous direct calculation for flow analysis to establish guidelines and criteria for designing turbomachinery blading in three-dimensional flow.

Acknowledgments

Support for this research work was provided by the Army Propulstion Directorate Grant No. NAG3-772, Mr. Pete Meitner, Technical Officer, and by Cummins Engine Co., Dr. H. Weber, Technical Monitor.

References

1 Borges, J. E., "Three-Dimensional Design of Turbomachinery," PhD Dissertation, Cambridge Univ., Cambridge, United Kingdom, Sept. 1986.

2 Celestina, M. L., Mulac, R. A., and Adamczyk, J. J., "A Numerical Simulation of the Inviscid Flow Through a Counterrotating Propeller," ASME JOURNAL OF TURBOMACHINERY, Vol. 108, 1986, pp. 187–193.

3 Civinskas, K. C., and Povinelli, L. A., "Application of a Quasi-Three-Dimensional Inviscid Flow and Boundary Layer Analysis to the Hub-Shroud Contouring of a Radial Turbine," Paper No. AIAA-84-1297, 1984.

4 Ghaly, W. S., "A Study and Design of Radial Turbomachinery Blading in Three-Dimensional Flow," Ph.D. Thesis, Department of Aero. and Astro., MIT, Cambridge, MA, Sept. 1986.

5 Hawthorne, W. R., and Tan, C. S., "Design of Turbomachinery Blading in 3-D Flow by the Circulation Method: A Progress Report," ICIDES-II, 1987, pp. 207–226.

6 Heidmann, J. D., and Beach, T. A., "An Analysis of the Viscous Flow Through a Compact Radial Flow Turbine by the Average Passage Approach," NASA TM 102471, 1990.

7 Kerwin, J. E., "Marine Propellers," *Annual Review of Fluid Mechanics*, Vol. 18, 1986.

8 Lamb, H., *Hydrodynamics*, 6th ed., Dover Publications, New York, 1932.

9 Lighthill, M. J., *Fourier Analysis and Generalized Functions*, Cambridge University Press, Cambridge, United Kingdom, 1958.

10 Smith, L. H., "Unducted Fan Aerodynamic Design," ASME JOURNAL OF TURBOMACHINERY, Vol. 109, 1987, pp. 313–324.

11 Tan, C. S., Hawthorne, W. R., McCune, J. E., and Wang, C., "Theory of Blade Design for Large Deflections," ASME *Journal of Engineering for Gas Turbines and Power*, Vol. 106, 1984, pp. 354–365.

12 Tan, C. S., "Vorticity Modeling of Blade Wakes Behind Isolated Annular Blade-Rows: Induced Disturbances in Swirling Flows," ASME *Journal of Engineering for Power*, Vol. 103, 1981, pp. 279–287.

13 Theodorsen, T., *Theory of Propellers*, McGraw-Hill, New York, 1948; University Press, 1959.

14 Yang, Y. L., "A Design Study of Radial Inflow Turbines in Three-Dimensional Flow," PhD Thesis, Department of Aero. and Astro., MIT, Cambridge, MA, 1991.

15 Zangeneh-Kazemi, M., "Three-Dimensional Design of Radial Inflow Turbines," PhD Thesis, Cambridge University, Cambridge, United Kingdom, 1988.

APPENDIX

The effect of blade thickness can be approximated by using a blockage distribution $b(r, z)$. As we assume that the flow field extends from the blade camber line so that the velocity, $\mathbf{W}$, and density, ρ, in the blade passage are extended to fill the entire space between camber lines, the continuity equation in the form

$$\nabla \cdot \rho \mathbf{W} = 0 \tag{A1}$$

will give too large a mass flow.

This may be seen from the relation

$$dm = \int_{\frac{\tau}{2}}^{\frac{2\pi}{B}-\frac{\tau}{2}} \rho \mathbf{W} \cdot \mathbf{n} d\theta \tag{A2}$$

where dm is the specific mass per blade pitch, $\mathbf{n}$ is the unit vector normal to the cross section across which the mass flow is determined, and τ is the angular thickness of the blade. It is therefore evident that

$$dm \le \int_0^{\frac{2\pi}{B}} \rho \mathbf{W} \cdot \mathbf{n} d\theta = \frac{2\pi}{B} \overline{\rho \mathbf{W}} \cdot \mathbf{n} \tag{A3}$$

We may approximate Eq. (A2) by writing

$$dm = \left(\frac{2\pi}{B} - \tau\right) \overline{\rho \mathbf{W}} \tag{A4}$$

and define

$$b = 1 - \frac{B\tau}{2\pi} \tag{A5}$$

as the blockage factor.

We may extend the blockage concept by assuming that each elementary volume of space between the camber lines has to be shrunk by a factor of b to represent the real volume in the blade passage, allowing us to write the dilation as

$$\nabla \cdot b\rho \mathbf{W} = 0 \tag{A6}$$

so that

$$\nabla \cdot \rho \mathbf{W} = -\rho \mathbf{W} \cdot \nabla \ln b \tag{A7}$$

Or

$$\nabla \cdot \mathbf{W} = -\mathbf{W} \cdot \nabla \ln \rho - \mathbf{W} \cdot \nabla \ln b \tag{A8}$$

$$\nabla \cdot \mathbf{W} = -\overline{\mathbf{W} \cdot \nabla \ln \rho} - \overline{\mathbf{W} \cdot \nabla \ln b} \tag{A9}$$

and subtracting

$$\nabla \cdot \tilde{\mathbf{V}} = \overline{\mathbf{W} \cdot \nabla \ln(\rho)} - \mathbf{W} \cdot \nabla \ln(\rho) - \tilde{\mathbf{V}} \cdot \nabla \ln b \tag{A10}$$

We might alternatively, as in thin airfoil theory, represent the thickness by a distribution of sources and sinks along the camber lines or surfaces of the blades, i.e., write

$$\nabla \cdot \rho \mathbf{W} = \mathrm{M}(r, z) \delta_p(\alpha) \tag{A11}$$

so that

$$\nabla \cdot \overline{\rho \mathbf{W}} = \mathrm{M} \tag{A12}$$

and comparing Eqs. (A7) and (A12)

$$\mathrm{M} = -\overline{\rho \mathbf{W}} \cdot \nabla \ln b = \frac{\overline{\rho \mathbf{W}} \cdot \left(\nabla \frac{B\tau}{2\pi}\right)}{b} \tag{A13}$$

which is to be compared with the relationship for the source

strength representing the thickness, t, of an isolated airfoil in two dimensions, i.e.,

$$\mathrm{M}(x) = \rho U_\infty \frac{dt}{dx} \tag{A14}$$

where U_∞ is the approaching velocity and x the axial coordinate.

Equation (A11) may also be written

$$\nabla \cdot \mathbf{W} = -\mathbf{W} \cdot \nabla \ln\rho + Q(r, z)\delta_p(\alpha) \tag{A15}$$

with a pitchwise mean value

$$\nabla \cdot \overline{\mathbf{W}} = -\overline{\mathbf{W} \cdot \nabla \ln\rho} + Q(r, z) \tag{A16}$$

where

$$Q(r, z) = \frac{\mathrm{M}}{\rho_{bl}} \tag{A17}$$

and comparing Eqs. (A16) and (A9)

$$Q(r, z) = -\overline{\mathbf{W}} \cdot \nabla \ln b \tag{A18}$$

Subtracting Eq. (A16) from Eq. (A15) we obtain

$$\nabla \cdot \tilde{\mathbf{V}} = \overline{\mathbf{W} \cdot \nabla \ln(\rho)} - \mathbf{W} \cdot \nabla \ln(\rho) + Q(r, z)\,(\delta_p(\alpha) - 1) \tag{A19}$$

which, on comparing Eq. (A19) with Eq. (A11), gives

$$Q(r, z)\,(\delta_p(\alpha) - 1) = -\mathbf{V} \cdot \nabla \ln b \tag{A20}$$

and substituting Eq. (A18)

$$(\delta_p(\alpha) - 1)\overline{\mathbf{W}} \cdot \nabla \ln b = \tilde{\mathbf{V}} \cdot \nabla \ln b \tag{A21}$$

Both sides of this equation are periodic in θ, but their form is not the same. The left-hand side is in fact the derivative of a sawtooth function and the right-hand side is approximately a sawtooth function. The use of the blockage in Eq. (A6) then can only approximately represent the blade thickness effect and will include the effect of sources and sinks distributed throughout the flow.

J. L. Boynton

R. Tabibzadeh

Rocketdyne Division,
Rockwell International Corporation,
Canoga Park, CA 91303

S. T. Hudson
NASA-Marshall Space Flight Center,
Huntsville, AL 35812

Investigation of Rotor Blade Roughness Effects on Turbine Performance

The cold air test program was completed on the SSME (Space Shuttle Main Engine) HPFTP (High-Pressure Fuel Turbopump) turbine with production nozzle vane rings and polished coated rotor blades with a smooth surface finish of 30 μin. (0.76 μm) rms (root mean square). The smooth blades were polished by an abrasive flow machining process. The test results were compared with the air test results from production rough-coated rotor blades with a surface finish of up to 400 μin. (10.16 μm) rms. Turbine efficiency was higher for the smooth blades over the entire range tested. Efficiency increased 2.1 percentage points at the SSME 104 percent RPL (Rated Power Level) conditions. This efficiency improvement could reduce the SSME HPFTP turbine inlet temperature by 57 R (32 K), increasing turbine durability. The turbine flow parameter increased and the midspan outlet swirl angle became more axial with the smooth rotor blades.

Introduction

The SSME HPFTP consists of a high-pressure hydrogen pump driven by a subsonic, axial flow, two-stage, reaction turbine. This low pressure ratio turbine is driven by fuel-rich oxygen–hydrogen combustion products consisting of steam and gaseous hydrogen. The turbine produces approximately 73,000 hp (54.6 mw) although the blade tip diameter is only 11 in. (28 cm). Near its design point the turbine inlet temperature and pressure are about 1900 R (1055 K) and 5200 psia (35.9 MPa), respectively. At these extreme operating conditions accurate turbine performance measurement is difficult. Therefore, there was a need to determine experimentally the efficiency and flow characteristics of the SSME HPFTP turbine at design and off-design points. To meet this need a "cold" flow test program was established at the National Aeronautics and Space Administration's Marshall Space Flight Center (MSFC) in Huntsville, AL. This program involves using model measurements and scaled performance parameters to establish the performance characteristics of the turbine. The testing of the baseline turbine with production rough-coated turbine rotor blades was reported by Hudson et al. (1991). Other rough coated rotor blades were polished to a smooth surface finish and installed in the turbine and tested. The polishing process, the profile changes, the performance test results, and the comparison of the smooth blades with the rough blades are the subjects of this paper.

1 Blade Polishing by Abrasive Flow Machining Process

The rough plasma-sprayed NiCrA1Y coating on the SSME HPFTP turbine first and second rotor blades prevents airfoil cracks during the severe engine start transient. The rough-coated blades were polished by Dynetics Corporation of Woburn, MA, using abrasive flow machining. Abrasive flow machining was done by moving an abrasive laden compound back and forth across the blade airfoil surface parallel to the gas flow under high pressure. Figure 1 shows a comparison of the rough plasma spray coated blades, both suction and pressure surfaces, and the polished coated blades from an earlier pol-

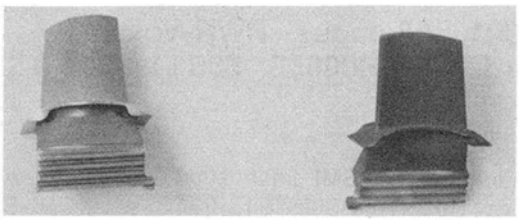

A. Plasma Spray Coating, Unpolished, Surface Finish 250–500 RA

B. Coating After Surface Polished, Surface Finish 20–40 RA

Fig. 1 Polished turbine blades: SSME HPFTP first stage

Contributed by the International Gas Turbine Institute and presented at the 37th International Gas Turbine and Aeroengine Congress and Exposition, Cologne, Germany, June 1–4, 1992. Manuscript received by the International Gas Turbine Institute February 28, 1992. Paper No. 92-GT-297. Associate Technical Editor: L. S. Langston.

ishing feasibility study program completed by Rocketdyne Materials Engineering and Technology group. The shiny polished blades were tested in this program. The airfoil and platform surfaces were polished to a surface finish of 30 μin. (0.76 μm) rms. The abrasive flow medium was a polymer compound laden with silicon carbide abrasive.

Figure 2 shows representative tip profile coordinate measurements of a coated blade profile before and after abrasive flow machining polishing as well as the nominal as-cast profile shape before coating. This figure is representative of the rough coating thickness and the polished coating thickness from diffracto measurements of six rotor blades, three first-stage and three second-stage, at hub and tip sections. Similar material removal occurred on both surfaces during polishing. The thickness measurements are summarized in Table 1 for near the leading and trailing edges and near the mid-chord. The measurements indicated the pressure surface coating was slightly thicker than drawing requirements at 0.008 in. (0.203 mm) before polishing, and suction surface coating was slightly thinner than required at 0.004 in. (0.102 mm). The coating thickness (before polishing) reduced the throat opening by 6.1 and 5.1 percent for the first and second rotor blades, respectively. The polishing, then, increased the throat opening from the coated values by 4.0 and 3.3 percent, respectively. The coated trailing edge thickness increased from the nominal 0.020 in. (0.51 mm) as-cast to 0.033 in. (0.84 mm). Polishing reduced the trailing edge thickness to 0.027 in. (0.69 mm). The average first and second rotor mean trailing edge blockages for nominal, rough-coated, and polished coated were 8, 13, and 11 percent, respectively (percent of trailing edge thickness to the sum of the throat opening and the trailing edge thickness).

2 Efficiency Prediction for Smooth Blades

Turbine efficiency correlations with surface roughness have been included in turbine performance prediction programs in the literature. These were developed for relatively lower Reynolds number applications and tend to predict greater changes than might occur in rocket turbines. The Craig and Cox method (1970–71) predicted an efficiency improvement of 3.4 percent for the smooth blades. An in-house method based on the Moody Friction Factor curve, relative roughness, the passage hydraulic diameter, outlet Reynolds number, trailing edge thickness, and fluid conditions predicted an efficiency improvement of 2.7 percent. The pretest prediction was a conservative average of the two methods at 3.0 percent (2.6 percentage points). This predicted efficiency improvement was applied to the rough blade air test results to predict the performance of the polished coated (smooth) rotor blades. At 104 percent RPL equivalent conditions, the predicted efficiency for the smooth blades increased from 85.79 percent to 88.36 percent. The 2.6 percentage-point increase in efficiency would reduce the turbine inlet temperature in the SSME by 69 R (38 K) increasing turbine reliability.

The Craig and Cox method indicated that the primary efficiency variable was surface finish at the high Reynolds numbers. Changes in throat area and trailing edge thickness had a small effect on efficiency (about 0.2 percentage points).

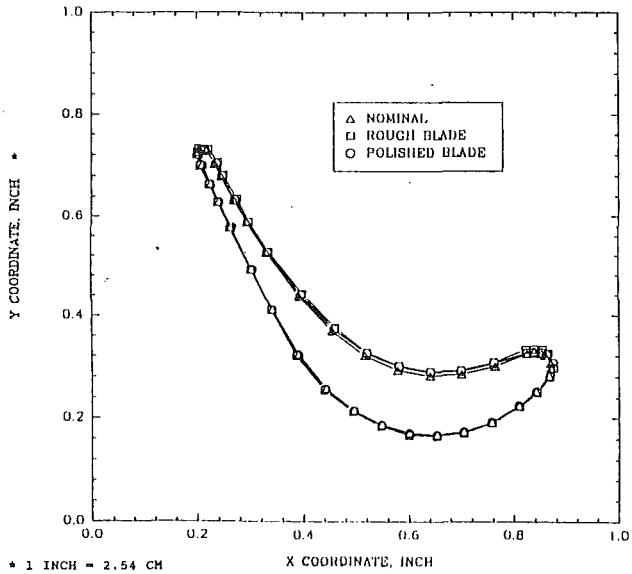

Fig. 2 Smooth coated turbine test blade coordinates before and after polishing

Table 1 SSME HPFTP turbine: rotor blade thickness and removal with polishing

	Measurements (mm)		
	Coating Thickness From *Nominal*	Polishing Removal of Coating	Remaining Coating
Suction Surface:			
Near leading edge	+0.102	-0.076	+0.025
Near mid-chord	+0.152	-0.102	+0.051
Near trailing edge	+0.102	-0.076	+0.025
Pressure Surface:			
Near leading edge	+0.203	-0.051	+0.152
Near mid-chord	+0.203	-0.102	+0.102
Near trailing edge	+0.178	-0.102	+0.076

The measured profile data indicated a 3.6 percent average increase in rotor area due to polishing the blades. A 3.0 percent increase in flow parameter was predicted at the 104 percent RPL equivalent condition.

3 NASA/MSFC Air Flow Turbine Test Facility

The test program was conducted in the NASA-Marshall Space Flight Center (MSFC) air flow Turbine Test Equipment (TTE) in Huntsville, AL. A schematic of the TTE is shown in Fig. 3. The TTE is a blowdown facility that operates by expanding high-pressure dry air from one or two 6000 cubic feet (170 cubic meters) tanks at 420 psig (2,896 kPa) to atmospheric

Nomenclature

U/Co = mean overall isentropic velocity ratio, T-T
U = mean blade speed
Co = overall isentropic velocity, total-to-total
EFF T-T = total-to-total efficiency
PTIN, PI = turbine inlet absolute total pressure
TTIN, TI = turbine inlet absolute total temperature
W = turbine inlet mass flow rate
PRT-T = turbine overall total-to-total pressure ratio
N = shaft rotational speed
RE AVG = average of Reynolds numbers at first stator mean outlet and second rotor mean outlet based on actual chord, blade row outlet velocity, and outlet density

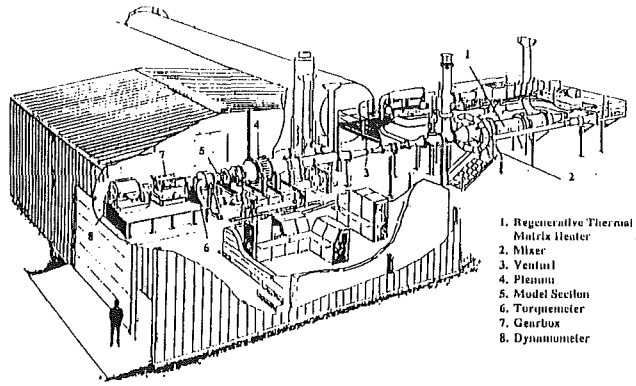

Fig. 3 Schematic of TTE

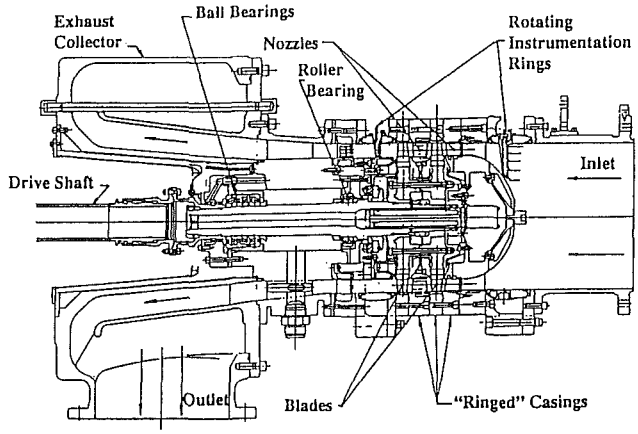

Fig. 4 Cross section of TTA

pressure. Air flows through a heater section, quiet trim control valve, calibrated subsonic venturi, and into a plenum section. The air passes through the test model and exhausts to atmosphere. Air can be delivered to the test model at 220 psia (1517 Pa) for run times to over five minutes. The heater controls tester inlet temperatures between 530 R (294 K) and 830 R (461 K). The TTE has manual set point closed-loop control of the model inlet total pressure, inlet total temperature, shaft speed, and pressure ratio. The facility accurately measures air mass flow rate, shaft torque, and horsepower. The facility measures up to 400 pressures, 120 temperatures, and various health monitoring variables. A more detailed facility description is given by Carter (1991).

4 Model Description

The model tested was a full-scale model of the SSME HPFTP turbine in the baseline configuration as shown in Fig. 4 except for the polished coated (smooth) rotor blades in both stages. The turbine design data for the SSME is shown in Table 2. The hot blade path data are listed in Table 3. The mean diameter of the air test turbine blading was constant at 10.069 in. (25.58 cm). The inlet dome and struts, nozzle rings, and rotor blades accurately duplicated the gas path geometry of the two-stage SSME HPFTP reaction turbine. The nozzle rings were production hardware. The model disks were designed to provide blade path alignment at the near-ambient test conditions of the nozzle vane and rotor blade hub and tip endwalls. The rotor blades were also production hardware, except that the airfoils and hub platforms had been polished smooth to a 30 μin. rms surface finish. The model inlet flow enters axially with zero swirl. The exit vanes were located downstream of the outlet instrumentation measuring at the second rotor outlet.

Table 2 SSME HPFTP turbine design data (104 percent rated thrust)

Power	MW	48.800
Speed	rpm	35,131
Flow rate	kg/sec	70.3
Inlet total pressure	MPa	35.76
Inlet total temperature	K	1018
Pressure ratio total-to-total	-	1.462
Overall velocity ratio	-	0.367
Mean diameter	cm	25.88
Stage work split	%	55/45
Stage mean reaction (1)	%	39/39
Reynolds number average	-	1.1 x 10E7

(1) Mean stage reaction defined as static pressure drop across rotor divided by static pressure drop across stage

Table 3 SSME HPFTP turbine blade path data: hot

Stage	1	1	2	2
Blade row	Nozzle	Rotor	Nozzle	Rotor
Blade number	41	63	39	59
Mean diameter (cm)	25.88	25.88	25.88	25.88
Blade height (cm)	2.25	2.25	2.50	2.50
Mean width (cm)	2.66	1.87	2.66	1.95
Tip clearance (mm) (1)	-	0.48	-	0.41
Axial space (cm)	0.89	0.97	0.91	
Mean inlet flow angle (deg A) (2)	0.00	38.21	-24.59	33.42
Mean outlet flow angle (deg A) (2)	66.75	63.04	66.17	-60.46
Mean outlet velocity (3) (m/sec)	779	693	730	625
Mean outlet mach number (3)	0.44	0.40	0.42	0.37
Surface finish, maximum micrometer RMS:				
Production	1.60	10.16	1.60	10.16
Polished	1.60	0.76	1.60	0.76
Trailing edge thickness (mm):				
Production	0.51	0.84	0.51	0.84
Polished	0.51	0.69	0.51	0.69

(1) Average radial tip clearance
(2) Angles in degrees from axial, positive in direction of rotor rotation
(3) Relative to blade row at 104% rated thrust

The SSME HPFTP turbine outlet circumferential pressure gradient resulting from the nonsymmetric rocket engine hot gas manifold was not simulated to get basic blading performance. The model exhausted into an axial annulus, which led to a collector. The collector diffused the flow and directed it radially downward into the exhaust system with no circumferential pressure gradient at the tester outlet. The rotor blade tip seal and platform seals were set at the engine nominal clearances. The blade shank coolant passages were sealed and the disk coolant flows were not simulated to evaluate the basic uncooled turbine blading performance.

5 Instrumentation

The turbine model was instrumented to measure aerothermodynamic performance and monitor model health to ensure safe operation. Figure 5 shows the model instrumentation. The turbine inlet and outlet plane conditions were measured by instrumented rings, which could be rotated 90 deg around the model centerline. Each ring contained four total pressure and four total temperature rakes with five radial kiel-head probes located in the centers of equal areas. The fixed inlet probes were axial and pitched to align with the flow around the inlet dome. The axial outlet rake probes are manually adjustable for swirl. Two auto-nulling, radial traversing cobra probes were mounted on each instrumentation ring 180 deg apart. The cobra probes measure total pressure, total temperature, and flow angle.

The model included static pressure measurements at six axial locations as shown in Fig. 5 at both the hub and the tip, with

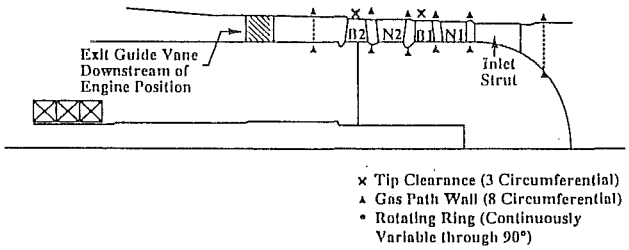

Fig. 5 Phase IA instrumentation

Table 4 Phase 1A test matrix

Test Part	Objective	Set Point Conditions
A	Determine 104 and 65% RPL performance, assess Reynolds number effects, and survey exit flow field	TTIN = 550 R (306 K) PTIN = 27, 35, 50,75, 100, 125, 150, 175, 200 psia (186, 241, 345, 517, 689, 862, 1,034, 1,207, 1,379 KPa)
B	Map 65 to 109% RPL performance and survey turbine exit flow field	TTIN = 550 R (306 K) PTIN = 100 psia (689 KPa) PR = 1.30, 1.35, 1.40, 1.45, 1.463, 1.50 N = 5,000, 5,500, 6,000, 6,500, 7,000, 7,500 rpm
C	Map startup and extreme off-design performance	TTIN = 550 R (306 K) PTIN = 100 psia (689 KPa) PR = 1.20, 1.30, 1.40, 1.50, 1.60 N = 2,000, 4,000, 5,000, 6,000, 7,000, 8,0000 10,000 rpm

Table 5 NASA/MSFC air tests: SSME HPFTP turbine; 104 percent RPL equivalent conditions

Rotor Blades		Rough Blades Averages	Smooth Blades Averages	Delta
PTIN	PSIAT (KPa)	99.46 (685.8)	99.41 (685.4)	
TTIN	R (K)	547.6 (304.2)	548.9 (304.9)	
Speed	rpm	7,007	7,008	
PRT–T exit	–	1.471	1.467	
U/Co	–	0.372	0.372	
Eff–Delta temp.	–	0.8579	0.8792	+2.48%
Eff–torq. cor.	–	0.8491	0.8722	+2.72%
Eff–torq. meas.	–	0.8311	0.8550	+2.87%
$W/\overline{T1}/P1$ (lb x (R) 0.5)/(sec x psia) (kg x (K) 0.5)/sec x KPa)		3.296 161.6	3.449 169.1	+4.64% +4.64%
Outlet swirl (1)		–2.1	+1.7	+3.8 deg

(1) Outlet swirl in degrees from axial, average of cobras 3 and 4 at 52.5% span, positive in direction of rotor rotation

Where:

Eff–Delta temp. = efficiency from total temperature and pressure measurements

Eff–torq. cor. = efficiency from measured torque corrected for tare and measured flow rate

Eff–torq. meas. = efficiency from measured torque and flow rate (no tare correction)

eight taps equally spaced circumferentially. The first and second-stage nozzle vanes had static surface taps at 10, 50, and 90 percent span and on the passage hub and tip endwalls.

Disk cavity gas temperatures and pressures were measured along with special purpose instrumentation including tip clearance probes, metal casing temperatures, bearing outer race metal temperatures, speed pickups, and accelerometers.

6 Test Plan

The Phase 1A testing was conducted in three parts as shown in Table 4. Part A was dedicated to testing the model performance at the "cold air" equivalent conditions of the SSME at 104 percent RPL. Inlet temperature was constant at 550 R. The reference inlet pressure was 100 psia. Reynolds number was varied at the 104 percent RPL equivalent conditions by varying turbine inlet pressure above and below the reference inlet pressure. The Reynolds number variation was also tested at the 65 percent RPL conditions. Part B assessed the turbine performance over the SSME steady-state operating range. Part C tested turbine performance over a very wide range within the facility and tester limits to cover the engine start and shutdown transient conditions. Ten frames or readings of the test data were averaged for each test point.

7 Efficiency Results

The average delta-temperature efficiency for the smooth blades at 104 percent RPL equivalent conditions was 87.92 percent. This is an efficiency improvement of 2.5 percent (2.1 percentage points) over the production (rough) blades compared in Table 5. This efficiency improvement could reduce the required SSME fuel turbine inlet temperature by 57 R (32 K), from 1832 R (1018 K), increasing turbine life. The 2.5 percent increase was within 0.5 percent of the 3.0 percent predicted. The efficiency from the temperature measurements was considered the most representative because the efficiency from the torque and mass flow measurements showed inconsistencies due to the tare correction.

The efficiency improvement of the smooth blades is shown directly in Fig. 6 compared with the rough blades. The efficiency improvement was over the entire range and will result in lower turbine temperatures at every engine system operating point. The maximum efficiency improvement was over 5 percent for start transient speeds. Variations due to pressure ratio were low due to the low, subsonic Mach numbers in the blading.

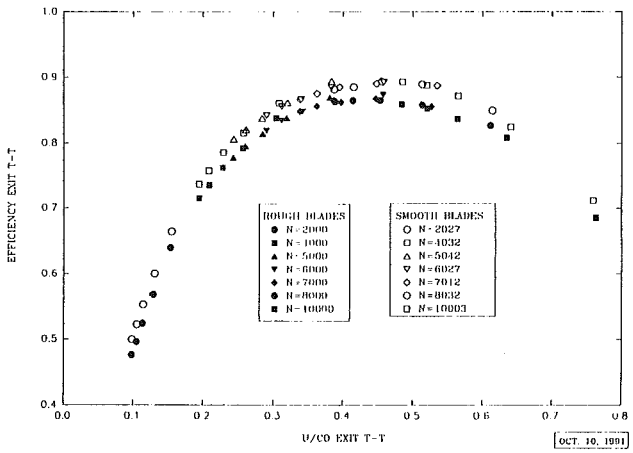

Fig. 6 NASA/MSFC TTE Rocketdyne HPFT: efficiency for Part C

The efficiency improvement for the polished coated (smooth) blades is significant to improve turbine durability. Heat transfer is also reduced with the smooth surface finish improving durability as discussed by Blair and Anderson (1989).

8 Flow Parameter Results

The turbine flow characteristic indicates the flow rate through the turbine for a given inlet pressure, inlet temperature, pressure ratio, shaft speed, and working fluid. The flow parameter evaluated for the air tests was mass flow multiplied by the square root of the absolute inlet temperature divided by the absolute inlet pressure. This parameter was used to determine the final standard air equivalent mass flow for the turbine flow

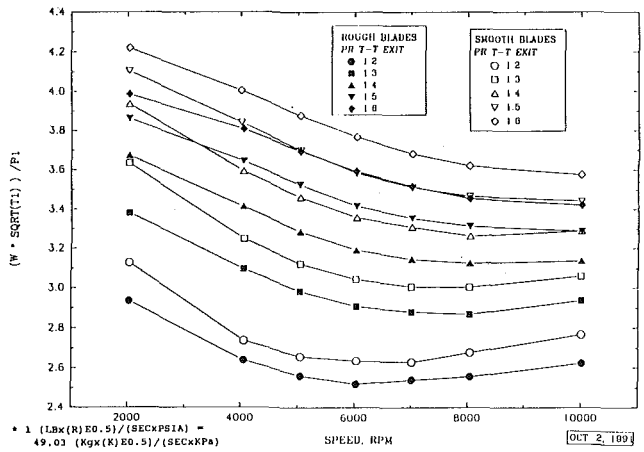

Fig. 7 NASA/MSFC TTE Rocketdyne HPFT: flow parameter for Part C

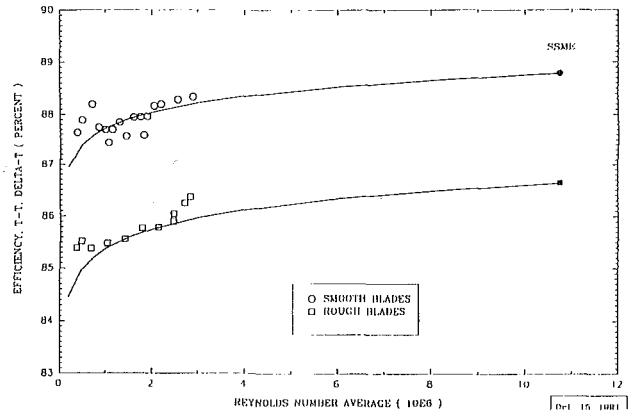

Fig. 9 NASA/MSFC air tests SSME HPFTP turbine 104 percent RPL equivalent conditions Reynolds number effects

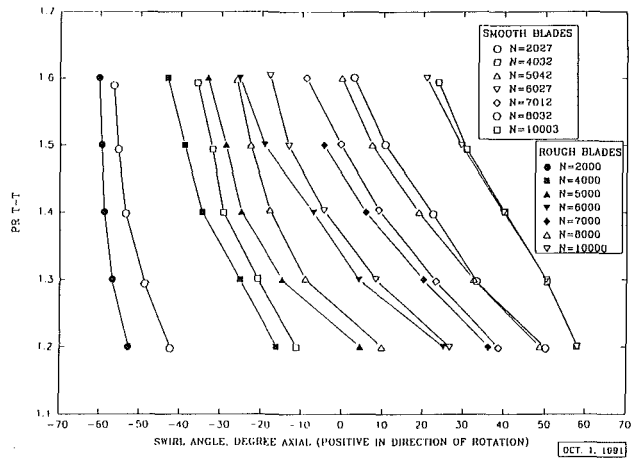

Fig. 8 NASA/MSFC TTE Rocketdyne HPFT Comparison of Swirl Angle for Part C

map. The flow parameter for the 10 frame averages of six tests at 104 percent RPL equivalent conditions was 3.449 (169.1 in SI units). The smooth blades average was compared in Table 5 with the rough blade test average of 3.296 (161.9 in SI units) indicating a 4.6 percent higher value for the smooth blades. This increase was higher than expected since the polishing had increased rotor throat area by only 3.6 percent. The remaining increase was probably due to significantly reduced boundary layer thicknesses for the polished blades.

The wide range mapping test data for the smooth blades was compared with the rough blades in Fig. 7. The lower flow parameter for the rough blades is shown for every point. At 7000 rpm and 1.2 pressure ratio, the minimum difference was 3.5 percent. The maximum difference was 5.2 percent at a pressure ratio of 1.4 with an average difference at 7000 rpm to 4.5 percent.

The smooth blade flow parameter was higher due to higher efficiency, larger rotor blade throat openings, and thinner trailing edges for the air-tested polished rotor blades. Coating the blades thicker and polishing closer to the drawing nominal coating thickness would reduce the flow parameter to closer to the current rough blade flow parameter.

9 Outlet Swirl Results

Outlet swirl is the angle of the turbine outlet absolute velocity measured from the axial in the direction of throughflow. The swirl angle is positive in the direction of rotation per Glassman (1973). Outlet swirl was measured using two cobra probes mounted 180 deg apart in the outlet plane survey ring.

The midspan outlet swirl angle at 104 percent RPL equivalent conditions was more positive (in the direction of rotation) and more axial for the smooth blades compared to the rough blades. The average of three smooth blades tests was + 1.7 deg from the axial as shown in Table 5 compared to the rough blades average of -2.1 deg for a difference of 3.8 deg.

The wide range mapping smooth blade swirl data were compared with the rough blade swirl data in Fig. 8. More positive swirl is shown for the smooth blades for almost every point over the wide range of shaft speeds and pressure ratios. The swirl angle changes between the smooth and rough blades were indicative of the higher efficiency and reduced resistance of the smooth rotor blades.

10 Reynolds Number Results

The average blade chord outlet Reynolds number for the first-stage nozzle and the second-stage rotor of the HPFTP turbine in the SSME engine is high at 1.1×10^7 for 104 percent RPL conditions. The maximum Reynolds number for the NASA/MSFC TTE is also high at 3×10^6. The Reynolds number for 100 psia inlet pressure and 104 percent RPL equivalent conditions is 1.5×10^6. The Reynolds number correction from the air test values to the SSME engine is not well established in the literature because the majority of testing has been done at Reynolds numbers significantly lower than allowable with the NASA/MSFC TTE. The pretest prediction of the Reynolds number trend was that the efficiency ratio was proportional to the Reynolds number ratio to the 0.038 power (Hudson et al., 1991).

The delta-temperature efficiency data were plotted versus average Reynolds number for the smooth and rough blades air tests in Fig. 9. The smooth blade data were represented by circles and the rough blade data by squares. These data are indicative of the accuracy potential of establishing Reynolds number trends. Shifts in the efficiency data of 0.3 to 0.5 percentage points are within the accuracy of the data (Hudson et al., 1991). The predicted trend lines were plotted through the 110 psia (758 kPa) inlet pressure point for the smooth blades and the 100 psia (689 kPa) point for the rough blades. The trend lines are approximately representative of the data for the higher Reynolds numbers: 1.0 to 3.0 $\times$ 10^6, but both sets deviate at the lower Reynolds numbers. The reason for the deviation has not been determined, but is believed to be associated with boundary layer transition effects. All the 104 percent RPL reference performance tests and all the Parts B and C mapping tests were run at 100 psia (689 kPa) inlet

pressure, which is in the data range that shows the expected Reynolds number trends.

The predicted trend lines were extended in Fig. 9 to the SSME engine Reynolds number values. The increase in efficiency due to Reynolds number effects by the predicted trend from the 100 psia (689 KPa) Reynolds number (about 1.5×10^6) was about one percentage point. The efficiency increase from the maximum tested Reynolds number (about 2.8×10^6) to the SSME engine Reynolds number was about 0.3 to 0.4 points.

The midspan (52.5 percent span) smooth blade outlet swirl angles were plotted versus Reynolds number average in Fig. 10. A swirl decrease (increasing positive value in the direction of rotation) is shown for increasing Reynolds number with a least-mean-square line through the data. Combining the swirl characteristic with the efficiency characteristic versus Reynolds number indicates that increasing Reynolds number increases efficiency and reduces exit swirl.

11 Interstage Static Pressure Results

Interstage static pressures are easily measured boundary conditions between each blade row that indicate the pressure distribution, stage reaction, and power split between stages in the turbine. Static pressures were measured upstream and downstream and at the hub and tip of the first-stage nozzle, second-stage nozzle, and downstream of the second-stage rotor. Each hub and tip location had eight static pressure taps, which were averaged in the data reduction program after assuring all measurements were representative.

Static pressures for rough and smooth blades at 104 percent RPL equivalent conditions, scaled using the engine and air test turbine inlet total pressure ratios to SSME 104 percent RPL turbine conditions, are compared in Figs. 11 and 12. Static pressures from the measurements are underlined and the delta pressures are in parentheses. The delta pressures were calculated for tip minus hub at each measurement plane and across each blade row at tip and hub as well as for each stage and overall.

The overall and stage delta pressures were essentially the same for rough and smooth blades. Smooth blade rotor tip and hub delta pressures were lower than the rough blades for both stages. This indicates reduced resistance of the smooth rotor blades resulting from the increased rotor efficiency and effective areas. These effects increase stage performance and reduce stage reaction and rotor blading axial thrust. The first and second-stage nozzle tip and hub and outlet radial delta pressures were correspondingly higher for the smooth rotor blades, indicating greater nozzle expansion and positive rotor blade incidence.

The static pressure changes for the smooth blades are interrelated with the efficiency improvement and the flow area changes compared with the rough blades. These results will be used in the analysis models to understand better the effects of surface finish on otherwise identical turbine geometries.

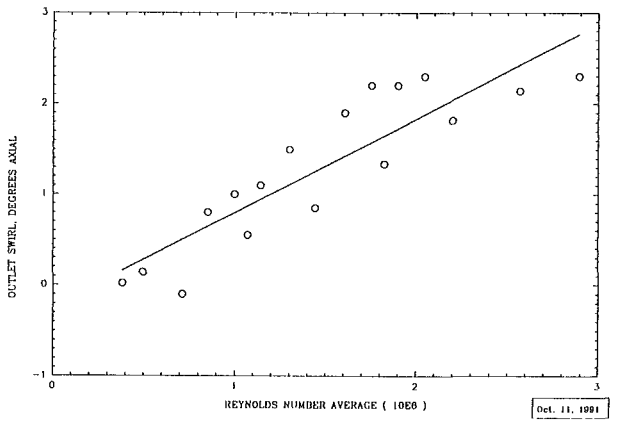

Fig. 10 NASA/MSFC TTE air test SSME blades: 104 percent RPL equivalent conditions Reynolds number effects (swirl positive in direction of rotation)

12 Uncertainty Analysis for Smooth Blade Tests

An uncertainty analysis was conducted to estimate the uncertainty of the calculated thermodynamic efficiency. The analysis followed the guidelines set forth by the ANSI/ASME Performance Test Code (PTC) 19.1 (1985, 1986) and Coleman and Steele (1989). An estimate of the efficiency bias and precision limits were computed for the design point and the extreme off-design points of Part C by propagating estimates of the bias and precision limits in the measured pressures and

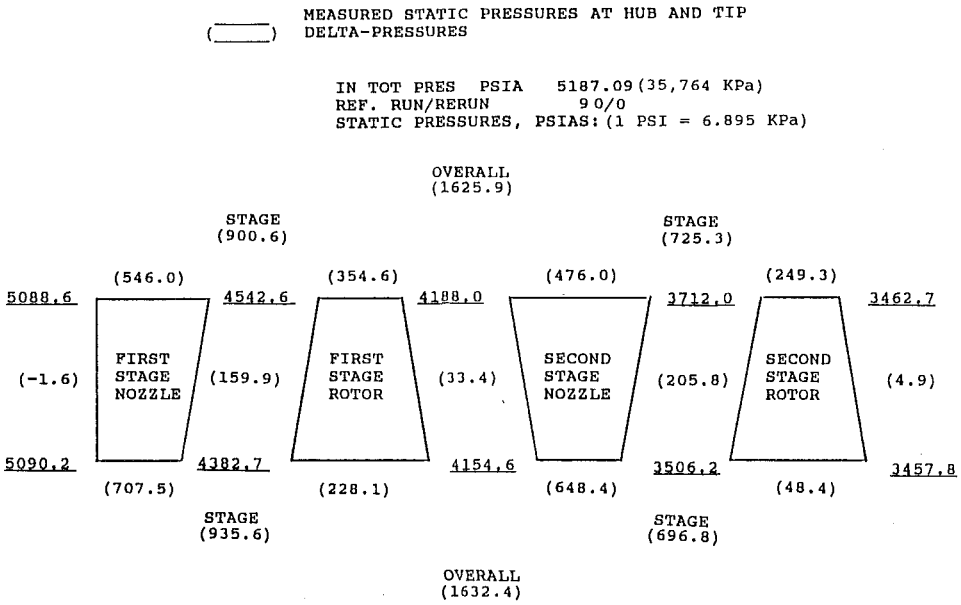

Fig. 11 NASA/MSCF TTE air test SSME HPFTP turbine: Smooth Blades; 104 percent RPL equivalent conditions scaled to SSME inlet pressure: Interstage Static Pressure Distribution

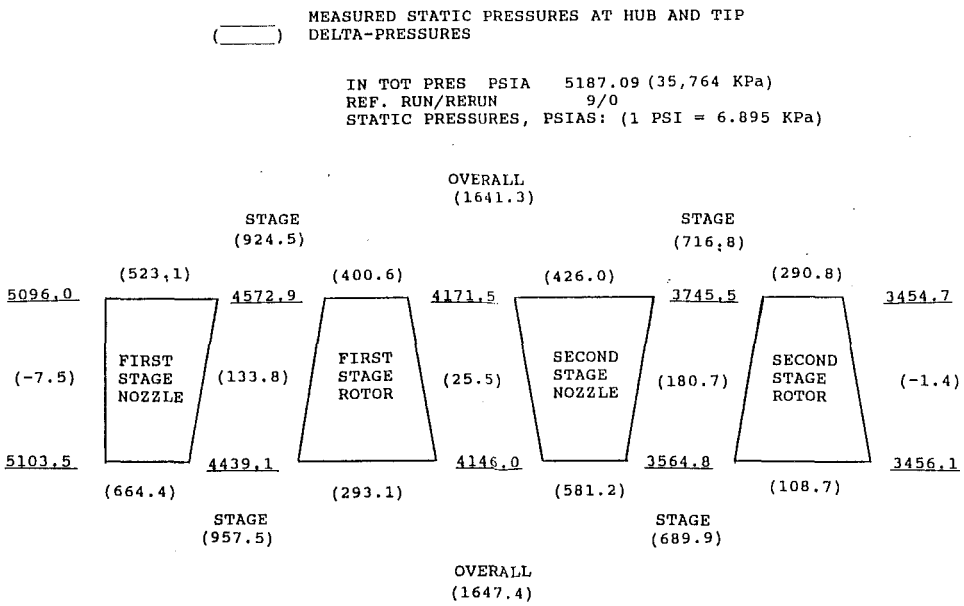

Fig. 12 NASA/MSFC TTE air test SSME HPFTP turbine: Rough Blades; 104 percent RPL equivalent conditions scaled to SSME inlet pressure; Interstage Static Pressure Distribution

temperatures. The efficiency bias and precision limits for each run were then combined using the root sum square (RSS) method to give a 95 percent confidence interval. At the design point the efficiency uncertainty was estimated to be +0.7 percentage points of efficiency. At the extreme off-design points the uncertainty was within +1.5 points of efficiency.

The uncertainty analysis for the rough blades tests was reported by Hudson et al. (1991).

13 Conclusions

The smooth blade turbine efficiency increased compared to the rough blades at every test point. The efficiency increase at the 104 percent RPL equivalent condition was 2.5 percent for the smooth blades. The efficiency improvement will reduce steady-state turbine operating temperatures in the SSME.

The polishing process improved the rotor blade surface finish from 400 μin. (10.16 μm) rms to 30 μin. (0.76 μm) rms. The process removed 0.002 to 0.004 in. (0.051 to 0.102 mm) of coating from each airfoil surface. The polished airfoils were representative of the coated blades but near the minimum tolerance.

The flow parameter increased 4.6 percent as a result of the higher efficiency, thinner boundary layers, and the material removal with polishing.

The outlet swirl angle decreased for the smooth blades at 104 percent RPL, indicating lower leaving energy with the higher efficiency.

The test results agreed with the expected Reynolds number trend with efficiency. The mapping tests were run in the range of the expected Reynolds number trend. The midspan outlet swirl decreased with increasing Reynolds number and increasing efficiency.

The interstage static pressure distribution indicated reduced stage reaction for the smooth blades as expected for reduced resistance for lower rotor blade axial thrust with higher efficiency.

Acknowledgments

The authors acknowledge Melody Lin of Rocketdyne for extensive assistance in the data reduction and plotting of test results, Wayne Bordelon of NASA/MSFC for the uncertainty analysis, and Rotadata Inc. for installation of the polished rotor blades in their turbine tester.

References

ANSI/ASME Power Test Code 19.1, 1985, 1986, Part 1, Measurement Uncertainty.

Blair, M. F., and Anderson, O. L., 1989, "The Effects of Reynolds Number, Rotor Incidence Angle and Surface Roughness on the Heat Transfer Distribution in a Large-Scale Turbine Rotor Passage," United Technologies Research Center, NASA Contract No. NAS8-37351.

Carter, J. A., 1991, "Blowdown Turbine Test Equipment Design Characteristics," NASA/MSFC Memo ED35-45-91.

Coleman, H. W., and Steele, W. G., Jr., 1989, *Experimentation and Uncertainty Analysis for Engineers*, Wiley, New York.

Craig, H. R. M., and Cox, H. J. A., 1970–71, "Performance Estimation of Axial Flow Turbine," *Proc. Instn. Mech. Engrs.*

Glassman, A., 1973, "Turbine Design and Application," NASA SP 290, Vols. 1, 2, and 3.

Hudson, S. T., Gaddis, S. W., Johnson, P. D., and Boynton, J. L., 1991, "Cold Flow Testing of the Space Shuttle Main Engine High Pressure Fuel Turbine Model," AIAA Paper No. 91-2503.